université
PARIS-SACLAY

Theoretical Study of Quantum Correlations and Nonlinear Fluctuations in Quantum Gases

Thèse de doctorat de l'Université Paris-Saclay

École doctorale n° 564, Physique en Île-de-France (PIF)
Spécialité de doctorat: Physique
Unité de recherche: Université Paris-Saclay, CNRS, LPTMS, 91405, Orsay, France
Référent: : Faculté des sciences d'Orsay

Thèse présentée et soutenue à Orsay, le 10 septembre 2020, par

Mathieu ISOARD

Composition du jury:

Christoph WESTBROOK Directeur de recherche, Institut d'Optique Graduate School Laboratoire Charles Fabry	Président
Matteo CONFORTI Chargé de recherche (HDR), Université de Lille Laboratoire PhLAM	Rapporteur
Patrik ÖHBERG Professeur, Heriot-Watt University Institute of Photonics and Quantum Sciences	Rapporteur
Élisabeth GIACOBINO Directrice de recherche émérite, Université Pierre et Marie Curie Laboratoire Kastler Brossel	Examinatrice
Sandro STRINGARI Professeur, Università di Trento INO-CNR BEC Center	Examinateur
Nicolas PAVLOFF Professeur, Université Paris-Saclay LPTMS	Directeur

Thèse de doctorat

NNT: 2020UPASP004

As you see, the war treated me kindly enough,
in spite of the heavy gunfire,
to allow me to get away from it all
and take this walk in the land of your ideas.

— Schwarzschild to Einstein, 22 December 1915

REMERCIEMENTS

Je voudrais tout d'abord remercier mon directeur de thèse, Nicolas Pavloff, sans qui ce travail n'aurait pas vu le jour. Travailler à ses côtés pendant ces trois dernières années a été un réel plaisir ; sa curiosité scientifique m'a permis de découvrir de nouveaux champs de la physique et d'acquérir de nouvelles connaissances, sa rigueur et sa ténacité m'ont appris à explorer toutes les pistes possibles d'un sujet pour en saisir tous les contours. Enfin, je retiendrai sa bonne humeur, sa gentillesse et son humour qui en font pour moi le meilleur directeur que j'aurais pu espérer.

Je remercie tous les membres de mon jury pour avoir pris le temps de lire ma thèse ; un grand merci à Matteo Conforti et Patrik Öhberg pour avoir été les rapporteurs de ma thèse.

Je remercie aussi Nicolas Cherroret d'avoir accepté d'être mon tuteur pendant mes trois années de doctorat.

Je souhaiterais ensuite remercier l'ensemble du LPTMS qui a contribué à rendre ces trois années de doctorat très agréables. Je remercie en particulier Claudine et Karolina pour leur aide et leur réactivité. Je remercie les permanents et post-docs pour les discussions matinales autour du café ; parmi eux, je remercie Christophe, pour l'aide qu'il m'a apportée pendant la préparation de la soutenance, et Guillaume, pour avoir été mon mentor.

Il m'est impossible de ne pas mentionner également notre bureau légendaire que j'ai eu la chance de partager avec mes amis Ivan, Samuel et Thibault ; le très fameux tableau d'Ivan rempli d'expressions françaises, Samuel et ses idées lumineuses sur les nombres hyperduaux, Thibault et ses feuilles volantes, les repas improvisés, les parties de fléchettes et les visites nombreuses de notre cher Aurélien resteront gravés dans ma mémoire. Je remercie aussi tous les doctorants que j'ai connus au cours de mes trois années de doctorat et avec lesquels je garderai une affection particulière et d'excellents souvenirs ; un merci tout particulier à Nina et Nadia que j'ai eu la chance de connaître.

Je remercie Scott Robertson pour les discussions stimulantes que nous avons eues sur le rayonnement de Hawking analogue. Je remercie également mon ami Maxime pour nos nombreuses discussions autour de la gravité analogue, pour m'avoir proposé de préparer un workshop avec lui et donc pour la confiance qu'il m'accorde, enfin pour son soutien.

Je voudrais remercier tous mes amis pour leur présence et les nombreuses soirées parisiennes que nous avons partagées ensemble; merci Thiébaut pour ton aide précieuse à la veille de la soutenance.

Je ne peux terminer ces remerciements sans évoquer ma famille. Un grand merci à mes proches, à mes parents, à mes grands-parents et à ma petite soeur pour m'avoir soutenu dans mes projets depuis tant d'années et qui m'ont permis d'arriver là où j'en suis.

CONTENTS

0 INTRODUCTION GÉNÉRALE

Cette thèse est dédiée à l'étude des phénomènes nonlinéaires dans deux fluides quantiques qui partagent de nombreuses similitudes : les condensats de Bose-Einstein [153] et les faisceaux optiques Gaussiens nonlinéaires (qui sont aussi considérés comme des "fluides de lumière" [35]).

Dans les condensats de Bose-Einstein, les effets nonlinéaires se manifestent par les interactions de contact entre bosons et affectent de façon importante les propriétés du gaz. En 1947, Bogoliubov a été le premier à proposer une nouvelle théorie des perturbations pour prendre en compte les interactions dans un condensat de Bose-Einstein faiblement interagissant [28] ; cette théorie a été d'une grande importance dans les développements qui ont suivi pour comprendre notamment les liens qui existent entre superfluidité et condensation [78, 144, 145, 152]. La théorie de champ moyen developpée par Bogoliubov prédit également que des excitations élémentaires sont induites par les fluctuations quantiques dans le condensat. Cette propriéte est très importante dans le domaine de la gravité analogue parce qu'elle permet de créer un fluide transsonique à l'aide d'un condensat de Bose-Einstein. Dans ce cas, un tel fluide pourra être considéré comme l'analogue acoustique d'une trou noir [71].

Le domaine de la gravité analogue est né environ sept ans après que Hawking a prédit que les trous noirs émettent un faible rayonnement [87]. Unruh suggère alors d'utiliser des analogues hydrodynamiques des trous noirs gravitationnels pour étudier leurs propriétés dans le laboratoire[182]. Un fluide transsonique, c'est-à-dire un fluide qui passe d'une région subsonique, où les ondes sonores peuvent se propager dans toutes les directions, à une région supersonique, où les ondes sont piégées et entraînées par le fluide en mouvement, joue le même rôle qu'un trou noir. En effet, de même que la lumière reste piégée à l'intérieur d'un trou noir gravitationnel, les ondes sonores, elles, ne peuvent s'échapper de la région supersonique.

Pour expliquer simplement ce phénomène, considérons une rivière au bout de laquelle se trouve une cascade, voir Figure 1. La vitesse du cours d'eau augmente à l'approche de la cascade. Imaginons maintenant que des poissons remontent le courant, tous à la même vitesse. Il est assez intuitif de penser qu'il existe un point de non-retour ("Point of no return" sur la Figure 1) au-delà duquel les poissons ne sont plus capables de remonter le courant tant la vitesse de la rivière devient grande. Dans ce cas, les poissons sont piégés et irrémédiablement entrainés jusqu'en bas de la cascade qui joue alors le rôle de la singularité d'un trou noir, comme indiqué sur la Figure 1 ; le point de non-retour est alors l'équivalent d'un horizon des événements pour les poissons.

Dans son article de 1981, Unruh n'a pas considéré des poissons dans une rivière, mais des ondes sonores se propageant dans un fluide en mou-

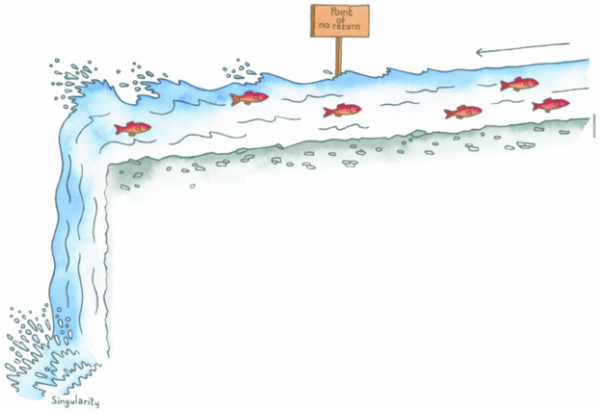

FIGURE 1: Des poissons remontent le cours d'eau d'une rivière. Dessin réalisé par Nascimbene pour montrer l'analogie entre les trous noirs hydrodynamiques et leur équivalent gravitationnel. La rivière se déplace de la droite vers la gauche et accélère à l'approche d'une cascade. Tous les poissons ont la même vitesse et tente de remonter le cours d'eau. Au-delà du panneau marron, dans la partie gauche de la rivière, la vitesse du cours d'eau est si importante que les poissons sont tous entraînés par la rivière vers la cascade. De façon équivalente à la lumière qui est piégée à l'intérieur d'un trou noir et se propage jusqu'à sa singularité, les poissons au-delà du point de non-retour (indiqué par le panneau marron) sont piégés et tombent jusqu'en bas de la cascade. Cette région joue donc le rôle de l'intérieur du trou noir analogue.

vement. L'idée reste toutefois identique : Si le courant, bien que stationnaire, devient supersonique dans une région de l'espace, une onde sonore qui se déplace dans cette région serait alors entrainée par le courant et ne pourrait plus atteindre la région subsonique située en amont. L'onde sonore serait dans ce cas piégée dans la partie supersonique, comme le poisson l'était au-delà du point de non-retour et comme la lumière l'est à l'intérieur d'un trou noir gravitationnel. La frontière entre les régions subsonique et supersonique est alors appelée un horizon acoustique. De tels systèmes transsoniques ont été appelés "trous muets" par Unruh.

Toutefois, le lien qui existe entre les trous noirs gravitationnels et les "trous muets" s'étend au-delà de cette simple analogie cinématique. En effet, en linéarisant les équations hydrodynamiques, Unruh a montré que la dynamique des ondes sonores dans le fluide en mouvement est la même que celle d'un champ scalaire dans un espace-temps courbe. Nous reproduirons les calculs qui l'ont mené à cette conclusion dans le premier chapitre de thèse.

De plus, dans le cas où le champ sonore serait quantifié, il devrait hériter des propriétés des champs quantiques qui se propagent dans un espace-temps courbe. En particulier, comme Unruh l'a montré dans son article et comme nous l'expliquerons dans le chapitre 2, l'horizon acoustique "déconnecte" complétement la partie subsonique de la partie supersonique, et cela doit nécessairement s'accompagner de l'émission spontanée de particules depuis cet horizon ; ce rayonnement doit no-

tamment jouir des mêmes propriétés thermiques que le rayonnement de Hawking émis par les trous noirs gravitationnels.

L'idée proposée par Unruh a suscité l'intérêt d'une large communauté ; la gravité analogue connaît en particulier un intérêt important depuis les deux dernières décennies, avec de nombreuses expériences d'analogues acoustiques réalisées dans des écoulements à la surface d'un bassin [59, 159, 192], dans les fibres optiques nonlinéaires [23, 50, 149, 184], dans les condensats d'excitons-polaritons [132] et dans les condensats de Bose-Einstein [102, 105, 131, 163, 170, 175, 177]. Parmi ces différentes plateformes, nous nous sommes concentrés au cours de la thèse sur les trous noirs acoustiques réalisés dans les condensats de Bose-Einstein transsonique et (quasi) unidimensionnel. Un tel condensat en mouvement a été réalisé expérimentalement par J. Steinhauer il y a dix ans [105] ; récemment, l'analogue du rayonnement de Hawking y a été observé [131, 177].

Dans le chapitre 2, nous revenons tout d'abord sur la découverte de Hawking. Nous soulignons l'universalité du rayonnement de Hawking en considérant tout d'abord le cas d'un miroir en accélération non uniforme [48, 69]. Ensuite, nous traitons le cas de l'effondrement gravitationnel d'une étoile menant à la formation d'un trou noir. La courbure de l'espace-temps est si affectée pendant cet effondrement que deux régions déconnectées apparaissent : l'intérieur et l'extérieur du trou noir. Nous montrons que ce processus est très similaire au problème du miroir en mouvement et donne également lieu à l'émission d'un rayonnement thermique [25, 87, 88].

Le chapitre 3 est dédié à l'étude du rayonnement de Hawking analogue dans les condensats de Bose-Einstein. Dans ces systèmes quantiques, les excitations sonores *entrantes* émergent des fluctuations quantiques du vide et donnent naissance aux excitations *sortantes* après un processus de diffusion à l'horizon acoustique. Ces ondes sonores sortantes se propagent le long du fluide dans les régions subsonique et supersonique, situées de part et d'autre de l'horizon acoustique, et induisent des corrélations de densité. Ainsi, comme suggéré pour la première fois en 2008 par des collaborateurs travaillant à Trente et Bologne [15], la détection expérimentale de ces corrélations constituerait une signature indirecte de la présence du rayonnement de Hawking analogue dans les condensats de Bose-Einstein.

Le chapitre 3 présente le travail réalisé pendant la thèse, à savoir l'étude détaillée des fluctuations quantiques près de l'horizon acoustique d'une condensat de Bose-Einstein transsonique.

Nous démontrons que la prise en compte des modes zéros, relatifs à la phase du condensat et aux fluctuations du nombre de particules dans ce dernier, est nécessaire dans un premier temps pour obtenir une description correcte des corrélations au voisinage de l'horizon acoustique. Cela mène dans un second temps à un excellent accord entre nos résultats théoriques et les données expérimentales obtenues par le groupe de J. Steinhauer en 2019 [131]. Cependant, en raison des effets dispersifs dans notre système, nous prouvons également que le rayonnement de

Hawking analogue émis depuis l'horizon acoustique dévie d'un spectre totalement Planckien, comme attendu gravitationnel [87, 88]. Ce caractère "non-thermique" est inhérent à tout système dispersif. Toutefois, nous montrons dans cette thèse qu'une procédure d'analyse des corrélations de densité peut "supprimer" les effets dispersifs et conduire à la conclusion erronée que le spectre de Hawking analogue est complétement thermique. Nous discutons en particulier l'analyse de données publiée par le groupe de J. Steinhauer [131] dans la dernière section du chapitre 3. Ce travail a donné lieu à une publication dans *Physical Review Letters*, cf. fin du chapitre 3. Certains des résultats discutés dans ce chapitre mèneront également à la publication d'un plus long article dans le futur.

Dans le chapitre 4, nous étudions l'intrication entre les excitations qui émergent des fluctuations quantiques de part et d'autre de l'horizon acoustique. En particulier, nous soulignons le lien fondamental qui existe avec le chapitre 2, c'est-à-dire l'existence de deux vides différents, menant alors à l'émission spontanée de particules. Nous montrons que ces deux vides sont liés par une transformation de Bogoliubov. De cette manière, ce que nous définissons comme le vide *entrant* peut être vu dans notre système analogue comme un état Gaussien à trois modes, de sorte que l'intrication est répartie entre ces trois modes.

Pour étudier cette intrication *tripartite*, nous introduisons tout d'abord la notion de matrice covariante et nous détaillons les différents outils qui permettent d'étudier la séparabilité d'un état quantique, tels que la violation de l'inégalité de Cauchy-Schwarz ou le critère PPT (*Positive Partial Transpose*). Ensuite, nous les appliquons au cas particulier de notre système, en suivant la procédure présentée dans la référence [4] pour les états Gaussiens et basée sur l'étude de l'inégalité CKW (*Coffman, Kundu, Wootters*) [40]. Cela nous permet de calculer le degré d'intrication *tripartite* qui ne dépend que de quantités accessibles expérimentalement [131, 176, 177] ; nous pensons donc qu'il serait possible dans le futur d'observer et de mesurer cette intrication *tripartite* dans les condensats de Bose-Einstein.

En sus de l'étude du rayonnement de Hawking analogue, nous nous sommes également intéressés aux liens qui existent entre la condensation de Bose-Einstein et l'optique nonlinéaire. En effet, la lumière qui se propage dans un milieu nonlinéaire se comporte comme un fluide dont la dynamique est gouvernée par une équation de Gross-Pitaevskii effective [108]. En particulier, les effets nonlinéaires, induits par la lumière dans le milieu dans lequel elle se propage, conduisent à une interaction effective entre photons. Cette analogie avec les condensats de Bose-Einstein a suscité beaucoup d'intérêt dans la communauté scientifique pour observer et sonder des phénomènes hydrodynamiques dans le contexte de l'optique nonlinéaire, telles que la superfluidité ou les excitations sonores de la lumière [34, 39, 66, 111, 128, 162, 187, 188].

Dans la seconde partie de la thèse, nous nous intéressons à un phénomène qui peut s'observer dans les systèmes non-dissipatifs, nonlinéaires et dispersifs : la formation d'ondes de choc dispersives [100]. La figure 2

souligne de nouveau le lien fort qui existe entre les systèmes optiques et les condensats de Bose-Einstein ; l'image de gauche, extraite de la référence [22], montre la propagation d'une onde de choc dispersive radiale dans un milieu optique nonlinéaire, tandis que l'image de droite, extraite de la référence [91], correspond à la propagation d'une telle onde dans un condensat de Bose-Einstein.

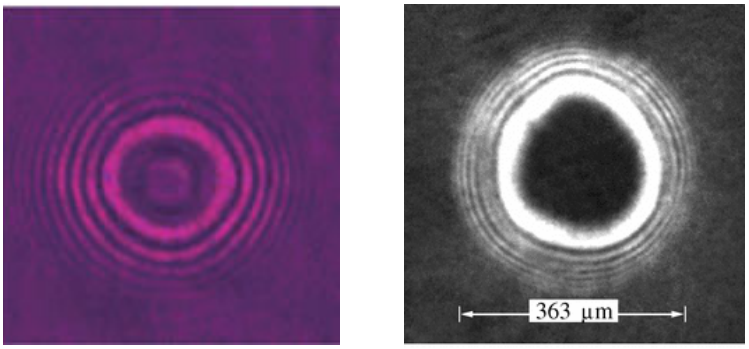

FIGURE 2: Propagation d'une onde de choc radiale
(Gauche) à travers un crystal photoréfractif [22], **©2007, Nature**.
(Droite) à travers un condensat de Bose-Einstein [91], **©2006, APS**.

Les ondes de choc dispersives proviennent des effets nonlinéaires qui rendent de plus en plus abrupt le profil d'une perturbation qui se propage plus vite que son propre front ; elle le rattrape donc inévitablement au bout d'un certain temps, appelé *temps de déferlement* ; Il en résulte alors un choc qui se traduit par la formation d'un train d'ondes, appelé onde de choc dispersive. L'émergence de telles ondes n'est pas restreinte aux condensats de Bose-Einstein ou à l'optique nonlinéaire, mais se produit aussi dans de nombreux autres systèmes : la figure 3a montre un *mascaret ondulant* observé en eaux peu profondes et la figure 3b montre une série de nuages enroulés sur eux-mêmes. Dans ce dernier exemple, une telle onde de choc se forme dans l'atmosphère quand deux masses d'air de températures différentes se rencontrent ; ce phénomène est connu sous le nom de *Morning Glory*. Ces différents exemples révèlent l'universalité de ce phénomène piloté par la compétition entre effets nonlinéaires et dispersifs.

Dans le chapitre 5, nous montrons tout d'abord que la propagation d'un faisceau optique (dans l'approximation paraxiale) dans un milieu nonlinéaire est gouvernée par une équation de Schrödinger nonlinéaire. Une approche hydrodynamique du problème, proposée en premier par le groupe de Khlokhlov en 1967 [8–11], revient à considérer que le faisceau optique se comporte comme un fluide de lumière, caractérisé par une densité et une vitesse. De plus, grâce à cette approche hydrodynamique, la propagation d'un tel fluide peut être étudiée à travers les *invariants de Riemann* et la méthode des caractéristiques. Ces notions sont introduites dans ce chapitre.

Dans le chapitre 6, nous étudions avec l'aide de la méthode de Riemann la première étape de l'évolution d'un fluide de lumière en présence

(a) Mascaret ondulant observé à Turnagain Arm, Alaska (copyright Scott Dickerson, 2013)

(b) Onde de choc dispersive observée dans l'atmosphère – appelée *Morning Glory* (copyright Mick Petroff, Creative Commons 3.0, 2009)

FIGURE 3: Exemples d'ondes de choc dispersives observées dans la nature.

d'un fond uniforme, c'est-à-dire avant l'apparition de l'onde de choc dispersive. Cette étape peut être décrite à travers une approche non dispersive qui conduit alors à un excellent accord avec les simulations numériques du problème. Nous appliquons en particulier la méthode de Riemann pour des distributions initiales non monotones. Dans ce cas, comme suggéré par Ludford [120], nous avons besoin de déplier le plan hodographique. Nous expliquons en détail cette procédure et comparons nos résultats théoriques avec des simulations numériques. Ce travail a conduit à deux publications : un article de conférence dans lequel nous considérons un faisceau optique Gaussien, cf. fin du chapitre 6 ; et la première partie d'un article publié dans *Physical Review A*, cf. fin du chapitre 7.

En outre, nous avons remarqué qu'il était possible d'obtenir une solution approximative et simple du problème de Riemann qui est en très bon accord avec les simulations. Nous avons généralisé cette approximation au cas des fluides non visqueux, et, en particulier, aux systèmes non-intégrables. Ce travail a été publié dans EPL (*Europhysics Letters*), cf. fin du chapitre 6

Dans le chapitre 7, nous étudions la seconde étape de l'évolution des fluides nonlinéaires lorsque les effets dispersifs entrent en jeu. Comme mentioné plus haut, les effets nonlinéaires couplés aux effets dispersifs conduisent à la formation et la propagation d'une onde de choc dispersive. Dans ce chapitre, nous décrivons la structure et la dynamique d'une telle onde dans le cas où le profil de densité initial a la forme d'une parabole inversée ; une description théorique peut en effet être obtenue pour un tel choix de distribution initiale. Nous montrons que deux *invariants de Riemann* varient de façon concomitante dans la région du choc et que le problème se réduit à la résolution d'une équation d'Euler-Poisson. Nous utilisons les résultats obtenus par Eisenhart [53] et la méthode proposée dans les références [56, 82] pour résoudre analytiquement cette équation ; nous montrons alors que les résultats théoriques sont en très bon accord avec les simulations numériques.

Cette approche est intéressante parce qu'elle permet aussi d'obtenir une description asymptotique de l'onde de choc dispersive. Nous sommes en particulier capables d'extraire des paramètres d'intérêt expérimental, comme le contraste des franges de l'onde de choc.

Au cours de la thèse, nous avons tout d'abord commencé par l'étude de la propagation d'une onde de choc dans le cas de l'équation de Korteweg-De Vries. Ce fut une première étape dans la compréhension de la méthode décrite dans les références [56, 82]. De plus, l'étape non dispersive de l'étalement peut être facilement étudiée grâce à la méthode des caractéristiques. Ce travail a été publié dans *Physical Review E*, cf. fin du chapitre 7.

Ensuite, nous nous sommes intéressés à l'équation de Schrödinger nonlinéaire. Dans ce cas, l'étude de l'étalement sans dispersion du fluide nonlinéaire est plus complexe et requiert l'utilisation de la méthode de Riemann (voir chapitre 6). Néanmoins, l'analyse de l'onde de choc dispersive est assez similaire à celle utilisée dans le cas de l'équation de Korteweg-De Vries (mais nécessite tout de même un traitement théorique un peu plus technique) ; ceci montre l'efficacité de la méthode suggérée dans les références [56, 82]. Ce travail a été publié dans *Physical Review A* et se trouve à la fin du chapitre 7.

Nous reviendrons enfin dans la conclusion sur les similarités entre les condensats de Bose-Einstein et les fluides de lumière ; nous discuterons en particulier les perspectives que nous envisageons pour étendre les travaux présentés dans cette thèse.

1

GENERAL INTRODUCTION

This thesis is dedicated to the study of nonlinear-driven phenomena in two quantum gases which bear important similarities: Bose-Einstein condensates of ultracold atomic vapors [153] and paraxial nonlinear laser beams (which are sometimes considered as pertaining to the wider class of "quantum fluid of light" [35])

In Bose-Einstein condensates nonlinearity arises from contact interactions between bosons and dramatically affect the properties of the gas. In 1947, Bogoliubov was the first to suggest a new perturbation theory to take account of interactions in a weakly-interacting Bose gas [28]. Bogoliubov theory is a first-principle mean-field theory of superfluidity which has been of tremendous importance in the development of the field of Bose-Einstein condensates of atomic vapors [78, 144, 145, 152]. It predicts the emergence of sound-like excitations from quantum fluctuations in the condensate. This aspect is of particular relevance in the domain of analogue gravity where a transonic flow is analyzed as an acoustic analogue of a black hole [71].

The domain of analogue gravity started around seven years after Hawking's prediction in 1974 that black holes emit a faint radiation [87], when Unruh suggested the use of hydrodynamic analogues of gravitational black holes to study their properties in the laboratory [182]. A transonic flow, from a subsonic region, where sound waves can propagate in all directions, to a supersonic region, where waves are trapped and dragged by the flow, could play the same role as a black hole, not by trapping light but sound excitations.

As a simple illustration of the phenomenon, let us consider a river flowing towards a waterfall. The flow velocity increases when the river approaches the waterfall. One also consider fish swinging against the current, with all the same velocity (see Figure 4). One understands that there must exist a point of no return beyond which the flow velocity becomes too important, so that fish are dragged by the flow and bound to fall down to the bottom of the waterfall, playing the role of a black hole singularity. Then, the point of no return, indicated by the brown panel in Figure 4, would be the equivalent of the event fish-horizon.

In his seminal paper, Unruh did not consider fish in a river, but sound waves propagating in a fluid flow. The idea is still the same though; if the flow, albeit stationary, happens to be supersonic in some region of space, a sound wave propagating in this region would be dragged by the flow and would not be able to reach the subsonic region upstream the supersonic one; the boundary between the subsonic and supersonic regions is then the acoustic horizon. One has constructed what Unruh called a "dumb hole".

However, this parallel to gravitational black holes extends further than this simple kinematic analogy; by deriving and linearizing the hy-

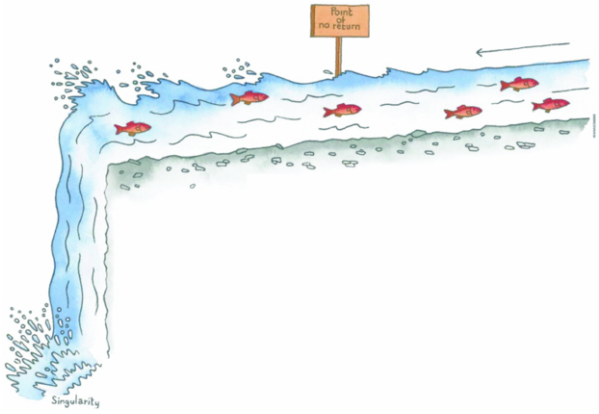

FIGURE 4: Drawing of a river with fish to understand the analogy between analogue black holes and their gravitational counterparts. The river flows from the right to the left and accelerates when approaching to the waterfall. All fish have the same velocity and try to move to the right. Beyond the brown panel, in the left part of the flow, the river velocity is so high that fish are not able to go upstream. Similarly to light which is trapped inside a black hole and propagates down to the black hole singularity, fish are trapped in this part of the flow and are bound to fall down to the waterfall. This region thus plays the role of the interior of the analogue black hole.

drodynamics equations, Unruh showed that the motion of sound waves in the fluid flow is equivalent to the one of a scalar field in a curved spacetime. We will reproduce his calculations in the first chapter of this thesis.

Then, if one quantizes the sound field, one should inherit the properties of quantum fields propagating in curved spacetime. In particular, as we shall explain in more detail in Chapter 2, the acoustic horizon completely disconnects the subsonic part from the supersonic one. Unruh showed in his paper that this *must* lead to spontaneous creation of particles from the acoustic horizon, thus to the emission of a radiation, having in principle the same thermal property as the one emitted by black holes.

Unruh's idea has triggered the interest of a large community; the analogue gravity field has particularly known a burst of interest in the last decade, with numerous experimental realizations of acoustic analogues in open-channel flows [59, 159, 192], in nonlinear optical fibers [23, 50, 149, 184], in exciton-polariton condensates [132] and in Bose-Einstein condensates [102, 105, 131, 163, 170, 175, 177]. Among them, we will focus on sonic black holes realized in (quasi) one-dimensional transonic Bose-Einstein condensates. Such a flow has been experimentally achieved by J. Steinhauer ten years ago [105] and, recently, he observed the analogous Hawking radiation [131, 177].

In Chapter 2 we will come back to Hawking's breakthrough. We will stress the universality of Hawking radiation by first considering the case of a non-uniform accelerating mirror; this acceleration will indeed cause

particle creation from vacuum [48, 69]. Then, we will treat the case of a gravitational collapse leading to the formation of a black hole. The spacetime curvature is so much affected during the collapse that two disconnected regions appear: the interior and the exterior of the black hole. We will show that this time-dependent process is very similar to the moving mirror problem and gives rise to the emission of a thermal radiation [25, 87, 88].

Chapter 3 is devoted to the study of analogue Hawking radiation in Bose-Einstein condensates. In these quantum systems, *ingoing* sound-like excitations will emerge from quantum vacuum fluctuations and scatter into *outgoing* excitations at the acoustic horizon. These outgoing sound waves will then propagate along the flow in both subsonic and supersonic regions and will induce density correlations. Therefore, as first suggested by a collaboration between teams from Trento and Bologna [15], the experimental detection of these correlations provides an indirect signature of the analogous Hawking radiation.

Chapter 3 presents the part of the original work of this thesis dedicated to the detailed analysis of quantum fluctuations close to the acoustic horizon realized in the transonic flow of a BEC.

We will first demonstrate that the taking into account of zero modes, pertaining to the phase of the condensate and the number of particles in the latter, is necessary to obtain a correct description of the correlations at the vicinity of the acoustic horizon; this will provide a safely grounded theory.

Then, we will show that, by means of the addition of the zero modes, our theoretical results compare well with the experimental data obtained by the Steinhauer's group in 2019 [131]. However, we will also prove that dispersive effects in our system does not lead to a fully thermal analogue Hawking radiation, as predicted by Hawking in the gravitational case [87, 88], but, on the contrary, presents some departure from thermality. This non-thermal feature is inherent to any dispersive system. Nevertheless, we show that a self-consistent procedure of data analysis "kill" dispersive effects and might lead to the erroneous conclusion that the analogue Hawking spectrum is completely thermal, where in reality it is not. This is the reason why we question the experimental data analysis published by J. Steinhauer's group [131] in the last section of Chapter 3. This work resulted in a publication in *Physical Review Letters*, see the article attached at the end of Chapter 3. Some of the results discussed in this chapter will also lead to a longer article in the future.

In Chapter 4 we study the entanglement between density waves emerging from quantum fluctuations on both sides of the acoustic horizon. In particular, we stress the fundamental connection with Chapter 2, i.e., the existence of two different vacua, leading to spontaneous emission of particles. We show that both vacua are linked through a Bogoliubov transformation and that the *ingoing* vacuum can be seen as a three mode Gaussian state, so that entanglement is shared among three modes.

To study this *tripartite* entanglement, we first introduce the notion of covariance matrix and we detail the different tools to analyze the separability of a quantum state, such as the violation of Cauchy-Schwarz inequality or the PPT criterion (*Positive Partial Transpose*). Then, we apply them to the particular case of our system, following the procedure presented in Ref. [4] for Gaussian states and based on the study of the CKW (*Coffman, Kundu, Wootters*) inequality [40]. By means of this procedure, we are able to compute the degree of *tripartite* entanglement, which only depends on quantities experimentally accessible [131, 176, 177]; thus, we think that it might be possible in the future to observe and measure the tripartite entanglement in Bose-Einstein condensates.

Besides the study of analogue Hawking radiation, we have been also interested in the connections that exist between Bose-Einstein condensation and nonlinear optics. The propagation of light in a nonlinear medium behaves as a fluid whose dynamics is governed by an effective Gross-Pitaevskii equation [108]. In particular, nonlinear effects induced by light in the medium lead to an effective photon-photon interaction. This analogy with Bose-Einstein condensates has triggered much interest in the scientific community to probe hydrodynamics phenomena in the context of nonlinear optics, such as superfluidity or sound-like excitations of light [34, 39, 66, 111, 128, 162, 187, 188].

In the second part of the thesis, we will be particularly interested in a specific phenomenon observed in nonlinear, dispersive, non-dissipative systems: the formation of dispersive shock waves [100]. In this respect, Figure 5 is a clear example of the strong analogy between Bose gas and optics. The left image extracted from Ref. [22] shows the propagation of a radial dispersive shock wave in a nonlinear optical medium, while the right image extracted from Ref. [91] corresponds to the propagation of such a wave in a Bose-Einstein condensate.

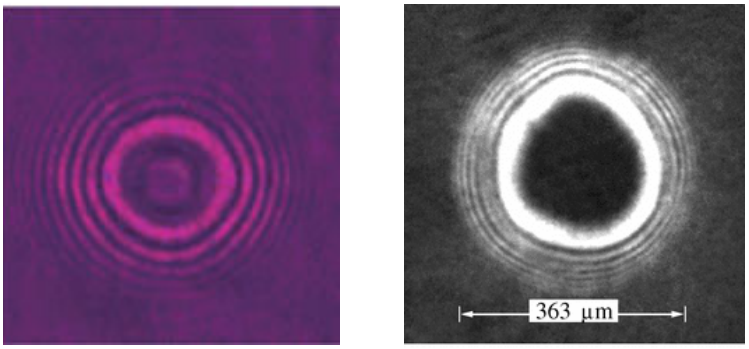

FIGURE 5: Propagation of a radial dispersive shock wave
(Left) through a photo-refractive crystal [22], **©2007, Nature**.
(Right) through a condensate [91], **©2006, APS**.

Dispersive shock waves arise from nonlinear effects which induce a wave steepening during the propagation of a nonlinear pulse on top of a background. This is rather intuitive: in the presence of a background, a part of the pulse propagates faster than the front edge and catches

it up at a certain time, called the *wave breaking time*; this results in a shock and the formation of a pattern of oscillations, called a dispersive shock wave. The emergence of such waves is not restricted to the fields of Bose-Einstein condensation and nonlinear optics, but also observed in many different systems: Figure 6a shows an example of *undular bores* in shallow waters and Figure 6b shows *morning glory roll clouds* in the atmosphere when two air masses of different temperatures collide. This undoubtedly reveals the universality of such a phenomenon driven by the competition between nonlinear and dispersive effects.

(a) Undular bore in Turnagain Arm, Alaska (copyright Scott Dickerson, 2013)

(b) Atmospheric dispersive shock waves – Morning glory roll cloud (copyright Mick Petroff, Creative Commons 3.0, 2009)

FIGURE 6: Examples of dispersive shock waves in nature.

In Chapter 5 we will first show that the paraxial propagation of an optical beam in a nonlinear medium is governed by the nonlinear linear Schrödinger equation. An hydrodynamic approach of the problem, first proposed by Khlokhlov's group in 1967 [8–11], amounts to consider the propagating optical beam as a fluids of light, characterized by a density and a velocity. Then, by means of this hydrodynamics approach, the motion of the beam can be studied by means of the Riemann invariants and through the method of characteristics. These notions are introduced in this chapter.

In Chapter 6, we study the short-time evolution of a fluid of light in the presence of a uniform background with the use of Riemann's method. This first stage of spreading can be described through a dispersionless approach and gives an excellent agreement with numerical simulations. We apply Riemann's method to the case of non-monotonic initial distributions. In this case, as proposed by Ludford [120], one needs to unfold the hodograph plane. We explain carefully this procedure and we compare our theoretical results to numerical simulations. This work led to two publications: a conference article where we considered a Gaussian optical beam, see article at the end of Chapter 6; and the first part of an article published in *Physical Review A*, see article at the end of Chapter 7.

In addition, we have noticed that it was possible to obtain a simple approximate solution of Riemann's problem which reproduced well the

simulations. We have generalized this approximation to the case of inviscid nonlinear pulses, and, in particular, to non-integrable systems. This work has been published in EPL (*Europhysics Letters*), see article at the end of Chapter 6.

In Chapter 7, we study the long-time evolution of nonlinear pulses when dispersive effects come into play. As mentioned earlier, nonlinear effects eventually lead to a gradient catastrophe when density gradients become infinite. In this case, a dispersive shock wave appears and starts propagating. In this chapter, we describe such a wave in the case of an initial density which has the form of an inverted parabola. A theoretical description of the dispersive shock waves can be obtained with such an initial condition. We show that two Riemann invariants vary concomitantly in the shock region and that the problem reduces to solve a Euler-Poisson equation. We resort to Eisenhart's work [53] and the method proposed in Refs. [56, 82] to solve the problem; we show that the theoretical results compare very well with numerical simulations.

An interesting outcome of this approach lies on the possibility to provide a weak shock theory, i.e., an asymptotic description of the dispersive shock wave, akin to the one describing the viscous shocks [197]. In particular, we are able to extract experimentally relevant parameters such as the contrast of the fringes of the dispersive shock waves.

We first described the propagation of dispersive shock waves in the case of the Korteweg-De Vries equation. This was a first step to use the method developed in Refs. [56, 82] and the dispersionless stage of spreading is easily treated using the method of characteristics. This resulted in a first publication in *Physical Review E*, attached at the end of Chapter 7.

Then, we turned our attention to the nonlinear Schrödinger equation. In this case, the description of the dispersionless spreading is more involved and requires the use of Riemann's approach (see Chapter 6). Nevertheless, the analysis of the dispersive shock wave is very similar to the one used in the case of the Korteweg-De Vries equation (but requires a more involved treatment) and show the effectiveness of the method suggested in Refs. [56, 82]. This work has been published in *Physical Review A* and is also attached at the end of Chapter 7.

We will come back to the similarities between Bose-Einstein condensates and fluids of light in the conclusion and we will discuss the future perspectives to extend the work presented in this thesis.

PUBLICATIONS

- *Analogue gravity:*

  ↪ Departing from thermality of analogue Hawking radiation in a Bose-Einstein condensate

  M. Isoard, N. Pavloff, Physical Review Letters **124**, 060401 (2020)

  doi: https://doi.org/10.1103/PhysRevLett.124.060401

  Attached to Chapter 3, see Section 3.4.

- *Nonlinear hydrodynamics:*

  ↪ Short-distance propagation of nonlinear optical pulses

  M. Isoard, A.M. Kamchatnov, N. Pavloff, 22e Rencontre du Non-Linéaire, Non-Linéaire Pub (2019)

  Attached to Chapter 6, see Section 6.3.

  ↪ Dispersionless evolution of inviscid nonlinear pulses

  M. Isoard, A.M. Kamchatnov, N. Pavloff, EPL **129**, 64003 (2020)

  doi: https://doi.org/10.1209/0295-5075/129/64003

  Attached to Chapter 6, see Section 6.4.

  ↪ Long-time evolution of pulses in the Korteweg–de Vries equation in the absence of solitons reexamined: Whitham method

  M. Isoard, A.M. Kamchatnov, N. Pavloff, Physical Review E **99**, 012210 (2019)

  doi: https://doi.org/10.1103/PhysRevE.99.012210

  Attached to Chapter 7, see Section 7.4.

  ↪ Wave breaking and formation of dispersive shock waves in a defocusing nonlinear optical material

  M. Isoard, A.M. Kamchatnov, N. Pavloff, Physical Review A **99**, 053819 (2019)

  doi: https://doi.org/10.1103/PhysRevA.99.053819

  Attached to Chapter 7, see Section 7.5.

Part I

ACOUSTIC BLACK HOLES IN BOSE-EINSTEIN CONDENSATES

2

FROM HAWKING RADIATION TO ANALOGUE GRAVITY

An accelerating observer will perceive a black-body radiation where an inertial observer would observe none. This is the so-called Davies-Fulling-Unruh effect, discovered by Davies, Fullies and Unruh in the 70's [47, 70, 181]. This means that a vacuum state for a inertial observer will be regarded as a thermal state for an uniformly accelerating observer. But the contrary is also true: an inertial observer will detect a thermal flux from a accelerating mirror that recedes from him [48, 69]. From a geometrical point of view these two situations are conformally equivalent [48], so it comes as no surprise to observe a thermal radiation in both cases.

However the latter case has a profound physical meaning: acceleration creates particles from vacuum. Let us examine this statement more precisely and resort to Einstein's equivalence principle; during its acceleration period, the moving mirror plays the same role as a time-dependent background geometry. And here is the fundamental issue: a time-dependent geometry, i.e., a time-dependent metric, breaks the time translation symmetry. Said differently, one cannot define a proper conserved energy and the construction of a vacuum state for a given field becomes ambiguous.

One can decide to expand a quantum field over a certain orthonormal set a modes and define the corresponding vacuum state with respect to this decomposition. Yet, in general relativity where spacetime is curved, one could expand this field over another set of modes and find a vacuum state different from the first one.

For instance, let us consider that $|0, \text{in}\rangle$ was the vacuum in the remote past, denoted as the *in* region. We assume that a quantum field was initially in this vacuum state. Then, for some reasons, the metric has evolved in time (for example during a gravitational collapse of a star, an expansion or a contraction of the universe,...), so that the vacuum is now $|0, \text{out}\rangle$ in the *out* region (the future of the *in* region). However, in the Heisenberg picture, the quantum field is still in the state $|0, \text{in}\rangle$, not considered as the vacuum for an observer living in the *out* region (for this observer the "true" vacuum would be $|0, \text{out}\rangle$). In that case, the observer will detect particles. The existence of both vacua will be discussed in Chapter 4.

In other words, this means that any time variation of the spacetime curvature induces spontaneous emission [142]; and there is one process in the universe which is able to dramatically affect the curvature of spacetime: the creation of a black hole from a gravitational collapse.

When the nuclear energy of the star is not enough to repel the gravitational attraction, the star shrinks and might form a black hole if the remnant mass of the star is sufficiently heavy (it should exceed three or

four solar masses [137]). All the mass of the star should collapse in one point of infinite density, the so-called black hole singularity. This singularity is hidden by an event horizon which marks the frontier between our universe and a region where nothing can escape, not even light. Any matter crossing the horizon is trapped and bound to propagate down to the singularity.

Intuitively, one can argue that nothing can escape the gravitational field of such a massive object. However, in 1974, by taking into account quantum effects at the vicinity of the event horizon, Hawking predicted that black holes are not black and should emit a faint black-body radiation, a flux which is able to elude the strong gravitational field [87, 88]; this is the so-called Hawking radiation.

Hawking's prediction in the 70's has resulted in a burst of studies around particle creation by black holes [48, 49, 69, 139, 141, 190]. However, as Hawking demonstrated in his paper [87], black holes radiate and loose mass (in other word they evaporate) until they disappear. This is an issue for quantum mechanics. Indeed, black holes are black bodies; thus, they all emit a thermal radiation that carries no information [25]. In terms of quantum mechanics, this means that any quantum field in a pure quantum state entering the black hole is transformed into a mixed state, when coming out from the black hole as a thermal radiation. As long as the black hole exists there is no issue since the full state is still pure (inside and outside the black hole), albeit the quantum field outside the black hole is mixed; this transition from pure to mixed states will be discussed in Chapter 4. The situation becomes problematic when the black hole has disappeared. Only the mixed state at the exterior of the black hole remains; thus, the information about the original quantum state has been destroyed and this leads to the so-called information loss paradox [89, 155]. Is this information really lost? If not, where it is stored? How is information retrieved in our universe? We will briefly discuss these issues which are still a matter of debate today[1] in the introduction of Chapter 4.

Actually, as indicated by the title of Unruh's paper in 1981, "Experimental Black-Hole Evaporation?" [182], it is precisely this process of evaporation that motivates Unruh to suggest the use of hydrodynamic analogues of black holes to explore this fundamental question.

In this chapter, we will first consider an analogy to the Hawking process by considering an accelerating mirror. This acceleration will cause creation of particles. We will then turn our attention to the gravitational collapse of a star leading to the formation of a black hole and the emission of Hawking radiation.

In the second part of this chapter, following Unruh's findings [182], we will demonstrate that the motion of sound waves propagating in a fluid flow is equivalent to the one of a massless scalar field in a curved spacetime. In particular, we will derive the metric that describes the space-

1 Note for instance that Hawking's latest paper is precisely about this question of information loss paradox [85], forty years after its discovery.

time curvature and comment on the emission of an analogue Hawking radiation, as soon as a sonic horizon exists.

2.1 HAWKING RADIATION

Hawking predicts in 1974 that a black hole should emit a thermal radiation. We will not enter into all the details of calculations and we will first consider a simple example to give an overall picture of the main results. In particular, we will focus on the universal process that gives rise to particle creation from vacuum fluctuations. This will give a first hint to understand how quantum sonic black holes can produce a spontaneous radiation from the acoustic horizon.

2.1.1 *Accelerating mirror*

In this section, following Refs. [25, 48, 69], we will show how a moving mirror can produce particles from vacuum. This example offers the following advantage: it gives the same result as for a gravitational collapse, but, here, the problem can be treated within a simpler framework.

Therefore, let us consider a mirror moving along the trajectory

$$x = z(t) < 0, \quad \text{with} \quad z(t) = 0, \quad t < 0. \tag{1}$$

Figure 7 shows this trajectory in the (t, x) plane (pink curve). In this plane, null rays[2] are such that $x - t =$ Constant or $x + t =$ Constant. Note that we choose units where the speed of light is unity: $c = 1$.

The mirror starts accelerating at $t = 0$ and reaches asymptotically the speed of light, so that its trajectory becomes tangent to the line $-t + v_0$, where v_0 is an arbitrary constant.

We now consider a field $\phi(t, x)$ satisfying the massless scalar wave equation

$$\frac{\partial^2 \phi}{\partial t^2} - \frac{\partial^2 \phi}{\partial x^2} = 0. \tag{2}$$

This field propagates to the right of the mirror $x > z(t)$ and will eventually reflect off the surface of the mirror, such that it also satisfies the boundary condition

$$\phi(z(t), t) = 0. \tag{3}$$

Such reflections are illustrated in Figure 7 by blue to red straight lines (the choice of colors will become clearer below). The dashed red line indicates the boundary between regions that we denote by I and II – this is the last reflected ray before the acceleration of the mirror at $t = 0$.

2 A null ray corresponds to a wave propagating at the speed of light.

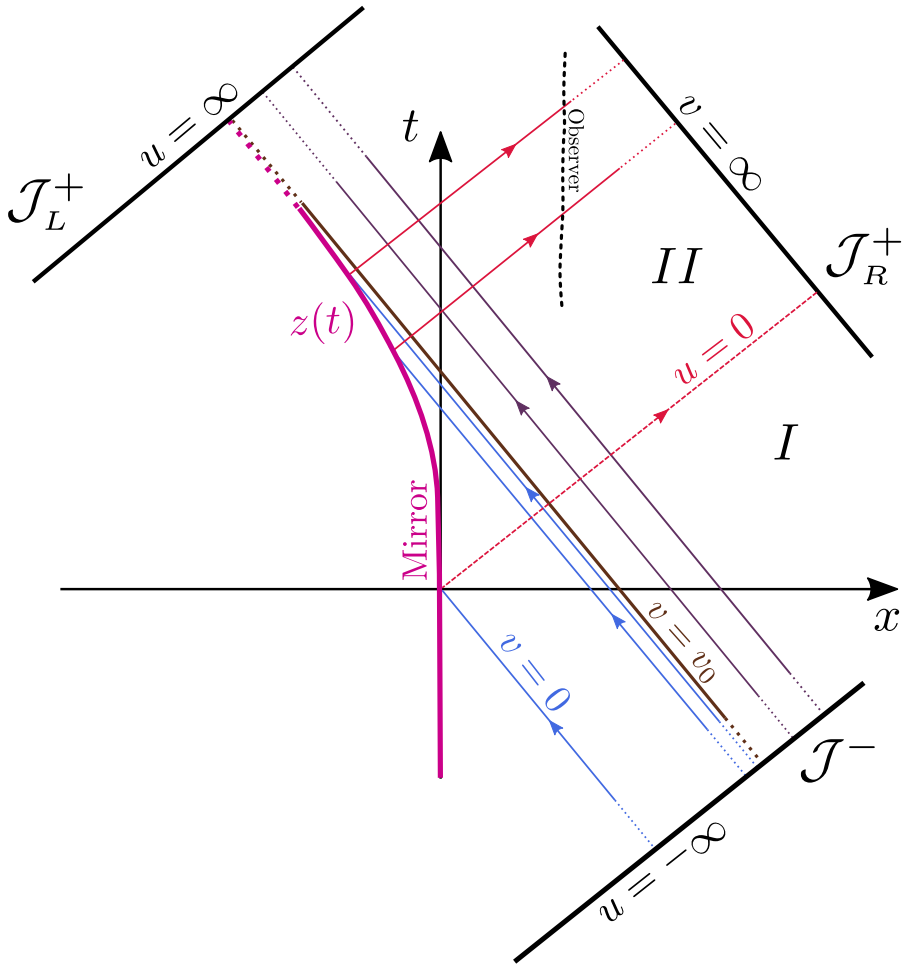

FIGURE 7: Accelerating mirror in two-dimensional Minkowski spacetime. The trajectory of the mirror $z(t)$ corresponds to the pink curve and is asymptotic to the left-moving null ray $v = t + x = v_0$ at late times – a null ray is a vector field that propagates at the speed of light, i.e., whose trajectory is a straight line oriented at 45° to the vertical. Left-moving null rays such that $v = t + x < v_0$ are indicated by blue lines and come from the past null infinity denoted as $\mathcal{J}^-$ (all left-moving null rays come from this hypersurface in the asymptotic past, see text). These rays reflect off the surface of the mirror, thus become right-moving rays and propagate until they reach the future null infinity denoted as $\mathcal{J}_R^+$ (all right-moving null rays converge to this hypersurface in the asymptotic future). Right-moving rays are colored in red because they undergo a (possibly infinite) redshift when they are reflected. One sees that, when traced back in time, right-moving rays come from left-moving rays which tend to crowd up along the line $v = v_0$. The red dashed line ($u = t - x = 0$) is the last reflected ray before the acceleration of the mirror. It also corresponds to the boundary between region I and region II defined in the text. All the left-moving null rays with $v = t + x > v_0$ (represented by the dark purple straight lines) do not reflect off the surface of the mirror and continue to propagate without any disturbance until they reach $\mathcal{J}_L^+$ (the future null infinity for the left-moving null rays). Note that in the absence of the mirror all the left-moving rays would have converged to this hypersurface in the asymptotic future. We have also drawn the trajectory of an observer (black dashed curve) in region II detecting reflected particles emitted from the surface of the mirror.

In region I, where the mirror is at rest, nothing surprising happens. The set of positive energy modes[3], solutions of equation (2), satisfying boundary condition (3), are given by

$$\phi^I_\omega(x,t) = \frac{1}{\sqrt{\pi\,\omega}}\,\sin(\omega x)\,e^{-i\omega t} = \frac{i}{\sqrt{4\,\pi\,\omega}}\,\left(e^{-i\omega v} - e^{-i\omega u}\right), \tag{4}$$

with

$$v = t + x, \quad \text{and} \quad u = t - x. \tag{5}$$

We introduce the past null infinity hypersurface[4] $\mathcal{J}^-$, which corresponds to $u = -\infty$. All the left-moving modes $v =$ Constant come from $\mathcal{J}^-$ in the asymptotic past $t \to -\infty$. Similarly, we also define the future null infinity hypersurfaces $\mathcal{J}^+_L$, corresponding to $u = +\infty$, and $\mathcal{J}^+_R$, corresponding to $v = +\infty$. These three hypersurfaces are indicated in Figure 7. Any null ray will converge to one of these surfaces (also called *lightlike infinity*).

The factor $\frac{1}{\sqrt{\pi\,\omega}}$ in expression (4) is a normalization factor. Indeed, the Lagrangian density, from which equation (2) is derived[5], is invariant under phase rotation. For any two solutions ϕ_1 and ϕ_2 of equation (2), this $U(1)$ symmetry implies the conservation of a scalar quantity [133] – the scalar product – of the form

$$(\phi_1, \phi_2) = -i \int_\Sigma \mathrm{d}\Sigma\,[\phi_1\,\partial_n\phi_2^\star - \partial_n\phi_1\,\phi_2^\star], \tag{6}$$

where Σ is a spacelike hypersurface and n a future-directed unit vector[6] orthogonal to Σ. Actually Σ can be any spacelike hypersurface, since the value of (ϕ_1, ϕ_2) is independent of the chosen surface Σ [25, 90]. One checks easily that ϕ^I_ω [see equation (4)] is normalized such that[7]

$$(\phi^I_\omega, \phi^I_{\omega'}) = \delta(\omega - \omega'). \tag{7}$$

In region II, where the mirror accelerates, reflected modes undergo a Doppler shift. Let us consider a solution of equation (2) of the form

$$\phi^{II}_\omega(t,x) = f_\omega(t-x) + g_\omega(t+x) = f_\omega(u) + g_\omega(v). \tag{8}$$

3 In the sense that they are eigenfunctions of the operator $\partial/\partial t$: $\frac{\partial}{\partial t}\phi_\omega = -i\,\omega\,\phi_\omega$, with $\omega > 0$.

4 A null hypersurface is such that its normal vector field $(ct, \mathbf{r})$ is a null vector, i.e., its norm equals zero: $c^2t^2 - \mathbf{r}^2 = 0$.

5 This Lagrangian density reads $\mathcal{L} = \frac{1}{2}\eta^{\mu\nu}\partial_\mu\phi^\star\,\partial_\nu\phi$, where η is the usual Minkowskian metric tensor (+,-,-,-).

6 Let $(\mathcal{M}, g)$ be the four-dimensional spacetime, g being the metric. A spacelike hypersurface $\Sigma \subset \mathcal{M}$ is a submanifold of dimension 3 with a timelike normal vector field $n = (ct, \mathbf{r})$, i.e., satisfying $c^2t^2 > \mathbf{r}^2$. In our 2-dimensional plane (t, x), a natural spacelike hypersurface is any curve $t =$ Constant, with normal vector $n = (1, 0)$.

7 The scalar product can be evaluated choosing the spacelike curve $t = 0$ with $n = (1, 0)$ in expression (6), and remembering that a mode of frequency ω is given by equation (4) for $x > z(t = 0) = 0$, 0 otherwise. The scalar product is also simply obtained for $\Sigma = \mathcal{J}^-$ or $\mathcal{J}^+$, whose normal vectors are $(1, -1)$ and $(1, 1)$, respectively.

The left-moving modes $g_\omega(v)$ are the same in regions I and II. Therefore, one finds immediately

$$g_\omega(v) = \frac{i}{\sqrt{4\,\pi\,\omega}}\, e^{-i\omega v}. \tag{9}$$

The right-moving modes are reflected modes. The function $f_\omega(u)$ can be found with the use of boundary condition (3):

$$0 = f_\omega(t-z(t))+g_\omega(t+z(t)) \Rightarrow f_\omega(t-z(t)) = \frac{-i}{\sqrt{4\,\pi\,\omega}}\, e^{-i\omega[t+z(t)]}, \tag{10}$$

so that

$$f_\omega(u) = \frac{-i}{\sqrt{4\,\pi\,\omega}}\, e^{-i\omega[2\tau-u]} \tag{11}$$

where τ is found implicitly through the relation:

$$\tau - z(\tau) = u. \tag{12}$$

The general set of solutions in region I and II is thus

$$\phi_\omega(u,v) = \frac{i}{\sqrt{4\,\pi\,\omega}} \left(e^{-i\omega v} - e^{-i\omega s(u)}\right), \tag{13}$$

with

$$s(u) = 2\tau - u, \quad \tau - z(\tau) = u. \tag{14}$$

Therefore, if one considers mode decomposition (13), the left-moving modes assume a simple form, whereas the right-moving modes do not, precisely because of the Doppler distortion when reflecting off the mirror.

One could actually find another decomposition, where the right-moving modes assume the simple form $\exp(-i\omega u)$. Then, these modes, when traced back in time and reflected off the mirror, will be left-moving modes with complicated complex exponential $\exp(i\omega s^{-1}(v))$, where s^{-1} is the inverse function of s defined in expression (14).

In addition, when the trajectory of the mirror approaches the asymptote $v = v_0$ as $t \to \infty$ (see the brown straight line in Figure 7), one has to be careful because left-moving modes are not reflected off the mirror for $v > v_0$, see the dark purple lines in Figure 7. In that case, the mode decomposition reads

$$\bar{\phi}_\omega(u,v) = \begin{cases} \dfrac{i}{\sqrt{4\,\pi\,\omega}} \left(e^{-i\omega s^{-1}(v)} - e^{-i\omega u}\right), & v < v_0, \\ \dfrac{i}{\sqrt{4\,\pi\,\omega}} \left(e^{-i\omega v} - e^{-i\omega u}\right), & v > v_0. \end{cases} \tag{15}$$

Despite their similarity, mode decomposition (13) and (15) are fundamentally different as we will see below.

Following quantum field theory in curved spacetime [25], one can expand the quantum field $\hat{\phi}$ over a complete set of modes, either choosing (13) or (15):

$$\hat{\phi} = \int_{\omega>0} \mathrm{d}\omega \, [\phi_\omega a_\omega + \phi^\star_\omega a^\dagger_\omega], \tag{16a}$$

$$\hat{\phi} = \int_{\omega>0} \mathrm{d}\omega \, [\bar{\phi}_\omega \bar{a}_\omega + \bar{\phi}^\star_\omega \bar{a}^\dagger_\omega], \tag{16b}$$

where a_ω and $a^\dagger_\omega$ are annihilation and creation operators pertaining to the mode ϕ_ω of frequency ω. Then, no mode ϕ_ω is present in the quantum vacuum state; we can thus define the vacuum $|0\rangle$ with respect to the set of modes (13):

$$a_\omega |0\rangle = 0, \quad \forall\, \omega. \tag{17}$$

Similarly, $\bar{a}_\omega$ and $\bar{a}^\dagger_\omega$ are annihilation and creation operators pertaining to the mode $\bar{\phi}_\omega$ of frequency ω. The vacuum state $|\bar{0}\rangle$ associated to the set of modes (15) thus reads

$$\bar{a}_\omega |\bar{0}\rangle = 0, \quad \forall\, \omega. \tag{18}$$

We can prove that modes $\bar{\phi}_\omega$ and ϕ_ω are connected through the following relations [25]:

$$\bar{\phi}_\omega = \int_{\omega>0} \mathrm{d}\omega' \, [\alpha^\star_{\omega'\omega} \, \phi_{\omega'} - \beta_{\omega'\omega} \phi^\star_{\omega'}], \tag{19}$$

or conversely

$$\phi_\omega = \int_{\omega>0} \mathrm{d}\omega' \, [\alpha_{\omega\omega'} \, \bar{\phi}_{\omega'} + \beta_{\omega\omega'} \bar{\phi}^\star_{\omega'}] \tag{20}$$

with

$$\alpha_{\omega\omega'} = (\phi_\omega, \bar{\phi}_{\omega'}), \quad \beta_{\omega\omega'} = -(\phi_\omega, \bar{\phi}^\star_{\omega'}), \tag{21}$$

where $(\cdot, \cdot)$ corresponds to the scalar product defined by expression (6) and provided $(\phi_\omega, \phi_{\omega'}) = \delta(\omega - \omega')$, $(\bar{\phi}_\omega, \bar{\phi}_{\omega'}) = \delta(\omega - \omega')$.

In addition, matrices coefficients (21) have the following properties:

$$\int_{k>0} \alpha_{\omega k} \alpha^\star_{\omega' k} - \beta_{\omega k} \beta^\star_{\omega' k} = \delta(\omega - \omega'), \tag{22a}$$

$$\int_{k>0} \alpha_{\omega k} \beta_{\omega' k} - \beta_{\omega k} \alpha_{\omega' k} = 0. \tag{22b}$$

Equating equations (16a) and (16b) and using expressions (19) and (20), we can find the relations between the operators a_ω and $\bar{a}_\omega$:

$$\bar{a}_\omega = \int_{\omega'>0} [\alpha_{\omega'\omega} a_{\omega'} + \beta^\star_{\omega'\omega} a^\dagger_{\omega'}] \tag{23a}$$

$$a_\omega = \int_{\omega'>0} [\alpha^\star_{\omega\omega'} \bar{a}_{\omega'} - \beta^\star_{\omega\omega'} \bar{a}^\dagger_{\omega'}] \tag{23b}$$

Transformations (23a) and (23b) between both sets of modes are called *Bogoliubov transformations*. We will introduce them in more detail in Section 4.1.

Let us now calculate α and β from equations (21) with the use of expressions (13) and (15). We choose to evaluate the scalar product on the spacelike hypersurface $t = 0$. The only non-trivial part for $\omega, \omega' > 0$, i.e., without taking into account the $\delta(\omega - \omega')$-terms[8], reads

$$\alpha_{\omega\omega'} \sim \frac{i}{\sqrt{4\pi\omega'}}(\phi^I_\omega, e^{-i\omega' s^{-1}(v)}), \quad \beta_{\omega\omega'} \sim \frac{-i}{\sqrt{4\pi\omega'}}(\phi^I_\omega, e^{i\omega' s^{-1}(v)}), \tag{24}$$

where the integration in expression (6) starts from $x = v = 0$ to $x = v = v_0$ ($x = v$ since $t = 0$). One easily obtains [25, 48]

$$\begin{cases} \alpha_{\omega\omega'} \\ \beta_{\omega\omega'} \end{cases} \sim \frac{\mp i}{2\pi\sqrt{\omega\omega'}} \int_0^{v_0} \{\omega \pm \omega'[s^{-1}(x)]'\}\, e^{\pm i\omega'\, s^{-1}(x)}\, \sin(\omega x)\, \mathrm{d}x, \tag{25}$$

where $[s^{-1}(x)]'$ is the derivative of $s^{-1}(x)$. An integration by parts in the previous integral yields

$$\begin{cases} \alpha_{\omega\omega'} \\ \beta_{\omega\omega'} \end{cases} \sim \pm\frac{1}{2\pi}\sqrt{\frac{\omega}{\omega'}} \int_0^{v_0} e^{\pm i\omega'\, s^{-1}(x) - i\omega x} \mathrm{d}x. \tag{26}$$

Therefore, when the function $s(x)$ is such that $\beta_{\omega\omega'} \neq 0$, positive modes $\bar{\phi}_\omega$ are decomposed into a mixing a positive and negative frequency modes $\phi_{\omega'}$ and $\phi^\star_{\omega'}$. In addition annihilation operators $\bar{a}_\omega$ are a sum of annihilation and creation operators $a_{\omega'}$ and $a^\dagger_{\omega'}$; this means necessarily that $|0\rangle \neq |\bar{0}\rangle$. In particular, we obtain from expressions (23a)

$$\langle 0|\bar{N}_\omega|0\rangle = \int_{\omega'>0} |\beta_{\omega'\omega}|^2\, \mathrm{d}\omega' \neq 0, \quad \bar{N}_\omega \equiv \bar{a}^\dagger_\omega\, \bar{a}_\omega, \tag{27}$$

thus leading to spontaneous creation of particles from vacuum.

Let us now consider the following asymptotic mirror trajectory

$$z(t) \to -t - A\, e^{-2\kappa t} + v_0, \quad \text{as} \quad t \to \infty. \tag{28}$$

The trajectory at earlier time is irrelevant because we will only concentrate our attention to the particle flux emitted by the mirror at late time. However, for the sake of completeness, we mention that one could take a trajectory of the form

$$z(t) = \begin{cases} -\kappa^{-1}\, \ln(\cosh \kappa t), & \text{if} \quad t > 0, \\ 0, & \text{if} \quad t \leq 0, \end{cases} \tag{29}$$

8 Indeed, here we are only interested in the non-trivial terms because they lead to particle creation. For instance, if $s = \mathbb{1}$ in equations (24), this implies $\alpha_{\omega\omega'} = \delta(\omega - \omega')$, $\beta_{\omega\omega'} = 0$, and thus the set of annihilation operators $\bar{a}_\omega$ can be expressed in terms of annihilation operators a_ω only [see, e.g., equation (23a)]. In that case both vacua $|0\rangle$ and $|\bar{0}\rangle$ are the same and, thus, there is no particle creation. Likewise, positive frequency modes $\bar{\phi}_\omega$ are only expanded over positive frequency modes ϕ_ω, see expression (19). As it will be shown in the following the situation becomes more interesting if $\beta_{\omega\omega'} \neq 0$, see equation (27).

whose asymptotic behavior corresponds to expression (28), with $A = \kappa^{-1}$ and $v_0 = \kappa^{-1} \ln 2$. From equations (14) and (28), one obtains the asymptotic form of $s(u)$:

$$s(u) \to v_0 - A\, e^{-\kappa(v_0+u)}, \quad \text{as} \quad u \to +\infty. \tag{30}$$

As one can see from Figure 7, when $u \to +\infty$, all the backward reflected rays pile up near the asymptotic line $v = v_0$. All the left-moving rays beyond that line (i.e.,$\forall\ v > v_0$) are not reflected off the mirror and will not be detected by an observer whose world line corresponds for instance to the dashed black line in Figure 7. Thus, the line $v = v_0$ behaves as a kind of horizon and this is precisely what makes this moving mirror problem so interesting.

As a result, when $u \to +\infty$, i.e., $v \to v_0$, we expect $s^{-1}(v)$ to be a rapidly varying function of v. Asymptotically, this yields

$$s^{-1}(v) \to -\kappa^{-1} \ln\left(\frac{v_0 - v}{A}\right) - v_0, \quad v \to v_0, \quad v < v_0. \tag{31}$$

In particular, one sees from the previous expression that asymptotic right-moving rays $u \to \infty$ undergo an infinite blueshift when traced back to $\mathcal{J}^-$ (this is the reason why we have colored in blue the left-moving rays close to $v = v_0$). In other words, at late time, any mode $\exp(-i\omega u)$ of finite frequency ω and detected by the observer (black dashed curve in Figure 7) originates from a left-moving mode $\exp[-i\omega s^{-1}(v)]$, infinitely close to $v = v_0$, with arbitrarily short wavelengths [as $s^{-1}(v \to v_0) \to +\infty$]; it corresponds to the so-called *trans-Planckian problem* [97, 158]. No definite answer to this problem has been yet given in the context of quantum gravity and, actually, this is an issue we do not encounter in analogue gravity by means of the addition of dispersive effects. For example, in Bose-Einstein condensates, there exists a natural cut-off Ω due to dispersive effects and beyond which analogue Hawking radiation ceases to be emitted, see Chapter 3.

Let us come back to our moving mirror problem and calculate matrices coefficients $\alpha_{\omega\omega'}$ and $\beta_{\omega\omega'}$ by inserting expression (31) in equations (26). To make the computation, we first assume that the asymptotic expression (31) is valid for all x. This is a reasonable assumption since most of the contribution to the integral comes from the region $v \to v_0$. Then, we let the lower bound of the integral going to $-\infty$; this amounts to consider large frequencies ω, which is valid here because the rapidly varying function $s^{-1}(v)$ near $v = v_0$ represents very high frequencies ω [25, 88].

By means of the above approximations, expressions (26) are easily computed and we obtain

$$\begin{cases} \alpha_{\omega\omega'} \\ \beta_{\omega\omega'} \end{cases} \sim \pm \frac{i\, e^{\pm\pi\omega'/2\kappa}}{2\pi\sqrt{\omega\omega'}}\, e^{\pm i\omega' D - i\omega v_0}\, \omega^{\pm i\omega'/\kappa}\, \Gamma(1 \mp i\omega'/\kappa), \tag{32}$$

with $D = \kappa^{-1} \ln A - v_0$. Then, using the identity

$$|\Gamma(1 + ix)|^2 = \frac{\pi x}{\sinh \pi x}, \quad x \in \mathbb{R}, \tag{33}$$

we obtain the final result

$$|\beta_{\omega\omega'}|^2 = \frac{1}{2\pi\kappa\,\omega}\left(\frac{1}{e^{\omega'/k_{\mathrm{B}}T}-1}\right), \quad \text{with} \quad k_{\mathrm{B}}T = \frac{\kappa}{2\pi}. \tag{34}$$

Using expression (27), this leads to

$$\langle 0|\bar{N}_\omega|0\rangle = \frac{1}{e^{\omega/k_{\mathrm{B}}T}-1}\int_0^{+\infty}\frac{\mathrm{d}\omega'}{2\pi\kappa\,\omega'}. \tag{35}$$

Therefore, an observer, whose world line corresponds to the dashed black line in Figure 7, will detect spontaneous emission from vacuum, and more precisely, will detect a thermal flux of temperature $T \sim \kappa$. The logarithmic divergence of expression (35) lies in the fact that the mirror continues to accelerate during an infinite amount of time, and thus accumulates an infinite number of quanta per mode. Note that the divergence can be removed by looking instead at the number of quanta emitted per unit time in the frequency range ω to $\omega + \mathrm{d}\omega$ [25, 139]:

$$\frac{\mathrm{d}\bar{N}_\omega}{\mathrm{d}t} = \frac{1}{e^{\omega/k_{\mathrm{B}}T}-1}\frac{\mathrm{d}\omega}{2\pi}. \tag{36}$$

2.1.2 *Penrose diagrams*

Before deriving Hawking's famous result in the case of the gravitational collapse of a star into a black hole, let us introduce important diagrams in General Relativity, the so-called *Penrose diagrams*.

Such diagrams are very similar to what is drawn in Figure 7. However, in a Penrose diagram, one is interested in looking at the whole spacetime, i.e., from the asymptotic past to the asymptotic future.

There is a simple way to glance at the past and the future at once by making the following change of variables

$$\bar{u} = 2\arctan u, \quad \bar{v} = 2\arctan v, \tag{37}$$

where we recall that $u = t - x$ and $v = t + x$. Note that we still consider here a two-dimensional Minkowski spacetime $\mathrm{d}s^2 = \mathrm{d}t^2 - \mathrm{d}x^2 = \mathrm{d}u\,\mathrm{d}v$.

One sees that the coordinate transformations (37) amount to shrink the asymptotic past and future to finite values. Indeed, the axis $x = 0$ which goes to $t = -\infty$ to $t = +\infty$ now starts from $\bar{u} = \bar{v} = -\pi$ to $\bar{u} = \bar{v} = \pi$. Similarly the axis $t = 0$ now goes from $\bar{v}(x = -\infty, t = 0) = -\bar{u}(-\infty, 0) = -\pi$ to $\bar{v}(\infty, 0) = -\bar{u}(\infty, 0) = \pi$, see Figure 8.

We denote by i^- and i^+ the past and future timelike infinities, since they correspond to $t = -\infty$, $\forall\, x$ ($\bar{u} = \bar{v} = -\pi$) and $t = +\infty$, $\forall\, x$ ($\bar{u} = \bar{v} = \pi$), respectively. In other words, any timelike vector field[9] comes from the past timelike infinity and converges to the future timelike infinity. The red dashed line drawn in the middle of Figure 8 from i^- to i^+ would be the world line of an object at rest in the universe from its asymptotic past $t = -\infty$ to its asymptotic future $t = +\infty$.

9 A timelike vector field $u = (ct, \mathbf{r})$ has a positive norm $u^\mu u_\mu$ if the chosen Minkowskian signature is $(+,-,-,-)$.

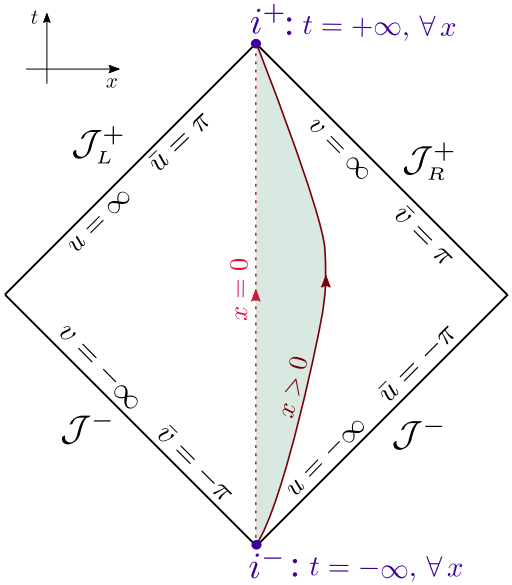

FIGURE 8: Penrose diagram. The distant past and future $t = -\infty$ and $t = +\infty$ become finite by means of the coordinate transformations (37). The past and future null infinities denoted as $\mathcal{J}^-$, $\mathcal{J}_L^+$ and $\mathcal{J}_R^+$ have been already introduced in Figure 7. All null rays, i.e., with $u = t - x =$ Constant or $v = t + x =$ Constant converge to these hypersurfaces. As discussed in the text, these null rays are represented as straight lines oriented at 45° from the vertical in a Penrose diagram. The conformal transformation leading to a Penrose diagram actually preserves the orientation of the light cone, and thus the notion of causality. Both points i^- and i^+ are the past and future timelike infinity, respectively. All timelike vector fields come from i^- [where $u = v = -\infty$ or $\bar{u} = \bar{v} = -\pi$, see expressions (37)] and converge to i^+ (where $u = v = +\infty$ or $\bar{u} = \bar{v} = \pi$). We have drawn two examples of timelike geodesics, corresponding to $x = 0$ – red dashed line — and $x > 0$ – brown curve. The presence of the green area will become clearer below.

Transformations (37) actually correspond to a conformal transformation to the metric, i.e.,

$$g_{\mu\nu} \to \bar{g}_{\mu\nu} = \Omega^2(x)\, g_{\mu\nu}, \tag{38}$$

with $\Omega^2(x) = \left(\frac{1}{4}\cos^{-2}\frac{\bar{u}}{2}\cos^{-2}\frac{\bar{v}}{2}\right)^{-1}$ [25]. The main interest of a conformal transformation lies in the fact that it changes lengths but not angles. Therefore, it leaves the light cone invariant: null rays, oriented at 45° to the vertical in the usual Minkowski spacetime $\mathrm{d}s^2 = \mathrm{d}t^2 - \mathrm{d}x^2$, remain at 45° after the conformal transformation. Therefore, the causality is the same as in the usual Minkowski spacetime [25, 117]. In particular, the null hypersurfaces $\mathcal{J}^-$, corresponding to $u, v = -\infty$ ($\bar{u}, \bar{v} = -\pi$), and $\mathcal{J}^+$, corresponding to $u, v = +\infty$ ($\bar{u}, \bar{v} = \pi$), are still at 45° to the vertical, see Figure 8.

MOVING MIRRORS Let us now apply what we have learned from the previous paragraph to draw the Penrose diagram in the case of an

accelerating mirror, as considered in Section 2.1.1. The left graph of Figure 9 shows such a diagram. The mirror trajectory starts from i^- ($t = -\infty$, $x = 0$ for the mirror at rest) and becomes asymptotic to the null ray[10] $v = v_0$, reaching eventually the future null infinity denoted as $\mathcal{J}_L^+$, see Figure 7. Actually, all the left-moving rays $v > v_0$ will reach this surface in the asymptotic future. A reflected ray off the mirror surface is also depicted in Figure 9; it will reach the asymptotic surface denoted as $\mathcal{J}_R^+$ at $t = +\infty$.

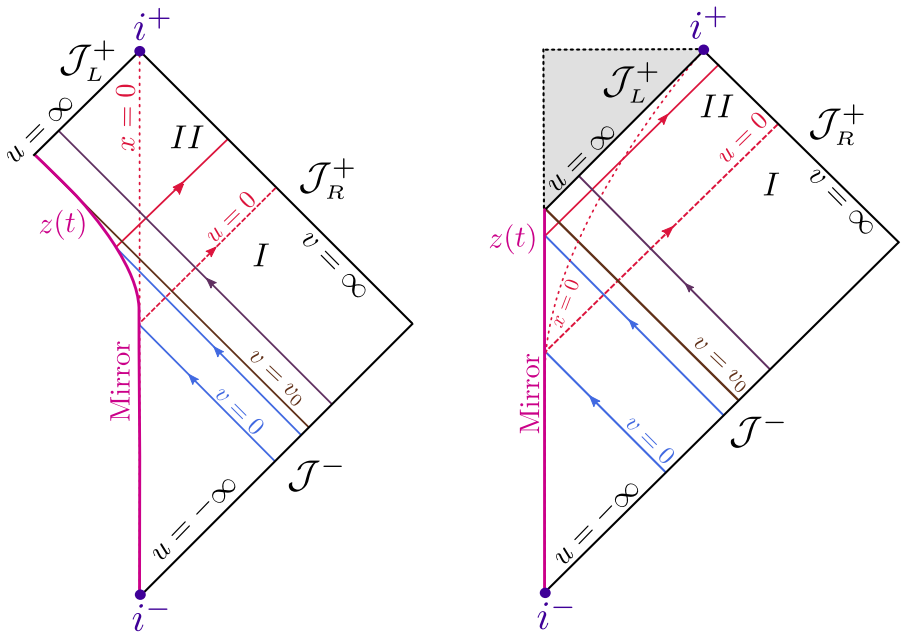

FIGURE 9: Penrose diagram in the case of the accelerating mirror problem. (Left) This diagram should be compared with Figure 7. Different reflected rays are depicted, as well as regions I and II. The region to the left of the mirror is not reachable, and thus not indicated on the diagram. The trajectory of the mirror becomes tangent to the line $v = v_0$ asymptotically.
(Right) The same situation after a conformal transformation which amounts to go to the rest frame of the mirror. In this case, the trajectory of the mirror is a straight line converging smoothly to $\mathcal{J}_L^+$ as it becomes tangent to the left-moving null ray $v = v_0$. Null rays are still straight lines oriented at 45° to the vertical since any conformal transformation preserves their orientation. The shaded area is not reachable (because it corresponds to a region outside spacetime), but is indicated for comparison with Figure 12 obtained in the case of a gravitational collapse. This shaded area would correspond to the interior of the black hole. Any left-moving rays with $v > v_0$ would not be reflected off the surface of the mirror and would fall inside the gray region. In this case, the hypersurface $\mathcal{J}_L^+$ would play the role of an event horizon.

However, one can also choose a new system of coordinates associated to the rest frame of the mirror. This is again a conformal transformation [48] and the resulting Penrose diagram corresponds to the right panel

10 We recall that a null ray corresponds to a wave propagating at the speed of light.

of Figure 9. One sees that the last reflected rays ending up on $\mathcal{J}_R^+$ is infinitely close to $\mathcal{J}_L^+$. The dashed lines delimiting the unreachable shaded area will become meaningful in the next subsection.

At the moment, the connection between a gravitational collapse and an accelerating mirror in the universe might be still unclear; a first glance at Figure 12, and a comparison of this figure with the right graph of Figure 9, may give a hint!

2.1.3 *Gravitational collapse*

In this subsection, we will derive the famous result obtained by Hawking in 1974 [87]. Note that, for simplicity, we will only consider the case of a two-dimensional spacetime (t, r), whereas Hawking considered the four-dimensional case. Despite this simplification, the final result will be similar to Hawking's findings. For a complete derivation we refer the reader to Refs. [25, 88].

In the case of a gravitational collapse, spacetime is not Minkowskian outside the collapsing body, but is rather described by the Schwarzschild metric introduced in the subsequent paragraph.

In addition, we only consider the case of a massless scalar field ϕ that propagates in a two-dimensional curved (Schwarzschild) spacetime, i.e.,

$$\nabla_\mu \nabla^\mu \phi = \frac{1}{\sqrt{-g}}\, \partial_\mu (\sqrt{-g}\, g^{\mu\nu}\, \partial_\nu \phi) = 0, \tag{39}$$

where $g = (\det g^{\mu\nu})^{-1}$ and $g^{\mu\nu}$ is the curved spacetime metric.

SCHWARZSCHILD METRIC This metric describes the spacetime curvature in the presence of a spherical object of mass m; it corresponds to an exact solution of Einstein's equations derived by Schwarzschild[11] [165] in 1915. It reads

$$\begin{aligned} \mathrm{d}s^2 &= \left(1 - \frac{2\,m}{r}\right) \mathrm{d}t^2 - \left(1 - \frac{2\,m}{r}\right)^{-1} \mathrm{d}r^2 - r^2(\mathrm{d}\theta^2 + \sin^2\theta\, \mathrm{d}\varphi^2) \\ &= g_{\mu\nu} \mathrm{d}x^\mu\, \mathrm{d}x^\nu, \end{aligned} \tag{40}$$

$g_{\mu\nu}$ being the matrix coefficients of the four-dimensional Schwarzschild metric. One sees that $r = 0$ and $r = 2\,m$ (called *Schwarzschild radius*) are singular.

First, let us notice that if $r > 2m$, $g_{00} = 1 - 2m/r > 0$ (where the subscript "0" stands for the time coordinate) and $g_{11} = -(1 - 2m/r)^{-1} < 0$ (where "1" is for the radial coordinate). However, when $r < 2m$, g_{00} and g_{11} switch signs; it means that the radial coordinate r becomes timelike and the time coordinate t becomes spacelike for

11 "As you see, the war treated me kindly enough, in spite of the heavy gunfire, to allow me to get away from it all and take this walk in the land of your ideas" – Letter excerpt from Schwarzschild to Einstein, 22 December 1915.
Schwarzschild derived the first exact solution of Einstein equations on the Russian front, the so-called Schwarzschild metric.

$r < 2m$. As shown in Figure 10, it implies that light cones – represented by the yellow areas – in the region $r < 2m$ are oriented towards the hypersurface $r = 0$ and are tilted by 90 degrees to those in the region $r > 2m$. Therefore, $r = 2m$ acts as a boundary between two causally disconnected regions; no signal in the region $r < 2m$ can be sent towards the region $r > 2m$ and any matter is bound to propagate towards the singularity $r = 0$. The hypersurface $r = 2m$, indicated by the red line in Figure 10, is nothing but an *event horizon*.

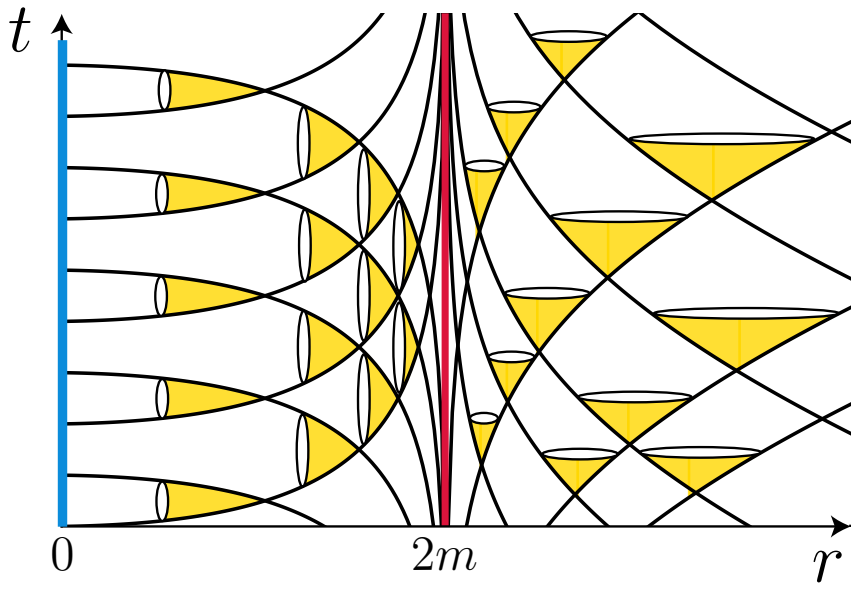

FIGURE 10: The black curves represent the null geodesics in the (r, t)-plane propagating in a Schwarzschild curved spacetime. Null rays in this spacetime correspond to $\widetilde{u}$ and $\widetilde{v}$ = constant, where $\widetilde{u}$ and $\widetilde{v}$ are defined in equation (41). The yellow areas correspond to light cones. The blue line located at $r = 0$ is the singularity of the black hole, while the red line, located at $r = 2m$, is the event horizon. Note that the time coordinate t in this graph would correspond to the time measured by an observer outside the black hole (in the region $r > 2m$). For such an observer, it would take an infinite amount of time for a light ray to cross the event horizon. This is completely different from the experience of someone who is actually falling into the black hole; their measure of time is called *proper time*. In this case, according to their watch, this person will cross the horizon in a finite amount of time.

Second, the singularity $r = 2\,m$ in the metric (40) is only apparent and can be removed by means of the following change of coordinates:

$$\widetilde{u} = t - r^\star, \quad \widetilde{v} = t + r^\star, \tag{41}$$

with

$$r^\star = r + 2m \, \ln \left| \frac{r}{2\,m} - 1 \right| . \tag{42}$$

Inserting the change of coordinates (41), (42) in expression (40) leads to the so-called Eddington–Finkelstein form:

$$\mathrm{d}s^2 = \left(1 - \frac{2\,m}{r}\right)\mathrm{d}\widetilde{v}^2 - 2\,\mathrm{d}\widetilde{v}\,\mathrm{d}r - r^2(\mathrm{d}\theta^2 + \sin^2\theta\,\mathrm{d}\varphi^2), \tag{43}$$

where the singularity $r = 0$ remains, but not $r = 2m$.

In the case of a two-dimensional spacetime (dropping the angular part), the previous metric reduces to

$$\mathrm{d}s^2 = C(r)\,\mathrm{d}\widetilde{u}\,\mathrm{d}\widetilde{v}, \quad C(r) = \left(1 - \frac{2\,m}{r}\right), \tag{44}$$

and this corresponds to a conformal transformation:

- For $r > 2m$, $C(r) > 0$. By taking $\Omega(r) = C^{-1/2}(r)$ in equation (38), one sees immediately that (44) is conformal to a two-dimensional Minkowski spacetime with signature $(+,-)$.
- For $r < 2m$, $C(r) < 0$. Thus, (44) is conformal to a two-dimensional Minkowski spacetime with signature $(-,+)$.

Therefore, the presence of an horizon (at $r = 2m$) splits the whole spacetime in two regions ($r > 2m$ and $r < 2m$), each of them being *conformally flat*, i.e., conformal to a Minkowski spacetime [117].

Let us make a last comment which will be of importance in the next section: if the radius $R(t)$ of a collapsing star shrinks below the Schwarzschild radius at a certain time denoted as t_0, an event horizon is formed at $r = 2m$ and the region $R(t > t_0) < r < 2m$ becomes the interior of the black hole, see for instance Figure 11. The singularity eventually appears when $R(t_{\text{sing}}) = 0$ (purple dot in Figure 11).

PENROSE DIAGRAM First, let us look at Figure 11, which corresponds to a schematic drawing of a gravitational collapse (we assume that the problem is spherically symmetric).

The black curves converging to the singularity $r = 0$ represent the surface of the collapsing body (the surface of a star for instance). We denote by $R(t)$ the radius of the collapsing body. The wavy line remaining at $r = 0$ at all times after the final collapse occurring at $t = t_{\text{sing}}$ is the singularity of the black hole. We have also drawn null rays passing through the collapsing body and which are deviated by the strong gravitational field in this region. As in Figure 9, they are colored blue and then red since they undergo an infinite redshift[12] when crossing the collapsing body, see below.

The last ray which escapes the singularity and which is directed towards the future timelike infinity i^+ forms the event horizon of the black hole. As we mentioned in the last paragraph, when considering a Schwarzschild metric, the horizon is formed at a certain time t_0 when the radius of the collapsing body equals the Schwarzschild radius, i.e., $R(t_0) = 2\,m$.

12 Contrary to the accelerating mirror, the redshift is not instantaneous here.

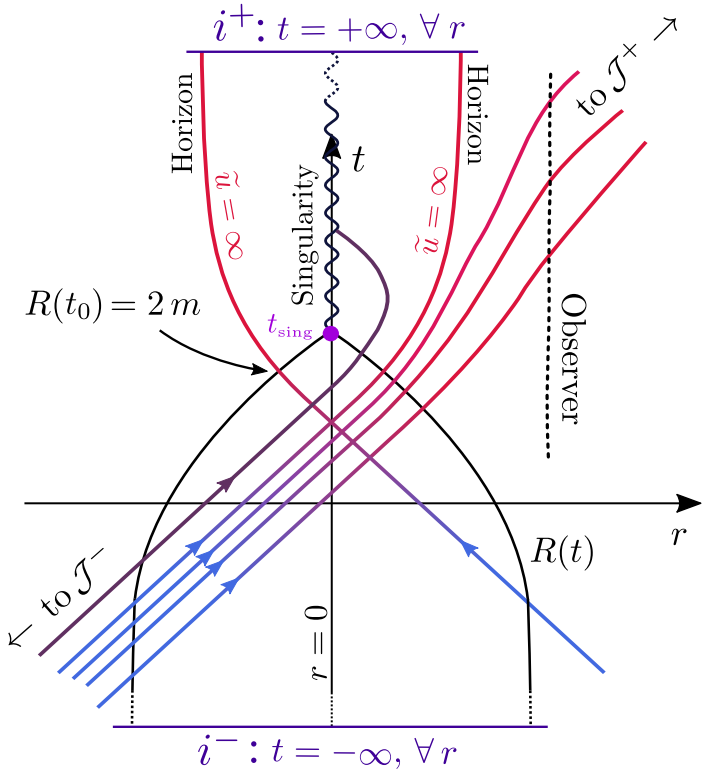

FIGURE 11: Schematic drawing of a gravitational collapse leading to the formation of a black hole. The surface of the collapsing body (assuming spherical and of mass m) is indicated by the black curves. We denote by $R(t)$ the object radius at time t, eventually shrinking to zero at a time denoted as t_{sing} and pinpointed by the purple dot. An infinite density point is then formed and called *black hole singularity*. Null rays, depicted as blue to red curves (since they undergo a – possibly infinite – redshift), come from $\mathcal{J}^-$, then pass though the collapsing body. They are distorted due to the strong gravitational field in the vicinity of the black hole region. The null ray going out from the collapsing body when its surface radius is $R(t_0) = 2\,m$ (i.e., the Schwarzschild radius in the case of a Schwarzschild spacetime, see text) is so distorted that it becomes a vertical straight line; it corresponds to the last ray that escapes the singularity and converges to the intersection between the future timelike infinity i^+ and the future null infinity $\mathcal{J}^+$, see Figure 12. The surface delimited by these two null rays (by symmetry, the second null ray goes out from the collapsing body when $R(t_0) = -2\,m$) forms the so-called *event horizon*. We have also indicated that these null rays correspond to $\widetilde{u} = \infty$, with $\widetilde{u}$ defined in expression (41). Any ray crossing the surface of the collapsing body at a later time $t > t_0$, such as the dark purple curve in the graph, is bound to propagate down to the singularity. We have also drawn the world line of an observer outside the black hole and able to detect null rays after they passed through the collapsing body.

Beyond that point, we enter the interior of the black hole; anything that propagates here is bound to fall down to the singularity[13] (see the dark purple null ray in Figure 11).

13 Note that the singularity is hidden by the event horizon delimiting the mysterious interior of the black hole – In the absence of an event horizon, the singularity is said

Now, we will draw the Penrose diagram of such a collapse. To model the spherical symmetry of the four-dimensional situation, we can restrict the problem to $r \geq 0$ and reflect the null rays at $r = 0$; this will reproduce the trajectory of incoming null rays inside the collapsing body through the center at $r = 0$, and then out of the body [25], see Figure 13 for instance. Such reflections will be achieved by imposing the boundary condition $\phi(r = 0, t) = 0$ for the field ϕ, exactly as we did in Section 2.1.1, see equation (3).

Figure 12 shows the two-dimensional Penrose diagram associated to the gravitational collapse of a spherical body. The center of the body $r = 0$ is a vertical line until it reaches the purple dot; this dot indicates the moment when the surface has shrunk to the the singularity. The surface of the body corresponds to the black curve; initially this curve comes from the past timelike infinity i^- and converges to the purple dot. The line appears distorted as a result of the coordinates transformation (37), where u and v should be replaced by the Kruskal coordinates[14].

The last left-moving null ray $\widetilde{v} = \widetilde{v}_0$ that escapes the singularity is reflected from the center $r = 0$, and then moves to the right until it reaches the intersection between the future timelike infinity i^+ and the null hypersurface $\mathcal{J}_R^+$. This ray goes out from the collapsing body just before the formation of the event horizon when $R(t \simeq t_0) \simeq 2m$, where we recall that $R(t)$ is the decreasing radius of the spherical body. Looking at equations (41) and (42), we find that this outgoing and right-moving ray thus corresponds to the null ray $\widetilde{u} = +\infty$ and is tangent to the hypersurface $\mathcal{J}_L^+$, see Figure 12.

Then, all the left-moving rays such that $\widetilde{v} > \widetilde{v}_0$ reflect off the center at a point located beyond the purple dot and thus propagate down to the singularity (see for instance the dark purple null ray in Figure 12). The fact that the singularity (corresponding to $r = 0$) is perpendicular to the black dashed vertical line $r = 0$ is a bit subtle: in fact, the Penrose diagram shown in Figure 12 hides two Penrose diagrams glued together along the curve $R(t)$! The green area corresponds to the interior of the collapsing body, whose spacetime is described by the conformally flat metric (46). Thus, the associated Penrose diagram simply looks like the green area in Figure 8. The other part of the diagram represents the exterior of the collapsing body, whose spacetime is described by the Schwarzschild metric (40). In this case, the associated Penrose diagram is a bit more complicated to draw and is a portion of the so-called *maximally extended Kruskal manifold* [25, 129].

Besides this subtle point, the gray area in Figure 12 is located beyond the event horizon and corresponds to the interior of the black hole. This region is equivalent to the shaded region in the right plot of Figure 9.

---

to be *naked*. R. Penrose postulated in 1969 that no naked singularity exists in our universe; this is known as the *cosmic censorship hypothesis* [146].

14 The Kruskal coordinates are defined by [25, 129]

$$u = \mp 4\, m e^{-\widetilde{u}/4m}, \quad v = 4\, m e^{\widetilde{v}/4m}, \tag{45}$$

with the minus (plus) sign for u if $r > 2m$ ($r < 2m$).

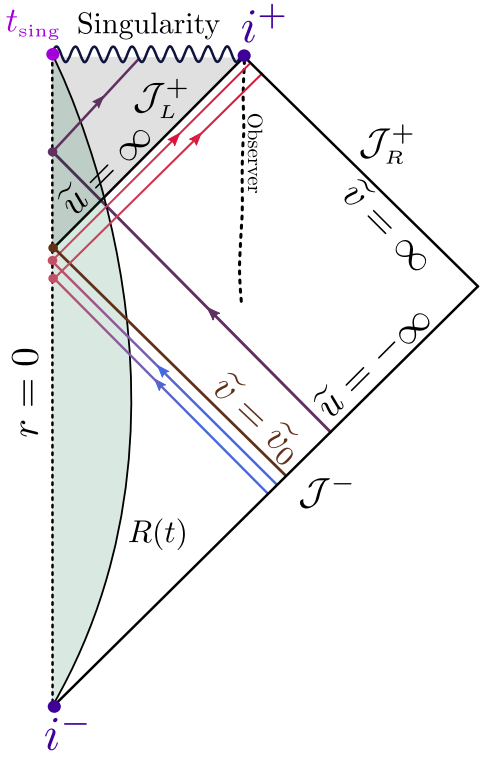

FIGURE 12: Penrose diagram of the gravitational collapse. To model the spherical symmetry of the four-dimensional situation, we have restricted the problem to $r \geq 0$ and reflected the null rays at $r = 0$. This procedure of reflection is better illustrated in Figure 13. Then, the problem becomes very similar to the case of the accelerating mirror, see the right diagram of Figure 9. The main difference lies in the fact that the redshift accumulated by null rays when crossing the collapsing body is not instantaneous, contrary to the case of the moving mirror. The surface of the collapsing body is represented by the black curve $R(t)$ and the interior corresponds to the green area. When the surface radius reaches $r = 0$ at $t = t_{\text{sing}}$, a singularity is formed. This event is indicated by the purple dot. The last reflected ray escaping from the singularity corresponds to $\widetilde{u} = \infty$ and comes from a left-moving null ray with $\widetilde{v} = \widetilde{v}_0$. Thus, the event horizon is nothing but the null hypersurface $\mathcal{J}_L^+$. All the left-moving rays with $\widetilde{v} > \widetilde{v}_0$ enter the interior of the black hole and propagate down to the singularity, as illustrated for instance with the dark purple null ray.

As in Figure 7, the dashed black curve in Figure 12 would correspond to the world line of an observer in our universe, outside the black hole, converging to the asymptotic future i^+ and observing the right-moving null rays passing through. In full analogy with the accelerating mirror, all the right-moving rays converge to $\mathcal{J}_R^+$. When traced back in the asymptotic past, they all converge to $\mathcal{J}^-$ and crowd up around $\widetilde{v} = \widetilde{v}_0$.

HAWKING RADIATION Let us now compute the expected spontaneous emission due to the gravitational collapse. This amounts to calcu-

late the relationship between the left-moving waves propagating from $\mathcal{J}^-$ to the center of the collapsing body, then come out and propagate to $\mathcal{J}^+_{\mathrm{R}}$, see the left graph of Figure 13. Equivalently, one can model the spherical symmetry of the four-dimensional situation by reflecting null rays from $r = 0$, see the right graph of Figure 13.

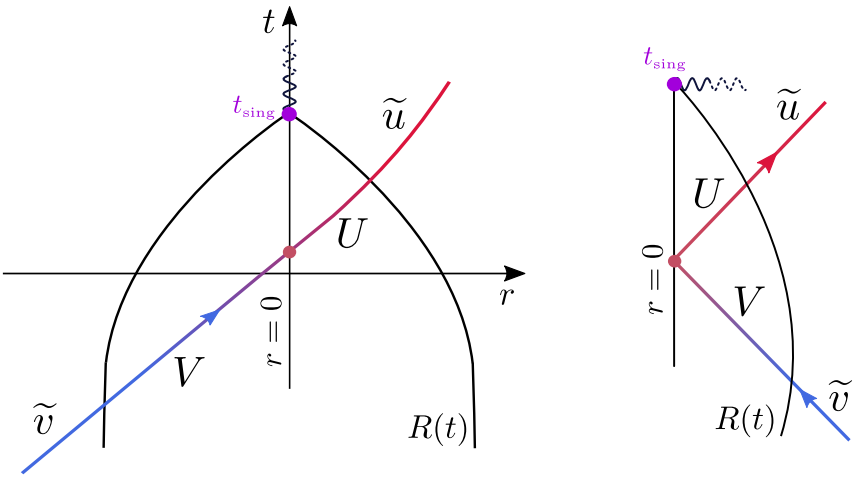

FIGURE 13: Portions of the graphs depicted in Figure 11 and Figure 12.
(Left) A null ray with $\widetilde{v}$ = Constant enters the collapsing body. In the interior of the body, we define new coordinates U and V, see expressions (46).
(Right) Portion of the Penrose diagram illustrated in Figure 12. The null ray is reflected at the center $r = 0$ of the collapsing body.

Inside the collapsing body, we introduce a new time coordinate τ and we assume that the spacetime is conformal to Minkowski spacetime [25, 87] with line element

$$\mathrm{d}s^2 = A(U,V)\,\mathrm{d}U\,\mathrm{d}V, \quad \text{where} \quad \begin{cases} U = \tau - r, \\ V = \tau + r. \end{cases} \tag{46}$$

We have introduced in the previous equation a new time coordinate τ inside the collapsing body. The coordinates U and V are indicated in Figure 13.

Outside the spherical body, we use the two-dimensional Schwarzschild metric given by expression (44), where $\widetilde{u}$ and $\widetilde{v}$ are defined in equations (41) and (42).

Then, the transformations between the interior and the exterior coordinates are given in terms of two functions denoted as α and β – These functions will be determined later:

$$U = \alpha(\widetilde{u}), \quad \widetilde{v} = \beta(V). \tag{47}$$

Now, let us consider an outgoing null ray going out from the collapsing body and propagating towards $\mathcal{J}^+_R$ with $\widetilde{u}$ = Constant. When traced back in time, such a ray had coordinate $U = \alpha(\widetilde{u})$ = Constant in the interior of the body, after passing through $r = 0$, see Figure 13. At the

center of the body $r = 0$, expressions (46) show that $V(\tau, 0) = U(\tau, 0)$ = Constant. Then, we can use the function β that connects V and $\widetilde{v}$ to obtain the full connection between $\widetilde{v}$ and $\widetilde{u}$:

$$\widetilde{v} = \beta(V) = \beta(U) = \beta \circ \alpha(\widetilde{u}) = \text{ Constant.} \tag{48}$$

Similarly to the case of the accelerating mirror, an ingoing wave $\exp(-i\omega\widetilde{v})$ will be converted into an outgoing wave $\exp[-i\omega\beta\circ\alpha(\widetilde{u})]$ when going out from the collapsing body; comparing with expression (13), this would correspond to $s = \beta \circ \alpha$.

We shall now find explicitly the functions α and β. To that end, we have to match the exterior and interior metrics (44) and (46) across the collapsing surface $r = R(t) = R(\tau)$, i.e.,

$$C[R(\tau)]\, \mathrm{d}\widetilde{u}\, \mathrm{d}\widetilde{v} = A(U, V) \mathrm{d}U\, \mathrm{d}V, \tag{49}$$

with

$$\begin{cases} \widetilde{u} = \tau - R(\tau) - 2\,m\, \ln\left|\dfrac{R(\tau)}{2\,m} - 1\right|, \\ \widetilde{v} = \tau + R(\tau) + 2\,m\, \ln\left|\dfrac{R(\tau)}{2\,m} - 1\right|, \end{cases} \quad \text{and} \quad \begin{cases} U = \tau - R(\tau), \\ V = \tau + R(\tau). \end{cases} \tag{50}$$

One finds easily from expression (49) both differential equations[15]

$$\begin{aligned} \alpha' &= \frac{\mathrm{d}U}{\mathrm{d}\widetilde{u}} = C\,(1 - \dot{R})\, \left\{[\dot{R}^2 + A\,C\,(1 - \dot{R}^2)]^{1/2} - \dot{R}\right\}^{-1}, \\ \beta' &= \frac{\mathrm{d}V}{\mathrm{d}\widetilde{v}} = C^{-1}\,(1 + \dot{R})^{-1}\, \left\{\dot{R}^2 - [A\,C\,(1 - \dot{R}^2)]^{1/2} + \dot{R}\right\}, \end{aligned} \tag{51}$$

where $\dot{R} = \mathrm{d}R/\mathrm{d}\tau$ and $(\dot{R}^2)^{1/2} = -\dot{R}$ because $\dot{R} < 0$.

To solve these differential equations let us make a comment related to what we have learned from the accelerating mirror problem: we noticed that the most redshifted right-moving rays were those coming from the region at the vicinity of $v = v_0$. In addition, due to this significant redshift, the major contribution to the integral (26) [which gives eventually the total number of emitted quanta from vacuum, see equation (27)] corresponds to $v \simeq v_0$.

In the gravitational case and by similarity with the mirror problem, we expect this strong redshift to occur close to $\widetilde{v} = \widetilde{v}_0$, i.e., for null rays coming out from the collapsing body at $R(t_0) \simeq 2\,m$ when the surface of the spherical body approaches the event horizon, see Figure 11.

Therefore, let us assume that $C(R) = (1 - 2m/R) \simeq 0$, so that equations (51) simplify to

$$\frac{\mathrm{d}U}{\mathrm{d}\widetilde{u}} = \frac{\dot{R} - 1}{2\,\dot{R}}\, C(R), \tag{52a}$$

$$\frac{\mathrm{d}V}{\mathrm{d}\widetilde{v}} = \frac{A\,(\dot{R} - 1)}{2\,\dot{R}}. \tag{52b}$$

15 Note that $r^\star = \int C^{-1}\, \mathrm{d}r$, where $r^\star$ and $C(r)$ are defined in equations (42) and (44), respectively.

Then, we expand $R(t)$ around $t = t_0$, where we recall that t_0 is the moment corresponding to the formation of the event horizon:

$$R(t) \simeq R(t_0) + \dot{R}(t_0)(t - t_0). \tag{53}$$

This leads to[16]

$$\frac{C}{2\,\dot{R}(t_0)} \simeq \kappa\,(t - t_0), \quad 1 - \dot{R}(t_0) \simeq \frac{U + R(t_0) - t_0}{t - t_0}, \tag{54}$$

where we have introduced

$$\kappa = \frac{1}{2}\left.\frac{\mathrm{d}C}{\mathrm{d}R}\right|_{R(t_0)} \underset{\text{our case}}{=} \frac{1}{4\,m}. \tag{55}$$

Actually, κ, called the *surface gravity*, measures how curved is the metric at the vicinity of the horizon. One sees that in the case of the Schwarzschild metric, the surface gravity is inversely proportional to the mass of the black hole.

Finally, by integrating equation (52a) with the use of (54), we obtain

$$\kappa\,\widetilde{u} = -\ln|U + R(t_0) - t_0| + \text{ Const.}, \quad \text{as} \quad \widetilde{u} \to +\infty. \tag{56}$$

Therefore, inverting the previous expression gives

$$U = e^{-\kappa\,\widetilde{u}} + t_0 - R(t_0), \quad \text{as} \quad \widetilde{u} \to +\infty. \tag{57}$$

At late times, i.e., for large values of $\widetilde{u}$, one sees from (56) and (57) that U does not really depend on $\widetilde{u}$ and equals $t_0 - R(t_0)$. Likewise, outgoing waves with such large values of $\widetilde{u}$ all pile up at the vicinity of $\widetilde{v} = \widetilde{v}_0$ when traced back in time. This implies that a narrow range of values for V and $\widetilde{v}$ covers a large area of $\mathcal{J}_R^+$. Therefore, if U and V do not vary too much when $\widetilde{u} \to +\infty$, we can assume that $A(U, V)$ is approximately constant in equation (52b) and integrate it:

$$V = \frac{A[\dot{R}(t_0) - 1]}{2\,\dot{R}(t_0)}\,(\widetilde{v}_0 - \widetilde{v}) + t_0 - R(t_0). \tag{58}$$

The integration constant in the previous expression has been found by taking the limit $\widetilde{v} \to \widetilde{v}_0$, which should correspond to $\widetilde{u} \to +\infty$. Inserting expression (58) in equation (56), then using the continuity condition $U = V$ at $r = 0$, we obtain

$$\widetilde{u} = -\kappa^{-1}\,\ln\left(\frac{\widetilde{v}_0 - \widetilde{v}}{\widetilde{A}}\right), \quad \text{as} \quad \widetilde{v} \to \widetilde{v}_0, \quad \widetilde{v} < \widetilde{v}_0, \tag{59}$$

with $\widetilde{A} = A[\dot{R}(t_0) - 1]/(2\,\dot{R}(t_0))$.

A glance at equation (31) confirms the high similarity between the gravitational collapse and the moving mirror problem. This lies on the

16 Using $U = t - R(t)$ at the surface of the collapsing body and making a Taylor expansion of C around t_0.

fact that the above analysis is based on geometric optics. Therefore, the Doppler shift acquired after the reflection on the surface of the mirror is equivalent to the effects of distortion in the background geometry during the gravitational collapse.

In addition, we have treated the case of a massless scalar field propagating in the Schwarzschild spacetime, but the above results can be derived in a more general framework for any quantum field in a black hole spacetime [25].

Then, from expression (59), we find that natural *outgoing* positive modes of energy $\hbar\,\omega > 0$ for an observer whose world line would be the black dashed curve in Figure 12 are

$$\bar{\phi}_\omega = \frac{i}{\sqrt{4\pi\omega}}\left(e^{i\omega\,\kappa^{-1}\,\ln[(\widetilde{v}_0-\widetilde{v})/\widetilde{A}]} - e^{-i\omega\widetilde{u}}\right), \quad \widetilde{v} < \widetilde{v}_0. \tag{60}$$

This positive mode is actually a superposition of *ingoing* positive and negative energy modes ϕ_ω and $\phi^\star_\omega$ [see expression (19)] given by

$$\phi_\omega = \frac{i}{\sqrt{4\pi\omega}}\left(e^{-i\omega\widetilde{v}} - e^{-i\omega\,(\widetilde{v}_0-\widetilde{A}\,e^{-\kappa\,\widetilde{u}})}\right). \tag{61}$$

Again, this is precisely this mixing of positive and negative energies which will lead to spontaneous emission. Indeed, using directly the results found in Section 2.1.1, we can compute the matrices coefficients (21) and arrive to the expected number of particles spontaneously emitted from vacuum [see equation (35), and also (34)]:

$$\langle 0|\bar{N}_\omega|0\rangle \propto \frac{1}{e^{\hbar\,\omega/k_{\rm B}T_{\rm H}}-1}, \tag{62}$$

where $T_{\rm H}$ is the so-called *Hawking temperature*,

$$T_{\rm H} = \frac{\hbar\,\kappa}{k_{\rm B}\,2\pi\,c}, \quad \kappa = \frac{c^4}{4G\,m}. \qquad \text{(with the right units)} \tag{63}$$

Expression (62) is nothing but the the so-called Hawking radiation emitted by black holes.

Let us conclude this section with some remarks. In the above calculations we assume that $\widetilde{u} \to +\infty$. This means that we have computed the expected flux of particles at late time. For an observer outside the black hole, this steady flux would be seen as emerging from the event horizon and would correspond to a thermal radiation of temperature $T_{\rm H}$. We note that the Hawking temperature is proportional to the surface gravity κ, and thus depends on the spacetime curvature at the vicinity of the horizon [see expression (55)]. As we will show below, the analogue Hawking temperature in the context of analogue gravity will be also proportional to a quantity that measures the "curvature" of the fluid flow near the acoustic horizon.

Moreover, it was proved that this positive energy flux converging to $\mathcal{J}^+_R$ should be balanced by a negative energy flux entering the black hole [88, 190]. Wald actually showed that particles are created by pair,

one of positive energy should travel towards $\mathcal{J}_R^+$ (and corresponds to a null ray $\widetilde{v}_{\rm pos} < \widetilde{v}_0$), and the other one, of negative energy, should be absorbed by the black hole (and actually correspond to the symmetric of $\widetilde{v}_{\rm pos}$ with respect to $\widetilde{v}_0$, i.e., $\widetilde{v}_{\rm neg} = 2\widetilde{v}_0 - \widetilde{v}_{\rm pos} > \widetilde{v}_0$) [190]; Both particles of opposite energy form what we call a *Hawking pair*.

As a last comment, we can estimate the expected Hawking temperature for typical black holes of mass $M \simeq 10\, M_\circ$, where $M_\circ$ is the mass of the sun. Expression (63) can be indeed approximated to

$$T_{\rm H} \simeq 10^{-6}\, \frac{M_\circ}{M}\, {\rm K}, \tag{64}$$

meaning that the Hawking temperature is about a μK, thus completely lost in the Cosmological Microwave Background.

2.2 ANALOGUE GRAVITY

The event horizon of a black hole can be seen as a point of no return: anything that crosses the horizon is trapped inside the black hole, cannot come back to our universe and is bound to propagate until it reaches the singularity.

In the general introduction we have compared a black hole to a river flowing towards a waterfall. Imagine that some fish are traveling in the river trying to go upstream the flow. Fish close to the waterfall are not able to swim up the river and are bound to fall down to the bottom of the waterfall, playing here the role of the black hole singularity. Therefore, the point where the flow velocity equals the velocity of the fish could be seen as the equivalent of the event horizon: beyond that point fish are trapped, see Figure 4 of the general introduction.

This idea of comparing black holes to hydrodynamic systems might seem rather naive at this stage; however, as we will see in this section, the similarity between analogue systems and black holes goes beyond the kinematic analogy discussed in the previous paragraph.

In the following, we will not consider fish in a river but rather sound waves propagating in a transonic flow, see Figure 14. We will first prove that the hydrodynamic equations for sound waves correspond to the wave equation of a massless scalar field in a curved spacetime. Then, using the seminal result obtained by Unruh in 1981 [182], we will show that an analogous Hawking radiation can be defined in analogue systems.

2.2.1 *Sound waves in curved spacetime*

Let us start with the usual inviscid hydrodynamic equations

$$\partial_t \rho + \nabla(\rho\, \mathbf{v}) = 0, \tag{65a}$$

$$\partial_t \mathbf{v} + (\mathbf{v}\cdot\nabla)\, \mathbf{v} = -\frac{1}{\rho}\nabla p, \tag{65b}$$

$$p = p(\rho), \tag{65c}$$

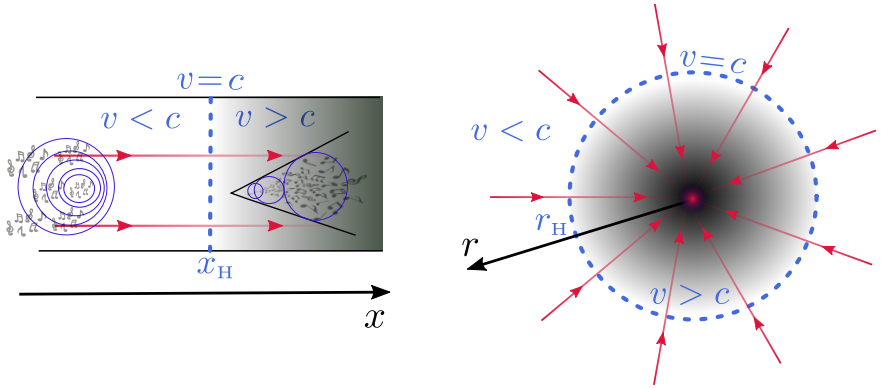

FIGURE 14: Different configurations of transonic flows.
(Left) One-dimensional flow such as considered in Chapter 3. The fluid moves from the left to the right. The subsonic region corresponds to the left part where $v < c$; then, the flow becomes supersonic ($v > c$) in the right region. The boundary between these two regions corresponds the blue dashed line (at $x = x_{\rm H}$) and plays the role of an acoustic horizon for sound waves. Indeed, a sound wave propagating in the supersonic region is dragged by the flow and forms a Cerenkov cone as shown in the figure. The supersonic region is the analogue of the interior of a black hole. On the contrary, a sound wave in the subsonic region can propagate in all directions.
(Right) Two-dimensional case with a spherical symmetry and where the flow velocity is only radial – this is the situation considered in Unruh's paper [182] and in this subsection. The blue dashed line located at a radius $r_{\rm H}$ corresponds to the acoustic horizon, beyond which sound waves are trapped.

where $\rho(\mathbf{r},t)$ is the fluid density, $\mathbf{v}(\mathbf{r},t)$ the flow velocity and $p(\mathbf{r},t)$ the pressure. We also assume that the flow is irrotational; we can thus define a scalar field $\psi(\mathbf{r},t)$ such that

$$\mathbf{v} = \nabla\psi. \tag{66}$$

We are interested in the small fluctuations around the background flow. We thus expand the physical quantities up to first order:

$$\begin{pmatrix}\psi(\mathbf{r},t)\\ \rho(\mathbf{r},t)\\ p(\mathbf{r},t)\end{pmatrix} = \begin{pmatrix}\psi_0(\mathbf{r},t)\\ \rho_0(\mathbf{r},t)\\ p_0(\mathbf{r},t)\end{pmatrix} + \varepsilon \begin{pmatrix}\psi_1(\mathbf{r},t)\\ \rho_1(\mathbf{r},t)\\ p_1(\mathbf{r},t)\end{pmatrix}, \tag{67}$$

where (ψ_0,ρ_0,p_0) is an exact solution of the set of equations (65) and ε is a small parameter. Then, we linearize the hydrodynamic equations at first order[17]. We find for equation (65a):

$$\partial_t\rho_1 + \nabla\cdot(\rho_0\nabla\psi_1 + \rho_1\nabla\rho_0) = 0 \tag{68}$$

17 Note that this is exactly what we will do in Chapter 3 in the context of Bose-Einstein condensates, see in particular the hydrodynamic equations (121) and the linearized version (123).

A linearization of equation (65c) leads to

$$p_1 = c^2(\rho_0)\,\rho_1, \quad \text{with} \quad c^2(\rho_0) = \frac{\mathrm{d}p}{\mathrm{d}\rho}(\rho_0), \tag{69}$$

with $c(\rho_0)$ the background sound velocity. Moreover, equation (65b) becomes at first order [109]

$$\rho_0(\partial_t\psi_1 + \nabla\psi_0 \cdot \nabla\psi_1) = -p_1. \tag{70}$$

Then, using together expressions (68), (69) and (70), we obtain

$$\partial_t\left[\frac{\rho_0}{c^2}(\partial_t\psi_1 + \mathbf{v}_0 \cdot \nabla\psi_1)\right] = \nabla \cdot \left[\rho_0\nabla\psi_1 - \frac{\rho_0}{c^2}(\partial_t\psi_1 + \mathbf{v}_0 \cdot \nabla\psi_1)\mathbf{v}_0\right], \tag{71}$$

where we have introduced $\mathbf{v}_0 = \nabla\psi_0$. Note that if $\mathbf{v}_0 = 0$, provided that the background density ρ_0 is constant (which leads to a constant sound velocity $c(\rho_0)$ along the fluid flow), expression (71) reduces to the wave equation (2), i.e., the wave equation for a massless scalar field in Minkowski spacetime.

CURVED SPACETIME METRIC The situation is more interesting when $\mathbf{v}_0 \neq 0$. Let us write expression (71) with Einstein notations, such that for example

$$\partial_t\left(\frac{\rho_0}{c^2}\mathbf{v}_0 \cdot \nabla\psi_1\right) = \partial_0\left(\frac{\rho_0}{c^2}\mathbf{v}_0^j\,\partial_j\psi_1\right), \tag{72}$$

where the subscript 0 corresponds to the time coordinate t and $j \in \{1,2,3\}$ stands for space coordinates x, y, z. Equation (71) then reads

$$\begin{aligned}&\partial_0\left(\frac{\rho_0}{c^2}\partial_0\psi_1\right) + \partial_0\left(\frac{\rho_0}{c^2}\mathbf{v}_0^j\,\partial_j\psi_1\right)\\ &\quad + \partial_j\left(\frac{\rho_0}{c^2}\,\mathbf{v}_0^j\partial_0\psi_1\right) + \partial_i\left(\frac{\rho_0\mathbf{v}_0^i\,\mathbf{v}_0^j - \rho_0\,c^2\delta^i_j}{c^2}\,\partial_j\psi_1\right) = 0.\end{aligned} \tag{73}$$

We would like now to identify the previous expression with the wave equation in curved spacetime (39). By defining

$$g^{\mu\nu} = \frac{1}{c\,\rho_0}\begin{pmatrix}1 & \mathbf{v}_0^j\\ \mathbf{v}_0^i & \mathbf{v}_0^i\,\mathbf{v}_0^j - c^2\delta^{ij}\end{pmatrix}, \quad \sqrt{-g} = (-\det g^{\mu\nu})^{-1} = \frac{\rho_0^2}{c}, \tag{74}$$

Expression (73) becomes

$$\partial_\mu(\sqrt{-g}\,g^{\mu\nu}\partial_\nu\psi_1) = 0. \tag{75}$$

Then, by multiplying the last equation by $1/\sqrt{-g}$, we obtain the expected wave equation of a massless scalar field in a curved spacetime

$$\nabla_\mu\,\nabla^\mu\psi_1 = \frac{1}{\sqrt{-g}}\,\partial_\mu(\sqrt{-g}\,g^{\mu\nu}\,\partial_\nu\psi_1) = 0, \tag{76}$$

whose metric tensor is

$$g_{\mu\nu} = \frac{\rho}{c}\begin{pmatrix} c^2 - \mathbf{v}_0^2 & (\mathbf{v}_0)_j \\ (\mathbf{v}_0)_i & -\delta_{ij} \end{pmatrix}. \tag{77}$$

The inverse metric tensor is given by expression (74). From equation (77), it is easy to prove that the line element in this spacetime is given by

$$\begin{aligned} \mathrm{d}s^2 &= g_{\mu\nu}\,\mathrm{d}x^\mu\,\mathrm{d}x^\nu \\ &= \frac{\rho_0}{c}[c^2\,\mathrm{d}t^2 - (\mathbf{v}_0^i\mathrm{d}t - \mathrm{d}x^i)\delta_{ij}(\mathbf{v}_0^j\mathrm{d}t - \mathrm{d}x^j)]. \end{aligned} \tag{78}$$

We can already guess from the form of the metric tensor (77) the intrinsic connection between black holes and transonic flows. First, if $\mathbf{v}_0 = 0$, we find the metric associated to a Minkowski spacetime $(+,-,-,-)$; this is what we already noticed in the last paragraph.

Now, if $\mathbf{v}_0 \neq 0$ and the flow becomes supersonic ($|\mathbf{v}_0| > c$) in a certain region, g_{00} becomes negative, exactly as it occurs for a Schwarzschild metric when r becomes lower than the Schwarzschild radius $2\,m$, see equation (40).

Thus, let us take the math a step further and show the full analogy between the metric (77) and the Schwarzschild metric (40). In polar coordinates (r,θ,φ) the metric (77) becomes

$$g_{\mu\nu} = \frac{\rho}{c}\begin{pmatrix} c^2 - \mathbf{v}_0^2 & \mathbf{v}_{0,r} & \mathbf{v}_{0,\theta} & \mathbf{v}_{0,\varphi} \\ \mathbf{v}_{0,r} & -1 & 0 & 0 \\ \mathbf{v}_{0,\theta} & 0 & -r^2 & 0 \\ \mathbf{v}_{0,\varphi} & 0 & 0 & -r^2\,\sin\theta \end{pmatrix}. \tag{79}$$

Then, if $\mathbf{v}_0$ is only radial (see e.g., the right drawing of Figure 14), i.e., $\mathbf{v}_{0,\theta} = \mathbf{v}_{0,\varphi} = 0$, the line element (78) becomes

$$\mathrm{d}s^2 = \frac{\rho_0}{c}[c^2\mathrm{d}t^2 - (\mathbf{v}_{0,r}\mathrm{d}t - \mathrm{d}r)^2 - r^2(\mathrm{d}\theta^2 + \sin^2\theta\mathrm{d}\varphi^2)]. \tag{80}$$

In this coordinates system, this line element exactly corresponds to the so-called *Painlevé -Gullstrand line element* [80, 140]. By making the following change of variable[18]

$$\tau = t + \int^r \frac{\mathbf{v}_{0,r}}{c^2 - \mathbf{v}_{0,r}^2}\,\mathrm{d}r', \tag{81}$$

we obtain

$$\mathrm{d}s^2 = \frac{\rho_0}{c}\left[\left(1 - \frac{\mathbf{v}_{0,r}^2}{c^2}\right)c^2\mathrm{d}\tau^2 - \left(1 - \frac{\mathbf{v}_{0,r}^2}{c^2}\right)^{-1}\mathrm{d}r^2 - r^2\,\mathrm{d}\Omega^2\right], \tag{82}$$

with $\mathrm{d}\Omega^2 = \mathrm{d}\theta^2 + \sin^2\theta\mathrm{d}\varphi^2$. We can already see the similarity with the Schwarzschild line element here. Let us now consider a transonic flow with radial velocity

$$\mathbf{v}_{0,r} = -c\sqrt{\frac{r_{\mathrm{H}}}{r}}, \tag{83}$$

18 Note that τ can be understood as a time coordinate only if $|\mathbf{v}_{0,r}| \ll c$.

where we assume that c is constant. Since $c > 0$, the minus sign in the previous expression ensures that the velocity is directed towards the center $r = 0$. Such a velocity splits the flow in two regions: for $r > r_{\rm H}$ the flow is subsonic ($|\mathbf{v}_{0,r}| < c$); for $r < r_{\rm H}$ the flow is supersonic ($|\mathbf{v}_{0,r}| > c$). The line element (82) becomes

$$\mathrm{d}s^2 = \frac{\rho_0}{c}\left[\left(1-\frac{r_{\rm H}^2}{r^2}\right)c^2\mathrm{d}\tau^2 - \left(1-\frac{r_{\rm H}^2}{r^2}\right)^{-1}\mathrm{d}r^2 - r^2\,\mathrm{d}\Omega^2\right], \tag{84}$$

and is conformally equivalent to the Schwarzschild metric (40), where $r_{\rm H}$ plays the role of the Schwarzschild radius. In our case, $r_{\rm H}$ is called *acoustic horizon*. In addition, if we define

$$C(r) = \frac{c^2 - \mathbf{v}_{0,r}^2}{c^2}, \quad r^\star = \int^r [C(r')]^{-1}\,\mathrm{d}r', \tag{85}$$

and

$$\widetilde{u} = \tau - r^\star/c, \quad \widetilde{v} = \tau + r^\star/c, \tag{86}$$

equation (82) becomes

$$\mathrm{d}s^2 = \rho_0(r)\,(c^2 - \mathbf{v}_{0,r}^2)\,\mathrm{d}\widetilde{u}\,\mathrm{d}\widetilde{v}, \tag{87}$$

where we dropped the angular part. Note the similarity between expressions (87) and (44). The structure of spacetime is exactly the same: the acoustic horizon splits the spacetime in two regions (subsonic and supersonic), each of them being conformally flat, but disconnected at the horizon [117, 158].

Note that using expression (81) in equations (86), we obtain

$$\widetilde{u} = t - \int^r \frac{\mathrm{d}r'}{c + \mathbf{v}_{0,r}(r')}, \quad \widetilde{v} = t + \int^r \frac{\mathrm{d}r'}{c - \mathbf{v}_{0,r}(r')}, \tag{88}$$

in agreement with Ref. [158]. Note also that here we assume that the sound velocity c is constant and absolute[19] – the latter assumption will not be true in the presence of dispersion, see e.g., Chapter 3.

Then, one can prove that the field ψ_1, solution of the wave equation (76), is also solution of [25]

$$\frac{\partial^2\psi_1}{\partial\widetilde{u}\,\partial\widetilde{v}} = 0. \tag{89}$$

In addition, if we define

$$k_{\widetilde{u}} = \frac{\omega}{c + \mathbf{v}_{0,r}}, \quad k_{\widetilde{v}} = -\frac{\omega}{c - \mathbf{v}_{0,r}}, \tag{90}$$

one finds

$$\begin{cases} \psi_1 \propto e^{\pm i\omega\widetilde{u}} = e^{\pm i(\omega t - \int^r k_{\widetilde{u}}(r')\mathrm{d}r')}, \\ \psi_1 \propto e^{\pm i\omega\widetilde{v}} = e^{\pm i(\omega t - \int^r k_{\widetilde{v}}(r')\mathrm{d}r')}, \end{cases} \tag{91}$$

19 In the sense that any sound wave propagates at the sound velocity, independently of its frequency or wavenumber; in other words we consider here a dispersionless theory.

with

$$\omega - \mathbf{v}_{0,r}\, k_{\widetilde{u}} = c\, k_{\widetilde{u}}, \quad \omega - \mathbf{v}_{0,r}\, k_{\widetilde{v}} = -c\, k_{\widetilde{v}}. \tag{92}$$

Therefore, a fixed frequency ω in the laboratory frame is related to the co-moving frequency $\omega_{\rm cm} = \omega - \mathbf{v}_{0,r}\, k$ via a Doppler shift. Then, the $\widetilde{u}$-modes correspond to $\omega_{\rm cm} = ck$ and the $\widetilde{v}$-modes to $\omega_{\rm cm} = -ck$. We also introduce the scalar product [158] [similar to expression (6)]:

$$(\psi_1, \psi_2) = -i \int_{\mathbb{R}} [\psi_1\, \partial_\eta \psi_2^\star - \partial_\eta \psi_1\, \psi_2^\star]\, \mathrm{d}r, \tag{93}$$

where $\partial_\eta = \partial_t + \mathbf{v}_{0,r}\partial_r$ is the partial derivative with respect to time in the co-moving frame.

2.2.2 *Analogue Hawking radiation*

Let us now turn our attention to the existence of an analogous Hawking radiation using what we have learned from the previous subsection.

Suppose first that the flow is subsonic or supersonic everywhere – in this case, the radial velocity is not given by expression (83). For simplicity, we assume that the radial velocity is constant $\mathbf{v}_{0,r} = V_r$, with $|V_r| < c$ in a subsonic flow and $|V_r| > c$ in a supersonic flow. Solutions of the wave equation (89) are

$$\psi_1^\omega \propto e^{\pm i\omega(t - \frac{r - r_{\rm H}}{c + V_r})}, \quad \text{or} \quad \psi_1^\omega \propto e^{\pm i\omega(t + \frac{r - r_{\rm H}}{c - V_r})}, \tag{94}$$

where $r_{\rm H}$ is just for the moment an integration constant used to compute integrals (88). Let us introduce the coordinates pertaining to the co-moving frame

$$\eta = t, \quad \xi = r - r_{\rm H} - V_r\, t. \tag{95}$$

Solutions (94) can be then recast in the form

$$\psi_{1,\rightarrow}^\omega \propto e^{\pm i\omega_{cm}(\eta - \xi/c)}, \quad \text{or} \quad \psi_{1,\leftarrow}^\omega \propto e^{\pm i\omega_{cm}(\eta + \xi/c)}, \tag{96}$$

and correspond to the right- (with the subscript $\rightarrow$) and left-moving modes (with the subscript $\leftarrow$) with respect to the co-moving frame. We recall that ω_{cm} is the co-moving frequency. Using the scalar product (93), it is easy to prove that the positive frequency modes in the subsonic region correspond to $\exp[-i\omega_{cm}(\eta \pm \xi/c)]$, while in the supersonic region they are $\exp[i\omega_{cm}(\eta \pm \xi/c)]$.

On the contrary, if the flow now becomes transonic[20] at a certain position $r_{\rm H}$, the subsonic and the supersonic regions are disconnected. Indeed, one sees from equations (88) that the variable $\widetilde{u}$ is ill-defined at

20 Note that the radial velocity is not necessarily given by (83) – the only requirement lies in the existence of a position $r_{\rm H}$ dividing the flow in a subsonic and a supersonic region.

the acoustic horizon. Approximating the flow velocity near the acoustic horizon by $\mathbf{v}_{0,r} \simeq -c + \alpha(r - r_{\mathrm{H}})$, we obtain

$$\widetilde{u} \simeq t - \frac{1}{\alpha} \ln\left(\frac{\alpha}{c}|r - r_{\mathrm{H}}|\right), \quad \alpha = \left.\frac{\mathrm{d}\mathbf{v}_{0,r}}{\mathrm{d}r}\right|_{r_{\mathrm{H}}} > 0, \tag{97}$$

which diverges when $r \to r_{\mathrm{H}}$. As shown in Figure 15, we need to define two variables $\widetilde{u}_{\mathrm{sub}}$ and $\widetilde{u}_{\mathrm{super}}$, each of them going from $-\infty$ to $+\infty$ and spanning the subsonic and the supersonic region, respectively. However these two parameters are totally disconnected between each other. Indeed, let us imagine the point of view of an observer living in the subsonic region and detecting a sound wave $\exp(-i\omega\widetilde{u}_{\mathrm{sub}})$ with $\widetilde{u}_{\mathrm{sub}} =$ Constant at a certain time t. When traced back in time, this wave packet would seem to originate infinitely close to the acoustic horizon, but would be still located in the subsonic region, so that no event occurring in the supersonic region could be witnessed by the observer in the subsonic part, see Figure 15. This figure can also be compared with Figure 10.

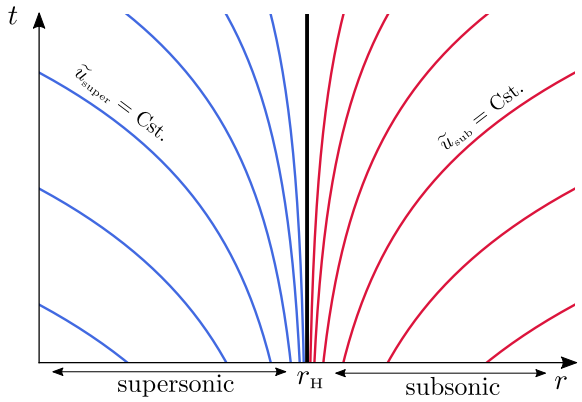

FIGURE 15: Trajectories of sound waves near the acoustic horizon located at $r = r_{\mathrm{H}}$, see equation (97). The subsonic and the supersonic regions are completely disconnected by the presence of the horizon. Any left-moving (right-moving) wave in the supersonic (subsonic) region has emerged infinitely close to the acoustic horizon in the asymptotic past. This figure can be compared with Figure 10.

The form of equation (97) is very similar to expressions (31) and (56) in the case of the moving mirror problem and the gravitational collapse – where α plays the role of the surface gravity κ. If we assume that in the asymptotic past the flow were subsonic everywhere, a right moving mode would be given by the simple expression (96) – this is what we call an *ingoing* mode. Then, if at a certain time the flow becomes transonic, the right moving modes in the subsonic part would be given in terms of the complicated function (97) near the acoustic horizon – we call them *outgoing* modes.

Exactly like the gravitational collapse and the moving mirror problems, the *ingoing modes* can be written as a sum of positive and nega-

tive frequency *outgoing* modes through a Bogoliubov transformation[21] of the form (19). Therefore, this mixing of positive and negative energy modes will lead to spontaneous creation of particles from vacuum if one quantizes the sound field as done by Unruh in 1981 [182]. He found that a thermal spectrum should be emitted from the acoustic horizon with temperature

$$T_{\mathrm{H}}^{\mathrm{analogue}} = \frac{\hbar\alpha}{2\pi k_{\mathrm{B}}}, \quad \alpha = \left.\frac{\mathrm{d}\mathbf{v}_{0,r}}{\mathrm{d}r}\right|_{r_{\mathrm{H}}}, \tag{98}$$

i.e., the analogous version of expression (63). In the case of analogue gravity, the analogous Hawking temperature depends on how fast is the transition from the subsonic to the supersonic region through the parameter α. In analogy to the surface gravity, this measures the "curvature" of the flow near the sonic horizon.

To conclude, we hope that we convinced the reader of the strong analogy between transonic flows and black holes. Unruh proved that analogue systems indeed give rise to spontaneous emission of particles. However, quantum fluctuations leading to analogue Hawking radiation are too small to be detected in classical platforms[22]. This is the reason why we will now turn our attention to quantum fluids – one-dimensional flow of Bose-Einstein condensates, where the (analogue) spontaneous Hawking radiation can be explored. This is what we discuss in the next chapter.

21 We do not detail this transformation here because we will discuss them later in the context of analogue gravity, see Chapter 4. Let us just mention that this mixing of positive and negative frequencies results from a problem of analyticity of expression (97) when crossing the acoustic horizon r_{H} from the subsonic to the supersonic region. This is similar to the problem encountered in Rindler space [25] where two regions of spacetime are also disconnected. Likewise, this is nicely discussed and detailed in the context of analogue gravity in Ref. [158].

22 Despite this fact, classical systems such as surface water experiments [59, 61, 159, 192] are still very exciting; for instance, one can use an external perturbation to create stimulated Hawking radiation.

3

HAWKING RADIATION IN BOSE-EINSTEIN CONDENSATES

Garay *et al* [71] were the first to propose the use of Bose-Einstein condensates (BECs) as acoustic analogues, followed by many others [18–21, 63, 76, 104, 164, 199, 202] in the last two decades. BECs are indeed excellent candidates to explore Hawking radiation in analogue systems for the following reasons:

First, the theory of Bose-Einstein condensation is well-established [148, 153]. This is an uncontested advantage for studying quantum fluctuations emerging in the condensate. Based on a Bogoliubov approach, a theoretical treatment of these fluctuations for one-dimensional flows of BECs was first suggested by Leonhardt *et al* in Refs. [115, 116].

In addition, BECs provide an excellent platform to explore the effect of these fluctuations on the condensate itself, the so-called backreaction. This might bring new perspectives in General Relativity, a theory which is not unequivocal when quantum effects are taken into account. This program exceeds the scope of this thesis, but we hope that a theoretical analysis of the backreaction problem for sonic black holes in BECs will be proposed in the future.

Second, BECs are quantum systems. Contrary to classical analogues, for which Hawking radiation can only result from a disturbance external to the system [59, 60, 159, 160], here, the analogous Hawking radiation may originate from quantum fluctuations in the system. Quasiparticles are spontaneously emitted from the acoustic horizon and propagate in opposite direction, exactly as it would occur at the vicinity of a gravitational black hole event horizon (see Section 3.2.1 and Figure 21). This gives rise to correlated and entangled currents emitted outside and inside the acoustic black hole.

This correlated signals can be identified and measured by means of the density-density correlation function. This was first proposed in 2008 by a collaboration between teams from Bologna and Trento [15]. Contrary to gravitational black holes, information can be extracted from the interior of a sonic black hole; it is then possible to measure experimentally the density correlations in the supersonic region. Likewise, density correlations are much less affected by thermal noise than a direct measurement of the Hawking effect (see, for instance, Section 3.2.5 and [156]).

Motivated by this promising idea, theoretical predictions for specific configurations of one-dimensional acoustic black holes in BECs have been obtained in Refs. [110, 124, 156]. One of these configurations was realistic enough to be implemented experimentally in 2010 by the

Technion Group [105]. A first measurement of density correlations was achieved in 2016 [177]. After several technical improvements of the experimental setup, a much less noisy measurement was performed in 2019 [131]. The theoretical results obtained during this PhD compare very well with experimental data of Ref. [131]. Therefore, we are able to conclude from this analysis that the Technion Group obtained a clear signature of Hawking radiation in a Bose-Einstein condensate, almost forty years after Unruh's suggestion to use hydrodynamic analogues of black holes [182].

In this chapter, we will first explain how a sonic horizon can be realized in a Bose-Einstein condensate. We will also discuss two specific configurations and the experimental realization of one of them. This will conclude Section 3.1.

Then, in Section 3.2, we will provide a detailed theoretical analysis of quantum fluctuations, within a Bogoliubov approach. The specificity of this thesis is to improve the theoretical treatment previously used in the field by taking into account the zero modes.

By means of this well-founded theory, we are able to reproduce with a nice accuracy the experimental results recently published by the Technion Group in Ref. [131]. Finally, although we confirm that the experimental determination of the Hawking temperature is reliable, we challenge some claims of Refs. [131, 177] in Section 3.3.

3.1 REALIZATION OF AN ACOUSTIC HORIZON IN A BOSE-EINSTEIN CONDENSATE

3.1.1 *The Gross-Pitaevskii equation*

The many body Hamiltonian describing N interacting bosons in the presence of an external potential V_{ext} is given, in second quantization, by [45, 106, 153]

$$\hat{H} = \int dr\, \hat{\Phi}^\dagger \left[-\frac{\hbar^2}{2\,m}\nabla^2 + V_{\text{ext}} + \frac{g_{3\text{D}}\,\hat{n}}{2} \right] \hat{\Phi}, \tag{99}$$

where $\hat{\Phi}(r,\,t) = \exp(i\,\hat{H}\,t/\hbar)\hat{\Phi}(r)\,\exp(-i\,\hat{H}\,t/\hbar)$ is the field operator in the Heisenberg representation, m the mass of the bosons, $\hat{n} = \hat{\Phi}^\dagger\hat{\Phi}$ the density operator and $g_{3\text{D}}$ is the coupling constant.

The time evolution of the field operator $\hat{\Phi}(r,\,t)$ is

$$\begin{aligned} i\,\hbar\partial_t\hat{\Phi}(r,\,t) &= [\hat{\Phi},\,\hat{H}] \\ &= -\frac{\hbar^2}{2\,m}\nabla^2\hat{\Phi}(r,\,t) + [V_{\text{ext}}(r) + g_{3\text{D}}\,\hat{n}]\,\hat{\Phi}(r,\,t). \end{aligned} \tag{100}$$

We recall that the form of the Hamiltonian (99) corresponds to an effective interaction between the particles $V_{\text{eff}}(r - r') = g_{3\text{D}}\,\delta(r - r')$ characterized by a single parameter $g_{3\text{D}}$. The coupling constant $g_{3\text{D}}$ and

the s-wave scattering length a are related through the relation [148, 153]

$$g_{3D} = \frac{4\pi\hbar^2 a}{m}. \tag{101}$$

This means that the details of the interaction potential, i.e., at the microscopic level, are ignored; only the scattering length a characterizes the effects of the interaction on the gas on a macroscopic scale[1]. Therefore, if we denote n_{3D} the density of the gas and d the interparticle distance, the use of this effective potential will be legitimate only if the condition

$$a \ll d = n_{3D}^{-1/3} \tag{102}$$

For ^{87}Rb, $a = 5.77$ nm [27]. With $n_{3D} \sim 10^{14}\ cm^{-3}$, $a^3\, n_{3D} < 10^{-3}$.

is fulfilled [153]. In this case, the system is said to be *dilute* or *weakly interacting*. We will always consider this mean-field regime in the following.

Bose-Einstein condensation occurs when the temperature is low enough and when there is a macroscopic occupation of the lowest energy state, i.e., when the number of atoms in this state becomes very large. In this case, the Bogoliubov approach [28] consists in writing

$$\hat{\Phi}(r,\, t) = \Phi(r,\, t) + \delta\hat{\phi}(r, t), \tag{103}$$

where $\Phi(r,\, t)$ is a classical field, called the order parameter of the condensate and $\delta\hat{\phi}(r, t)$ is a quantum correction which describes the quantum fluctuations of the interacting Bose gas. The condensate density is given by $n(r,\, t) = |\Phi(r,\, t)|^2$, while the density operator still reads $\hat{n} = |\hat{\Phi}|^2$.

Within this Bogoliubov approach, one needs to work in the grand canonical ensemble since the number of particles in the condensate fluctuates [37]. We will explain this point in more detail in Section 3.2 with the addition of zero modes in the theory. Therefore, in the following, instead of the Hamiltonian (99), we shall consider $\hat{H}_{GC} = \hat{H} - \mu\,\hat{N}$, where μ is the chemical potential and $\hat{N} = \int dr\,\hat{n}$ is the number of particles. Inserting decomposition (103) in equation (100) leads, at zero order, to the well-known time-dependent Gross-Pitaevskii equation [78, 152]:

$$i\,\hbar\partial_t\Psi(r,\, t) = -\frac{\hbar^2}{2\,m}\nabla^2\Psi(r,\, t) + [V_{ext}(r) + g_{3D}\,\hat{n} - \mu]\,\Psi(r,\, t), \tag{104}$$

with $\Psi(r,\, t) = \Phi(r,\, t)\,\exp(i\,\mu\,t/\hbar)$.

3.1.2 *One-dimensional flow of Bose-Einstein condensates*

We consider a quasi one-dimensional Bose-Einstein condensate: the gas is elongated in the longitudinal direction x and radially confined by

1 In this thesis, we will only consider repulsive interactions, i.e., when $a > 0$ and $g_{3D} > 0$.

a strong harmonic potential $V_\perp(r_\perp) = m\,\omega_\perp^2\,r_\perp^2/2$ of frequency $\omega_\perp$. A schematic view and an experimental realization of a quasi-1D Bose-Einstein condensate are shown in Figure 16.

We consider the possibility of adding a longitudinal external potential $U(x)$. Its importance and its precise form will be discussed in Section 3.1.3.

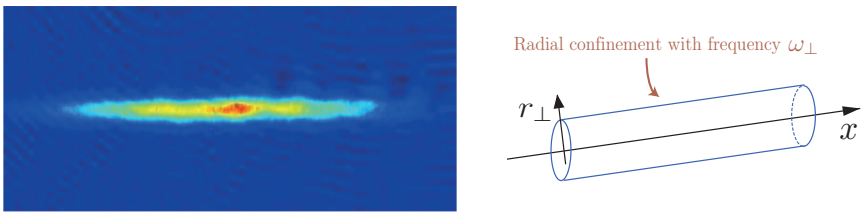

FIGURE 16: (Left) Experimental realization of an elongated Bose-Einstein condensate [79]. (Right) Schematic view of a quasi one-dimensional Bose-Einstein condensate, whith x the longitudinal coordinate and $r_\perp$ the radial coordinate.

One uses the following Ansatz to describe the condensate wave function: $\Psi(r,\,t) = \psi(x,t)\,\varphi_\perp(r_\perp;\,n)$, where $n(x,t) = \int dr_\perp |\Psi|^2 = |\psi(x,t)|^2$ [95, 113]. The Gross-Pitaevskii equation (104) becomes [153]

$$i\,\hbar\partial_t\psi(x,t) = -\frac{\hbar^2}{2\,m}\partial_{xx}\psi(x,t) + \left[U(x) + g\,|\psi(x,t)|^2 - \mu\right]\psi(x,t), \quad (105)$$

where $g = 2\,\hbar\,\omega_\perp\,a$ [135] is an effective one-dimensional nonlinear coupling constant.

1D MEAN-FIELD REGIME The validity of equation (105) relies on several conditions. As mentioned in the previous section, the total number of atoms should be large and the temperature low enough to reach the condensed phase. Moreover, even at zero temperature, one needs to respect the following inequalities

$$\left(\frac{a}{a_\perp}\right)^2 \ll n\,a \ll 1, \quad (106)$$

where a is the scattering length and $a_\perp = \sqrt{\hbar/\omega_\perp\,m}$ is the harmonic oscillator length.

The left inequality ensures that the transverse dimension of the cloud should be sufficiently large with respect to the scattering length a to avoid the *Tonks-Girardeau regime*. This condition is equivalent to requiring $\xi \gg d$ [153], where $d = n^{-1}$ is the one-dimensional inter-particle distance and $\xi = \hbar/\sqrt{m\,g\,n}$ is the healing length [45], i.e., the typical length scale on which the interaction energy balances quantum pressure [the kinetic term in equation (105)]. Say differently, if this condition is not satisfied, the mean-field regime is no longer valid.

The right inequality ensures that the 1D dynamics does not triggers excitations of the transverse degrees of freedom to avoid the 3D-like *transverse Thomas-Fermi regime*.

A last important remark at this point: note that a one-dimensional Bose-Einstein condensate cannot exist due to the absence of long-range order[2] [130, 154]. However, a quasi-condensed phase can be reached with a large occupation number of the ground state.

STATIONARY AND TRANSONIC FLOW Let us now consider a quasi one-dimensional condensate moving from the left to right (in the positive x direction) at some velocity V. Moreover, the flow is taken stationary, meaning that the condensate wave function ψ does not depend on time. Thus, in the following, we will only consider the stationary Gross-Pitaevskii equation

$$\mu\,\psi(x) = -\frac{\hbar^2}{2\,m}\partial_{xx}\psi(x) + [U(x) + g\,n(x)]\,\psi(x), \tag{108}$$

The previous equation describes the background density. Then, density fluctuations around this background may appear in the condensate. These elementary excitations emerge from quantum fluctuations [see the second term of the right-hand side of the Bogoliubov expansion (103)] and behave as sound waves at low energy (i.e., in the long-wavelength limit, see Figure 20).

In Bose-Einstein condensate, the sound velocity at which these excitations propagate is given by

$$c = \sqrt{\frac{g\,n}{m}}. \tag{109}$$

Note that the sound velocity is well-defined when the density $n(x)$ in the previous expression is constant. The local sound velocity is indeed an approximate concept, only rigorously valid where the condensate density varies over typical length scales much larger than the healing length.

To realize a sonic black hole configuration, one should modulate the sound velocity and the flow velocity along the condensate to create a subsonic region, where $V < c$, and a supersonic region, where $V > c$. One may achieve such a dissymmetry along the flow by a proper chosen external potential $U(x)$ in equation (108). Indeed, in the presence of such a potential, the density profile changes along the condensate, and so does the sound velocity through the relation (109). Then, using the

2 If $\hat{\Psi}$ is the field operator which describes the one-dimensional system, the one-body density matrix is $n^{(1)}(x,x') = \left\langle \hat{\Psi}(x)\,\hat{\Psi}(x') \right\rangle$. In this case, a long-range order exists if

$$n^{(1)}(x,x') \xrightarrow[|x-x'|/\xi\to\infty]{} n_0, \tag{107}$$

where ξ is the healing length and n_0 the condensate density.
One shows that this limit diverges when using the Bogoliubov approach. However, an exact derivation [130, 154] demonstrates that off-diagonal terms of the the one-body density matrix tends to zero. This proves that no long-range order exists, and hence, neither does a one-dimensional condensed phase [92, 127]. A nice discussion about this problem can be found in Ref. [109].

stationarity of the flow, one has (when the density does not vary too much to ensure the validity of the sound velocity)

$$n\,V = \text{Cst} \Rightarrow c^2\,V = \text{Cst}. \tag{110}$$

This means that the flow velocity is also modulated. Therefore, one can tune the parameters to obtain a region of higher density (and thus of slower flow velocity) and an other region of lower density (and thus of faster flow velocity), such that the first region is subsonic and the second one is supersonic. In this case, the flow becomes transonic.

NOTATIONS AND CONSERVATION LAWS The external potential $U(x)$ in equation (108) plays the role of an obstacle. Furthermore, we will consider cases where $U(x)$ is discontinuous at $x = 0$, and define the subscripts u for upstream ($x < 0$) and d for downstream ($x > 0$) this obstacle. We also introduce the Mach numbers $m_{u,d} = V_{u,d}/c_{u,d}$, where V_u (V_d) is the upstream (downstream) flow velocity and c_u (c_d) the upstream (downstream) local sound velocity. The analogous black hole is realized in a situation where the far upstream ($x \to -\infty$) flow is subsonic ($m_u < 1$), and the far downstream one ($x \to +\infty$) is supersonic ($m_d > 1$). Here, the condensate wave function, solution of equation (108), is

$$\psi(x) = \begin{cases} \sqrt{n_u}\exp(\mathrm{i}k_u x)\phi_u(x) & \text{for} \quad x < 0\,, \\ \sqrt{n_d}\exp(\mathrm{i}k_d x)\phi_d(x) & \text{for} \quad x > 0\,. \end{cases} \tag{111}$$

In expression (111) we have separated the upstream and downstream expressions of $\psi(x)$ because $U(x)$ is discontinuous at $x = 0$. The quantities $\phi_u(x)$ and $\phi_d(x)$ will be determined later; we demand that $\lim_{x\to-\infty}\phi_u(x)$ and $\lim_{x\to+\infty}\phi_d(x)$ are constant complex numbers of modulus unity, so that n_u and $\hbar k_u/m = V_u > 0$ (n_d and $\hbar k_d/m = V_d > 0$) are the upstream (downstream) asymptotic density and velocity. The asymptotic healing lengths and sound velocities are $\xi_{u,d}$ and $c_{u,d}$, with $\hbar^2/(m\xi_\alpha^2) = mc_\alpha^2 = g_\alpha n_\alpha$ ($\alpha = u$ or d) where $g_{u,d} = \lim_{x\to\mp\infty} g(x)$. We allow for a position-dependent effective atomic interaction $g(x)$ for being able to consider the model configuration introduced in Refs. [15, 36] and in Section 3.1.3, which we denote as "flat profile" below.

Inserting the asymptotic limits of (111) (when $x \to \mp\infty$) in the stationary Gross-Pitaevskii equation (108) gives the conservation laws

$$n_u V_u = n_d V_d\,, \quad \frac{\hbar k_u^2}{2m} + U_u + g_u n_u = \frac{\hbar k_d^2}{2m} + U_d + g_d n_d\,, \tag{112}$$

where $U_{u,d} = \lim_{x\to\mp\infty} U(x)$. The first of these equations is the current conservation relation and the second one can be considered as a conservation of the local chemical potential (one can indeed define such a local quantity in regions where the density varies weakly over a distance of the order of the healing length).

3.1.3 *Theoretical configurations*

FLAT PROFILE CONFIGURATION This configuration has been introduced in Refs. [15, 36], as an idealized structure in which the background density profile is a plane wave of constant amplitude and velocity: $n_u = n_d \equiv n_0$, $k_u = k_d \equiv k_0$ and $\phi_u(x) = \phi_d(x) \equiv 1$. A transonic configuration is achievable in such a set-up when

$$U(x) = \begin{cases} U_u \ \text{ for } x < 0 \,, \\ U_d \ \text{ for } x > 0 \,, \end{cases} \qquad g(x) = \begin{cases} g_u \ \text{ for } x < 0 \,, \\ g_d \ \text{ for } x > 0 \,, \end{cases} \tag{113}$$

$$\text{and} \ \ g_u n_0 + U_u = g_d n_0 + U_d \,.$$

In this case one has a constant flow velocity $V_0 = \hbar k_0/m$ and

$$\frac{c_d}{c_u} = \frac{m_u}{m_d} = \frac{\xi_u}{\xi_d} < 1 \,. \tag{114}$$

An experimental realization of this idealized configuration seems difficult. First, the coupling constant $g(x)$ varies along the condensate; obtaining such a local monitoring of $g(x)$ is certainly a great challenge. Second, one needs to control very precisely the external potential $U(x)$ to compensate the variations of the coupling constant and to keep constant the chemical potential $\mu = \hbar^2 k_0^2/(2m) + U(x) + g(x)\, n_0$.

This is why another configuration, called "waterfall profile" or "step-like profile", has been suggested in Ref. [110] and has been realized experimentally [102, 105, 131, 175, 177] (see next paragraph and Section 3.1.4).

WATERFALL CONFIGURATION The condensate is accelerated in the downstream region $x > 0$ by an attractive step-like potential $U(x) = -U_0 \Theta(x)$, where Θ is the Heaviside function and $U_0 > 0$ (see Figure 17). The nonlinear parameter g is constant throughout the system. In this transonic configuration the order parameter [equation (111)] corresponds upstream to half a grey soliton and downstream to a plane wave [114]:

$$\phi_u(x) = \cos\theta \, \tanh\left(x \, \cos\theta/\xi_u\right) - \mathrm{i} \sin\theta \,, \quad \text{and} \quad \phi_d(x) = -\mathrm{i} \,, \tag{115}$$

where $\sin\theta = m_u$.

Contrary to the flat profile configuration in which the upstream and downstream Mach numbers can be chosen independently, here, once m_u is fixed all the other dimensionless parameters of the flow are determined by equations (112) and by imposing continuity of ψ at $x = 0$. This yields

$$\begin{cases} \dfrac{V_d}{V_u} = \dfrac{n_u}{n_d} = \dfrac{1}{m_u^2} = m_d = \left(\dfrac{\xi_d}{\xi_u}\right)^2 = \left(\dfrac{c_u}{c_d}\right)^2 \,, \\ \dfrac{U_0}{g n_u} = \dfrac{m_u^2}{2} + \dfrac{1}{2\, m_u^2} - 1. \end{cases} \tag{116}$$

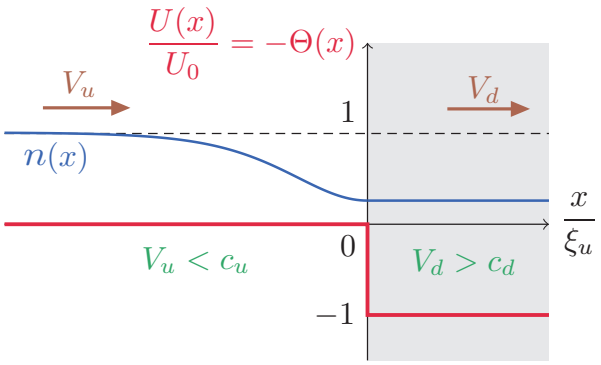

FIGURE 17: Waterfall configuration. The red curve is a step-like potential whose discontinuity is located at $x = 0$. The blue curve is the condensate density profile, corresponding to half a grey soliton in the upstream region (see equation (115)) and constant in the downstream region. The sound velocity can be found from the background density profile through equation (109) and is shown in Figure 18. Asymptotic upstream and downstream sound velocities are denoted c_u and c_d, respectively. The flow moves from the left to to right in the lab frame as indicated on the graph by brown arrows. Upstream and downstream flow velocities are denoted V_u and V_d, respectively. The interior of the sonic black hole, i.e., the supersonic region corresponds to the gray shaded region.

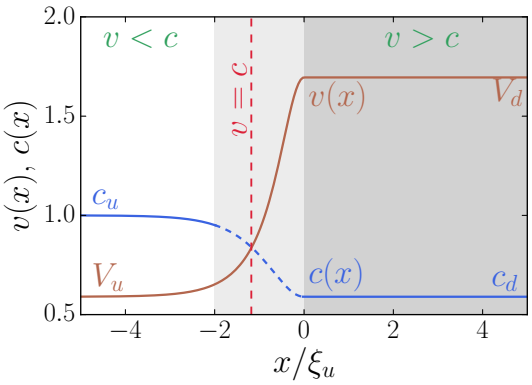

FIGURE 18: Flow velocity $v(x)$ and sound velocity $c(x)$ along the condensate. Asymptotic upstream and downstream values are mentioned on the graph. The dashed red line indicates the boundary between the subsonic and supersonic regions where $v = c$. The light gray shaded region (upstream the obstacle located at $x = 0$) corresponds to a region where the condensate density varies over typical length scales much larger than the healing length. Thus, the local sound velocity c cannot be properly defined in this shaded area and the concept of sonic horizon becomes ill defined. The dark gray shaded region is the interior of the sonic black hole.

LOCATION OF THE ACOUSTIC HORIZON As noticed in Refs. [109, 110], the acoustic horizon, which is at the boundary between the subsonic and the supersonic regions (i.e., where $v = c$), is not exactly located at $x = 0$ but slightly upstream the obstacle (see Figure 18).

In addition, as already discussed in the last paragraph, the sound velocity is only well-defined when the density varies over typical length scales much larger than the healing length. Therefore, the concept of sonic horizon is ill defined, and this is the reason why the region at the vicinity of $x = 0$ is shaded in Figure 18.

However, it will not be a problem in the following: we just need to remember that the position $x = 0$ is the location of the potential discontinuity, where one has to be careful with matching conditions between the upstream and the downstream regions (see Section 3.2).

3.1.4 *Experimental realization of an acoustic horizon*

In this subsection, we discuss the experimental realization by the Technion group of an acoustic black hole in a Bose-Einstein condensate using a step-like external potential [131, 177]. The one-dimensional Bose-Einstein condensate consists of 8.000 ^{87}Rb atoms. The region $x < 0$ is illuminated with an additional laser beam that creates a positive potential as shown in Figure 19. Thus, a step-like potential whose discontinuity is located at $x = 0$ is formed: this is a waterfall configuration. Then, the potential is put in motion at a constant speed to the left, creating a subsonic and a supersonic region as explained in the previous subsection. Figure 19 shows the experimental density profiles of the condensate obtained in 2016 [177] and 2019 [131]. The resulting density profiles fit quite well with the theoretical and expected profile (115), as shown in Figure 19 where the green curves correspond to half a grey soliton[3].

We now optimize our theoretical parameters such that they are the closest from the experimental configuration. This will be useful in the following to compare our theoretical results with experimental ones (see Section 3.2.5 and Section 3.3). First, we know from continuity equations (116) that, in a waterfall configuration, once one of the parameters is fixed (for instance the upstream Mach number m_u) all the others are set as well. Second, the experiment is not a 'true' waterfall configuration, in the sense that experimental parameters do not exactly respect the equalities imposed by conditions (116).

Thus, we should fix the right parameter to obtain the best configuration with respect to the experimental setup. A table with experimental and theoretical parameters can be found in Appendix A. In this table, we compare different configurations, whose parameters are fixed by one of the equalities of (116). For instance, the experimental downstream Mach number is $m_d^{\text{exp}} = 2.9$ [131]. If we choose the same value for the theoretical downstream Mach number, then, all the other theoretical parameters can be calculated with conditions (116). Actually, this choice (fixing $m_d = 2.9$) leads to the best agreement between experimental and theoretical parameters.

3 The agreement is slightly less good in 2019 (graph (c) in Figure 19) than in 2016 (inset of graph (b) in Figure 19). Notwithstanding this point, we will nicely reproduce the experimental density correlations signal showing the robustness of the theoretical description, see below.

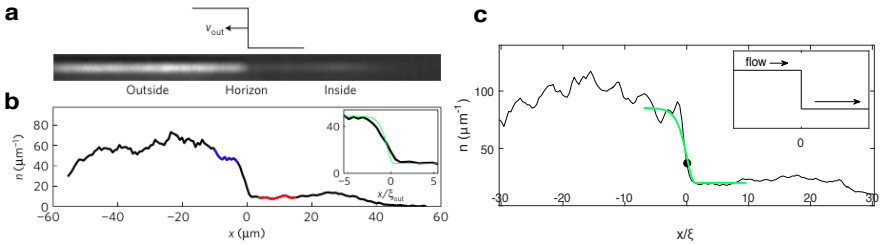

FIGURE 19: (a) Image of the experimental one-dimensional Bose-Einstein condensate obtained in the presence of a step-like external potential [177]. The step-like function is shown on top of the figure and moves to the left. The image is obtained by absorption of light: the brightest region is the outside of the sonic black hole (high-density area), while the darkest region is the inside (low-density area).
(b) Density profile obtained from (a). The green curve in the inset is half a grey soliton.
(c) Density profile obtained in Ref. [131]. The green curve corresponds to the expected theoretical background density for a waterfall configuration with $m_u = 0.59$ (see the text). The inset shows the step-like potential which moves to the left in the free-falling frame, implying that the flow moves to the right in the lab frame.

3.2 DENSITY CORRELATIONS IN BOSE-EINSTEIN CONDENSATES

We have seen hitherto how to construct an acoustic black hole in a Bose-Einstein condensate. The questions we would like to address in this section are:

- How could we define an analogue of Hawking radiation in Bose-Einstein condensate?
- How to detect such a signal?

3.2.1 *Bogoliubov approach*

First, the analogue of Hawking radiation originates from quantum fluctuations emerging from the condensate.

To describe these fluctuations, let us start by decomposing the total field operator $\hat{\Psi}(x)$ using a Bogoliubov approach, as done in (103):

$$\hat{\Psi}(x) = \psi(x) + \delta\hat{\psi}(x,t), \tag{117}$$

where $\delta\psi(\hat{x},t)$ is as small quantum perturbation. For the moment, we consider $\delta\hat{\psi}(x,t)$ as a small classical field, denoted as $\delta\psi$, with $\psi + \delta\psi$ solution of the time-dependent Gross-Pitaevskii equation (105).

Linearizing this equation (see, e.g., Ref. [65]) leads to the well-known Bogoliubov-De Gennes equations

$$i\,\hbar\partial_t \begin{pmatrix} \delta\psi \\ \delta\psi^\star \end{pmatrix} = \begin{pmatrix} \mathcal{H} & g\,\psi^2 \\ -g\,(\psi^\star)^2 & -\mathcal{H} \end{pmatrix} \begin{pmatrix} \delta\psi \\ \delta\psi^\star \end{pmatrix}, \tag{118}$$

where $\mathcal{H} = -\frac{\hbar^2}{2m}\partial_x^2 + 2\,g\,|\psi|^2 + U(x) - \mu$.

DISPERSIVE HYDRODYNAMICS EQUATIONS It is interesting at this point to establish the connection with Chapter 2. To this end, we describe the condensate wave function in terms of number density and phase by means of the Madelung representation:

For the moment we do not assume stationarity of the flow.

$$\psi(x,t) = \sqrt{n_0(x,t)}\, e^{i\,\theta_0(x,t)}, \tag{119}$$

where n_0 is the condensate density and θ_0 its phase; the phase being connected to the flow velocity V by the formula

$$V(x,t) \equiv \frac{\hbar}{m}\,\partial_x\,\theta_0. \tag{120}$$

From the Gross-Pitaevskii equation (105) one finds two equations for n_0 and θ_0:

$$\begin{aligned}
&\partial_t\, n_0 + \partial_x\,(n_0\, V) = 0\ ,\\
&\partial_t\, V + V\,\partial_x\, V + \frac{g}{m\,\rho_0}\partial_x\, P + \frac{\hbar^2}{2\,m^2}\partial_x\,\Pi + \frac{1}{m}\,\partial_x U(x) = 0,\\
&P = \frac{n_0^2}{2}, \quad \text{and} \quad \Pi = -\frac{1}{\sqrt{n_0}}\,\partial_{xx}\sqrt{n_0},
\end{aligned} \tag{121}$$

where P is an effective pressure induced by nonlinearities and Π is the quantum pressure [153].

The set of equations (121) are the hydrodynamics equations: the first one is the continuity equation, the second one is the Euler equation. However, one sees a main (and dramatic) difference with the hydrodynamics equations introduced in Chapter 2: the addition of dispersive effects in the system through the quantum pressure term in the second equation of (121) will prevent us to define a proper metric[4] (see below).

LAGRANGIAN DENSITY AND METRIC Let us now imagine that the density and the phase slightly fluctuate, such that the total classical field which describes the system becomes

This is nothing but the Bogoliubov decomposition (117)

$$\begin{aligned}
&\Psi = \sqrt{n_0 + n_1}\, e^{i\,(\theta_0+\theta_1)} = \sqrt{n_0} e^{i\,\theta_0} + \delta\psi,\\
&\text{with} \quad \delta\psi = \sqrt{n_0} e^{i\,\theta_0}\left(\frac{n_1}{2\,n_0} + i\,\theta_1\right)
\end{aligned} \tag{122}$$

Using the linearized version of the time-dependent Gross-Pitaevskii equation, namely the Bogoliubov-De Gennes equations [see equation (118)], one finds [119]

$$(\partial_t + v_0\,\partial_x)\,\theta_1 = -\frac{m\,c^2(-i\,\partial_x)}{\hbar\,n_0}\,n_1, \tag{123a}$$

$$(\partial_t + \partial_x\,v_0)\,(\partial_t + v_0\,\partial_x)\theta_1 - c^2(-i\,\partial_x)\,\partial_x^2\,\theta_1 = 0, \tag{123b}$$

4 As we already mentioned in Chapter 2, dispersive effects are totally absent in general relativity. For massless fields, the speed of light c is the speed of waves, regardless of their frequency or wavevector. The wave speed is absolutely fixed.

where $c^2(-i\,\partial_x)$ is an operator which takes into account the dispersion in the system:

$$c^2(-i\,\partial_x) = c^2 - \frac{\hbar^2}{4\,m^2}\,\partial_x^2, \tag{124}$$

with $c = \sqrt{n_0\,g/m}$, the usual sound velocity.

Note that the set of equations (123) are obtained assuming that n_0 is constant. Albeit this is true for the flat profile configuration, this assumption is incorrect for the waterfall configuration in the subsonic region at the vicinity of the horizon (see Figure 17). However the density tends reasonably fast to its constant value n_u (for a specific case of experimental interest where $n(x) \simeq n_u$ for $x < -3\,\xi_u$). In any case, as we already mentioned in Section 3.1.3, one is not able to define a proper sound velocity when the density varies on scales of the order of the healing length[5].

Despite this assumption, equations (123) are very instructive and meaningful. The field $\theta_1(x,t)$ is solution of a (massless) wave equation in curved spacetime. Indeed, when $c^2(-i\partial_x) = c^2$, i.e., in the dispersionless regime, equation (123b) can be written in terms of a metric $g_{\mu\nu}$:

$$\frac{1}{\sqrt{-\mathcal{G}}}\partial_\mu(\sqrt{-\mathcal{G}}\,g^{\mu\,\nu}\partial_\nu\theta_1) = 0, \tag{125}$$

with $\mathcal{G} = \det\, g_{\mu\nu}$. One finds in this case

$$g_{\mu\nu} = \frac{n_0}{m\,c}\begin{pmatrix} c^2 - v_0^2 & v_0 \\ v_0 & -1 \end{pmatrix}, \tag{126}$$

which is equivalent to the metric derived in Chapter 2 [see equation (77)]. Equivalently, the field $\theta_1(x,t)$ can be seen as a massless field propagating in a 1+1D curved spacetime whose metric is given by equation (126).

In presence of dispersion, we are forced to abandon the concept of metric, which is strictly valid in a *dispersionless regime*. However one can still write a Lagrangian density from which equation (123b) is derived [158]. We introduce a complex field $\theta(x,t)$ solution of the massless wave equation (125), such that $\theta_1 = \theta + \theta^\star$. This ensures that θ_1 defined in expression (122) is real and solution of equation (123b). Then, the Lagrangian density reads

$$\mathcal{L} = \frac{1}{2}\,|(\partial_t + v\,\partial_x)\,\theta|^2 - \frac{1}{2}\,|c(-i\,\partial_x)\,\partial_x\,\theta|^2. \tag{127}$$

Similarly, we also introduce $n(x,t)$, a solution of equation (123a) such that $n_1 = n + n^\star$.This field is related to the canonical momentum π associated to θ through the relation

$$\pi = \frac{\partial\mathcal{L}}{\partial(\partial_t\,\theta^\star)} = (\partial_t + v\,\partial_x)\,\theta \underset{(123a)}{=} -\frac{m\,c^2(-i\,\partial_x)}{\hbar\,n_0}\,n. \tag{128}$$

5 Equations (123) are derived in Ref [119] with a varying density, but neglecting dispersive effects. The derivation also leads to a generalized Klein-Gordon equation.

SCALAR PRODUCT From the Lagrangian density (127) we can also derived a conserved current [133]

$$\mathcal{J}_i = i\left[\frac{\partial\mathcal{L}}{\partial(\partial_i\,\theta^\star)}\,\theta^\star - \frac{\partial\mathcal{L}}{\partial(\partial_i\,\theta)}\theta\right], \quad \text{where} \quad i\in\{t,x\}. \tag{129}$$

The current $\mathcal{J}_t$ can be understood as a density of charge and is associated to a conserved quantity – the *scalar product* – defined as [158]

$$\langle\theta_k|\theta_l\rangle = i\int_{\mathbb{R}}\mathcal{J}_t\,dx = i\int_{\mathbb{R}}dx\;\left(\theta_k^\star\,\pi_l - \theta_l\,\pi_k^\star\right), \tag{130}$$

where $\theta_{k,l}$ are two solutions of equation (123) and $\pi_{k,l}$ are derived from equation (128). Introducing $\Lambda_k = (-\pi_k + i\,\theta_k,\,-\pi_k - i\,\theta_k)^{\mathrm{T}}$, the scalar product (130) becomes

$$\langle\Lambda_k|\Lambda_l\rangle = \int_{\mathbb{R}}dx\,\Lambda_k^\dagger\,\sigma_z\,\Lambda_l, \tag{131}$$

with $\sigma_z = \mathrm{diag}(1,\,-1)$. This scalar product will be of importance in the following to normalize correctly the excitation modes emerging from quantum fluctuations. Indeed, from this scalar product, one can define the norm $\mathcal{N}$ of an excitation mode: $\mathcal{N} = \langle\theta|\theta\rangle = -\langle\theta^\star|\theta^\star\rangle$, or equivalently $\mathcal{N} = \langle\Lambda|\Lambda\rangle = -\langle\sigma_x\,\Lambda^\star|\sigma_x\,\Lambda^\star\rangle$, where σ_x is the Pauli matrix.

DISPERSION RELATION Let us now consider a plane wave $\theta(x,t) = A\,\exp[-i\,(\omega\,t - q\,x)]$, solution of equation (123b). We obtain immediately the corresponding dispersion relation

$$(\omega - V\,q)^2 = \omega_{\mathrm{B}}^2(q), \quad \text{with} \quad \omega_{\mathrm{B}}(q) = \sqrt{c^2\,q^2 + \left(\frac{\hbar\,q^2}{2\,m}\right)^2}, \tag{132}$$

$\omega_{\mathrm{B}}(q)$ being the so-called Bogoliubov dispersion relation[6].

If the condensate were at rest, i.e., $V = 0$, the elementary excitations would have frequency $\omega = \omega_{\mathrm{B}}$, as expected in Bose-Einstein condensation theory using a Bogoliubov approach. Yet, when the condensate is moving, dispersion relation (132) implies that the frequency undergoes a Doppler shift, which is in some sense a very intuitive result. Therefore, in the *free-falling frame* (where the condensate is at rest) the emitted excitation has frequency ω_{B}, while in the *lab frame* (where the condensate is moving), it has frequency ω, related to ω_{B} via equation (132).

6 Let us add a brief comment on the Bogoliubov dispersion relation. This expression can be rewritten in terms of dimensionless parameters and reads in this case [148, 153]

$$\hbar\,\omega_{\mathrm{B}}(Q)/(m\,c^2) = Q\sqrt{1 + \frac{Q^2}{4}}, \tag{133}$$

with $Q = \xi\,q$. Low energy excitations (when $Q \ll 1$) travel at the sound velocity with energy $\hbar\omega_{\mathrm{B}} = c\,p$ ($p = \hbar\,q$). These quasiparticles are sound waves and are called phonons. When $Q \gg 1$, excitations become free particles with energy $\hbar\omega_{\mathrm{B}} = p^2/(2m) + mc^2$.
Denoting λ the wavelength of the excitation, one sees that the turning point between the phonon (where interactions dominate) and the free particles regimes (where quantum pressure dominates) takes place around $\lambda \sim \xi$, which corresponds to the proper definition of the healing length [45, 148, 153] introduced in Section 3.1.2.

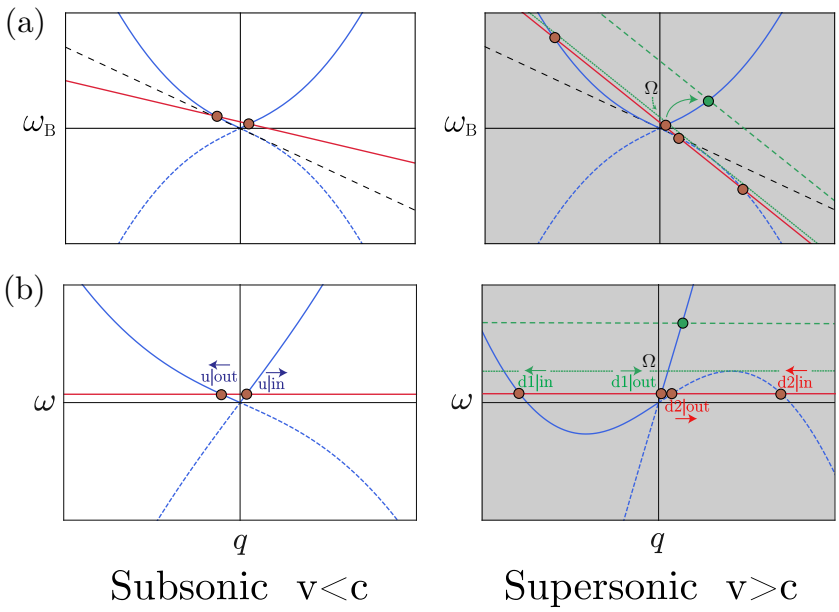

FIGURE 20: (a) Free-falling frame – Blue curve: Bogoliubov dispersion relation $\omega_B(q)$ in units of energy $m\,c^2$. Dashed blue curves indicate branches of negative norm. Red lines: $(\omega - v\,q)^2$ with $v < c$ in the subsonic region (left) and $v > c$ in the supersonic region (right). The lab frequency ω is fixed. The dashed black line corresponds to $-c\,q$ and is tangent to $\omega_B(q)$ for $q \ll 1$. The intersections between straight lines and $\omega_B(q)$ are solutions of equation (132) with real wavenumbers and are indicated by brown dots. Two other solutions of equation (132) also exist, but with imaginary wavenumbers: the evanescent channels. The dotted green line in the supersonic region (right) shows the frequency threshold Ω above which two intersection points disappear and become evanescent waves. For $\omega > \Omega$, the dashed green line intersects two times the Bogoliubov dispersion relation (green dot, the other one is out of bounds of the figure), similarly to the subsonic region (left).
(b) Lab frame – The blue curve is the dispersion relation (132) in the lab frame, where dashed branches are of negative norm. The lab frequency ω is fixed and one recovers the same intersection points as in the above figure (a). The same dotted and dashed green lines are indicated in the supersonic region (right). The different propagation channels are labeled $\alpha|$in or $\alpha|$out, depending if they travel in the subsonic ($\alpha = u$) or the supersonic ($\alpha = d$) region, towards (*in*) or away from (*out*) the horizon. We indicate with an arrow their direction of propagation.

In our case, $V = V_\alpha$, with $\alpha = u$ in the subsonic (upstream) region, and $\alpha = d$ in the supersonic (downstream) region. Figure 20 shows the dispersion relation in the free-falling frame [i.e., when $\omega = \omega_B(q)$] and in the lab frame[7]. Note that the solid lines are branches of positive norm,

7 Note that in Figure 20 we use dimensionless units: the frequency is in units of $m\,c^2$ and the wavenumber in units of ξ^{-1}, with ξ the healing length.

i.e., when $\langle\theta|\theta\rangle > 0$, while dashed curves are branches of negative norm [$\langle\theta|\theta\rangle < 0$].

By means of equation (132), one sees that the possible modes of emission in each region (subsonic or supersonic), can be found graphically as the intersections between straight lines $\omega(q) - V_\alpha\, q$ and the Bogoliubov dispersion relation $\omega_{\rm B}(p)$. This is what is outlined Figure 20. For a fixed frequency ω, since the tangent of $\omega_{\rm B}(q)$ equals cq in the long-wavelength limit ($\xi\, q \ll 1$, with ξ the healing length), one finds two possible modes of excitation in the subsonic region (because, here, $V_u < c$). In the supersonic region ($V_d > c$) the situation is more complex: below a certain threshold Ω there are four modes of excitations; when $\omega > \Omega$, two modes become evanescent and the line $\omega(q) - V_d\, q$ intersects $\omega_{\rm B}(q)$ only two times.

SCATTERING CHANNELS As one can see from Figure 20, these excitation modes are labeled $\ell = \alpha|\text{in}$ or $\ell = \alpha|\text{out}$, with $\alpha = u, d$, depending if the excitation travels in the upstream or the downstream region, towards (*ingoing*-modes) or away (*outgoing*-modes) from the obstacle located at $x = 0$. Each of them takes part of three different scattering processes induced by a *ingoing*-mode. For example, a *ingoing*-mode emitted in the upstream region and propagating to the right ($\ell = u|\text{in}$) will scatter at the horizon and be converted in *outgoing*-modes, either propagating in the upstream region against the flow or in the downstream region in the direction of the flow. This process of *mode conversion* is schematically represented in Figure 21. Two other scattering processes can be induced by $\ell = d1|\text{in}$ or $\ell = d2|\text{in}$. Note that the evanescent modes, characterized by a complex wavenumber q, are also mentioned in Figure 21.

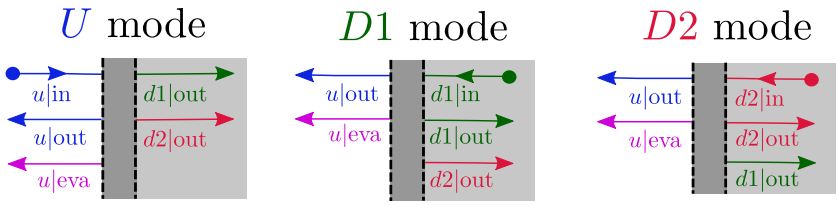

FIGURE 21: Sketch of the different channels contributing to the incoming quantum modes U, $D1$ and $D2$. In each plot the background condensate propagates from left to right, the white region corresponds to the upstream subsonic flow, the gray one to the interior of the analogous black hole (downstream supersonic flow) and the region of the horizon is represented by the dark gray shaded interface (see also Figure 18). The labels indicate the different modes of emission shown in Figure 20. Each mode (U, $D1$ and $D2$) is seeded by a ingoing channel ($u|\text{in}$, $d1|\text{in}$ and $d2|\text{in}$) propagating towards the horizon.

BASIS SET FOR EXPANDING THE ELEMENTARY EXCITATIONS We learned from the aforementioned paragraphs that quantum fluctuations in a moving condensate result in the emission of quasiparticles.

These excitations are plane waves characterized by their frequency ω ($\omega_{\rm B}$ in the free-falling frame), their wavenumber q, and also their norm. They can be emitted in different modes, whose notations are detailed in the previous paragraph. Positive (negative) norm modes carry a positive (negative) charge, i.e., a positive (negative) scalar product.

We shall now expand the small classical field $\delta\psi$ (see Equation 117) over a complete set of eigenvectors. We look for *stationary modes*[8] of the form

$$\begin{pmatrix} \delta\,\psi_\omega \\ \delta\,\psi_\omega^\star \end{pmatrix} = \Xi\, e^{-i\,\omega\,t} = \begin{pmatrix} u(x) \\ v(x) \end{pmatrix} e^{-i\,\omega\,t}, \tag{134}$$

where $u(x)$ and $v(x)$ are the Bogoliubov amplitudes. Inserting (134) in the Bogoliubov-De Gennes equations (118) leads to well-known diagonalization problem of the Bogoliubov-De Gennes Hamiltonian

$$\hbar\,\omega\,\Xi = \mathcal{L}_{\rm BG}\,\Xi\,, \quad \text{with} \quad \mathcal{L}_{\rm BG} = \begin{pmatrix} \mathcal{H} & g\,\psi^2 \\ -g\,(\psi^\star)^2 & -\mathcal{H} \end{pmatrix}, \tag{135}$$

where we recall that $\mathcal{H} = -\frac{\hbar^2}{2m}\partial_x^2 + 2\,g\,|\psi|^2 + U(x) - \mu$. Thus, Ξ is an eigenvector with eigenvalue $\hbar\,\omega$. Note that the symmetry property of the Bogoliubov-De Gennes equations [65] implies that for each solution $\Xi = (u,\, v)^{\rm T}$ of energy $\epsilon = \hbar\,\omega$ of equation (135), the quantity $\Upsilon = (v^\star,\, u^\star)^{\rm T} = \sigma_x\,\Xi^*$ is also a solution of energy $-\epsilon = -\hbar\,\omega$.

From equation (131), one checks that the norm

$$\langle\Xi|\Xi\rangle = \int_{\mathbb{R}} dx\,\Xi^\dagger\,\sigma_z\,\Xi \tag{136}$$

is conserved. Moreover, if $\langle\Xi|\Xi\rangle > 0$, then $\langle\Upsilon|\Upsilon\rangle < 0$. For a certain mode Ξ emitted with frequency ω and wavenumber q, it is worth noticing that the sign of its norm only depends on the sign of $\omega_{\rm B}(|q|)$, i.e., the frequency of this mode in the free-falling frame[9]. Therefore, looking at Figure 20, we notice that the $D2$-mode has a negative norm, or say differently, carries a negative charge, while the U and $D1$-modes are positive norm modes.

This last remark is very important. Indeed, we can already guess where the analogous Hawking radiation in BECs comes from: each scattering processes shown in Figure 21 gives birth to a positive norm mode $u|$out propagating away from the horizon outside the acoustic black hole, and a negative norm mode $d2|$out also propagating away from the horizon inside the black hole. These two modes are nothing but the analogous Hawking pair in our system. The specificity of acoustic black holes in BECs lies in the fact that an other outgoing positive norm

8 The existence of stationary modes is ensured by the time invariance of the Lagrangian density (127) [133].

9 Indeed, this directly comes from equation (131). Going to the free-falling frame, one sees that $\pi = \partial_{t'}\theta$, with $t' = t$, $x' = x - v_0\,t$, and $\partial_{t'} = \partial_t + v_0\,\partial_x$. Then, by considering a stationary mode $\theta(x',t') = \widetilde{\theta}(x')\,\exp[-i\,\omega_{\rm B}(|q|)\,t']$, the norm is $\langle\theta|\theta\rangle = 2\,\omega_{\rm B}(|q|)\int_{\mathbb{R}} dx\,|\widetilde{\theta}|^2$.

mode $d1|\text{out}$ is also emitted during the scattering process, leading to tripartite entanglement (see Chapter 4).

Then, combining the different channels with appropriate matching conditions at $x = 0$ one can build modes defined on all the real axis which form a basis set for expanding the elementary excitations. We choose to build solutions on well defined ingoing channels $u|\text{in}$, $d1|\text{in}$, and $d2|\text{in}$, as shown in Figure 21. The corresponding wave-functions are denoted as Ξ_U, Ξ_{D1} and Ξ_{D2}, with $\Xi_L(x) = (u_L(x), v_L(x))^T$. They have the form,

$$\begin{aligned}
\text{for } x<0 \,:\quad & \Xi_U(x) = S_{u,u}\,\Xi_{u|\text{out}}(x) + S^{\text{eva}}_{u,u}\,\Xi_{u|\text{eva}}(x) + \Xi_{u|\text{in}}(x)\,,\\
& \Xi_{D1}(x) = S_{u,d1}\,\Xi_{u|\text{out}}(x) + S^{\text{eva}}_{u,d1}\,\Xi_{u|\text{eva}}(x)\,,\\
& \Xi_{D2}(x) = S_{u,d2}\,\Xi_{u|\text{out}}(x) + S^{\text{eva}}_{u,d2}\,\Xi_{u|\text{eva}}(x)\,;\\
\text{for } x>0 \,:\quad & \Xi_U(x) = S_{d1,u}\,\Xi_{d1|\text{out}}(x) + S_{d2,u}\,\Xi_{d2|\text{out}}(x)\,,\\
& \Xi_{D1}(x) = S_{d1,d1}\,\Xi_{d1|\text{out}}(x) + S_{d2,d1}\,\Xi_{d2|\text{out}}(x) + \Xi_{d1|\text{in}}(x)\,,\\
& \Xi_{D2}(x) = S_{d1,d2}\,\Xi_{d1|\text{out}}(x) + S_{d2,d2}\,\Xi_{d2|\text{out}}(x) + \Xi_{d2|\text{in}}(x)\,,
\end{aligned} \tag{137}$$

with

$$\Xi_\ell(x) \equiv \begin{pmatrix} u_\ell(x) \\ v_\ell(x) \end{pmatrix} = e^{i\,q_\ell\,x} \begin{pmatrix} e^{i\,m\,V_\alpha\,x/\hbar}\,\mathcal{U}_\ell(x) \\ e^{-i\,m\,V_\alpha\,x/\hbar}\,\mathcal{V}_\ell(x) \end{pmatrix}, \tag{138}$$

where the labels ℓ refer to the possible modes of emission ($\ell = \alpha|\text{in}$ or $\ell = \alpha|\text{out}$), and V_α is the flow velocity in the subsonic ($\alpha = u$) or the supersonic ($\alpha = d$) region. In the flat profile configuration, and also in the downstream region of the waterfall configuration (where ϕ_α, defined in equation (111), is constant) the solution of equation (135) are plane waves. In the upstream region of the waterfall configuration the solutions are also known, see, e.g., Ref. [24] and the explicit expressions of $\mathcal{U}_\ell(x)$ and $\mathcal{V}_\ell(x)$ are given in Ref. [110]. In equation (138) q_ℓ's are the wave vector of the Bogoliubov modes, solutions of the dispersion relation (132). The S's in equation (137) are reflection and transmission coefficients: for instance $S_{u,d1}(\omega)$ describes how the amplitude of a wave of angular frequency ω initiated in the $d1|\text{in}$ channel is scattered onto the $u|\text{out}$ one. Note that in the above expressions all quantities depend on ω.

The classical field $\delta\psi$ can be now expanded over the basis formed by eigenvectors Ξ_L and Υ_L:

$$\begin{aligned}
\boldsymbol{\delta\psi}(x,t) &= \begin{pmatrix} \delta\psi(x,t) \\ \delta\psi^\star(x,t) \end{pmatrix} \\
&= \int_0^{+\infty} d\omega \sum_{L\in\{U,\,D1\}} \Xi_L(\omega,x)\,e^{-i\,\omega\,t}\,b_L(\omega) + \Upsilon_L(\omega,x)\,e^{i\,\omega\,t}\,b_L^\star(\omega) \\
&\quad + \int_0^{\Omega} d\omega\,\Upsilon_{D2}(\omega,x)\,e^{i\,\omega\,t}\;b_{D2}(\omega) + \Xi_{D2}(\omega,x)\,e^{-i\,\omega\,t}\;b_{D2}^\star(\omega)\,,
\end{aligned} \tag{139}$$

with

$$\begin{cases} b_L(\omega) = \langle \Xi_L | \boldsymbol{\delta\psi} \rangle \,, \quad \text{and} \quad b^\star_L(\omega) = -\langle \Upsilon_L | \boldsymbol{\delta\psi} \rangle \,, \quad \text{if} \quad L \in \{U, D1\}, \\ b_{D2}(\omega) = \langle \Upsilon_{D2} | \boldsymbol{\delta\psi} \rangle \,, \quad \text{and} \quad b^\star_{D2}(\omega) = -\langle \Xi_{D2} | \boldsymbol{\delta\psi} \rangle \,. \end{cases} \tag{140}$$

In equation (139), Ω is the threshold above which the mode $D2$ disappears. Note that in the case of the $D2$-mode the positive norm mode is $\Upsilon_{D2}(\omega, x)\, e^{i\,\omega\, t}$ for $\omega > 0$[10]. The validity of equation (139) is based on a correct normalization of Ξ_L, i.e.,

$$\left\langle \Xi_{L'}(\omega) | \Xi_L(\omega') \right\rangle = \nu_L \delta_{L,L'} \delta(\omega - \omega') \,, \tag{141}$$

with $\nu_U = \nu_{D1} = 1$ and $\nu_{D2} = -1$. Using expansion (137), one sees that this normalization imposes the following relation between the S-coefficients:

$$S^\dagger \eta S = \eta \,, \quad \text{where} \quad S = \begin{pmatrix} S_{u,u} & S_{u,d1} & S_{u,d2} \\ S_{d1,u} & S_{d1,d1} & S_{d1,d2} \\ S_{d2,u} & S_{d2,d1} & S_{d2,d2} \end{pmatrix} \,, \tag{142}$$

and with $\eta = \mathrm{diag}(1, 1, -1)$. Note that the evanescent are not involved in equation (142) because they do not carry any current [110].

3.2.2 *Zero modes*

The decomposition (139) does not form a complete basis. Indeed, the linear operator $\mathcal{L}_{\mathrm{BG}}$ [see equation (135)] is not self-adjoint and one cannot build *a priori* a complete basis set from the eigenfunctions Ξ_L. A general technique has been exposed in Ref. [26] for building a Jordan representation of $\mathcal{L}_{\mathrm{BG}}$ which, besides its normalized eigenvalues, admits also solutions of zero energy and zero norm.

Indeed, within the Bogoliubov approach, the phase of the condensate wave function is fixed, implying that the global $U(1)$ symmetry is broken. This symmetry breaking is actually associated to a zero energy solution of equation (135): for any fixed θ, the quantity $\psi_\theta(x) = \psi(x) \exp(\mathrm{i}\theta)$ is also solution of the stationary Gross-Pitaevskii (108). Since one can write $\psi_\theta \simeq \psi + \mathrm{i}\theta\, \psi$ it follows that $i\,\theta\, \psi$ is a solution of the linearized Gross-Pitaevskii equation with $\omega = 0$.

The corresponding solution of equation (135) reads (the term $i\,\theta$ has been factorized out)

$$P = \begin{pmatrix} \psi \\ -\psi^\star \end{pmatrix} \,, \quad \text{with} \quad \mathcal{L}_{\mathrm{BG}}\, P = 0 \,. \tag{143}$$

10 For completeness we mention that another possible expansion for the $D2$-mode would have been

$$\ldots + \int_{-\Omega}^{0} d\omega\, \Xi_{D2}(\omega, x)\, e^{-i\,\omega\, t}\, \langle \Xi_{D2} | \Delta \rangle - \Upsilon_{D2}(\omega, x)\, e^{i\,\omega\, t}\, \langle \Upsilon_{D2} | \Delta \rangle \,.$$

We recall that $\psi(x)$ is the condensate wave function and takes a different form in the upstream and the downstream regions, see expressions (111). This is the reason why we introduce

$$P_\alpha(x) = \begin{pmatrix} \sqrt{n_\alpha}\, e^{i\,k_\alpha\,x}\,\phi_\alpha(x) \\ -\sqrt{n_\alpha}\, e^{-i\,k_\alpha\,x}\,\phi_\alpha^\star(x) \end{pmatrix}, \quad \text{with} \quad \mathcal{L}_{\rm BG}\,P_\alpha = 0\,, \tag{144}$$

where $k_\alpha = m\,V_\alpha/\hbar$ and, as usual, $P = P_u$ for negative x and $P = P_d$ for positive x. These modes have zero norm: $\langle P_\alpha | P_\alpha\rangle = 0$.

As we noticed earlier, for each solution of the Bogoliubov-De Gennes equations (118) with $\epsilon = \hbar\,\omega > 0$, one solution of negative energy $-\epsilon$ also exists. Thus, we expect that an another mode of zero energy should be associated to the mode P_α. This mode of excitation actually corresponds to addition of particles to the system [148]. Indeed, if the number of particles varies, so does the chemical potential μ. Thus, let us consider a family of solutions of the Gross-Pitaevskii equation (105) parameterised by μ:

$$\psi_{\mu,\alpha}(x,t) = \psi^{\rm st}_{\mu,\alpha}(x)\,e^{-i(\mu-\mu_0)\,t}\,, \tag{145}$$

with $\alpha \in \{u,d\}$ and where $\psi^{\rm st}_{\mu=\mu_0,\alpha}(x) = \sqrt{n_\alpha}\,\exp(i\,k_\alpha\,x)\,\phi_\alpha(x)$ is a stationary solution of equation (108) with $\mu = \mu_0$. If the chemical potential varies around μ_0, $\delta\psi = \psi_{\mu_0+\delta\mu} - \psi_{\mu_0}$ is a solution of the linearised Gross-Pitaevskii equation (118) when $\delta\mu \to 0$:

$$i\,\hbar\,\partial_t \begin{pmatrix} \partial_\mu\psi_{\mu,\alpha}|_{\mu=\mu_0} \\ \partial_\mu\psi^\star_{\mu,\alpha}|_{\mu=\mu_0} \end{pmatrix} = \mathcal{L}_{\rm BG} \begin{pmatrix} \partial_\mu\psi_{\mu,\alpha}|_{\mu=\mu_0} \\ \partial_\mu\psi^\star_{\mu,\alpha}|_{\mu=\mu_0} \end{pmatrix}, \tag{146}$$

with $\partial_\mu\psi_{\mu,\alpha}|_{\mu=\mu_0} = \partial_\mu\psi^{\rm st}_{\mu,\alpha}|_{\mu=\mu_0} - i\,\frac{t}{\hbar}\,\psi^{\rm st}_{\mu_0,\alpha}$. One finds

$$\mathcal{L}_{\rm BG}\,Q_\alpha = \frac{i}{M_{\rm eff}}\,P_\alpha, \quad \text{with} \quad Q_\alpha = \begin{pmatrix} q_\alpha(x) \\ -q^\star_\alpha(x) \end{pmatrix}, \tag{147}$$

where $q_\alpha(x) = i\,\partial_N\psi^{\rm st}_{\mu,\alpha}|_{\mu=\mu_0}$ and where $1/M_{\rm eff} = d\mu/dN$ [26, 148, 157] plays the role of an effective mass (N being the number of particles in the system). One has also $\langle Q_\alpha | Q_\alpha\rangle = 0$.

In our case, the system is infinite and, thus, $M_{\rm eff} \to \infty$. Indeed, if we slightly anticipate on Section 3.2.3, the phase of the condensate deviates from its initial value and this is known as the phenomenon of phase diffusion [118]. However, the inertia associated to the change of the global phase of a system of infinite number of particles is infinite and this imposes $M_{\rm eff} \to \infty$ [see equation (161) of Section 3.2.3]. Therefore, the mode Q_α is also solution of $Q_\alpha\,\mathcal{L}_{\rm BG} = 0$.

In the following, we only explicit the expressions of Q_α for the flat profile and the waterfall configurations. The details of calculations can be found in Appendix B.

FLAT PROFILE

$$\begin{aligned}\bar{Q}_u &= D\, e^{\Lambda_u X_u} \begin{pmatrix} -i\,\frac{\Lambda_u}{2} - m_u \\ -i\,\frac{\Lambda_u}{2} + m_u \end{pmatrix} , \\ \bar{Q}_d &= A \begin{pmatrix} 1 \\ -1 \end{pmatrix} \\ &\quad + D\,E\, e^{i\,K_0\,X_d} \begin{pmatrix} \frac{K_0}{2} - m_d \\ \frac{K_0}{2} + m_d \end{pmatrix} + D\,E^{\star}\, e^{-i\,K_0\,X_d} \begin{pmatrix} -\frac{K_0}{2} - m_d \\ -\frac{K_0}{2} + m_d \end{pmatrix} ,\end{aligned} \tag{148}$$

with

$$\begin{aligned} Q_\alpha &= \begin{pmatrix} e^{i\,k_\alpha\,x} & 0 \\ 0 & e^{-i\,k_\alpha\,x} \end{pmatrix} \bar{Q}_\alpha \\ X_\alpha &= x/\xi_\alpha,\; K_0 = 2\,\sqrt{m_d^2 - 1}, \quad \text{and} \quad \Lambda_u = 2\,\sqrt{1 - m_u^2}\,, \\ A &= D\,[m_d\,(E + E^{\star}) - m_u]\,, \\ E &= -\frac{\Lambda_u}{2\,m_d\,K_0^2}\,\frac{\xi_d}{\xi_u}\,\left(\Lambda_u\,m_d + i\,m_u\,K_0\right)\,. \end{aligned} \tag{149}$$

The parameter D in equations (148) and (149) can be found numerically for different configurations $m_u = V_u/c$ and $m_d = V_d/c$, see Appendix B. This gives an approximate expression for D:

$$D = \frac{m_u^2\,K_0^2}{8\,(1 + m_u)\,(m_d^2 - m_u^2)} \Rightarrow A = -\frac{m_u}{2\,(1 + m_u)}. \tag{150}$$

WATERFALL CONFIGURATION

$$\begin{aligned}\bar{Q}_u &= D\,\left[\chi(X_u) - \frac{\Lambda}{2}\right]^2\, e^{\Lambda_u\,X_u} \begin{pmatrix} 1 \\ 1 \end{pmatrix} , \\ \bar{Q}_d &= A \begin{pmatrix} \phi_d \\ -\phi_d^{\star} \end{pmatrix} \\ &\quad + E\, e^{i\,K_0\,X_d} \begin{pmatrix} [\frac{K_0}{2} - m_d]\,\phi_d \\ [\frac{K_0}{2} + m_d]\,\phi_d^{\star} \end{pmatrix} + E\, e^{-i\,K_0\,X_d} \begin{pmatrix} [-\frac{K_0}{2} - m_d]\,\phi_d \\ [-\frac{K_0}{2} + m_d]\,\phi_d^{\star} \end{pmatrix} ,\end{aligned} \tag{151}$$

with

$$\begin{aligned} Q_\alpha &= \begin{pmatrix} e^{i\,k_\alpha\,x} & 0 \\ 0 & e^{-i\,k_\alpha\,x} \end{pmatrix} \bar{Q}_\alpha \\ \chi(X) &= \sqrt{1 - m_u^2}\,\tanh\left(\sqrt{1 - m_u^2}\,X\right) \\ A &= i\,D\,\frac{(1 - m_u^2)\,(1 + 2\,m_u^2)}{2\,(1 + m_u^2)}, \quad \text{and} \quad E = i\,D\,\frac{m_u^2\,(m_u^2 - 1)}{4\,(1 + m_u^2)}\,. \end{aligned} \tag{152}$$

The parameter D in equations (151) and (152) can be also found numerically. In this case,

$$D = i\,\frac{a\,m_u + b}{1 - m_u}, \tag{153}$$

with $a = 0.175$ and $b = -4.56\,10^{-3}$. Note that for the waterfall configuration, $m_d = 1/m_u^2$.

Once the zero modes have been derived with the correct matching conditions at $x = 0$, the basis is complete and the small classical field $\delta\psi(x,t)$ is decomposed as follows

$$\begin{aligned}\boldsymbol{\delta\psi}(x,t) = \begin{pmatrix}\delta\psi(x,t)\\ \delta\psi^\star(x,t)\end{pmatrix} &= -i\,P\,\langle Q|\Delta\rangle + i\,Q\,\langle P|\Delta\rangle \\ &+ \int_0^{+\infty} d\omega \sum_{L\in\{U,\,D1\}} \Xi_L(\omega,x)\,e^{-i\omega t}\,b_L(\omega) + \Upsilon_L(\omega,x)\,e^{i\omega t}\,b_L^\star(\omega) \\ &+ \int_0^{\Omega} d\omega\,\Upsilon_{D2}(\omega,x)\,e^{i\omega t}\,b_{D2}(\omega) + \Xi_{D2}(\omega,x)\,e^{-i\omega t}\,b_L^\star(\omega)\,,\end{aligned} \tag{154}$$

with the correct normalization between P and Q, i.e., $\langle Q|P\rangle = i$.

3.2.3 *Quantization*

The quantization is directly obtained from expression (154): the field operator $\delta\hat{\psi}$ associated to the elementary excitations is expanded over the scattering modes and reads

$$\begin{aligned}\boldsymbol{\delta\hat{\psi}}(x,t) = \begin{pmatrix}\delta\hat{\psi}\\ \delta\hat{\psi}^\dagger\end{pmatrix} &= -i\,P\,\hat{\mathcal{Q}} + i\,Q\,\hat{\mathcal{P}} \\ &+ \int_0^{+\infty} d\omega \sum_{L\in\{U,\,D1\}} \Xi_L(\omega,x)\,e^{-i\omega t}\,\hat{b}_L(\omega) + \Upsilon_L(\omega,x)\,e^{i\omega t}\,\hat{b}_L^\dagger(\omega) \\ &+ \int_0^{\Omega} d\omega\,\Upsilon_{D2}(\omega,x)\,e^{i\omega t}\,\hat{b}_{D2}(\omega) + \Xi_{D2}(\omega,x)\,e^{-i\omega t}\,\hat{b}_{D2}^\dagger(\omega)\,,\end{aligned} \tag{155}$$

where $\hat{b}_L(\omega)$ and $\hat{b}_L^\dagger(\omega)$ are respectively the annihilation and creation operators pertaining to a scattering process induced by an ingoing mode $L|\text{in}$, $L \in \{u, d1, d2\}$. They are the quantized version of $b_L(\omega)$ and $b_L^\star(\omega)$ defined in equation (140):

$$\begin{cases}\hat{b}_L(\omega) = \left\langle \Xi_L|\boldsymbol{\delta\hat{\psi}}\right\rangle \\ \qquad\quad = \displaystyle\int_{\mathbb{R}} dx\,u_L^\star\,\delta\hat{\psi}(x,t) - v_L^\star\,\delta\hat{\psi}^\dagger(x,t), \quad \text{if} \quad L\in\{U,\,D1\}, \\ \hat{b}_{D2}(\omega) = \left\langle \Upsilon_{D2}|\boldsymbol{\delta\hat{\psi}}\right\rangle = \displaystyle\int_{\mathbb{R}} dx\,v_{D2}\,\delta\hat{\psi}(x,t) - u_{D2}\,\delta\hat{\psi}^\dagger(x,t),\end{cases} \tag{156}$$

Zero modes operators $\hat{\mathscr{P}}$ and $\hat{\mathscr{Q}}$ are given by

$$\begin{aligned}\hat{\mathscr{Q}} &= \left\langle Q|\boldsymbol{\delta\hat{\psi}}\right\rangle = \int_{\mathbb{R}} dx\,\left[q^\star(x)\,\hat{\psi}(x,t) + q(x)\,\hat{\psi}^\dagger(x,t)\right]\,, \\ \hat{\mathscr{P}} &= \left\langle P|\boldsymbol{\delta\hat{\psi}}\right\rangle = \int_{\mathbb{R}} dx\,\left[\psi^\star(x)\,\hat{\psi}(x,t) + \psi(x)\,\hat{\psi}^\dagger(x,t)\right]\,,\end{aligned} \tag{157}$$

where $\psi(x) = \sqrt{n_\alpha}\, e^{i\, k_\alpha\, x}\, \phi_\alpha(x)$ [see equation (111)]. The operator $\hat{\mathscr{Q}}$ is the phase operator of the condensate, while $\hat{\mathscr{P}}$ corresponds to the fluctuations of the number of particles.

This quantization yields the correct commutation relations

$$\left[\hat{b}_L(\omega), \hat{b}^\dagger_{L'}(\omega')\right] = \delta_{L,L'}\delta(\omega-\omega'), \quad \text{and} \quad [\hat{\mathscr{Q}}, \hat{\mathscr{P}}] = \langle Q|P\rangle = i. \tag{158}$$

The taking into account of the zero modes, with the proper normalization of mode Q ensures that the field operator $\delta\hat{\psi}$ verifies the correct commutation relation

$$\left[\delta\hat{\psi}(x,t), \delta\hat{\psi}^\dagger(x',t)\right] = \delta(x-x')\,. \tag{159}$$

The importance of the zero modes to obtain a correct normalization is stressed in Figure 22. One sees that the zero modes cannot be neglected to have a well-founded theory based on a proper normalization.

Once the zero modes have been included, the quadratic Hamiltonian which describes the quantum fluctuations is [26]

$$\begin{aligned}\hat{H}_{\text{quad}} &= \frac{1}{2}\int_{\mathbb{R}} dx\, \hat{\Delta}^\dagger\, \sigma_z\, \mathcal{L}_{\text{BG}}\, \hat{\Delta} \\ &= \frac{\hat{\mathscr{P}}^2}{2\, M_{\text{eff}}} + \sum_{L\in\{U,\, D1,D2\}} \nu_L \int_0^{\Omega_L} d\omega\, \hbar\,\omega\, \hat{b}^\dagger_L(\omega)\, \hat{b}_L(\omega),\end{aligned} \tag{160}$$

with $\Omega_U = \Omega_{D1} = \infty$ and $\Omega_{D2} = \Omega$, $\nu_U = \nu_{D1} = 1$, and $\nu_{D2} = -1$. The first term of equation (160) has the form of a free kinetic energy, with no restoring force and is associated with the zero eigenvalue of the Bogoliubov-De Gennes Hamiltonian $\mathcal{L}_{\text{BG}}$ [26]. Thus, the operator $\hat{\mathscr{P}}$ can be identified with a momentum operator and the parameter M_{eff} may be indeed interpreted as an effective mass. The second contribution to equation (160) is a system of independent oscillators of energies $\hbar\,\omega$. Then, the ground state $|0\rangle$ of the Hamiltonian (160) consists of an oscillator ground state such that $\hat{b}_L\,|0\rangle = 0$, $L \in \{U, D1, D2\}$, and of a zero-momentum plane wave state such that $\hat{\mathscr{P}}\,|0\rangle = 0$ [26].

In addition one has also

$$\left[\hat{\mathscr{Q}},\, \hat{H}_{\text{quad}}\right] = i\,\frac{\hat{\mathscr{P}}}{M_{\text{eff}}}. \tag{161}$$

Equation (161) implies that the phase operator $\hat{\mathscr{Q}}(t)$ is not stationary and deviates from its initial value $\hat{\mathscr{Q}}(t=0)$. This is the phenomenon of phase diffusion (see, e.g, Ref. [118]). In our case, $M_{\text{eff}} \to \infty$ and no phase diffusion occurs. The physical interpretation of this phenomenon was already mentioned in Section 3.2.2 and corresponds to the inertia associated to the change of the global phase of a system with infinite number of particles.

Let us conclude this subsection with a last remark: the decomposition (154) is not unique. Indeed, one would be tempted to define *outgoing operators* $\hat{c}_L$ and $\hat{c}^\dagger_L$, the annihilation and creation operators for outgoing modes $L|\text{out}$, with $L \in \{u, d1, d2\}$, i.e., which destroy or create

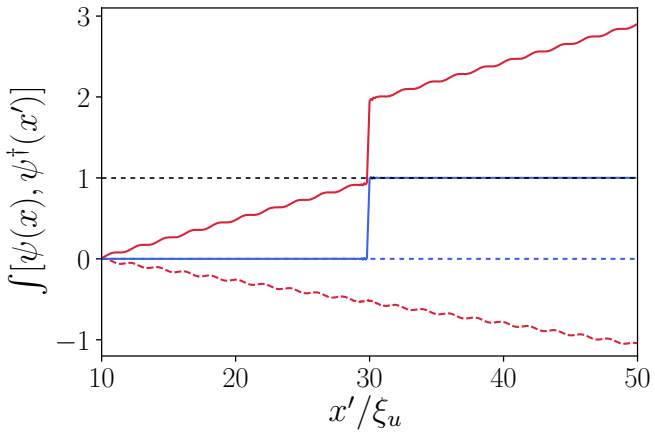

FIGURE 22: Commutation relation $\left[\hat{\psi}(x,t),\hat{\psi}^\dagger(x',t)\right]$ calculated with or without the zero modes and integrated over x'/ξ_u, for $x = 30\,\xi_u$. The solid red curve corresponds to the real part of the resulting integration, while the dashed red curve refers to as the imaginary part. When the zero modes are taken into account, one obtains the blue curves: a Heaviside function for the real part (solid blue) and zero for the imaginary part (dashed blue), thus yielding the correct normalization (159).

a quasiparticle in one of the outgoing channels u, $d1$ or $d2$. Inserting expressions (137) in equation (154), one would find another decomposition in terms of this new operators $\hat{c}$'s. This would also provide the relation between *ingoing operators*[11] $\hat{b}_L$ and *outgoing operators* $\hat{c}_L$,

$$\begin{pmatrix} \hat{c}_U \\ \hat{c}_{D1} \\ \hat{c}^\dagger_{D2} \end{pmatrix} = \begin{pmatrix} S_{u,u} & S_{u,d1} & S_{u,d2} \\ S_{d1,u} & S_{d1,d1} & S_{d1,d2} \\ S_{d2,u} & S_{d2,d1} & S_{d2,d2} \end{pmatrix} \begin{pmatrix} \hat{b}_U \\ \hat{b}_{D1} \\ \hat{b}^\dagger_{D2} \end{pmatrix}, \tag{162}$$

known as a Bogoliubov transformation. We will discuss this important point in Chapter 4.

3.2.4 *Density correlations*

The study of density correlations to explore the analogous Hawking radiation has been first proposed in 2008 by a collaboration between teams from Trento and Bologna [15]. We already discussed in the introduction of this chapter the numerous interests of studying the density-density correlation function $G^{(2)}$; among them the possible experimental detection of the analogous Hawking signal, weakly affected by experimental noises.

11 Note here the subtle sense of *ingoing*: this does not correspond to an ingoing wave $l|\text{in}$, but instead refers to as the whole scattering process induced by one of the ingoing channel $l|\text{in}$, $l \in \{u, d1, d2\}$.

The density correlation function is defined by

$$\begin{aligned} G^{(2)}(x,x') =& \langle :\hat{n}(x,t)\hat{n}(x',t):\rangle - \langle \hat{n}(x,t)\rangle \langle \hat{n}(x',t)\rangle \\ \simeq& \psi(x)\psi^\star(x')\langle \delta\hat{\psi}^\dagger(x,t)\,\delta\hat{\psi}(x',t)\rangle \\ &+ \psi(x)\psi(x')\langle \delta\hat{\psi}^\dagger(x,t)\,\delta\hat{\psi}^\dagger(x',t)\rangle + \text{c.c.} \end{aligned} \tag{163}$$

In this equation, the symbol ":" denotes normal ordering and the final expression is obtained within the Bogoliubov approach, encompassing the effects of quantum fluctuations at leading order. The function $\psi(x)$ corresponds to the condensate wave function defined in equation (111). At zero temperature, the average $\langle \cdots \rangle$ in equation (163) is taken over the state $|0\rangle$, the *vacuum* state[12] for the ingoing operators $\hat{b}_L$. Although this state is thermodynamically unstable and cannot support a thermal distribution, finite temperature effects can still be included as explained for instance in Refs. [62, 124, 156].

Using the results derived in Ref. [156] and adding the contribution from the zero modes, equation (163) can be rewritten

$$G^{(2)}(x_1,x_2) = G^{(2)}_{\text{ZM}}(x_1,x_2) + \sqrt{n_1\,n_2}\int_0^{+\infty}\frac{d\omega}{2\,\pi}\gamma(x_1,x_2,\omega), \tag{164}$$

where $G^{(2)}_{\text{ZM}}(x_1,x_2)$ accounts for the zero modes contribution, $n_i = n_u$ (n_d) if $x_i < 0$ $(x_i > 0)$, $i \in \{1,2\}$ and $\gamma(x_1,x_2,\omega)$ is split in a zero-temperature contribution γ_0 and a thermal term γ_{T}:

$$\gamma(x_1,x_2,\omega) = \gamma_0(x_1,x_2,\omega) + \gamma_{\text{T}}(x_1,x_2,\omega). \tag{165}$$

The zero-temperature term is [110]

$$\begin{aligned} \gamma_0(x_1,x_2,\omega) =& \sum_{L\in\{U,D1\}} \widetilde{v}^\star_L(x_1)\,\widetilde{r}_L(x_2) \\ &+ \Theta(\Omega-\omega)\,\widetilde{u}^\star_{D2}(x_1)\,\widetilde{r}_{D2}(x_2) + \text{c.c.}, \end{aligned} \tag{166}$$

with $\widetilde{u}_L(x_i) = e^{-i\,k_i\,x_i}\,\phi_i^\star(x_i)\,u_L(x_i)$, $\widetilde{v}_L(x_i) = e^{i\,k_\alpha\,x_i}\,\phi_i(x_i)\,v_L(x_i)$, and $\widetilde{r}_L(x_i) = \widetilde{u}_L(x_i) + \widetilde{v}_L(x_i)$. In these expressions, $\phi_i = \phi_u$ $(= \phi_d)$ and $k_i = k_u$ $(= k_d)$ if $x_i < 0$ $(x_i > 0)$[13].

The other contribution to equation (165) reads [110]

$$\gamma_{\text{T}}(x_1,x_2,\omega) = \sum_{L\in\{U,D1,D2\}} \widetilde{r}^\star_L(x_1)\,\widetilde{r}_L(x_2)\,n_L(\omega) + \text{c.c.}, \tag{167}$$

where $n_L(\omega)$ is the occupation number for each of the scattering mode L. For instance $n_U(\omega) = n_{\text{th}}[\omega_{\text{B}}(q_{u|\text{in}})]$, with ω_{B} the Bogoliubov dispersion relation and $n_{\text{th}}(\omega) = (\exp(\omega/T)-1)^{-1}$ the thermal Bose occupation factor (the condensate is initially at thermal equilibrium at temperature T).

12 Here, *vacuum* means no elementary excitations, i.e., $\hat{b}_L\,|0\rangle = 0$, $L \in \{U, D1, D2\}$ [see also the discussion below the quadratic Hamiltonian (160) of Section 3.2.3].

13 we recall that $\phi_i = 1$ for the flat profile configuration, while for the waterfall configuration the expression is given in equation (115). We also recall that $k_\alpha = m\,V_\alpha/\hbar$.

We now turn our attention to the first contribution to equation (164): the two-body density matrix of the zero modes $G^{(2)}_{\rm ZM}$. Inserting the zero modes contribution to the quantum operator (154) in equation (163) gives

$$\begin{aligned} G^{(2)}_{\rm ZM}(x_1,x_2) = {} & 2\,i\,\psi(x_1)\,Q^\star(x_1)\,\mathrm{Im}[\psi^\star(x_2)\,Q(x_2)]\left\langle \hat{\mathscr{P}}^2\right\rangle \\ & - 2\,i\,\psi(x_1)\,P^\star(x_1)\,\mathrm{Im}[\psi^\star(x_2)\,Q(x_2)]\left\langle \hat{\mathscr{Q}}\,\hat{\mathscr{P}}\right\rangle \\ & - 2\,i\,\psi(x_1)\,Q^\star(x_1)\,\mathrm{Im}[\psi^\star(x_2)\,P(x_2)]\left\langle \hat{\mathscr{P}}\,\hat{\mathscr{Q}}\right\rangle \\ & + 2\,i\,\psi(x_1)\,P^\star(x_1)\,\mathrm{Im}[\psi^\star(x_2)\,P(x_2)]\left\langle \hat{\mathscr{Q}}^2\right\rangle + \text{c.c}, \end{aligned} \tag{168}$$

with $\psi(x_i)$ the condensate wave function defined in equation (111). Using the fact that $\hat{\mathscr{P}}\,|0\rangle = 0$ (see Section 3.2.3) and $\psi^\star(x_i)\,P(x_i) = |\psi(x_i)|^2$, equation (168) reduces to the simple expression:

$$G^{(2)}_{\rm ZM}(x_1,x_2) = 2\,|\psi(x_1)|^2\,\mathrm{Im}[\psi^\star(x_2)\,Q(x_2)]. \tag{169}$$

Finally, in order to compare our results with the experimental data obtained by the Technion group [131, 177], we shall normalize the correlation function (163) in the same way:

$$g^{(2)}(x,x') = \sqrt{\frac{\xi_u\,\xi_d}{n_u\,n_d}}\,G^{(2)}(x,x'). \tag{170}$$

This normalization will become meaningful later when we compute the Fourier transform of the density-density correlation function (see Section 3.3.2).

Figure 23 shows the normalized density-density correlation function (170) computed at zero temperature for a waterfall configuration. We mention that we also take into account the position dependence of the background density $\psi(x)$ in the upstream region [see equation (115)], as well as the evanescent channels close to the horizon.

Three dashed straight lines have been added in this figure: each of them corresponds to the correlation lines where a large correlated signal is expected. Indeed, to understand this point let us consider the following simple picture: correlated outgoing waves (induced by the *same* scattering process) are emitted from the horizon at a certain time t_0. These waves propagate either in the upstream subsonic region (this would correspond to a $u|$out mode) or in the downstream supersonic region (this would correspond to a $d1|$out or a $d2|$out mode) at their group velocity, denoted here $V_g(q) = \partial\omega/\partial q$, with ω their frequency and q their wavenumber. For simplicity, we assume that these quasiparticles are phonons (i.e., low energy excitations). Therefore, using the dispersion relation (132) and neglecting the dispersive contribution, we find their respective positions at equal propagation time t:

$$\begin{aligned} & x_{u|\rm out} = (V_u - c_u)\,t < 0, \quad x_{d1|\rm out} = (V_d + c_d)\,t > 0, \\ & \text{and} \quad x_{d2|\rm out} = (V_d - c_d)\,t > 0. \end{aligned} \tag{171}$$

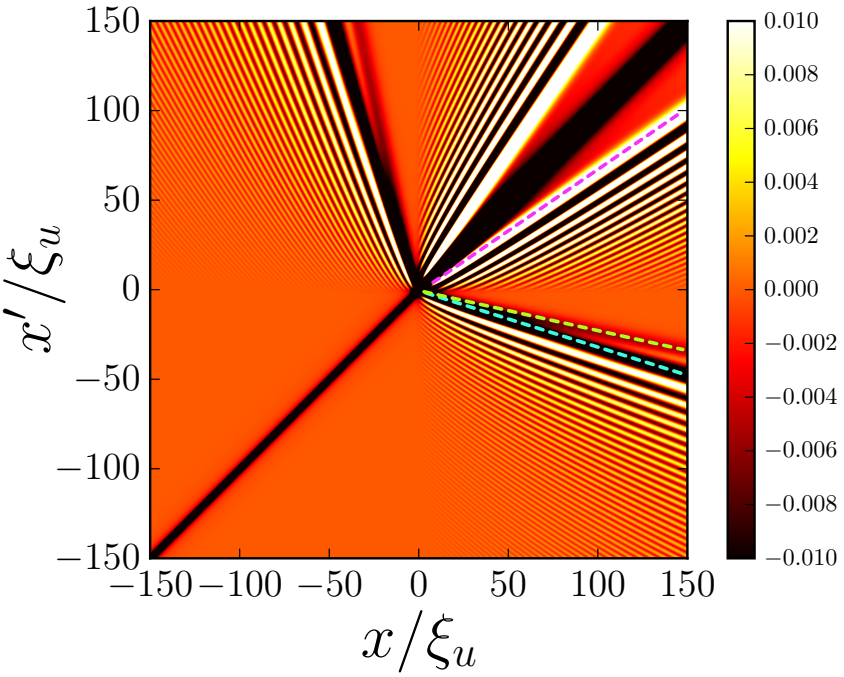

FIGURE 23: Intensity plot of the density-density correlation function $g^{(2)}(x, x')$ at zero temperature for a waterfall configuration with $m_u = 0.42$ and taking into account all contributions to equation (164). The parameter ξ_u is the healing length in the upstream region. The dashed straight lines correspond to the correlation lines where a large correlated signal is expected: Hawking-Partner correlations (blue dashed), $u|$out-$d1|$out correlations (green dashed), and $d1|$out-$d2|$out correlations (pink dashed).

Thus, we expect a high correlation signal along their trajectories, i.e., lines of slopes

$$\frac{x_{u|\text{out}}}{x_{d2|\text{out}}} = \frac{V_u - c_u}{V_d - c_d} < 0, \quad \frac{x_{u|\text{out}}}{x_{d1|\text{out}}} = \frac{V_u - c_u}{V_d + c_d} < 0, \quad \text{and} \quad \frac{x_{d2|\text{out}}}{x_{d1|\text{out}}} = \frac{V_d - c_d}{V_d + c_d} > 0. \tag{172}$$

The three dashed lines in Figure 23 correspond to lines whose slopes are given by expressions (172). We are particularly interested in the blue dashed line of slope $(V_u - c_u)/(V_d - c_d)$. This line indicates a large correlation signal induced by a $u|\text{out} - d2|\text{out}$ pair. This exactly corresponds to the emission of a correlated Hawking-Partner pair, as it would occur at the vicinity of a gravitational black hole: an excitation emitted in the $u|$out mode propagates in the subsonic region, outside the acoustic black hole and has a positive charge (in the sense of positive norm), while an excitation emitted in the $d2|$out mode propagates inside the black hole, in the supersonic region, and carries a negative charge.

Therefore, this correlation line is the signature of the analogous Hawking effect in Bose-Einstein condensates induced by quantum fluctuations.

It is also worth noticing that the correlation lines $u|\text{out} - d1|\text{out}$ and $u|\text{out} - d2|\text{out}$, which separate at large distance from the horizon, merge close to the horizon (this is clear from Figure 24).

To conclude this subsection, we would like to emphasize the importance of the zero modes in the calculation. The correlation signal computed along a longitudinal cut (this cut is drawn in the left plot of Figure 24) clearly shows that the zero modes cannot be neglected to give a correct description of the correlations. Indeed, as we can notice from the right plot of the same figure, zero modes 'kill' the spurious oscillations of the blue curve (obtained when the zero modes are neglected).

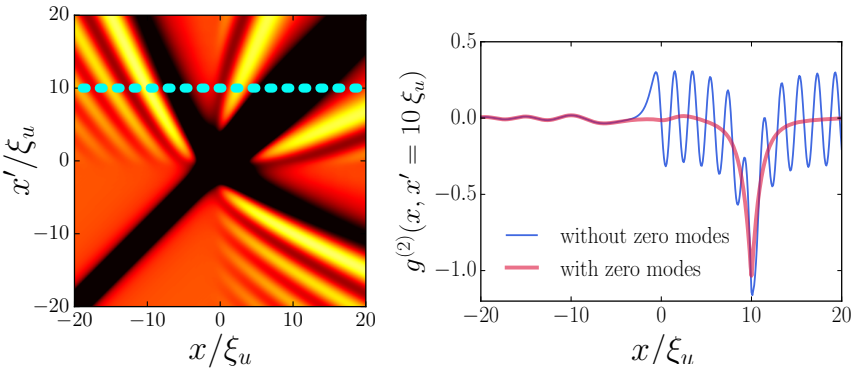

FIGURE 24: (Left) Intensity plot of density correlations for x/ξ_u and x'/ξ_u close to the horizon for a waterfall configuration with $m_u = 0.59$ (this value is of experimental interest – see Section 3.1.4). As in Figure 23, all contributions to equation (164) are included in the calculation. The blue dashed line indicates a longitudinal cut along x/ξ_u for $x' = 10\,\xi_u$.
(Right) Correlation signal along this cut computed either by taking into account the zero modes (red curve) or neglecting them (blue curve).

3.2.5 *Comparison to experiment*

We shall now compare our theoretical results with experimental data obtained recently by the Technion group [131], whose experimental setup has been already presented in Section 3.1.4. So far, such a comparison between the experiment and the theory was not possible: the experimental correlations have been acquired close to the horizon, a region where the correlations are difficult to be obtained theoretically because one cannot neglect the position dependence of the condensate density and the evanescent channels. However, by means of the addition of the zero modes, we are now able to obtain a correct theoretical description of the correlations at the vicinity of the horizon. This enables us to safely compare experimental and theoretical results.

Figure 25 shows a 2D plot of the density correlation pattern. The function $g^{(2)}(x, x')$ has been computed at zero temperature for a waterfall configuration with Mach numbers $m_u = V_u/c_u = 0.59$ and $m_d = V_d/c_d = 2.9$. The downstream Mach number m_d is chosen to reproduce the experimental configuration studied in Ref. [131], as discussed in Section 3.1.4. In this figure, the correlation line of the Hawking-Partner pair is visible in both theoretical and experimental plots and is indicated by a green dashed line. We can first compare the slope of these lines, denoted $p_{\rm th}$ (theoretical) and $p_{\rm exp}$ (experimental). We find

$$|p_{\rm th}| = 0.45 - 0.55, \quad \text{and} \quad |p_{\rm exp}| = 0.57 - 0.62. \tag{173}$$

The theoretical slope $p_{\rm th}$ ranges from -0.55 to -0.45 because this slope tends to increase at the vicinity of the horizon (see Figure 26).The slight discrepancy between experimental and theoretical slopes might come from several causes: albeit our theoretical value for the downstream Mach number m_d coincides with the experimental one, it is not the case for the upstream Mach number m_u (the experimental value is 0.44, while the continuity relations (116) impose $m_u = 0.59$ for $m_d = 2.9$). This could indicate that the experimental setup is not a perfect waterfall configuration. Therefore, the slope could be slightly shifted with respect to an ideal situation where the external potential is a perfect step-like function. It is also possible that the experiment is not completely stationary which makes the slope shift. Indeed, in a recent publication of the Technion group [102] the time evolution of an analogue black hole is studied in a configuration close to that of Ref. [131] ($m_u^{\rm exp} = 0.37$ and $m_d^{\rm exp} = 3.3$). Several 2D plots of the density-density correlation function are shown at different times after the formation of the horizon. In these plots, the slope of the Hawking-Partner correlation line varies between -0.79 and -0.58 with an average of -0.62 in agreement with Ref. [131].

Besides this point, a similar feature is observed in experimental and theoretical results: the slopes of the Hawking-Partner correlation lines extracted from Figure 25 deviate by an angle of $\simeq$-9° from the predicted slopes given by (172) and obtained in a dispersionless regime for phonon-like excitations. This deviation is a first indication that elementary excitations are not emitted with the same group velocity due to the presence of dispersive effects in Bose-Einstein condensates.

HAWKING-PARTNER CORRELATIONS A more precise comparison between experimental and theoretical results can be achieved by following the procedure used in Ref. [131], which consists in averaging $g^{(2)}$ over the region inside the green rectangle represented in Figure 25. As shown in the left plot of Figure 26, one defines a local coordinate x'' which is orthogonal to the locus of the minima of $g^{(2)}$ (indicated by black dots), and one plots the averaged $g^{(2)}$ (denoted as $g^{(2)}_{\rm av}$) as a function of the variable x''. This is done in the right plot of Figure 26. Our theoretical approach (red and green curves) is in good agreement with experimental data (blue dots with error bars extracted from Ref. [131]). We recall that theoretical results are obtained for a configuration whose downstream Mach number $m_d = 2.9$ leads to theoretical parameters

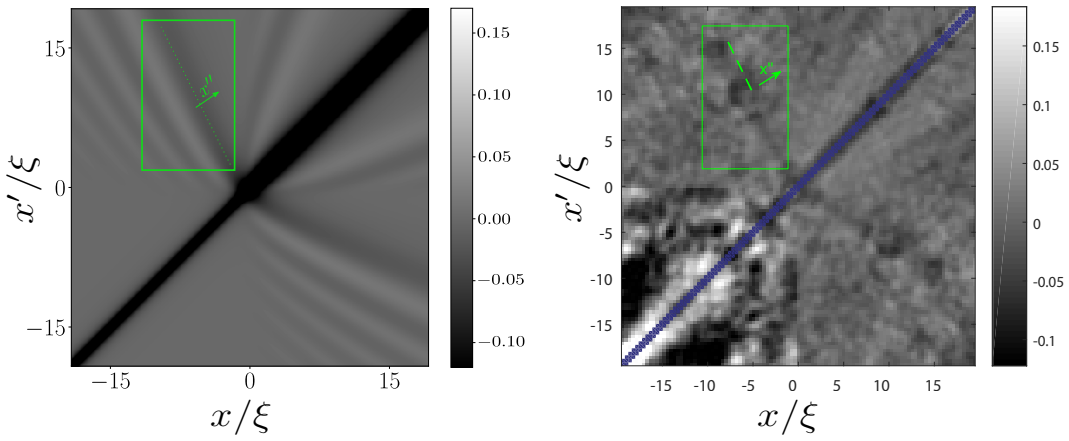

FIGURE 25: (Left) Theoretical density correlation pattern obtained close to the horizon at zero temperature for a waterfall configuration with Mach numbers $m_u \equiv V_u/c_u = 0.59$ and $m_d = V_d/c_d = 2.9$. The parameter $\xi = \sqrt{\xi_u\,\xi_d}$ is the geometrical mean of the healing lengths ξ_u and ξ_d, where $\xi_{(u/d)} = \hbar(mgn_{(u,d)})^{-1/2}$. The line of anti-correlation in the upper left and lower right quadrants corresponds to the merging close to the horizon of the Hawking-partner $(u|\text{out}-d2|\text{out})$ and Hawking-companion $(u|\text{out}-d1|\text{out})$ correlations. The green rectangle delimits the region where we average $g^{(2)}$ for comparison with experimental data (see Figure 26). (Right) Experimental density correlation pattern taken from Ref. [131]. A line of anti-correlation is visible in the upper left and lower right quadrants. Here also, the Hawking-partner correlations merge with those of the Hawking-companion close to the horizon. The green rectangle also delimits the region where experimental correlations have been averaged (see Figure 26).

closest from experimental ones (see Section 3.1.4). If one fixes an other parameter (for instance $m_u = 0.44$) to determine the others through relations (116), the theoretical configuration is further away from the experimental one, and that yields a less good agreement between the experimental and theoretical Hawking-Partner correlated signals[14]. We insist that the good agreement between our approach and experimental results can only be achieved through a correct description of the quantum fluctuations – equation (155) – including the contribution of zero modes and of evanescent channels.

Let us notice that the analogue Hawking temperature T_{H} appears in the legend of the right plot of Figure 26. However, we did not explain so far how we could define such an analogue Hawking temperature in a Bose-Einstein condensate. We call the reader to be patient until the first subsection of Section 3.3, where the definition of this mysterious temperature is unveiled.

14 Hence, we computed the density-density correlation function for $m_u = 0.44$ and $m_u = 0.51$ and we observed a less good agreement with experimental data than for $m_u = 0.59$. These results are not shown in Figure 26 for a better readability.

To conclude this section, our theoretical results (which could not have been obtained without the strong theoretical background provided by previous studies [15, 36, 62, 110, 113, 156, 158]) confirms the experimental observation of the spontaneous analogue Hawking effect in a Bose-Einstein condensate. We hope that we convinced the reader of the importance (the necessity) of the zero modes to obtain a well-founded theory that correctly describes the quantum fluctuations in an acoustic black hole formed in a Bose-Einstein condensate. As we mentioned in the introduction of this chapter, the description of density correlations at the vicinity of the acoustic horizon is a further step towards possible studies on the backreaction problem, i.e., the influence of quantum fluctuations on the background density profile.

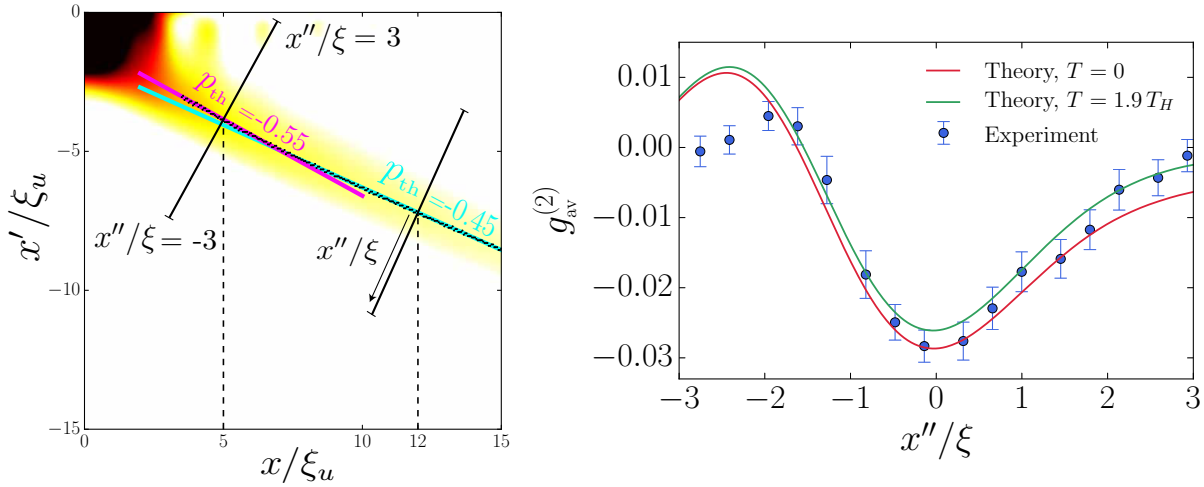

FIGURE 26: (Left) 2D plot of the density-density correlation signal overexposed to enhance the Hawking-Partner correlation line. Black dots indicate the locus of the minima of $g^{(2)}$. The pink line is tangent to the black dots in the near-horizon region, while the light blue line is tangent to the black dots a little further from the horizon. The slopes of these lines are denoted $p_{\rm th}$ and their corresponding values are written on the graph and in equation (173). Two perpendicular cuts to the Hawking-Partner correlation line at $x = 5\,\xi_u$ and $x = 12\,\xi_u$ are also shown. We define a local coordinate denoted x'' which varies along these cuts.
(Right) Intensity of the averaged $g^{(2)}$ (denoted as $g^{(2)}_{\rm av}$) as a function of the variable x''/ξ computed over the region inside the green rectangle shown in Figure 25 (or say differently, the correlation signal $g^{(2)}$ is averaged over perpendicular cuts to the Hawking-Partner correlation line). We recall that $\xi = \sqrt{\xi_u\,\xi_d}$ is the geometrical mean of the healing lengths ξ_u and ξ_d. The red curve exemplifies the theoretical results obtained at zero temperature, while the green one shows the result for a non-zero temperature $T = 1.9\,T_{\rm H}$, with $T_{\rm H}$ the analogue Hawking temperature. The computation of this Hawking temperature is explained in Section 3.3.1. The blue dots are experimental data extracted from Ref. [131].

3.3 DEPARTING FROM THERMALITY OF ANALOGUE HAWKING RADIATION

We learned from the last section that the study of density correlations was an efficient way to detect the signature of the Hawking effect in Bose-Einstein condensates. Thus, such quantum systems are promising candidates to explore the spontaneous Hawking radiation in more detail. However, are there some limitations to the analogy between the spontaneous emission of quasiparticles in BECs and the predicted Hawking radiation emitted by gravitational black holes? How far can we push the analogy further?

In this section we discuss these questions. We show in particular that dispersive effects affect significantly the Hawking spectrum and lead to a departure from the thermal radiation predicted by Hawking for gravitational black holes (see the discussion in Chapter 2 and Refs. [87, 88]).

Actually we have already mentioned some effects of dispersion in BECs. First, we are not able to properly define a metric such as (126) in the presence of dispersion. This is the most dramatic issue of the analogy between dispersive acoustic black holes and general relativity. Second, density correlations are affected by dispersive effects, in particular the slope of the Hawking-Partner correlation line which deviates from the dispersionless prediction. In addition, the asymmetry of the Hawking-Partner correlation signal shown in the right plot of Figure 26 is another hint of the presence of dispersion [156].

Therefore, in line with the aforementioned comments, it is not surprising that dispersion dramatically affects the Hawking signal.

In the following, we first define the analogous Hawking temperature in our system and explain how this value can be obtained. Then, we show that the Hawking spectrum can be found from the Fourier transform of the density-density correlation function. We also show that the windowing to compute the Fourier transform should be chosen very carefully and might lead to the erroneous conclusion that the Hawking spectrum in BECs is thermal. We finally draw conclusions about the thermality of acoustic black holes in BECs.

3.3.1 *Hawking temperature*

For gravitational black holes, the Hawking radiation is the signal emitted outside the black hole propagating away from the horizon. In our case, as mentioned in the previous section, the analogue of a Hawking particle is a quasiparticle emitted in the $u|$out mode (see for instance Figure 21). Thus, the Hawking radiation spectrum, i.e., the number of emitted quanta in the $u|$out mode at frequency ω, is

$$\mathcal{N}_{\rm H}(\omega) = \left\langle \hat{c}^\dagger_U(\omega)\, \hat{c}_U(\omega) \right\rangle , \tag{174}$$

where $\hat{c}^\dagger_U$ ($\hat{c}_U$) is the creation (annihilation) operator for the outgoing mode $u|$out [this operator has been already defined at the end of Sec-

tion 3.2.3 and is related to the *ingoing* operators $\hat{b}_L$ and $\hat{b}_L^\dagger$ through relation (162)]. As in equation (163), the average $\langle\cdots\rangle$ in equation (174) is taken over the state $|0\rangle$, the vacuum state for the ingoing operators $\hat{b}_L$. Using equation (162), one finds

$$\begin{aligned}\mathcal{N}_{\rm H}(\omega) = |S_{u,u}(\omega)|^2 \left\langle \hat{b}_U^\dagger \hat{b}_U \right\rangle + |S_{u,d1}(\omega)|^2 \left\langle \hat{b}_{D1}^\dagger \hat{b}_{D1} \right\rangle \\ + |S_{u,d2}(\omega)|^2 \left\langle \hat{b}_{D2} \hat{b}_{D2}^\dagger \right\rangle \\ \underset{T=0}{=} |S_{u,d2}(\omega)|^2,\end{aligned} \tag{175}$$

for $T = 0$. Equation (175) should be compared with equation (62) of Chapter 2. In both equations, $\mathcal{N}_{\rm H}$ is given in terms of the transmission coefficient associated to the scattering process induced by the ingoing negative norm mode [in Chapter 2 this coefficient would correspond to $\beta_{\omega\omega'}$, see expressions (19) and (21)]. The left plot of Figure 27 exemplifies the Hawking radiation spectrum for a waterfall configuration with upstream Mach number $m_u = 0.59$. In the long-wavelength limit (dispersionless regime) $\mathcal{N}_{\rm H}$ can be approximated by a thermal radiation $n_{T_{\rm H}}$ of temperature $T_{\rm H}$:

$$\mathcal{N}_{\rm H}(\omega) = |S_{u,d2}|^2 \simeq \frac{1}{e^{\hbar\omega/k_B T_{\rm H}} - 1} \equiv n_{T_{\rm H}}(\omega), \tag{176}$$

where $T_{\rm H}$ plays the role of the analogue Hawking temperature. The red curve in the left plot of Figure 27 shows the approximated thermal radiation $n_{T_{\rm H}}$ leading to $T_{\rm H} = 0.102\, g n_u$ in this particular case (with μ the chemical potential). In fact, the analogue Hawking temperature can be calculated analytically from the low-ω behavior of the scattering matrix coefficient $S_{u,d2}$ (see, e.g, Ref. [110] where the analytic formula for $T_{\rm H}$ is given).

Another measure of the analogue Hawking temperature can be obtained through the correlation spectrum of the Hawking radiation, i.e., the Hawking-Partner correlations measured in k-space: $\langle \hat{c}_U(\omega)\, \hat{c}_{D2}(\omega)\rangle$, with $\hat{c}_{D2}$ the outgoing annihilation operator pertaining to the $d2|$out mode. Let us assume that, in the scattering process schematically illustrated in Figure 21 for the $D2$-mode, the companion $d1|$out channel plays a negligible role, so that the $|S_{d1,d2}|^2$ term can be omitted in the normalization condition $|S_{d2,d2}|^2 = 1 + |S_{u,d2}|^2 + |S_{d1,d2}|^2$ of the S-matrix (see, e.g., Ref. [156]). Then one obtains in the long-wavelength limit

$$|\,\langle \hat{c}_U(\omega)\, \hat{c}_{D2}(\omega)\rangle\,|^2 = |S_{u,d2}|^2\, |S_{d2,d2}|^2 \simeq n_{T_{\rm H}}(\omega)\,[1 + n_{T_{\rm H}}(\omega)]\,. \tag{177}$$

The right plot of Figure 27 shows the correlation spectrum for a waterfall configuration with $m_u = 0.59$. Similarly to the left graph of the same figure, the red curve is obtained from equation (177) by approximating the Hawking radiation by a thermal radiation $n_{T_{\rm H}}$. In this case, the best fit between the blue and the red curves leads to $T_{\rm H} = 0.106\, g n_u$, slightly different from the result obtained from the Hawking radiation spectrum $\left\langle \hat{c}_U^\dagger \hat{c}_U \right\rangle$. This discrepancy results from the fact that we neglect the $d1|$out channel in the calculation of (177).

In the following we choose to use equation (177) to determine the Hawking temperature to be in agreement with the choice made by the experimental group [131, 177].

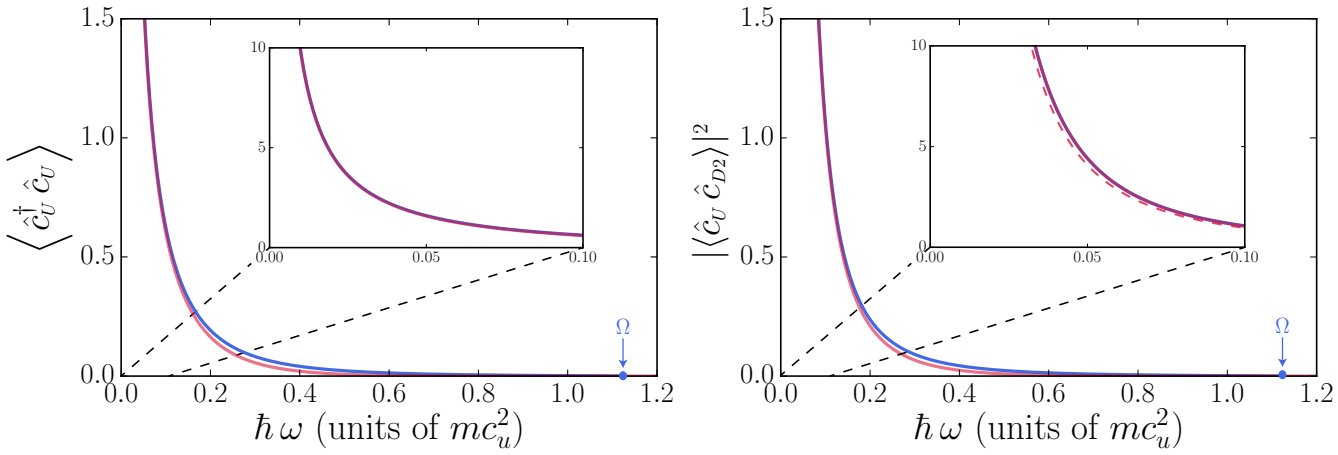

FIGURE 27: Here, we consider a waterfall configuration whose upstream Mach number is $m_u = 0.59$.
(Left) The blue curve is the Hawking radiation spectrum $\mathcal{N}_{\rm H}$ as a function of the energy $\hbar\omega$ in units of mc_u^2. The red curve corresponds to a thermal radiation $n_{T_{\rm H}}$ of temperature $T_{\rm H} = 0.102\, g n_u$ [see equation (176)]. The inset shows a zoom on the low energy sector. We recall that Ω is the threshold frequency above which the $d2$ modes disappear.
(Right) The blue curve corresponds to the correlation spectrum (177) as a function of the energy $\hbar\omega$ in units of mc_u^2, while the red curve is obtained from equation (177) by approximating the Hawking radiation by a thermal radiation $n_{T_{\rm H}}$, with $T_{\rm H} = 0.106\, g n_u$. The inset shows a zoom on the low energy sector. The dashed red curve drawn in this inset is obtained from a thermal radiation with $T_{\rm H} = 0.102\, g n_u$, i.e., the Hawking temperature determined from the Hawking radiation spectrum $\mathcal{N}_{\rm H}$.

3.3.2 *Fourier transform of* $g^{(2)}$

It is actually possible to obtain the correlation spectrum (177) from the Fourier transform of density correlations. Indeed, Figure 28 shows the result of the Fourier transform of $g^{(2)}$ computed over the upper left region of Figure 23. One can observe a more pronounced signal for certain pairs (k, k'). For instance, the brightest signal corresponds to Hawking-Partner pairs (u|out-$d2$|out). Indeed, for each frequency ω one can calculate wavevectors $k = k_{\rm H}(\omega)$ and $k' = k_{\rm P}(\omega)$, the momenta relative to the condensate of a Hawking quantum (H) and its Partner (P) obtained from the dispersion relation (132). This calculation leads to the green curve in Figure 28 that fits perfectly with the bright signal obtained from the computation of the Fourier transform. Another signal is much less bright and corresponds to Hawking-Companion pairs (u|out-$d1$|out). The red curve corresponds to $k' = k_{d1|\rm out}(\omega)$ as a func-

tion of $k = k_{\rm H}(\omega)$, and indeed follows the signal computed from the Fourier transform (this signal is more visible in the inset of Figure 28).

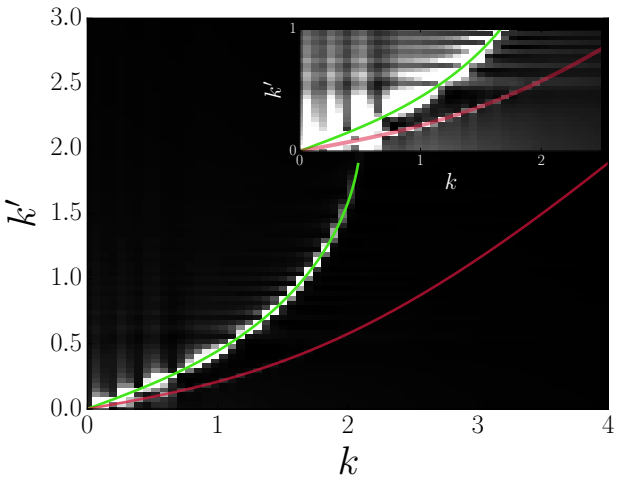

FIGURE 28: Fourier transform of $g^{(2)}$ computed over the upper left region of Figure 23. The green curve corresponds to $k = k_{\rm H}$ and $k' = k_{\rm P}$, the momenta relative to the condensate of a Hawking quantum and its partner obtained from the dispersion relation (132). The red curve corresponds to $k = k_{\rm H}$ and $k' = k_{d1|\rm out}$. The inset shows the same plot, but overexposed to enhance the Hawking-Companion ($u|$out-$d1|$out) correlation signal.

Figure 29 illustrates the computation of the Fourier transform of $g^{(2)}$ computed over the green rectangle of Figure 25 for both theoretical and experimental results. One sees a clear damping of the signal compared to Figure 28 when the region of integration of the Fourier transform becomes relatively narrow: this is a first hint of the importance of the windowing of the Fourier transform. The signal pertaining to Hawking-Companion pairs ($u|$out-$d1|$out) has completely disappear. This might lead us to believe that no quasiparticles are emitted in the mode $d1|$out, while this is not the case since a signal is clearly visible in k-space (see Figure 28) and in real space (see Figure 23).

Let us go further in the analysis: if we perform the Fourier transform of $g^{(2)}$ at fixed ω, for wavevectors $k_{\rm H}(\omega)$ and $k_{\rm P}(\omega)$ ($u|$out-$d2|$out channels) having an energy $\hbar\omega$ in the laboratory frame, one obtains (see Appendix C)

$$\begin{aligned}&\frac{\mathcal{S}_0^{-1}}{\sqrt{n_u n_d L_u L_d}}\int_{-L_u}^{0}dx\int_{0}^{L_d}dx'\,e^{-i(k_{\rm H}x+k_{\rm P}x')}\,g^{(2)}(x,x')\\&=d(\omega)\,\langle\hat{c}_U(\omega)\hat{c}_{D2}(\omega)\rangle=d(\omega)\,S_{u,d2}\,S^{\star}_{d2,d2}.\end{aligned}\tag{178}$$

In equation (178) $d(\omega)$ is a damping factor which depends on the windowing of the Fourier transform [see below, equation (179)]. $\mathcal{S}_0(\omega) = (u_{k_{\rm H}} + v_{k_{\rm H}})(u_{k_{\rm P}} + v_{k_{\rm P}})$ is the static structure factor, where the u_k's and the v_k's are the standard Bogoliubov amplitudes of excitations of momentum k (see, e.g., Refs. [148, 153]). The integration region

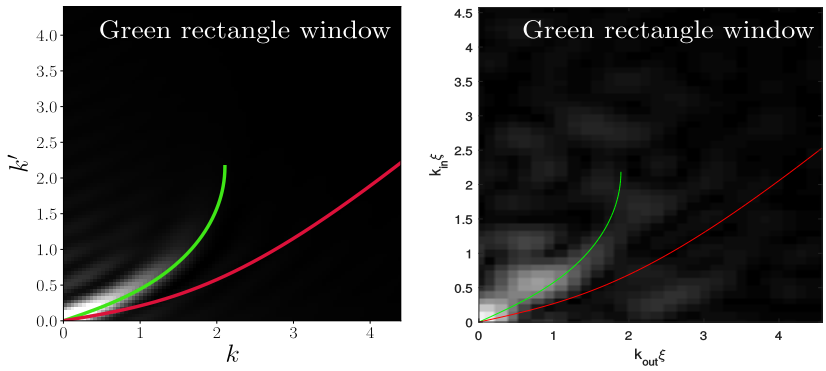

FIGURE 29: Fourier transform of $g^{(2)}$ computed over the green rectangle of Figure 25 – (Left) Theoretical result (Right) Experimental result extracted from Ref. [131]. The green curve corresponds to $k = k_{\rm H}$ and $k' = k_{\rm P}$, the momenta relative to the condensate of a Hawking quantum and its partner obtained from the dispersion relation (132). The red curve corresponds to $k = k_{\rm H}$ and $k' = k_{d1|\rm out}$.

$[-L_u, 0] \times [0, L_d]$ lies in the upper left quadrant of Figure 23. Equation (178) remains valid as long as $k_{\rm H}\, L_u \gg 1$ and $k_{\rm P}\, L_d \gg 1$ (see Appendix C).

The damping factor $d(\omega)$ in equation (178) can be calculated (see Appendix C) and is

$$\begin{aligned} &d(\omega) = \frac{1}{\sqrt{a(\omega)}}, \text{ if } a(\omega) \geq 1, \quad \text{and} \quad d(\omega) = \sqrt{a(\omega)}, \text{ if } a(\omega) \leq 1, \\ &\text{with} \quad a(\omega) = \frac{L_d\, |V_g(k_{\rm H})|}{L_u\, V_g(k_{\rm P})}. \end{aligned} \tag{179}$$

In equation (179) $V_{g,\rm H}(\omega) = \partial\omega/\partial q|_{q=k_{\rm H}}$ $[V_{g,\rm P}(\omega)]$ is the group velocity of a Hawking quantum [of a partner] of energy $\hbar\omega$. One sees that there is no damping ($d(\omega) = 1$) if and only if

$$\frac{L_u}{|V_{g,\rm H}(\omega)|} = \frac{L_d}{V_{g,\rm P}(\omega)}, \tag{180}$$

We recover exactly the same condition as the one mentioned in Refs. [62, 134]. Therefore, it is clear from equation (180) that the integration region $[-L_u, 0] \times [0, L_d]$ should be adapted for each value of ω. This result will be of paramount importance in the following: if one does not adapt the integration region, the Fourier transform (178) is automatically damped and, thus, one does not obtain the true correlation spectrum (177). This could lead to the erroneous conclusion that the analogous Hawking radiation is thermal (see Section 3.3.3).

The red curve of Figure 30 shows the correlation spectrum (177) normalized by the static structure factor $\mathcal{S}_0(\omega)$. The green dots are obtained from the numerical computation of the Fourier transform of $g^{(2)}$ [equation (178)] and, in this case, the windowing $[-L_u, 0] \times [0, L_d]$ is adapted for each frequency ω using relation (180). One observes a

nice agreement between the theoretical prediction and numerical results, except for low energies where conditions $k_{\rm H}\, L_u \gg 1$ and $k_{\rm P}\, L_d \gg 1$ are violated. The blue curve is obtained for an other choice of windowing that does not respect condition (180): here, we choose $L_u\, V_{g,{\rm P}}(0) = L_d\, |V_{g,{\rm H}}(0)|$, i.e., the long-wavelength limit of equation (180). Thus, L_u and L_d are the same for all frequencies. The brown stars are obtained from the numerical computation of the Fourier transform of $g^{(2)}$ and agree well with the damped correlation spectrum predicted by equation (178).

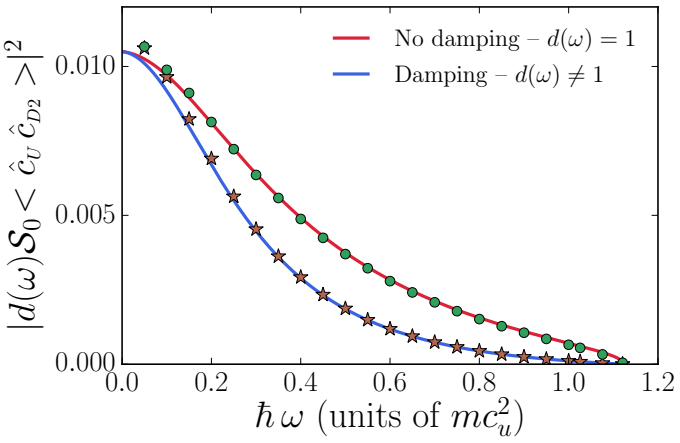

FIGURE 30: Hawking-Partner correlation signal. The red curve is the correlation spectrum obtained from the right hand side of equation (178) with $d(\omega) = 1, \forall\, \omega$. The green dots corresponds to the numerical computation of the Fourier transform of $g^{(2)}$ [see the left hand side of equation (178)], where the integration region $[-L_u, 0] \times [0, L_d]$ is adapted for each frequency ω to respect condition (180). The blue curve also corresponds to the right hand side of equation (178), but with $d(\omega) \neq 1$. In this particular case, we choose $L_u\, V_{g,{\rm P}}(0) = L_d\, |V_{g,{\rm H}}(0)|$ leading to $[d(\omega)]^2 = |V_{g,{\rm H}}(0)|\, V_{g,{\rm P}}(\omega)/[V_{g,{\rm P}}(0)\, |V_{g,{\rm H}}(\omega)|] < 1$. The brown stars are obtained from the numerical computation of the Fourier transform of $g^{(2)}$ with $L_u\, V_{g,{\rm P}}(0) = L_d\, |V_{g,{\rm H}}(0)|$.

3.3.3 *Thermality?*

Hawking predicted that black holes should emit a thermal radiation, characterized by an effective temperature, the Hawking temperature [87, 88]. This important property comes from the fact that dispersive effects are totally absent in General Relativity: a massless field propagates at the speed of light regardless of its frequency or wavevector. The wave speed is absolutely fixed.

The thermality of Hawking radiation is crucial because it ensures the correctness of the analogy between analogue gravity and General Relativity. However, we argued several times in the previous subsections that dispersion does play an important role in Bose-Einstein condensates. However, it is commonly accepted that the spectrum of analo-

gous Hawking radiation only weakly departs from thermality [41, 42, 183]. This general consensus has been recently reinforced by the experimental results obtained by the Technion group, claiming that the experimental analogous Hawking radiation is thermal [102, 131].

In this subsection we demonstrate that dispersive effects lead to a significant departure from thermality, at least from a theoretical point of view. We also use the findings of Section 3.3.2 to show that a self-consistent procedure might lead to the unfounded conclusion that the analogous Hawking radiation is fully thermal.

DISPERSIONLESS AND THERMAL MODEL To explain this claim, let us first consider a simple dispersionless and thermal model: we only take into account correlations between Hawking-Partner pairs and we approximate all the coefficients of the scattering matrix by their long-wavelength limit; one has in particular $|S_{u,d2}|^2 = n_{T_{\rm H}}(\omega)$, $\forall\,\omega$, with $n_{T_{\rm H}}$ a Bose thermal distribution of temperature $T_{\rm H}$ [see Section 3.3.1 and equation (177)]. In this case we obtain the following result for $g^{(2)}$ in a waterfall configuration [156]:

$$\begin{aligned} g^{(2)}(x,x') &= \frac{c_u^2}{|V_{u|\rm out}|\,V_{d2|\rm out}\,m_u}\int_0^\Sigma \frac{d\varepsilon}{2\,\pi}\,f(\varepsilon,x,x')\ , \\ f(\varepsilon,x,x') &= \frac{\varepsilon\,e^{\varepsilon/(2\,T_{\rm H})}}{e^{\varepsilon/T_{\rm H}}-1}\,\cos\left[\frac{c_u\,\varepsilon}{\xi_u}\left(\frac{x}{V_{d2|\rm out}}-\frac{x'}{V_{u|\rm out}}\right)\right]. \end{aligned} \tag{181}$$

In equation (181), $V_{u|\rm out} = c_u\,(m_u-1)$ and $V_{d2|\rm out} = c_d\,(m_d-1)$ are the group velocity of the Hawking and partner quanta in the dispersionless regime. The parameter $\Sigma = \hbar\,\Omega/(mc_u^2)$ is the usual cut-off above which $d2$-modes cease to exist. Expression (181) can be re-written in terms of the local coordinate x'', orthogonal to the locus of the minima of $g^{(2)}$, defined in Section 3.2.5 and indicated in Figure 25 and Figure 26. One finds

$$\begin{cases} x'' = \dfrac{x-x'/\gamma}{\sqrt{1+\gamma^2}}, \\ g^{(2)}(x'') = \dfrac{c_u^2}{|V_{u|\rm out}|\,V_{d2|\rm out}\,m_u}\displaystyle\int_0^\Sigma \frac{d\varepsilon}{2\,\pi}\,\frac{\varepsilon\,e^{\varepsilon/(2\,T_{\rm H})}}{e^{\varepsilon/T_{\rm H}}-1}\,\cos\left(\frac{\varepsilon}{l}\,x''\right), \end{cases} \tag{182}$$

with $\gamma = V_{u|\rm out}/V_{d2|\rm out}$ and $l = \sqrt{m_u}\,(1-m_u)/\sqrt{\gamma^2-1}$. The density-density correlation function (182) is shown in the left plot of Figure 31 (brown curve, with $m_u = 0.59$ and $T_{\rm H} = 0.106\,gn_u$). We also display for comparison the theoretical correlation signal in the presence of dispersion (red curve) and experimental data (blue dots) already shown in Figure 26. We recall that $g^{(2)}_{\rm av}$ means that the experimental blue dots and the theoretical red curve have been obtained after averaging the correlation signal over cuts perpendicular to the Hawking-Partner correlation line.

The symmetry of the dispersionless profile in Figure 31 is a feature of the absence of dispersion [156]. However, one sees that neither the symmetry nor the width and the depth of the dispersionless profile match well with the red curve or the experimental blue dots.

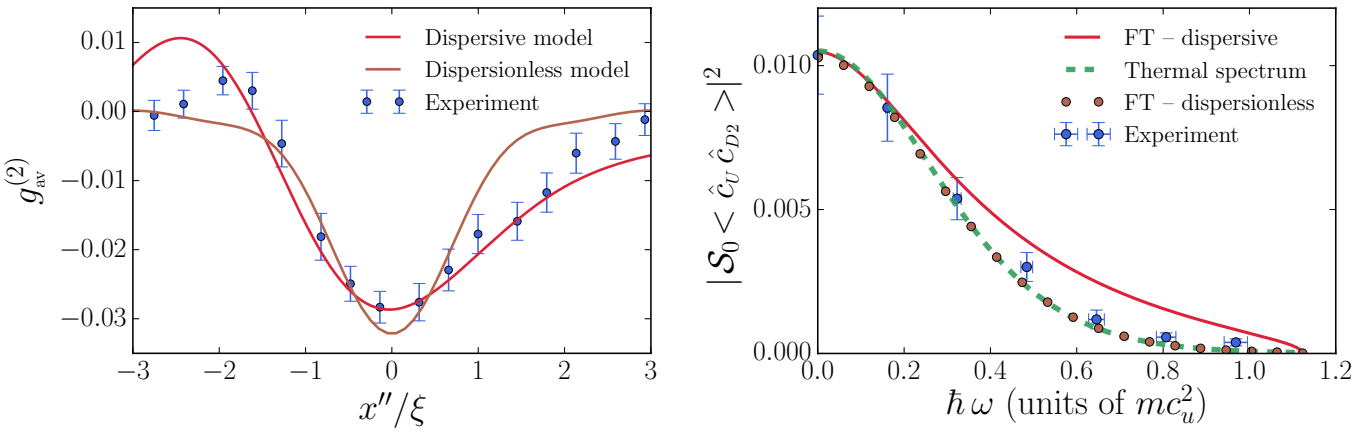

FIGURE 31: Here we consider a waterfall configuration with $m_u = 0.59$.
(Left) Experimental blue dots and the theoretical red curve have been obtained after averaging the correlation signal over cuts perpendicular to the Hawking-Partner correlation line (see for instance Figure 26). The brown curve corresponds to the dispersionless model, whose density-density correlation function is made explicit in equation (182).
(Right) The red curve corresponds to the Fourier transform of $g^{(2)}$ in the presence of dispersion, while the brown dots are obtained from the Fourier transform of the dispersionless profile (181). The dashed green curve is a thermal spectrum with effective temperature $T_{\rm H} = 0.106\,gn_u$. The blue dots with error bars are from Ref. [131]. They are obtained after processing the experimental result for $g^{(2)}$.

Therefore, we would not expect *a priori* that the Hawking correlation spectrum $|\,\langle \hat{c}_U(\omega)\,\hat{c}_{D2}(\omega)\rangle\,|^2$ of the dispersionless model coincides with those obtained from the dispersive model and experimental results; and this is indeed the case for the theoretical result: the red curve in the right plot of Figure 31 corresponds to the Fourier transform of $g^{(2)}$ in the presence of dispersion, while the brown dots are obtained from the Fourier transform of the dispersionless profile (181). By virtue of equations (178) and (177), the brown dots should match with a thermal correlation spectrum of temperature $T_{\rm H}$[15]. This is indeed the case as shown in the right plot of Figure 31 where the dashed green curve corresponds to a thermal spectrum with an effective temperature $T_{\rm H} = 0.106\,gn_u$. Moreover, as expected, the red curve and the brown dots coincide in the dispersionless regime, i.e., in the long-wavelength limit ($\hbar\,\omega \to 0$). Then, the red curve deviates from the thermal spectrum due to dispersive effects. Thus, we can conclude that the analogous Hawking radiation significantly departs from thermality in a Bose-Einstein condensate.

It is clear from the left plot of Figure 31 that the experimental blue dots are closer from the dispersive red curve than the dispersionless brown curve. Therefore, the natural question that arises from this comment is: why the experimental correlation spectrum shown in the right

15 Note that here the windowing of the Fourier transform does not need to be adapted, since condition (180) does not depend on the frequency in the dispersionless regime.

plot of Figure 31 does not follow the theoretical (dispersive) expectation, but, on the contrary, seems to coincide with a thermal spectrum?

To answer this question or, at least, suggest a procedure which might lead to this outcome, we need to keep in mind the results obtained in the previous subsection. Indeed, we noticed in Section 3.3.2 that the windowing of the Fourier transform of $g^{(2)}$ plays a significant role in the result: if the region of integration is not adapted for each frequency ω, the correlation spectrum is automatically damped by a factor $d(\omega)$ made explicit in equation (179). Figure 32 illustrates the consequence of this remark: the left plot of this figure shows the expected ('true') correlation spectrum (177) for a waterfall configuration with $m_u = 0.59$ (red curve), as well as the damped correlation spectrum obtained with a region of integration fixed by the long-wavelength limit of equation (180) with $m_u = 0.59$ (blue curve)[16]. The dashed gray curve represents a thermal spectrum with an effective temperature $T_{\rm H} = 0.106\, g n_u$. One sees that the blue curve is very close to the thermal spectrum and this would make us think that analogous Hawking radiation is thermal. We hope to convince the reader of the importance of the windowing of the Fourier transform (178) here.

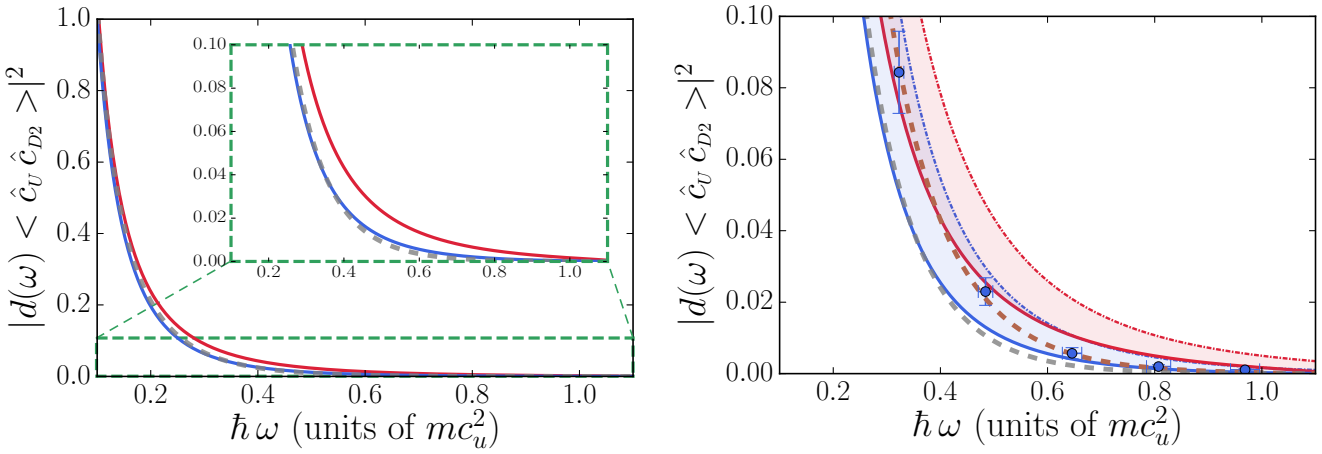

FIGURE 32: (Left) Red curve: true correlation spectrum with no damping. Blue curve: damped correlation spectrum, computed from (178) with a region of integration that corresponds to the long-wavelength limit of condition (180). The dashed gray curve is a thermal spectrum with effective temperature $T_{\rm H} = 0.106\, g n_u$. The inset is a zoom on the dashed green rectangle region. Here, we consider a waterfall configuration with $m_u = 0.59$.
(Right) The light red (light blue) region is the expected (damped) correlation spectrum obtained in a waterfall configuration for different upstream Mach numbers, ranging from $m_u = 0.51$ (dashed dotted red and blue curves) to $m_u = 0.59$ (solid red and blue curves). The blue dots are extracted from Ref. [131]. The dashed gray and the dashed borwn curves correspond to thermal spectra whose temperatures are $T_{\rm H} = 0.106\, g n_u$ and $T_{\rm H} = 0.124\, g n_u$, respectively.

16 This figure actually corresponds to Figure 30 without the normalization factor $\mathcal{S}_0$.

The right plot of Figure 32 corresponds to the inset of the left graph. Blue dots are obtained after processing the experimental data for $g^{(2)}$ and are extracted from Ref. [131]. The light red (light blue) region is the true (damped) correlation spectrum obtained for different upstream Mach numbers, ranging from $m_u = 0.51$ (dashed dotted red and blue curves) to $m_u = 0.59$ (solid red and blue curves). In the long-wavelength limit, experimental points belong to the light red and the light blue regions. Then, they slightly deviate to the lower bound of the blue region and they stay there up to the cut-off frequency Ω. The brown curve is a thermal spectrum of effective temperature $T_{\mathrm{H}} = 0.124\, g n_u$, corresponding to the experimental value found in Ref. [131].

Therefore, several conclusions can be drawn from the above comments. It is quite possible that dispersive effects only play a negligible role in the experiment and, in this case, it is not surprising to find a nice agreement with a thermal spectrum[17]. However, it is clear from the procedure described and used in Ref. [131] to analyze experimental data that the windowing has not been adapted for each frequency. Thus, the analysis of experimental data could have been dramatically affected by the windowing of the Fourier transform, leading to a damping of the correlation spectrum. Results shown in Figure 32 are totally consistent with this explanation.

In conclusion, from a theoretical point of view, the analogous Hawking radiation is not fully thermal, except in the long-wavelength limit. We also explained that a data analysis procedure might lead to the erroneous conclusion that the Hawking radiation spectrum is thermal: the only manner to obtain the true correlation spectrum is to adapt the window of the Fourier transform such as prescribed by condition (180). Despite this fact, the agreement between the thermal spectrum and the true spectrum in the dispersionless regime leads to the correct determination of the Hawking temperature.

17 The angle of the Hawking-Partner correlation line shown in Figure 25 (which deviates from the dispersionless result) and the asymmetry of the experimental profile shown in Figure 26 would let us think that dispersion does have an effect in the experiment.

3.4 ARTICLE: DEPARTING FROM THERMALITY OF ANALOGUE HAWKING RADIATION IN A BOSE-EINSTEIN CONDENSATE

↪ Departing from thermality of analogue Hawking radiation in a Bose-Einstein condensate

M. Isoard, N. Pavloff, Physical Review Letters **124**, 060401 (2020)

doi: https://doi.org/10.1103/PhysRevLett.124.060401

We study the quantum fluctuations in a one dimensional Bose-Einstein condensate realizing an analogous acoustic black hole. The taking into account of evanescent channels and of zero modes makes it possible to accurately reproduce recent experimental measurements of the density correlation function. We discuss the determination of Hawking temperature and show that in our model the analogous radiation presents some significant departure from thermality.

Departing from Thermality of Analogue Hawking Radiation in a Bose-Einstein Condensate

M. Isoard and N. Pavloff
Université Paris-Saclay, CNRS, LPTMS, 91405 Orsay

(Received 5 September 2019; accepted 9 January 2020; published 10 February 2020)

We study the quantum fluctuations in a one-dimensional Bose-Einstein condensate realizing an analogous acoustic black hole. The taking into account of evanescent channels and of zero modes makes it possible to accurately reproduce recent experimental measurements of the density correlation function. We discuss the determination of Hawking temperature and show that in our model the analogous radiation presents some significant departure from thermality.

DOI: 10.1103/PhysRevLett.124.060401

The Hawking effect [1] being of kinematic origin [2] can be transposed to analogue systems, as first proposed by Unruh [3]. Among the various platforms that have been proposed for observing induced or spontaneous analogous Hawking radiation and related phenomena, the ones for which the experimental activity is currently the most intense are surface water waves [4–10], nonlinear light [11–17], excitonic polaritons [18], and Bose-Einstein condensed atomic vapors [19–22].

Because of their low temperature, their intrinsic quantum nature, and the high experimental control achieved in these systems, Bose-Einstein condensates (BECs) seem particularly suitable for studying analogue Hawking effect. Steinhauer and colleagues have undertaken several studies of quasiunidimensional configurations, making it possible to realize analogue black hole horizons in BEC systems, and made claims of observation of Hawking radiation [20–22]. Their results have triggered the interest of the community [23–33] and generated a vivid debate [34,35]. One of the goals of the present Letter is to contribute to this debate, and to partially close it, at least in what concerns density correlations around an analogue black hole horizon. A definite theoretical answer can be obtained thanks to a remark that had been overlooked in previous works: one needs to develop the quasiparticle operator on a complete basis set for properly describing the density fluctuations. This is achieved in the first part of this Letter, and we apply this theoretical approach to the analysis of the experimental results of Ref. [22].

While in general relativity the thermality of the Hawking radiation is constrained by the laws of black hole thermodynamics, no such general principle is expected to hold for analogue systems [2]. It is nonetheless commonly accepted that the spectrum of analogous Hawking radiation only weakly departs from thermality [36–38], and that all relevant features of an analogue system can be understood on the basis of a hydrodynamical, long wavelength description. However, the phenomenology of analogous systems provides mechanisms supporting the impossibility of a perfectly thermal analogue Hawking radiation [39]. In the second part of this Letter we argue that in the BEC case we are considering, it is legitimate to determine a Hawking temperature from the information encoded in the density correlation function, but we show that some features of the radiative process at hand significantly depart from thermality and propose a procedure for confirming our view.

We consider a one-dimensional configuration in which the quantum field $\hat{\Psi}(x,t)$ is a solution of the Gross-Pitaevskii equation

$$i\hbar\partial_t\hat{\Psi} = -\frac{\hbar^2}{2m}\partial_x^2\hat{\Psi} + [g\hat{n} + U(x)]\hat{\Psi}. \tag{1}$$

In this equation m is the mass of the atoms, $\hat{n} = \hat{\Psi}^\dagger\hat{\Psi}$, and the term $g\hat{n}$ describes the effective repulsive atomic interaction ($g > 0$). We have studied several external potentials $U(x)$ making it possible to engineer a sonic horizon, but we only present here the results for a step function: $U(x) = -U_0\Theta(x)$ with $U_0 > 0$. The reason for this choice is twofold: (i) This potential has been realized experimentally in Refs. [21,22]; (ii) from the three configurations analyzed in Ref. [31], this is the one that leads to the signal of quantum nonseparability which is the largest and the most resilient to temperature effects.

In the spirit of Bogoliubov's approach, we write the quantum field as

$$\hat{\Psi}(x,t) = \exp(-i\mu t/\hbar)[\Phi(x) + \hat{\psi}(x,t)], \tag{2}$$

where μ is the chemical potential. $\Phi(x)$ is a classical field describing the stationary condensate and $\hat{\psi}(x,t)$ accounts for small quantum fluctuations. Although such a separation is not strictly valid in one dimension, it has been argued in Ref. [31] that it constitutes a valid approximation over a large range of one-dimensional densities. In the case we

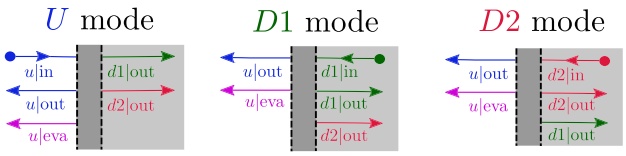

FIG. 1. Sketch of the different channels contributing to the incoming quantum modes U, $D1$, and $D2$. In each plot the background BEC propagates from left to right, the white region corresponds to the upstream subsonic flow, the gray one to the interior of the analogous black hole (downstream supersonic flow), and the region of the horizon is represented by the dark gray shaded interface. The Hawking channel and its partner are labeled $u|$out and $d2|$out. The $d1|$out channel is a companion propagating away from the horizon, inside the analogous black hole region. Each mode (U, $D1$, and $D2$) is seeded by an ingoing channel ($u|$in, $d1|$in, and $d2|$in) whose group velocity is directed towards the horizon.

consider, Φ is a solution of the classical Gross-Pitaevskii equation describing a sonic horizon: the $x<0$ profile is half a dark soliton [40], with $\Phi(x\to-\infty)=\sqrt{n_u}\exp(ik_u x)$, where n_u and $V_u=mk_u/\hbar$ (>0) are the upstream asymptotic density and velocity, respectively. The downstream ($x>0$) flow of the condensate corresponds to a plane wave: $\Phi(x>0)=\sqrt{n_d}\exp(ik_d x-i\pi/2)$. The asymptotic upstream and downstream sound velocities are $c_{(u,d)}=\sqrt{gn_{(u,d)}/m}$. The analogous black hole configuration corresponds to a flow that is asymptotically upstream subsonic ($V_u<c_u$) and downstream supersonic ($\hbar k_d/m=V_d>c_d$).

We describe the quantum fluctuations on top of this classical field within a linearized approach. The relevant modes are identified by using the asymptotic ingoing (i.e., directed towards the acoustic horizon) and outgoing channels, far from the horizon. As discussed in previous references [41–45] and recalled in [46], the Bogoliubov dispersion relation supports a decomposition of $\hat{\psi}$ onto three incoming modes that we denote as U, $D1$, and $D2$. For instance, the U mode is seeded by an upstream incoming wave that we denote as $u|$in, which propagates towards the horizon with a long wavelength group velocity V_u+c_u. It is scattered onto two outgoing transmitted channels (propagating in the analogue black hole away from the horizon), which we denote as $d1|$out and $d2|$out with respective long wavelength group velocities V_d+c_d and V_d-c_d (both positive) and one outgoing reflected channel (propagating away from the horizon, outside of the analogue black hole, with long wavelength group velocity $V_u-c_u<0$). The corresponding three scattering coefficients are denoted as $S_{d1,u}$, $S_{d2,u}$, and $S_{u,u}$. There is also an upstream evanescent wave ($u|$eva) that carries no current, does not contribute to the S matrix, but is important for fulfilling the continuity relations at $x=0$. The situation is schematically depicted in Fig. 1.

The frequency-dependent boson operators associated to the three incoming modes U, $D1$, and $D2$ are denoted as $\hat{b}_U$, $\hat{b}_{D1}$, and $\hat{b}_{D2}$; they obey the commutation relations $[\hat{b}_L(\omega),\hat{b}^\dagger_{L'}(\omega')]=\delta_{L,L'}\delta(\omega-\omega')$. In addition, Bose-Einstein condensation is associated with a spontaneously broken $U(1)$ symmetry that implies the existence of supplementary zero modes of the linearized version of (1). As discussed in Ref. [50], one is lead to introduce two new operators $\hat{\mathcal{P}}$ and $\hat{\mathcal{Q}}$ accounting for the global phase degree of freedom, and the correct expansion of the quantum fluctuation field reads

$$\begin{aligned}\hat{\psi}(x,t)=&-i\Phi(x)\hat{\mathcal{Q}}+iq(x)\hat{\mathcal{P}}+\int_0^\infty\frac{d\omega}{\sqrt{2\pi}}\sum_{L\in\{U,D1\}}\\&\times[u_L(x,\omega)e^{-i\omega t}\hat{b}_L(\omega)+v_L^*(x,\omega)e^{i\omega t}\hat{b}_L^\dagger(\omega)]\\&+\int_0^\Omega\frac{d\omega}{\sqrt{2\pi}}[u_{D2}(x,\omega)e^{-i\omega t}\hat{b}^\dagger_{D2}(\omega)\\&+v^*_{D2}(x,\omega)e^{i\omega t}\hat{b}_{D2}(\omega)].\end{aligned}\tag{3}$$

In this expression the u_L's and v_L's are the usual Bogoliubov coefficients (their explicit form is given for instance in Ref. [44]), and the quantization of the $D2$ mode is atypical, as discussed in several previous references [41,42,51]. The function $q(x)$ is one of the components of the zero eigenmodes; see [46]. Omitting the contribution of the zero mode operators $\hat{\mathcal{P}}$ and $\hat{\mathcal{Q}}$ would correspond to using an incomplete basis set for the expansion of the quantum fluctuations; in other words, their contribution is essential for verifying the correct commutation relation $[\hat{\psi}(x,t),\hat{\psi}^\dagger(y,t)]=\delta(x-y)$. The operator $\hat{\mathcal{Q}}$ is associated with the global phase of the condensate. $\hat{\mathcal{P}}$ is the canonical conjugate operator ($[\hat{\mathcal{Q}},\hat{\mathcal{P}}]=i$) that typically appears in the quadratic Hamiltonian $\hat{H}_{\rm quad}$ describing the dynamics of the quantum fluctuations with a $\hat{\mathcal{P}}^2$ contribution, while $\hat{\mathcal{Q}}$ does not [50,52,53]. This means that the degree of liberty associated with the broken symmetry has no restoring force—as expected on physical grounds—and that the zero excitation quantum state $|\mathrm{BH}\rangle$ describing the analogous black hole configuration verifies $\hat{\mathcal{P}}|\mathrm{BH}\rangle=0$ and $\hat{b}_L(\omega)|\mathrm{BH}\rangle=0$ for $L\in\{U,D1,D2\}$.

Once the appropriate expansion (3) has been performed, and the correct quantum state $|\mathrm{BH}\rangle$ has been identified, one can compute the density correlation function,

$$\begin{aligned}G_2(x,y)=&\langle{:}\hat{n}(x,t)\hat{n}(y,t){:}\rangle-\langle\hat{n}(x,t)\rangle\langle\hat{n}(y,t)\rangle\\\simeq&\,\Phi(x)\Phi^*(y)\langle\hat{\psi}^\dagger(x,t)\hat{\psi}(y,t)\rangle\\&+\Phi(x)\Phi(y)\langle\hat{\psi}^\dagger(x,t)\hat{\psi}^\dagger(y,t)\rangle+\text{c.c.}\end{aligned}\tag{4}$$

In this equation, the symbol ${:}$ denotes normal ordering and the final expression is the Bogoliubov evaluation of G_2, encompassing the effects of quantum fluctuations at leading order. At zero temperature, the average $\langle\cdots\rangle$ in Eq. (4) is taken over the state $|\mathrm{BH}\rangle$. Although this state is thermodynamically unstable and cannot support a thermal

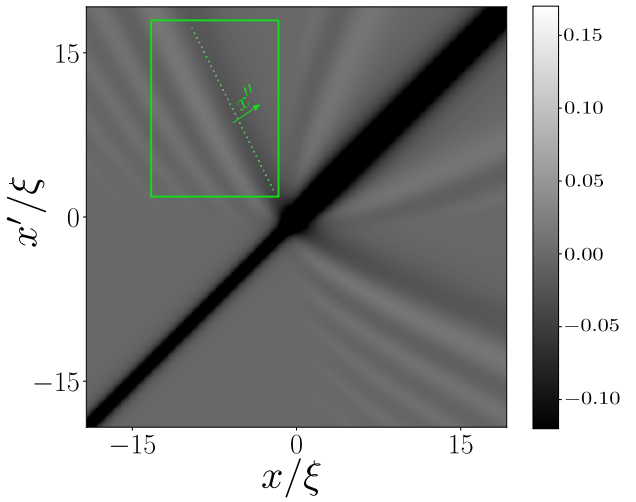

FIG. 2. Intensity plot of the dimensionless correlation function $\xi(n_u n_d)^{-1/2} G_2(x, x')$ for x and x' close to the horizon. The parameter $\xi = \sqrt{\xi_u \xi_d}$ is the geometrical mean of the healing lengths ξ_u and ξ_d, where $\xi_{(u/d)} = \hbar(mgn_{(u,d)})^{-1/2}$. The line of anticorrelation in the upper left and lower right quadrants corresponds to the merging close to the horizon of the Hawking-partner $(u|\text{out} - d2|\text{out})$ and Hawking-companion $(u|\text{out} - d1|\text{out})$ correlations. The green rectangle delimits the region where we average G_2 for comparison with experimental data (see Fig. 3).

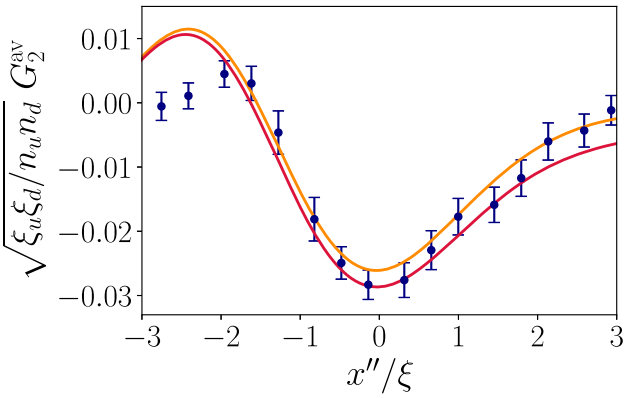

FIG. 3. Red solid line: zero temperature density correlation function $G_2^{\text{av}}(x, x')$ plotted as a function of x''. The blue dots with error bars are the results of Ref. [22]. The orange solid line is the finite temperature result for $k_B T = 0.2 g n_u$, i.e., $T \simeq 1.9 T_H$.

distribution, finite temperature effects can still be included as explained for instance in Refs. [31,41,42].

In 2008 a collaboration between teams from Bologna and Trento [54,55] pointed out that, in the presence of a horizon, G_2 should exhibit nonlocal features resulting from correlations between the different outgoing channels, in particular, between the Hawking quantum and its partner $(u|\text{out} - d2|\text{out}$ correlation in our terminology). The importance of this remark lies in the fact that, due to the weak Hawking temperature T_H (at best one fourth of the chemical potential [44]), the direct Hawking radiation is expected to be hidden by thermal fluctuations, whereas density correlations should survive temperature effects in typical settings [42]. This idea has been used to analyze the Hawking signal in Ref. [22], where a stationary correlation pattern was measured in the vicinity of the horizon. In this region, it is important for a theoretical treatment to account for the position dependence of the background density and to include the contribution of the evanescent channels in the expansion (3). We also checked that it is essential to take into account the contribution of the zero modes to obtain a sensible global description of the quantum fluctuations. The corresponding two-dimensional plot of the density correlation pattern is represented in Fig. 2. G_2 has been computed at zero temperature, for $V_d/c_d = 2.90$, which imposes $V_u/c_u = 0.59$ [44,46]. This value is chosen to reproduce the experimental configuration studied in Ref. [22]. The dotted line in the upper left quadrant of Fig. 2 marks the anticorrelation curve that results from the Hawking-partner $(u|\text{out} - d2|\text{out})$ and Hawking-companion $(u|\text{out} - d1|\text{out})$ correlations. We find that these two correlation lines, which separate at large distance from the horizon [42,44,55], merge close to the horizon, as also observed experimentally.

A precise comparison of our results with experiment can be achieved by following the procedure used in Ref. [22], which consists in averaging G_2 over the region inside the green rectangle represented in Fig. 2. One defines a local coordinate x'' that is orthogonal to the locus of the minima of G_2, and one plots the averaged G_2 (denoted as G_2^{av}) as a function of the variable x''. This is done in Fig. 3. We insist that the good agreement between our approach and the experimental results can only be achieved through a correct description of the quantum fluctuations—Eq. (3)—including the contribution of zero modes and evanescent channels.

It has been noticed by Steinhauer [56] that the determination of $G_2(x, x')$ in the upper left (or lower right) quadrant of the (x, x') plane makes it possible to evaluate the Hawking temperature thanks to the relation

$$S_{u,d2}(\omega) S^*_{d2,d2}(\omega) = \langle \hat{c}_U(\omega) \hat{c}_{D2}(\omega) \rangle = \frac{\mathcal{S}_0^{-1}}{\sqrt{n_u n_d L_u L_d}} \int_{-L_u}^{0} dx \int_{0}^{L_d} dx' e^{-i(k_H x + k_P x')} G_2(x, x'). \tag{5}$$

In this expression S is the matrix that describes the scattering of the different channels onto each other, and $\mathcal{S}_0(\omega) = (u_{k_H} + v_{k_H})(u_{k_P} + v_{k_P})$ is the static structure factor, where the u_k's and the v_k's are the standard Bogoliubov amplitudes of excitations of momentum k (see, e.g., Refs. [57,58]). The $\hat{c}_L$'s are outgoing modes related to the incoming ones by the S matrix [42]

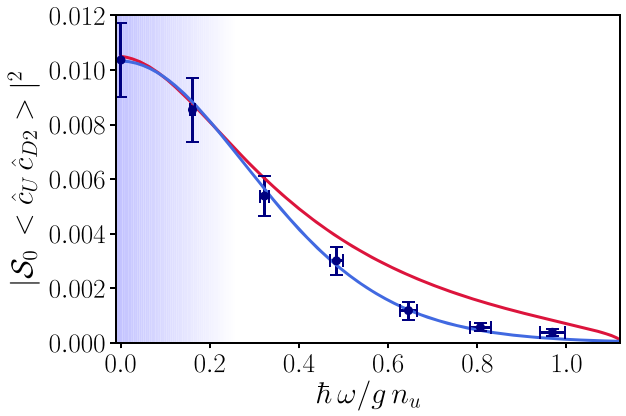

FIG. 4. Hawking-partner correlation signal represented as a function of the dimensionless energy. The red solid curve is the theoretical result from Eq. (5). The dots with error bars are from Ref. [22]. They are obtained after processing the experimental result for G_2 by means of the Fourier transform (5). The blue region corresponds to a domain where the ratio of Hawking and partner wave vectors is equal to its long wavelength value within a 10% accuracy. The blue solid curve is the theoretical result obtained by neglecting dispersive effects in Eq. (5) and discarding the contribution of the companion $d1|$out channel (see the text).

$$\begin{pmatrix} \hat{c}_U \\ \hat{c}_{D1} \\ \hat{c}^\dagger_{D2} \end{pmatrix} = \begin{pmatrix} S_{u,u} & S_{u,d1} & S_{u,d2} \\ S_{d1,u} & S_{d1,d1} & S_{d1,d2} \\ S_{d2,u} & S_{d2,d1} & S_{d2,d2} \end{pmatrix} \begin{pmatrix} \hat{b}_U \\ \hat{b}_{D1} \\ \hat{b}^\dagger_{D2} \end{pmatrix}. \quad (6)$$

The Fourier transform of G_2 in Eq. (5) is performed at fixed ω, for wave vectors $k_H(\omega)$ and $k_P(\omega)$, which are the momenta relative to the condensate of a Hawking quantum and its partner ($u|$out and $d2|$out channels in our terminology) having an energy $\hbar\omega$ in the laboratory frame. The integration region $[-L_u, 0] \times [0, L_d]$ lies in the upper left quadrant of Fig. 2, and should be adapted for each value of ω in such a way that [31,59]

$$\frac{L_u}{|V_{g,H}(\omega)|} = \frac{L_d}{V_{g,P}(\omega)}, \quad (7)$$

where $V_{g,H}(\omega)$ [$V_{g,P}(\omega)$] is the group velocity of a Hawking quantum (of a partner) of energy $\hbar\omega$. We have checked that once the prescription (7) is fulfilled, formula (5) is very well verified [46]. It is then intriguing to observe that, while theory and experiment both agree on the value of G_2 in real space (Fig. 3), they do not for the correlation $\langle \hat{c}_U(\omega)\hat{c}_{D2}(\omega)\rangle$: as can bee seen in Fig. 4, the agreement is restricted to the low energy regime. This is the bluish region in the figure, which corresponds to a domain where the ratio $k_H(\omega)/k_P(\omega)$ is equal to its long wavelength value $(c_u - V_u)/(c_d - V_d)$ with an error less that 10%.

Let us discuss this discrepancy in some detail. The interest of Eq. (5) lies in the fact that the scattering matrix coefficient $S_{u,d2}$ is the equivalent of the Hawking β parameter: its squared modulus is expected to behave as a Bose thermal distribution $n_{T_H}(\omega)$ with an effective temperature T_H, the Hawking temperature [1]. In an analogous system such as ours, because of dispersive effects, this equivalence is only valid in the long wavelength limit, typically in the blue region of Fig. 4. This suggests a possible manner to reconcile theory and experiment: we assume that the ratio $k_H(\omega)/k_P(\omega)$ is ω independent and equal to its low energy value, $(c_u - V_u)/(c_d - V_d)$ (this value is denoted as $\tan\theta$ in Refs. [21,22]). We also assume that, in the scattering process schematically illustrated in Fig. 1 for the $D2$ mode, the companion $d1|$out channel plays a negligible role, so that the $|S_{d1,d2}|^2$ term can be omitted in the normalization condition $|S_{d2,d2}|^2 = 1 + |S_{u,d2}|^2 + |S_{d1,d2}|^2$ of the S matrix (see, e.g., Ref. [42]). Then one obtains

$$|S_{u,d2}|^2 |S_{d2,d2}|^2 \simeq n_{T_H}(\omega)[1 + n_{T_H}(\omega)]. \quad (8)$$

Using the experimental values from Ref. [22] for V_α and c_α ($\alpha \in \{u, d\}$) and for the Hawking temperature T_H leads, within approximation (8), to the blue curve of Fig. 4 that agrees with the results published in Ref. [22] (blue dots with error bars). It is important to note that this procedure is self-consistent in the following sense: If one performs numerically the Fourier transform (5) over a domain that, instead of fulfilling the relation (7), verifies the ω-independent condition $L_u/|V_u - c_u| = L_d/(V_d - c_d)$, appropriate in a nondispersive, long wavelength approximation, one obtains a result (not shown for legibility, but see [46]) close to a thermal spectrum, i.e., to the blue curve in Fig. 4. Although this procedure is self-consistent, it is not fully correct, as can be checked by the fact that the resulting value of $\langle \hat{c}_U(\omega)\hat{c}_{D2}(\omega)\rangle$ only agrees with the exact one (red curve in Fig. 4) in the long wavelength limit. Stated differently: this procedure leads to the erroneous conclusion that the radiation is fully thermal. However, since all approaches coincide in the long wavelength regime (blue colored region of Fig. 4), they all lead to the correct determination of the Hawking temperature. For a flow with $V_d/c_d = 2.9$, our theoretical treatment yields $k_B T_H/(g n_u) = 0.106$, whereas the experimental value reported for this quantity in Ref. [22] is 0.124 (corresponding to a Hawking temperature $T_H = 0.35$ nK).

In conclusion, our work sheds a new light on the study of quantum correlations around an analogous black hole horizon, and on the corresponding Hawking temperature. From a theoretical point of view, we argue that the contribution of zero modes is essential for constructing a complete basis set necessary to obtain an accurate description of the quantum fluctuations. This claim is supported by the excellent agreement we obtain when comparing our results with recent experimental ones. On the experimental side, we substantiate the determination of the Hawking

temperature presented in Ref. [22], although we find that the Hawking spectrum is not thermal for all wavelengths. We identify a natural but unfounded procedure for analyzing the information encoded in $G_2(x,x')$ that leads to the opposite conclusion; we show that, within our approach, an alternative analysis of the correlation pattern accurately accounts for nonhydrodynamical effects. It would thus be interesting to reanalyze the data published in Ref. [22] to investigate if the windowing (7) we propose for Eq. (5) modifies the experimental conclusion for the Hawking-partner correlation signal and confirms the departure from thermality we predict.

We acknowledge fruitful discussions with I. Carusotto, M. Lewenstein, and J. Steinhauer, whom we also thank for providing us with experimental data.

[1] S. W. Hawking, Nature (London) **248**, 30 (1974); Commun. Math. Phys. **43**, 199 (1975).
[2] M. Visser, Phys. Rev. Lett. **80**, 3436 (1998).
[3] W. G. Unruh, Phys. Rev. Lett. **46**, 1351 (1981).
[4] G. Rousseaux, C. Mathis, P. Maïssa, T. G. Philbin, and U. Leonhardt, New J. Phys. **10**, 053015 (2008).
[5] S. Weinfurtner, E. W. Tedford, M. C. J. Penrice, W. G. Unruh, and G. A. Lawrence, Phys. Rev. Lett. **106**, 021302 (2011).
[6] L.-P. Euvé, F. Michel, R. Parentani, T. G. Philbin, and G. Rousseaux, Phys. Rev. Lett. **117**, 121301 (2016).
[7] V. Cardoso, A. Coutant, M. Richartz, and S. Weinfurtner, Phys. Rev. Lett. **117**, 271101 (2016).
[8] T. Torres, S. Patrick, A. Coutant, M. Richartz, E. W. Tedford, and S. Weinfurtner, Nat. Phys. **13**, 833 (2017).
[9] L.-P. Euvé, S. Robertson, N. James, A. Fabbri, and G. Rousseaux, arXiv:1806.05539.
[10] H. Goodhew, S. Patrick, C. Gooding, and S. Weinfurtner, arXiv:1905.03045.
[11] T. G. Philbin, C. Kuklewicz, S. Robertson, S. Hill, F. König, and U. Leonhardt, Science **319**, 1367 (2008).
[12] F. Belgiorno, S. L. Cacciatori, M. Clerici, V. Gorini, G. Ortenzi, L. Rizzi, E. Rubino, V. G. Sala, and D. Faccio, Phys. Rev. Lett. **105**, 203901 (2010).
[13] E. Rubino, F. Belgiorno, S. L. Cacciatori, M. Clerici, V. Gorini, G. Ortenzi, L. Rizzi, V. G. Sala, M. Kolesik, and D. Faccio, New J. Phys. **13**, 085005 (2011).
[14] M. Elazar, V. Fleurov, and S. Bar-Ad, Phys. Rev. A **86**, 063821 (2012).
[15] K. E. Webb, M. Erkintalo, Y. Xu, N. G. R. Broderick, J. M. Dudley, G. Genty, and S. G. Murdoch, Nat. Commun. **5**, 4969 (2014).
[16] D. Vocke, C. Maitland, A. Prain, K. E. Wilson, F. Biancalana, E. M. Wright, F. Marino, and D. Faccio, Optica **5**, 1099 (2018).
[17] J. Drori, Y. Rosenberg, D. Bermudez, Y. Silberberg, and U. Leonhardt, Phys. Rev. Lett. **122**, 010404 (2019).
[18] H. S. Nguyen, D. Gerace, I. Carusotto, D. Sanvitto, E. Galopin, A. Lemaître, I. Sagnes, J. Bloch, and A. Amo, Phys. Rev. Lett. **114**, 036402 (2015).
[19] O. Lahav, A. Itah, A. Blumkin, C. Gordon, S. Rinott, A. Zayats, and J. Steinhauer, Phys. Rev. Lett. **105**, 240401 (2010).
[20] J. Steinhauer, Nat. Phys. **10**, 864 (2014).
[21] J. Steinhauer, Nat. Phys. **12**, 959 (2016).
[22] J. R. M. de Nova, K. Golubkov, V. I. Kolobov, and J. Steinhauer, Nature (London) **569**, 688 (2019).
[23] F. Michel and R. Parentani, Phys. Rev. A **91**, 053603 (2015).
[24] F. Michel, J.-F. Coupechoux, and R. Parentani, Phys. Rev. D **94**, 084027 (2016).
[25] M. Tettamanti, S. L. Cacciatori, A. Parola, and I. Carusotto, Europhys. Lett. **114**, 60011 (2016).
[26] J. R. M. de Nova, S. Finazzi, and I. Carusotto, Phys. Rev. A **94**, 043616 (2016).
[27] A. Finke, P. Jain, and S. Weinfurtner, New J. Phys. **18**, 113017 (2016).
[28] Y.-H. Wang, T. Jacobson, M. Edwards, and C. W. Clark, SciPost Phys. **3**, 022 (2017).
[29] A. Parola, M. Tettamanti, and S. L. Cacciator, Europhys. Lett. **119**, 50002 (2017).
[30] S. Robertson, F. Michel, and R. Parentani, Phys. Rev. D **96**, 045012 (2017).
[31] A. Fabbri and N. Pavloff, SciPost Phys. **4**, 019 (2018).
[32] A. Coutant and S. Weinfurtner, Phys. Rev. D **97**, 025006 (2018).
[33] J. M. Gomez Llorente and J. Plata, J. Phys. B **52**, 075004 (2019).
[34] U. Leonhardt, Ann. Phys. (Berlin) **530**, 1700114 (2018).
[35] J. Steinhauer, Ann. Phys. (Berlin) **530**, 1700459 (2018).
[36] W. G. Unruh, Phys. Rev. D **51**, 2827 (1995).
[37] S. Corley and T. Jacobson, Phys. Rev. D **54**, 1568 (1996).
[38] S. Corley, Phys. Rev. D **55**, 6155 (1997).
[39] T. Jacobson, Phys. Rev. D **44**, 1731 (1991).
[40] P. Leboeuf, N. Pavloff, and S. Sinha, Phys. Rev. A **68**, 063608 (2003).
[41] J. Macher and R. Parentani, Phys. Rev. A **80**, 043601 (2009).
[42] A. Recati, N. Pavloff, and I. Carusotto, Phys. Rev. A **80**, 043603 (2009).
[43] A. Coutant, R. Parentani, and S. Finazzi, Phys. Rev. D **85**, 024021 (2012).
[44] P.-É. Larré, A. Recati, I. Carusotto, and N. Pavloff, Phys. Rev. A **85**, 013621 (2012).
[45] D. Boiron, A. Fabbri, P.-É. Larré, N. Pavloff, C. I. Westbrook, and P. Ziń, Phys. Rev. Lett. **115**, 025301 (2015).
[46] See Supplemental Material at http://link.aps.org/supplemental/10.1103/PhysRevLett.124.060401 which recalls previous results, details some characteristics of the zero modes and of the analysis of the Hawking spectrum and includes Refs. [47–49].
[47] P. Villain, M. Lewenstein, R. Dum, Y. Castin, L. You, A. Imamoğlu, and T. A. B. Kennedy, J. Mod. Opt. **44**, 1775 (1997).
[48] N. Bilas and N. Pavloff, Phys. Rev. A **72**, 033618 (2005).
[49] P. Deuar, A. G. Sykes, D. M. Gangardt, M. J. Davis, P. D. Drummond, and K. V. Kheruntsyan, Phys. Rev. A **79**, 043619 (2009).
[50] M. Lewenstein and L. You, Phys. Rev. Lett. **77**, 3489 (1996).
[51] U. Leonhardt, T. Kiss, and P. Öhberg, J. Opt. B **5**, S42 (2003).

[52] P. Ring and P. Shuck, *The Nuclear Many-Body Problem* (Springer-Verlag, Berlin, 1980).
[53] J. P. Blaizot and G. Ripka, *Quantum Theory of Finite Systems* (MIT Press, Cambridge, MA, 1986).
[54] R. Balbinot, A. Fabbri, S. Fagnocchi, A. Recati, and I. Carusotto, Phys. Rev. A **78**, 021603(R) (2008).
[55] I. Carusotto, S. Fagnocchi, A. Recati, R. Balbinot, and A. Fabbri, New J. Phys. **10**, 103001 (2008).
[56] J. Steinhauer, Phys. Rev. D **92**, 024043 (2015).
[57] C. J. Pethick and H. Smith, *Bose-Einstein Condensation in Dilute Gases* (Cambridge University Press, Cambridge, England, 2002).
[58] L. P. Pitaevskii and S. Stringari, *Bose-Einstein Condensation*, International Series of Monographs on Physics (Oxford University Press, Oxford, United Kingdom, 2016).
[59] J. R. M. de Nova, F. Sols, and I. Zapata, New J. Phys. **17**, 105003 (2015).

Supplemental material to: Departing from thermality of analogue Hawking radiation in a Bose-Einstein condensate

M. Isoard[1] and N. Pavloff[1]

[1] *Université Paris-Saclay, CNRS, LPTMS, 91405 Orsay, France*

THE BACKGROUND FLOW AND DENSITY PROFILES

We recall here the properties of the background transonic flow $\Phi(x)$ realizing an analogue black hole horizon [1]. $\Phi(x)$ is solution of the classical stationary Gross-Pitaevskii equation

$$\mu\Phi = -\frac{\hbar^2}{2m}\partial_x^2\Phi + [g\,n(x) + U(x)]\,\Phi\ , \tag{S1}$$

with $n(x) = |\Phi(x)|^2$ and $U(x) = -U_0\Theta(x)$, where Θ is the Heaviside step function and $U_0 > 0$. There exists a stationary solution of this equation which is half a dark soliton glued at $x = 0$ to a plane wave [2]:

$$\Phi(x) = \begin{cases} \sqrt{n_u}\,\exp(ik_u x)\,\chi_u(x) \equiv \Phi_u(x) & \text{for } x \le 0, \\ \sqrt{n_d}\,\exp(ik_d x - i\pi/2) \equiv \Phi_d(x) & \text{for } x \ge 0. \end{cases} \tag{S2}$$

where

$$\chi_u(x) = \cos\theta\,\tanh(x\cos\theta/\xi_u) - i\sin\theta. \tag{S3}$$

In these equations n_u and n_d are the asymptotic upstream and downstream densities, $\xi_u = \hbar(mgn_u)^{-1/2}$ is the upstream healing length and $\sin\theta = V_u/c_u$ where V_u and $c_u = \hbar/(m\xi_u)$ are the asymptotic flow and sound velocities. The downstream flow and sound velocity are $V_d = \hbar k_d/m$ and $c_d = \sqrt{gn_d/m}$. The chemical potential μ in Eq. (S1) verifies

$$\mu = \tfrac{1}{2}mV_u^2 + gn_u = \tfrac{1}{2}mV_d^2 + gn_d - U_0. \tag{S4}$$

The matching conditions at $x = 0$ impose

$$\frac{V_d}{V_u} = \frac{n_u}{n_d} = \left(\frac{c_u}{V_u}\right)^2 = \frac{V_d}{c_d}. \tag{S5}$$

Hence, in this configuration, which we denote as "waterfall", the upstream and downstream Mach numbers (V_u/c_u and V_d/c_d) are not independent. We chose to take the same downstream Mach number than in the experiment [3]: $V_d/c_d = 2.9$. From (S5) this imposes $V_u/c_u = 0.59$, different from the experimental value ($V_u/c_u|_{\rm exp} = 0.44$). This difference indicates that the experiment is not exactly in a waterfall configuration. This is probably due to the fact that the experimental external potential is not exactly a Heaviside function. It could also be that the experimental flow has not yet reached a fully stationary state. This difference does not preclude a very good agreement with the experimental density correlation pattern (as observed in Fig. 3 of the main text); however, it explains why we cannot reproduce with the same accuracy the behavior of the density correlation function $G_2(x, x')$ in all the quadrants of Fig. 2 of the main text: the $d1|\text{out} - d2|\text{out}$ correlation line (upper right quadrant of Fig. 2 of the main text) does not exactly superimposes with the experimental one. We take the same value of V_d/c_d as in the experiment, because this is the choice which gives the better account of experiment in the upper left quadrant of Fig. 2 of the main text, which is the core of the discussion of Ref. [3].

THE BOGOLIUBOV-DE GENNES EQUATIONS

In this section we present the construction of expansion (3) of the main text. The first part of the section is devoted to the definition of the usual Bogoliubov modes, and is an abridged version of a discussion which can be found in Ref. [1]; the second part concerns the construction of the zero modes and comprises a general discussion (from Refs. [4–6]) followed by the explicit form of these modes in the situation we consider [Eqs. (S14) and (S15)].

The simplest way to set up an eigen-basis set for expanding the quantum fluctuation operator is to treat $\hat\psi$ as a small classical field, denoted as ψ, with $\exp(-i\mu t/\hbar)(\Phi + \psi)$ solution of the classical version of Eq. (1) of the main text. One then looks for a normal mode of the form

$$\psi(x,t) = u(x,\omega)e^{-i\omega t} + v^*(x,\omega)e^{i\omega t} \tag{S6}$$

For such a normal mode, the linearization of the Gross-Pitaevskii equation leads to the so-called Bogoliubov-de Gennes equation which reads $\mathcal{L}\,\Xi = \hbar\omega\,\Xi$, where $\Xi(x,\omega) = (u(x,\omega)\,,\,v(x,\omega))^T$ and

$$\mathcal{L} = \begin{pmatrix} H & \Phi^2(x) \\ -(\Phi^*(x))^2 & -H \end{pmatrix}, \tag{S7}$$

with $H = \frac{\hbar^2}{2m}\partial_x^2 + U(x) - 2gn(x) - \mu$. Far upstream, the background density being constant, the eigen-modes behave as plane waves of the form

$$\Xi(x,\omega) = \begin{pmatrix} u(x,\omega) \\ v(x,\omega) \end{pmatrix} \underset{x\to-\infty}{\longrightarrow} e^{iqx} \begin{pmatrix} \exp(ik_u x)\,\mathcal{U}_\omega \\ \exp(-ik_u x)\,\mathcal{V}_\omega \end{pmatrix} \tag{S8}$$

where $\mathcal{U}_\omega$ and $\mathcal{V}_\omega$ are complex constants, their explicit expression can be found in Ref. [1], together with the general expression of $u(x,\omega)$ and $v(x,\omega)$. The same type of behavior is observed downstream. The corresponding dispersion relations are of the form

$$(\omega - V_\alpha q)^2 = \omega_{\rm B}^2(q), \tag{S9}$$

where $\alpha = u$ far upstream and $\alpha = d$ downstream and

$$\omega_{\rm B}(q) = c_\alpha q\sqrt{1 + q^2\xi_\alpha^2/4} \tag{S10}$$

is the Bogoliubov dispersion relation. The asymptotic upstream and downstream dispersion relations are represented in Fig. SF1. One sees in this figure that, for each value of ω, there exists three incoming channels, i.e., three plane waves which group velocity is directed towards the horizon. One of these plane waves lies in the upstream region, we denote it as $u|$in, the two others lie in the downstream region: $d1|$in and $d2|$in.

Once the eigen-modes Ξ has been found for all non-zero frequencies, the eigen-basis needs to be completed with the addition of zero modes for which $\omega = 0$. First, it is clear that $\mathcal{L}$ admits a simple zero mode:

$$\mathcal{L}\,\mathrm{P} = 0\,, \quad \text{where} \quad \mathrm{P} = \begin{pmatrix} \Phi(x) \\ -\Phi^*(x) \end{pmatrix}. \tag{S11}$$

The physical interpretation of the existence of this zero mode is the following: it results from the U(1) symmetry breaking of the condensate wave function and it is a collective mode with no restoring force, which is sometimes denoted as a spurious mode [4, 5]. Indeed, if Φ is a stationary solution of the Gross-Pitaevskii equation, for any arbitrary constant θ, $\Phi_\theta(x) = \Phi(x)\,e^{i\theta}$ is also a stationary solution. Φ_θ tends continuously to Φ when $\theta \to 0$, hence $\delta\Phi = \Phi_\theta - \Phi \simeq i\,\theta\,\Phi$ is a solution of the linearized Gross-Pitaevskii equation. This immediately translates into the fact that $(\delta\Phi, \delta\Phi^*)^T = i\,\theta\,\mathrm{P}$ is a zero mode of $\mathcal{L}$.

Another mode of excitation corresponds to addition of particles to the system [6]. By differentiating the Gross-Pitaevskii equation with respect to the number of particles N, we find the mode Q associated to P:

$$\mathrm{Q} = \begin{pmatrix} q(x) \\ -q^*(x) \end{pmatrix}, \quad \text{with} \quad \mathcal{L}\,\mathrm{Q} = -i\,\frac{d\,\mu}{dN}\,\mathrm{P}, \tag{S12}$$

where μ is the chemical potential of the condensate. The two modes Q and P complete the eigen-basis of $\mathcal{L}$, or, more precisely, make it possible to write $\mathcal{L}$ in a Jordan normal form. The field operator $\hat\psi$ which describes the quantum fluctuations can be now expanded over the scattering modes and the zero modes:

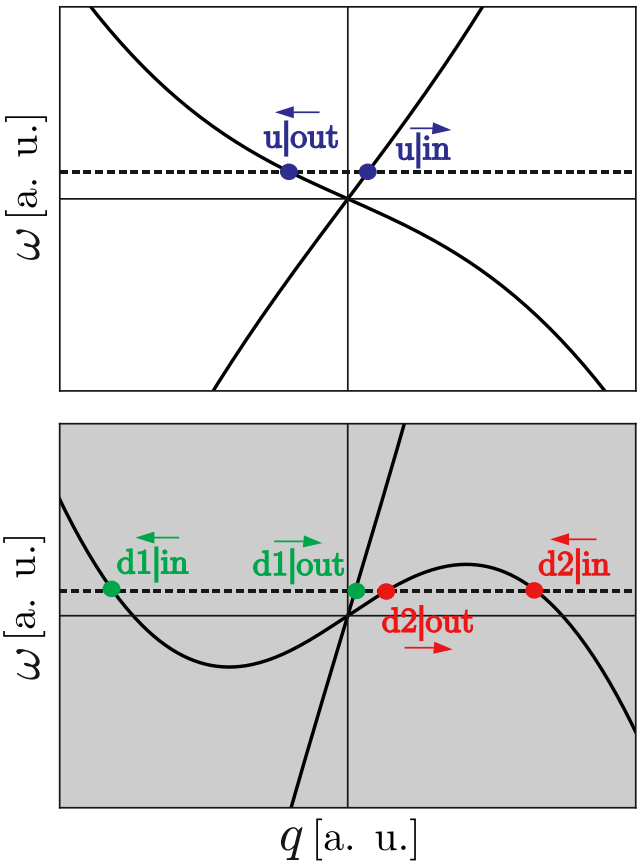

FIG. SF1: Graphical representation of the dispersion relation, i.e., of the solutions of Eq. (S9) in the far upstream (upper plot) and far downstream (lower plot) regions. In the upstream region, for a given ω (represented by a horizontal dashed line) one finds two real solutions of Eq. (S9) which we denote as $q_{u|\rm in}$ and $q_{u|\rm out}$. The intercept of the horizontal dashed line with the corresponding dispersion relation is marked with a colored dot labeled $u|$in or $u|$out, as appropriate. The situation is different downstream: there exists a threshold energy below which Eq. (S9) admits 4 real solutions which we denote as $q_{d1|\rm in}$, $q_{d1|\rm out}$, $q_{d2|\rm in}$ and $q_{d2|\rm out}$. Both $d2$ solutions disappear above the threshold. All these solutions correspond to the channels identified in the main text. They are denoted as "in" ("out") is their group velocity – schematically represented by an arrow – is directed towards (away from) the horizon.

$$\begin{aligned}\hat\psi(x,t) = &-i\Phi(x)\hat{\mathcal{Q}} + iq(x)\hat{\mathcal{P}} + \int_0^\infty \frac{d\omega}{\sqrt{2\pi}} \sum_{L\in\{U,D1\}} \\ &[u_L(x,\omega)e^{-i\omega t}\,\hat b_L(\omega) + v_L^*(x,\omega)e^{i\omega t}\,\hat b_L^\dagger(\omega)] \\ &+ \int_0^\Omega \frac{d\omega}{\sqrt{2\pi}}[u_{D2}(x,\omega)e^{-i\omega t}\,\hat b_{D2}^\dagger(\omega) \\ &+ v_{D2}^*(x,\omega)e^{i\omega t}\,\hat b_{D2}(\omega)].\end{aligned} \tag{S13}$$

In this expression the u_L's and the v_L's are linear combinations of terms of the form (S8) involving the S-matrix (see Refs. [1, 7]), and $\hat{\mathcal{Q}}$ is the phase operator of the condensate, while $\hat{\mathcal{P}}$ corresponds to the fluctuations of the number of particles. The quadratic Hamiltonian $\hat{H}_{\rm quad}$ describing the linear dynamics of the elementary excitations of the system contains a term $\hat{\mathcal{P}}^2/2\,M_{\rm eff}$, where $1/M_{\rm eff} = d\mu/dN$ [4–6]. Thus, the operator $\hat{\mathcal{P}}$ can be identified with a momentum operator and $M_{\rm eff}$ with an effective mass. In addition, the commutation relation $[\hat{\mathcal{Q}}, \hat{H}_{\rm quad}] = i\,\hat{\mathcal{P}}/M_{\rm eff}$ indicates that the phase operator $\hat{\mathcal{Q}}(t)$ is not stationary and deviates from its initial value $\hat{\mathcal{Q}}(t=0)$. This is the phenomenon of phase diffusion, see, e.g, Ref. [8].

In our case, the system is infinite: no phase diffusion can occur and $M_{\rm eff} \to \infty$. The physical interpretation of this phenomenon is that the inertia associated to the change of the global phase of a system of infinite number of particles is infinite. Therefore, the mode Q is also solution of $\mathcal{L}\,\mathrm{Q} = 0$ [see Eq. (S12) with $^{d\mu}/_{dN} \to 0$]. Moreover, the operator $\mathcal{L}$ has a different expression for $x<0$ and $x>0$, just because Φ does [see Eq. (S2)]. As a result, $\mathcal{L}$ admits zero energy eigen-states ($\omega = 0$) which have different forms in the upstream and the downstream region. The modes P and Q should be written as linear combinations of these zero modes. In particular, in the upstream region the density profile is a portion of dark soliton [see Eq. (S2)], and the expression of the corresponding zero modes can be found, e.g., in Ref. [9]. One obtains

$$\mathrm{P}(x<0) = \begin{pmatrix} \Phi_u(x) \\ -\Phi_u^*(x) \end{pmatrix} \quad \text{and} \quad \mathrm{P}(x>0) = \begin{pmatrix} \Phi_d(x) \\ -\Phi_d^*(x) \end{pmatrix}, \tag{S14}$$

while

$$\begin{aligned} \mathrm{Q}(x<0) &= i\sqrt{n_u}\,A\left[\cos\theta\tanh(x\cos\theta/\xi_u) - \frac{\Lambda_u}{2}\right]^2 e^{\Lambda_u\,x/\xi_u}\begin{pmatrix} e^{i\,k_u\,x} \\ e^{-i\,k_u\,x}\end{pmatrix} \quad \text{and} \\ \mathrm{Q}(x>0) &= B\begin{pmatrix} \Phi_d(x) \\ -\Phi_d^*(x)\end{pmatrix} + C\,e^{i\,K_0\,x/\xi_d}\begin{pmatrix} [K_0/2 - M_d]\,\Phi_d(x) \\ [K_0/2 + M_d]\,\Phi_d^*(x)\end{pmatrix} + C\,e^{-i\,K_0\,x/\xi_d}\begin{pmatrix} [-K_0/2 - M_d]\,\Phi_d(x) \\ [-K_0/2 + M_d]\,\Phi_d^*(x)\end{pmatrix}, \end{aligned} \tag{S15}$$

with $\Lambda_u = 2\sqrt{1-M_u^2} = 2\cos\theta$ and $K_0 = 2\sqrt{M_d^2-1}$, where M_u and M_d are the upstream and downstream Mach numbers ($M_\alpha = V_\alpha/c_\alpha$). In expression (S15), the normalization factors A, B and C are dimensionless real numbers which are determined by imposing the matching conditions at $x=0$ and the commutation relation between $\hat{\mathcal{Q}}$ and $\hat{\mathcal{P}}$: $[\hat{\mathcal{Q}}, \hat{\mathcal{P}}] = i$, or equivalently, $\mathrm{Q}^\dagger\,\sigma_z\,\mathrm{P} = i$, where σ_z is the third Pauli matrix.

FOURIER TRANSFORM OF THE DENSITY CORRELATION FUNCTION

The computation of the Fourier transform of the G_2 function gives access to the correlation signal between the Hawking pair $[k_{\rm H}(\omega), k_{\rm P}(\omega)]$ in momentum space for a fixed energy $\hbar\omega$ in the lab frame, see Eq. (5) of the main text. The wave vectors $k_{\rm H} = q_{u|\rm out}(\omega)$ and $k_{\rm P} = -q_{d2|\rm out}(\omega)$ are the momenta relative to the condensate of the Hawking quantum and of its partner (see the discussion in Ref. [7]). We define

$$I(\omega) = \frac{1}{\sqrt{n_u\,n_d\,L_u\,L_d}} \times \int_{-L_u}^{0} dx \int_0^{L_d} dx'\, e^{-i(k_{\rm H}(\omega)\,x + k_{\rm P}(\omega)\,x')}\,G_2(x,x'), \tag{S16}$$

where G_2 is the density correlation function [Eq. (4) of the main text]. The quantities n_u and n_d are the asymptotic densities in both regions (when $x \to -\infty$ and $x' \to +\infty$).

As proved in Refs. [7, 10], the integration in Eq. (S16) should be performed over a domain $[-L_u, 0] \times [0, L_d]$ which is adapted to each Hawking pair $[k_{\rm H}(\omega), k_{\rm P}(\omega)]$: one should verify

$$L_u\,V_{g,\rm P}(\omega) = L_d\,|V_{g,\rm H}(\omega)|\ , \tag{S17}$$

where

$$V_{g,\rm I}(\omega) \equiv \left.\frac{\partial\omega}{\partial k}\right|_{k_{\rm I}}, \ \mathrm{I} \in \{\mathrm{H},\,\mathrm{P}\}. \tag{S18}$$

This condition has a physical interpretation: the time taken by an elementary excitation pertaining to the Hawking channel to go from the horizon to the center of the upstream window $[-L_u, 0]$ has to be the same as the time taken by its partner to go from the horizon to the center of the downstream window $[0, L_d]$. The Fourier transform can be calculated theoretically for $L_u,\ L_d \to +\infty$ [still verifying (S17)] and this leads to Eq. (5) of the main text, i.e.:

$$I(\omega) = \mathcal{S}_0\,S_{ud2}(\omega)\,S_{d2d2}^*(\omega). \tag{S19}$$

Fig. SF2 compares the numerical computation of the Fourier transform (S16) (black dots), when the choice of

the window $[-L_u, 0] \times [0, L_d]$ respects condition (S17), with the theoretical expectation [left hand side of Eq. (S19), red curve in the figure]. We observe a nice agreement, except, of course, for long wavelengths where the validity condition of Eq. (S19): $k_{\rm H} L_u$ and $k_{\rm P} L_d \gg 1$ is violated.

The choice of the window is crucial; for example, the orange triangles in Fig. SF2 are obtained for another prescription which corresponds to the long wavelength limit of Eq. (S17):

$$L_u \, V_{g,\rm H}(0) = L_d \, |V_{g,\rm P}(0)| \, , \tag{S20}$$

where $V_{g,\rm H}(0) = V_u - c_u$ and $V_{g,\rm P}(0) = V_d - c_d$ are the group velocities of the Hawking quantum $k_{\rm H}$ and its partner $k_{\rm P}$ in the long wavelength limit. As expected, the result deviates from the evaluation which uses the correct condition (S17).

To recover the numerical result obtained by using the prescription (S20), we use the following approximations: (i) we assume that $k_{\rm H}(\omega) = \omega/(V_u - c_u)$ and $k_{\rm P}(\omega) = \omega/(V_d - c_d)$, as if we were in the dispersionless regime for all frequencies ω, and (ii) we also assume that $S_{ud2}(\omega) \simeq n_{T_{\rm H}}(\omega)$, with $n_{T_{\rm H}}(\omega)$ (the Bose thermal distribution at the Hawking temperature) and that $|S_{ud2}|^2 \, |S^*_{d2d2}|^2 \simeq n_{T_{\rm H}}(\omega)(1 + n_{T_{\rm H}}(\omega))$ [Eq. (8) of the main text]. Then, we compute expression (S19) using both approximations (i) and (ii): we obtain the dark blue curve in Fig. SF2 which agrees well with the orange triangles.

In conclusion, one may numerically analyse the information contained in the density distribution G_2 by using Eq. (S16) within the oversimplified long wavelength prescription (S20) and still get an equality between the two terms of Eq. (S19). However, this approach could lead to the erroneous conclusion that the analogous Hawking radiation is thermal for all frequencies ω. In our system, where dispersion plays an important role, only the result represented by the red curve in Fig. SF2 should be considered as correct, and it clearly deviates from the thermal result (dark blue curve in Fig. SF2).

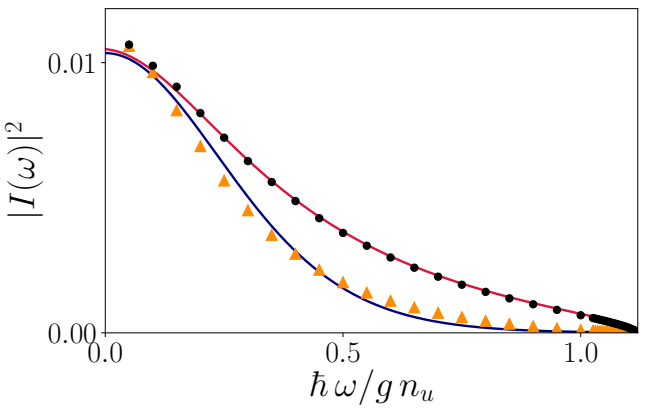

FIG. SF2: Fourier transform of the G_2 function, denoted as $I(\omega)$ and given by expression (S16), plotted as a function of ω. The red curve indicates the theoretical expectation: right hand side of Eq. (S19). The black dots are obtained by the numerical computation of the Fourier transform (S16) with condition (S17). The orange triangles are also obtained numerically, but for a different choice of window corresponding to prescription (S20). The dark blue curve is obtained from (S19) but in the long wavelength approximation, where the analogous Hawking signal is thermal.

EFFECT OF TEMPERATURE ON THE DENSITY CORRELATION FUNCTION

In this section, we discuss how to account for temperature effects in our system. We first note that the stationary configuration we consider is thermodynamically unstable, and cannot support a thermal state. However, a thermal-like occupation of the states can be defined as detailed for instance in Ref. [7]. Previous studies [11] have already highlighted the robustness of the correlation signal, even if the temperature of the system is greater than the Hawking temperature. Our results confirm this point, as shown in Fig. 3 of the main text (the orange solid line is the finite temperature result for $k_B \, T = 0.2 \, g n_u \simeq 1.9 \, T_{\rm H}$). At finite temperature, the density correlation function $G_2(x, x')$ splits in two parts [1, 11]:

$$G_2(x, x') = G_2^0(x, x') + G_2^T(x, x'), \tag{S21}$$

where G_2^0 is the zero temperature contribution and G_2^T accounts for the additional temperature effects. As already mentioned in Refs. [11, 12], G_2^T contains a term which corresponds to a thermal enhancement of zero temperature correlations, together with additional contributions involving scattering processes specific to the $T \neq 0$ case. This results in a practical disappearance of the $u|\text{out} - d1|\text{out}$ correlation for $k_B \, T \simeq 0.2 \, g n_u$, while the $u|\text{out} - d2|\text{out}$ Hawking signal is robust up to $k_B \, T \simeq g n_u$, see the discussion in Ref. [11]. This confirms the interest of using analog system to investigate analog Hawking radiation: the non-local correlation pattern in G_2 is weakly affected by temperature and a noticeable signal can be recorded even if T is larger than $T_{\rm H}$.

The finite T result presented in the main text is obtained by computing the two contributions in (S21) separately, in a regime which has been denoted as the "weakly interacting quasicondensate regime" in Ref. [13], and which holds when the following conditions are met:

$$\frac{4 \, \tau_\alpha^2}{(\xi_\alpha \, n_\alpha)^4} \ll \frac{1}{(\xi_\alpha \, n_\alpha)^2} \ll 1, \tag{S22}$$

where $\alpha \in \{u, d\}$ and $\tau_\alpha = k_B \, T/(g \, n_\alpha)$ is the reduced temperature. We use typical experimental parameters of Ref. [3] to evaluate the order of magnitude of the

different terms in the inequalities (S22): $\xi_u = 1.4\,\mu$m, $\xi_d = 2.38\,\mu$m, $n_u \simeq 70-90\,\mu\text{m}^{-1}$ and $n_d \simeq 20\,\mu\text{m}^{-1}$. We obtain $(\xi_u\, n_u)^{-2} \simeq 6.3\times10^{-5} - 10^{-4} \ll 1$, $(\xi_d\, n_d)^{-2} \simeq 4.4\times10^{-4} \ll 1$. By computing the left hand part of (S22) in the upstream and downstream regions, we find that the more stringent condition reads $k_B\, T \ll 8.3\, g n_u$, i.e., our approach is valid up to $k_B\, T \simeq 0.8-1\, g n_u \gg T_{\text{H}}$.

[1] P.-É. Larré, A. Recati, I. Carusotto, and N. Pavloff, Phys. Rev. A **85**, 013621 (2012).

[2] P. Leboeuf, N. Pavloff and S. Sinha, Phys. Rev. A **68**, 063608 (2003).

[3] J. R. M. de Nova, K. Golubkov, V. I. Kolobov, and J. Steinhauer, Nature (London) **569**, 688 (2019).

[4] P. Ring and P. Shuck, *The Nuclear Many-Body Problem* (Springer-Verlag, Berlin, 1980).

[5] J. P. Blaizot and G. Ripka, *Quantum Theory of Finite Systems* (MIT Press, Cambridge, MA, 1986).

[6] C. J. Pethick and H. Smith, *Bose-Einstein Condensation in Dilute Gases*, (Cambridge University Press, Cambridge, England, 2002).

[7] A. Fabbri and N. Pavloff, SciPost Phys. **4**, 019 (2018).

[8] P. Villain, M. Lewenstein, R. Dum, Y. Castin, L. You, A. Imamoğlu, and T. A. B. Kennedy, J. Mod. Optics **44**, 1775 (1997).

[9] N. Bilas and N. Pavloff Phys. Rev. A **72**, 033618 (2005).

[10] J. R. M. de Nova, F. Sols and I. Zapata, New. J. Phys. **17**, 105003 (2015).

[11] A. Recati, N. Pavloff and I. Carusotto, Phys. Rev. A **80**, 043603 (2009).

[12] J. Macher and R. Parentani, Phys. Rev. A **80**, 043601 (2009).

[13] P. Deuar, A. G. Sykes, D. M. Gangardt, M. J. Davis, P. D. Drummond and K. V. Kheruntsyan, Phys. Rev. A **79**, 043619 (2009).

4

TRIPARTITE ENTANGLEMENT IN ANALOGUE GRAVITY

Hawking pairs emitted at the vicinity of a gravitational black hole are entangled. This peculiar property of quantum systems has triggered much interest in general relativity [48, 49, 69, 139, 141, 190] in connection to the so-called information loss paradox [12, 85, 89, 96, 122, 125, 126, 155, 181, 185, 203] and the vivid debate around it [178] . Indeed, if black holes radiate a thermal radiation, as predicted by Hawking in 1974 [87], they slowly evaporate and should disappear in a finite amount of time. As long as the black hole exists, the Hawking particle and its "Partner" emitted from each side of the event horizon are entangled. From an observer outside the black hole (and thus only able to detect the presence of Hawking particles) the quantum state is perceived as a mixed state, but the full state (Hawking + partner) remains a pure entangled state. However, after the evaporation process, the quantum field will remain entangled with the quantum field observables inside the past black hole – even though the black hole has evaporated completely. This means that any quantum field in a pure state evolves to a mixed state and the knowledge of the final state is not sufficient to determine the initial state; in other words, there is a violation of unitarity [185] and information has been lost during this evaporation process; in particular, one can wonder what happens for the entangled Hawking pair when the black hole has disappeared?

These questions are still debated today and several suggestions have been proposed to overcome this paradox [185]: no complete evaporation of the black hole, information coming out in a final burst, a firewall formed on the horizon – a barrier significantly diminishing entanglement across the horizon, but requiring the quantum field to be singular on the horizon.

However, no theory is known today to solve unambiguously the problem. A natural question we might ask ourselves in this thesis: is analogue gravity able to give some insights on this fundamental issue of information loss paradox? A recent publication indeed suggested to use a plasma laser to mimic an accelerating relativistic mirror[1], giving rise to emission of Hawking pairs from vacuum fluctuations [38]. Partner particles are trapped beyond an horizon, while Hawking particles, reflected from the mirror, can be detected. Then, in the proposed experiment, the plasma mirror is suddenly stopped to imitate the final evaporation of a black hole and to observe how trapped partner particles are released.

In our case, acoustic analogues in Bose-Einstein condensates (BECs) do not evaporate. However, quanta emitted spontaneously from vacuum fluctuations, i.e., elementary excitations on top of the condensate, share

1 see Section 2.1.1 for more details about particle creation by accelerating mirrors.

entanglement with each other. The study of entanglement in BECs is a first step to explore the peculiar quantum properties emerging from the presence of an horizon. It might be interesting in the future to suggest new experimental setups in BECs to delve into the information loss paradox; and our theoretical studies addressing several possible tools for evaluating the amount of bipartite (or tripartite) entanglement constitute a preliminary step in this direction.

This chapter is entirely dedicated to the study of entanglement emerging in sonic analogues in BECs. We show in particular that our system gives rise to tripartite entanglement and we are able to determine the degree of entanglement between the three outgoing modes emitted spontaneously from the acoustic horizon.

First, we need to introduce Bogoliubov transformations and precise their specific properties in the case we consider. Then, we present some tools to quantify and measure entanglement. In a third part, we study tripartite entanglement.

4.1 BOGOLIUBOV TRANSFORMATIONS

In this section, we consider linear transformations that preserve canonical commutation rules for boson operators. We will restrict ourselves to the case of unitary transformations.

4.1.1 *General case*

Let us consider N creation and annihilation boson operators $\mathbf{b} = (\hat{b_1}, \dots, \hat{b}_N, \hat{b}_1^\dagger, \dots, \hat{b}_N^\dagger)^{\mathrm{T}}$, with the usual commutation relation

$$[\mathbf{b}_i,\, \mathbf{b}_j] = \widetilde{\Omega}_{ij}, \tag{183}$$

where

$$\widetilde{\Omega} = \begin{pmatrix} 0 & \mathbb{1}_N \\ -\mathbb{1}_N & 0 \end{pmatrix}. \tag{184}$$

Consider now the following transformation acting on the $\hat{b}$'s operators:

$$\mathbf{c}_i = \sum_{j=1}^{2N} \mathscr{T}_{ij}\, \mathbf{b}_j, \quad \text{or equivalently} \quad \mathbf{c} = \mathscr{T}\, \mathbf{b}, \tag{185}$$

with $\mathbf{c} = (\hat{c}_1, \dots, \hat{c}_N, \hat{c}_1^\dagger, \dots, \hat{c}_N^\dagger)^{\mathrm{T}}$ the transformed operators, and

$$\mathscr{T} = \begin{pmatrix} \alpha^* & -\beta^* \\ -\beta & \alpha \end{pmatrix}. \tag{186}$$

In expression (186), α and β are $N \times N$ matrices. Written in a more explicit form, the transformation reads

$$\begin{pmatrix} \hat{c}_1 \\ \vdots \\ \hat{c}_N \end{pmatrix} = \alpha^* \begin{pmatrix} \hat{b}_1 \\ \vdots \\ \hat{b}_N \end{pmatrix} - \beta^* \begin{pmatrix} \hat{b}_1^\dagger \\ \vdots \\ \hat{b}_N^\dagger \end{pmatrix}, \tag{187}$$

and

$$\begin{pmatrix} \hat{c}_1^\dagger \\ \vdots \\ \hat{c}_N^\dagger \end{pmatrix} = -\beta \begin{pmatrix} \hat{b}_1 \\ \vdots \\ \hat{b}_N \end{pmatrix} + \alpha \begin{pmatrix} \hat{b}_1^\dagger \\ \vdots \\ \hat{b}_N^\dagger \end{pmatrix}. \tag{188}$$

One sees that, if $\beta \neq 0$, the transformation mixes creation and annihilation operators.

In addition, as mentioned in the introduction of this section, we consider here linear transformations that preserve the bosonic commutation rule, i.e., the set of transformed operators $\mathbf{c}$ must respect the commutation relation (183). This leads to the condition

$$\mathscr{T}\,\widetilde{\Omega}\,\mathscr{T}^{\mathrm{T}} = \widetilde{\Omega}, \tag{189}$$

meaning that $\mathscr{T}$ belongs to the symplectic group[2] $Sp(2N, \mathbb{K})$, where $\mathbb{K} = \mathbb{R}$ or $\mathbb{C}$. Condition (189) imposes the following relations between the matrices α and β:

$$\begin{aligned} &\alpha\,\alpha^\dagger - \beta\,\beta^\dagger = \mathbb{1}_N, \quad \alpha\,\beta^{\mathrm{T}} - \beta\,\alpha^{\mathrm{T}} = 0 \\ &\alpha^\dagger\,\alpha - \beta^{\mathrm{T}}\,\beta^* = \mathbb{1}_N, \quad \alpha^{\mathrm{T}}\,\beta^* - \beta^\dagger\,\alpha = 0. \end{aligned} \tag{190}$$

Moreover, since $\mathscr{T}$ is a symplectic matrix, one finds immediately

$$\mathscr{T}^{-1} = -\widetilde{\Omega}\,\mathscr{T}^{\mathrm{T}}\,\widetilde{\Omega} = \begin{pmatrix} \alpha^{\mathrm{T}} & \beta^\dagger \\ \beta^{\mathrm{T}} & \alpha^\dagger \end{pmatrix}. \tag{191}$$

To the canonical transformation (185) there corresponds in general a unitary scalar operator T acting in Fock space such that:

$$\mathbf{c} = T^\dagger\,\mathbf{b}\,T. \tag{192}$$

Equation (192) should be understood as

$$\begin{cases} \hat{c}_1 = T^\dagger\,b_1\,T, \\ \quad\vdots \\ \hat{c}_N = T^\dagger\,b_N\,T, \end{cases} \qquad \begin{cases} \hat{c}_1^\dagger = T^\dagger\,b_1^\dagger\,T, \\ \quad\vdots \\ \hat{c}_N^\dagger = T^\dagger\,b_N^\dagger\,T, \end{cases} \tag{193}$$

and similarly for the inverse transformation (using the fact that T is a unitary operator, i.e., $T^{-1} = T^\dagger$):

$$\mathbf{b} = T\,\mathbf{c}\,T^\dagger. \tag{194}$$

Then, one shows that in our case this operator should be of the form [26]

$$T = e^{\frac{1}{2}\mathbf{b}^{\mathrm{T}}\,Q\,\mathbf{b}}, \tag{195}$$

2 We recall that the symplectic group is the set of linear transformations of a $2N$-dimensional vector space over $\mathbb{K}$ ($= \mathbb{R}$ or $\mathbb{C}$) which preserve a non-singular skew-symmetric bilinear form, here represented by the skew-symmetric matrix $\widetilde{\Omega}$.

with Q a $2N\times 2N$ matrix, assumed symmetric without loss of generality. Such a quadratic operator gives rise to linear transformations[3]. Indeed, it is not difficult to show that the unitary operator defined in (195) leads to[4]

$$\mathbf{c}_i = T^{-1}\,\mathbf{b}_i\,T = \sum_{j=1}^{2N} \mathscr{T}'_{ij}\,\mathbf{b}_j, \quad \text{or equivalently} \quad \mathbf{c} = \mathscr{T}'\,\mathbf{b}, \tag{197}$$

with

$$\mathscr{T}' = \begin{pmatrix} \mathscr{T}'_{11} & \mathscr{T}'_{12} \\ \mathscr{T}'_{21} & \mathscr{T}'_{22} \end{pmatrix} = e^{\widetilde{\Omega}\,Q} \tag{198}$$

a symplectic matrix, thus respecting condition (189), but *a priori* not equal to $\mathscr{T}$ defined in equation (186). In expression (198), $\mathscr{T}'_{ij}$ are $N\times N$ matrices. In addition to the symplectic property of $\mathscr{T}'$, the unitarity of T adds another constraint. Indeed, let us define the matrix $\gamma = \Sigma_z\,\widetilde{\Omega}$, with $\Sigma_z = \mathrm{diag}(\mathbb{1}_N, -\mathbb{1}_N)$. By noticing that $\mathbf{c}^\dagger = \mathbf{c}^{\mathrm{T}}\,\gamma$, one finds

$$\begin{aligned} \mathbf{c}^\dagger &= \mathbf{b}^\dagger\,\gamma\,(\mathscr{T}')^{\mathrm{T}}\,\gamma, \\ \mathbf{c}^\dagger &= \mathbf{b}^\dagger\,(\mathscr{T}')^\dagger. \end{aligned} \tag{199}$$

Thus, we obtain another condition on $\mathscr{T}'$:

$$(\mathscr{T}')^* = \gamma\,\mathscr{T}'\,\gamma, \tag{200}$$

leading to $(\mathscr{T}'_{11})^* = \mathscr{T}'_{22} \equiv \alpha$ and $(\mathscr{T}'_{12})^* = \mathscr{T}'_{21} \equiv -\beta$. Therefore we find $\mathscr{T}' = \mathscr{T}$, where $\mathscr{T}$ is defined in (186).

We also define vacua with respect to each set of annihilation operators:

$$\hat{b}_i\,|0\rangle_b = 0, \quad \text{and} \quad \hat{c}_i\,|0\rangle_c = 0, \quad i \in \{1,\dots,N\}. \tag{201}$$

Note that both vacua are identical if $\beta = 0$, i.e., when $\hat{c}_i$ does not contain any creation operators $\hat{b}_i^\dagger$ [see equation (187)]. Actually, Both vacua are linked through the relation

$$|0\rangle_b = T\,|0\rangle_c, \quad \text{and} \quad |0\rangle_c = T^\dagger\,|0\rangle_b. \tag{202}$$

Indeed, $\hat{b}_i\,|0\rangle_b = T\,\hat{c}_i\,T^\dagger\,T\,|0\rangle_c = T\,\hat{c}_i\,|0\rangle_c = 0$, where we used the inverse transformation (194) and $\hat{c}_i\,|0\rangle_c = 0$.

3 We precise that the transformation is *linear* at the level of the operators: $\hat{c}$'s operators are linear combinations of $\hat{b}$'s and $\hat{b}^\dagger$'s operators.

4 One can use the well know operator identity

$$e^{\hat{A}}\,\hat{B}\,e^{-\hat{A}} = \hat{B} + [\hat{A},\hat{B}] + \frac{1}{2!}[\hat{A},[\hat{A},\hat{B}]] + \cdots. \tag{196}$$

CANONICAL DECOMPOSITION Let us consider three special types of transformation.

• The first type is

$$T^{(1)} = e^{\frac{1}{2}\mathbf{b}^{\mathrm{T}} Q^{(1)} \mathbf{b}}, \quad \text{with} \quad Q^{(1)} = \begin{pmatrix} 0 & 0 \\ 0 & X \end{pmatrix}, \tag{203}$$

the $N \times N$ matrix X being symmetric. Expressions (197) and (198), applied to a unitary operator of the form (203), lead to

$$\mathscr{T}^{(1)} = e^{\widetilde{\Omega} Q^{(1)}} = \begin{pmatrix} \mathbb{1}_N & X \\ 0 & \mathbb{1}_N \end{pmatrix}, \tag{204}$$

and thus,

$$c_i = b_i + \sum_{j=1}^{N} X_{ij}\, b_j^\dagger, \quad \text{and} \quad \hat{c}_i^\dagger = b_i^\dagger, \quad \forall i \in \{1, \ldots, N\}. \tag{205}$$

The creation operators are left invariant under this transformation.

• The second type does not mix the creation and the annihilation operators. The matrix $Q \equiv Q^{(2)}$ defined in (195) has the form

$$Q^{(2)} = \begin{pmatrix} 0 & Y^{\mathrm{T}} \\ Y & 0 \end{pmatrix}. \tag{206}$$

Expressions (197) and (198), with Q given by the matrix (206), gives

$$\mathscr{T}^{(2)} = \begin{pmatrix} e^{Y} & 0 \\ 0 & e^{-Y^{\mathrm{T}}} \end{pmatrix}. \tag{207}$$

• The third type is similar to the first one, but leaves invariant the annihilation operators:

$$Q^{(3)} = \begin{pmatrix} Z & 0 \\ 0 & 0 \end{pmatrix}, \text{ with } Z^{\mathrm{T}} = Z \Rightarrow \mathscr{T}^{(3)} = \begin{pmatrix} \mathbb{1}_N & 0 \\ -Z & \mathbb{1}_N \end{pmatrix}, \tag{208}$$

that is to say, under the effect of $\mathscr{T}^{(3)}$ one has:

$$c_i = b_i, \quad \text{and} \quad \hat{c}_i^\dagger = b_i^\dagger - \sum_{j=1}^{N} Z_{ij}\, b_j, \quad \forall i \in \{1, \ldots, N\}. \tag{209}$$

These three transformations actually generate the most general unitary Bogoliubov transformation since any matrix $\mathscr{T}$ can be decomposed as follows:

$$\begin{aligned} \mathscr{T} = \mathscr{T}^{(1)}\, \mathscr{T}^{(2)}\, \mathscr{T}^{(3)} &= \begin{pmatrix} \mathbb{1}_N & X \\ 0 & \mathbb{1}_N \end{pmatrix} \begin{pmatrix} e^{Y} & 0 \\ 0 & e^{-Y^{\mathrm{T}}} \end{pmatrix} \begin{pmatrix} \mathbb{1}_N & 0 \\ -Z & \mathbb{1}_N \end{pmatrix} \\ &= \begin{pmatrix} e^{Y} - X\, e^{-Y^{\mathrm{T}}} Z & X\, e^{-Y^{\mathrm{T}}} \\ -e^{-Y^{\mathrm{T}}} Z & e^{-Y^{\mathrm{T}}} \end{pmatrix}. \end{aligned} \tag{210}$$

Indeed, provided $\det(\alpha) \neq 0$, and by means of the symmetry of X and Z, as well as the group law property (189), matrices X, Y, and Z can be found in terms of the $\mathscr{T}$-coefficients. One obtains [16, 123]

$$X = -\beta^* \, \alpha^{-1}, \quad Z = \alpha^{-1} \, \beta, \quad e^{-Y^{\mathrm{T}}} = \alpha. \tag{211}$$

This property follows from equations (197) and (186).

Then, we can use the following property for product of bosons transformations:

$$e^{\frac{1}{2}\mathbf{b}^{\mathrm{T}} \, Q^{(1)} \, \mathbf{b}} \dots e^{\frac{1}{2}\mathbf{b}^{\mathrm{T}} \, Q^{(n)} \, \mathbf{b}} = e^{\frac{1}{2}\mathbf{b}^{\mathrm{T}} \, Q \, \mathbf{b}}, \tag{212}$$

where $Q^{(1)}, \dots, Q^{(n)}$ and Q are all symmetric, and satisfy

$$e^{\widetilde{\Omega} \, Q^{(1)}} \dots e^{\widetilde{\Omega} \, Q^{(n)}} = e^{\widetilde{\Omega} \, Q}, \text{ i.e., } \mathscr{T}^{(1)} \dots \mathscr{T}^{(n)} = \mathscr{T}. \tag{213}$$

This shows that the operator T can be uniquely decomposed into the product [16, 123]

$$T = T^{(1)} \, T^{(2)} \, T^{(3)}, \quad \text{where} \quad T^{(i)} = e^{\frac{1}{2}\mathbf{b}^{\mathrm{T}} \, Q^{(i)} \, \mathbf{b}}, \; i \in \{1, 2, 3\}, \tag{214}$$

with $Q^{(1),(2),(3)}$ given in equations (203), (206), and (208). Expression (214) can be written explicitly as

$$\begin{aligned} T = (\det \alpha)^{-1/2} \exp \left[\frac{1}{2} \sum_{i,j=1}^{N} X_{i,j} \, \hat{c}_i^\dagger \, \hat{c}_j^\dagger \right] \\ \times \exp \left[\sum_{i,j=1}^{N} Y_{i,j} \, \hat{c}_i^\dagger \, \hat{c}_j \right] \exp \left[\frac{1}{2} \sum_{i,j=1}^{N} Z_{i,j} \, \hat{c}_i \, \hat{c}_j \right], \end{aligned} \tag{215}$$

where we used the fact that[5] $\mathbf{b}^{\mathrm{T}} \, Q \, \mathbf{b} = \mathbf{c}^{\mathrm{T}} \, Q \, \mathbf{c}$, for any symmetric matrix Q.

The interest of the previous expression lies in the fact that all annihilation operators have been put to the right. Therefore, when acting on the vacuum $|0\rangle_c$, we obtain

$$|0\rangle_b = (\det \alpha)^{-1/2} \exp \left[\frac{1}{2} \sum_{i,j} X_{i,j} \, \hat{c}_i^\dagger \, \hat{c}_j^\dagger \right] |0\rangle_c, \tag{216}$$

with $X = -\beta^* \, \alpha^{-1}$.

4.1.2 *Two-mode squeezed state*

Let us apply the results derived in the last section to a simple example. We consider here a two-mode squeezed operator, that is to say

$$T_{\mathrm{sq2}}(\phi_\omega) = \exp \left[\phi_\omega \left(b_1^\dagger \, b_2^\dagger - b_1 \, b_2 \right) \right], \tag{217}$$

5 Indeed, using equation (197), one has $\mathbf{b}^{\mathrm{T}} \, Q \, \mathbf{b} = \mathbf{c}^{\mathrm{T}} \, (\mathscr{T}^{-1})^{\mathrm{T}} \, Q \, \mathscr{T}^{-1} \, \mathbf{c}$. Equation (186) and symplectic properties of the matrix $\mathscr{T}$ (189) and (191) lead to $\mathbf{b}^{\mathrm{T}} \, Q \, \mathbf{b} = \mathbf{c}^{\mathrm{T}} \, Q \, \mathbf{c}$. Note that we used $\widetilde{\Omega}^2 = -\mathbb{1}_{2N}$.

with $\tanh r_\omega = \exp(-c\,\pi\omega/\kappa)$. The meaning of c, κ and ω will become clearer below. Equation (217) can be written in the form used in the previous section:

$$T_{\mathrm{sq2}}(r_\omega) = e^{\frac{1}{2}\mathbf{b}^{\mathrm{T}}\,Q_{\mathrm{sq2}}\,\mathbf{b}} = e^{\frac{1}{2}\mathbf{c}^{\mathrm{T}}\,Q_{\mathrm{sq2}}\,\mathbf{c}}, \tag{218}$$

where here

$$\mathbf{b} = \begin{pmatrix} \hat{b}_1 \\ \hat{b}_2 \\ \hat{b}_1^\dagger \\ \hat{b}_2^\dagger \end{pmatrix}, \quad \mathbf{c} = \begin{pmatrix} \hat{c}_1 \\ \hat{c}_2 \\ \hat{c}_1^\dagger \\ \hat{c}_2^\dagger \end{pmatrix}, \tag{219}$$

are the creation and annihilation operators linked by the Bogoliubov transformation

$$\mathbf{c} = T_{\mathrm{sq2}}^\dagger(r_\omega)\,\mathbf{b}\,T_{\mathrm{sq2}}(r_\omega). \tag{220}$$

In equation (218), Q_{sq2} is given by

$$\text{and} \quad Q_{\mathrm{sq2}} = \begin{pmatrix} 0 & -r_\omega & 0 & 0 \\ -r_\omega & 0 & 0 & 0 \\ 0 & 0 & 0 & r_\omega \\ 0 & 0 & r_\omega & 0 \end{pmatrix}. \tag{221}$$

One finds from equation (186)

$$\mathscr{T}_{\mathrm{sq2}} = \begin{pmatrix} \alpha_{\mathrm{sq2}} & -\beta_{\mathrm{sq2}} \\ -\beta_{\mathrm{sq2}} & \alpha_{\mathrm{sq2}} \end{pmatrix}, \tag{222}$$

with

$$\alpha_{\mathrm{sq2}} = \begin{pmatrix} \cosh r_\omega & 0 \\ 0 & \cosh r_\omega \end{pmatrix}, \ \beta_{\mathrm{sq2}} = -\begin{pmatrix} 0 & \sinh r_\omega \\ \sinh r_\omega & 0 \end{pmatrix}. \tag{223}$$

The Bogoliubov transformation associated to the unitary operator (217) between two vectors $\mathbf{b}$ and $\mathbf{c}$ is

$$\hat{c}_{1\,(2)} = \cosh r_\omega\,\hat{b}_{1\,(2)} + \sinh r_\omega\,\hat{b}_{2\,(1)}^\dagger, \tag{224}$$

i.e.,

$$\begin{pmatrix} \hat{c}_1 \\ \hat{c}_2 \end{pmatrix} = \alpha_{\mathrm{sq2}} \begin{pmatrix} \hat{b}_1 \\ \hat{b}_2 \end{pmatrix} - \beta_{\mathrm{sq2}} \begin{pmatrix} \hat{b}_1^\dagger \\ \hat{b}_2^\dagger \end{pmatrix}. \tag{225}$$

Equation (216) becomes in this case

$$|0\rangle_b = (\cosh r_\omega)^{-1} e^{\tanh r_\omega \hat{c}_1^\dagger\,\hat{c}_2^\dagger}\,|0\rangle_c. \tag{226}$$

PHYSICAL INTERPRETATION Let us expand equation (226) over a Fock space associated to the c's operators[6],

$$|0\rangle_b = (\cosh r_\omega)^{-1} \sum_{n=0}^{\infty} e^{-n\,c\,\pi\,\omega/\kappa} |n\rangle_1 \, |n\rangle_2, \tag{227}$$

where $|n\rangle_i$ is a state with n particles in mode i ($i \in \{1, 2\}$), and where we used $\tanh r_\omega = \exp(-c\pi\omega/\kappa)$. One sees that $|0\rangle_b$ is a pure state. On the contrary the reduced density matrix with respect to mode 1 [in the sense that we trace out over mode 2] is

$$\begin{aligned} \hat{\rho}^{(1)} &= \sum_{n'=0}^{\infty} {}_2\langle n'|0\rangle_b \, {}_b\langle 0|n'\rangle_2 \\ &= (\cosh r_\omega)^{-2} \sum_{n=0}^{\infty} (\tanh r_\omega)^{2n} \; |n\rangle_1 \, {}_1\langle n|. \\ &= (1 - e^{-2\,c\,\pi\,\omega/\kappa}) \sum_{n=0}^{\infty} e^{-2\,n\,c\,\pi\,\omega/\kappa} \, |n\rangle_1 \, {}_1\langle n|. \end{aligned} \tag{228}$$

The density matrix (228) describes a mixed state.

Let us go further in the interpretation: imagine an observer restricted to a region where he can only have access to mode 1. If this observer measures an observable $\mathcal{O}$, with associated operator $\hat{\mathcal{O}}$, in the quantum state $|0\rangle_b$, then the measure is given by

$${}_b\langle 0|\hat{O}|0\rangle_b = \mathrm{Tr}(\hat{O}\,\hat{\rho}^{(1)}). \tag{229}$$

Therefore, if one takes the particle number operator for mode 1, $\hat{\mathcal{N}}_1 = \hat{c}_1^\dagger \, \hat{c}_1$, the observer will measure

$${}_b\langle 0|\hat{\mathcal{N}}_1|0\rangle_b = \frac{1}{(\coth r_\omega)^2 - 1} = \frac{1}{e^{\hbar\omega/k_B T_{\text{eff}}} - 1}, \tag{230}$$

with

$$T_{\text{eff}} \equiv \frac{\hbar\omega}{2\,k_{\text{B}}\,\ln(\coth r_\omega)}. \tag{231}$$

Note that, in equation (230), the parameter ω plays the role of a frequency. Using $\coth r_\omega = \exp(c\,\pi\omega/\kappa)$, one finds

$$T_{\text{eff}} = \frac{\hbar\kappa}{2\pi c} \equiv T_{\text{H}} \tag{232}$$

Thus, this observer perceives a thermal radiation emitted from a certain source with an effective temperature T_{H}, independent of the frequency ω. From equation (232), one sees that this temperature is nothing but the Hawking temperature derived in Chapter 2.

What can we learn from this paragraph? A pure state appears as a mixed state for an observer confined in a certain region, where he

6 One has in particular $(c_i^\dagger)^n \, |0\rangle_c = \sqrt{n!}\, |n\rangle_i$, $i \in \{1, 2\}$.

has only access to modes emitted in this subsystem. This is exactly the situation that occurs after a gravitational collapse leading to the formation of a black hole. The event horizon hides the information inside the black hole and this entails a loss of information [25] (this is clear since we obtain a mixed state and not a pure state).

Thus, a quantum field in a pure state will be seen in a mixed state for an observer located outside the black hole. Said differently, the vacuum $|0\rangle_b$ is no longer the physical vacuum for an outside observer to the black hole, since the 'true' vacuum would be now $|0\rangle_c$; any detector positioned outside the black hole will register the presence of a thermal radiation given by the Planck spectrum (230), i.e., the so-called Hawking radiation. A similar result can be found for an expanding universe where the acceleration is responsible from the emission of quanta [25].

A mixed state is associated to a non-zero entropy, i.e., a loss of information (see Section 4.2.4).

GENERALIZATION The results derived in this section can be generalized to a n mode squeezed operator given by

$$T_{\rm sqn}(z) = e^{\frac{1}{2}\mathbf{b}^{\rm T} Q_{\rm sqn}\, \mathbf{b}}, \tag{233}$$

with

$$\mathbf{b} = \begin{pmatrix} \hat{b}_1 \\ \vdots \\ \hat{b}_N \\ \hat{b}_1^\dagger \\ \vdots \\ \hat{b}_N^\dagger \end{pmatrix}, \quad \text{and} \quad Q_{\rm sqn} = \begin{pmatrix} -z^\dagger & 0 \\ 0 & z \end{pmatrix}, \tag{234}$$

where z is a $N \times N$ symmetric matrix. This matrix can be decomposed into a product of an Hermitian matrix and a unitary matrix $z = r\, \exp(i\,\phi)$, with r (positive semi-definite) and ϕ two Hermitian matrices. This is called a *polar decomposition*. In this case, the Bogoliubov transformation associated to the operator $T_{\rm sqn}(z)$ between two sets of creation and annihilation operators $\mathbf{b}$ and $\mathbf{c}$ reads [123]

$$\mathbf{c} = T_{\rm sqn}^\dagger(z)\, \mathbf{b}\, T_{\rm sqn}(z) = \mathscr{T}_{\rm sqn}\, \mathbf{b}, \tag{235}$$

with

$$\mathscr{T}_{\rm sqn} = \begin{pmatrix} \cosh(r) & \sinh(r)\, e^{i\,\phi} \\ \sinh(r^{\rm T})\, e^{i\,\phi^{\rm T}} & \cosh(r^{\rm T}) \end{pmatrix}. \tag{236}$$

The matrix (236) is the generalized version of expression (222).

4.1.3 *Bogoliubov transformations in BECs*

Let us now apply the previous results to the case of Bogoliubov transformations in our BEC system. Actually, we have already mentioned

the presence of a Bogoliubov transformation in Chapter 3 [given by equation (162)]:

$$\begin{pmatrix} \hat{c}_U \\ \hat{c}_{D1} \\ \hat{c}^\dagger_{D2} \end{pmatrix} = \begin{pmatrix} S_{u,u} & S_{u,d1} & S_{u,d2} \\ S_{d1,u} & S_{d1,d1} & S_{d1,d2} \\ S_{d2,u} & S_{d2,d1} & S_{d2,d2} \end{pmatrix} \begin{pmatrix} \hat{b}_U \\ \hat{b}_{D1} \\ \hat{b}^\dagger_{D2} \end{pmatrix}, \tag{237}$$

where $\hat{c}_I$ ($\hat{b}_I$), $I \in \{U, D1, D2\}$ are the annihilation operators associated to *outgoing* (*ingoing*) modes. In equation (237), $S_{i,j}$, $i, j \in \{u, d1, d2\}$ are the coefficients of the scattering matrix introduced in Chapter 3. Note that in expression (237) all coefficients depend on the energy $\hbar\omega$.

Let us now define the sets of ingoing and outgoing operators $\mathbf{b} = (\hat{b}_U, \hat{b}_{D1}, \hat{b}_{D2}, \hat{b}^\dagger_U, \hat{b}^\dagger_{D1}, \hat{b}^\dagger_{D2})^{\mathrm{T}}$ and $\mathbf{c} = (\hat{c}_U, \hat{c}_{D1}, \hat{c}_{D2}, \hat{c}^\dagger_U, \hat{c}^\dagger_{D1}, \hat{c}^\dagger_{D2})^{\mathrm{T}}$. Equation (237) can be re-written in the form used in this chapter

$$\mathbf{c} = \mathscr{T}\,\mathbf{b} = \begin{pmatrix} \alpha^* & -\beta^* \\ -\beta & \alpha \end{pmatrix} \mathbf{b}, \tag{238}$$

with

$$\alpha = \begin{pmatrix} S^*_{u,u} & S^*_{u,d1} & 0 \\ S^*_{d1,u} & S^*_{d1,d1} & 0 \\ 0 & 0 & S_{d2,d2} \end{pmatrix}, \; \beta = -\begin{pmatrix} 0 & 0 & S^*_{u,d2} \\ 0 & 0 & S^*_{d1,d2} \\ S_{d2,u} & S_{d2,d1} & 0 \end{pmatrix}. \tag{239}$$

Applying expression (216) to our case gives immediately

$$|0\rangle_b = |S_{d2,d2}|^{-1} \exp\left[\frac{1}{2}\sum_{I,J} X_{I,J}\,\hat{c}^\dagger_I\,\hat{c}^\dagger_J\right]|0\rangle_c, \tag{240}$$

with $|0\rangle_b$ and $|0\rangle_c$ both vacua associated to the b's ans c's operators, respectively, and

$$X = \begin{pmatrix} 0 & 0 & \frac{S_{u,d2}}{S_{d2,d2}} \\ 0 & 0 & \frac{S_{d1,d2}}{S_{d2,d2}} \\ \frac{S_{u,d2}}{S_{d2,d2}} & \frac{S_{d1,d2}}{S_{d2,d2}} & 0 \end{pmatrix}, \quad \text{with} \quad X = -\beta^*\,\alpha^{-1}. \tag{241}$$

Expression (240) takes the simple form

$$|0\rangle_b = |S_{d2,d2}|^{-1} e^{\left(X_{U,D2}\,\hat{c}^\dagger_U + X_{D1,D2}\,\hat{c}^\dagger_{D1}\right)\hat{c}^\dagger_{D2}}|0\rangle_c. \tag{242}$$

Expanding expression (242) over a Fock space gives[7]

$$|0\rangle_b = \frac{1}{|S_{d2,d2}|}\sum_{n=0}^{+\infty}\sum_{n'=0}^{+\infty}\sqrt{\binom{n+n'}{n'}}\,X^{n'}_{U,D2}\,X^{n}_{D1,D2} \times |n'\rangle_{(U)}\,|n\rangle_{(D1)}\,|n+n'\rangle_{(D2)}. \tag{243}$$

7 Where $|n\rangle_{(I)} = \frac{1}{\sqrt{n!}}(\hat{c}^\dagger_I)^n\,|0\rangle_c$

Expression (243) shows that the state we consider is a three-mode pure state[8] (since $\hat{\rho}_b = |0\rangle_{b\,b}\langle 0|$ is a pure state). Then, the reduced density matrix with respect to mode I, $I \in \{U, D1, D2\}$ is

$$\hat{\rho}^{(I)} = (\cosh r_I)^{-2} \sum_{n=0}^{\infty} (\tanh r_I)^{2n} \; |n\rangle_{(I)\,(I)}\langle n|, \tag{244}$$

where we introduced a parameter r_I for each mode U, $D1$, and $D2$:

$$\begin{aligned}
\tanh[r_U(\omega)] &= \frac{|S_{u,d2}(\omega)|}{\sqrt{1+|S_{u,d2}(\omega)|^2}}, \\
\tanh[r_{D1}(\omega)] &= \frac{|S_{d1,d2}(\omega)|}{\sqrt{1+|S_{d1,d2}(\omega)|^2}}, \\
\tanh[r_{D2}(\omega)] &= \frac{\sqrt{|S_{d2,d2}(\omega)|^2-1}}{|S_{d2,d2}(\omega)|}.
\end{aligned} \tag{245}$$

In particular, one has $\sinh r_U = |S_{u,d2}|$, $\sinh r_{D1} = |S_{d1,d2}|$, and $\sinh r_{D2} = \sqrt{|S_{d2,d2}|^2 - 1}$. By virtue of the scattering matrix normalization (142), the three parameters r_U, r_{D1}, and r_{D2} are linked through the relation

$$(\sinh r_U)^2 + (\sinh r_{D1})^2 = (\sinh r_{D2})^2. \tag{246}$$

THERMALITY Expression (244) is exactly the same as equation (228). The reduced density matrix $\hat{\rho}^{(I)}$ is associated to a thermal state [see below, equation (284)] and describes a two mode squeezed vacuum state $T_{\text{sq2}}(r_I)\,|0\rangle_c$ [see equations (217) and (226)]. Therefore, using equation (230), one immediately obtains the number of emitted quanta in the $u|$out mode at frequency ω, i.e., the Hawking radiation spectrum already defined in Section 3.3.1,

$$\mathcal{N}_{\text{H}}(\omega) = \left\langle \hat{c}^{\dagger}_U(\omega)\, \hat{c}_U(\omega) \right\rangle = \frac{1}{e^{\hbar\omega/k_B T_{\text{eff}}} - 1}, \tag{247}$$

with

$$T_{\text{eff}}(\omega) = \frac{\hbar\omega}{2\, k_{\text{B}}\, \ln[\coth r_U(\omega)]}. \tag{248}$$

Thus, we obtain a thermal radiation of effective temperature $T_{\text{eff}}(\omega)$, compare with expression (62) obtained in Chapter 2. In this sense, the analogue Hawking radiation in BECs is indistinguishable from a radiation emitted by a thermal source at the same temperature [74]. However, this thermality is different from the one discussed in Section 3.3.3. Indeed, Hawking radiation emitted by black holes is a black-body radiation with an effective temperature which does not depend on the energy

8 This state can be also seen as a two-mode squeezed vacuum state, formed by the mode $D2$ and a superposition of the modes U and $D1$ [see below, starting from equation (250), and, in particular, equations (256) and (258)].

$\hbar\omega$ [see expression (63) of Chapter 2], at variance with the temperature determined in expression (248). In this sense, the analogue Hawking spectrum is clearly not thermal, albeit one naturally recovers the definition of analogue Hawking temperature in the long-wavelength limit [110]

$$T_{\text{eff}}(\omega) \xrightarrow[\omega\to 0]{} T_{\text{H}}. \tag{249}$$

The effective temperature T_{eff}, as well as the analogue Hawking temperature T_{H}, are shown in Figure 33 for a waterfall configuration[9] with upstream Mach number $m_u = V_u/c_u = 0.59$.

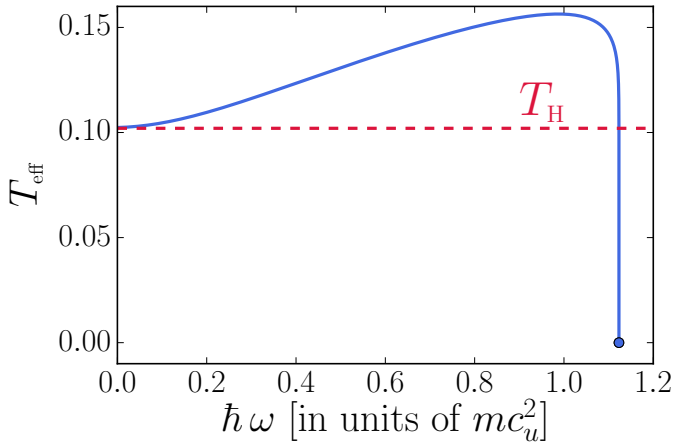

FIGURE 33: Effective temperature T_{eff} computed from equation (248) for a waterfall configuration with upstream Mach number $m_u = V_u/c_u = 0.59$ (see Section 3.1.3). The red dashed line indicates the long-wavelength limit, for which the effective temperature matches with the definition of the analogue Hawking radiation T_{H} defined in equation (176) in Section 3.3.1. Note also that the temperature decreases to zero at $\omega = \Omega$, where Ω is the cut-off frequency defined in Figure 20 of Chapter 3.

TWO MODE SQUEEZED VACUUM STATE We conclude this section with a last remark: it is in fact possible to show that expression (242) corresponds to a two mode squeezed vacuum state. This comes from the fact that one can factor out the creation operator $c^\dagger_{D2}$ in equation (242).

To demonstrate this point, let us first introduce some notations: the coefficients of the scattering matrix are complex, and thus we define the phase $\varphi_{i,j}$, such that $S_{i,j} = |S_{i,j}| \exp(i\,\varphi_{i,j})$, $\forall i, j \in \{u, d1, d2\}$. Then we introduce new annihilation and creation operators $\hat{e}_I$, $I \in \{U, D1, D2\}$:

$$\hat{e}_U = e^{-i\,\varphi_{u,d2}}\hat{c}_U, \quad \hat{e}_{D1} = e^{-i\,\varphi_{d1,d2}}\hat{c}_{D1}, \quad \hat{e}_{D2} = e^{i\,\varphi_{d2,d2}}\hat{c}_{D2}. \tag{250}$$

9 The definition of a waterfall configuration is given in Section 3.1.3.

The transformation between operators $\hat{e}_I$ and $\hat{c}_I$ is unitary and corresponds to a rotation operator

$$R(\varphi) = \exp\left(i \sum_{IJ} \hat{c}_I^\dagger \, \varphi_{i,j} \, \hat{c}_J \right), \tag{251}$$

with $\varphi = \mathrm{diag}(-\varphi_{u,d2}, -\varphi_{d1,d2}, \varphi_{d2,d2})$. One has indeed

$$\mathbf{e} = R^\dagger(\varphi)\, \mathbf{c}\, R(\varphi) = \Phi\, \mathbf{c}, \tag{252}$$

with $\mathbf{e} = (\hat{e}_U, \hat{e}_{D1}, \hat{e}_{D2}, \hat{e}_U^\dagger, \hat{e}_{D1}^\dagger, \hat{e}_{D2}^\dagger)^{\mathrm{T}}$, and

$$\Phi = \begin{pmatrix} \Phi_{\mathrm{d}} & 0 \\ 0 & \Phi_{\mathrm{d}}^\dagger \end{pmatrix}. \tag{253}$$

In expression (253), $\Phi_{\mathrm{d}} = \mathrm{diag}(e^{-i\,\varphi_{u,d2}}, e^{-i\,\varphi_{d1,d2}}, e^{i\,\varphi_{d2,d2}})$. Note that expression (253) is a peculiar form of the matrix $\mathscr{T}$ defined in equation (186), which does not mix annihilation and creation operators.

Then, one can write the full transformation from the set of operators $\mathbf{b}$ to the set $\mathbf{e}$:

$$\mathbf{e} = R^\dagger(\varphi)\, T^\dagger \mathbf{b}\, T\, R(\varphi) = \Phi\, \mathscr{T}\, \mathbf{b}, \tag{254}$$

where T corresponds to the unitary Bogoliubov transformation between $\mathbf{b}$ and $\mathbf{c}$, and $\mathscr{T}$ is given by equations (238) and (239).

Then, we also define an angle $\theta(\omega)$ such that:

$$\cos(\theta) \equiv \frac{|X_{U,D2}|}{\tanh r_{D2}} \quad \text{and} \quad \sin(\theta) \equiv \frac{|X_{D1,D2}|}{\tanh r_{D2}}, \tag{255}$$

where we recall that $X_{I,J}$ are the coefficients of the matrix X [see expression (241)]. This enables us to introduce a new annihilation operator

$$\hat{e}_\theta = \cos(\theta)\, \hat{e}_U + \sin(\theta)\, \hat{e}_{D1}. \tag{256}$$

Note that $\sinh r_U = \cos(\theta)\, \sinh r_{D2}$ and $\sinh r_{D1} = \sin(\theta)\, \sinh r_{D2}$.

By means of these new notations, expression (242) becomes

$$\begin{aligned} |0\rangle_b &= (\cosh r_{D2})^{-1} e^{\tanh r_{D2}\, \hat{e}_\theta^\dagger\, \hat{e}_{D2}^\dagger} |0\rangle_c \\ &= T_{\mathrm{sq2}}(r_{D2})\, |0\rangle_c, \end{aligned} \tag{257}$$

with

$$T_{\mathrm{sq2}}(r_{D2}) = \exp\left[r_{D2} \left(\hat{e}_\theta^\dagger\, \hat{e}_{D2}^\dagger - \hat{e}_\theta\, \hat{e}_{D2} \right) \right]. \tag{258}$$

Therefore, $|0\rangle_b$ is indeed a two mode squeezed vacuum state. This will make it possible to write the covariance matrix (280) in a standard form (see Section 4.2.1). Moreover, note that the change of basis (256) could be seen as the equivalent of the action of beamsplitter in a quantum optics setup; we will come back to this analogy in Section 4.3.1.

4.2 MEASURING ENTANGLEMENT

In this section we discuss the different possibilities for measuring entanglement. The first subsection is devoted to the definition of the so-called covariance matrices. These matrices provide a powerful tool for characterizing entanglement through symplectic eigenvalues, and we will use them throughout the following sections.

Then, we define Cauchy-Schwarz inequality or, equivalently in our case, the DGCZ criterion [52] (where DGCZ are the co-authors of Ref. [52]). A violation of this inequality ensures the non-separability of a bipartite state. Several studies in the field of acoustic black holes [32, 33, 62] used this criterion to study entanglement properties of pairs of quanta emitted in BECs from vacuum fluctuations.

In this thesis, as mentioned in the introduction of this chapter, we wish to study tripartite entanglement. Previous works pertaining to quantum information theory [3–6, 166, 167, 169] developed numerous tools to explore entanglement of multipartite states. In particular, Peres-Horodecki (PPT) criterion is used in this community to study non-separability, and this is the reason why one subsection is dedicated to its analysis. However, this criterion does not measure the degree of entanglement. Since our aim is to characterize the degree of entanglement of a tripartite state, we need to use a computable measure that is able to quantify entanglement sharing, such as the Von-Neuman entropy or the logarithmic negativity. Therefore, we end this section by their definition.

PPT means 'Positive Partial Transpose'.

4.2.1 *Gaussian states and covariance matrices*

GAUSSIAN STATES By definition, a quantum state[10]

$$\hat{\rho} = \sum_i p_i \left|\psi_i\right\rangle \left\langle\psi_i\right| \tag{259}$$

is Gaussian if and only if its associated characteristic Wigner function

$$\chi_{\mathrm{W}}(\boldsymbol{\lambda}) = \mathrm{Tr}\left[\hat{\rho}\,\hat{D}(\boldsymbol{\lambda})\right] \tag{260}$$

is a Gaussian function [72].

In equation (260), $\boldsymbol{\lambda} = (\lambda_1, \ldots, \lambda_N, -\lambda_1^*, \ldots, -\lambda_N^*)^{\mathrm{T}}$, with $\lambda_i \in \mathbb{C}$, and $\hat{D}(\boldsymbol{\lambda})$ is a displacement operator defined as

$$\hat{D}(\boldsymbol{\lambda}) = e^{\boldsymbol{\lambda}^{\mathrm{T}}\mathbf{b}}, \quad \text{with} \quad \mathbf{b} = (\hat{b}_1, \ldots, \hat{b}_N, \hat{b}_1^\dagger, \ldots, \hat{b}_N^\dagger)^{\mathrm{T}}. \tag{261}$$

Consider a pure Gaussian state $\hat{\rho}_{\mathrm{G}} = \left|\psi_{\mathrm{G}}\right\rangle \left\langle\psi_{\mathrm{G}}\right|$ and a unitary Bogoliubov transformation

$$\left|\psi\right\rangle = T\left|\psi_{\mathrm{G}}\right\rangle. \tag{262}$$

10 The density matrix $\hat{\rho}$ is also referred to as the quantum state in the quantum information community.

We define for convenience

$$\chi_{\mathrm{W}}^{\mathrm{G}}(\boldsymbol{\lambda}) \equiv \mathrm{Tr}\left[\hat{\rho}_{\mathrm{G}}\,\hat{D}(\boldsymbol{\lambda})\right]. \tag{263}$$

Then, $\hat{\rho} = |\psi\rangle\langle\psi|$ is also a Gaussian state. Indeed, first we notice that

$$\hat{\rho} = T\,\hat{\rho}_{\mathrm{G}}\,T^{\dagger}. \tag{264}$$

Therefore, by using the cyclicity of the trace and equation (197),

$$\begin{aligned}\chi_{\mathrm{W}}(\boldsymbol{\lambda}) &= \mathrm{Tr}\left[\hat{\rho}\,\hat{D}(\boldsymbol{\lambda})\right]\\ \mathrm{Tr}\left[T\,\hat{\rho}_{\mathrm{G}}\,T^{\dagger}\,\hat{D}(\boldsymbol{\lambda})\right] &= \mathrm{Tr}\left[\hat{\rho}_{\mathrm{G}}\,T^{\dagger}\,\hat{D}(\boldsymbol{\lambda})\,T\right]\\ &= \mathrm{Tr}\left[\hat{\rho}_{\mathrm{G}}\,e^{\boldsymbol{\lambda}^{\mathrm{T}}\,T^{\dagger}\,\mathbf{b}\,T}\right]\mathrm{Tr}\left[\hat{\rho}_{\mathrm{G}}\,e^{\boldsymbol{\lambda}^{\mathrm{T}}\,\mathscr{T}\,\mathbf{b}}\right] = \mathrm{Tr}\left[\hat{\rho}_{\mathrm{G}}\,\hat{D}(\mathscr{T}^{\mathrm{T}}\,\boldsymbol{\lambda})\right],\end{aligned} \tag{265}$$

and thus

$$\chi_{\mathrm{W}}(\boldsymbol{\lambda}) = \chi_{\mathrm{W}}^{\mathrm{G}}(\mathscr{T}^{\mathrm{T}}\,\boldsymbol{\lambda}). \tag{266}$$

Equation (266) proves that the Wigner characteristic function $\chi_{\mathrm{W}}(\boldsymbol{\lambda})$, associated to the quantum state $\hat{\rho}$, is a Gaussian function, meaning that $\hat{\rho}$ is indeed a Gaussian state.

In our case, since we consider a Bogoliubov transformation $|0\rangle_c = T^{\dagger}\,|0\rangle_b$, the Gaussian character of the vacuum $|0\rangle_b$ is preserved through this transformation, and thus $|0\rangle_c$ is also a Gaussian state; and this result is expected: $|0\rangle_c$ is an oscillator ground state such that $\hat{c}_I\,|0\rangle_c = 0$, $I \in \{U, D1, D2\}$, thus necessarily Gaussian. Recalling expression (243), the Bogoliubov transformation associated to the scattering process (237) leads to a three-mode Gaussian pure state.

COVARIANCE MATRICES Let us now introduce the vector of quadrature operators

$$\boldsymbol{\xi} = \sqrt{2}\,(\hat{q}_1, \hat{p}_1, \ldots, \hat{q}_N, \hat{p}_N)^{\mathrm{T}}, \tag{267}$$

with $\hat{q}_i$ and $\hat{p}_i$ the position and momentum operators related to mode i, and defined in terms of the creation and annihilation operators as[11]

$$\hat{q}_i = \frac{\hat{b}_i + \hat{b}_i^{\dagger}}{\sqrt{2}}, \quad \text{and} \quad \hat{p}_i = \frac{\hat{b}_i - \hat{b}_i^{\dagger}}{\sqrt{2}\,i}, \ \forall\, i \in \{1, \ldots, N\}. \tag{268}$$

Therefore we can define a (unitary) matrix U such that

$$\boldsymbol{\xi} = U\,\mathbf{b}, \quad \mathbf{b} = U^{\dagger}\,\boldsymbol{\xi}. \tag{269}$$

Using equation (269), one sees that the vector $\boldsymbol{\xi}$ must respect the commutation relation

$$[\boldsymbol{\xi}_i, \boldsymbol{\xi}_j] = 2\,i\,\Omega_{ij}, \ \forall\, i, j \in \{1, \ldots 2N\}, \tag{270}$$

11 The factor $\sqrt{2}$ in the definition of ξ in equation (267) seems useless, since it cancels with the factor $1/\sqrt{2}$ in the definition of the position and momentum operators [expressions (268)]. However, we decided to keep this factor in expression (267) to follow the conventions used in Ref. [4], in particular for the normalization of the covariance matrix and the symplectic eigenvalues (see below).

with

$$\Omega = -\frac{i}{2}\, U\, \widetilde{\Omega}\, U^{\mathrm{T}} = \bigoplus_{1}^{N} \omega, \quad \omega = \begin{pmatrix} 0 & 1 \\ -1 & 0 \end{pmatrix}. \tag{271}$$

We define the covariance matrix σ, a real symmetric positive-definite matrix, such that:

$$\sigma_{i,j} \equiv \frac{1}{2}\, \langle \hat{\xi}_i\, \hat{\xi}_j + \hat{\xi}_j\, \hat{\xi}_i \rangle - \langle \hat{\xi}_i \rangle\, \langle \hat{\xi}_j \rangle. \tag{272}$$

Let us consider now a unitary transformation, decomposed into a Bogoliubov transformation (we denote the corresponding operator T to respect the notations used in the previous sections) and a rotation transformation [the corresponding operator is denoted $R(\varphi)$].

In the Heisenberg picture, the quadrature operators ξ are transformed by this unitary transformation. Indeed, it is easy to prove that in this case

$$R^{\dagger}(\varphi)\, T^{\dagger}\, \boldsymbol{\xi}\, T\, R(\varphi) = U \Phi\, \mathscr{T}\, U^{\dagger} \boldsymbol{\xi} \equiv \mathscr{J}(U)\, \boldsymbol{\xi}, \tag{273}$$

where $\mathscr{J}(U) = U\, \Phi\, \mathscr{T}\, U^{\dagger} \in \mathrm{Sp}(2N, \mathbb{R})$ [172]. Denoting $\Phi(U) = U\, \Phi\, U^{\dagger}$ and $\mathscr{T}(U) = U\, \mathscr{T}\, U^{\dagger}$, one might prefer to write $\mathscr{J}(U) = \Phi(U)\, \mathscr{T}(U)$. The covariance matrix (272) associated to this transformation is

$$\sigma'_{i,j} = \frac{1}{2}\, \langle \hat{\xi}'_i\, \hat{\xi}'_j + \hat{\xi}'_j\, \hat{\xi}'_i \rangle - \langle \hat{\xi}'_i \rangle\, \langle \hat{\xi}'_j \rangle, \tag{274}$$

where we have introduced the transformed vector

$$\boldsymbol{\xi}' = (\hat{\xi}'_1, \ldots, \hat{\xi}'_N) = \mathscr{J}(U)\, \boldsymbol{\xi}. \tag{275}$$

Thus expression (274) becomes

$$\sigma'_{i,j} = \frac{1}{2} \sum_{kl} [\mathscr{J}(U)]_{ik}\, \langle \hat{\xi}_k\, \hat{\xi}_l + \hat{\xi}_l\, \hat{\xi}_k \rangle - \langle \hat{\xi}_k \rangle\, \langle \hat{\xi}_l \rangle\, [\mathscr{J}(U)^{\mathrm{T}}]_{lj}, \tag{276}$$

showing that

$$\sigma' = \mathscr{J}(U)\, \sigma\, \mathscr{J}(U)^{\mathrm{T}}. \tag{277}$$

We could also write it in the form

$$\sigma' = \Phi(U)\, \mathscr{T}(U)\, \sigma\, \mathscr{T}(U)^{\mathrm{T}}\, \Phi(U)^{\mathrm{T}}, \tag{278}$$

where the decomposition into a Bogoliubov transformation and a rotation becomes clearer.

Note that, if $\Phi = \mathrm{diag}(\Phi_{\mathrm{d}}, \Phi_{\mathrm{d}}^{\dagger})$, with $\Phi_{\mathrm{d}} = \mathrm{diag}[\exp(i\, \varphi_1), \ldots, \exp(i\, \varphi_N)]$,

$$\Phi(U) = \begin{pmatrix} R_{\varphi_1} & & \\ & \ddots & \\ & & R_{\varphi_N} \end{pmatrix}, \quad R_{\varphi_i} = \begin{pmatrix} \cos(\varphi_i) & \sin(\varphi_i) \\ -\sin(\varphi_i) & \cos(\varphi_i) \end{pmatrix}. \tag{279}$$

In this case, the matrix $\Phi(U)$ is diagonal and corresponds for each mode $i \in \{1, \ldots, N\}$ to a rotation of angle φ_i. One sees from equation (253) that we are exactly in this case.

Let us summarize the action of a Bogoliubov transformation followed by a rotation on an initial covariance matrix σ_{G}. Using expression (272), the covariance matrix can be written explicitly in terms of the position and the momentum operators

$$\sigma_{\mathrm{G}} = \begin{pmatrix} \sigma_1 & \varepsilon_{12} & \cdots & \varepsilon_{1N} \\ \varepsilon_{12}^{\mathrm{T}} & \ddots & \ddots & \vdots \\ \vdots & \ddots & \ddots & \varepsilon_{N-1N} \\ \varepsilon_{1N}^{\mathrm{T}} & \cdots & \varepsilon_{N-1N}^{\mathrm{T}} & \sigma_N \end{pmatrix}, \tag{280}$$

with

$$\sigma_i = 2 \begin{pmatrix} \langle \hat{q}_i^2 \rangle & \langle \{\hat{q}_i, \hat{p}_i\} \rangle \\ \langle \{\hat{q}_i, \hat{p}_i\} \rangle & \langle \hat{p}_i^2 \rangle \end{pmatrix}, \; \varepsilon_{ij} = 2 \begin{pmatrix} \langle \hat{q}_i \hat{q}_j \rangle & \langle \hat{q}_i \hat{p}_j \rangle \\ \langle \hat{p}_i \hat{q}_j \rangle & \langle \hat{p}_i \hat{p}_j \rangle \end{pmatrix}, \tag{281}$$

where $\langle \{\hat{q}_i, \hat{p}_i\} \rangle = \frac{1}{2} \left(\langle \hat{q}_i \hat{p}_i \rangle + \langle \hat{p}_i \hat{q}_i \rangle \right)$, $i \in \{1, \ldots, N\}$.

In equations (280) and (281) the position and momentum operators $\hat{q}_i$ and $\hat{p}_i$, $i \in \{1, \ldots, N\}$ are linked to the initial set of annihilation and creation operators $\mathbf{b}$ through relation (269), or explicitly through relation (268). After the unitary transformation, using equations (272) and (277) one finds that the covariance matrix σ has the same form as equation (280), but now

$$\hat{q}_i \to \hat{q}_i' = \frac{\hat{e}_i + \hat{e}_i^\dagger}{\sqrt{2}}, \quad \text{and} \quad \hat{p}_i \to \hat{p}_i' = \frac{\hat{e}_i - \hat{e}_i^\dagger}{\sqrt{2}\, i}, \tag{282}$$

where $\hat{e}_i$ ($\hat{e}_i^\dagger$) are the transformed annihilation (creation) operators [see, e.g., expression (254)].

SIMPLE CASES In this paragraph we just mention some simple covariance matrices, which will be useful in the following:

• Vacuum state – The covariance matrix associated to a vacuum state $|0\rangle$ is

$$\sigma_0 = \mathbb{1}. \tag{283}$$

This result is immediate from equation (281).

• Thermal state – A thermal state is described by a density matrix of the form

$$\rho^{\mathrm{th}}(\bar{n}) = \frac{1}{\bar{n}+1} \sum_{n=0}^{\infty} \left(\frac{\bar{n}}{\bar{n}+1} \right)^n |n\rangle \langle n|. \tag{284}$$

Note that, as mentioned earlier, the reduced density matrices $\rho^{(I)}$ derived in equation (244) are thermal states with $\bar{n} = \sinh^2(r_I)$, $\forall\, I \in$

$\{U, D1, D2\}$. One checks that $\bar{n}$ is indeed the mean occupation number for each mode I, since $\sinh^2(r_I) = \langle \hat{c}_I^\dagger \hat{c}_I \rangle$.

Here also, one finds from equation (281) that the covariance matrix $\sigma^{\rm th}$ associated to the density matrix (284) is

$$\sigma^{\rm th} = (2\,\bar{n} + 1)\mathbb{1}_2. \tag{285}$$

WICK THEOREM Gaussian states are fully characterized by the first and second moments of the vector $\boldsymbol{\xi}$. One can always impose $\langle \boldsymbol{\xi} \rangle = 0$ by using some local displacement operations. Therefore, the covariance matrix reduces to $\sigma_{i,j} = \frac{1}{2}\langle \hat{\xi}_i \hat{\xi}_j + \hat{\xi}_j \hat{\xi}_i \rangle$ and entirely describes the corresponding Gaussian state of density operator $\hat{\rho}$. This is an important remark: the covariance matrix σ characterizes the entanglement of the corresponding Gaussian state.

We mention for completeness that higher order moments can be evaluated by using the Wick theorem

$$\langle \hat{\mathcal{O}}_1 \dots \hat{\mathcal{O}}_N \rangle = \sum \langle \hat{\mathcal{O}}_{i_1} \hat{\mathcal{O}}_{i_2} \rangle \dots \langle \hat{\mathcal{O}}_{i_{N-1}} \hat{\mathcal{O}}_{i_N} \rangle, \tag{286}$$

where the sum is taken over all different manners to associate the initial operators $\hat{\mathcal{O}}_i$, and with $i_j < i_{j+1}$, $j \in \{1, \dots, N-1\}$.

WILLIAMSON'S THEOREM For any real symmetric positive-definite $2N \times 2N$ matrix σ there exists $\mathcal{S} \in {\rm Sp}(2N, \mathbb{R})$ such that the so-called symplectic transform of σ by $\mathcal{S}$ has the canonical diagonal form, unique up to the ordering of the ν_j,

$$\nu = \mathcal{S}\,\sigma\,\mathcal{S}^{\rm T} = {\rm diag}(\nu_1, \nu_1, ..., \nu_N, \nu_N), \quad \text{with} \quad \nu_j \in \mathbb{R}^+. \tag{287}$$

The quantities $\{\nu_j\}$ are called the symplectic eigenvalues of σ and they can be computed as the eigenvalues of the matrix $|i\Omega\sigma|$, where Ω has been defined in equation (271) [12].

In addition, one sees from equation (285) that the diagonal form ν of any covariance matrix σ is associated to a density matrix

$$\rho_\nu = \bigotimes_{j=1}^{N} \rho^{\rm th}(\nu_j), \tag{289}$$

where $\rho^{\rm th}(\nu_j)$ is defined in equation (284). Therefore Williamson's theorem proves that any Gaussian states can be decomposed into thermal states, whose mean occupation number $\bar{n}$ are the symplectic eigenvalues ν_j.

UNCERTAINTY RELATION A bona fide covariance matrix σ has to satisfy the uncertainty relation [172]

$$\sigma + i\,\Omega \geq 0. \tag{290}$$

12 This statement can be proven on the canonical diagonal form [166]. Indeed, one has $\Omega^{-1} = \Omega^{\rm T} = -\Omega$, $\Omega^2 = -\mathbb{1}$ and $\mathcal{S}^{-1} = \Omega^{-1}\,\mathcal{S}^T\,\Omega$ leading to

$$\Omega\,\nu = \Omega\,\mathcal{S}\,\sigma\,\mathcal{S}^{\rm T} = (\mathcal{S}^{\rm T})^{-1}\,\Omega\,\sigma\,\mathcal{S}^{\rm T}. \tag{288}$$

Let us prove this property. Using the Williamson's theorem, we know that there exists a symplectic matrix $\mathcal{S}$ such that $\nu = \mathcal{S}\,\sigma\,\mathcal{S}^{\mathrm{T}}$. Thus,

$$\nu + i\,\Omega = \mathcal{S}\,(\sigma + i\,\Omega)\,\mathcal{S}^{\mathrm{T}}, \tag{291}$$

where we used $\mathcal{S}\,\Omega\,\mathcal{S}^{\mathrm{T}} = \Omega$. The explicit expression of $\nu + i\,\Omega$ is easily obtained and reads

$$\nu + i\,\Omega = \bigoplus_{i=1}^{N} \varpi_i, \quad \text{where} \quad \varpi_i = \begin{pmatrix} \nu_i & 1 \\ -1 & \nu_i \end{pmatrix}. \tag{292}$$

Thus, since the eigenvalues of ϖ_i are $\nu_i \pm 1$, $\nu + i\,\Omega \geq 0$ if and only if $\nu_i \geq 1$, $i \in \{1, \ldots, N\}$. By noticing that $\nu_i = 2\,\langle \hat{q}_i^2 \rangle = 2\,\langle \hat{p}_i^2 \rangle = \mathrm{Tr}(\hat{\rho}_\nu\,\hat{p}_i^2)$, where $\hat{\rho}_\nu$ is given by expression (284), one obtains

$$\nu_i \geq 1 \Rightarrow (\Delta\hat{q}_i)^2\,(\Delta\hat{p}_i)^2 \geq \frac{1}{4}, \tag{293}$$

which corresponds exactly to the Heisenberg uncertainty relation, and which is always verified for a pair of canonical operators $\{\hat{q}_i, \hat{p}_i\}$. This ensures that $\nu + i\,\Omega \geq 0$. Then, since the transformation (291) preserves the positive-semi-definiteness, $\sigma + i\,\Omega \geq 0$.

4.2.2 *Cauchy-Schwarz inequality*

DUAN *et al.* CRITERION (also called the *DGCZ criterion*) As discussed in Ref. [52], there exists a general inequality for Gaussian states, which is a sufficient and necessary condition for two modes to be entangled. The covariance matrix associated to two modes, say 1 and 2, is explicitly

$$\sigma_{12} = \begin{pmatrix} \sigma_1 & \varepsilon_{12} \\ \varepsilon_{12}^{\mathrm{T}} & \sigma_2 \end{pmatrix}, \tag{294}$$

where σ_1, σ_2 and ε_{12} are 2×2 matrices given by (281). This covariance matrix is said to be in its *standard form* when it is of the form

$$\sigma_{12} = \begin{pmatrix} n_1 & 0 & \ell_1 & 0 \\ 0 & n_2 & 0 & \ell_2 \\ \ell_1 & 0 & m_1 & 0 \\ 0 & \ell_2 & 0 & m_2 \end{pmatrix}, \tag{295}$$

where n_1, n_2, m_1, $m_2 \geq 1$, and ℓ_1, $\ell_2 \in \mathbb{R}$. In this case, Duan *et al.* [52] proved that a sufficient and necessary condition for these two modes to be entangled is

$$\begin{cases} |\ell_1| > \sqrt{(n_1 - 1)\,(m_1 - 1)} \\ |\ell_2| > \sqrt{(n_2 - 1)\,(m_2 - 1)} \end{cases} \tag{296}$$

In our case, we consider two modes I and J among U, $D1$, and $D2$. As explained in the previous subsection, the corresponding two

mode covariance matrix can be calculated in terms of the transformed annihilation and creation operators $\hat{e}_I$ and $\hat{e}_I^\dagger$ defined in expression (254):

$$\sigma_I = (1 + 2\,\langle \hat{e}_I^\dagger\, \hat{e}_I\rangle)\,\mathbb{1}_2 = (1 + 2\,\langle \hat{c}_I^\dagger\, \hat{c}_I\rangle)\,\mathbb{1}_2,\ \forall I \in \{U, D1, D2\}, \tag{297}$$

and

$$\varepsilon_{IJ} = \begin{cases} 2|\langle \hat{c}_I\, \hat{c}_J\rangle|\,\sigma_z, & \text{if} \quad I \in \{U, D1\},\ J = D2, \\ 2|\langle \hat{c}_I\, \hat{c}_J^\dagger\rangle|\,\mathbb{1}_2, & \text{if} \quad I, J \in \{U, D1\}, \end{cases} \tag{298}$$

where we recall that c's operators annihilate or create an excitation in one of the outgoing modes $u|\text{out}$, $d1|\text{out}$, or $d2|\text{out}$ [see equation (237)]. Note that in equation (298), the result is written in terms of $\hat{c}_I$ ($\hat{c}_I^\dagger$) and not $\hat{e}_I$ ($\hat{e}_I^\dagger$). This will be indeed more convenient for future discussions, since c's operators have a real physical meaning and are linked to e's operators just by a phase factor [see equation (250)].

We immediately see that the covariance matrix described by matrices (297) and (298) is in its *standard form*, with

$$\begin{aligned} &n_1 = n_2 = (1 + 2\,\langle \hat{c}_I^\dagger\, \hat{c}_I\rangle), \\ &m_1 = m_2 = (1 + 2\,\langle \hat{c}_J^\dagger\, \hat{c}_J\rangle), \\ &\ell_1 = \begin{cases} -\ell_2 = 2|\langle \hat{c}_I\, \hat{c}_J\rangle|, & \text{if} \quad I \in \{U, D1\},\ J = D2, \\ \ell_2 = 2|\langle \hat{c}_I\, \hat{c}_J^\dagger\rangle|, & \text{if} \quad I, J \in \{U, D1\}. \end{cases} \end{aligned} \tag{299}$$

Thus, using the DGCZ criterion (296), we state that two modes I and J are entangled if and only if

$$\begin{cases} |\langle \hat{c}_I\, \hat{c}_J\rangle|^2 > \langle \hat{c}_I^\dagger\, \hat{c}_I\rangle\,\langle \hat{c}_J^\dagger\, \hat{c}_J\rangle, & \text{if} \quad I \in \{U, D1\},\ J = D2, \\ |\langle \hat{c}_I\, \hat{c}_J^\dagger\rangle|^2 > \langle \hat{c}_I^\dagger\, \hat{c}_I\rangle\,\langle \hat{c}_J^\dagger\, \hat{c}_J\rangle, & \text{if} \quad I, J \in \{U, D1\}. \end{cases} \tag{300}$$

The set of inequalities (300) exactly corresponds to a violation of the Cauchy-Schwarz inequality [75, 174].

ENTANGLEMENT Let us now use inequalities (300) to determine if there is entanglement in our system. First, we write the covariance matrix in terms of the parameters r_I introduced in equation (245):

$$\sigma_I = \cosh(2\,r_I)\,\mathbb{1}_2,\ \forall I \in \{U, D1, D2\}, \tag{301}$$

and

$$\varepsilon_{IJ} = \begin{cases} 2\,\sinh(r_I)\,\cosh(r_J)\,\sigma_z, & \text{if} \quad I \in \{U, D1\},\ J = D2, \\ 2\,\sinh(r_I)\,\sinh(r_J)\,\mathbb{1}_2, & \text{if} \quad I, J \in \{U, D1\}. \end{cases} \tag{302}$$

Therefore, we obtain

$$\begin{cases} \dfrac{\langle \hat{c}_I^\dagger\, \hat{c}_I\rangle\,\langle \hat{c}_J^\dagger\, \hat{c}_J\rangle}{|\langle \hat{c}_I\, \hat{c}_J\rangle|^2} = [\tanh(r_{D2})]^2, \ \text{if } I \in \{U, D1\},\ J = D2, \\ \dfrac{\langle \hat{c}_I^\dagger\, \hat{c}_I\rangle\,\langle \hat{c}_J^\dagger\, \hat{c}_J\rangle}{|\langle \hat{c}_I\, \hat{c}_J^\dagger\rangle|^2} = 1, \ \text{if } I, J \in \{U, D1\}. \end{cases} \tag{303}$$

One sees that the first inequality of (300) is always verified [$\tanh(r_{D2}) < 1$], meaning that the Cauchy-Schwarz inequality is violated. This means that pairs of quanta $U - D2$ and $D1 - D2$ are entangled.

However, the second inequality of (300) is not true: indeed, according to equation (303), $\langle \hat{c}^\dagger_U \hat{c}_U \rangle \langle \hat{c}^\dagger_{D1} \hat{c}_{D1} \rangle = |\langle \hat{c}_U \hat{c}^\dagger_{D1} \rangle|^2$. This means that a pair of quanta $U - D1$ is not entangled, but instead separable.

Therefore, one guesses how tripartite entanglement emerges. Three outgoing quanta, emitted from the acoustic horizon in the mode U, $D1$, and $D2$, respectively, share entanglement with each other in a particular manner: positive energy modes U and $D1$ are not entangled, but each of them is entangled with the negative mode $D2$. This renders the whole system entangled.

4.2.3 *PTT criterion*

Another important criterion is the PPT ('*Positive Partial Transpose*') criterion which will reveal more useful than the DGCZ criterion for studying tripartite entanglement. Consider a density matrix $\hat{\rho}$ which acts on a Hilbert space of the form $\mathcal{H}_A \otimes \mathcal{H}_B$. The partial transpose with respect to subsystem A is defined as[13]

$$\hat{\rho}^{\mathrm{T_A}} = (\mathtt{T} \otimes \mathbb{1})(\hat{\rho}), \tag{304}$$

where $\mathtt{T}$ is the transposition map applied to A and $\mathbb{1}$ is the identity map applied to B.

The Peres-Horodecki (or PPT) criterion states that a necessary and sufficient condition [171, 193] for a state $\hat{\rho}$ to be separable is that $\hat{\rho}^{\mathrm{T_A}}$ (or $\hat{\rho}^{\mathrm{T_B}}$) must be positive semidefinite, i.e., all its eigenvalues are positive. Therefore, if one of the eigenvalues is negative after the partial transpose operation[14], the state is entangled. Therefore, PTT criterion helps to decide if two subsystems are entangled or not.

The covariance matrix appears to be a very powerful tool to use PPT criterion. Indeed, it has been proven that the covariance matrix $\hat{\sigma}^{\mathrm{T_A}}$ of the partially transposed state $\hat{\rho}^{\mathrm{T_A}}$ with respect to subsystem A is [171]

$$\hat{\sigma}^{\mathrm{T_A}} = \mathfrak{T}\,\sigma\,\mathfrak{T}, \quad \text{with} \quad \mathfrak{T} = \bigoplus_1^m \sigma_z \oplus \mathbb{1}_{2n}, \tag{305}$$

where m is the dimension of subsystem A, n is the dimension of subsystem B, σ_z is the usual 2×2 Pauli matrix, and $\mathbb{1}_{2n}$ is the $2n$-dimensional identity matrix.

If we consider now a $[1 + (n-1)]$-mode Gaussian state (in the sense that subsystem A is one-dimensional and subsystem B is $(n-1)$-dimensional), in analogy with condition (293), the PPT criterion can

13 Such a density matrix can be written as $\hat{\rho} = \sum \rho_{ijkl} \, |i_A \, j_B\rangle\langle k_A \, l_B|$. Then the transposition map applied to subsystem A leads to $\hat{\rho}^{\mathrm{T_A}} = \sum \rho_{kjil} \, |i_A \, j_B\rangle\langle k_A \, l_B|$.

14 One does not need to partial transpose with respect to A, and then to B to conclude on the separability or not of the state. Indeed, it suffices to partial transpose with respect to one of both subsystems, say A for example. Then, because $\hat{\rho}^{\mathrm{T_B}} = (\hat{\rho}^{\mathrm{T_A}})^{\mathrm{T}}$, the spectrum of $\hat{\rho}^{\mathrm{T_B}}$ is the same as the spectrum of $\hat{\rho}^{\mathrm{T_A}}$.

be expressed as a condition of the *symplectic eigenvalues*[15] $\{\nu_j^{\mathrm{T_A}}\}$ of $\hat{\sigma}^{\mathrm{T_A}}$. The $[1+(n-1)]$-mode Gaussian state is separable

$$\text{if and only if} \quad \nu_j^{\mathrm{T_A}} \geq 1, \quad \forall\, j \in \{1,\ldots,n\}. \tag{306}$$

A violation of the previous inequality by one of the symplectic eigenvalues $\{\nu_j^{\mathrm{T_A}}\}$ ensures the non-separability of the state. This condition can be also written

$$\sigma^{\mathrm{T_A}} + i\,\Omega \geq 0, \tag{307}$$

in full analogy with inequality (290).

DETERMINATION OF THE SYMPLECTIC EIGENVALUES We give here the explicit expression of the symplectic eigenvalues in the case of a two-mode Gaussian state.

We denote $\nu_\pm$ the symplectic eigenvalues associated to the density matrix $\hat{\rho}$, which describes the two-mode Gaussian state. The symplectic eigenvalues of the partially transposed density matrix $\hat{\rho}^{\mathrm{T_1}}$ with respect to the first mode[16] is denoted $\nu_\pm^{\mathrm{T_1}}$.

Then, as in expression (294), we define the two-mode covariance matrix as

$$\sigma_{12} = \begin{pmatrix} \sigma_1 & \varepsilon_{12} \\ \varepsilon_{12}^{\mathrm{T}} & \sigma_2 \end{pmatrix}, \tag{308}$$

where the 2×2 matrices $\sigma_{1,2}$ and ε_{12} are defined in (281).

One can find easily the symplectic eigenvalues associated to σ_{12} [169, 186]. First, using the Williamson's theorem, which states that any covariance matrix σ can be put into a diagonal form ν through a symplectic transform, we can find a symplectic matrix $\mathcal{S}$ such that $\nu_{12} = \mathcal{S}\,\sigma_{12}\,\mathcal{S}^{\mathrm{T}}$, with $\nu_{12} = \mathrm{diag}(\nu_-,\nu_-,\nu_+,\nu_+)$.

Then, to find the explicit expressions of ν_- and ν_+, we use the fact that $\det\sigma_{12}$ and the quantity defined by $\Delta_{12} = \det\sigma_1 + \det\sigma_2 + 2\det\varepsilon_{12}$ are symplectic invariant, i.e., invariant under a symplectic transform [169]. This means that $\det\nu_{12} = \nu_-\,\nu_+ = \det\sigma_{12}$ and $\Delta_{12}(\nu_{12}) = \nu_-^2 + \nu_+^2 = \Delta_{12}(\sigma_{12})$, thus leading to

$$2\,\nu_\pm^2 = \Delta_{12} \pm \sqrt{\Delta_{12}^2 - 4\,\det\,\sigma_{12}}. \tag{309}$$

In addition, one can prove easily that partial transpose operation changes the sign in front of $\det\varepsilon_{12}$ in the expression of Δ_{12} [171]. Therefore, the symplectic eigenvalues associated to $\hat{\sigma}_{12}^{\mathrm{T_1}}$ are given by

$$2\,(\nu_\pm^{\mathrm{T_1}})^2 = \Delta_{12}^{\mathrm{T_1}} \pm \sqrt{(\Delta_{12}^{\mathrm{T_1}})^2 - 4\,\det\sigma_{12}}, \tag{310}$$

15 We recall that the *symplectic eigenvalues* $\{\nu\}$ are the eigenvalues of $|i\,\Omega\,\sigma|$, with Ω defined in equation (271) and σ is the covariance matrix associated to a density matrix $\hat{\rho}$. The existence of the *symplectic eigenvalues* is ensured by the Williamson's theorem (see Section 4.2.1).

16 We changed the notation $\hat{\rho}^{\mathrm{T_A}}$ to $\hat{\rho}^{\mathrm{T_1}}$ for simplicity.

with $\Delta_{12}^{\mathrm{T}_1} = \det\sigma_1 + \det\sigma_2 - 2\det\varepsilon_{12}$.

For a two-mode state, PPT criterion reduces to whether or not $\nu_-^{\mathrm{T}_1}$ is greater than one. Indeed, if the bipartite state is separable, it follows immediately that $\nu_+^{\mathrm{T}_1} \geq 1$; if the bipartite state is entangled, one can prove that necessarily $\det\varepsilon_{12} < 0$ [171], meaning that $\Delta_{12}^{\mathrm{T}_1} > \Delta_{12}$, and thus, $\nu_+^{\mathrm{T}_1} > \nu_-$. Using the uncertainty principle (293), one obtains $\nu_+^{\mathrm{T}_1} \geq \nu_- \geq 1$. In all cases (separable or entangled), $\nu_+^{\mathrm{T}_1} \geq 1$. Therefore, condition (306) can only be violated by $\nu_-^{\mathrm{T}_1}$ and the necessary and sufficient condition PPT condition for the separability of the state reduces to

$$\nu_-^{\mathrm{T}_1} \geq 1. \tag{311}$$

In our case, it is simple to show that the symplectic eigenvalue $\nu_-^{\mathrm{T}_U}$ (where the notation T_U means that we partial transpose with respect to mode U) of the reduced covariance matrix σ_{UD1} is greater than one, meaning that a pair of quanta $U-D1$ is separable. On the contrary, the eigenvalues $\nu_-^{\mathrm{T}_{D2}}$ of the reduced covariance matrix σ_{UD2} and σ_{D1D2} are lower than one. This implies that pairs of quanta $U-D2$ or $D1-D2$ are entangled, thus leading to the same results as those obtained with the Cauchy-Schwarz inequality in Section 4.2.2.

The use of PPT criterion, and in particular of the *symplectic eigenvalues* $\{\nu_j^{\mathrm{T_A}}\}$ (or equivalently $\{\nu_j^{\mathrm{T}_1}\}$) will become clear in the next subsection, where we introduce the *logarithmic negativity* as a measure of the degree of entanglement.

4.2.4 *Degree of entanglement*

We introduced two criteria heretofore to determine the separability of a bipartite state. We would like now to measure the degree of entanglement, provided by the *negativity* $\mathcal{N}$.

LOGARITHMIC NEGATIVITY The *negativity* of a quantum state $\hat{\rho}$ is defined as [204]

$$\mathcal{N}(\hat{\rho}) \equiv \frac{\|\hat{\rho}^{\mathrm{T_A}}\|_1 - 1}{2}, \tag{312}$$

where $\|\hat{\mathcal{O}}\|_1 = \mathrm{Tr}\sqrt{\hat{\mathcal{O}}^\dagger\hat{\mathcal{O}}}$ is the trace norm, and $\hat{\rho}^{\mathrm{T_A}}$ is the partially transposed density matrix with respect to subsystem A; for instance, with respect to mode 1 for a $[1+(n-1)]$-mode Gaussian state. One can have an intuition of this measure: equation (312) quantifies the extent to which $\hat{\rho}^{\mathrm{T_A}}$ fails to be positive. Indeed, since $\|\hat{\rho}\|_1 = 1$ by definition of a density matrix, if one eigenvalue of $\hat{\rho}^{\mathrm{T_A}}$ is negative, $\|\hat{\rho}^{\mathrm{T_A}}\|_1 < 1$ and $\mathcal{N}(\hat{\rho}) < 0$; the more $\hat{\rho}^{\mathrm{T_A}}$ has negative eigenvalues the more $\mathcal{N}(\hat{\rho})$ becomes negative.

Let us now introduce the *logarithmic negativity*

$$E_{\mathcal{N}}(\hat{\rho}) \equiv \ln\|\hat{\rho}^{\mathrm{T_A}}\|_1. \tag{313}$$

Identically to condition (312),the *logarithmic negativity* also measures the extent to which $\hat{\rho}^{\mathrm{T_A}}$ fails to be positive, and equals zero if the bipartite state is separable.

Here again, the covariance matrix represents a powerful tool. For a two-mode Gaussian state, one can prove that [5, 186]

$$E_{\mathcal{N}}^{1|2}(\hat{\rho}) = \max[0, -\ln \nu_{-}^{\mathrm{T_1}}], \tag{314}$$

where $\nu_{-}^{\mathrm{T_1}}$ is the lowest symplectic eigenvalues of the partially transposed density matrix $\hat{\rho}^{\mathrm{T_1}}$ with respect to mode 1 defined in equation (310). Note that, in (314), the notation 1|2 means that we consider the state of the bipartition composed of mode 1 and mode 2.

Since the explicit expression of $\nu_{-}^{\mathrm{T_1}}$ is given in (310), we can calculate expression (314) for a two-mode Gaussian pure state. Here, we present the approach for a pure state because (i) the calculation of expression (314) for a mixed state is more tedious, (ii) our system is a pure state, (iii) the generalization from a two-mode Gaussian pure state to a $[1 + (N-1)]$-mode Gaussian pure state (in our case $N = 3$) has been studied in Ref. [6] and is given below [see equation (318), which will be useful later for the computation of the degree of tripartite entanglement, see equation (338)]. First, we use the fact that any covariance matrix can be put into its standard form (295) through local linear unitary Bogoliubov transformations[17] (LLUBO) [52].

For a pure state the standard form of the covariance matrix reduces to [3]

$$\sigma_{12}^{\mathbf{p}} = \begin{pmatrix} a & 0 & \sqrt{a^2-1} & 0 \\ 0 & a & 0 & -\sqrt{a^2-1} \\ \sqrt{a^2-1} & 0 & a & 0 \\ 0 & -\sqrt{a^2-1} & 0 & a \end{pmatrix}, \tag{316}$$

17 Consider a covariance matrix σ_{12} of the form (308); A local linear Bogoliubov transformation is such that the transformed covariance matrix reads

$$\sigma'_{12} = S\,\sigma_{12}\,S^{\mathrm{T}}, \tag{315}$$

with $S = \mathrm{diag}\,(S_1, S_2) \in \mathrm{Sp}(2,\mathbb{R}) \otimes \mathrm{Sp}(2,\mathbb{R})$, S_1 and S_2 being 2×2 symplectic matrices [52, 171]. Equation (315), together with the form of the symplectic matrix S, imply that locally $\sigma'_1 = S_1\,\sigma_1\,S_1^{\mathrm{T}}$, $\sigma'_2 = S_2\,\sigma_2\,S_2^{\mathrm{T}}$, $\varepsilon'_{12} = S_1\,\varepsilon_{12}\,S_2^{\mathrm{T}}$. Since $\det S_1 = \det S_2 = \pm 1$ (recall that S_1 and S_2 are symplectic), $\det \sigma'_1 = \det \sigma_1$, $\det \sigma'_2 = \det \sigma_2$, and $\det \varepsilon'_{12} = \det \varepsilon_{12}$. Thus, Δ_{12}, $\Delta_{12}^{\mathrm{T_1}}$, and $\det\,\sigma_{12}$ are also symplectic invariants. This property can be extended straightforwardly to any $2N \times 2N$ covariance matrix $\sigma_{1\ldots N}$ by defining $S = \mathrm{diag}\,(S_1, \ldots, S_N) \in \mathrm{Sp}(2,\mathbb{R}) \otimes \ldots \otimes \mathrm{Sp}(2,\mathbb{R})$. In this case, $\det \sigma_i$ and $\det \varepsilon_{ij}$, $\forall\, i,j \in \{1,\ldots,N\}$ are symplectic invariants – for instance, note that $\Phi(U)$ defined in equation (279) is such a LLUBO transformation applied to a N-mode Gaussian state.
In our case, the covariance matrix is already in its standard form [see the set of equations (297), (298), and (299)]. Indeed, we considered the covariance matrix associated to the full transformation (254), i.e., the transformation from the set of operators **b** to the set **e**. If we have considered instead the transformation between **b** and **c** only, the covariance matrix would not have been in its standard form. One sees from equations (278) and (279) that we used a LLUBO transformation [expression (279)] between the set of operators **c** and **e**.

where $a = \sqrt{\det \sigma_1}$ is called the *local mixedness*; the notation σ^{P} means that we consider here a pure state. Using expression (316), one computes easily $\Delta_{12}^{\mathrm{T}_1}$ defined below (310). We obtain $\Delta_{12}^{\mathrm{T}_1} = 4\,a^2 - 1$, and thus, $\nu_{\pm}^{\mathrm{T}_1} = a \pm \sqrt{a^2 - 1}$. This leads to

$$E_{\mathcal{N}}^{1|2}(\hat{\rho}) = -\mathrm{arcsinh}\,(\sqrt{a^2 - 1}). \tag{317}$$

Actually, inasmuch as $\nu_{+}^{\mathrm{T}_1} \geq \nu_{-} \geq 1$, this implies $a \geq 1$.

• if $a = 1$, $\nu_{+}^{\mathrm{T}_1} = \nu_{-}^{\mathrm{T}_1} = 1$, thus the state is separable by virtue of the PPT criterion (311).

• If $a > 1$, $\nu_{+}^{\mathrm{T}_1} > 1$, leading to $\nu_{-}^{\mathrm{T}_1} < 1$. Therefore, the PPT criterion (311) affirms that the state is entangled, and, indeed, $E_{\mathcal{N}}^{1|2}(\hat{\rho}) \neq 0$ in this case.

Expressions (314) and (317) can be generalized to $[1 + (N-1)]$-mode Gaussian pure states, i.e., to each bipartite state $i|i_1 \ldots i_N$, where $i \in \{1, \ldots N\}$ and $i_j \neq i$, $\forall\, j \in \{1, \ldots, N-1\}$. Indeed, in this case, it was proven in Ref. [6] that

$$E_{\mathcal{N}}^{i|i_1 \ldots i_N}(\hat{\rho}) = -\mathrm{arcsinh}\left(\sqrt{a_i^2 - 1}\right), \tag{318}$$

with $a_i = \sqrt{\det \sigma_i}$ the local mixedness pertaining to mode i, σ_i being defined in expression (280).

In the following, we will use the *squared logarithmic negativity*, i.e.,

$$E_{\tau}(\hat{\rho}) \equiv \ln^2 \|\hat{\rho}^{\mathrm{T}_1}\|_1\,, \tag{319}$$

where $\hat{\rho}^{\mathrm{T}_1}$ means that the density matrix $\hat{\rho}$ has been partial transposed with respect to mode 1. One finds from equation (318) that

$$E_{\tau}^{i|i_1 \ldots i_N}(\hat{\rho}) = \mathrm{arcsinh}^2\left(\sqrt{a_i^2 - 1}\right). \tag{320}$$

4.3 TRIPARTITE ENTANGLEMENT IN BECS

In this section, we use the results derived previously to study tripartite entanglement emerging in an acoustic black hole. It is worth recalling that these results apply to Gaussian states only. We can safely use them here, since we proved in Section 4.1.3, together with the results derived in Section 4.2.1, that the Bogoliubov transformation associated to the scattering process (237) led to expression (243), i.e., a three-mode Gaussian pure state.

$\hat{\rho}_b = |0\rangle_b\,{}_b\langle 0|$ *is a pure state.*

4.3.1 *Tripartite system and parametric down-conversion*

Before computing the degree of tripartite entanglement in our system, let us write the 6×6 covariance matrix σ associated to the three-mode Gaussian pure state (243). We already computed the submatrices σ_I,

$I \in \{U, D1, D2\}$ and ε_{IJ}, $I, J \in \{U, D1, D2\}$, $I \neq J$ of σ in equations (301) and (302), see Section 4.2.2.

It will be convenient to express all the quantities appearing in the covariance matrix σ in terms of the local mixedness

$$a_I = \sqrt{\det \sigma_I} \tag{321}$$

related to each mode I, $I \in \{U, D1, D2\}$. Using (301), one finds easily

$$a_I = \cosh(2r_I), \quad I \in \{U, D1, D2\}, \tag{322}$$

where the parameters r_I have been defined in equation (245). One can also write the scattering matrix normalization (246) in terms of the local mixedness:

$$a_U + a_{D1} - a_{D2} = 1 \tag{323}$$

Then, the covariance matrix reads

$$\sigma = \begin{pmatrix} \sigma_{D2} & \varepsilon_{UD2} & \varepsilon_{D1D2} \\ \varepsilon_{UD2}^{\mathrm{T}} & \sigma_U & \varepsilon_{UD1} \\ \varepsilon_{D1D2}^{\mathrm{T}} & \varepsilon_{UD1}^{\mathrm{T}} & \sigma_{D1} \end{pmatrix}, \tag{324}$$

with

$$\sigma_I = \begin{pmatrix} a_I & 0 \\ 0 & a_I \end{pmatrix}, \quad I \in \{U, D1, D2\}, \tag{325}$$

and

$$\varepsilon_{UD2} = \begin{pmatrix} \sqrt{a_U - 1}\sqrt{a_{D2} + 1} & 0 \\ 0 & -\sqrt{a_U - 1}\sqrt{a_{D2} + 1} \end{pmatrix}, \tag{326a}$$

$$\varepsilon_{D1D2} = \begin{pmatrix} \sqrt{a_{D1} - 1}\sqrt{a_{D2} + 1} & 0 \\ 0 & -\sqrt{a_{D1} - 1}\sqrt{a_{D2} + 1} \end{pmatrix}, \tag{326b}$$

$$\varepsilon_{UD1} = \begin{pmatrix} \sqrt{a_U - 1}\sqrt{a_{D1} - 1} & 0 \\ 0 & \sqrt{a_U - 1}\sqrt{a_{D1} - 1} \end{pmatrix}. \tag{326c}$$

Recall that this covariance matrix is expressed in the basis $\hat{e}_U$, $\hat{e}_{D1}$ and $\hat{e}_{D2}$ and is of standard form.

As noticed in Refs. [44, 168], it is possible to concentrate the tripartite entanglement of our system on a two mode state by applying a unitary transformation; this procedure is called *entanglement localization*. Actually, this is exactly what we already did in Section 4.1.3 by defining a new annihilation operator $\hat{e}_\theta$ in equation (256):

$$\hat{e}_\theta = \cos\theta\, \hat{e}_U + \sin\theta\, \hat{e}_{D1}, \tag{327}$$

with

$$\cos\theta = \frac{\sinh r_U}{\sinh r_{D2}} = \sqrt{\frac{a_U - 1}{a_{D2} - 1}}, \sin\theta = \frac{\sinh r_{D1}}{\sinh r_{D2}} = \sqrt{\frac{a_{D1} - 1}{a_{D2} - 1}}. \tag{328}$$

Therefore, the unitary transformation associated to this change of basis, from $\{\hat{e}_{D2}, \hat{e}_U, \hat{e}_{D1}\}$ to $\{\hat{e}_{D2}, \hat{e}_\theta, \hat{e}_{\theta+\frac{\pi}{2}}\}$, is

$$U_\theta = \begin{pmatrix} 1 & 0 & 0 & 0 & 0 & 0 \\ 0 & 1 & 0 & 0 & 0 & 0 \\ 0 & 0 & \cos\theta & 0 & \sin\theta & 0 \\ 0 & 0 & 0 & \cos\theta & 0 & \sin\theta \\ 0 & 0 & -\sin\theta & 0 & \cos\theta & 0 \\ 0 & 0 & 0 & -\sin\theta & 0 & \cos\theta \end{pmatrix}. \tag{329}$$

Then, using the fact that under any local linear Bogoliubov transformation U the covariance matrix transforms as $\sigma' = U\sigma U^{\mathrm{T}}$ [52, 171], we find here

$$\sigma_\theta = U_\theta\, \sigma\, U_\theta^{\mathrm{T}} = \begin{pmatrix} \sigma_{\mathrm{sq}} & 0 \\ 0 & \mathbb{1}_2 \end{pmatrix}, \tag{330}$$

with

$$\sigma_{\mathrm{sq}} \equiv \begin{pmatrix} \cosh(2r_{D2}) & 0 & \sinh(2r_{D2}) & 0 \\ 0 & \cosh(2r_{D2}) & 0 & -\sinh(2r_{D2}) \\ \sinh(2r_{D2}) & 0 & \cosh(2r_{D2}) & 0 \\ 0 & -\sinh(2r_{D2}) & 0 & \cosh(2r_{D2}) \end{pmatrix}, \tag{331}$$

i.e., σ_{sq} is the covariance matrix associated to a two mode squeezed state with squeezing parameter r_{D2}. This was expected: the covariance matrix σ_θ corresponds to the two mode squeezed vacuum state (258). The tripartite entanglement between the three modes U, $D1$ and $D2$ is equivalent to the one of a two mode squeezed state between $D2$ and $U - D1$, where the mode $U - D1$ [the mode "θ", see equation (327)] is in fact a linear combination of U and $D1$.

Likewise, one can draw a nice analogy with a quantum optics system: parametric down-conversion generates a two modes squeezed state (here $\hat{e}_\theta$). This mode directed to a beamsplitter generates a linear combination between the two outgoing channels (here, $\hat{e}_U$ and $\hat{e}_{D1}$), see Figure 34. Note that the pair $U - D1$ is indeed separable and each of these modes share entanglement with the remaining mode $D2$. Such a setup with parametric down-conversion was suggested for instance in Ref. [44].

The interest of the system we consider is to generate such a combination of states through the Bogoliubov transform (237): tripartite entanglement naturally emerges from quantum fluctuations around a sonic horizon.

Besides this analogy, one can compute very easily the symplectic eigenvalues associated to the covariance matrix $\sigma_\theta^{\mathrm{T_{D2}}}$ of the partially transposed state $\hat{\rho}^{\mathrm{T_{D2}}}$ from (330). Indeed, two of them are trivially 1, and the remaining ones are those of a two mode squeezed state with

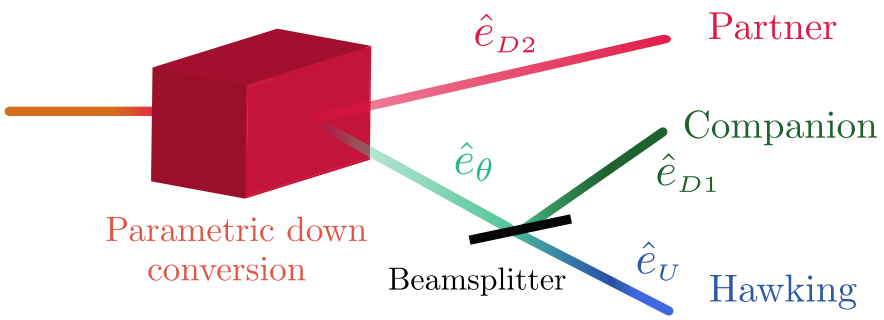

FIGURE 34: Example of a tripartite entangled system generated by parametric down-conversion and the use of a beamsplitter to create a linear combination between two separable modes. The modes $D2$ (the partner), and 'θ' form a squeezed state, see expression (258). Then the mode 'θ' splits in two modes by means of a beamsplitter, see equation (327); They correspond to the Hawking (mode U) and the companion (mode $D1$) quanta.

covariance matrix (331); they can be easily computed from (310). Therefore, we obtain[18]

$$\{\nu_j^{\mathrm{T}_{D2}}\} = \{e^{2r_{D2}}, e^{2r_{D2}}, e^{-2r_{D2}}, e^{-2r_{D2}}, 1, 1\}. \tag{332}$$

One sees in particular that the PPT criterion (306) is always violated for all $r_{D2} > 0$. We can also use expression (314) to compute the logarithmic negativity between the bipartite system formed by the mode $D2$ and the mode $U-D1$ (corresponding to a two mode squeezed state of parameter r_{D2}). This gives the squared logarithmic negativity:

$$E_\tau^{D2|UD1} = 4\, r_{D2}^2 = \mathrm{arcsinh}^2\left(\sqrt{a_{D2}^2 - 1}\right), \tag{333}$$

in agreement with expression (320).

A local unitary transformation also exists for the modes U and $D1$. In that case, the transformed covariance matrix will be of the form (330), with σ_{sq} a covariance matrix associated to a two mode squeezed state with squeezing parameter r_U or r_{D1}. Indeed, by computing the eigenvalues of the matrix $|i\,\Omega\,\sigma^{\mathrm{T}_I}|$, with $I \in \{U, D1\}$, one finds easily that

$$\begin{cases} \{\nu_j^{\mathrm{T}_U}\} = \{e^{2r_U}, e^{2r_U}, e^{-2r_U}, e^{-2r_U}, 1, 1\}, \\ \{\nu_j^{\mathrm{T}_{D1}}\} = \{e^{2r_{D1}}, e^{2r_{D1}}, e^{-2r_{D1}}, e^{-2r_{D1}}, 1, 1\}. \end{cases} \tag{334}$$

Then, the uniqueness of these eigenvalues, which correspond to those of a covariance matrix of the form $\sigma = \mathrm{diag}(\sigma_{\mathrm{sq}}, \mathbb{1}_2)$, indicates that such a local unitary transformation also exists for U and $D1$.

18 Note that these symplectic eigenvalues are also those associated to the covariance matrix $\sigma^{\mathrm{T}_{D2}}$ of the partially transposed state $\hat{\rho}^{\mathrm{T}_{D2}}$, where σ is given by (324), with submatrices (325) and (326). This property lies in the uniqueness of the symplectic eigenvalues, see Williamson's theorem, Section 4.2.1.

Therefore, similarly to (333), expression (314) leads to

$$\begin{aligned} E_\tau^{D1|UD2} &= 4\, r_{D1}^2 = \operatorname{arcsinh}^2\left(\sqrt{a_{D1}^2 - 1}\right), \\ E_\tau^{U|D1D2} &= 4\, r_U^2 = \operatorname{arcsinh}^2\left(\sqrt{a_U^2 - 1}\right), \end{aligned} \tag{335}$$

in agreement with (320). The above results will be useful in the following section to compute the degree of entanglement of the tripartite system.

More generally, note that any bisymmetric $(m+n)$-mode Gaussian state with a covariance matrix σ can be brought, by means of a local unitary operation, with respect to the $m \times n$-mode bipartition, to a tensor product of single mode uncorrelated states and of a two mode Gaussian state [168].

4.3.2 *CKW inequality*

Entanglement is usually shared between a pair of objects, forming a bipartite state; in this sense, entanglement is monogamous: it cannot be freely shared among many objects. Indeed, if a pair of particles is maximally entangled[19], then, these two particles cannot share entanglement with a third one. Consequently, several inequalities to study how entanglement is shared among multipartite states have been derived in the past and are known as *CKW inequalities* (Coffman, Kundu and Wootters) [40]. In Ref. [40], Coffman, Kundu and Wootters considered the case of pure states of three qubits. Later, these results have been extended for three-mode Gaussian states and all symmetric Gaussian states[20] with an arbitrary number of modes [4]. We are particularly interested in the latter achievement since we consider here a three-mode Gaussian state. The CKW inequality for a tripartite system reads

$$\tau_{\text{res}} \geq 0, \quad \text{with} \quad \tau_{\text{res}} = \tau^{(1|23)} - \tau^{(1|2)} - \tau^{(1|3)}, \tag{336}$$

where τ, called the *tangle*, is a proper measure of bipartite entanglement for continuous variables, e.g., the *squared logarithmic negativity* defined in Section 4.2.4; for instance, $\tau^{(1|23)}$ measures the bipartite entanglement between 1 and the composite subsystem $\{2-3\}$. In expression (336), τ_{res} is called the *residual tangle* and quantifies the tripartite entanglement between 1, 2 and 3.

The inequality (336) means that the entanglement shared between 1 and 2, tracing out 3, in addition to the entanglement shared between 1 and 3, tracing out 2, cannot exceed the total entanglement shared between 1 and the pair $\{2,3\}$. Figure 35 shows a qualitative sketch of the CKW monogamy inequality with Borromean rings. On the left-hand side of the picture rings are all entangled with each other: this exemplifies the tripartite entanglement ($\equiv \tau_{\text{res}}$). Then, one might consider the blue and green rings as one subsystem. In this case, one study how the

19 A state is maximally entangled when the degree of entanglement is maximized – this can be measured through the logarithmic negativity for example.

20 A symmetric N-mode Gaussian state is such that all local mixedness a_i, $i \in \{1,\ldots,N\}$, defined below equation (318), are all equal to each other.

red ring is entangled with the 'blue-green' ring ($\equiv \tau^{(1|23)}$). The other configurations in Figure 35 consist of tracing out one of the ring to study the entanglement between each bipartite systems (red and blue rings – $\tau^{(1|2)}$ – or red and green rings – $\tau^{(1|3)}$).

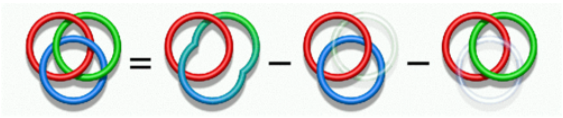

FIGURE 35: Borromean rings extracted from Ref. [58] to illustrate the tripartite entanglement. The CKW inequality states that the entanglement shared between 1 and 2 (red and blue rings), tracing out 3, in addition to the entanglement shared between 1 and 3 (red and green rings), tracing out 2, cannot exceed the total entanglement shared between 1 (red ring) and the pair $\{2,3\}$ (green and blue rings). The positive difference between these quantities corresponds to the left-hand side of the equality and is called the residual tangle; it measures the tripartite entanglement shared among all the three modes and is represented by the three entangled rings.

However, expression (336) depends on which mode (among the three) is mode 1, then mode 2 and mode 3. To encompass all possible cases, we consider instead

$$\tau_{\text{res}} \equiv \min_{i,j,k} [\tau^{(i|jk)} - \tau^{(i|j)} - \tau^{(i|k)}], \tag{337}$$

where $i,j,k \in \{1,2,3\}$. Equation (337) ensures that, if $\tau_{\text{res}} > 0$, the system does exhibit tripartite entanglement.

4.3.3 *Computation of the residual tangle*

To calculate the residual tangle τ_{res} defined in expression (336), we use as it was shown in Ref. [4] the *squared logarithmic negativity* E_τ as a measure of entanglement.

We already know from Section 4.2.4 that

$$\tau^{(1|23)} = E_\tau^{1|23}(\hat{\rho}) = \text{arcsinh}^2\left(\sqrt{a_1^2 - 1}\right), \tag{338}$$

where $\hat{\rho}$ is the density matrix associated to the three-mode Gaussian state and $a_1 \equiv \sqrt{\det \sigma_1}$ is the local mixedness related to mode 1 [see equation (320)]. We also recall that σ_1 is one of the submatrices of the matrix (280).

The computation of $E_\tau^{1|2}(\hat{\rho})$ and $E_\tau^{1|3}(\hat{\rho})$ is more difficult since the density matrices of composite subsystems $\{1-2\}$ and $\{1-3\}$ correspond to mixed states[21].

21 Indeed, while the whole system is a three-mode pure state, the restrictions to two modes (tracing out the remaining mode) are described by mixed states.

For such mixed states, it was proven in Ref. [3] that

$$\begin{aligned} Q^{(1)} &\stackrel{\text{def}}{=} E_\tau^{1|2}(\hat{\rho}) + E_\tau^{1|3}(\hat{\rho}) \\ &= \operatorname{arcsinh}^2\left[\sqrt{m^2(a_1,s,d)-1}\right] \\ &\qquad + \operatorname{arcsinh}^2\left[\sqrt{m^2(a_1,s,-d)-1}\right], \end{aligned} \tag{339}$$

with

$$s = \frac{a_2+a_3}{2}, \quad \text{and} \quad d = \frac{a_2-a_3}{2}, \tag{340}$$

$m = m_-$ ($m = m_+$) if $D \leq 0$ ($D > 0$) [4]:

$$\begin{aligned} &k_\pm = a_1^2 \pm (s+d)^2, \\ &D = 2\,(s-d) - \sqrt{2\left[k_-^2 + 2\,k_+ + |k_-|\,(k_-^2 + 8\,k_+)^{1/2}\right)]/k_+}, \\ &m_- = \frac{|k_-|}{(s-d)^2-1}, \\ &\frac{m_+}{\sqrt{2}} = \frac{\sqrt{2\,a_1^2\,(1+2\,s^2+2\,d^2) - (4\,s^2-1)\,(4\,d^2-1) - a_1^4 - \sqrt{\delta}}}{4\,(s-d)}, \\ &\delta = (a_1-2\,d-1)\,(a_1-2\,d+1)\,(a_1+2\,d-1)\,(a_1+2\,d+1) \\ &\quad \times\,(a_1-2\,s-1)\,(a_1-2\,s+1)\,(a_1+2\,s-1)\,(a_1+2\,s+1). \end{aligned} \tag{341}$$

In our case, there are some simplifications in equations (341). Indeed, using equation (323), we have immediately $\delta = 0$.

We now specify two different cases:

1. $a_1 = a_U$ (or $a_1 = a_{D1}$), $a_2 = a_{D1}$ (or $a_2 = a_U$), and $a_3 = a_{D2}$.

   We obtain

   $$\begin{aligned} m_-(a_1,s,d) &= \frac{|a_1-a_2|}{a_3-1}, \quad \text{and} \quad m_-(a_1,s,-d) = \frac{a_1+a_3}{1+a_2} \\ m_+(a_1,s,d) &= \sqrt{\frac{a_1\,a_2}{a_3}}, \quad \text{and} \quad m_+(a_1,s,-d) = \sqrt{\frac{a_1\,a_3}{a_2}}, \end{aligned} \tag{342}$$

   and $D \geq 0$, $\forall\,\{a_1,a_2\}$, with of course $a_{1,2} \geq 1$ [with D defined in (341)]. Therefore, we shall choose $m = m_+$ in equation (339).

   Besides, we also know that state $1|2 = U|D1$ is separable (or we can just check easily that $d < -(a_1^2-1)/(4s)$ [4]). Thus, $E_\tau^{1|2} = 0$ and we have at the end

   $$Q^{(1)} = E_\tau^{1|3} = \operatorname{arcsinh}^2\left(\sqrt{\frac{a_1\,a_3-a_2}{a_2}}\right) \tag{343}$$

2. $a_1 = a_{D2}$, $a_2 = a_U$ (or $a_2 = a_{D1}$), and $a_3 = a_{D1}$ (or $a_3 = a_U$).

   In this case,

   $$s = \frac{a_U + a_{D1}}{2} = \frac{a_{D2}+1}{2} = s^{\min}, \tag{344}$$

which is the minimum value of s and this is expected: s reaches its minimal value when the reduced bipartition $2|3 = U|D1$ is separable [4]; and we know from the Cauchy-Schwartz inequality that U and $D1$ are not entangled.

The parameter D is always negative and we obtain [4]

$$m_-(a_1, s^{\min}, \pm d) = \frac{1 + 3\,a_1 \pm 2\,d}{3 + a_1 \mp 2\,d}, \tag{345}$$

which leads to the corresponding $Q^{(1)}$ computed from (339):

$$\begin{aligned} Q^{(1)} &= E_\tau^{1|2} + E_\tau^{1|3} \\ &= \operatorname{arcsinh}^2\left(\frac{2}{1+a_2}\sqrt{(a_2+a_3)\,(a_3-1)}\right) \\ &\quad + \operatorname{arcsinh}^2\left(\frac{2}{1+a_3}\sqrt{(a_2+a_3)\,(a_2-1)}\right). \end{aligned} \tag{346}$$

At the end we obtain for the tripartite entanglement:

$$\tau_{res} = \min_{(1)=U,D1,D2}[\operatorname{arcsinh}^2\left(\sqrt{a_{(1)}^2 - 1}\right) - Q^{(1)}], \tag{347}$$

where $Q^{(1)}$ is computed from equation (343) or equation (346) depending on the chosen case. Actually, it was proven by Adesso *et al.* that the minimum in equation (347) is reached for the lowest local mixedness [4]. Figure 36 shows the curves associated to the three local mixedness a_U, a_{D1} and a_{D2} as functions of the frequency[22] ω. The results are obtained for a waterfall configuration with upstream Mach number $m_u = 0.59$ (see Section 3.1.3 for the definition of this specific configuration). We can identify two regimes: below a frequency denoted as ω_{thr} (=0.56 for $m_u = 0.59$) the lowest local mixedness is a_{D1}; above this frequency threshold[23], the minimum value becomes a_U. We also note that all local mixedness tend to 1 when $\omega \to \Omega$, where Ω corresponds to the vanishing of the $D2$ mode, see Figure 20 for the definition of Ω; this means in particular that the population in the different modes vanish:

$$\langle \hat{c}_U^\dagger(\Omega)\,\hat{c}_U(\Omega)\rangle = \langle \hat{c}_{D1}^\dagger(\Omega)\,\hat{c}_{D1}(\Omega)\rangle = \langle \hat{c}_{D2}^\dagger(\Omega)\,\hat{c}_{D2}(\Omega)\rangle = 0, \tag{348}$$

since $a_I = 1 + \sinh^2(r_I) = 1 + \langle \hat{c}_I^\dagger\,\hat{c}_I\rangle$, $I \in \{U, D1, D2\}$.

We decided to compute the residual tangle (347) in the three cases $(1) = U, D1, D2$ to check *a posteriori* that the minimum tangle was indeed reached for the lowest local mixedness. We denote by $\tau_{res}^{(I)}$ the residual tangle such that $(1) = I$ in equation (347), $I \in \{U, D1, D2\}$. The result is shown in Figure 37 for the same configuration ($m_u = 0.59$). One sees that the system exhibits tripartite entanglement, which diverges when the energy tends to zero. Then, the residual tangle decreases rapidly to zero and completely vanishes at the upper bound frequency Ω.

As shown in Figure 38, one has indeed $\tau_{res}^{(U)} < \tau_{res}^{(D1)}$ for $\omega > \omega_{\text{thr}}$, i.e., when $a_U < a_{D1}$; the difference between both tangles is very tiny though.

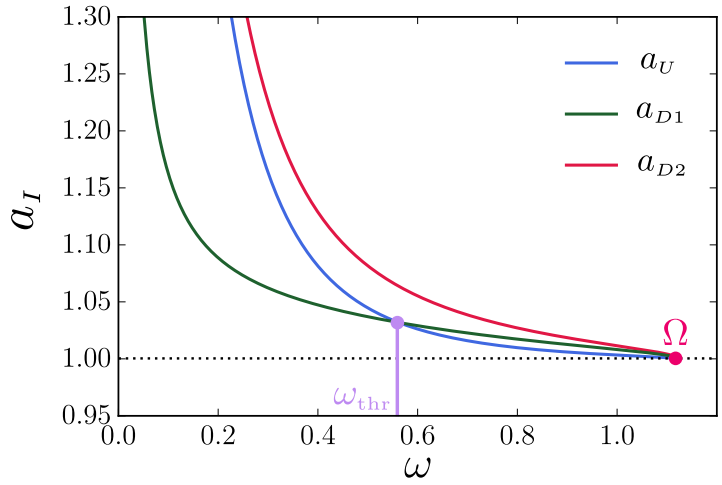

FIGURE 36: Local mixedness defined in equation (322) for each mode U, $D1$ and $D2$ as functions of the parameters r_I. These parameters depend on the frequency ω and their explicit expressions are given in terms of the scattering matrix coefficients in equations (245). The scattering matrix coefficients are computed for a waterfall configuration with upstream Mach number $m_u = 0.59$, see Section 3.1.3 for the definition of this specific configuration. The frequency $\omega_{\rm thr}$ indicates the turning point above which a_U becomes lower than a_{D1}. The upper bound frequency Ω corresponds to the vanishing of the $D2$ mode, see Figure 20.

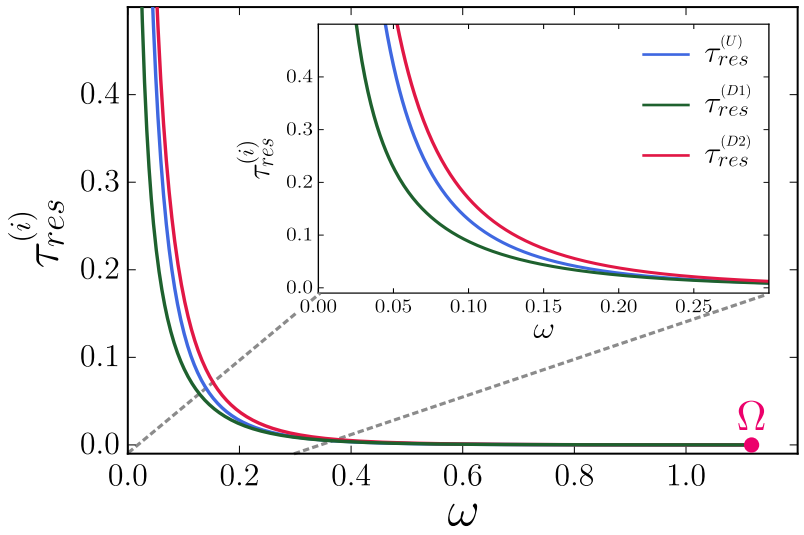

FIGURE 37: Residual tangle calculated from equations (338), (343) and (346), where the subscript "1" is replaced by either U, $D1$ – case 1, equation (343) – or $D2$ – case 2, equation (346). We denote by $\tau_{res}^{(I)}$, $I \in \{U, D1, D2\}$ the corresponding tangle. The inset of the figure corresponds to a zoom over the low energy sector. The upper bound frequency Ω corresponds to the vanishing of the $D2$ mode, see Figure 20. We recall that this result is obtained for a waterfall configuration with upstream Mach number $m_u = 0.59$, see Section 3.1.3 for the definition of this specific configuration.

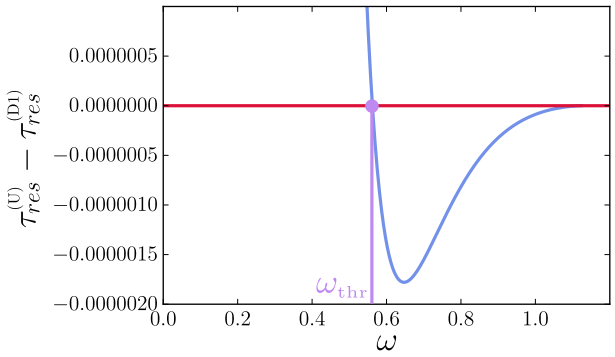

FIGURE 38: Difference between the residual tangles $\tau_{res}^{(U)}$ and $\tau_{res}^{(D1)}$, computed from equations (338) and (343). The frequency ω_{thr} indicates the turning point above which a_U becomes lower than a_{D1}, see Figure 36.

In conclusion, the presence of negative energy modes renders the acoustic black hole energetically unstable [71]; this leads to creation of entangled quanta of positive and negative energies emerging at the acoustic horizon from quantum vacuum fluctuation and propagating in the subsonic and the supersonic regions.

Said differently, the total absence of *ingoing* modes in the system does not mean that no *outgoing* modes are emitted from the scattering process occurring at the acoustic horizon. In that sense, one can perceive the analogue Hawking radiation (and also the Hawking radiation in the gravitational case) as an amplification process [158]: the mode conversion of *ingoing* modes into negative energy *outgoing* modes must result in an increase of positive energy *outgoing* modes.

This also means that the *in*-vacuum associated to the *ingoing* modes is different from the *out*-vacuum associated to the *outgoing* modes. In the gravitational case, the *in*-vacuum is seen as a thermal state for an observer outside a black hole [25, 87, 88]. Therefore, this observer will perceive a thermal radiation emitted from the event horizon of the black hole, the so-called Hawking radiation, see Chapter 2.

In this chapter, we proved that the same process occurs in sonic black hole, the mode conversion at the acoustic horizon and the 'mixing' of positive and negative energy modes corresponds to a Bogoliubov transformation. In particular, the *in*-vacuum in our analogue system can be seen as an effective two mode squeezed vacuum state between a negative energy mode – $D2$ – and a linear combination of positive energy modes – U and $D1$. We showed that an observer in the subsonic region will then perceive a 'thermal' radiation, whose effective temperature depends on the energy of the mode. From this point of view, the analogue Hawking spectrum is thermal, but it is not Planckian since the temperature depends on the energy.

22 Recall that the local mixedness defined in equations (322) depend on the parameters r_I, $I \in \{U, D1, D2\}$, which depend themselves on the energy $\hbar\omega$, see equations (245).

23 We have noticed that this threshold decreases when m_u decreases.

Besides this question of thermality, we also proved that the tripartite system formed by the *outgoing* quanta gives rise to tripartite entanglement. We were able to quantify the degree of entanglement in our system in the last section of this chapter. Interestingly, the result only depends on the local mixedness a_I defined in equation (322), which are linked to the occupation number $\langle \hat{c}_I^\dagger \hat{c}_I \rangle$ in each mode. Since these quantities can be accessible through the density-density correlation function and the static structure factor [176, 177], it might be possible in the future to observe and measure experimentally the tripartite entanglement in BECs analogue systems.

Part II

PROPAGATION OF DISPERSIVE SHOCK WAVES IN NONLINEAR MEDIA

5

FLUIDS OF LIGHT

The propagation of light in a nonlinear material is amenable to a hydrodynamic treatment [8–11, 179]. This approach amounts to consider the propagating optical beam as a fluid of light. In fact, nonlinear effects induced by light in the medium lead to an effective photon-photon interaction, similarly to atomic Bose gases where nonlinearity arises from contact interactions between bosons. This rich analogy suggests that many hydrodynamic phenomena studied in the context of Bose-Einstein condensation can be also explored in nonlinear optics. In particular, the study of fluids of light resulted in a burst of interest for probing many-body physics quantum phenomena, such as superfluidity or sound-like excitations of light [34, 39, 66, 111, 128, 162, 187, 188].

In addition, we mention that this analogy to hydrodynamics can be also used to explore analogue gravity, such as optical event horizons [57], ergo regions [189], stimulated Hawking radiation [50]; as already discussed in the first part of this thesis, this confirms the universality of Hawking radiation as soon as an horizon is present.

Another phenomenon of interest for us (which will be studied in detail in the next chapters) is the formation of dispersive shock waves in nonlinear media. Many studies have been carried out in nonlinear optics to observe and describe the propagation of such waves [22, 43, 64, 191, 200, 201]. In this thesis, we will analyze more specifically the nonlinear spreading of a region of increased light intensity in the presence of a uniform constant background, leading eventually to the formation of a dispersive shock wave.

In the absence of background and for a smooth initial intensity pattern, the spreading is mainly driven by the nonlinear defocusing and can be treated analytically in some simple cases [179].

The situation is more interesting in the presence of a constant background: The pulse splits in two parts, each eventually experiencing nonlinear wave breaking, leading to the formation of a dispersive shock wave which cannot be described within the framework of perturbation theory, even if the region of increased intensity corresponds to a perturbation of the flat pedestal. This scenario indeed fits with the hydrodynamic approach of nonlinear light propagation and is nicely confirmed by the experimental observations of Refs. [191, 200].

In this chapter, we show that a propagating optical beam can be seen as a fluid of light. We also introduce the notion of characteristics and Riemann invariants, before applying them in simple cases. Then, in the next chapter, we use and generalize these important mathematical tools to describe the dispersionless evolution of nonlinear pulses, such as the short-time evolution of the fluid of light in the presence of a uniform

background light intensity. Indeed, during this first stage of spreading, the pulse can be described within a nondispersive approximation by means of Riemann's approach.

Eventually, at later times, nonlinear effects induce wave steepening, which results in a gradient catastrophe and wave breaking. After the wave breaking time, dispersive effects can no longer be omitted and a shock is formed; in this case we resort to Whitham modulation theory [197] to describe the time evolution of the pulse. The theoretical study of the propagation of the dispersive shock wave is addressed in the last chapter. The difficulty, here, lies in the fact that two Riemann invariants vary concomitantly. In addition, an interesting outcome of our theoretical treatment is an asymptotic determination of experimentally relevant parameters of the dispersive shock, such as a simple estimate of the contrast of the fringes of the dispersive shock waves.

5.1 NONLINEAR SCHRÖDINGER EQUATION AND HYDRODYNAMIC APPROACH

Let us consider the propagation of a monochromatic optical beam in a nonlinear dielectric medium, such as a hot Rubidium atomic vapor [66]. The propagation of the beam induces local electric dipole moments, leading to a polarization of the dielectric material. The electric displacement field is defined as

$$\mathbf{D}(\mathbf{r},t) = \varepsilon_0\,\mathbf{E}(\mathbf{r},t) + \mathbf{P}(\mathbf{r},t), \tag{349}$$

where ε_0 is the vacuum permittivity, and $\mathbf{P}(\mathbf{r},t)$ is the density of induced electric dipole moments in the material, called the *polarization density*. Here, we consider a nonlinear medium in which $\mathbf{P}$ depends nonlinearly on $\mathbf{E}$:

$$\mathbf{P}(\mathbf{r},t) = \mathbf{P}^{\mathrm{L}}(\mathbf{r},t) + \mathbf{P}^{\mathrm{NL}}(\mathbf{r},t), \tag{350}$$

where $\mathbf{P}^{\mathrm{L}}$ is the linear polarization and $\mathbf{P}^{\mathrm{NL}}$ is the nonlinear polarization. Their components are[1]

$$\left.\begin{aligned}\mathbf{P}^{\mathrm{L}}_{\mu}(\mathbf{r},t) &= \varepsilon_0\,[\underset{\sim}{\chi}^{(1)}]_{\mu\nu}\,\mathbf{E}_{\nu}\\ \mathbf{P}^{\mathrm{NL}}_{\mu}(\mathbf{r},t) &= \varepsilon_0\,[\underset{\sim}{\chi}^{(3)}]_{\mu\nu\alpha\beta}\,\mathbf{E}_{\nu}\,\mathbf{E}_{\alpha}\,\mathbf{E}_{\beta}\end{aligned}\right\}, \quad \text{with} \quad \mu \in \{x,y,z\}, \tag{351}$$

where $\underset{\sim}{\chi}^{(1)}$ is the linear susceptibility and the fourth rank tensor $\underset{\sim}{\chi}^{(3)}$ is the third-order susceptibility. We discarded the second-order $\underset{\sim}{\chi}^{(2)}$ contribution to the nonlinear polarization because we consider an inversion invariant medium in which the response is not affected when $\mathbf{E} \to -\mathbf{E}$.

In a non magnetic dielectric material Maxwell equations read [108]

$$\boldsymbol{\nabla}\times\mathbf{E} = -\partial_t\mathbf{B},\ \boldsymbol{\nabla}\times\mathbf{B} = \frac{1}{\varepsilon_0\,c^2}\partial_t\,\mathbf{D},\ \boldsymbol{\nabla}\cdot\mathbf{D} = 0,\ \boldsymbol{\nabla}\cdot\mathbf{B} = 0, \tag{352}$$

1 Note that we use Einstein notations in equation (351), i.e., $[\underset{\sim}{\chi}^{(1)}]_{\mu\nu}\,\mathbf{E}_{\nu} = [\underset{\sim}{\chi}^{(1)}]_{\mu x}\mathbf{E}_x + [\underset{\sim}{\chi}^{(1)}]_{\mu y}\mathbf{E}_y + [\underset{\sim}{\chi}^{(1)}]_{\mu z}\mathbf{E}_z$.

leading to

$$\Delta\mathbf{E} - \boldsymbol{\nabla}\left(\boldsymbol{\nabla}\cdot\mathbf{E}\right) = \frac{1}{c^2}\,\partial_t^2\mathbf{E} + \frac{1}{\varepsilon_0\,c^2}\,\partial_t^2\mathbf{P}. \tag{353}$$

Assuming that $\boldsymbol{\nabla}\cdot\mathbf{E} = 0$ (this will be justified *a posteriori*), one obtains

$$\Delta\mathbf{E} = \frac{1}{c^2}\,\partial_t^2\mathbf{E} + \frac{1}{\varepsilon_0\,c^2}\,\partial_t^2\mathbf{P}. \tag{354}$$

We consider now a linearly polarized beam, of the form

$$\mathbf{E}(\mathbf{r},t) = \frac{1}{2}\left(E(\mathbf{r})\,e^{-i\omega_0 t} + \text{c.c.}\right)\vec{x}, \tag{355}$$

where $E(\mathbf{r})$ is a complex function, which does not depend on time. This will be denoted as a stationary beam. In this case, one has in particular

$$\mathbf{P}(\mathbf{r},t) = \varepsilon_0\left[\chi^{(1)} + \frac{3}{4}\,\chi^{(3)}\,|E(\mathbf{r})|^2\right]\mathbf{E}(\mathbf{r},t), \tag{356}$$

where it is customary to simply write $\chi^{(1)} \equiv [\underset{\sim}{\chi}^{(1)}]_{xx}$, $\chi^{(3)} \equiv [\underset{\sim}{\chi}^{(3)}]_{xxxx}$ in an isotropic medium, and where terms $\propto \exp(-3i\omega_0 t)$, corresponding to third harmonic generation, have been discarded.

Therefore, using equation (354), we obtain

$$\Delta\mathbf{E} - \frac{1}{c^2}\left[1 + \chi^{(1)} + \frac{3}{4}\,\chi^{(3)}\,|E(\mathbf{r})|^2\right]\partial_t^2\mathbf{E} = 0 \tag{357}$$

In the following, one considers a slowly modulated plane wave in the paraxial approximation

$$E(\mathbf{r}) = A(\vec{r}_\perp, z)\,e^{i\beta_0 z}, \quad \text{where} \quad |\partial_z A| \le \beta_0\,|A|. \tag{358}$$

Inserting the previous expression in equation (357) yields[2]

$$i\partial_z A = -\frac{1}{2\,\beta_0}\boldsymbol{\nabla}_\perp^2 A - k_0\,n_2\,|A|^2\,A, \tag{360}$$

where $\boldsymbol{\nabla}_\perp$ is the transverse Laplacian, and

$$k_0 = \frac{\omega_0}{c}, \quad \beta_0 = n_0\,k_0, \quad n_2 = \frac{3}{8\,n_0}\chi^{(3)}, \quad n_0 = (1+\chi^{(1)})^{1/2}. \tag{361}$$

We also define the optical beam intensity $I \equiv |A|^2$ and the nonlinear refractive index $\Delta n \equiv n_2\,I = n_2\,|A|^2$.

2 First, note that in the paraxial approximation one neglects $\partial_{zz}A$, leading to a first-order differential equation with respect to z:

$$2\,i\,\beta_0\,\partial_z A + \boldsymbol{\nabla}_\perp^2 A = -\frac{\omega_0^2}{c^2}\left(1 + \chi^{(1)} - \frac{c^2}{\omega_0^2}\beta_0^2 + \frac{3}{4}\,\chi^{(3)}\,|A|^2\right)A. \tag{359}$$

Second, by discarding nonlinear effects for a perfect plane wave, i.e., constant A, one finds $\beta_0 = n_0\,k_0$, where $n_0 = (1+\chi^{(1)})^{1/2}$ is the linear index refraction.

We can already notice the similarity between equation (360) and the nonlinear Schrödinger equation. The nonlinear term, which contained the nonlinear refractive index, is interpreted as an effective photon-photon interaction induced by the Kerr nonlinearity, i.e., the nonlinear polarization of the dielectric material where the optical beam propagates.

If $\chi^{(3)} > 0$, the process is said *self-focusing*[3] and corresponds to an effective attractive interaction between photons. On the contrary, if $\chi^{(3)} < 0$, the process is said *self-defocusing* and leads to an effective repulsive interaction between photons [31, 66, 162].

Let us now justify that $\boldsymbol{\nabla} \cdot \mathbf{E}$ can be indeed neglected in equation (353). One finds easily that

$$\boldsymbol{\nabla} \cdot \mathbf{E} = -\frac{2\, n_0\, n_2}{1 + \chi^{(1)} + 2 n_0 n_2 |E(\mathbf{r})|^2}\, E(\mathbf{r})\, \partial_x |E(\mathbf{r})|^2. \tag{362}$$

The previous expression is non zero only through the transverse derivative of the slowly varying envelope A. It is additionally small because the nonlinear contribution is small[4] ($n_2 |E|^2 \leq 1$): thus, it can be safely neglected.

In the following, we consider the case of a *defocusing* nonlinearity ($n_2 < 0$, $\chi^{(3)} < 0$); that is, as shown in the paragraph below, one finds an equation analogous to the Gross-Pitaevskii equation, where the nonlinearity is mediated by repulsive interactions between bosons. Therefore, as mentioned in the introduction of this chapter, one understands the strong analogy with weakly interacting Bose gases; within an hydrodynamic approach [9, 10, 179], the propagation of the optical beam in the nonlinear material can be seen as a fluid of light where fundamental phenomena, such as superfluidity [128], can be explored.

NONLINEAR SCHRÖDINGER EQUATION We define dimensionless units by choosing a reference intensity I_{ref} and introducing the nonlinear length[5] $z_{\text{NL}} = (k_0 |n_2| I_{\text{ref}})^{-1}$ and the transverse healing length $\xi_\perp = (z_{\text{NL}}/n_0 k_0)^{1/2}$. We consider a geometry where the transverse profile is translationally invariant and depends on a single Cartesian coordinate (see Figure 39). One thus writes $\vec{\nabla}_\perp^2 = \xi_\perp^{-2} \partial_x^2$ where x is the dimensionless transverse coordinate and we define an effective "time" $t = z/z_{\text{NL}}$. The quantity $\psi(x,t) = A/\sqrt{I_{\text{ref}}}$ is then a solution of the dimensionless nonlinear Schrödinger equation equation

$$i\, \partial_t \psi = -\tfrac{1}{2} \partial_{xx} \psi + |\psi|^2 \psi\ , \tag{363}$$

which can be compared with equation (105) of Chapter 3 (removing the external potential $U(x)$ and the chemical potential μ). Therefore,

3 The Kerr nonlinearity induces a change in refractive index n of the material: $n = n_0 + \Delta n$, with $\Delta n = n_2\, I$. When $n_2 > 0$, i.e., $\chi^{(3)} > 0$, the refractive index becomes larger in the areas where the intensity is higher, usually at the center of a beam, creating a focusing density profile.

4 In typical experiments, one has indeed $|A|^2 \simeq 10^5$ W.m^{-2} and $n_2 \simeq 10^{-10}$ W.m^{-2}.

5 The nonlinear length is the typical length above which nonlinear effects become predominant.

the propagation of an optical beam in a nonlinear dielectric material is entirely described by equation (363), where the longitudinal direction z plays the role of an effective time t.

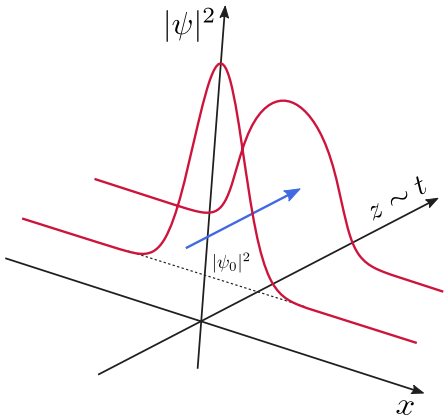

FIGURE 39: Evolution of an optical beam propagating in a nonlinear dielectric material. It propagates along the z axis, as indicated by the blue arrow. The propagation direction plays the role of an effective "time" $t = z/z_{\text{NL}}$, where we introduced the nonlinear length $z_{\text{NL}} = (k_0|n_2|I_{\text{ref}})^{-1}$. In the last expression, n_2 is proportional to the third-order Kerr nonlinearity $\chi^{(3)}$ [see equations (361)], and I_{ref} is a reference intensity [see the text above equation (363)]. The vertical axis corresponds to the quantity $|\psi|^2 = I/I_{\text{ref}}$, where I is the intensity of the beam. The parameter $|\psi_0|^2$ corresponds to the background intensity. As mentioned in the introduction of this chapter, this leads eventually to the formation of a dispersive shock wave, which will be studied in Chapter 7. The transverse profile is translationally invariant and depends on a single Cartesian coordinate x.

HYDRODYNAMIC APPROACH Our objectives in this thesis lies in the theoretical description of the propagation of such a fluid of light. The derivation of hydrodynamic equations which govern its evolution will enable us to efficiently use powerful tools, such as the Riemann invariants, the Riemann method, or the Whitham modulational theory, to completely characterize its short and long-time propagation. As we have already proceeded in Chapter 3, let us use a Madelung transformation such that[6]

$$\psi(x,t) = \sqrt{\rho(x,t)}\, e^{i\,S(x,t)}, \tag{364}$$

where the phase $S(x,t)$ is connected to the fluid velocity $u(x,t)$ through the relation

$$u(x,t) \equiv \partial_x S. \tag{365}$$

6 We consider here the case of a one-dimensional fluid flow, but the results of this paragraph can be generalized straightforwardly to two dimensions.

In full analogy with the set of equations (121) obtained in Chapter 3, one obtains from the nonlinear Schrödinger equation (363) the system

$$\begin{cases} \partial_t \rho + \partial_x(\rho\, u) = 0, \\ \partial_t u + u\, \partial_x u + \dfrac{1}{\rho}\, \partial_x P + \dfrac{1}{2}\, \partial_x \Pi = 0, \end{cases} \tag{366}$$

with

$$P = \frac{\rho^2}{2}, \quad \text{and} \quad \Pi = -\frac{1}{\sqrt{\rho}}\, \partial_{xx} \sqrt{\rho}. \tag{367}$$

In expression (367), P is an effective pressure due to nonlinear effects, and Π is associated to a *quantum pressure* term (also called *quantum potential*) due to dispersive effects in the system. The first equation of the system (366) is the continuity equation, while the second one is the Euler equation. In the dispersionless approach, when density gradients of the initial density $\rho(x, t = 0)$ are weak, one can neglect the quantum pressure. In this case, the set of hydrodynamic equations becomes

$$\begin{cases} \partial_t \rho + \partial_x(\rho\, u) = 0, \\ \partial_t u + u\, \partial_x u + \partial_x \rho = 0. \end{cases} \tag{368}$$

5.2 CHARACTERISTICS AND RIEMANN INVARIANTS

In this section we introduce the concept of *characteristics* and *Riemann invariants*. There are indeed powerful tools to solve partial differential equations (PDE) and we will use them throughout this and the subsequent chapters.

Characteristics are curves on which certain quantities, the Riemann invariants are conserved. We first introduce them with a simple example, the Hopf equation, before considering the case of a polytropic gas flow, characterized by a density ρ, a pressure $P(\rho) = \rho^\gamma/\gamma$ and a sound velocity $c(\rho) = \rho^{(\gamma-1)/2}$, up to normalization constants; for adiabatic flow of an ideal gas, the adiabatic index γ is equal to the ratio $\gamma = C_\mathrm{P}/C_\mathrm{V}$ of the specific heat capacities at constant pressure (C_P) and at constant volume (C_V).

A fluid of light, as considered in the previous section, whose evolution is governed by the nonlinear Schrödinger equation (363) (or equivalently a Bose gas described by the Gross-Pitaevskii equation) corresponds to $\gamma = 2$ [$P(\rho) = \rho^2/2$, see equation (367)].

5.2.1 *Hopf equation*

Consider a function $u(x, t)$ solution of the Hopf equation

$$\partial_t u + u\, \partial_x u = 0. \tag{369}$$

In the plane (t, x) there exists a vector field

$$\mathbf{a} \equiv (1, u), \tag{370}$$

such that equation (369) can be rewritten

$$(\mathbf{a}\,\boldsymbol{\nabla})\,u = 0, \tag{371}$$

where $\boldsymbol{\nabla} = (\partial_t, \partial_x)$. The previous expression implies that u is constant along integral curves Γ generated by the vector field $\mathbf{a}$. If the point $(t = 0, x = x_0)$ in the plane (t, x) corresponds to an initial value $u = u_0$, then equation (371) implies that $u(x, t)$ is constant along the curve Γ_0 generated by $\mathbf{a}_0 \equiv (1, u_0)$.

Let us introduce a parameter s along Γ_0, such that

$$\boldsymbol{\ell} = (t(s), x(s)), \quad \text{and} \quad \mathbf{a}_0 = \frac{d\boldsymbol{\ell}}{ds}. \tag{372}$$

The notations are summarized in Figure 40.

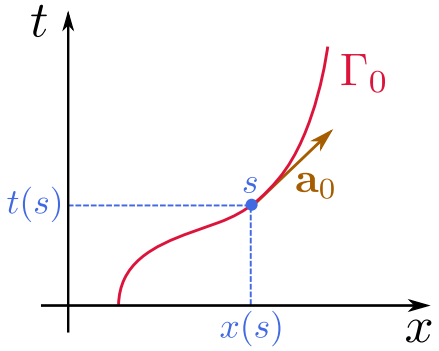

FIGURE 40: Sketch of the curve Γ_0 in the plane (t, x). This curve is defined parametrically by $(t = t(s), x = x(s))$, with s a parameter moving along Γ_0. The brown arrow corresponds to the tangent vector to the point of coordinates $(t(s), x(s))$; this vector is denoted $\mathbf{a}_0$.

This yields the following equations

$$\frac{\mathrm{d}t}{\mathrm{d}s} = 1, \quad \text{and} \quad \frac{\mathrm{d}x}{\mathrm{d}s} = u_0, \tag{373}$$

leading to

$$t = s, \quad \text{and} \quad x = u_0\, s + x_0. \tag{374}$$

Therefore, given an initial point $(t = 0, x = x_0, u = u_0)$ in the three dimensional Cartesian coordinate system (t, x, u), the value u_0 corresponding to the initial coordinate x_0 is carried after time t to the point x given by equation (374). In this case, the curves Γ are straight lines, called *characteristics*, and generate a surface from the initial curve $(0, x, u(x, t = 0))$.

In addition, in the exceptional case where the initial conditions would be defined on a characteristic curve Γ, one would not be able to use a Taylor series expansion to calculate $u(x, t)$ in the vicinity of Γ, i.e., the Cauchy Problem for equation (369) cannot be solved. Indeed, we cannot calculate from equation (369) the derivatives of $u(x, t)$ along any direction intersecting the characteristic curve Γ, precisely because expression (371) shows that information only propagates along this curve. We will use this important remark in the following to derive the *Riemann invariants*.

5.2.2 *Polytropic gas flow*

We have introduced the main idea of the *method of characteristics* in the previous subsection: given the initial data, one finds a set of curves, the *characteristics*, along which a quantity is conserved. In the case of Hopf equation, the conserved quantity is directly given by $u(x,t)$ and the characteristics are straight lines [see equation (374)].

Let us now generalize this method to the case of polytropic gas flow described by a density $\rho(x,t)$ and a velocity $u(x,t)$, solutions of the set of equations[7]

$$\begin{cases} \partial_t \rho + \rho\, \partial_x u + u\, \partial_x \rho = 0, \\ \partial_t u + u\, \partial_x u + \dfrac{c^2}{\rho}\, \partial_x \rho = 0, \end{cases} \tag{375}$$

with $c^2 = \rho^{\gamma-1}$.

As mentioned in Section 5.2.1, if the initial data are given on a characteristic curve, one is not able to solve the Cauchy problem associated to the system (375). We will use this remark to find the characteristics.

Indeed, let us consider in the plane (t,x) such a characteristic curve, denoted Γ and defined parametrically by $(t = f(s), x = g(s))$, with s a parameter along the curve. We introduce an angle ϕ such that the components of the vector tangent to Γ read

$$\frac{\mathrm{d}x}{\mathrm{d}s} = \cos\phi, \quad \text{and} \quad \frac{\mathrm{d}t}{\mathrm{d}s} = \sin\phi, \tag{376}$$

Assuming that the initial data for $\rho(x,t)$ and $u(x,t)$ are given on the curve Γ, one can calculate their derivatives along Γ:

$$\begin{cases} \dfrac{\mathrm{d}\rho}{\mathrm{d}s} = \partial_x \rho\, \cos\phi + \partial_t \rho\, \sin\phi, \\ \dfrac{\mathrm{d}u}{\mathrm{d}s} = \partial_x u\, \cos\phi + \partial_t u\, \sin\phi. \end{cases} \tag{377}$$

The set of equations (375), together with equations (377), is a system of four equations of four unknown functions $\partial_t\rho$, $\partial_x\rho$, $\partial_t u$, $\partial_x u$. Since Γ is a characteristic curve, this system does not have a solution[8] and, thus, its determinant Δ_Γ equals 0:

$$\Delta_\Gamma = \begin{vmatrix} 1 & u & 0 & \rho \\ 0 & \frac{c^2}{\rho} & 1 & u \\ \sin\phi & \cos\phi & 0 & 0 \\ 0 & 0 & \sin\phi & \cos\phi \end{vmatrix} = 0 \tag{378}$$

$$\Leftrightarrow\ \Delta_\Gamma = (\cos\phi - u\, \sin\phi)^2 - c^2\, \sin^2\phi = 0.$$

7 We will follow the method presented by A. Kamchatnov in his book [100].

8 Otherwise the derivatives of ρ and u would be known along directions intersecting the characteristic curve Γ and the Cauchy problem would be solved.

The previous equation has two solutions

$$\cot \phi_{\pm} = u \pm c. \tag{379}$$

Therefore, there exists two characteristic curves $\Gamma^{\pm}$ defined parametrically by $(t = f(s^{\pm}), x = g(s^{\pm}))$, whose tangent vectors are $\mathbf{a}_{\Gamma^{\pm}} = (\sin \phi_{\pm}, \cos \phi_{\pm})$.

In addition, it is worth noticing that solutions of equation (378) are real here: the system is called *hyperbolic*. When the solutions are complex, the system is called *elliptic*; for instance, such a configuration can be encountered in mean-field game theory [29, 30].

Now, we will find the conserved quantities along $\Gamma^{\pm}$, namely the Riemann invariants, denoted $\lambda^{\pm}$. Multiplying the first equation of the system (375) by $(\cos \phi_{\pm} - u \sin \phi_{\pm})$ and the second equation by $-c^2/\rho \sin \phi_{\pm}$, then using equations (377) and (378), yields

$$\frac{\mathrm{d}u}{\mathrm{d}s^{\pm}} \pm \frac{c}{\rho} \frac{\mathrm{d}\rho}{\mathrm{d}s^{\pm}} = 0. \tag{380}$$

We define two functions $\lambda^{\pm}(\rho, u)$ such that

$$\frac{\partial \lambda^{\pm}}{\partial u} = \frac{1}{2}, \quad \text{and} \quad \frac{\partial \lambda^{\pm}}{\partial \rho} = \pm \frac{c}{2\,\rho}. \tag{381}$$

In this case, equations (380) and (381) lead to

$$\frac{\mathrm{d}\lambda^{\pm}}{\mathrm{d}s^{\pm}} = 0, \tag{382}$$

meaning that λ^{+} (λ^{-}) is a conserved quantity along Γ^{+} (Γ^{-}). Solving equations (381) gives

$$\lambda^{\pm}(\rho, u) = \frac{u}{2} \pm \frac{1}{2} \int^{\rho} \frac{c(\rho')}{\rho'}\, d\rho'. \tag{383}$$

For a polytropic gas flow, where $c^2(\rho) = \rho^{\gamma - 1}$, we obtain the explicit expressions

$$\lambda^{\pm}(\rho, u) = \frac{u}{2} \pm \frac{c(\rho)}{\gamma - 1}. \tag{384}$$

In particular, when $\gamma = 2$ [which corresponds to the hydrodynamic equations (368)], $\lambda^{\pm} = \frac{u}{2} \pm \sqrt{\rho}$.

We end this section with a last comment: the determination of the Riemann invariant makes it possible to put the system in an effectively diagonal form. Indeed, one may also consider $\lambda^{\pm}$ as functions of t and x. Equation (382) would give in this case

$$\partial_t \lambda^{\pm} + v_{\pm}\, \partial_x \lambda^{\pm} = 0, \quad \text{where} \quad v_{\pm} \equiv \cot \phi_{\pm}. \tag{385}$$

Therefore, one sees that solving the initial system of equations (375) reduces to find both Riemann invariants $\lambda^{\pm}(x, t)$, solutions of equations

(385). Writing $v_\pm = u \pm c$ [see equation (379)] in terms of $\lambda^\pm$, in the case of a polytropic flow, differential equations (385) become

$$\begin{cases} \partial_t \lambda^+ + \dfrac{1}{2}\left[(1+\gamma)\,\lambda^+ + (3-\gamma)\,\lambda^-\right]\,\partial_x \lambda^+ = 0, \\ \partial_t \lambda^- + \dfrac{1}{2}\left[(3-\gamma)\,\lambda^+ + (1+\gamma)\,\lambda^-\right]\,\partial_x \lambda^- = 0. \end{cases} \tag{386}$$

If one of the Riemann invariants is always constant in some region of space $x \in I \subset \mathbb{R}$, say for instance $\lambda^+(x,t) = \lambda_0^+, \forall x \in I$, this region is called a *simple-wave region*. The problem is then automatically solved: the first equation of (386) is trivially satisfied, and the second one reduces to a Hopf equation

$$\partial_t v_- + v_- \partial_x v_- = 0. \tag{387}$$

Solutions of the previous equation have been already discussed in Section 5.2.1. Therefore, the characteristic curves in a *simple-wave region* are straight lines in the plane (t,x), along which v_- and λ^- are constant. Therefore, in turn, one is able to find $\lambda^-(x,t)$ for each position x and time t.

The second set of characteristic curves Γ^+, with tangent vector $\mathbf{a}_\Gamma = (\sin\phi_+, \cos\phi_+)$ and $v_+ = \cot\phi_+$, can be found with equation

$$\frac{dx}{dt} = v_+(x,t) = \frac{1}{2}\left[(1+\gamma)\,\lambda^+(x,t) + (3-\gamma)\,\lambda^-(x,t)\right], \tag{388}$$

where $\lambda^+(x,t)$ and $\lambda^-(x,t)$ are known in the simple-wave region. Thus, Integrating the differential equation (388) yields the trajectories of the characteristic curves Γ^+. This problem is discussed in more detail in Ref. [100], where the simple wave approach is applied to a polytropic gas in expansion into an empty half-space.

Solving the system of partial differential equations (385), when both Riemann invariants vary concomitantly in some regions, is a more difficult problem and requires more involved mathematical tools, such as Riemann's method, a generalization of the method of characteristics. The different situations of interest for us necessitate the use of such a method; this is the reason why the next chapter is dedicated to its study.

6

DISPERSIONLESS EVOLUTION OF NONLINEAR PULSES

As we showed in Chapter 3 and Chapter 5, Bose-Einstein condensates and their photonic counterparts, the fluids of light, are described by the same type of nonlinear equations. In both cases, the problem can be mapped onto dispersive hydrodynamic equations, through a Madelung transformation [see, e.g., equations (121) and (366)]. This hydrodynamic approach has triggered much interest experimentally, as we already mentioned in the previous chapter. However, this analogy is also a powerful tool to address numerous theoretical problems. Indeed, in Chapter 3, we used the mapping to hydrodynamic equations to show that the motion of excitations emerging in a flowing Bose-Einstein condensate was the one of a massless scalar field in a curved spacetime. In Chapter 5, we noticed that the dynamics of Bose gases and fluids of light, in the absence of dispersion, was described by the same hydrodynamic equations as those governing the inviscid gas dynamics:

$$\begin{cases} \partial_t \rho + \rho\, \partial_x u + u\, \partial_x \rho = 0, \\ \partial_t u + u\, \partial_x u + \dfrac{c^2(\rho)}{\rho}\, \partial_x \rho = 0, \end{cases} \tag{389}$$

where $c(\rho) = \sqrt{\rho}$ is the sound velocity. In fact, this is a particular case of polytropic gases, for which

$$c(\rho) = \rho^{\frac{\gamma-1}{2}} \tag{390}$$

where γ is the adiabatic index ($\gamma > 1$). However, even in this apparently simple case for which a number of exact solutions have been obtained for various problems [107], solving the system of equations (389) becomes quite complicated if the parameter

$$\beta = \frac{3-\gamma}{2\,(\gamma-1)} \tag{391}$$

is not an integer number (which is the case for Bose gases and fluids of light where $\gamma = 2$ and $\beta = \frac{1}{2}$).

The aim of this chapter is to present a theoretical method to describe the dispersionless evolution of nonlinear pulses, whose dynamics is governed by hydrodynamic equations (389).

Many physical models lead to this one-dimensional hydrodynamic description and can be addressed by this method. We first consider the general case of polytropic gases. Then, we particularize the solutions to the case of nonlinear optical pulses in the presence of a uniform constant background, when density gradients of the density ρ are sufficiently

weak to neglect dispersive effects[1]. A last example illustrates the case of a non-integrable system: a zero temperature Bose-Einstein condensate transversely confined in an atomic wave guide.

6.1 HODOGRAPH TRANSFORMATION AND RIEMANN'S METHOD

We introduced the Riemann invariants $\lambda^+(x,t)$ and $\lambda^-(x,t)$ in Chapter 5. These invariants are conserved along characteristic curves and they "diagonalize" the system of hydrodynamic equations (389). We proved that they were given by

$$\lambda^{\pm}(x,t) = \frac{u(x,t)}{2} \pm \frac{1}{2}\int^{\rho(x,t)} \frac{c(\rho')}{\rho'}\,d\rho', \tag{392}$$

and solutions of the partial differential equations

$$\partial_t\lambda^{\pm} + v_{\pm}(\lambda^+,\lambda^-)\,\partial_x\lambda^{\pm} = 0, \quad v_{\pm}(\lambda^+,\lambda^-) = u \pm c(\rho). \tag{393}$$

If one solves the nonlinear equations given by (393) and finds the corresponding Riemann invariants $\lambda^+(x,t)$ and $\lambda^-(x,t)$, one immediately knows the density and velocity distributions for each position x and at any time t:

$$\begin{aligned} &\lambda^+(x,t) + \lambda^-(x,t) = u(x,t),\\ &\lambda^+(x,t) - \lambda^-(x,t) = \int^{\rho(x,t)} \frac{c(\rho')}{\rho'}\,d\rho'. \end{aligned} \tag{394}$$

Therefore, the problem consists of solving equations (393). In addition, we can notice from equations (394) that $c(\rho)$ is a function of $\lambda^+ - \lambda^-$. Thus, we obtain

$$v_{\pm}(\lambda^+,\lambda^-) = \lambda^+ + \lambda^- \pm c(\lambda^+ - \lambda^-). \tag{395}$$

In the first subsection, we show that these equations can be linearized by considering x and t as functions of the Riemann invariants:

$$x = x(\lambda^+,\lambda^-), \quad t = t(\lambda^+,\lambda^-). \tag{396}$$

This is known as a hodograph transformation [100, 107]. This procedure leads to a Euler-Poisson equation[2], whose solutions can be found by means of the Riemann's method [173]. This method is discussed in the second subsection.

1 The formation of a dispersive shock wave resulting from a gradient catastrophe will be studied in Chapter 7.

2 In the case of complex Riemann invariants, one finds a Laplace equation and a nice mapping to an electrostatic problem [29].

6.1.1 *Hodograph transformation*

This transformation consists in considering x and t as functions of the independent variables $\lambda^{\pm}$ [see equation (396)] and leads to the following system of linear equations (see Appendix D):

$$\begin{aligned} \frac{\partial x}{\partial \lambda^+} - v_-(\lambda^+, \lambda^-)\frac{\partial t}{\partial \lambda^+} = 0, \\ \frac{\partial x}{\partial \lambda^-} - v_+(\lambda^+, \lambda^-)\frac{\partial t}{\partial \lambda^-} = 0. \end{aligned} \tag{397}$$

We look for the solutions of these equations in the form

$$\begin{aligned} x - v_+(\lambda^+, \lambda^-)t = w_+(\lambda^+, \lambda^-), \\ x - v_-(\lambda^+, \lambda^-)t = w_-(\lambda^+, \lambda^-). \end{aligned} \tag{398}$$

A simple test of consistency shows that the unknown functions $w_{\pm}(\lambda^+, \lambda^-)$ should verify the Tsarev equations [180]

$$\begin{aligned} \frac{1}{w_+ - w_-}\frac{\partial w_+}{\partial \lambda^-} = \frac{1}{v_+ - v_-}\frac{\partial v_+}{\partial \lambda^-}, \\ \frac{1}{w_+ - w_-}\frac{\partial w_-}{\partial \lambda^+} = \frac{1}{v_+ - v_-}\frac{\partial v_-}{\partial \lambda^+}. \end{aligned} \tag{399}$$

Now we notice that since the velocities $v_{\pm}$ are given by expressions (395), the right-hand sides of both equations (399) are equal to each other:

$$\frac{1}{v_+ - v_-}\frac{\partial v_+}{\partial \lambda^-} = \frac{1}{v_+ - v_-}\frac{\partial v_-}{\partial \lambda^+} = \frac{1 - c'(\lambda^+ - \lambda^-)}{2\,c(\lambda^+ - \lambda^-)}, \tag{400}$$

where $c'(\lambda) \equiv \mathrm{d}c(\lambda)/\mathrm{d}\lambda$, $\lambda = \lambda^+ - \lambda^-$. Consequently $\partial w_+/\partial \lambda^- = \partial w_-/\partial \lambda^+$ and $w_{\pm}$ can be sought in the form

$$w_{\pm} = \frac{\partial W}{\partial \lambda^{\pm}}. \tag{401}$$

Substitution of equations (400) and (401) into equations (399) shows that the function W obeys the Euler-Poisson equation

$$\frac{\partial^2 W}{\partial \lambda^+ \partial \lambda^-} - \frac{1 - c'(\lambda^+ - \lambda^-)}{2c(\lambda^+ - \lambda^-)}\left(\frac{\partial W}{\partial \lambda^+} - \frac{\partial W}{\partial \lambda^-}\right) = 0. \tag{402}$$

A formal solution of equation (402) in the (λ^+, λ^-) plane (the so-called hodograph plane) can be obtained with the use of the Riemann method (see subsection below and Ref. [173]).

In conclusion, the system of hydrodynamic equations (389) can be mapped onto an Euler-Poisson equation (402), where W plays the role of a potential. The knowledge of this potential determines the functions $w_{\pm}$ through expression (401). Then, the Riemann invariants $\lambda^+(x,t)$ and $\lambda^-(x,t)$ can be obtained as functions of x and t by inverting the system of equations (398). Ultimately, the density $\rho(x,t)$ and the velocity $u(x,t)$ can be determined with equations (394).

The above procedure might give the impression to be cumbersome and unnecessary. However, it constitutes a powerful tool to address hydrodynamic problems: indeed, we started from nonlinear equations (389) and we arrived to a linear equation (402), whose solutions are well know in numerous cases. Besides, in certain problems, one can even obtain a physical interpretation of the potential W, which appears naturally from the hodograph transformation [29, 30].

6.1.2 *Riemann's method*

Let us consider a linear differential equation of second order of the form[3]

$$\mathscr{L}(W) \equiv \frac{\partial^2 W}{\partial\lambda^+\,\partial\lambda^-} + a(\lambda^+,\lambda^-)\frac{\partial W}{\partial\lambda^+} + b(\lambda^+,\lambda^-)\frac{\partial W}{\partial\lambda^-} = 0, \quad (403)$$

where $\mathscr{L}$ is a differential operator. We define the so-called adjoint differential operator

$$\mathscr{M}(R) \equiv \frac{\partial^2 R}{\partial\lambda^+\,\partial\lambda^-} - \frac{\partial\,(aR)}{\partial\lambda^+} - \frac{\partial\,(bR)}{\partial\lambda^-}, \quad (404)$$

where R, called the *Riemann function*, needs to be determined [see below, equations (412)]. One shows easily that

$$R\,\mathscr{L}(W) - W\,\mathscr{M}(R) = \frac{\partial U}{\partial\lambda^+} - \frac{\partial V}{\partial\lambda^-}, \quad (405)$$

with

$$\begin{cases} U = \dfrac{1}{2}\left(R\,\dfrac{\partial W}{\partial\lambda^-} - W\,\dfrac{\partial R}{\partial\lambda^-}\right) + aRW, \\ V = \dfrac{1}{2}\left(W\,\dfrac{\partial R}{\partial\lambda^+} - R\,\dfrac{\partial W}{\partial\lambda^+}\right) - bRW. \end{cases} \quad (406)$$

We now assume that the initial data $\lambda^+(x,t=0)$ and $\lambda^-(x,t=0)$ are known. This corresponds to the schematic curve $\mathcal{C}_0$ represented in the hodograph plane (λ^+,λ^-) and shown in Figure 41 for two cases: $\lambda^-(x,0)$ is a decreasing (or increasing) function of $\lambda^+(x,0)$. Therefore, using equations (398) and (401), one can determine W along the curve $\mathcal{C}_0$:

$$\left.\frac{\partial W}{\partial\lambda^+}\right|_{\mathcal{C}_0} = \left.\frac{\partial W}{\partial\lambda^-}\right|_{\mathcal{C}_0} = x(\lambda^+,\lambda^-). \quad (407)$$

Then, we show below that, from the knowledge of the values of λ^+ and λ^- on the initial curve $\mathcal{C}_0$, one is able to calculate the potential W at any point $P(\lambda^+=\xi,\lambda^-=\eta)$ in the hodograph plane. As illustrated in Figure 41, we denotes A (B) the intersection point between the straight line $\lambda^-=\eta$ ($\lambda^+=\xi$) and $\mathcal{C}_0$. The dark green region in Figure 41

3 In this subsection, we mainly follow the procedure presented in Sommerfeld's book [173]

corresponds to the interior of PAB; this surface is denoted $\mathcal{S}$. using the Stokes theorem and equation (405) one finds[4]

$$\begin{aligned}\int_{\mathcal{S}} [R\,\mathscr{L}(W) - W\mathscr{M}(R)]\,\mathrm{d}\lambda^+\,\mathrm{d}\lambda^- \\ = \int_{\mathcal{S}} \left(\frac{\partial U}{\partial \lambda^+} - \frac{\partial V}{\partial \lambda^-}\right) \mathrm{d}\lambda^+\,\mathrm{d}\lambda^- \\ = \oint_{\partial\mathcal{S}} V\,\mathrm{d}\lambda^+ + U\,\mathrm{d}\lambda^-,\end{aligned} \tag{408}$$

where the path of integration along $\partial\mathcal{S}$ is anticlockwise, as indicated by the blue arrows in Figure 41.

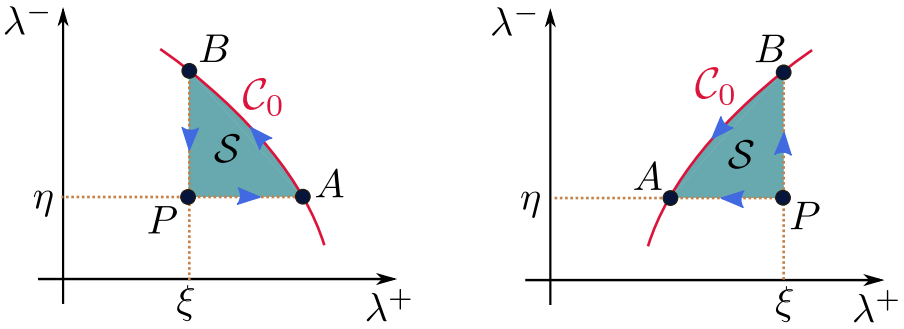

FIGURE 41: Initial curve $\mathcal{C}_0$ drawn in the hodograph plane (λ^+, λ^-) for two different configurations. We define three points: P of coordinates (ξ, η) ; A, the intersection point between the characteristic curve $\lambda^- = \eta$ and $\mathcal{C}_0$; B, the intersection point between the characteristic curve $\lambda^+ = \xi$ and $\mathcal{C}_0$. The dark green region corresponds to the interior of the surface $\mathcal{S}$ delimited by PAB. The blue arrows indicate the path of integration (anticlockwise) along $\partial\mathcal{S}$ in equation (408).

Using explicit expressions of U and V [see equations (406)] and an integration by parts, we obtain easily in the case where $\lambda^-(x, 0)$ is a decreasing function of $\lambda^+(x, 0)$ (this situation corresponds to the left plot of Figure 41)

$$\begin{aligned}\int_P^A V\,\mathrm{d}\lambda^+ = \frac{1}{2}(RW)_P - \frac{1}{2}(RW)_A \\ + \int_P^A W\left(\frac{\partial R}{\partial \lambda^+} - bR\right)\mathrm{d}\lambda^+,\end{aligned} \tag{409}$$

and

$$\begin{aligned}\int_B^P U\,\mathrm{d}\lambda^- = \frac{1}{2}(RW)_P - \frac{1}{2}(RW)_B \\ - \int_B^P W\left(\frac{\partial R}{\partial \lambda^-} - aR\right)\mathrm{d}\lambda^-.\end{aligned} \tag{410}$$

4 This is also known as *Green's theorem*

Therefore, one finds

$$\begin{aligned}&\int_{\mathcal{S}}[R\mathscr{L}(W)-W\mathscr{M}(R)]\,\mathrm{d}\lambda^+\,\mathrm{d}\lambda^-\\&=(RW)_P-\frac{1}{2}(RW)_A-\frac{1}{2}(RW)_B+\int_{\mathcal{C}_0}V\,\mathrm{d}\lambda^++U\,\mathrm{d}\lambda^-\\&+\int_P^A W\left(\frac{\partial R}{\partial\lambda^+}-bR\right)\mathrm{d}\lambda^+-\int_B^P W\left(\frac{\partial R}{\partial\lambda^-}-aR\right)\mathrm{d}\lambda^-.\end{aligned}\tag{411}$$

We know from equation (403) that $\mathscr{L}(W)=0$ anywhere in the interior of $\mathcal{S}$. Moreover, we can choose the Riemann function $R(\lambda^+,\lambda^-;\xi,\eta)$ in a convenient way for us; we demand that this function respects the following conditions:

$$\mathscr{M}(R)=0 \text{ in } \mathcal{S},\tag{412a}$$

$$R(P)=R(\xi,\eta;\xi,\eta)=1,\tag{412b}$$

$$\begin{aligned}&\frac{\partial R}{\partial\lambda^+}-bR=0,\ \text{on the characteristic } \lambda^-=\eta,\\&\frac{\partial R}{\partial\lambda^-}-aR=0,\ \text{on the characteristic } \lambda^+=\xi.\end{aligned}\tag{412c}$$

In this case, conditions (412) and expression (411) lead to

$$W(P)=\frac{1}{2}(RW)_A+\frac{1}{2}(RW)_B\mp\int_A^B V\,\mathrm{d}\lambda^++U\,\mathrm{d}\lambda^-,\tag{413}$$

with the 'minus' sign if one considers the case depicted in the left plot of Figure 41, and the 'plus' sign in the case exemplified in the right plot of the same figure.

Consequently, the knowledge of initial data suffices to determine the function W for any point P in the hodograph plane, provided the Riemann function R is known [computed from equations (412)].

RIEMANN FUNCTION In the case of the Euler-Poisson equation (402) [and comparing with the differential equation (403)], one obtains

$$a(\lambda^+,\lambda^-)=\frac{c'(\lambda^+-\lambda^-)-1}{2c(\lambda^+-\lambda^-)}=-b(\lambda^+,\lambda^-).\tag{414}$$

Then, conditions (412c) and (412b) yield

$$\begin{aligned}R(\lambda^+,\eta;\xi,\eta)&=\sqrt{\frac{c(\xi-\eta)}{c(\lambda^+-\eta)}}\exp\left(\int_{\xi-\eta}^{\lambda^+-\eta}\frac{\mathrm{d}\lambda}{2\,c(\lambda)}\right),\\R(\xi,\lambda^-;\xi,\eta)&=\sqrt{\frac{c(\xi-\eta)}{c(\xi-\lambda^-)}}\exp\left(\int_{\xi-\eta}^{\xi-\lambda^-}\frac{\mathrm{d}\lambda}{2\,c(\lambda)}\right),\end{aligned}\tag{415}$$

where $R(\lambda^+,\eta;\xi,\eta)$ is the Riemann function along the characteristic $\lambda^-=\eta$ (i.e., along PA, see Figure 41), and $R(\xi,\lambda^-;\xi,\eta)$ is the Riemann function along the characteristic $\lambda^+=\xi$ (i.e., along PB). Expressions (415) suggest that R can be sought in the form

$$R(\lambda^+,\lambda^-;\xi,\eta)=\mathscr{R}(\lambda^+-\lambda^-,\xi-\eta)\,F(\lambda^+,\lambda^-;\xi,\eta),\tag{416}$$

where $F(\lambda^+, \eta; \xi, \eta) = 1 = F(\xi, \lambda^-; \xi, \eta)$ and

$$\begin{aligned} \mathscr{R}(\lambda_1, \lambda_2) &= \sqrt{\frac{c(\lambda_2)}{c(\lambda_1)}} \exp\left(\int_{\lambda_2}^{\lambda_1} \frac{\mathrm{d}\lambda}{2\, c(\lambda)} \right) \\ &= \sqrt{\frac{c(\lambda_2)\rho(\lambda_1)}{c(\lambda_1)\rho(\lambda_2)}}. \end{aligned} \tag{417}$$

The final expression in the above formula has been obtained by means of a change of variable $\rho = \rho(\lambda)$ in the integral, where the function $\rho(\lambda)$ is the reciprocal function of $\lambda(\rho)$ given in (394)

$$\lambda(\rho) = \int^{\rho} \frac{c(\rho')\mathrm{d}\rho'}{\rho'}, \tag{418}$$

and $c(\lambda) = c(\rho(\lambda))$, so that $\mathrm{d}\lambda/c(\lambda) = \mathrm{d}\rho/\rho$.

INITIAL CONDITIONS We now consider the case where initial density and velocity distributions are given by

$$\rho(x, 0) = \bar{\rho}(x), \quad \text{and} \quad u(x, 0) = 0. \tag{419}$$

The density $\bar{\rho}(x)$ can be non-monotonic, as illustrated in the right margin. For simplicity, we assumed the existence of one global maximum reached at $x = 0$; we also assume that the density distribution is symmetric. The generalization to non-symmetric distributions is straightforward. We denote the regions $x < 0$ and $x > 0$ as regions 1 and 3, respectively. Since $u(x, 0) = 0$, one deducts from equations (394) that

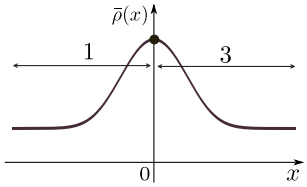

$$\lambda^+(x, 0) = -\lambda^-(x, 0), \quad \lambda^+(x, 0) = \int_0^{\bar{\rho}(x)} \frac{c(\rho)}{\rho}\, d\rho. \tag{420}$$

Thus, in this case, the initial curve $\mathcal{C}_0$ is a straight line in the hodograph plane (λ^+, λ^-). We introduce the monotonous functions $\bar{\lambda}^{(1)}(x) \equiv \lambda^+(x < 0, 0)$ and $\bar{\lambda}^{(3)}(x) \equiv \lambda^+(x \geq 0, 0)$. Their reciprocal functions are denoted $\bar{x}^{(1)}(\lambda)$ and $\bar{x}^{(3)}(\lambda)$, respectively. Here, since the initial density distribution is symmetric, we define

$$\bar{\lambda}(x) \equiv \bar{\lambda}^{(3)}(x) = \bar{\lambda}^{(1)}(-x), \quad \bar{x}(\lambda) \equiv \bar{x}^{(3)}(\lambda) = -\bar{x}^{(1)}(\lambda). \tag{421}$$

We obtain for the value of x on the curve $\mathcal{C}_0$:

$$x = \begin{cases} \bar{x}(\lambda) & \text{if } x \geq 0, \\ -\bar{x}(\lambda) & \text{if } x < 0. \end{cases} \tag{422}$$

The functions $\bar{\lambda}(x)$ and $\bar{x}(\lambda)$ are illustrated in the schematic graphs of Figure 42.

Besides that, since at $t = 0$ the values $\lambda^+ = \bar{\lambda}$ and $\lambda^- = -\bar{\lambda}$ correspond to the same value of x, we find that $\bar{x}(\lambda)$ is an even function, $\bar{x}(-\lambda) = \bar{x}(\lambda)$. All these notations are summarized in Figure 42, where, in particular, the minimum and the maximum of $\lambda^+(x, t = 0)$ are denoted λ_0 and λ_m, respectively.

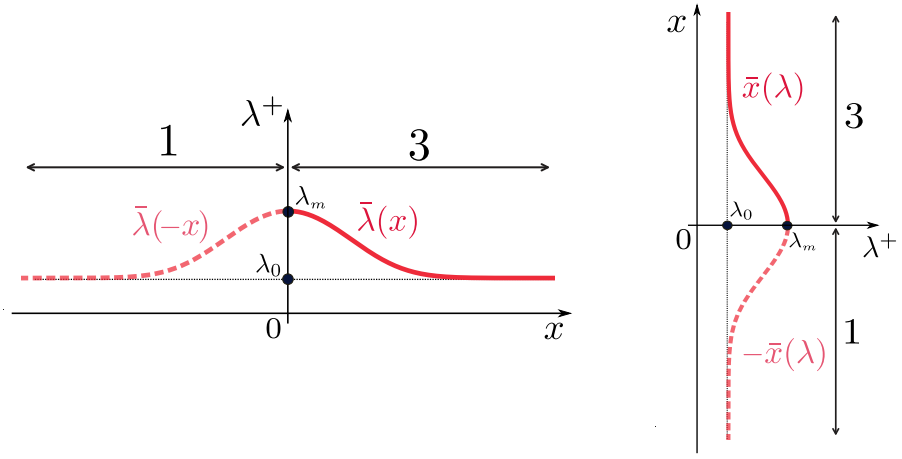

FIGURE 42: (Left) Sketch of $\lambda^+(x, t = 0)$ and, in particular, $\bar\lambda(x) \equiv \lambda^+(x \geq 0, 0)$. This curve can be obtained from the initial density distribution $\bar\rho(x)$ through expression (420). Since we consider a symmetric density distribution here, the dashed part of the red curve is the symmetric of the solid curve and thus corresponds to $\bar\lambda(-x)$. The minimum and the maximum of $\bar\lambda(x)$ are denoted λ_0 and λ_m, respectively.
(Right) Reciprocal function of $\bar\lambda(x)$, denoted $\bar x(\lambda)$ [see equation (422)].

For the specific initial conditions (419), since $\lambda^+(x, 0) = -\lambda^-(x, 0)$, equation (407) shows that W is constant along the initial curve $\mathcal{C}_0$. The value of this constant is immaterial, we take $W|_{\mathcal{C}_0} = 0$ for simplicity.

However, the non-monotonicity of $\bar\rho$ adds a slight difficulty here. Indeed, depending on which region we are, $x = \bar x(\lambda)$ – region 3 – or $x = -\bar x(\lambda)$ – region 1 – [see equation (422)]; this leads for instance to an ambiguity about the choice of x in (407), and so does for expressions of U and V [see equations (406)].

An elegant way to solve this problem has been proposed by Ludford and consists in unfolding the hodograph plane [120], as shown in Figure 44. The red curve in both graphs corresponds to $\mathcal{C}_0$ and a sketch of the initial Riemann invariants $\lambda^+(x, 0) = -\lambda^-(x, 0)$, for a specific non-monotonic density distribution $\bar\rho(x)$, is depicted in the left plot of Figure 43. Region 1 then corresponds to the upper left domain of the right plot of Figure 44, while region 3 corresponds to the bottom right domain: this amounts to define a distinct hodograph plane for each monotonous part of the initial distribution.

For $t > 0$, the initial hump of density $\bar\rho(x)$ splits in two parts and both Riemann invariants λ^+ and λ^- propagate in opposite direction, as illustrated by the green arrows in the right plot of Figure 43. A new region appears: it corresponds to the domain where λ^+ and λ^- have the same monotonicity. We denote this region as region 2. Then, one is able to extract from this graph $\lambda^+(x, t > 0)$ as a function of $\lambda^-(x, t > 0)$ in order to draw the corresponding curve in the hodograph plane; we obtain the blue curve shown in Figure 44, either when the hodograph

plane is not unfolded (left plot) or when it is (right plot). One sees from the right plot of this figure that region 2 corresponds to the bottom left domain of the graph[5].

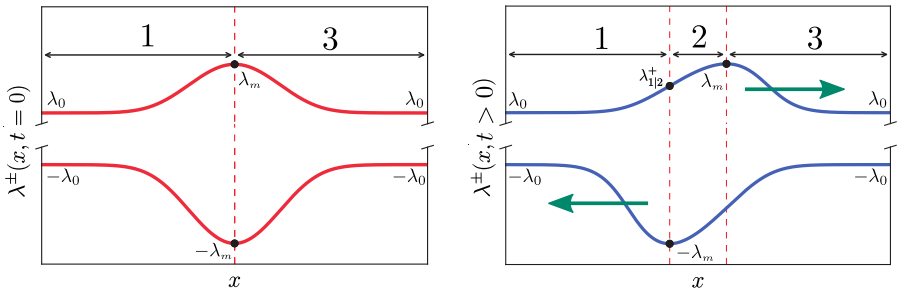

FIGURE 43: Sketch of the distributions $\lambda^{\pm}(x,t)$ at time $t=0$ (Left) and at finite time $t>0$ (Right). In each panel the upper solid curve represents λ^+ (always larger than λ_0), and the lower one λ^- (always lower than $-\lambda_0$). For $t>0$, as indicated by the green arrows, λ^+ (λ^-) moves to the right (to the left) and regions 1 and 3 start to overlap. This leads to the configuration represented in panel (Right) where a new region (labeled region 2) has appeared. The value of λ^+ at the interface between regions 1 and 2 is denoted as $\lambda^+_{1|2}$. These graphs actually correspond to a situation where the initial density distribution is given by (432) (see below, Section 6.2.1).

In conclusion, we obtain three different regions that we need to treat separately. Expression (413) takes a different form in each of these domains.

Let us first consider region 1 and 3 and a point P of coordinates (ξ,η) in the hodograph plane where we would like to evaluate the potential W (see Figure 44). Recalling that $W|_{\mathcal{C}_0}=0$ and using equations (406) and (407), expressions of U and V along $\mathcal{C}_0$ read

$$\begin{aligned} U(\lambda) = -V(\lambda) &= -\frac{\bar{x}(\lambda)}{2}\, R(\lambda,-\lambda;\xi,\eta) \quad \text{in region 1,} \\ U(\lambda) = -V(\lambda) &= \frac{\bar{x}(\lambda)}{2}\, R(\lambda,-\lambda;\xi,\eta) \quad \text{in region 3,} \end{aligned} \tag{423}$$

where (ξ,η) are the corresponding coordinates of P in each region of the hodograph plane (see Figure 44). Then, the expression of $W(P)$ is immediate from equation (413):

$$W^{(1,3)}(\xi,\eta) = \mp \int_{-\eta}^{\xi} \bar{x}(\lambda) R(\lambda,-\lambda;\xi,\eta)\mathrm{d}\lambda, \tag{424}$$

where the sign $-$ ($+$) applies in region 1 (3).

The computation of W in region 2 cannot be directly obtained from (413). In this region, one can also use the Stokes theorem (408) in the interior of the surface delimited by PA_2CB_2 (see Figure 44 for the

5 The gray region is unreachable in our problem.

notations). Similarly to equation (413), we can split the integral over the different segments and we easily obtain

$$\begin{aligned} W^{(2)}(\xi,\eta) = {} & [RW^{(1)}]_{B_2} + [RW^{(3)}]_{A_2} \\ & + \int_{A_2}^{C} \left(\frac{\partial R}{\partial \lambda^-} - aR\right)_{\lambda^+=\lambda_m} W^{(3)}(\lambda_m,\lambda^-)\,\mathrm{d}\lambda^- \\ & - \int_{C}^{B_2} \left(\frac{\partial R}{\partial \lambda^+} - bR\right)_{\lambda^-=-\lambda_m} W^{(1)}(\lambda^+,-\lambda_m)\,\mathrm{d}\lambda^+. \end{aligned} \tag{425}$$

Therefore, equations (424) and (425) solve the problem. Using equation (401) one finds the expressions of $w_\pm$ in each region. Inverting the system of equations (398) gives $\lambda^\pm$ as functions of x and t.

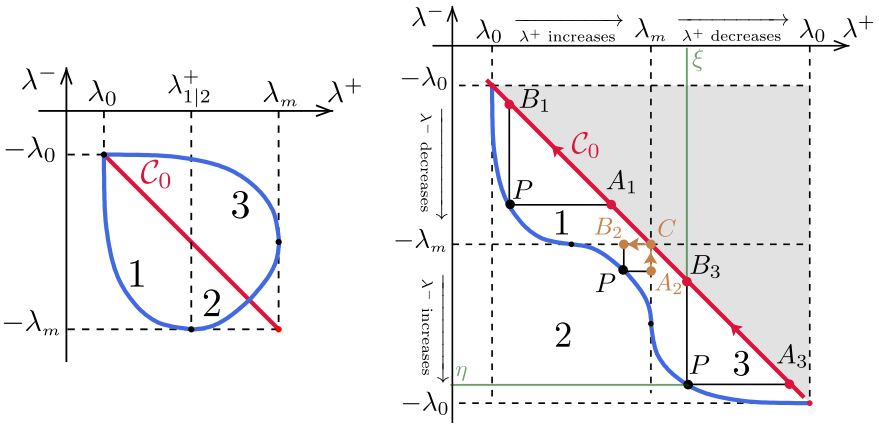

FIGURE 44: (Left) Behavior of the Riemann invariants in the hodograph plane at a given time t. The red straight line is the curve $\mathcal{C}_0$. The blue solid line is the curve with parametric equation $(\lambda_+(x,t>0),\lambda_-(x,t>0))$. The corresponding Riemann invariants $\lambda_\pm(x,t>0)$ (as functions of x) are shown in the right plot of Figure 43.
(Right) The same curves on the four-sheeted unfolded surface. The regions 1, 2 and 3 correspond to the different regimes of monotonicity identified in Figure 43. In our problem, the whole gray shaded domain above $\mathcal{C}_0$ is unreachable. A generic point P has coordinates (ξ,η), as indicated for instance in region 3, and points A_1, B_1, A_3, B_3 and C lie on the initial curve $\mathcal{C}_0$. Points A_2 and B_2 lie on a boundary between two regions. The arrows indicate the direction of integration in equations (413) and (425).

APPROXIMATE SOLUTIONS We would like to simplify expressions (424) and (425). First, in region 2, we notice that, at short time, the coordinates ξ and η of point P are close to λ_m and $-\lambda_m$, respectively (see Figure 44). This leads to the approximation

$$\left(\frac{\partial R}{\partial \lambda^-} - aR\right)_{\lambda^+=\lambda_m} \simeq \left(\frac{\partial R}{\partial \lambda^+} - bR\right)_{\lambda^-=-\lambda_m} \simeq 0, \tag{426}$$

by virtue of equations (412c). This assumption amounts to discard both integrals in expression (425). Actually, using equations (416) and (417), approximation (426) is equivalent to

$$F(\lambda^+, \lambda^-; \xi, \eta) \simeq 1. \tag{427}$$

Similarly, in expression (424) for $W^{(1)}$ and $W^{(3)}$, since at short time $-\eta$ and ξ are close, the integration variable λ is close to ξ and one can again assume that $F \simeq 1$. That is to say, we are led to make in the whole hodograph plane the approximation

$$R(\lambda^+, \lambda^-; \xi, \eta) \simeq \mathscr{R}(\lambda^+ - \lambda^-, \xi - \eta). \tag{428}$$

We can now write the final approximate results, making the replacements $\xi \to \lambda^+$, $\eta \to \lambda^-$ in the above expressions, so that they can be used in equation (401), and then in expressions (398):

$$\begin{aligned} W^{(1,3)}(\lambda^+, \lambda^-) &\simeq \mp \int_{-\lambda^-}^{\lambda^+} \bar{x}(\lambda)\, \mathscr{R}(2\lambda, \lambda^+ - \lambda^-) \mathrm{d}\lambda, \\ W^{(2)}(\lambda^+, \lambda^-) &\simeq \mathscr{R}(\lambda^+ + \lambda_m, \lambda^+ - \lambda^-)\, W^{(1)}(\lambda^+, -\lambda_m) \\ &\quad + \mathscr{R}(\lambda_m - \lambda^-, \lambda^+ - \lambda^-)\, W^{(3)}(\lambda_m, \lambda^-), \end{aligned} \tag{429}$$

where $\mathscr{R}$ is given by equation (417). It is important to stress that equation (417) has a universal form and can be applied to any physical system with known dependence $c(\lambda^+ - \lambda^-)$, see equations (394) and (395).

6.2 APPLICATION OF RIEMANN'S APPROACH

Le us now apply the Riemann's method described above to some peculiar cases of interest. We start with polytropic gases, which encompasses the specific case of adiabatic index $\gamma = 2$, corresponding to the nonlinear Schrödinger equation (363). This is relevant to the study of the propagation of an optical beam in a nonlinear medium in the presence of a constant background (see, e.g., Figure 39 in Chapter 5), before the formation of a dispersive shock wave, whose description will be addressed in Chapter 7.

6.2.1 *Polytopic gases and nonlinear optics*

In the case of the dynamics of a polytropic gas with $c(\rho) = \rho^{(\gamma-1)/2}$, an easy calculation gives

$$\mathscr{R}(\lambda_1, \lambda_2) = \left(\frac{\lambda_1}{\lambda_2}\right)^{\beta}, \quad \text{where} \quad \beta = \frac{3-\gamma}{2(\gamma-1)}. \tag{430}$$

It is worth noticing that the approximation (428) yields the exact expression of the Riemann function for a classical monoatomic gas with $\gamma = 5/3$ ($\beta = 1$). For other values of β the function F in (416) can be

shown to obey the hypergeometric equation (see, e.g., Ref. [173]) and our approximation corresponds to the first term in its series expansion. Thus, we obtain

$$\begin{aligned} W^{(1,3)}(\lambda^+,\lambda^-) &\simeq \mp\left(\frac{2}{\lambda^+-\lambda^-}\right)^{\beta}\int_{-\lambda^-}^{\lambda^+}\lambda^{\beta}\,\bar{x}(\lambda)\mathrm{d}\lambda, \\ W^{(2)}(\lambda^+,\lambda^-) &\simeq \left(\frac{2}{\lambda^+-\lambda^-}\right)^{\beta} \\ &\quad\times\left\{\int_{-\lambda^-}^{\lambda_m}\lambda^{\beta}\,\bar{x}(\lambda)\mathrm{d}\lambda+\int_{\lambda^+}^{\lambda_m}\lambda^{\beta}\,\bar{x}(\lambda)\mathrm{d}\lambda\right\}. \end{aligned} \tag{431}$$

The case $\beta = 1/2$ corresponds to the propagation of an optical beam in a nonlinear dielectric material and the dynamics of a Bose-Einstein condensed system [94].

INITIAL CONDITIONS One sees that expressions (431) are given in terms of $\bar{x}(\lambda)$, the reciprocal function of $\bar{\lambda}(x) \equiv \lambda^+(x \geq 0, 0)$, where $\lambda^+(x \geq 0, 0)$ can be calculated from (420). Here, we take an initial profile of the form[6]

$$\overline{\rho}(x) = \rho_0 + \rho_1 \exp(-x^2/x_0^2)\,, \tag{432}$$

with ρ_0 and $\rho_1 > 0$. One obtains from (420),

$$\bar{x}(\lambda) = x_0\sqrt{\ln\rho_1 - \ln\left[\left|(\gamma-1)\,\lambda\right|^{\frac{2}{\gamma-1}} - \rho_0\right]}. \tag{433}$$

For such a "single-bump" type of initial conditions, there exist two values $\lambda_m = \bar{\lambda}(0)$ and $\lambda_0 = \bar{\lambda}(x \to \infty)$ $(\lambda_m > \lambda_0 > 0)$ such that $\lambda^+(x,t) \in [\lambda_0, \lambda_m]$ and $\lambda^-(x,t) \in [-\lambda_m, -\lambda_0]$. This situation corresponds exactly to the graphs shown in Figure 42.

PROCEDURE Once $W(\lambda^+,\lambda^-)$ is known in all three regions 1, 2 and 3 by means of equations (431), it is possible to compute $\lambda^+(x,t)$ and $\lambda^-(x,t)$, and then $\rho(x,t)$ and $u(x,t)$, following the procedure below:

- One first determines the value $\lambda^+_{1|2}(t)$ reached by λ^+ at the boundary between regions 1 and 2, see the right panel of Figure 43. This boundary corresponds to the point where $\lambda^- = -\lambda_m$ at time t. From equations (398), $\lambda^+_{1|2}(t)$ is thus determined by solving

$$\frac{w_+^{(1)}(\lambda^+_{1|2},-\lambda_m) - w_-^{(1)}(\lambda^+_{1|2},-\lambda_m)}{v_+(\lambda^+_{1|2},-\lambda_m) - v_-(\lambda^+_{1|2},-\lambda_m)} + t = 0\,, \tag{434}$$

  where $w_+^{(1)} = \partial W^{(1)}/\partial\lambda^+$. We then know that, in region 1 at time t, λ^+ takes all possible values between λ_0 and $\lambda^+_{1|2}(t)$ (cf. Figure 43 and Figure 44).

6 In the case of nonlinear optics this initial profile corresponds to a Gaussian beam, which can be easily set up experimentally.

- One then lets λ^+ vary in $[\lambda_0, \lambda_m]$. From equations (398), at time t, the other Riemann invariant λ^- is solution of

$$\frac{w_+^{(1,2)}(\lambda^+,\lambda^-) - w_-^{(1,2)}(\lambda^+,\lambda^-)}{v_+(\lambda^+,\lambda^-) - v_-(\lambda^+,\lambda^-)} + t = 0\,, \tag{435}$$

  where the superscript should be 1 if $\lambda^+ \in [\lambda_0, \lambda^+_{1|2}(t)]$ and 2 if $\lambda^+ \in [\lambda^+_{1|2}(t), \lambda_m]$, see Figure 43.

- At this point, for each value of t and λ^+ we have determined the value of λ^-. The position x is then obtained by either one of equations (398). Thus, for given t and λ^+ in regions 1 and 2, one has determined the values of λ^- and x. In region 3 we use the symmetry of the problem and write $\lambda^{\pm}(x,t) = -\lambda^{\mp}(-x,t)$.

The above procedure defines a mapping of the whole physical (x,t) space onto the hodograph (λ^+,λ^-) space. The density and velocity profiles are then obtained by means of equations (392).

RESULTS The results are compared with numerical simulations in Figure 45 for $\gamma = 2$ and for an initial profile (432) with $x_0 = 20$, $\rho_0 = 0.5$ and $\rho_1 = 1.5$. The simulations have been performed by solving numerically the nonlinear Schrödinger equation of the form

$$\mathrm{i}\psi_t = -\tfrac{1}{2}\psi_{xx} + \rho\,\psi, \tag{436}$$

[see also equation (363) in Chapter 5] where $\rho(x,t) = |\psi|^2$, $u(x,t) = (\psi^*\psi_x - \psi\,\psi_x^*)/(2\mathrm{i}\rho)$ and $\psi(x,0) = \sqrt{\rho}(x,0)$. Equation (436) reduces to the system (389) with the speed of sound $c^2(\rho) = \sqrt{\rho}$ in the dispersionless limit.

One can notice in Figure 45 that our solution of the hydrodynamic equations (389) agrees very well with the numerical simulations of the dispersive equation (436) at short time. For larger times the profile steepens, eventually reaching a point of gradient catastrophe. One sees in particular the formation of oscillations at both edges of the numerical density profiles for $t > 16$. These oscillations correspond to the onset of a dispersive shock wave, which occurs at a time denoted as the wave breaking time: t_{WB}. It is thus expected that for $t \simeq t_{\mathrm{WB}}$ the solution of the dispersionless system (389) departs from the numerical simulations, as seen in the figure. However, this difference is not a sign of a failure of our approximation, but it rather points to the breakdown of the hydrodynamic model (389). After t_{WB} the system (389) leads to a multi-valued solution if not corrected to account for dispersive effects, as can be seen in Figure 45. The occurrence of the gradient catastrophe, when the dispersionless profile becomes multi-valued at both edges, is an efficient way to estimate the wave breaking time, as shown in the next paragraph.

WAVE BREAKING TIME We now turn to the determination of the wave breaking time t_{WB}, the moment at which a shock is formed and the

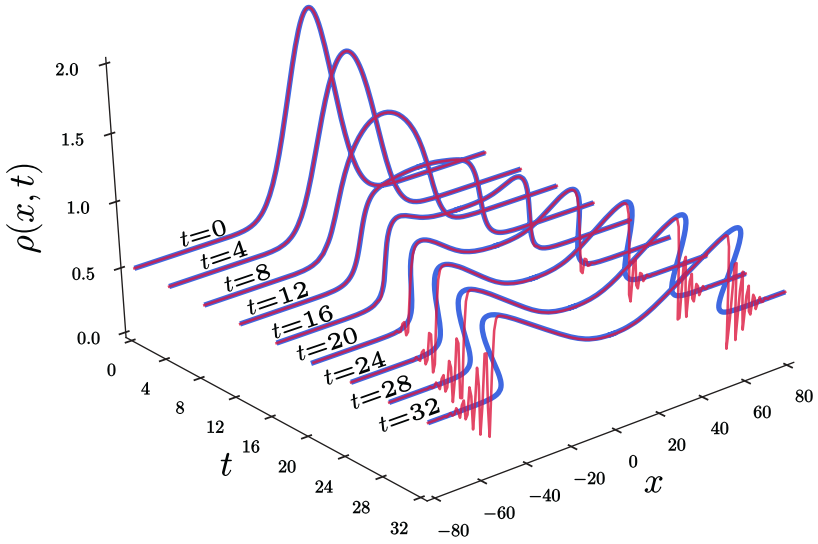

FIGURE 45: Density profile $\rho(x,t)$ for different times of propagation t. The initial density distribution $\bar{\rho}(x)$ is Gaussian, with $x_0 = 20$, $\rho_0 = 0.5$ and $\rho_1 = 1.5$ [see equations (419) and (432)]. The blue curves correspond to the theoretical results obtained from expressions (431), with $\beta = \frac{1}{2}$ ($\gamma = 2$). For this specific value of the adiabatic index γ, the nonlinear Schrödinger equation (436) can be indeed mapped onto hydrodynamic equations (389) in the dispersionless limit [or equation (366) when dispersion is taken into account]. The red curves are obtained with numerical simulations of the dispersive equation (436). The formation of oscillations around $t \simeq 20$ correspond to the birth of a dispersive shock wave.

dispersionless approach fails. As mentioned in the above paragraph, this corresponds to a *gradient catastrophe*, i.e., a point of infinite gradient $\partial\lambda^{\pm}/\partial x = \infty$. If one considers for instance the right part of the profile (region 3), from equations (398), this occurs at a time t such that

$$t = -\frac{\partial w_+^{(3)}/\partial\lambda_+}{1 + c'(\lambda_+ - \lambda_-)} = -\frac{\partial w_+^{(3)}/\partial\lambda_+}{1 + \left.\frac{\mathrm{d}\ln c}{\mathrm{d}\ln\rho}\right|_{\lambda_+ - \lambda_-}}, \tag{437}$$

and t_{WB} is the smallest of the times[7] (437).

One can easily compute t_{WB} approximately when the point of largest gradient in $\overline{\rho}(x)$ lies in a region where $\overline{\rho} \simeq \rho_0$. This occurs for some specific initial distributions (such as the inverted parabola considered in Section 6.2.3) or when the initial bump is only a small perturbation

7 It is worth noticing that this formula yields an expression for the breaking time obtained from our approximate solution of the initial value problem and in this sense it provides less general but more definite result than the upper estimate of the breaking time obtained by Lax in Ref. [112].

of the background. In this case, it is legitimate to assume that wave breaking is reached for $\lambda^- \simeq -\lambda_0$ and this yields

$$\lambda^+ - \lambda^- \simeq \tfrac{1}{2}\int_0^{\rho} \frac{c(\rho')}{\rho'}\mathrm{d}\rho' + \tfrac{1}{2}\int_0^{\rho_0} \frac{c(\rho')}{\rho'}\mathrm{d}\rho'. \tag{438}$$

Equations (401) and (429) then lead to $w_+^{(3)} \simeq \bar{x}(\lambda^+)$ and (437) becomes

$$t \simeq -\frac{2}{1+\left.\frac{\mathrm{d}\ln c}{\mathrm{d}\ln\rho}\right|_{\overline{\rho}}} \times \frac{\overline{\rho}}{c(\overline{\rho})\,\frac{\mathrm{d}\overline{\rho}}{\mathrm{d}x}}\,, \tag{439}$$

where $\overline{\rho}$ stands for $\overline{\rho}(\bar{x}(\lambda^+))$. Within our hypothesis, it is legitimate to assume that the shortest of times t is reached close to the point $\bar{x}(\lambda^+)$ for which $|\mathrm{d}\overline{\rho}/\mathrm{d}x|$ is maximal[8]. We note x^* the coordinate of this point and $\rho^* = \overline{\rho}(x^*)$. One thus obtains

$$t_{\mathrm{WB}} \simeq \frac{2}{1+\left.\frac{\mathrm{d}\ln c}{\mathrm{d}\ln\rho}\right|_{\rho^*}} \times \frac{\rho^*}{c(\rho^*)\cdot\max\left|\frac{\mathrm{d}\overline{\rho}}{\mathrm{d}x}\right|}\,. \tag{440}$$

For an initial density distribution of the form (432) with $c(\rho) = \sqrt{\rho}$ ($\gamma = 2$), one obtains

$$t_{\mathrm{WB}} \simeq \frac{4}{3}\sqrt{\frac{e}{2}}\,x_0\,\frac{\sqrt{\rho_0 + e^{-1/2}\rho_1}}{\rho_1}. \tag{441}$$

For the specific initial conditions of Figure 45: $x_0 = 20$, $\rho_0 = 0.5$, and $\rho_1 = 1.5$, expression (441) yields $t_{\mathrm{WB}} \simeq 17.4$, in good agreement with numerical simulations.

6.2.2 *Example on a non-integrable system*

We now study in some details a case where the dependence of c on ρ is less simple than the one of equation (390): this is the case of a zero temperature Bose-Einstein condensate transversely confined in an atomic wave guide. For a harmonic trapping, the transverse averaged chemical potential can be represented by the interpolating formula [73]

$$\mu_\perp(\rho) = \hbar\omega_\perp\sqrt{1+4a\rho}, \tag{442}$$

where $\omega_\perp$ is the angular frequency of the transverse harmonic potential, $a > 0$ is the s-wave scattering length, $\rho(x,t) = |\psi(x,t)|^2$ is the linear density of the condensate, and $\psi(x,t)$ is the one-dimensional condensate wave function[9]. In this case, the dynamics of the condensate is governed by an effective one-dimensional Gross-Pitaevskii equation

$$i\hbar\partial_t\,\psi = -\frac{\hbar^2}{2m}\partial_{xx}\psi + \mu_\perp(|\psi|^2)\,\psi, \tag{443}$$

8 Indeed, the gradient catastrophe is likely to occur at the point where the initial density gradient is maximal.

9 We note that other expressions for $\mu_\perp$ have also been proposed in the literature [101, 161].

with m the mass of the atoms in the Bose gas. When $a\rho \ll 1$, one recovers the transverse Gaussian regime with $\mu_\perp(\rho) \simeq \hbar\omega_\perp + g|\psi|^2$, where $g = 2\hbar\omega_\perp a$ [135] is an effective one-dimensional nonlinear coupling constant (see Section 3.1.2 where the 1D mean-field regime is discussed in more detail).

Expression (442) yields the correct sound velocity $mc^2 = \rho\, \mathrm{d}\mu_\perp/\mathrm{d}\rho$ both in the low ($a\rho \ll 1$) and in the high ($a\rho \gg 1$) density regimes. In these two limiting cases the dispersionless dynamics of the system is thus correctly described by the hydrodynamic equations (389) with, in appropriate dimensionless units[10]

$$c^2(\rho) = \frac{\rho}{\sqrt{1+\rho}}\,, \tag{444}$$

where one has made the changes of variables $4a\rho \to \rho$, $u/u_0 \to u$, $x/x_0 \to x$ and $t/t_0 \to t$, where $2mu_0^2 = \hbar\omega_\perp$ and $t_0 = x_0/u_0$. The length x_0 used to non-dimensionalize the dispersionless equations is a free parameter: we will chose it equal to the parameter x_0 appearing in the initial condition[11] (432). Note that in dimensionless units equation (443) becomes

$$\mathrm{i}\psi_t = -\tfrac{1}{2}\psi_{xx} + 2\,\psi\sqrt{1+|\psi|^2}, \tag{445}$$

which is a non-integrable equation.

Let us now apply the Riemann's method. In the case characterized by equations (442) and (444), expressions (417) and (418) yield

$$\mathscr{R}(\lambda_1,\lambda_2) = \left(\frac{\rho^2(\lambda_1)+\rho^3(\lambda_1)}{\rho^2(\lambda_2)+\rho^3(\lambda_2)}\right)^{1/8}, \tag{446}$$

where $\rho(\lambda)$ is the reciprocal function of

$$\lambda(\rho) = 2\int_0^{\sqrt{\rho}} \frac{\mathrm{d}u}{(1+u^2)^{1/4}}. \tag{447}$$

We can now insert the above expressions in equations (429) and use the procedure described in Section 6.2.1 to obtained theoretically the density and velocity distributions $\rho(x,t)$ and $u(x,t)$. The results are shown and compared with numerical simulations in Figure 46 for an initial profile (432) with $\rho_0 = 1$ and $\rho_1 = 1$. The simulations have been performed by solving numerically a generalized nonlinear Schrödinger equation (445).

Once again, as already observed in Figure 45, the approximate expressions (429) give an excellent agreement with the numerical simulations

10 This can be easily proven using a Madelung transformation $\psi = \sqrt{\rho}\,\exp(i\,S)$, with $\partial_x S(x,t) = u(x,t)$, $\rho(x,t)$ and $u(x,t)$ being the density and the velocity distributions of the gas.

11 We note here that the initial condition (432) can be realized by several means in the context of BEC physics. One can for instance suddenly switch on at $t = 0$ a blue detuned focused laser beam [13]. An alternative method has been demonstrated in Ref. [86]: by monitoring the relative phase of a two species condensate, one can implement a bump (or a through) in one of the components.

and confirm the efficiency of Riemann's method to describe the propagation of nonlinear pulses.

We can also estimate the wave breaking time using expression (440); for a sound velocity of the form (444), we find

$$t_{\mathrm{WB}} \simeq \sqrt{\frac{e}{2}} \frac{8(1+\rho^*)}{6+5\rho^*} \frac{x_0}{c(\rho^*)} \frac{\rho^*}{\rho_1}. \tag{448}$$

The location x_{WB} of the wave breaking event can be obtained from (398). Within our approximation scheme, this yields, for the right part of the profile:

$$x_{\mathrm{WB}} \simeq x^* + c(\rho^*) t_{\mathrm{WB}}. \tag{449}$$

These results are compared in Figure 47 with the values determined from the Riemann approach. The overall agreement is excellent. We also note that replacing ρ^* by ρ_0 in equations (448) and (449) gives a result which is less accurate, but still quite reasonable, see Figure 47.

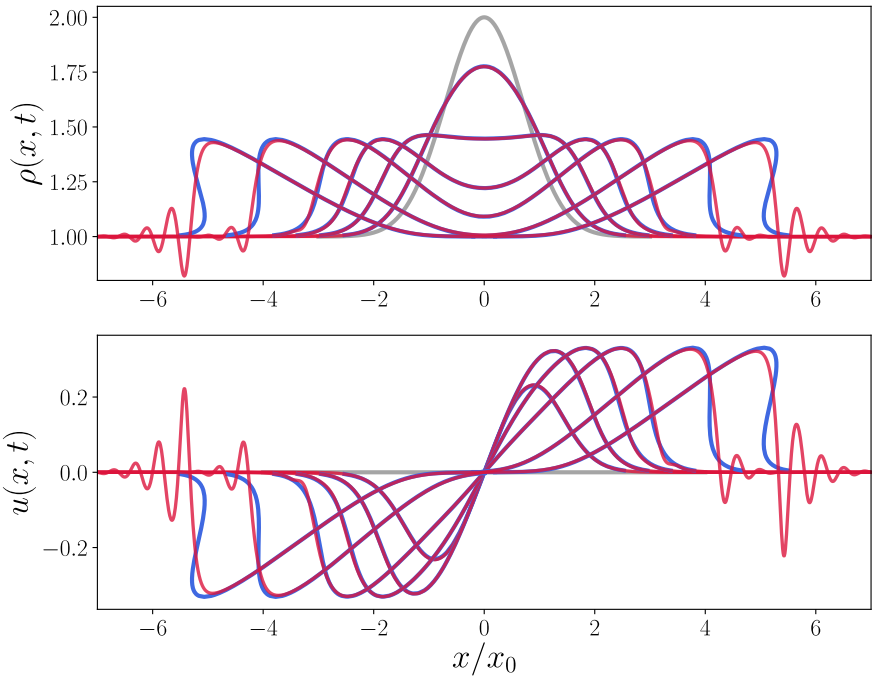

FIGURE 46: Density and velocity plotted as a function of x/x_0 for dimensionless times $t/t_0 = 0.5$, 1, 1.5, 2, 3 and 4 respectively. The initial conditions are given by equations (419) and (432) with $\rho_0 = 1$ and $\rho_1 = 1$, they are represented by the gray solid lines. The blue solid lines are the results of the hydrodynamic system (389) obtained from the approximate Riemann's approach described in Section 6.1.2. The red curves are the results of the numerical simulations of equations (445).

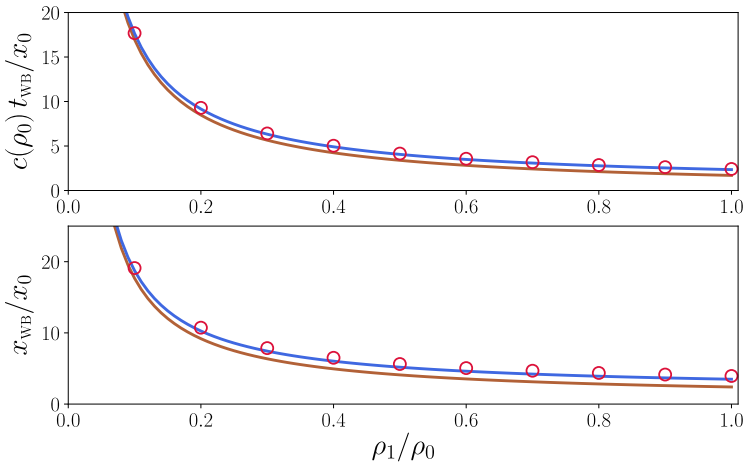

FIGURE 47: Wave breaking time t_{WB} and position of the wave breaking event x_{WB} for different values of ρ_1/ρ_0. The system considered is a quasi-1D Bose-Einstein condensate for which the speed of sound is given by (444). The initial distributions given by equation (432) and $u(x, t = 0) = 0$. The blue solid lines are the approximate results (448) and (449). The red dots are the results obtained from Riemann's approach. The brown solid lines are obtained by replacing ρ^* by ρ_0 in equations (448) and (449), see the paragraph 'Wave breaking time' of Section 6.2.1, and, in particular, expressions (439) and (440).

6.2.3 *Nonlinear optics with specific initial conditions*

We conclude this chapter with a last example, when the initial density distribution is not Gaussian, as in equation (432), but has the form of an inverted parabola:

$$\bar{\rho}(x) \equiv \rho(x, 0) = \begin{cases} \rho_0 + \rho_1(1 - x^2/x_0^2) & \text{if} \quad |x| < x_0, \\ \rho_0 & \text{if} \quad |x| \geq x_0, \end{cases} \tag{450}$$

and

$$u(x, 0) = 0. \tag{451}$$

We still consider the propagation of an optical beam in a nonlinear material. Therefore, the dynamics of the fluid of light is governed by the nonlinear Schrödinger equation (436), i.e., a specific case of polytropic gases with adiabatic index $\gamma = 2$. The sound velocity is thus $c(\rho) = \sqrt{\rho}$ and the Riemann invariants are given by $\lambda^{\pm} = \frac{1}{2}u + \sqrt{\rho}$.

Equations (421) and (422) are in the considered case:

$$x = \begin{cases} \bar{x}^{(3)}(\lambda) & \text{if } x > 0, \\ \bar{x}^{(1)}(\lambda) & \text{if } x < 0, \end{cases} \tag{452}$$

with

$$\bar{x}^{(3)}(\lambda) = -\bar{x}^{(1)}(\lambda) = x_0 \sqrt{1 - \frac{\lambda^2 - \rho_0}{\rho_1}}. \tag{453}$$

The emergence of simple wave regions renders the situation slightly more tricky than the procedure we described in the previous sections. Indeed, Figure 48 shows the evolution of the Riemann invariants with respect to time. The green arrows indicate the direction of propagation of each Riemann invariant.

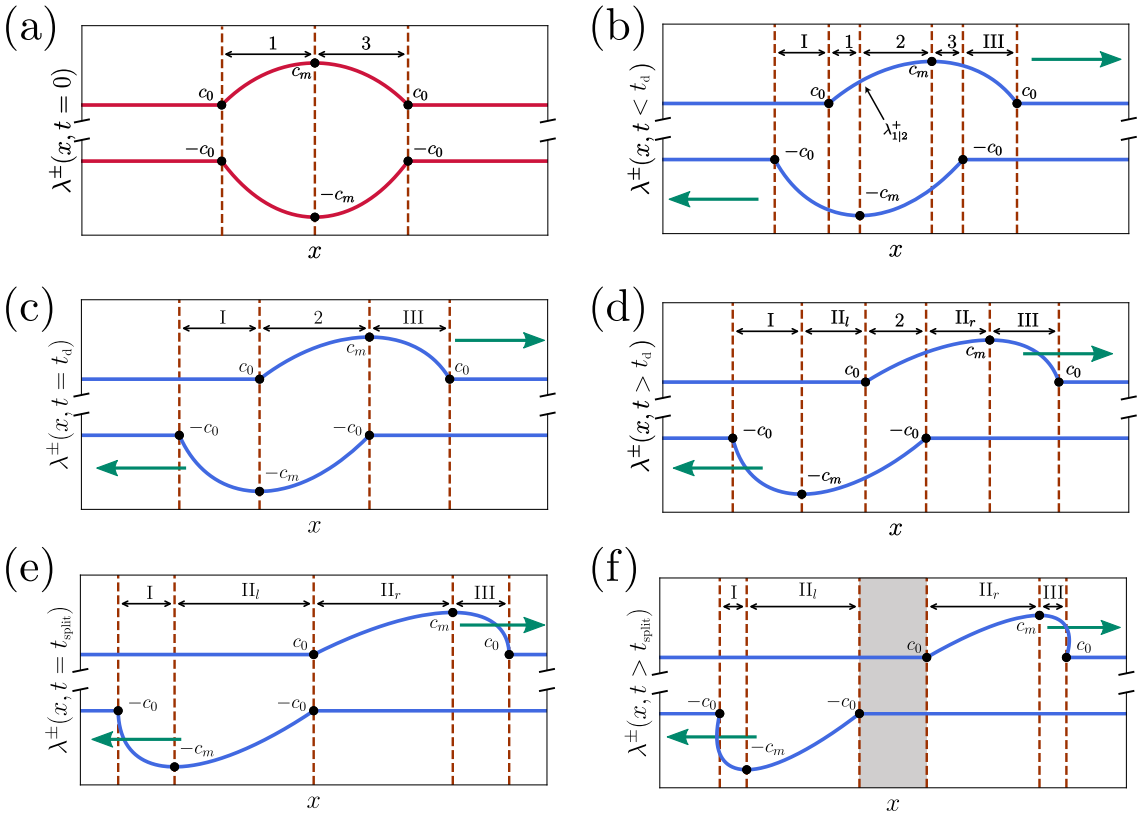

FIGURE 48: Sketch of the distributions $\lambda^{\pm}(x, t)$ at several times. In each panel the upper solid curve represents λ^+ (always larger than c_0), and the lower one λ^- (always lower than $-c_0$), both plotted as functions of x. Panel (a) corresponds to the initial distribution. Two subsequent relevant stages of evolution are represented in panels (b) and (c). For $t > 0$, λ^+ (λ^-) moves to the right (to the left) as indicated by the green arrows. This behavior initially leads to the configuration represented in panel (b) where a new region (labeled region 2) has appeared. We spot in this panel the value $\lambda^+_{1|2}(t_1)$ of the Riemann invariant λ^+ at the boundary between regions 1 and 2, as we already did in Figure 43. For longer time [panel (c)], at $t = t_d$, defined in equation (454), region 2 remains while regions 1 and 3 vanish. Then, for $t > t_d$, new simple wave regions II$_l$ and II$_r$ appear [panel (d)]. At even larger times, for $t \geq t_{split}$, where t_{split} is given by equation (455), region 2 also vanishes and only simple-wave regions remain: the initial pulse has split into two simple-wave pulses propagating in opposite directions [panels (e) and (f)].

We introduce $c_0 = \sqrt{\rho_0} = \lambda^+(x_0, 0)$ and $c_m = \sqrt{\rho_0 + \rho_1} = \lambda^+(0, 0)$. This means that $\lambda^+ \in [c_0, c_m]$ and $\lambda^- \in [-c_m, -c_0]$. The simple-wave

regions, where one of the Riemann invariants is constant, are denoted I, II_l, II_r and III (see Figure 48).

Before entering into the details, we introduce two important times t_d and t_split which define three stages during the propagation of the pulse:

- Time t_d corresponds to the vanishing of regions 1 and 3 [see graph (c) of Figure 48]. At this precise moment, $\lambda^+ = c_m$ and $\lambda^- = -c_0$. Thus, using equation (435), we obtain

$$t_\mathrm{d} = -\frac{w_+^{(2)}(c_m,-c_0) - w_-^{(2)}(c_m,-c_0)}{v_+(c_m,-c_0) - v_-(c_m,-c_0)}, \tag{454}$$

  with $w_\pm^{(2)} = \partial W^{(2)}/\partial\lambda^\pm$ and $v_\pm(\lambda^+,\lambda^-)$ given by expression (395). In the case a polytropic gas with adiabatic index $\gamma = 2$, $v_+ - v_- = \lambda^+ - \lambda^-$.

- Time t_split defines the moment for which the pulse splits into two simple-wave pulses propagating in opposite directions. This situation corresponds to the graph (e) of Figure 48. Likewise, this is also the exact point in time for which region 2 disappears and $\lambda^\pm = \pm c_0$ at the position where the pulse splits (in our case, this occurs exactly at $x = 0$, see graph (e) of Figure 48). Therefore,

$$t_\mathrm{split} = -\frac{w_+^{(2)}(c_0,-c_0) - w_-^{(2)}(c_0,-c_0)}{v_+(c_0,-c_0) - v_-(c_0,-c_0)}. \tag{455}$$

  This gives

$$t_\mathrm{split} = \frac{x_0}{c_0} + \frac{1}{4\,c_0^{5/2}}\int_{c_0}^{c_m}\sqrt{\lambda}\,[\bar{x}^{(3)}(\lambda) - \bar{x}^{(1)}(\lambda)]\mathrm{d}\lambda\,. \tag{456}$$

  For an initial profile of the form (450), $\bar{x}^{(1,3)}(\lambda)$ are given by expressions (453), and this leads to

$$t_\mathrm{split} = \frac{x_0}{c_0}\Big(1 + G(\rho_1/\rho_0)\Big)\,, \tag{457}$$

  where

$$G(X) = \frac{X}{4}\int_0^1 \frac{\sqrt{1-u}}{(1+Xu)^{1/4}}du\,. \tag{458}$$

The three stages thus corresponds to:

- $0 \le t \le t_\mathrm{d}$

  This stage of the propagation is illustrated in the graphs (a), (b) and (c) of Figure 48. The simple-wave regions, where one of the Riemann invariants is constant, are denoted I and III. As shown in graph (b) of Figure 48, region I corresponds to $\lambda^+(x \in \mathrm{I}, t) = c_0$, and region III to $\lambda^-(x \in \mathrm{III}, t) = -c_0$. Region 2 appears, exactly as it occurred in the previous section for a Gaussian pulse. Therefore, in regions 1, 2 and 3, one can safely apply the procedure

described in Section 6.2.1 where the potential $W^{(n)}$, $n \in \{1,2,3\}$ is given by expressions (431), with $\beta = \frac{1}{2}$.

For any time t, such that $0 \leq t \leq t_{\rm d}$, the boundary between region I and 1 located at a position denoted $x_{\rm I-1}$ can be found as follows: one fixes $\lambda^+ = c_0$. Then, one finds the corresponding value of $\lambda^- = \lambda^-_{c_0}$, solving equation (435) with the superscript 1. Ultimately, using equations (398), we obtain

$$x_{\rm I-1} = v_-(c_0, \lambda^-_{c_0})\, t + w^{(1)}_-(c_0, \lambda^-_{c_0}), \tag{459}$$

where $w^{(1)}_- = \partial W^{(1)}/\partial \lambda^-$.

Once $x_{\rm I-1}$ is determined, region I corresponds to $x \leq x_{\rm I-1}$, with

$$x = v_-(c_0, \lambda^-)\, t + w^{(1)}_-(c_0, \lambda^-), \quad x \in {\rm I}, \tag{460}$$

for $\lambda^- \in [\lambda^-_{c_0}, -c_0]$. The Riemann invariants in the area located at the left of region I are simply $\lambda^\pm = \pm c_0$, see graph (b) of Figure 48.

The boundary between regions 3 and III is simply determined by symmetry of the problem[12]: $x_{\rm 3-III} = -x_{\rm I-1}$, $\lambda^+({\rm 3-III}, t) = -\lambda^-_{c_0}$, and $\lambda^- = -c_0$ (see graph (b) of Figure 48). Then, region III corresponds to $x \geq x_{\rm 3-III}$, with

$$x = v_+(\lambda^+, -c_0)\, t + w^{(3)}_+(\lambda^+, -c_0), \quad x \in {\rm III}, \tag{461}$$

for $\lambda^+ \in [c_0, -\lambda^-_{c_0}]$.

At the precise time $t_{\rm d}$, when regions 1 and 3 vanish (see graph (c) of Figure 48), the boundary between I and 2, denoted $x_{\rm I-2}$, and between 2 and III, denoted $x_{\rm 2-III}$, are given by

$$\begin{aligned} x_{\rm I-2} &= v_-(c_0, -c_m)\, t + w^{(2)}_-(c_0, -c_m), \\ x_{\rm 2-III} &= v_+(c_m, -c_0)\, t + w^{(2)}_+(c_m, -c_0), \end{aligned} \tag{462}$$

that is to say $\lambda^-_{c_0} = -c_m$ in equation (459), see graph (c) of Figure 48.

- $t_{\rm d} < t < t_{\rm split}$

  This stage corresponds to the graph (d) of Figure 48. Regions I and 2 become disconnected, as well as regions 2 and III. Two new simple-wave regions denoted ${\rm II}_l$ and ${\rm II}_r$ emerge and fill the gap between the disconnected regions (see graph (d) of Figure 48).

  First, in region I and III, the determination of $x_{\rm I-2}$ and $x_{\rm 2-III}$ still holds [see equations (462)]. We denote these positions $x_{\rm I-II_l}$

12 In the case of a non-symmetric problem – corresponding to $u(x,0) \neq 0$, i.e., $\lambda^+(x,0) \neq -\lambda^-(x,0)$–, one can still use equation (435) with $\lambda^- = -c_0$ and find the corresponding value of λ^+.

and $x_{\mathrm{II_r}-\mathrm{III}}$, since they locate now the boundaries between I and II_l and between II_r and III, respectively:

$$\begin{aligned} x_{\mathrm{I}-\mathrm{II_l}} &= v_-(c_0,-c_m)\,t + w_-^{(2)}(c_0,-c_m), \\ x_{\mathrm{II_r}-\mathrm{III}} &= v_+(c_m,-c_0)\,t + w_+^{(2)}(c_m,-c_0), \end{aligned} \tag{463}$$

Then, one can use equations (460) and (461), to determine the positions associated to $\lambda^+ = c_0$, $\lambda^- \in [-c_m,-c_0]$ (region I) or $\lambda^+ \in [c_0,c_m]$, $\lambda^- = -c_0$ (region III).

Second, the boundaries between regions II_l and 2 and between 2 and II_r are determined exactly as explained above equation (459): one fixes $\lambda^+ = c_0$. Then, one finds the corresponding value of $\lambda^- = \lambda^-_{c_0}$, solving equation (435), now with the superscript 2. Using equations (398), we obtain

$$\begin{aligned} x_{\mathrm{II_l}-2} &= v_-(c_0,\lambda^-_{c_0})\,t + w_-^{(2)}(c_0,\lambda^-_{c_0}), \\ x_{2-\mathrm{II_r}} &= -x_{\mathrm{II_l}-2}. \end{aligned} \tag{464}$$

Then, for $x_{\mathrm{I}-\mathrm{II_l}} \le x \le x_{\mathrm{II_l}-2}$ (region II_l),

$$x = v_-(c_0,\lambda^-)\,t + w_-^{(2)}(c_0,\lambda^-), \quad \lambda^- \in [-c_m,\lambda^-_{c_0}], \tag{465}$$

and, for $x_{2-\mathrm{II_r}} \le x \le x_{\mathrm{II_r}-\mathrm{III}}$ (region II_r),

$$x = v_+(\lambda^+,-c_0)\,t + w_+^{(2)}(\lambda^+,-c_0), \quad \lambda^+ \in [-\lambda^-_{c_0},c_m]. \tag{466}$$

- $t \ge t_{\mathrm{split}}$

  This stage corresponds to graphs (e) and (f) of Figure 48. When $t = t_{\mathrm{split}}$, region 2 vanishes, see graph (e). The boundary between regions II_l and II_r amounts to take $t = t_{\mathrm{split}}$ and the limit $\lambda^-_{c_0} \to -c_0$ in equation (464). The other boundaries (between I and II_l and between II_r and III) are determined as explained in the previous point [see equations (463)]. Note that now all regions are simple-wave regions.

  For $t > t_{\mathrm{split}}$ [see graph (f)], one determines easily the boundaries between the different regions; the only change with respect to graph (e) is the separation between regions II_l and II_r and the emergence of the grey area where $\lambda^\pm = \pm c_0$. The boundary between this grey region and II_l still corresponds to the limit $\lambda^-_{c_0} \to -c_0$ in equation (464).

  Note the multi-valued regions at the left edge of λ^- and the right edge of λ^+ in graph (f) of Figure 48. This indicates that this graph is obtained after the wave breaking time. Here, the wake breaking thus occurs after the splitting of the initial pulse into two pulses, i.e., $t_{\mathrm{WB}} > t_{\mathrm{split}}$; this is not always the case, see below and, in particular, Figure 50.

One obtains an excellent description of the initial dispersionless stage of evolution of the pulse, as demonstrated by the very good agreement between theory and numerical simulations illustrated in Figure 49. The graphs in this figure compare at different times the theoretical density profile $\rho(x,t)$ with the one obtained by numerical integration of equation (436), taking the initial condition $u(x,0)=0$ and $\rho(x,0)$ given by (450) with $x_0=20$, $\rho_0=0.5$ and $\rho_1=1.5$. One sees that the profile is multi-valued at both edges for $t=10$ and $t=15$; this means that the gradient catastrophe already occurred, and thus $t_{\rm WB}<10$. An exact calculation will yield $t_{\rm WB}\simeq 6.3$ (see next paragraph), confirming this observation.

WAVE BREAKING TIME The wave breaking exactly occurs at the position $x_{\rm WB}=x_0$, since this position corresponds to the highest density gradient [see equation (450)]. Using (437) and the expression of $w_+^{(3)}$, obtained from $W^{(3)}$ [see equations (431)], an easy computation leads to the exact result

Remember that $\gamma=2$ and $\beta=\frac{1}{2}$.

$$t_{\rm WB}=\frac{2}{3}\left|\frac{{\rm d}\bar{x}^{(3)}}{{\rm d}\lambda}\right|_{\lambda=c_0}=\frac{2\,c_0\,x_0}{3\,\rho_1}, \tag{467}$$

where we used the expression of $\bar{x}^{(3)}(\lambda)$ given by (453).

Taking $x_0=20$, $\rho_0=0.5$ and $\rho_1=1.5$, one obtains $t_{\rm WB}\simeq 6.3$ in excellent agreement with the emergence of a multi-valued profile when using the Riemann's method.

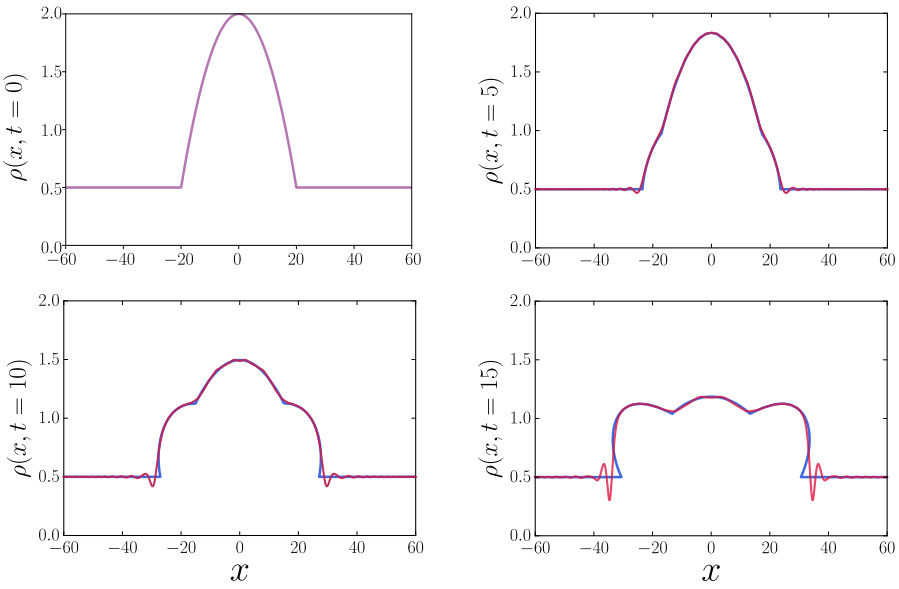

FIGURE 49: Comparison between theoretical results obtained from Riemann's method (blue curves) and numerical simulations of equation (436) (red curves) for different times of propagation $t=0$, 5, 10 and 15. The initial density distribution $\bar{\rho}(x)$ is given by expression (450).

Figure 50 displays several typical density profiles in a "phase space" with coordinates ρ_1/ρ_0 and t. The curves $t_{\rm split}(\rho_1/\rho_0)$ [as given by equations (457) and (458)] and $t_{\rm WB}(\rho_1/\rho_0)$ [equation (467)] separate this

plane in four regions, labeled as (a), (b), (c) and (d) in the figure. These two curves cross at a point represented by a white dot whose coordinates we determined numerically as being $\rho_1/\rho_0 = 0.60814$ and $c_0\, t/x_0 = 1.09623$. These coordinates are universal in the sense that they have the same value for any initial profile of inverted parabola type, such as given by equation (450), with $u(x,0) = 0$. Other types of initial profile would yield different precise arrangements of these curves in phase space, but the qualitative behavior illustrated by Figure 50 is generic. For instance, when $t_{\rm WB} < t < t_{\rm split}$, the wave breaking has already occurred while the profile is not yet split in two separated humps. This situation is represented by the inset (b). This is the situation which has been considered in Refs. [191] and [200].

The physical situation depicted in Figure 50 corresponds to physical intuition: a larger initial hump (larger ρ_1/ρ_0) experiences earlier wave breaking, and needs a longer time to be separated in two contrapropagating pulses. On the contrary, a small perturbation, with $\rho_1 \ll \rho_0$, will split much before experiencing a wave breaking. Moreover, we can learn from Figure 50 that perturbation theory always fails in describing correctly the propagation of a nonlinear pulse at large times. Indeed, any hump on top of a background ($\rho_1 > 0$), no matter how small it is, will lead to the formation of a dispersive shock wave at some finite time; this time can be very large ($t_{\rm WB} \to +\infty$, when $\rho_1 \to 0$, see Figure 50), but is never infinite.

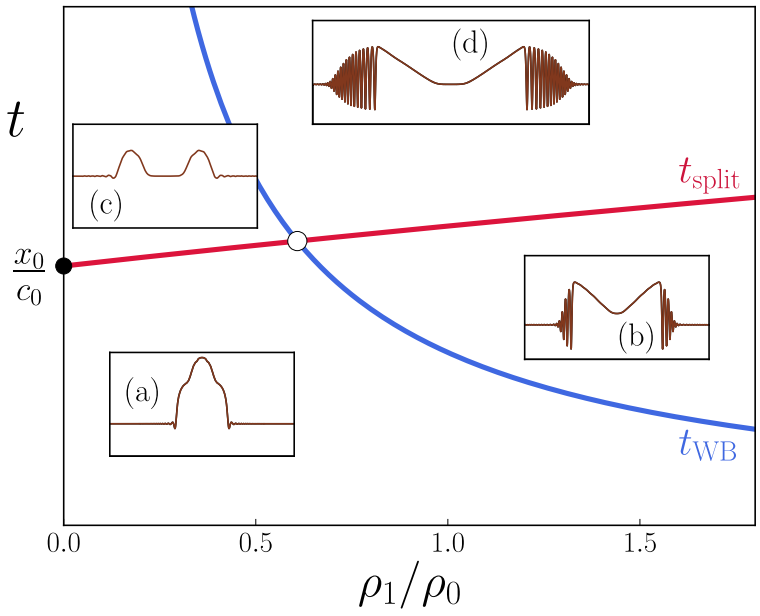

FIGURE 50: Behavior of the light intensity profile $\rho = |\psi|^2$ [see equation (436)] in the plane $(\rho_1/\rho_0, t)$. The plane is separated in four regions by the curves $t = t_{\rm WB}$ [see equation (467)] and $t = t_{\rm split}$ [see equations (457) and (458)]. These curves cross at the point represented by a white dot (of coordinates $\rho_1/\rho_0 = 0.60814$ and $c_0\, t/x_0 = 1.09623$). Typical profiles obtained numerically are displayed in the insets (a), (b), (c) and (d) which represent $\rho(x,t)$ plotted as a function of x for fixed t.

We conclude this chapter by stressing that Riemann's method is a powerful tool to describe the propagation of a pulse within a dispersionless approximation. In the case of an optical beam propagating in a medium, we have used Riemann's approach for two different initial conditions: an inverted parabola and a Gaussian beam. The latter is more realistic experimentally, but the description of the dispersive shock wave is a bit more difficult than for the inverted parabola. Indeed, as we will see in the next chapter, if one takes a Gaussian beam initially, four Riemann invariants vary concomitantly in the region of the dispersive shock wave, which renders the study quite involved. Moreover, in this case, the determination of the breaking time and of the boundary of the DSW can only be determined approximately. On the contrary, in the case of an inverted parabola, the description of the short-time propagation using Riemann's method is more tedious, since one has to worry about the emergence of simple wave regions (which do not exist for a Gaussian beam). However, the wave breaking time and the position of the dispersive shock wave can be determined exactly. In addition, only two Riemann invariants vary in the region of the dispersive shock wave. In this case, as we will see in Chapter 7, we know how to describe the dispersive shock wave using both Whitham modulational theory and the method presented in Refs. [56, 82].

6.3 ARTICLE: SHORT-DISTANCE PROPAGATION OF NONLINEAR OPTICAL PULSES

↪ Short-distance propagation of nonlinear optical pulses

M. Isoard, A.M. Kamchatnov, N. Pavloff, 22e Rencontre du Non-Linéaire, Non-Linéaire Pub (2019)

We theoretically describe the quasi one-dimensional transverse spreading of a light pulse propagating in a defocusing nonlinear optical material in the presence of a uniform background light intensity. For short propagation distances the pulse can be described within a nondispersive approximation by means of Riemann's approach. The theoretical results are in excellent agreement with numerical simulations.

Short-distance propagation of nonlinear optical pulses

Mathieu Isoard[1], A. M. Kamchatnov[2,3] & N. Pavloff[1]

[1] LPTMS, UMR 8626, CNRS, Univ. Paris-Sud, Université Paris-Saclay, 91405 Orsay, France
[2] Institute of Spectroscopy, Russian Academy of Sciences, Troitsk, Moscow, 108840, Russia
[3] Moscow Institute of Physics and Technology, Institutsky lane 9, Dolgoprudny, Moscow region, 141701, Russia
mathieu.isoard@u-psud.fr

Résumé. Nous étudions la propagation transverse d'un pulse lumineux quasi-unidimensionnel dans un milieu optique non-linéaire, en présence d'un fond d'intensité lumineuse constante. Dans un premier temps, le signal initial se divise en deux parties qui se propagent dans des directions opposées. Ce phénomène peut être décrit théoriquement à l'aide d'une approche non dispersive en utilisant une modification de la méthode de Riemann proposée par Ludford. Les résultats sont en excellent accord avec les simulations numériques.

Abstract. We theoretically describe the quasi one-dimensional transverse spreading of a light pulse propagating in a defocusing nonlinear optical material in the presence of a uniform background light intensity. For short propagation distances the pulse can be described within a nondispersive approximation by means of Riemann's approach. The theoretical results are in excellent agreement with numerical simulations.

1 Introduction

It has long been realized that light propagating in a nonlinear medium was amenable to a hydrodynamic treatment [1,2]. In the present work we use such an approach to study a model configuration which has been realized experimentally in a one-dimensional situation in the defocusing regime in Ref. [3]: the nonlinear spreading of a region of increased light intensity in the presence of a uniform constant background. In the absence of background, and for a smooth initial intensity pattern, the spreading is mainly driven by the nonlinear defocusing and can be treated analytically in some simple cases [1]. The situation is more interesting in the presence of a constant background: the pulse splits in two parts, each eventually experiencing nonlinear wave breaking, leading to the formation of dispersive shock waves at both extremities of the split pulse. In the present work we concentrate on the pre-shock period and demonstrate that it can be very accurately described within a non-dispersive nonlinear approximation.

The paper is organized as follows: In Sec. 2 we present the model and the set-up we aim at studying. The spreading and the splitting stage of evolution is accounted for in Sec. 3 within a dispersionless approximation which holds when the pulse region initially presents no large intensity gradient. The problem is first mapped onto an Euler-Poisson equation in Sec. 3.1. This equation is solved in Sec. 3.2 by using Riemann-Ludford method. In Sec. 3.3 the theoretical results are compared with numerical simulations. Our conclusions are presented in Sec. 4.

2 The model

In the paraxial approximation, the stationary propagation of the complex amplitude $A(\boldsymbol{r})$ of the electric field of a monochromatic beam is described by the equation (see, e.g., Ref. [4])

$$\mathrm{i}\partial_z A = -\frac{1}{2n_0 k_0}\boldsymbol{\nabla}_\perp^2 A - k_0 \delta n\, A\ .$$

In this equation, n_0 is the linear refractive index, $k_0 = 2\pi/\lambda_0$ is the carrier wave vector, z is the longitudinal coordinate along the beam, $\boldsymbol{\nabla}_\perp^2$ the transverse Laplacian and δn is a nonlinear contribution to the index. In a non absorbing defocusing Kerr nonlinear medium one can write $\delta n = -n_2|A|^2$, with $n_2 > 0$.

We consider a system with a uniform background light intensity, denoted as I_0, on top of which an initial pulse is added at the entrance of the nonlinear cell. To study the propagation of this pulse along the beam (direction z), we introduce the following characteristic quantities: the nonlinear length $z_{\rm NL} = (k_0 n_2 I_0)^{-1}$ and the transverse healing length $\beta_\perp = (z_{\rm NL}/n_0 k_0)^{1/2}$. Since the transverse profile depends on a single Cartesian coordinate, we write $\boldsymbol{\nabla}_\perp^2 = \beta_\perp^{-2}\partial_x^2$ where x is the dimensionless transverse coordinate, and also define an effective "time" $t = z/z_{\rm NL}$. In this framework, the quantity $\psi(x,t) = A(x,t)/\sqrt{I_0}$ is solution of the dimensionless nonlinear Schrödinger (NLS) equation

$$\mathrm{i}\,\psi_t = -\tfrac{1}{2}\psi_{xx} + |\psi|^2\psi\ . \tag{1}$$

The initial $\psi(x,t=0)$ is real (i.e., no transverse velocity or, in optical context, no focusing of the light beam at the input plane), with a dimensionless intensity $\rho(x,t) = |\psi|^2$ which departs from the constant background value (which we denote as ρ_0) only in the region near the origin where it forms a bump. To be specific, we consider the typical case where

$$\rho(x,0) = \rho_0 + \rho_1 \exp\left(-2\,x^2/x_0^2\right)\ , \quad \text{and} \quad u(x,0) = 0\ . \tag{2}$$

The maximal density of the initial profile is $\rho(0,0) = \rho_0 + \rho_1 \equiv \rho_m$.

3 The dispersionless stage of evolution

The initial pulse splits into two signals propagating in opposite directions of x axis. The aim of this section is to theoretically describe this splitting within a dispersionless approximation.

3.1 Riemann variables and Euler-Poisson equation

By means of the Madelung substitution $\psi(x,t) = \sqrt{\rho(x,t)}\exp\left(\mathrm{i}\int^x u(x',t)\,dx'\right)$, the NLS equation (1) can be cast into a hydrodynamic-like form for the density $\rho(x,t)$ and the flow velocity $u(x,t)$:

$$\rho_t + (\rho u)_x = 0\ , \quad u_t + u u_x + \rho_x + \left(\frac{\rho_x^2}{8\rho^2} - \frac{\rho_{xx}}{4\rho}\right)_x = 0\ . \tag{3}$$

These equations are to be solved with the initial conditions (2). The last term of the left hand-side of the second of Eqs. (3) accounts for the dispersive character of the fluid of light. In the first stage of spreading of the bump, if the density gradients of the initial density are weak (i.e., if $x_0 \gg \min\{\rho_0^{-1/2}, \rho_1^{-1/2}\}$), the effects of dispersion can be neglected, and the system (3) simplifies to

$$\rho_t + (\rho u)_x = 0\ , \quad u_t + u u_x + \rho_x = 0\ . \tag{4}$$

The above equations can be written in a more symmetric form by introducing the Riemann invariants

$$\lambda^\pm(x,t) = \tfrac{1}{2}u(x,t) \pm \sqrt{\rho(x,t)}\ , \tag{5}$$

which evolve according to the system [equivalent to (4)]:

$$\partial_t\lambda^\pm + v_\pm(\lambda^-,\lambda^+)\,\partial_x\lambda^\pm = 0\ , \quad \text{with} \quad v_\pm(\lambda^-,\lambda^+) = \tfrac{1}{2}(3\lambda^\pm + \lambda^\mp) = u \pm \sqrt{\rho}\ . \tag{6}$$

The Riemann velocities $v_\pm$ in (6) have a simple physical interpretation for a smooth velocity and density distribution: v_+ (v_-) corresponds to a signal which propagates downstream (upstream) at the local velocity of sound $c = \sqrt{\rho}$ and which is dragged by the background flow u.

The system (6) can be linearized by means of the hodograph transform (see, e.g., Ref. [5]) which consists in considering x and t as functions of λ^+ and λ^-. One readily obtains

$$\partial_\pm x - v_\mp \partial_\pm t = 0, \tag{7}$$

where $\partial_\pm \equiv \partial/\partial\lambda^\pm$. One introduces two auxiliary (yet unknown) functions $W_\pm(\lambda^-, \lambda^+)$ such that

$$x - v_\pm(\lambda^-, \lambda^+)\, t = W_\pm(\lambda^-, \lambda^+). \tag{8}$$

Inserting the above expressions in (7) shows that the $W_\pm$'s are solution of Tsarev equations [6]

$$\frac{\partial_- W_+}{W_+ - W_-} = \frac{\partial_- v_+}{v_+ - v_-}, \quad \text{and} \quad \frac{\partial_+ W_-}{W_+ - W_-} = \frac{\partial_+ v_-}{v_+ - v_-}. \tag{9}$$

From Eqs. (6) and (9) one can verify that $\partial_- W_+ = \partial_+ W_-$, which shows that W_+ and W_- can be sought in the form

$$W_\pm = \partial_\pm \chi, \tag{10}$$

where $\chi(\lambda^-, \lambda^+)$ plays the role of a potential. Substituting expressions (10) in one of the Tsarev equations shows that χ is a solution of the following Euler-Poisson equation

$$\frac{\partial^2 \chi}{\partial\lambda^+ \partial\lambda^-} - \frac{1}{2\,(\lambda^+ - \lambda^-)} \left(\frac{\partial \chi}{\partial \lambda^+} - \frac{\partial \chi}{\partial \lambda^-} \right) = 0\,. \tag{11}$$

3.2 Solution of the Euler-Poisson equation

We use Riemann's method (see, e.g., Ref. [7]) to solve the Euler-Poisson equation (11) in the (λ^+, λ^-)–plane which we denote below as the "characteristic plane". We follow here the procedure exposed in Ref. [8] which applies to non-monotonous initial distributions, such as the one corresponding to Eq. (2).

We first schematically depict in Fig. 1(a) the initial spatial distributions $\lambda^\pm(x, 0)$ of the Riemann invariants (left panel). The initial condition (2) yields $\lambda^\pm(x, 0) = \pm\sqrt{\rho(x, 0)}$. A later stage of evolution is shown in the right panel of Fig. 1. We introduce notations for some remarkable values of the Riemann invariants: $\lambda^\pm(-\infty, t) = \lambda^\pm(\infty, t) = \pm\sqrt{\rho_0} \equiv \pm c_0$ and $\lambda^\pm(0, 0) = \pm\sqrt{\rho_m} \equiv \pm c_m$. We also define as part A (part B) the branch of the distribution of the $\lambda^\pm$'s which is at the right (at the left) of the extremum $\pm c_m$. These notations are summarized in Fig. 1(a).

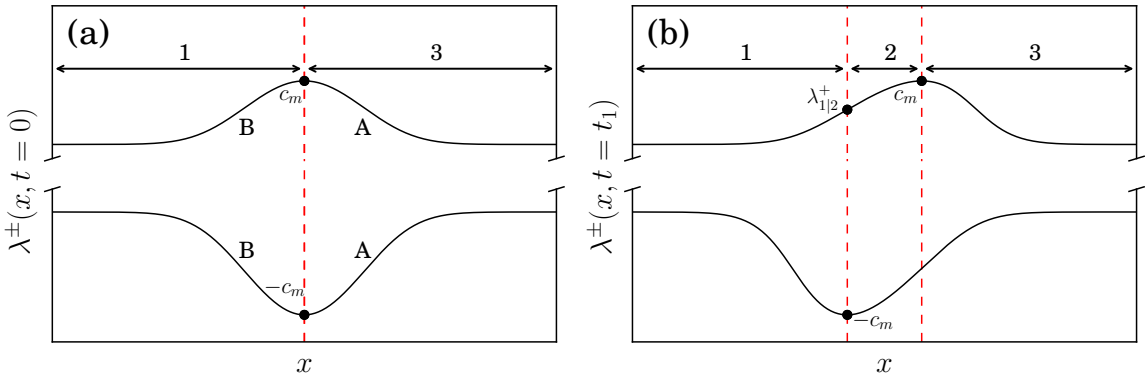

Figure 1. Sketch of the distributions $\lambda^\pm(x, t)$ at time $t = 0$ (left panel) and at finite time $t > 0$ (right panel). In each panel the upper solid curve represent λ^+ (always larger than c_0), and the lower one λ^- (always lower than $-c_0$). Panel (a) corresponds to the initial distribution, in which part B corresponds to region 1 and part A to region 3 (see the text). For $t > 0$, λ^+ (λ^-) moves to the right (to the left) and part B of λ^+ starts to overlap with part A of λ^-. This leads to the configuration represented in panel (b) where a new region (labeled region 2) has appeared. For later convenience, the value $\lambda^+_{1|2}(t_1)$ is added in this panel. It corresponds to the value of λ^+ at the boundary between regions 1 and 2 (see the discussion in Sec. 3.3).

At a given finite time, the x axis can be considered as divided in three domains, each requiring a specific treatment. Each domain is characterized by the behavior of the Riemann invariants. In domain

3 (domain 1 respectively), λ^+ is decreasing (increasing) while λ^- is increasing (decreasing); in domain 2 both are increasing, see Fig. 1(b). The theoretical description of this nonlinear wave is challenging because in each regions *both* Riemann invariants (λ^+ and λ^-) depend on position (i.e., there is no simple wave region).

The values of the Riemann invariants corresponding to Fig. 1(b) are represented in the characteristic plane in Fig. 2(a). The red curve $\mathcal{C}^0$ in Figs. 2(a) and (b) corresponds to the initial conditions depicted in Fig. 1(a). Since $\lambda^+(x,0) = -\lambda^-(x,0)$, the curve $\mathcal{C}^0$ lies along the anti-diagonal in the characteristic plane. The (blue) curvy lines correspond to regions where both Riemann invariants depend on position: the domains 1, 2 and 3. In each of these three domains the solution χ of the Euler-Poisson equation has a different expression. In order to describe these three branches, following Ludford [8], we introduce several sheets in the characteristic plane by unfolding the domain $[c_0, c_m] \times [-c_m, -c_0]$ into a four times larger region as illustrated in Fig. 2(b). We remark here that the whole region above $\mathcal{C}^0$ — shaded in Fig. 2(b) — is unreachable for the initial distribution we consider: for instance, the upper shaded triangle in region 1 would correspond to a configuration in which $\lambda^+_{\text{region1}}(x,t) > |\lambda^-_{\text{region1}}(x,t)|$, which does not occur in our case, see Fig. 1(b). The potential $\chi(\lambda^-, \lambda^+)$ can now take a different form in each of the regions labeled as 1, 2 and 3 in Fig. 2(b) and still be considered as single-valued. In each of the three domains, we use Riemann-Ludford method to solve Eq. (11). This yields, to a very good approximation (a thorough analysis can be found in Ref. [9])

$$\chi^{(n)}(\lambda^-, \lambda^+) = \frac{\sqrt{2}}{\sqrt{\lambda^+ - \lambda^-}} \int_{-\lambda^-}^{\lambda^+} \sqrt{r}\; w^{\mathrm{A/B}}(r)\, dr \;, \tag{12}$$

for regions $n = 1$ and 3. In the above formula, the superscript A should be used when $n = 3$, and the superscript B when $n = 1$, and w^{A} (w^{B}) is the inverse function of the initial λ profiles in part A (part B). For the initial condition (2) one has

$$x = w^{\mathrm{A/B}}(\lambda) = \pm x_0 \sqrt{-\frac{1}{2} \ln \frac{\lambda^2 - \rho_0}{\rho_1}} \quad \text{if } \; x \gtrless 0 \;.$$

In region 2, the formulae (12) are replaced by

$$\chi^{(2)}(\lambda^-, \lambda^+) = \frac{\sqrt{2}}{\sqrt{\lambda^+ - \lambda^-}} \left(\int_{c_m}^{\lambda^+} \sqrt{r}\, w^{\mathrm{B}}(r)\, dr + \int_{-\lambda^-}^{c_m} \sqrt{r}\, w^{\mathrm{A}}(r)\, dr \right) \;. \tag{13}$$

3.3 Results and comparison with numerical simulations

Once $\chi^{(n)}(\lambda^-, \lambda^+)$ has been determined in each of the three regions ($n = 1$, 2 or 3), the problem is solved. One first computes $W^{(n)}_{\pm}(\lambda^-, \lambda^+)$ in each region from Eqs. (10), (12) and (13). Then, the procedure to obtain the values of λ^+ and λ^- as functions of x and t is the following:

• One starts by determining the value of λ^+ for which $\lambda^- = -c_m$ at time t. This value of λ^+ defines the boundary between regions 1 and 2. We denoted it as $\lambda^+_{1|2}(t)$; it is represented in Fig. 1(b). From Eqs. (8), $\lambda^+_{1|2}(t)$ is a solution of

$$\frac{W^{(1)}_+(-c_m, \lambda^+_{1|2}) - W^{(1)}_-(-c_m, \lambda^+_{1|2})}{v_+(-c_m, \lambda^+_{1|2}) - v_-(-c_m, \lambda^+_{1|2})} + t = 0 \;. \tag{14}$$

We then know that, in region 1 at time t, λ^+ takes all possible values between c_0 and $\lambda^+_{1|2}(t)$.

• One picks a value of λ^+ in $[c_0, c_m]$. From Eqs. (8), λ^- is then solution of

$$\frac{W^{(n)}_+(\lambda^-, \lambda^+) - W^{(n)}_-(\lambda^-, \lambda^+)}{v_+(\lambda^-, \lambda^+) - v_-(\lambda^-, \lambda^+)} + t = 0 \;, \tag{15}$$

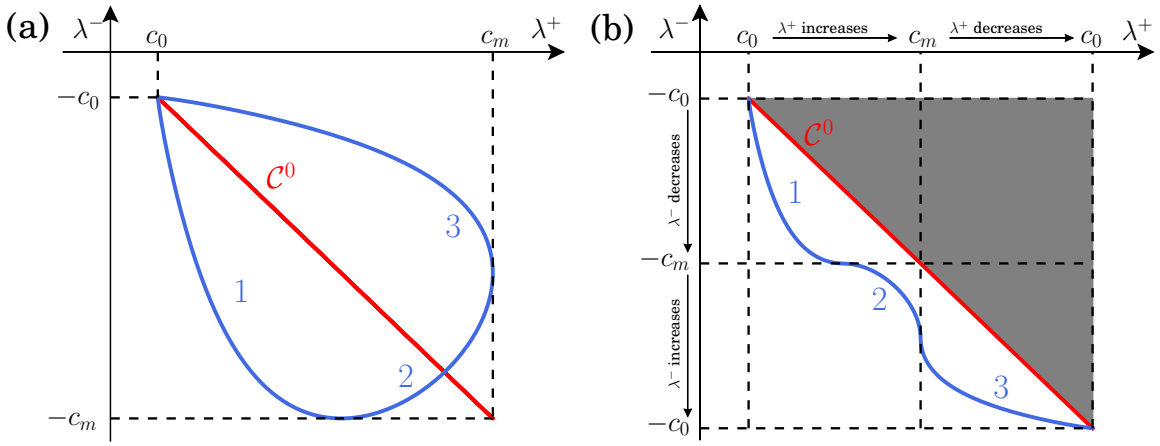

Figure 2. (a) Behavior of the Riemann invariants in the characteristic plane at a given time t (blue curve). The red curve $\mathcal{C}^0$ corresponds to the initial condition $[\lambda^-(x,0) = -\lambda^+(x,0)]$. (b) The same curves in the four-sheeted unfolded surface. In our problem, the whole gray shaded domain above $\mathcal{C}^0$ is unreachable.

with $n = 1$ if $\lambda^+ \in [c_0, \lambda^+_{1|2}(t)]$ and $n = 2$ if $\lambda^+ \in [\lambda^+_{1|2}(t), c_m]$. This determines the value of the Riemann invariants in regions 1 and 2. In region 3 one uses the symmetry of the problem and writes $\lambda^\pm(x,t) = -\lambda^\mp(-x,t)$, see Fig. 1(b).

• At this point, for each value of t and λ^+ we know the value of the other Riemann invariant λ^-. The position x is then simply obtained by either one of Eqs. (8). So, for given t and λ^+ in region n, one has determined the values of λ^- and x. In practice, this makes it possible to associate a couple (λ^-, λ^+) to each (x,t). The density and velocity profiles are then obtained through Eqs. (5).

The results of the above approach are compared in Fig. 3 with the numerical solution of Eq. (1), taking the initial condition given by Eq. (2) with $\rho_0 = 0.5$, $\rho_1 = 1.5$ and $x_0 = 20$. One reaches an excellent agreement for the density profile and also for the velocity profile (not shown in the figure) up to $t \simeq 20$. As time increases, the profile steepens and oscillations become visible at both ends of the pulse at $t \gtrsim 16$. There exists a certain time, the wave breaking time $t_{\rm WB}$, at which nonlinear nondispersive spreading leads to a gradient catastrophe; our approximation subsequently predicts a nonphysical multivalued profile, as can be seen in Fig. 3 (for $t > 20$). The time $t_{\rm WB}$ can be computed by noticing that the wave breaking occurs for the value $\lambda^+_{\rm WB} = (\rho_0 + \rho_1/\sqrt{e}\,)^{1/2}$ which is associated in the initial profile with the largest gradient in $\partial_x \rho$. At the wave-breaking time the profile of λ^+ in region 3 has a vertical tangent line: $\partial x/\partial \lambda^+ = 0$. For simplicity we also assume that the wave breaking occurs in a region where one can safely approximate $\lambda^- = -c_0$. Differentiation of (7) then yields

$$t_{\rm WB} = \frac{2}{3}\left|\frac{dW^{(3)}_+(-c_0,\lambda^+)}{d\lambda^+}\right|_{\lambda^+_{\rm WB}} = \left|\frac{\int_{c_0}^{\lambda^+}\sqrt{r}w^{\rm A}(r)dr}{\sqrt{2}(\lambda^+ + c_0)^{5/2}} + \frac{\sqrt{2}(c_0-\lambda^+)w^{\rm A}(\lambda^+)}{3\sqrt{\lambda^+}(\lambda^+ + c_0)^{3/2}} + \frac{2}{3}\sqrt{\frac{2\lambda^+}{\lambda^+ + c_0}}\frac{dw^{\rm A}}{d\lambda^+}\right|_{\lambda^+_{\rm WB}} . \quad (16)$$

The numerical value of $t_{\rm WB}$ is found to be $\simeq 19.15$ for our choice of initial condition, in good agreement with numerical simulations. Note also that for a small bump ($\rho_1 \ll \rho_0$) the wave breaking time becomes very large. From (16), and for an initial profile of type (2), one gets at leading order in ρ_1/ρ_0:

$$t_{\rm WB} \simeq \frac{2\sqrt{e}}{3}\frac{x_0}{c_0}\left(\frac{\rho_0}{\rho_1}\right) . \quad (17)$$

This means that the breaking time is much greater than the time $\sim x_0/c_0$ of propagation of sound along the pulse profile. In our optical system the wave breaking is regularized by the formation of a dispersive

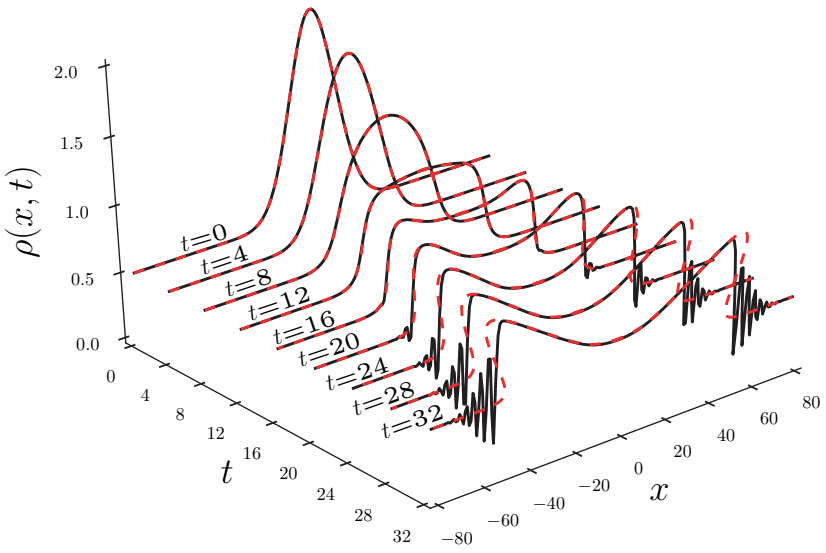

Figure 3. Density profile $\rho(x,t)$ corresponding to the initial conditions (2) with $\rho_0 = 0.5$, $\rho_1 = 1.5$ and $x_0 = 20$. The red dashed line corresponds to the exact solution of the dispersionless system (6) (see the text), while the black curve displays the density obtained from the numerical solution of Eq. (1).

shock wave which is a region with large oscillations of intensity and phase, whose extend increases with time, as can be seen in Fig. 3. Its description requires a nonlinear treatment able to account for dispersive effects and this goes beyond te scope of the present letter (see, e.g., Ref. [9]).

4 Conclusion

In this work we demonstrate that a nondispersive hydrodynamic approach to the spreading and splitting of an optical pulse compares extremely well with the results of numerical simulations up to the wave breaking time. At larger time, one observes the formation of an optical dispersive shock wave, which can be studied within Whitham modulation theory. In the case of the initial distribution given by Eq. (2), the shock should be described by four varying Riemann invariants and this requires a thorough investigation. Work in this direction is in progress.

References

1. V. I. Talanov, Radiophys. **9**, 138 (1965).
2. S. A. Akhmanov, A. P. Sukhorukov and R. V. Khokhlov, Usp. Fiz. Nauk **93**, 19 (1967).
3. W. Wan, S. Jia, and J. W. Fleischer, Nature Phys. **3**, 46 (2007).
4. L. D. Landau and E. M. Lifshitz, *Electrodynamics of Continuous Media*, Course of Theoretical Physics vol. 8 (Elsevier Butterworth-Heinemann, Oxford, 2006).
5. A. M. Kamchatnov, *Nonlinear Periodic Waves and Their Modulations—An Introductory Course*, (World Scientific, Singapore, 2000).
6. S. P. Tsarev, Math. USSR Izv. **37**, 397 (1991).
7. A. Sommerfeld, *Partial Differential Equations in Physics*, (Lectures on Theoretical Physics volume VI) (Academic Press, New York, 1964).
8. G. S. S. Ludford, Proc. Camb. Phil. Soc. **48**, 499 (1952).
9. M. Isoard, A.M. Kamchatnov, N. Pavloff, arXiv:1902.06975 [nlin.PS] (2019).

6.4 ARTICLE: DISPERSIONLESS EVOLUTION OF INVISCID NONLINEAR PULSES

↪ Dispersionless evolution of inviscid nonlinear pulses

M. Isoard, A.M. Kamchatnov, N. Pavloff, EPL **129**, 64003 (2020)

doi: https://doi.org/10.1209/0295-5075/129/64003

We consider the one-dimensional dynamics of nonlinear non-dispersive waves. The problem can be mapped onto a linear one by means of the hodograph transform. We propose an approximate scheme for solving the corresponding Euler-Poisson equation which is valid for any kind of nonlinearity. The approach is exact for monoatomic classical gas and agrees very well with exact results and numerical simulations for other systems. We also provide a simple and accurate determination of the wave breaking time for typical initial conditions.

A Letters Journal Exploring the Frontiers of Physics

March 2020

EPL, **129** (2020) 64003
doi: 10.1209/0295-5075/129/64003

www.epljournal.org

Dispersionless evolution of inviscid nonlinear pulses

M. Isoard[1], A. M. Kamchatnov[2,3] and N. Pavloff[1]

[1] *Université Paris-Saclay, CNRS, LPTMS - 91405 Orsay, France*
[2] *Institute of Spectroscopy, Russian Academy of Sciences - Troitsk, Moscow, 108840, Russia*
[3] *Moscow Institute of Physics and Technology - Institutsky lane 9, Dolgoprudny, Moscow region, 141701, Russia*

received 8 December 2019; accepted in final form 13 April 2020
published online 27 April 2020

PACS 47.40.-x – Compressible flows; shock waves
PACS 42.65.Sf – Dynamics of nonlinear optical systems; optical instabilities, optical chaos and complexity, and optical spatio-temporal dynamics
PACS 02.30.Jr – Partial differential equations

Abstract – We consider the one-dimensional dynamics of nonlinear non-dispersive waves. The problem can be mapped onto a linear one by means of the hodograph transform. We propose an approximate scheme for solving the corresponding Euler-Poisson equation which is valid for any kind of nonlinearity. The approach is exact for monoatomic classical gas and agrees very well with exact results and numerical simulations for other systems. We also provide a simple and accurate determination of the wave breaking time for typical initial conditions.

Introduction. – In the long wavelength limit, many physical models lead, in the one-dimensional regime, to equations of wave propagation equivalent to the equations of inviscid gas dynamics

$$\rho_t + (\rho u)_x = 0, \qquad u_t + u u_x + \frac{c^2}{\rho}\rho_x = 0, \tag{1}$$

where u is interpreted as a local "flow velocity", and $c = c(\rho)$ has a meaning of a local "sound velocity" which depends on a local "density" ρ. These nonlinear equations were studied very intensively in the framework of gas dynamics (see, *e.g.*, ref. [1]) and a number of exact solutions have been obtained for various problems in the particular case of polytropic gases for which, up to a normalization constant which can be rescaled to unity,

$$c(\rho) = \rho^{(\gamma-1)/2}, \tag{2}$$

where γ is the adiabatic index ($\gamma > 1$). However, even in this apparently simple case, the solutions become quite complicated if the parameter

$$\beta = \frac{3-\gamma}{2(\gamma-1)} \tag{3}$$

is not an integer number. This difficulty is encountered for instance in the study of the evolution of a nonlinear pulse with initial density and velocity distributions

$$\rho(x,0) = \overline{\rho}(x), \qquad u(x,0) = 0, \tag{4}$$

where $\overline{\rho}$ is a specified function of x; see, *e.g.*, the solution of the problems pulse evolution in optical systems with Kerr nonlinearity [2] or of collision of two rarefaction waves in the dynamics of a Bose-Einstein condensed system [3], for which $\gamma = 2$ (and $\beta = 1/2$).

In refs. [4,5] it was noticed that for the case $\gamma = 2$ one can obtain a very accurate and simple *approximate* solution of the problem of evolution of the pulse (4). The aim of the present paper is to generalize this approach to arbitrary dependence $c = c(\rho)$. We first present the hodograph transform which maps the nonlinear system onto a linear Euler-Poisson equation which can be solved by Riemann's method. We then propose an approximate expression for the Riemann function which leads to a simple solution of the problem. The approach is discussed and compared with numerical simulations. We also discuss an approximate determination of the time of shock formation in the system.

Hodograph transform and Riemann method. – The term in ρ_x in (1) being positive, the system is hyperbolic. It can be cast to a diagonal form by introducing the Riemann invariants

$$r_\pm(x,t) = \frac{1}{2}u(x,t) \pm \frac{1}{2}\int_0^{\rho(x,t)} \frac{c(\rho')\mathrm{d}\rho'}{\rho'}. \tag{5}$$

r_+ and r_- obey dynamical equations equivalent to (1) which take the form

$$\frac{\partial r_\pm}{\partial t} + v_\pm \frac{\partial r_\pm}{\partial x} = 0, \tag{6}$$

where

$$v_\pm = u \pm c \tag{7}$$

can be expressed in terms of the Riemann invariants. Indeed, it follows from eq. (5) that the physical variables u and c can be written as

$$u = r_+ + r_-, \qquad c = c(r_+ - r_-), \tag{8}$$

where the expression of c as a function of $r_+ - r_-$ is obtained by inverting the relation[1]

$$r_+ - r_- = \int_0^\rho \frac{c(\rho')\mathrm{d}\rho'}{\rho'} \tag{9}$$

and substituting $\rho(r_+ - r_-)$ into $c = c(\rho)$. Then, the velocities $v_\pm$ in eq. (7) can be considered as known functions of r_+ and r_-:

$$v_\pm(r_+, r_-) = r_+ + r_- \pm c(r_+ - r_-). \tag{10}$$

Equations (6) can be linearized by the hodograph transform (see, *e.g.*, refs. [1,6]). This consists in considering x and t as functions of the independent variables $r_\pm$ and leads to the following system of linear equations:

$$\begin{aligned} \frac{\partial x}{\partial r_+} - v_-(r_+, r_-)\frac{\partial t}{\partial r_+} = 0, \\ \frac{\partial x}{\partial r_-} - v_+(r_+, r_-)\frac{\partial t}{\partial r_-} = 0. \end{aligned} \tag{11}$$

We look for the solutions of these equations in the form

$$\begin{aligned} x - v_+(r_+, r_-)t = w_+(r_+, r_-), \\ x - v_-(r_+, r_-)t = w_-(r_+, r_-). \end{aligned} \tag{12}$$

A simple test of consistency shows that the unknown functions $w_\pm(r_+, r_-)$ should verify the Tsarev equations [7]

$$\begin{aligned} \frac{1}{w_+ - w_-}\frac{\partial w_+}{\partial r_-} = \frac{1}{v_+ - v_-}\frac{\partial v_+}{\partial r_-}, \\ \frac{1}{w_+ - w_-}\frac{\partial w_-}{\partial r_+} = \frac{1}{v_+ - v_-}\frac{\partial v_-}{\partial r_+}. \end{aligned} \tag{13}$$

Now we notice that since the velocities $v_\pm$ are given by expressions (10), the right-hand sides of both eqs. (13) are equal to each other:

$$\frac{1}{v_+ - v_-}\frac{\partial v_+}{\partial r_-} = \frac{1}{v_+ - v_-}\frac{\partial v_-}{\partial r_+} = \frac{1 - c'(r_+ - r_-)}{2\,c(r_+ - r_-)}, \tag{14}$$

[1] The dependence of c on $r_+ - r_-$ is different from its dependence on ρ. In the following, we always specify the argument of c to avoid confusion.

where $c'(r) \equiv \mathrm{d}c(r)/\mathrm{d}r$. Consequently $\partial w_+/\partial r_- = \partial w_-/\partial r_+$ and $w_\pm$ can be sought in the form

$$w_\pm = \frac{\partial W}{\partial r_\pm}. \tag{15}$$

Substitution of eqs. (14) and (15) into eqs. (13) shows that the function W obeys the Euler-Poisson equation

$$\frac{\partial^2 W}{\partial r_+ \partial r_-} - \frac{1 - c'(r_+ - r_-)}{2c(r_+ - r_-)}\left(\frac{\partial W}{\partial r_+} - \frac{\partial W}{\partial r_-}\right) = 0. \tag{16}$$

A formal solution of eq. (16) in the (r_+, r_-) plane (the so-called hodograph plane) can be obtained with the use of the Riemann method (see, *e.g.*, ref. [8]). We introduce the notation

$$a(r_+, r_-) = \frac{c'(r_+ - r_-) - 1}{2c(r_+ - r_-)} = -b(r_+, r_-), \tag{17}$$

and the so-called Riemann function $R(r_+, r_-; \xi, \eta)$ which satisfies an equation conjugate to (16)

$$\frac{\partial^2 R}{\partial r_+ \partial r_-} - \frac{\partial (aR)}{\partial r_+} - \frac{\partial (bR)}{\partial r_-} = 0, \tag{18}$$

with the boundary conditions:

$$\begin{aligned} &\frac{\partial R}{\partial r_+} - bR = 0 \quad \text{along the characteristic} \quad r_- = \eta, \\ &\frac{\partial R}{\partial r_-} - aR = 0 \quad \text{along the characteristic} \quad r_+ = \xi, \end{aligned} \tag{19}$$

and

$$R(\xi, \eta; \xi, \eta) = 1. \tag{20}$$

Then, at a point P with coordinates (ξ, η) of the hodograph plane, W can be expressed as

$$W(P) = \frac{1}{2}(RW)_A + \frac{1}{2}(RW)_B - \int_A^B (V\,\mathrm{d}r_+ + U\,\mathrm{d}r_-), \tag{21}$$

where

$$\begin{aligned} U = \frac{1}{2}\left(R\frac{\partial W}{\partial r_-} - W\frac{\partial R}{\partial r_-}\right) + aRW, \\ V = \frac{1}{2}\left(W\frac{\partial R}{\partial r_+} - R\frac{\partial W}{\partial r_+}\right) - bRW. \end{aligned} \tag{22}$$

We use here doubled notation for the coordinates in the hodograph plane: (ξ, η) and (r_+, r_-). $P = (\xi, \eta)$ is the "observation" point and the integral in (21) is taken over the curve $\mathcal{C}$ of the initial data in this plane which has parametric equation $(r_+(x, 0), r_-(x, 0))$. The points A and B are projections of P onto $\mathcal{C}$ along the r_+- and r_--axis, respectively. The advantage of the expression (21) is that it gives the value of W at P in terms of its values (and of the one of its derivatives) along the curve $\mathcal{C}$ of initial conditions.

Once the Riemann function R has been determined, eq. (21) gives the solution of the problem under consideration.

Approximate solution. – We now proceed and consider the specific problem formulated in the introduction. To simplify the discussion we assume that the initial distribution $\overline{\rho}(x)$ reaches an extremum at $x = 0$ and is an even function of x: $\overline{\rho}(-x) = \overline{\rho}(x)$. The generalization to non-symmetric distributions is straightforward.

First of all, we have to understand how the initial profile (4) fixes the boundary conditions for W on curve $\mathcal{C}$ in the hodograph plane. To this end, we compute the initial distribution of the Riemann invariant r_+ for positive x at $t = 0$:

$$\overline{r}(x) \equiv r_+(x > 0, t = 0) = \frac{1}{2}\int_0^{\overline{\rho}(x)} \frac{c(\rho)\mathrm{d}\rho}{\rho}. \tag{23}$$

Denoting as $\overline{x}(r)$ the reciprocal function, we obtain for the value of x on the curve $\mathcal{C}$:

$$x = \begin{cases} \overline{x}(r), & \text{if } x > 0, \\ -\overline{x}(r), & \text{if } x < 0. \end{cases} \tag{24}$$

Besides that, since at $t = 0$ the values $r_+ = \overline{r}$ and $r_- = -\overline{r}$ correspond to the same value of x, we find that $\overline{x}(r)$ is an even function, $\overline{x}(-r) = \overline{x}(r)$. As an illustration, for an initial profile of the form

$$\overline{\rho}(x) = \rho_0 + \rho_1 \exp(-x^2/x_0^2) \tag{25}$$

(with ρ_0 and $\rho_1 > 0$), one obtains in the case of a polytropic gas (2):

$$\overline{x}(r) = x_0\sqrt{\ln\rho_1 - \ln\left[\left|(\gamma-1)\,r\right|^{\frac{2}{\gamma-1}} - \rho_0\right]}. \tag{26}$$

For such a "single-bump" type of initial conditions which we consider, there exist two values $r_m = \overline{r}(0)$ and $r_0 = \overline{r}(x \to \infty)$ ($r_m > r_0 > 0$) such that $r_+(x,t) \in [r_0, r_m]$ and $r_-(x,t) \in [-r_m, -r_0]$. At a given time t, the space can be separated in three different regions 1, 2 and 3, depending on the values of $\partial r_\pm/\partial x$, as illustrated in fig. 1. In each region both r_+ and r_- vary concomitantly, and this is the reason why we have to resort to Riemann's method[2]. For determining the value of W in each of the three regions 1, 2 and 3, we follow Ludford [9] and unfold the hodograph plane into three sheets as illustrated in fig. 2(b).

For the specific initial condition (4), the curve $\mathcal{C}$ is represented by the anti-diagonal ($r_- = -r_+$) and the points A and B of eq. (21) have coordinates $A(-\eta, \eta)$ and $B(\xi, -\xi)$. Equations (12) with $t = 0$ give

$$\left.\frac{\partial W}{\partial r_+}\right|_{\mathcal{C}} = \left.\frac{\partial W}{\partial r_-}\right|_{\mathcal{C}} = x.$$

This implies that W keeps a constant value along $\mathcal{C}$. The value of this constant is immaterial, we take $W|_{\mathcal{C}} = 0$ for simplicity, and eqs. (22) then reduce to

$$U = \frac{x}{2}R(r, -r; \xi, \eta), \qquad V = -\frac{x}{2}R(r, -r; \xi, \eta). \tag{27}$$

We thus obtain from (21) $W = \int_{-\eta}^{\xi} xR\mathrm{d}r$ which gives in regions 1 and 3 the explicit expressions

$$W^{(1,3)}(\xi, \eta) = \mp\int_{-\eta}^{\xi} \overline{x}(r)R(r, -r; \xi, \eta)\mathrm{d}r, \tag{28}$$

where the sign $-$ ($+$) applies in region 1 (3). The difference in signs comes from the fact that $x = \mp\overline{x}(r)$ depending on if one is in region 1 or 3 (see eq. (24)).

When P is in region 2 one applies formula (21) with an integration path different from the one used in regions 1 and 3, see fig. 2. Upon integrating by parts one obtains

$$\begin{aligned} W^{(2)}(P) = &\left(RW^{(1)}\right)_{B_2} + \left(RW^{(3)}\right)_{A_2} \\ &+ \int_{A_2}^{C}\left(\frac{\partial R}{\partial r_-} - aR\right)_{r_+=r_m} W^{(3)}\mathrm{d}r_- \\ &- \int_{C}^{B_2}\left(\frac{\partial R}{\partial r_+} - bR\right)_{r_-=-r_m} W^{(1)}\mathrm{d}r_+, \end{aligned} \tag{29}$$

where the coordinates of the relevant points are: $A_2(r_m, \eta)$, $B_2(\xi, -r_m)$ and $C(r_m, -r_m)$ (see fig. 2).

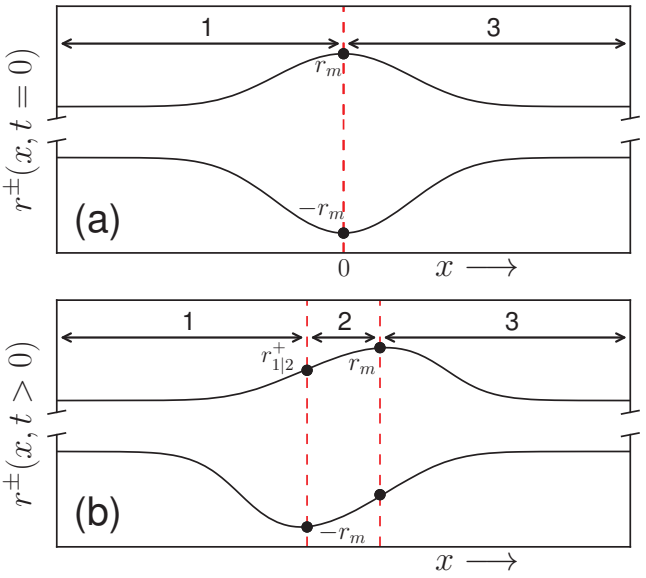

Fig. 1: Sketch of the distributions $r^{\pm}(x,t)$ at time $t = 0$ (a) and at finite time $t > 0$ (b). In each panel the upper solid curve represents r^+ (always larger than r_0), and the lower one r^- (always lower than $-r_0$). For $t > 0$, r^+ (r^-) moves to the right (to the left) and regions 1 and 3 start to overlap. This leads to the configuration represented in panel (b) where a new region (labeled region 2) has appeared. The value of r^+ at the interface between regions 1 and 2 is denoted as $r^+_{1|2}$.

[2]We note that for some initial conditions there might also exist simple-wave regions which cannot be tackled by the Riemann method. The density and velocity profiles in such regions are easily described (see the case studied in ref. [4]) and we do not consider here their possible occurrence so as not to burden the discussion.

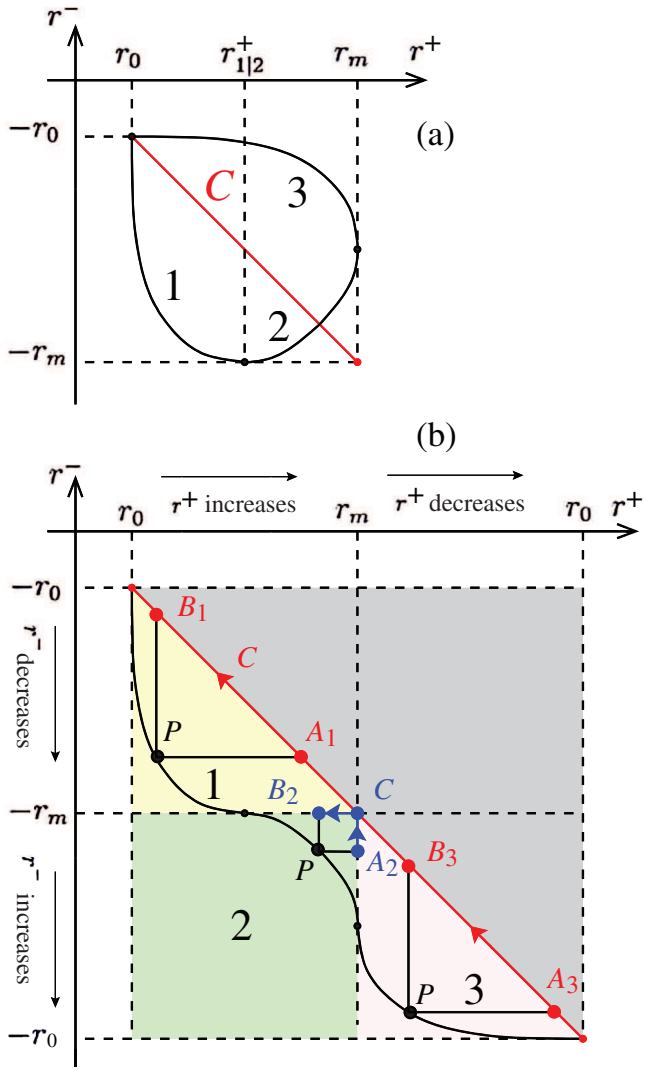

Fig. 2: (a) Behavior of the Riemann invariants in the characteristic plane at a given time t. The red straight line is the curve $\mathcal{C}$. The black solid line is the curve with parametric equation $(r_+(x,t), r_-(x,t))$. (b) The same curves on the four-sheeted unfolded surface. The colored regions 1, 2 and 3 are the same as the ones identified in fig. 1. In our problem, the whole gray shaded domain above $\mathcal{C}$ is unreachable. A generic point P of has coordinates (ξ, η) and points A_1, B_1, A_3, B_3 and C lie on the initial curve $\mathcal{C}$. Points A_2 and B_2 lie on a boundary between two regions. The arrows indicate the direction of integration in eqs. (21) and (29).

For small enough time of evolution, ξ is close to r_m and η is close to $-r_m$, the integrand functions in eq. (29) are then small by virtue of eqs. (19). A simple approximation thus consists in keeping only the two first terms in the right-hand side of (29).

It now remains to determine the Riemann function R for computing expression (28) of W in regions 1 and 3 and completely solving the problem. One first remarks that the conditions (19) and (20) yield

$$\begin{aligned} R(r_+,\eta;\xi,\eta) &= \sqrt{\frac{c(\xi-\eta)}{c(r_+-\eta)}}\exp\left(\int_{\xi-\eta}^{r_+-\eta}\frac{\mathrm{d}r}{2\,c(r)}\right), \\ R(\xi,r_-;\xi,\eta) &= \sqrt{\frac{c(\xi-\eta)}{c(\xi-r_-)}}\exp\left(\int_{\xi-\eta}^{\xi-r_-}\frac{\mathrm{d}r}{2\,c(r)}\right). \end{aligned} \tag{30}$$

These expressions suggest that R can be sought in the form

$$R(r_+,r_-;\xi,\eta) = \mathscr{R}(r_+-r_-,\xi-\eta)F(r_+,r_-;\xi,\eta), \tag{31}$$

where $F(r_+,\eta;\xi,\eta) = 1 = F(\xi,r_-;\xi,\eta)$ and

$$\begin{aligned} \mathscr{R}(r_1,r_2) &= \sqrt{\frac{c(r_2)}{c(r_1)}}\exp\left(\int_{r_2}^{r_1}\frac{\mathrm{d}r}{2\,c(r)}\right) \\ &= \sqrt{\frac{c(r_2)\rho(r_1)}{c(r_1)\rho(r_2)}}. \end{aligned} \tag{32}$$

The final expression in the above formula has been obtained by means of a change of variable $\rho = \rho(r)$ in the integral, where the function $\rho(r)$ is the reciprocal function of $r(\rho)$ given in (9)

$$r(\rho) = \int_0^\rho \frac{c(\rho')\mathrm{d}\rho'}{\rho'}, \tag{33}$$

and $c(r) = c(\rho(r))$, so that $\mathrm{d}r/c(r) = \mathrm{d}\rho/\rho$.

We note here that the approximation previously used for discarding the integrated terms in the right-hand side of eq. (29) amounts to assume that $F \simeq 1$. Similarly, in expression (28) for $W^{(1)}$ and $W^{(3)}$, since at short time $-\eta$ and ξ are close, the integration variable r is close to ξ and one can again assume that $F \simeq 1$. That is to say, we are led to make in the whole hodograph plane the approximation

$$R(r_+,r_-;\xi,\eta) \simeq \mathscr{R}(r_+-r_-,\xi-\eta). \tag{34}$$

We can now write the final approximate results, making the replacements $\xi \to r_+$, $\eta \to r_-$ in the above expressions, so that they can be used in eqs. (12) and (15):

$$\begin{aligned} W^{(1,3)}(r_+,r_-) &\simeq \mp\int_{-r_-}^{r^+}\overline{x}(r)\,\mathscr{R}(2r,r_+-r_-)\mathrm{d}r, \\ W^{(2)}(r_+,r_-) &\simeq \mathscr{R}(r_++r_m,r_+-r_-)\,W^{(1)}(r_+,-r_m) \\ &\quad +\mathscr{R}(r_m-r_-,r_+-r_-)\,W^{(3)}(r_m,r_-), \end{aligned} \tag{35}$$

where $\mathscr{R}$ is given by eq. (32). Formulae (34) and (35) are the main results of the present work. It is important to stress that eq. (32) has a universal form and can be applied to any physical system with known dependence $c(r_+-r_-)$, see eqs. (8) and (9).

Examples. – In the case of the dynamics of a polytropic gas with $c(\rho) = \rho^{(\gamma-1)/2}$, an easy calculation gives

$$\mathscr{R}(r_1, r_2) = \left(\frac{r_1}{r_2}\right)^{\beta}, \quad \text{where} \quad \beta = \frac{3-\gamma}{2(\gamma-1)}. \tag{36}$$

It is worth noticing that the approximation (34) yields the exact expression of the Riemann function for a classical monoatomic gas with $\gamma = 5/3$ ($\beta = 1$). For other values of β the function F in (31) can be shown to obey the hypergeometric equation (see, *e.g.*, ref. [8]) and our approximation corresponds to the first term in its series expansion. Thus, we obtain

$$\begin{aligned} W^{(1,3)}(r_+, r_-) &\simeq \mp \left(\frac{2}{r_+ - r_-}\right)^{\beta} \int_{-r_-}^{r_+} r^{\beta}\, \overline{x}(r)\mathrm{d}r, \\ W^{(2)}(r_+, r_-) &\simeq \left(\frac{2}{r_+ - r_-}\right)^{\beta} \\ &\quad \times \left\{ \int_{-r_-}^{r_m} r^{\beta}\, \overline{x}(r)\mathrm{d}r + \int_{r_+}^{r_m} r^{\beta}\, \overline{x}(r)\mathrm{d}r \right\}. \end{aligned} \tag{37}$$

For the case of "shallow water" equations with $\gamma = 2$ ($\beta = 1/2$) these formulae reproduce the results of refs. [4,5]. The approximation (37) cannot be distinguished from the exact result of Riemann's approach for the type of initial condition considered in ref. [4].

We now study in some details a case where the dependence of c on ρ is less simple than the one of eq. (2): this is the case of a zero temperature Bose-Einstein condensate transversely confined in an atomic wave guide. For a harmonic trapping, the transverse averaged chemical potential can be represented by the interpolating formula [10]

$$\mu_\perp(\rho) = \hbar\omega_\perp \sqrt{1 + 4a\rho}, \tag{38}$$

where $\omega_\perp$ is the angular frequency of the transverse harmonic potential, $a > 0$ is the s-wave scattering length, and $\rho(x,t)$ is the linear density of the condensate. We note that other expressions for $\mu_\perp$ have also been proposed in the literature [11,12]. Expression (38) yields the correct sound velocity $mc^2 = \rho\, \mathrm{d}\mu_\perp/\mathrm{d}\rho$ both in the low ($a\rho \ll 1$) and in the high ($a\rho \gg 1$) density regimes. In these two limiting cases the long wave length dynamics of the system is thus correctly described by the hydrodynamic equations (2) with, in appropriate dimensionless units:

$$c^2(\rho) = \frac{\rho}{\sqrt{1+\rho}}, \tag{39}$$

where one has made the changes of variables $4a\rho \to \rho$, $u/u_0 \to u$, $x/x_0 \to x$ and $t/t_0 \to t$, where $2mu_0^2 = \hbar\omega_\perp$ and $t_0 = x_0/u_0$. The length x_0 used to non-dimensionalize the dispersionless equations is a free parameter: we will chose it equal to the parameter x_0 appearing in the initial condition (25). We note here that the initial condition (25) can be realized by several means in the context of BEC physics. One can for instance suddenly switch on at $t = 0$ a blue detuned focused laser beam [13]. An alternative method has been demonstrated in ref. [14]: by monitoring the relative phase of a two species condensate, one can implement a bump (or a through) in one of the components.

In the case characterized by eqs. (38) and (39), expressions (32) and (33) yield

$$\mathscr{R}(r_1, r_2) = \left(\frac{\rho^2(r_1) + \rho^3(r_1)}{\rho^2(r_2) + \rho^3(r_2)}\right)^{1/8}, \tag{40}$$

where $\rho(r)$ is the reciprocal function of

$$r(\rho) = 2\int_0^{\sqrt{\rho}} \frac{\mathrm{d}u}{(1+u^2)^{1/4}}. \tag{41}$$

In order to evaluate W it then suffices to determine $\overline{x}(r)$ by inverting the relation (23) and to compute the appropriate integrals (35). Once $W(r_+, r_-)$ is known in all three regions 1, 2 and 3, it is possible to compute $r_+(x,t)$ and $r_-(x,t)$, and then $\rho(x,t)$ and $u(x,t)$ as explained in refs. [4,5]:

– One first determines the value $r^+_{1|2}(t)$ reached by r^+ at the boundary between regions 1 and 2, see fig. 1(b). This boundary corresponds to the point where $r^- = -r_m$ at time t. From eqs. (12), $r^+_{1|2}(t)$ is thus determined by solving

$$\frac{w_+^{(1)}(r^+_{1|2}, -r_m) - w_-^{(1)}(r^+_{1|2}, -r_m)}{v_+(r^+_{1|2}, -r_m) - v_-(r^+_{1|2}, -r_m)} + t = 0, \tag{42}$$

where $w_+^{(1)} = \partial W^{(1)}/\partial r^+$. We then know that, in region 1 at time t, r^+ takes all possible values between r_0 and $r^+_{1|2}(t)$ (cf. figs. 1 and 2).

– One then let r^+ vary in $[r_0, r_m]$. From eqs. (12), at time t, the other Riemann invariant r^- is solution of

$$\frac{w_+^{(1,2)}(r^+, r^-) - w_-^{(1,2)}(r^+, r^-)}{v_+(r^+, r^-) - v_-(r^+, r^-)} + t = 0\,, \tag{43}$$

where the superscript should be (1) if $r^+ \in [r_0, r^+_{1|2}(t)]$ and (2) if $r^+ \in [r^+_{1|2}(t), r_m]$.

– At this point, for each value of t and r^+ we have determined the value of r^-. The position x is then obtained by either one of eqs. (12). So, for given t and r^+ in regions 1 and 2, one has determined the values of r^- and x. In region 3 we use the symmetry of the problem and write $r^{\pm}(x,t) = -r^{\mp}(-x,t)$.

The above procedure defines a mapping of the whole physical (x,t) space onto the hodograph (r^+, r^-) space. The density and velocity profiles are then obtained by means of eqs. (5). The results are compared with numerical simulations in fig. 3 for an initial profile (25) with

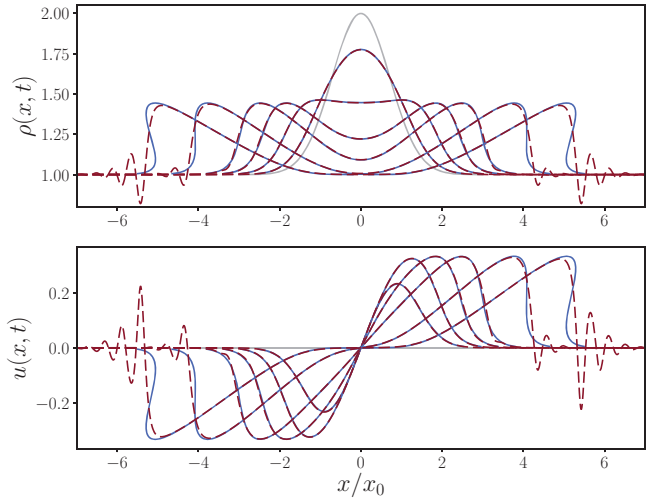

Fig. 3: Density and velocity plotted as a function of x/x_0 for dimensionless times $t/t_0 = 0.5$, 1, 1.5, 2, 3 and 4, respectively. The initial conditions are given by eqs. (4) and (25) with $\rho_0 = 1$ and $\rho_1 = 1$, they are represented by the gray solid lines. The blue solid lines are the results of the hydrodynamic system (1) obtained from the approximate Riemann's approach described in the text. The dashed lines are the results of the numerical simulations of eq. (44).

$\rho_0 = 1$ and $\rho_1 = 1$. The simulations have been performed by solving numerically a generalized nonlinear Schrödinger equation of the form

$$\mathrm{i}\psi_t = -\frac{1}{2}\psi_{xx} + 2\,\psi\sqrt{1+\rho}, \tag{44}$$

where $\rho(x,t) = |\psi|^2$, $u(x,t) = (\psi^*\psi_x - \psi\,\psi_x^*)/(2\mathrm{i}\rho)$ and $\psi(x,0) = \sqrt{\rho}(x,0)$. This effective Gross-Pitaevskii equation reduces to the system (1) with the speed of sound (39) in the dispersionless limit[3]. It yields an excitation spectrum always of Bogoliubov type, which is incorrect in the large density limit ($\rho \gg 1$). However, one can show that eq. (44) is acceptable even in this limit provided one remains in the long wavelength, hydrodynamic regime. It is not appropriate when rapid oscillations appear in the density and velocity (if $\rho \gg 1$) such as observed in fig. 3 for $t/t_0 = 3$. These oscillations correspond to the onset of a dispersive shock wave, which occurs at a time denoted as the wave breaking time: t_{WB}. For $t > t_{\mathrm{WB}}$ the numerical simulations can be considered as accurately describing the physical system only when $\rho \ll 1$. But for $t > t_{\mathrm{WB}}$ our dispersionless approach also fails (see below): we are thus safe when comparing our results with numerical simulations at earlier times.

One sees in fig. 3 that our solution of the hydrodynamic equations (1) agrees very well with the numerical simulations of the dispersive equation (44) at short time. For larger times the profile steepens, eventually reaching a point of gradient catastrophe at time t_{WB}. It is thus expected that for $t \simeq t_{\mathrm{WB}}$ the solution of the dispersionless system (1) departs from the numerical simulations, as seen in the figure. However, this difference is not a sign of a failure of our approximation, but it rather points to the breakdown of the hydrodynamic model (1). After t_{WB} the system (1) leads to a multi-valued solution if not corrected to account for dispersive effects, as can be seen in fig. 3.

Wave breaking time. – We now turn to the determination of the wave breaking time t_{WB} at which a shock is formed. After t_{WB} the system (1) has to be modified in order to account for viscous and/or dispersive effects, depending on the physical situation under consideration.

We treat the case of an initial profile roughly of the type (25): a bump over a uniform background. Wave breaking corresponds to the occurrence of a gradient catastrophe for which $\partial r_\pm/\partial x = \infty$. If one considers for instance the right part of the profile (region 3), from eq. (12), this occurs at a time t such that

$$t = -\frac{\partial w_+^{(3)}/\partial r_+}{1 + c'(r_+ - r_-)} = -\frac{\partial w_+^{(3)}/\partial r_+}{1 + \left.\dfrac{\mathrm{d}\ln c}{\mathrm{d}\ln\rho}\right|_{r_+ - r_-}}, \tag{45}$$

and t_{WB} is the smallest of the times (45). It is worth noticing that this formula yields an expression for the breaking time obtained from our approximate solution of the initial value problem and in this sense it provides less general but more definite result than the upper estimate of the breaking time obtained by Lax in ref. [15].

One can easily compute t_{WB} approximately when the point of largest gradient in $\overline{\rho}(x)$ lies in a region where $\overline{\rho} \simeq \rho_0$. This occurs for some specific initial distributions (such as the inverted parabola considered in ref. [4]) or when the initial bump is only a small perturbation of the background. In this case, it is legitimate to assume that wave breaking is reached for $r_- \simeq -r_0$ and that

$$r_+ - r_- \simeq \frac{1}{2}\int_0^{\rho} \frac{c(\rho')}{\rho'}\mathrm{d}\rho' + \frac{1}{2}\int_0^{\rho_0} \frac{c(\rho')}{\rho'}\mathrm{d}\rho'. \tag{46}$$

Equations (15) and (35) then lead to $w_+^{(3)} \simeq \overline{x}(r_+)$ and (45) becomes

$$t \simeq -\frac{2}{1 + \left.\dfrac{\mathrm{d}\ln c}{\mathrm{d}\ln\rho}\right|_{\overline{\rho}}} \times \frac{\overline{\rho}}{c(\overline{\rho})\,\dfrac{\mathrm{d}\overline{\rho}}{\mathrm{d}x}}, \tag{47}$$

where $\overline{\rho}$ stands for $\overline{\rho}(\overline{x}(r^+))$. Within our hypothesis, it is legitimate to assume that the shortest of times t is reached close to the point $\overline{x}(r^+)$ for which $|\mathrm{d}\overline{\rho}/\mathrm{d}x|$ is maximal. We note x^* the coordinate of this point and $\rho^* = \overline{\rho}(x^*)$. One thus obtains

$$t_{\mathrm{WB}} \simeq \frac{2}{1 + \left.\dfrac{\mathrm{d}\ln c}{\mathrm{d}\ln\rho}\right|_{\rho^*}} \times \frac{\rho^*}{c(\rho^*)\cdot\max\left|\dfrac{\mathrm{d}\overline{\rho}}{\mathrm{d}x}\right|}\,. \tag{48}$$

In a "shallow water" case with $\gamma = 1/2$ and for an initial profile where the bump is an inverted parabola, such as considered in ref. [4], the above formula is exact.

[3]It would be easier and more natural to compare our approximate Riemann approach with the numerical solution of eqs. (1). However, the difference between the two results is so small that the discussion of this comparison has little interest.

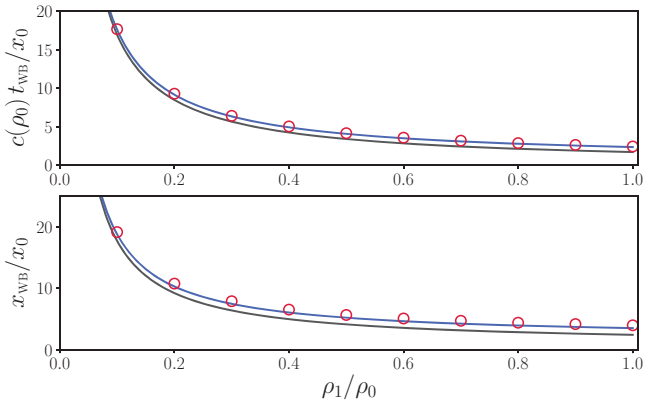

Fig. 4: Wave breaking time $t_{\rm WB}$ and position of the wave breaking event $x_{\rm WB}$ for different values of ρ_1/ρ_0. The system considered is a quasi-1D BEC for which the speed of sound in given by (39). The initial profile is given by eqs. (4) and (25). The blue solid lines are the approximate results (49) and (50). The red dots are the results obtained from Riemann's approach. The black solid lines are obtained by replacing ρ^* by ρ_0 in eqs. (49) and (50), see the text.

For the initial profile (25), in the case where the speed of sound is given by (39), formula (48) yields

$$t_{\rm WB} \simeq \sqrt{\frac{e}{2}}\, \frac{8(1+\rho^*)}{6+5\rho^*}\, \frac{x_0}{c(\rho^*)}\, \frac{\rho^*}{\rho_1}. \tag{49}$$

The location $x_{\rm WB}$ of the wave breaking event can be obtained from (12). Within our approximation scheme, this yields, for the right part of the profile:

$$x_{\rm WB} \simeq x^* + c(\rho^*) t_{\rm WB}. \tag{50}$$

These results are compared in fig. 4 with the values determined from the Riemann approach. The overall agreement is excellent. We also note that replacing ρ^* by ρ_0 in eqs. (49) and (50) gives a result which is less accurate, but still quite reasonable, see fig. 4.

Conclusion. – We have presented an approximate method for describing the hydrodynamic evolution of a nonlinear pulse. The method is quite general and applies for any type of nonlinearity. It has been tested for cases of experimental interest in the context of nonlinear optics in ref. [4] and here for studying the spreading of a nonlinear pulse in a guided atomic Bose-Einstein condensate. This last example is of particular interest for bench-marking the approach because the nonlinearity at hand has a non-trivial density dependence.

One could imagine to extend the present study in several directions. A possible track would be to solve the dispersionless shallow water equations (eqs. (1) and (2) with $\gamma = 2$) for more general initial conditions than discussed in the present work, as considered for instance in refs. [16,17] in the context of the initial stage of formation of a tsunami. Future studies could also test the present approach in the optical context for pulses propagating in a nonlinear photo-refractive material, where, up to now, no theoretical method was known for dealing with the dispersionless stage of evolution. In this context we note that the simple and accurate approximate analytic results obtained for $t_{\rm WB}$ and $x_{\rm WB}$ (eqs. (49) and (50)) should be helpful for determining the best parameters for an experimental observation of the wave breaking phenomenon.

We finally stress that the approximate scheme presented in this work, providing an accurate account of the stage of non-dispersive propagation of a pulse, is an important and necessary step for studying the post wave breaking dynamics, and particularly the formation of dispersive shock waves in non-integrable systems.

REFERENCES

[1] Landau L. D. and Lifshitz E. M., *Fluid Mechanics* (Pergamon, Oxford) 1987.
[2] Forest M. G., Rosenberg C.-J. and Wright III O. C., *Nonlinearity*, **22** (2009) 2287.
[3] Ivanov S. K. and Kamchatnov A. M., *Phys. Rev. A*, **99** (2019) 013609.
[4] Isoard M., Kamchatnov A. M. and Pavloff N., *Phys. Rev. A*, **99** (2019) 053819.
[5] Isoard M., Kamchatnov A. M. and Pavloff N., in *Compte-rendus de la 22^e rencontre du Non Linéaire*, edited by Falcon E., Lefranc M., Pétrélis F. and Pham C.-T. (Non-Linéaire Publications, Saint-Étienne du Rouvray) 2019, p. 33.
[6] Kamchatnov A. M., *Nonlinear Periodic Waves and Their Modulations—An Introductory Course* (World Scientific, Singapore) 2000.
[7] Tsarev S. P., *Math. USSR Izv.*, **37** (1991) 397.
[8] Sommerfeld A., *Partial Differential Equations in Physics* (Academic Press, New York) 1964.
[9] Ludford G. S. S., *Proc. Cambridge Philos. Soc.*, **48** (1952) 499.
[10] Gerbier F., *Europhys. Lett.*, **66** (2004) 771.
[11] Salasnich L., Parola A. and Reatto L., *Phys. Rev. A*, **65** (2002) 043614.
[12] Kamchatnov A. M. and Shchesnovich V. S., *Phys. Rev. A*, **70** (2004) 023604.
[13] Andrews M. R., Kurn D. M., Miesner H.-J., Durfee D. S., Townsend C. G., Inouye S. and Ketterle W., *Phys. Rev. Lett.*, **79** (1998) 553.
[14] Hall D. S., Matthews M. R., Wieman C. E. and Cornell E. A., *Phys. Rev. Lett.*, **81** (1998) 1543.
[15] Lax P. D., *J. Math. Phys.*, **5** (1964) 611.
[16] Pelinovsky E. N. and Rodin A. A., *Izv. Atmos. Ocean. Phys.*, **49** (2013) 548.
[17] Rodin A. A., Rodina N. A., Kurkin A. A. and Pelinovsky E. N., *Izv. Atmos. Ocean. Phys.*, **55** (2019) 374.

7

FORMATION AND PROPAGATION OF DISPERSIVE SHOCK WAVES

This chapter is devoted to the study of dispersive shock waves. An optical beam propagating in a nonlinear dielectric material might experience a gradient catastrophe leading to the formation of a dispersive shock wave (DSW).

It has been shown by Talanov [179] that a smooth localized light pulse sent in a nonlinear medium, spreads smoothly and can be described through the dispersionless hydrodynamic equations. However, the situation becomes quite different for a hump on top of a uniform background light intensity: the hump splits in two parts which propagate in opposite directions. The front and the rear edge of the hump have the same intensity as the background and accordingly propagate at the background sound velocity c_0, while the points of larger intensity propagate at larger velocity. When these points catch up the front edge (see Figure 51), this leads to the formation of a shock. In other words, when this situation occurs, density gradients at the front edge of the left an right-moving humps become infinite: this is a *gradient catastrophe*.

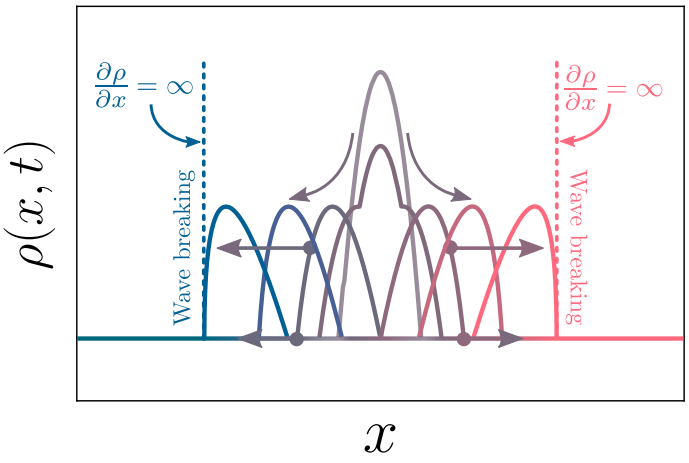

FIGURE 51: Evolution of a hump on top of a background. The initial bump splits in two parts, each of them propagating in opposite direction, as indicated by the arrows. The front and the rear edge of the hump have the same intensity as the background and accordingly propagate at the background sound velocity. On the contrary, all the points of larger intensity move at a higher velocity; this is illustrated by the arrows attached to each pulse and longer than those located at each edge. Therefore, at a certain time, called *wave breaking time*, the points of larger intensity catch up the front edge (for the left and right-moving bumps), leading to infinite density gradients: this is a *gradient catastrophe*. The wave breaking is indicated by the vertical dashed lines at both edges of each pulse.

As we discussed in the previous chapter, no matter how small is the hump on top of the background, a DSW is formed at each edge of each pulse moving away from each other. Therefore, perturbation theory always fails at describing such a situation, whereas the dispersionless approach leads to a non-physical multi-valued density distribution. This is the reason why we shall turn our attention to a theory which is able to encompass dispersive effects after the shock has formed. This theory does exist and has been developed by Whitham [194–197], then used by Gurevich and Pitaevskii [84] to describe a DSW as a slowly modulated nonlinear wave. The existence of two scales between fast oscillations in the shock and slow evolution of certain parameters along the shock, such as its wavelength or its amplitude, led them to the idea of using Whitham modulational theory for DSW; this is what we discuss in the first section of this chapter.

Then, we apply the Gurevich-Pitaevskii approach to the nonlinear Schrodinger equation (NLS). We show in particular that the theoretical treatment compares very well with numerical simulations. This approach also provides an asymptotic description of the DSW, namely a *weak shock theory*, from which we can extract experimentally relevant parameters such as the contrast of the fringes of the DSW.

7.1 WHITHAM MODULATIONAL THEORY

7.1.1 *General idea*

The main idea of Whitham modulational theory consists of describing modulations of nonlinear periodic waves which cannot be approximated by linear waves. The approach is based on the existence of two scales. We consider fast oscillations with wavelength $L(x,t)$, which slowly depends on space and time, and thus change little in one wavelength. We also assume that the amplitude of the wave does not vary too much in one wavelength. An example of such a slowly modulated wave is illustrated in Figure 52. The red dashed inset represents a portion of the fast oscillating wave. One sees that the wavelength, denoted L, and the amplitude of the wave, denoted A, do not vary much over several wavelengths.

Consequently, we can average the equations of motion which govern the variations of these parameters (wavelength, amplitude,...) along the nonlinear wave over fast oscillations; these averaged modulation equations are called the *Whitham equations*.

Let us consider a differential equation in the form

$$\phi(u, \partial_t u, \partial_x u, \partial_{tt} u, \partial_{tx} u, \partial_{xx} u, \ldots) = 0, \tag{468}$$

where $\partial_{i_1 \ldots i_n} = \partial^n / \partial i_1 \ldots \partial i_n$, with $i_1, \ldots, i_n \in \{t, x\}$. Now we suppose that the wave variable $u(x,t)$ depends on x and t only through $\xi = x - Vt$. Thus, multiplying equation (468) by $\partial_\xi u$ and integrating it, one obtains

$$u_\xi^2 = F(u, V, A_i), \tag{469}$$

where A_i are a set of parameters, such as the amplitude or the wavelength of the wave packet, which arise from the integration of (468). Periodic solutions correspond to oscillations of u between two zeros[1] of F, denoted as $u_1(V, A_i)$ and $u_2(V, A_i)$, with $u_1 < u_2$. Let us introduce ξ_1 and ξ_2 such that

$$u(\xi_1, V, A_i) = u_1(V, A_i), \quad u(\xi_2, V, A_i) = u_2(V, A_i). \tag{470}$$

Then, the wavelength corresponding to this periodic solution reads

$$L = L(V, A_i) = 2\int_{\xi_1}^{\xi_2} \mathrm{d}\xi = 2\int_{u_1}^{u_2} \frac{\mathrm{d}u}{\sqrt{F(u, V, A_i)}}, \tag{471}$$

where we used a change of variable and expression (469). The wavector k and the frequency ω are equal to

$$k = k(V, A_i) = \frac{2\pi}{L(V, A_i)}, \quad \omega = \omega(V, A_i) = Vk(V, A_i). \tag{472}$$

Since we consider here a slowly modulated wave $u(\xi, V, A_i)$, the parameters V and A_i are slow functions of x and t, and thus change little in one wavelength L. We would like to average these parameters over fast oscillations of the wave according to the rule

$$\widetilde{\mathcal{F}}(\xi, V, A_i) = \frac{1}{2\Delta}\int_{\xi-\Delta}^{\xi+\Delta} \mathcal{F}(\xi', V, A_i)\,\mathrm{d}\xi', \tag{473}$$

where the interval Δ should be much longer than the wavelength L and much shorter that any characteristic size ℓ in the problem, see Figure 52. Thus, one considers here

$$L \ll \Delta \ll \ell. \tag{474}$$

Following Whitham approach, it is more convenient to average conservation laws, such as for example

$$\partial_t \mathcal{P} + \partial_x \mathcal{Q} = 0, \tag{475}$$

where $\mathcal{P}(\xi, V, A_i)$ and $\mathcal{Q}(\xi, V, A_i)$ are two functions which can be derived from (468). By averaging over fast oscillations according to (473), we find that the averaged conservation law can be written as

$$\partial_t \widetilde{\mathcal{P}}(\xi, V, A_i) + \partial_x \widetilde{\mathcal{Q}}(\xi, V, A_i) = 0. \tag{476}$$

As one can see from the inset of Figure 52 and from the difference of scales (474), the wavelength remains constant up to small corrections in the interval 2Δ. Therefore, we can replace the average over 2Δ in expression (473) by the average over the wavelength, i.e.,

$$\overline{\mathcal{F}}(V, A_i) = \frac{1}{L}\int_{\xi}^{\xi+L} \mathcal{F}(\xi, V, A_i)\,\mathrm{d}\xi, \tag{477}$$

1 Think about F as the opposite of the potential energy and u_ξ^2 as proportional to an effective kinetic energy.

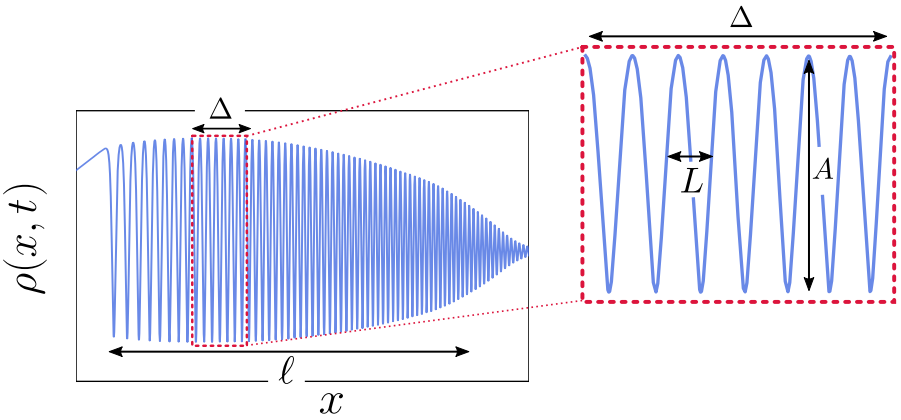

FIGURE 52: Different scales along the dispersive shock wave. The amplitude A and the wavelength L vary over a length ℓ, but can be considered almost constant along the interval Δ, as illustrated in the inset of the figure. In addition, Δ is much longer than the wavelength L. The existence of these two scales, between fast oscillations and slowly modulated parameters (wavelength, amplitude,...) along the DSW, is at the heart of Whitham modulational theory.

where the explicit dependence of $\overline{\mathcal{F}}$ on x and t disappears by means of the periodicity of $\mathcal{F}$. As a result, equation (476) becomes

$$\partial_t \overline{\mathcal{P}}(V, A_i) + \partial_x \overline{\mathcal{Q}}(V, A_i) = 0, \tag{478}$$

where the dependence of x and t only appear through the slowly varying parameters V and A_i. The averaged conservation laws of the form (478) are the Whitham equations. One should find as many Whitham equations as there are parameters (V, A_i) to describe the evolution of each of them. Then, we know the evolution of the nonlinear wave variable $u(x - Vt, V, A_i)$, since it only depends on the set of parameters (V, A_i).

ILLUSTRATIVE EXAMPLE Even though we will consider nonlinear waves in the following, let us first examine an instructive example of modulation of a linear wave governed by equation

$$\partial_{tt} u - \partial_{xx} u + \frac{1}{4} \partial_{xxxx} u = 0, \tag{479}$$

This differential equation actually corresponds to a linearized version of the Gross-Pitaevskii equation [see equation (123b) with $v_0 = 0$]. We seek periodic solutions of equation (479) in the form $u(\xi) = u(x - Vt)$. They are given by

$$u(x - Vt, V, a) = a \sin[2\sqrt{V^2 - 1}(\xi - \xi_0)], \tag{480}$$

where a plays the role of the wave amplitude. In the following we take $\xi_0 = 0$; this initial phase will indeed disappear after the averaging process (477).

Then, the wavenumber and the frequency are given by

$$k = 2\sqrt{V^2 - 1}, \quad \omega = 2V\sqrt{V^2 - 1}. \tag{481}$$

They are linked through the so-called Bogoliubov dispersion relation

$$\omega = k\sqrt{\frac{k^2}{4}+1}. \tag{482}$$

To completely describe the slowly linear modulated wave (480), we should find the evolution equations of V and a, meaning that we need two conservation laws in the form of (475) to solve the problem. These two laws can be derived from (479) and read

$$\begin{aligned} &(-u_t\,u_x)_t + \left[\frac{1}{8}u_{xx}^2 + \frac{1}{2}u_t^2 + \frac{1}{2}u_x^2 - \frac{1}{4}u_{xxx}\,u_x\right]_x = 0, \\ &\left[\frac{1}{8}u_{xx}^2 + \frac{1}{2}u_t^2 + \frac{1}{2}u_x^2\right]_t + \left[-u_t\,u_x - \frac{1}{4}u_{tx}\,u_{xx} + \frac{1}{4}u_t\,u_{xxx}\right]_x = 0, \end{aligned} \tag{483}$$

where we used the shortcut notation $u_{i_1\dots i_n} \equiv \partial_{i_1\dots i_n} u$, with $i_1 \dots i_n \in \{t, x\}$. Averaging these conservation laws according to the rule (478) leads to the set of equations

$$\left[a^2 V(V^2-1)\right]_t + \left[a^2(V^2-1)(2\,V^2-1)\right]_x = 0, \tag{484a}$$

$$\left[a^2 V^2(V^2-1)\right]_t + \left[a^2 V(V^2-1)(2\,V^2-1)\right]_x = 0, \tag{484b}$$

i.e., the Whitham equations. Multiplying equation (484a) by V and subtracting (484b) gives

$$\frac{\partial V}{\partial t} + \frac{2\,V^2-1}{V}\frac{\partial V}{\partial x} = 0. \tag{485}$$

By using expressions (481) and (482), one finds

$$\partial_t k + \omega'(k)\partial_x k = 0, \quad \text{where} \quad \omega'(k) = \frac{k^2/2+1}{\sqrt{k^2/4+1}}. \tag{486}$$

Equivalently, noticing that $\partial_x \omega = \omega'(k)\partial_x k$, we also obtain

$$\partial_t k + \partial_x \omega = 0. \tag{487}$$

Despite its apparent simplicity, expression (487), called equation of the *conservation of waves*, has a profound meaning. For linear waves this result is expected: indeed, the phase of a linear periodic train wave is given by $\theta = kx - \omega t$. Thus, $k = \partial_x\theta$ and $\omega = -\partial_t\theta$, and equation (487) comes from the fact that $\partial_x\partial_t\theta = \partial_t\partial_x\theta$. However, relation (487) is a direct consequence of Whitham equations (478) and is based on the existence of a slowly varying phase. Therefore, equation (487) will remain true within relatively small intervals in the case of nonlinear waves.

Moreover, let us develop further: equation (486) is nothing but a Hopf equation (see Section 5.2.1). Therefore, the wave vector k is constant along characteristic curves determined by

$$\frac{\mathrm{d}x}{\mathrm{d}t} = V_g(k), \quad \text{where} \quad V_g(k) \equiv \omega'(k), \tag{488}$$

and thus propagates at the group velocity along characteristics. We will use this important property later in the next section.

7.1.2 *Whitham equations for NLS equation*

In the case of the defocusing nonlinear Schrödinger equation

$$i\,\partial_t\psi = -\frac{1}{2}\partial_{xx}\psi + |\psi|^2\,\psi, \tag{489}$$

which can be mapped onto hydrodynamic equations [see equation (366)] through a Madelung transformation $\psi = \sqrt{\rho}\exp(i\int u\,\mathrm{d}x)$, nonlinear periodic solutions can be written in terms of four parameters $\lambda_1 \le \lambda_2 \le \lambda_3 \le \lambda_4$ in the form [100]

$$\begin{aligned}\rho(x,t) &= \tfrac{1}{4}(\lambda_4-\lambda_3-\lambda_2+\lambda_1)^2 + (\lambda_4-\lambda_3)(\lambda_2-\lambda_1)\\ &\quad\times \mathrm{sn}^2\left(\sqrt{(\lambda_4-\lambda_2)(\lambda_3-\lambda_1)}\,(x-Vt), m\right),\\ u(x,t) &= V - \frac{C}{\rho(x,t)},\end{aligned} \tag{490}$$

where sn is the Jacobi elliptic sine function (see. e.g., Ref. [2]),

$$V = \tfrac{1}{2}\sum_{i=1}^{4}\lambda_i\,, \quad m = \frac{(\lambda_2-\lambda_1)(\lambda_4-\lambda_3)}{(\lambda_4-\lambda_2)(\lambda_3-\lambda_1)}\,, \tag{491}$$

and

$$\begin{aligned}C = \tfrac{1}{8}(-\lambda_1-\lambda_2+\lambda_3+\lambda_4)\times(-\lambda_1+\lambda_2-\lambda_3+\lambda_4)\\ \times(\lambda_1-\lambda_2-\lambda_3+\lambda_4)\,.\end{aligned} \tag{492}$$

For constant λ_i's, expressions (490), (491) and (492) correspond to an exact (single phase) solution of the NLS equation, periodic in time and space, where oscillations have the amplitude

$$a = (\lambda_2-\lambda_1)(\lambda_4-\lambda_3)\,, \tag{493}$$

and the spatial wavelength

$$L = \frac{2\,\mathrm{K}(m)}{\sqrt{(\lambda_4-\lambda_2)(\lambda_3-\lambda_1)}}\,. \tag{494}$$

As explained in the previous section, the great insight of Gurevich and Pitaevskii [84] has been to describe a dispersive shock wave as a slowly modulated nonlinear wave of type (490). Solution (490) being entirely characterized by the knowledge of the four slowly varying parameters $\lambda_i(x,t)$, one needs four Witham equations (478) to solve the problem. They read [100, 197]

$$\partial_t\lambda_i + v_i(\lambda_1,\lambda_2,\lambda_3,\lambda_4)\,\partial_x\lambda_i = 0, \quad i = 1,2,3,4. \tag{495}$$

One sees immediately that the λ_i's are the Riemann invariants of the Whitham equations [compare for instance with equations (385)]. Equations (495) were first found in Refs. [67, 143]. The v_i's are the associated

characteristic velocities; their explicit expressions can be obtained from the relation[2] [82, 100]

$$v_i = V - \frac{1}{2}\frac{L}{\partial_i L}, \quad i = 1, 2, 3, 4\ , \tag{496}$$

where $\partial_i = \partial/\partial\lambda_i$. This yields

$$\begin{aligned}
v_1 &= V - \frac{(\lambda_4-\lambda_1)(\lambda_2-\lambda_1)\mathrm{K}(m)}{(\lambda_4-\lambda_1)\mathrm{K}(m) - (\lambda_4-\lambda_2)\mathrm{E}(m)},\\
v_2 &= V + \frac{(\lambda_3-\lambda_2)(\lambda_2-\lambda_1)\mathrm{K}(m)}{(\lambda_3-\lambda_2)\mathrm{K}(m) - (\lambda_3-\lambda_1)\mathrm{E}(m)},\\
v_3 &= V - \frac{(\lambda_4-\lambda_3)(\lambda_3-\lambda_2)\mathrm{K}(m)}{(\lambda_3-\lambda_2)\mathrm{K}(m) - (\lambda_4-\lambda_2)\mathrm{E}(m)},\\
v_4 &= V + \frac{(\lambda_4-\lambda_3)(\lambda_4-\lambda_1)\mathrm{K}(m)}{(\lambda_4-\lambda_1)\mathrm{K}(m) - (\lambda_3-\lambda_1)\mathrm{E}(m)},
\end{aligned} \tag{497}$$

where m is given by equation (491) and $\mathrm{E}(m)$ is the complete elliptic integrals of the second kind.

In our case, as shown in Figure 53, for $x > 0$, the left edge of the DSW, connected to the dispersionless part of the profile, is called *solitonic edge* and corresponds to the limit $m \to 1$; the first oscillation is indeed a dark soliton, see equation (498). The right edge, glued to the background, is called *small amplitude edge* or *harmonic edge* and corresponds to $m \to 0$, see equation (500). We detail these two limiting cases in the subsequent paragraphs.

SOLITONIC EDGE In this case, $m \to 1$ ($\lambda_2 = \lambda_3$), $\mathrm{sn}(x, m) \to \tanh(x)$ and expression (490) describes a dark soliton (for which $L \to \infty$):

$$\rho(x,t) = \frac{1}{4}(\lambda_4-\lambda_1)^2 - \frac{(\lambda_2-\lambda_1)(\lambda_4-\lambda_2)}{\cosh^2[\sqrt{(\lambda_2-\lambda_1)(\lambda_4-\lambda_2)}\xi]} \tag{498}$$

with $\xi = x - \frac{1}{2}(\lambda_1 + 2\lambda_2 + \lambda_3)t$.

The Whitham velocities reduce to

$$\begin{aligned}
&v_1 = \tfrac{1}{2}(3\lambda_1 + \lambda_4), \quad v_2 = v_3 = \tfrac{1}{2}(\lambda_1 + 2\lambda_2 + \lambda_4),\\
&v_4 = \tfrac{1}{2}(\lambda_1 + 3\lambda_4).
\end{aligned} \tag{499}$$

HARMONIC EDGE In the limit $m \to 0$ ($\lambda_1 = \lambda_2$ or $\lambda_3 = \lambda_4$), $\mathrm{sn}(x, m) \to \sin(x)$, and equation (490) describes a small amplitude sinusoidal wave oscillating around a constant density background ρ_0. The specific example shown in Figure 53 corresponds to $\lambda_3 \to \lambda_\mathrm{H}$, where

2 The fact that one can write the Whitham velocities in the form of (496) is a general property of Whitham equations; this was indeed indicated independently by Gurevich *et al.* [81] and Kudashev [103] for the Korteweg-De Vries equation and by Kamchatnov [99] for the derivative nonlinear Schrödinger equation.

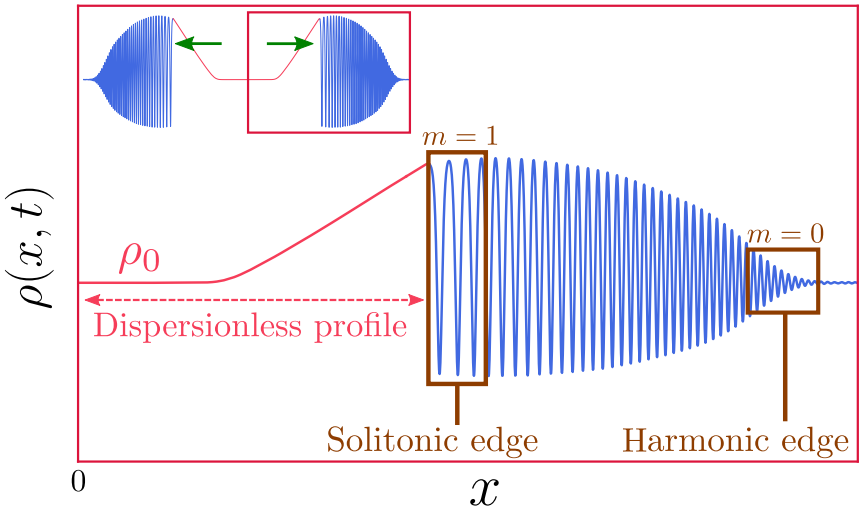

FIGURE 53: The inset shows the full density distribution after the formation of dispersive shock waves at the left (right) edge of the pulse propagating to the left (right). The green arrows indicate the propagation direction of each pulse.
The red rectangle represents a zoom over the dispersive shock wave (DSW) formed by the pulse propagating in the region $x > 0$. The DSW is connected to the dispersionless (smooth) profile at the left edge, corresponding to the limit $m \to 1$ in equation (490); this edge is called *solitonic edge* because the first oscillation is described by a dark soliton, see equation (498). The right edge of the DSW is often called *small amplitude edge* or *harmonic edge* and corresponds to $m \to 0$; this edge is indeed described by small linear oscillations over a constant background, see equation (500).

we have introduced $\lambda_{\rm H} \equiv \lambda_4(m \to 0)$, see Figure 54. In this case, the solution (490) reduces to

$$\rho(x,t) \simeq \rho_0 + a^2(x,t)\sin^2\left(\frac{\pi\xi}{L}\right), \tag{500}$$

where $\rho_0 = \frac{1}{4}(\lambda_1 - \lambda_2)^2$, and where $a^2(x,t) = 2\,c_0(\lambda_{\rm H} - \lambda_3)$ is a small amplitude ($\lambda_{\rm H} - \lambda_3 \to 0$ because at this edge $\lambda_3 \to \lambda_{\rm H} \equiv \lambda_4$). In addition, one has

$$L = \frac{2\,\pi}{k} = \frac{\pi}{\sqrt{(\lambda_{\rm H} - \lambda_1)(\lambda_{\rm H} - \lambda_2)}}, \tag{501}$$

and $\xi = x - Vt$, with $V = \frac{1}{2}(\lambda_1 + \lambda_2) + \lambda_{\rm H}$ [computed from (491)].

The Whitham velocities reduce to[3] (with $m \to 0$ when $\lambda_3 \to \lambda_H \equiv \lambda_4$)

$$\begin{aligned} &v_1 = \tfrac{1}{2}(3\lambda_1 + \lambda_2), \quad v_2 = \tfrac{1}{2}(\lambda_1 + 3\lambda_2), \\ &v_3 = v_4 \equiv v_H = 2\lambda_H + \frac{(\lambda_2 - \lambda_1)^2}{2(\lambda_1 + \lambda_2 - 2\lambda_H)}. \end{aligned} \tag{503}$$

In this limit, one of the Whitham equations (495) reads

$$\frac{\partial \lambda_H}{\partial t} + v_H \frac{\partial \lambda_H}{\partial x} = 0, \tag{504}$$

with $\lambda_H = \lambda_4$ and $v_H = v_4$.

In the particular case where $\lambda_2 = -\lambda_1 = c_0$, which will actually correspond to the situation considered in the following sections, $V(m \to 0) = \lambda_H$. In addition, using dimensionless units (i.e., putting $c_0 = 1$), one finds from equations (503)

with c_0 the background sound velocity.

$$v_H(\lambda_H) = 2\lambda_H - \frac{1}{\lambda_H} = \frac{2V^2 - 1}{V}, \tag{505}$$

and from expression (501)

$$k_H \equiv k(\lambda_H) = 2\sqrt{\lambda_H^2 - 1} = 2\sqrt{V^2 - 1}. \tag{506}$$

Expression (506) exactly corresponds to equation (481). Inserting equation (505) in equation (504) and using $V = \lambda_H$, valid in the harmonic limit when $\lambda_2 = -\lambda_1$, the Whitham equation (504) becomes

$$\frac{\partial V}{\partial t} + \frac{2V^2 - 1}{V}\frac{\partial V}{\partial x} = 0, \tag{507}$$

which is exactly equal to equation (485), i.e., the Whitham equation obtained for the linear differential equation (479). This is not surprising, since in the harmonic limit, the solution is described by a linear wave oscillating around a constant background [see equation (500)]. Therefore, using the results derived in Section 7.1.1, one sees that the harmonic edge of the DSW, denoted x_H (see Figure 54), moves at a velocity $v_H(\lambda_H)$:

$$\frac{\mathrm{d}x_H}{\mathrm{d}t} = v_H(\lambda_H). \tag{508}$$

In addition, this velocity indeed corresponds to the expected group velocity of the Bogoliubov waves, since, as already shown in Section 7.1.1,

$$v_H(\lambda_H) = \frac{k_H^2/2 + 1}{\sqrt{k_H^2/4 + 1}} = \omega'(k_H), \tag{509}$$

3 For the sake of completeness, we also mention that in the other small amplitude limit ($\lambda_1 \to \lambda_2$), the Whitham velocities read

$$\begin{aligned} &v_1 = v_2 = 2\lambda_1 + \frac{(\lambda_4 - \lambda_3)^2}{2(\lambda_3 + \lambda_4 - 2\lambda_1)}, \\ &v_3 = \tfrac{1}{2}(3\lambda_3 + \lambda_4), \quad v_4 = \tfrac{1}{2}(\lambda_3 + 3\lambda_4). \end{aligned} \tag{502}$$

with $\omega(k) = k\sqrt{\frac{k^2}{4}+1}$, and where we used equations (505) and (506).

This property of the small-amplitude edge is especially important in the theory of DSWs for non-integrable equations (see, e.g., Refs. [54, 55]).

To conclude this section, if one is able to find the solutions of Whitham equations (495), by inserting the corresponding Riemann invariants $\lambda_i(x,t)$, $i = 1,2,3,4$ in expressions (490), one knows the evolution of the density and velocity profiles along the DSW; this is exactly what we intend to do in the following section.

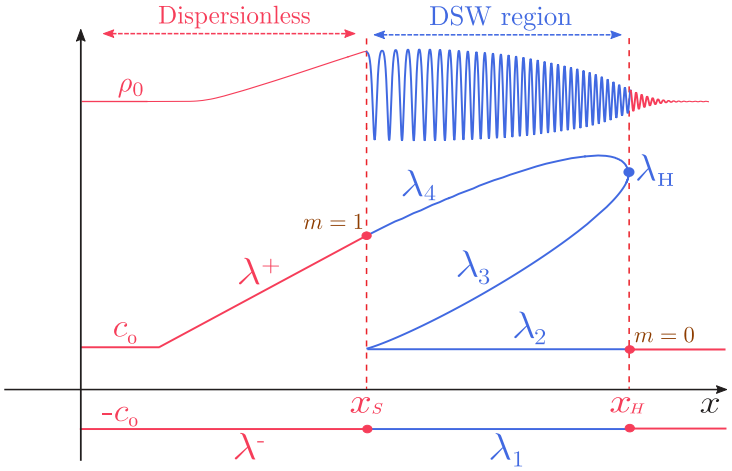

FIGURE 54: Sketch of the Riemann invariants λ_1, λ_2, λ_3, λ_4 along the DSW region, represented in blue. The dispersionless part of the profile, described by the Riemann invariants λ^+ and λ^-, is depicted in pink. As explained in Section 7.2, in our specific case, two Riemann invariants (λ_1 and λ_2) remain constant in the shock region. They are connected to the dispersionless Riemann invariants $\lambda^+ = c_0$ and $\lambda^- = -c_0$ at the right edge (harmonic edge, $m = 0$). Furthermore, $\lambda_3 \to \lambda_H \equiv \lambda_4$ at this edge. At the left and solitonic edge ($m = 1$), λ_1 is still connected to λ^-, while λ^+ is now glued to λ_4. In the other hand, $\lambda_2 = \lambda_3 = c_0$ at this edge. The position of the left edge (right edge) is denoted as x_S (x_H).

7.2 SOLUTIONS OF WHITHAM EQUATIONS

In this section, we present the solutions of Whitham equations (495), in the case where two Riemann invariants remain constant along the DSW. This situation arises when considering an initial density profile of the form of an inverted parabola, see expression (450).

First, as explained in the introduction of this chapter, the initial hump on top of a background splits in two parts; later, each of them experiences a wave breaking and this leads to the formation of a DSW at both edges. This exactly corresponds to the situation depicted in the inset (d) of Figure 50.

The Riemann invariants $\lambda^{\pm}$, which describe the dispersionless evolution of the nonlinear pulse, propagate in opposite direction, as shown in Figure 48.

Then, if we concentrate our attention to the region $x > 0$ (the region $x < 0$ can be obtained by symmetry of the problem), the right edge of λ^{+}, glued to the background, becomes multi-valued at a certain time, as illustrated in the graph (f) of Figure 48; this indicates a sign of the failure of the dispersionless approach after the wave breaking. The form of λ^{+} in this multi-valued region, and the fact that $\lambda^{-} = -c_0$ there, suggests to take $\lambda_1 = \lambda^{-} = -c_0$ and $\lambda_2 = \lambda^{+} = c_0$. Then, only $\lambda_3(x,t)$ and $\lambda_4(x,t)$ vary along the DSW and must match with the dispersionless profile at both edges of the DSW, see Figure 54.

Therefore, in the following, we consider in the shock region

$$\lambda_1(x,t) = -c_0, \quad \lambda_2(x,t) = c_0, \tag{510}$$

which trivially satisfy the Whitham equations (495), and the remaining Whitham equations for $\lambda_3(x,t)$ and $\lambda_4(x,t)$:

$$\frac{\partial \lambda_{3,4}}{\partial t} + v_{3,4}(-c_0, c_0, \lambda_3, \lambda_4)\frac{\partial \lambda_{3,4}}{\partial x} = 0. \tag{511}$$

7.2.1 *Generalized hodograph transform*

The nonlinear Whitham equations (511) are very similar to equations (393). This suggests to use the same trick to 'linearize' the Whitham equations by means of a hodograph transform (see Section 6.1.1). This procedure consists of writing x and t as functions of the Riemann invariants:

$$x = x(\lambda_3, \lambda_4), \quad t = t(\lambda_3, \lambda_4). \tag{512}$$

By introducing two functions $w_3(\lambda_3, \lambda_4)$ and $w_4(\lambda_3, \lambda_4)$ such that

$$x - v_{3,4}(-c_0, c_0, \lambda_3, \lambda_4)t = w_{3,4}(\lambda_3, \lambda_4), \tag{513}$$

and by using the results of Section 6.1.1, this leads to the Tsarev equations (399), where the superscripts $+$ and $-$ should be replaced by 3 and 4, respectively.

By means of expressions (496), one can prove easily that w_3 and w_4 verify the Tsarev equations if and only if

$$\partial_4[(\partial_3 k)\, w_3] = \partial_3[(\partial_4 k)\, w_4], \tag{514}$$

with $\partial_i = \partial/\partial\lambda_i$ and $k = 2\pi/L$. The previous equation suggests that $(\partial_3 k)\, w_3$ and $(\partial_4 k)\, w_4$ may be expressed in terms of a potential W, such that [82]

$$(\partial_i k) w_i = \partial_i (kW), \quad \text{with} \quad i \in \{3,4\}. \tag{515}$$

This yields

$$\begin{aligned} w_i(\lambda_3, \lambda_4) &= \left(1 - \frac{L}{\partial_i L}\partial_i\right) W \\ &= W + 2(v_i - V)\partial_i W, \quad i \in \{3,4\}, \end{aligned} \tag{516}$$

where we used $k/\partial_i k = -L/\partial_i L = 2(v_i - V)$ [see equation (496)]. Inserting (516) in the Tsarev equations, together with expressions of the Whitham velocities given by (496), shows that the potential W is solution of the following Euler-Poisson equation:

$$\frac{\partial^2 W}{\partial\lambda_3\partial\lambda_4} - \frac{1}{2(\lambda_3-\lambda_4)}\left(\frac{\partial W}{\partial\lambda_3} - \frac{\partial W}{\partial\lambda_4}\right) = 0. \tag{517}$$

Exactly as it already occurs in Chapter 6, we have transformed the set of nonlinear equations (511) into a linear differential equation (517). We could certainly solve the problem using Riemann's method, as we proceeded in Chapter 6. However, we found it more convenient to follow the method described in Refs. [56, 82]. In these works, the authors used a general solution of (517) derived by Eisenhart in 1918 [53].

7.2.2 *Solutions in the shock region*

A general solution of (517) is given by [53]

$$W(\lambda_3,\lambda_4) = \int_{c_0}^{\lambda_3} \frac{\psi(\mu)\,d\mu}{\sqrt{\lambda_3-\mu}\sqrt{\lambda_4-\mu}} + \int_{c_0}^{\lambda_4} \frac{\varphi(\mu)\,d\mu}{\sqrt{|\lambda_3-\mu|}\sqrt{\lambda_4-\mu}}, \tag{518}$$

where $\psi(\mu)$ and $\varphi(\mu)$ are two functions determined by boundary conditions.

In our case, as it was first understood in Ref. [83], the propagation of the DSW occurs in two steps after the wave breaking. Indeed, if the initial density distribution is non monotonous, as illustrated for instance in Figure 48, the first parts which become multi-valued are the left edge of $\lambda^-(x,t)$ and the right edge of $\lambda^+(x,t)$ (see for instance graph (f) of Figure 48).

To clarify the discussion, let us assume that we aim at describing the DSW long time after the wave breaking when the initial pulse has split in two parts[4], i.e., $t > t_{\text{split}}$, see for instance the inset of Figure 53. In this case, as shown in graph (f) of Figure 48, λ^+ is made of two simple wave regions: II_r and III; the latter being glued to the background.

Since for λ^+ the wave breaking occurs at the boundary between region III and the background, region III is the first which is gradually absorbed in the DSW. The part of region III absorbed in the DSW at a given time t is denoted as region A, see Figure 55. In that case, the left edge of region A, corresponding to the solitonic edge, is connected to the remaining dispersionless part of the simple wave region III[5].

Then, at a time that denoted as $t_{\text{A|B}}$, region III is completely absorbed; it is now the turn of region II_r to be swallowed by the DSW, see graph (f) of Figure 48. The shock region is now divided in two domains A and B, whose boundary corresponds to $\lambda_4 = c_m$, with $c_m = \max[\lambda^+(x, t=0)]$, and is indicated by the green solid curve in Figure 55.

4 This is actually a reasonable assumption since Whitham modulational theory is correct at large enough values of time, when the DSW is well formed with a large number of oscillations [84].

5 Indeed, one may glance at graph (f) of Figure 48 to be convinced that region A is indeed connected to region III in the first few moments after the shock has formed.

Therefore, we need to treat separately both regions. The solution of the Euler-Poisson equation (517) in region A (B) is denoted as W^{A} (W^{B}). The matching condition between these two solutions reads

$$W^{\mathrm{A}}(\lambda_3, c_m) = W^{\mathrm{B}}(\lambda_3, c_m), \tag{519}$$

and is realized at a position that we denote by x_m. We also denote by x_{S} and x_{H} the positions of the solitonic edge [$m \to 1$ in expressions (490)] and of the harmonic edge [$m \to 0$ in expressions (490)], see Figure 55 where all these notations are summarized.

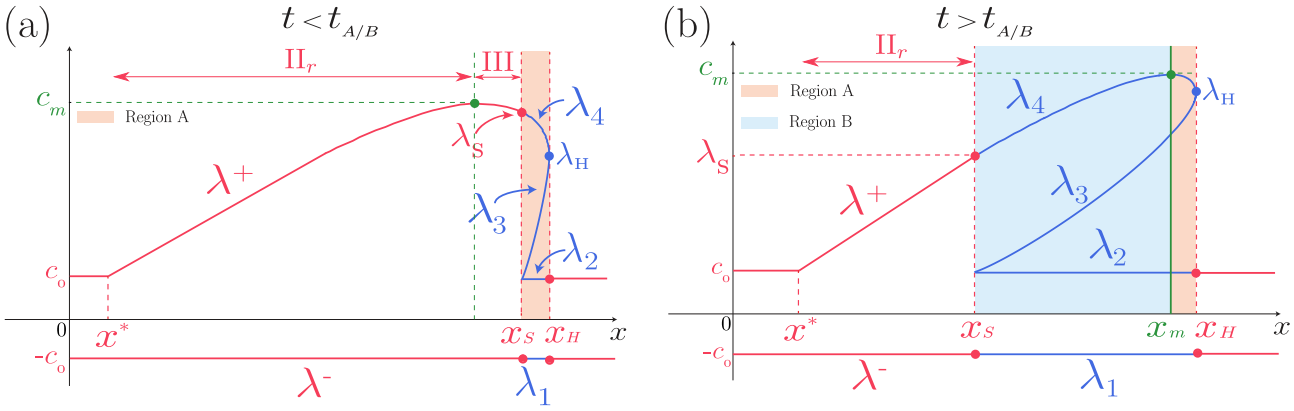

FIGURE 55: Schematic plots of the position dependence of the Riemann invariants inside (blue solid curves) and outside (pink solid curves) the DSW (colored region).
(a) For $t < t_{\mathrm{A/B}}$, the DSW is connected to the simple wave region III of the smooth dispersionless profile, see graph (f) of Figure 48. At $t = t_{\mathrm{A/B}}$, region III is completely absorbed by the DSW. Thus, for this time, the shock wave connects to the smooth profile exactly at $\lambda_+(x_{\mathrm{S}}(t), t) = c_m$.
(b) For $t > t_{\mathrm{A/B}}$, the DSW is connected at its left edge at a point belonging to region II_r of the smooth dispersionless profile, see graph (f) of Figure 48. In this case the shock wave is divided in two regions A and B, separated by the green vertical line in the plot. The continuity along the separation line between the two regions (i.e., at $x = x_m(t)$) is ensured by equation (519).
In both plots we introduce $\lambda_{\mathrm{S}} = \lambda_4(x_{\mathrm{S}}(t), t)$, the value of λ_4 at the solitonic edge of the DSW. The position $x^\star$ locates the left boundary of the simple wave region II_r, where λ^+ equals c_0. As in Figure 54, positions x_{S} and x_{H} locate the solitonic and harmonic edges of the DSW, respectively.

BOUNDARY CONDITIONS The general solution of the Euler-Poisson equation is made explicit in equation (518). We define two functions ψ^{A} and φ^{A}, such that

$$W^{\mathrm{A}}(\lambda_3, \lambda_4) = \int_{c_0}^{\lambda_3} \frac{\psi^{\mathrm{A}}(\mu)\, d\mu}{\sqrt{\lambda_3 - \mu}\sqrt{\lambda_4 - \mu}} + \int_{c_0}^{\lambda_4} \frac{\varphi^{\mathrm{A}}(\mu)\, d\mu}{\sqrt{|\lambda_3 - \mu|}\sqrt{\lambda_4 - \mu}} \tag{520}$$

is the solution of equation (517) in region A. Then, we can use the boundary conditions of the problem to find the expressions of both functions ψ^{A} and φ^{A}.

- The solitonic edge, located at position $x_{\rm S}$, connects region A (if $t < t_{\rm A|B}$) or region B (if $t \geq t_{\rm A|B}$) and the dispersionless profile (region III or II$_r$). Thus, one has at this edge

$$\lambda_1 = -c_0, \quad \lambda_2 = \lambda_3 = c_0, \quad \lambda_4 = \lambda^+(x_{\rm S}, t) \equiv \lambda_{\rm S}(t), \tag{521}$$

see Figure 55. The precise determination of $\lambda_{\rm S}(t)$ is given in Section 7.2.3.

Then, using equations (513), (499), (461) and (466), one obtains[6]

$$\begin{aligned} x_{\rm S} - \frac{1}{2}(3\lambda_{\rm S} - c_0)t &= w_4(c_0, \lambda_{\rm S}), \\ x_{\rm S} - \frac{1}{2}(3\lambda_{\rm S} - c_0)t &= w_+^{(i)}(\lambda_{\rm S}, -c_0), \end{aligned} \tag{522}$$

with the superscript $(i) = (3)$ if $t < t_{\rm A|B}$ or $(i) = (2)$ if $t \geq t_{\rm A|B}$. In the second equation of (522), the function $w_+^{(i)}(\lambda_{\rm S}, -c_0)$ has been defined in Chapter 6 [see equation (398)], and corresponds to $\partial W^{(i)}/\partial\lambda^+(\lambda_{\rm S}, -c_0)$, where $W^{(i)}$ is given by (431).

The set of equations (522) shows that $w_4(c_0, \lambda_{\rm S}) = w_+^{(i)}(\lambda_{\rm S}, -c_0)$. Using expression (516), this leads to

$$W^{\rm A,B}(c_0, \lambda_{\rm S}) + (2\,\lambda_{\rm S} - c_0)\frac{\partial W^{\rm A,B}}{\partial \lambda_4}(c_0, \lambda_{\rm S}) = w_+^{(i)}(\lambda_{\rm S}, -c_0), \tag{523}$$

where the superscript A corresponds to the superscript $(i) = (1)$, and B to $(i) = (2)$. Differential equation (523) can be easily solved and we arrive to the first boundary condition:

$$W^{\rm A}(c_0, \lambda_{\rm S}) = \frac{1}{2\sqrt{\lambda_{\rm S} - c_0}} \int_{c_0}^{\lambda_{\rm S}} \frac{w_+^{(3)}(r, -c_0)}{\sqrt{r - c_0}}\,{\rm d}r, \tag{524a}$$

$$\begin{aligned} W^{\rm B}(c_0, \lambda_{\rm S}) = &- \frac{1}{2\sqrt{\lambda_{\rm S} - c_0}} \int_{\lambda_{\rm S}}^{c_m} \frac{w_+^{(2)}(r, -c_0)}{\sqrt{r - c_0}} dr \\ &+ \frac{1}{2\sqrt{\lambda_{\rm S} - c_0}} \int_{c_0}^{c_m} \frac{w_+^{(3)}(r, -c_0)}{\sqrt{r - c_0}} dr\ , \end{aligned} \tag{524b}$$

where the second term of equation (524b) ensures that condition (519) is fulfilled.

- For the harmonic edge, at the right boundary of the DSW, one sees from Figure 54 and Figure 55 that $\lambda_3 \to \lambda_{\rm H} \equiv \lambda_4$. The second boundary equation consists of requiring that

$$W^{\rm A}(\lambda_3 = \lambda_{\rm H}, \lambda_4 = \lambda_{\rm H}) \text{ does not diverge.} \tag{525}$$

- Lastly, For $t \geq t_{\rm A|B}$, one needs to respect the boundary condition (519) connecting $W^{\rm A}$ and $W^{\rm B}$.

- The expression of $t_{\rm A|B}$ is determined in Section 7.2.3, see equation (534).

6 we also used $v_+(\lambda^+, \lambda^-) = \frac{1}{2}(3\lambda^+ + \lambda^-)$, see equation (395) with $c(\lambda^+ - \lambda^-) = \frac{1}{2}(\lambda^+ - \lambda^-)$ for an adiabatic index $\gamma = 2$.

SOLUTION IN REGION A Expression (520) with $\lambda_3 = c_0$ and the first boundary condition (524a) yield[7]

$$\varphi^{\mathrm{A}}(\mu) = \frac{1}{2\pi\sqrt{\mu - c_0}} \int_{c_0}^{\mu} \frac{w_+^{(3)}(r, -c_0)\,\mathrm{d}r}{\sqrt{\mu - r}} \,. \tag{526}$$

Then, the second boundary condition (525) imposes

More details can be found in Appendix E.

$$\psi^{\mathrm{A}}(\mu) = -\varphi^{\mathrm{A}}(\mu), \tag{527}$$

leading to the solution

$$W^{\mathrm{A}}(\lambda_3, \lambda_4) = \int_{\lambda_3}^{\lambda_4} \frac{\varphi^{\mathrm{A}}(\mu)\,\mathrm{d}\mu}{\sqrt{\mu - \lambda_3}\sqrt{\lambda_4 - \mu}} \,, \tag{528}$$

where φ^{A} is given by formula (526).

SOLUTION IN REGION B We look for a solution in this region in the form

$$W^{\mathrm{B}}(\lambda_3, \lambda_4) = W^{\mathrm{A}}(\lambda_3, \lambda_4) + \int_{\lambda_4}^{c_m} \frac{\varphi^{\mathrm{B}}(\mu)\,d\mu}{\sqrt{\mu - \lambda_3}\sqrt{\mu - \lambda_4}}, \tag{529}$$

The above expression ensures that W^{B}, (i) being the sum of two solutions of the Euler-Poisson equation, is also a solution of this equation and (ii) verifies the boundary condition (519) since the second term of the right-hand side of (529) vanishes when $\lambda_4 = c_m$.

Using the boundary condition (524b) for region B leads to the determination of $\varphi^{\mathrm{B}}(\mu)$:

See also Appendix E

$$\varphi^{\mathrm{B}}(\mu) = \frac{1}{2\pi\sqrt{\mu - c_0}} \int_{\mu}^{c_m} \frac{w_+^{(3)}(r, -c_0) - w_+^{(2)}(r, -c_0)}{\sqrt{r - \mu}} dr \,. \tag{530}$$

Inserting expression (530) in equation (529) gives the solution of the Euler-Poisson equation in region B.

Consequently, equation (528) together with equation (529) solve the problem in the shock region[8]. Before detailing the procedure to obtain the Riemann invariants λ_3 and λ_4 as functions of x and t (see Section 7.2.4), let us analyze more carefully the edges of the shock. This will determine the position of each edge $x_{\mathrm{S}}(t)$ and $x_{\mathrm{H}}(t)$ for any given time t, the value $\lambda_4(x_{\mathrm{S}}, t) = \lambda_{\mathrm{S}}(t)$, and also the time $t_{\mathrm{A|B}}$ when region B start arising.

7 To demonstrate this expression, we used the inverse Abel transformation [1], see Appendix E.

8 Expressions of W^{A} and W^{B} in term of a single integral can be found in Appendix E, see equations (625) and (627).

7.2.3 *Edges of the shock*

SOLITONIC EDGE We recall that the solitonic edge is located in our case at the left edge of the DSW (for the part of the pulse propagating to the right), see Figure 53. At this edge, the Riemann invariants are made explicit (521). The corresponding Whitham velocities are $v_3 = (\lambda_S + c_0)/2$ and $v_4 = (3\lambda_S - c_0)/2$ [see equations (499)], and both equations (513) read[9]

$$\begin{aligned} x_S - \frac{1}{2}(3\lambda_S - c_0)t &= w_4^\alpha(c_0, \lambda_S) = w_+^{(i)}(\lambda_S, -c_0), \\ x_S - \frac{1}{2}(\lambda_S + c_0)t &= w_3^\alpha(c_0, \lambda_S) = W^\alpha(c_0, \lambda_S), \end{aligned} \tag{531}$$

where we have introduced w_4^α and w_3^α:

$$w_i^\alpha(\lambda_3, \lambda_4) = W^\alpha + 2(v_i - V)\partial_i W^\alpha, \quad i \in \{3, 4\}, \tag{532}$$

with $\alpha = A$ ($\alpha = B$) in region A (in region B). In the set of equations (531) the superscripts are $\alpha = A$ and $(i) = (3)$ if $t < t_{A|B}$ or $\alpha = B$ and $(i) = (2)$ if $t \geq t_{A|B}$. This gives at once

$$t(\lambda_S) = \frac{1}{\lambda_S - c_0}\left[W^\alpha(c_0, \lambda_S) - w_+^{(i)}(\lambda_S, -c_0)\right], \tag{533a}$$

$$x_S(\lambda_S) = c_0\, t + \frac{1}{2}\left[3W^\alpha(c_0, \lambda_S) - w_+^{(i)}(\lambda_S, -c_0)\right], \tag{533b}$$

where $W^\alpha(c_0, \lambda_S)$, $\alpha = A, B$ are given by expressions (524). In particular, one can determine from equation (533a) the explicit expression of $t_{A|B} = t(\lambda_S = c_m)$:

$$t_{A|B} = \frac{-1}{(c_m - c_0)^{3/2}} \int_{c_0}^{c_m} \sqrt{r - c_0}\, \frac{dw_+^{(3)}(r, -c_0)}{dr}\, dr, \tag{534}$$

where we used an integration by parts in equation (524a).

In addition, for a given time t, the expression of $\lambda_S(t)$ is given implicitly by expression (533a). Once $\lambda_S(t)$ is determined, the position of the left edge $x_S(t)$ can be computed from equation (533b).

HARMONIC EDGE This edge corresponds to the right edge of the DSW in our case. For any given time t, this boundary is located at $x = x_H(t)$, where $\lambda_2 = -\lambda_1 = c_0$ and $\lambda_3 \to \lambda_H(t) \equiv \lambda_4(t)$, see Figure 54 and Figure 55. Note that this edge is always at the border with region A. Therefore, we obtain from (516):

$$x_H - v_H t = w_4^A(\lambda_H, \lambda_H), \tag{535}$$

where w_4^A is given by expression (532) and $v_H = 2\lambda_H - \frac{c_0^2}{\lambda_H}$ [see equation (503)]. Using the fact that $v_H = \mathrm{d}x_H/\mathrm{d}t$ [see equation (508)], differentiation of (535) with respect to time gives

$$t = -\frac{1}{\mathrm{d}v_H/\mathrm{d}\lambda_H}\frac{\mathrm{d}w_4^A(\lambda_H, \lambda_H)}{\mathrm{d}\lambda_H}. \tag{536}$$

9 Note that $w_3^\alpha(c_0, \lambda_S) = W^\alpha(c_0, \lambda_S)$ since $[v_3 - V](-c_0, c_0, c_0, \lambda_S) = 0$ and $\partial_3 W^\alpha(c_0, \lambda_S)$ remains finite, see equation (532).

Then, using together equations (532) and (528) leads to

$$w_4^{\mathrm{A}}(\lambda_{\mathrm{H}},\lambda_{\mathrm{H}}) = \pi\,\varphi^{\mathrm{A}}(\lambda_{\mathrm{H}}) + \pi\left(\lambda_{\mathrm{H}} - \frac{c_0^2}{\lambda_{\mathrm{H}}}\right)\frac{\mathrm{d}\varphi^{\mathrm{A}}}{\mathrm{d}\mu}(\lambda_{\mathrm{H}})\,, \tag{537}$$

and

$$\begin{aligned}\frac{\mathrm{d}w_4^{\mathrm{A}}(\lambda_{\mathrm{H}},\lambda_{\mathrm{H}})}{\mathrm{d}\lambda_{\mathrm{H}}} = \pi\left(2+\frac{c_0^2}{\lambda_{\mathrm{H}}^2}\right)\frac{\mathrm{d}\varphi^{\mathrm{A}}}{\mathrm{d}\mu}(\lambda_{\mathrm{H}}) \\ + \pi\left(\lambda_{\mathrm{H}} - \frac{c_0^2}{\lambda_{\mathrm{H}}}\right)\frac{\mathrm{d}^2\varphi^{\mathrm{A}}}{\mathrm{d}\mu^2}(\lambda_{\mathrm{H}})\,,\end{aligned} \tag{538}$$

where φ^{A} is given by expression (526). Inserting equation (538) in equation (536) yields

$$t = -\pi\,\frac{\mathrm{d}\varphi^{\mathrm{A}}}{\mathrm{d}\mu}(\lambda_{\mathrm{H}}) - \pi\,\frac{\lambda_{\mathrm{H}}^2 - c_0^2}{2\lambda_{\mathrm{H}}^2 + c_0^2}\,\frac{\mathrm{d}^2\varphi^{\mathrm{A}}}{\mathrm{d}\mu^2}(\lambda_{\mathrm{H}}). \tag{539}$$

Thus, for a fixed time t, the value of $\lambda_{\mathrm{H}}(t)$ is determined implicitly by means of the previous equation. Then, the position of the harmonic edge $x_{\mathrm{H}}(t)$ can be obtained from equation (535) with the use of expression (537).

WEAK SHOCK THEORY Let us examine the asymptotic behaviour of the shock at large time $t \to \infty$. In this case, $t > t_{\mathrm{A|B}}$ and $\lambda_{\mathrm{S}} \to c_0$; using expression (533a) with $\alpha = B$ and performing an integration by parts for each integral of equation (524b), leads to

$$t(\lambda_{\mathrm{S}} \to c_0) \simeq \frac{\mathcal{A}}{(\lambda_{\mathrm{S}} - c_0)^{3/2}}, \tag{540}$$

with

$$\begin{aligned}\mathcal{A} = -\left(\int_{c_m}^{c_0}\sqrt{r-c_0}\,\frac{\mathrm{d}w_+^{(2)}(r,-c_0)}{\mathrm{d}r}\,\mathrm{d}r\right. \\ \left. + \int_{c_0}^{c_m}\sqrt{r-c_0}\,\frac{\mathrm{d}w_+^{(3)}(r,-c_0)}{\mathrm{d}r}\,\mathrm{d}r\right).\end{aligned} \tag{541}$$

We thus obtain the asymptotic expressions

$$\lambda_{\mathrm{S}}(t\to\infty) \simeq c_0 + \left(\frac{\mathcal{A}}{t}\right)^{2/3}, \quad x_{\mathrm{S}}(t\to\infty) \simeq c_0\,t + \frac{3\mathcal{A}^{2/3}}{2}\,t^{1/3}\,. \tag{542}$$

At large enough time, the dispersionless profile between $x^\star$ and x_{S} (corresponding to the simple-wave region II_r, see Figure 55) depends only on the self-similar variable[10] $(x - x^\star)/t$, and so does λ^+. In addition, one sees from graph (e) of Figure 48 that $x^\star(t_{\mathrm{split}}) = 0$, and thus $x^\star(t) = c_0(t - t_{\mathrm{split}})$; at large time, one can consider that $x^\star(t) \simeq c_0\,t$.

10 Indeed, asymptotically, as one can guess from expressions (542), the details of the initial distribution are lost; it is thus reasonable to consider that the dispersionless profile only depends on a self-similar variable of type x/t.

This approximation and the self-similarity of the profile in region II_r, together with the use of equation (393), lead to

$$\lambda^+ = c_0 + \frac{2}{3}\frac{x - x^\star}{t}, \quad \lambda^+ \in \mathrm{II}_r, \quad t \gg t_{\mathrm{WB}}. \tag{543}$$

Then, one can extract from the second equation of (394) the corresponding density profile in this simple-wave region:

$$\rho(x,t) = \left(c_0 + \frac{1}{3}\frac{x - x^\star}{t}\right)^2, \quad x \in [x^\star, x_{\mathrm{S}}], \quad t \gg t_{\mathrm{WB}}. \tag{544}$$

Using the second equation of (542), we obtain

$$\int_{x^\star}^{x_{\mathrm{S}}} \left(\sqrt{\rho(x,t)} - c_0\right)^{1/2} = \frac{\mathcal{A}}{\sqrt{2}}, \tag{545}$$

where $\mathcal{A}$ is given by expression (541) and is thus associated to a conserved quantity during the propagation of the dispersive nonlinear pulse. First, it is worth noticing that we found the same type of conserved quantity in the case of the Korteweg-de Vries equation [93]. Second, our results obtained for dispersive shock waves provide the counterpart of the weak viscous shock theory [197] : (i) a nonlinear pattern of triangular shape (see the dispersionless profile depicted in Figure 53) may also appear at the rear edge of a (viscous) shock, (ii) the details of the initial distribution are lost at large time (as in the present case) and (iii) a conserved quantity of the type (545) also exists.

7.2.4 *Procedure of resolution and results*

PROCEDURE OF RESOLUTION It is now possible to completely describe the evolution of the DSW during its propagation using the results obtained in Section 7.2.2 and in Section 7.2.3.

First, one needs to compute the time $t_{\mathrm{A|B}}$ from expression (534). Then,

- for $t \leq t_{\mathrm{A|B}}$ (see graph (a) of Figure 55),

  One starts to calculate $\lambda_{\mathrm{S}}(t)$ by inverting expression (533a) and $\lambda_{\mathrm{H}}(t)$ by solving equation (539). Then, one picks $\lambda_4 \in [\lambda_{\mathrm{H}}, \lambda_{\mathrm{S}}]$ and finds the corresponding value for λ_3 by solving

  $$t = -\frac{w_4^{\mathrm{A}}(\lambda_3,\lambda_4) - w_3^{\mathrm{A}}(\lambda_3,\lambda_4)}{v_4(\lambda_3,\lambda_4) - v_3(\lambda_3,\lambda_4)}, \tag{546}$$

  where we used the shortcut notation $v_i(\lambda_3,\lambda_4) = v_i(-c_0, c_0, \lambda_3, \lambda_4)$, $i \in \{3,4\}$, and where w_i^{A}, $i \in \{3,4\}$ are determined[11] from equations (532). Once λ_3 is determined, all the Riemann invariants are known and can be inserted in equations (490) to find the corresponding density and velocity distributions $\rho(x,t)$ and $u(x,t)$. The position x associated to a set of Riemann invariants $\{\lambda_3,\lambda_4\}$ can be computed from one of the equations (513).

11 The potential $W^{\mathrm{A}}(\lambda_3,\lambda_4)$ (and its first derivative with respect to λ_3 or to λ_4) can be easily computed numerically from expression (625).

- for $t \geq t_{\mathrm{A|B}}$, (see graph (b) of Figure 55)

  The situation is not much more difficult than the previous point. One also determines $\lambda_{\mathrm{S}}(t)$ and $\lambda_{\mathrm{H}}(t)$ from equations (533a) and (539). Then, the procedure is divided in two steps:

  – For $\lambda_4 \in [\lambda_{\mathrm{S}}, c_m]$, one finds the corresponding value for λ_3 by solving[12]

  $$t = -\frac{w_4^{\mathrm{B}}(\lambda_3, \lambda_4) - w_3^{\mathrm{B}}(\lambda_3, \lambda_4)}{v_4(\lambda_3, \lambda_4) - v_3(\lambda_3, \lambda_4)}. \tag{547}$$

  – For $\lambda_4 \in [\lambda_{\mathrm{H}}, c_m]$, one finds the corresponding value for λ_3 by solving equation (546).

  Then, the problem is solved: one computes the density and velocity distributions by means of equations (490), and the position x associated to a set of Riemann invariants $\{\lambda_3, \lambda_4\}$ from one of the equations (513).

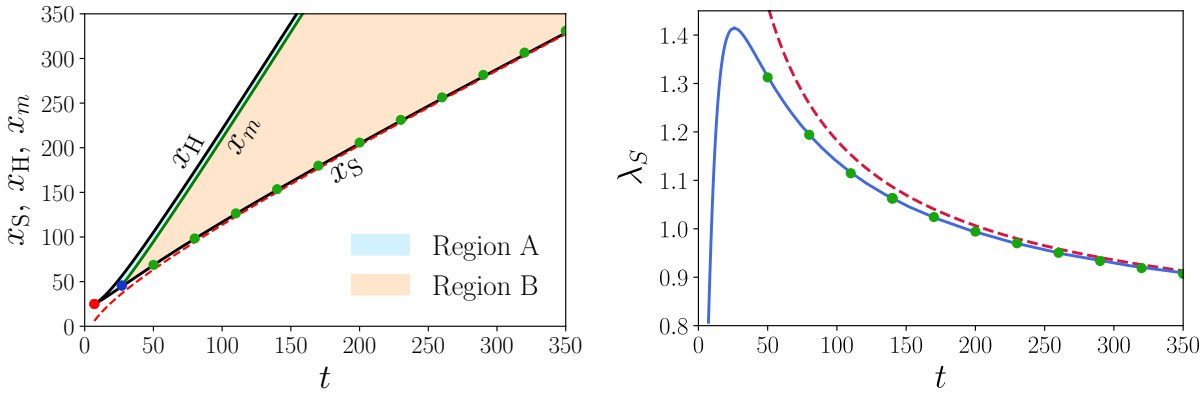

FIGURE 56: (Left) Black solid curves: time evolution of $x_{\mathrm{S}}(t)$ and $x_{\mathrm{H}}(t)$ calculated from equations (533b) and (535). Green solid curve: time evolution of $x_m(t)$ computed from equation (548), for which $\lambda_4(x_m(t), t) = c_m$. This position delimits region A from region B. Red dashed line: asymptotic behavior of $x_{\mathrm{S}}(t)$, from the second equation of (542). The green points indicate the position $x_{\mathrm{S}}(t)$ extracted from simulations, for an initial condition (450) with $\rho_0 = 0.5$, $\rho_1 = 1.5$ and $x_0 = 20$ [we also take initially $u(x, t = 0) = 0$]. The red dot marks the birth of the DSW [at time $t_{\mathrm{WB}} \simeq 6.3$, see equation (467)], while the blue one initiates region B [at time $t_{\mathrm{A|B}} \simeq 25.9$, computed from equation (534)]. (Right) Blue solid curve: time evolution of $\lambda_{\mathrm{S}}(t)$ from equation (533a). Red dashed line: asymptotic behavior, from the first equation of (542). The green points are extracted from simulations for different times, for the initial profile (450) with $\rho_0 = 0.5$, $\rho_1 = 1.5$ and $x_0 = 20$ [and $u(x, t = 0) = 0$].

12 The potential $W^{\mathrm{B}}(\lambda_3, \lambda_4)$ (and its first derivative with respect to λ_3 or to λ_4) can be easily computed numerically from expression (627).

RESULTS The position $x_m(t)$ at the boundary between region A and B is computed as follows: one determines the value of λ_3^m associated to $\lambda_4(x_m(t),t) = c_m$ by solving equation (546). Once λ_3^m is found, one can use equation (513) to compute $x_m(t)$:

$$x_m(t) = v_4(\lambda_3^m, c_m)\, t + w_4^{\mathrm{A}}(\lambda_3^m, c_m). \tag{548}$$

The left plot of Figure 56 shows $x_{\mathrm{S}}(t)$, $x_m(t)$ and $x_{\mathrm{H}}(t)$ computed from equations (533b), (548) and (535), respectively. The blue and green dots are extracted from simulations and match well with the theoretical results. The red dashed line corresponds to the asymptotic behaviour of $x_{\mathrm{S}}(t)$, see equation (542).

The blue curve in the right plot of Figure 56 corresponds to $\lambda_4(x_{\mathrm{S}}(t),t) = \lambda_{\mathrm{S}}(t)$ [computed from (533a)], while the red dashed curve represents its asymptotic behaviour, extracted from (542). The green dots are obtained from simulations and nicely agree with the theoretical expectation.

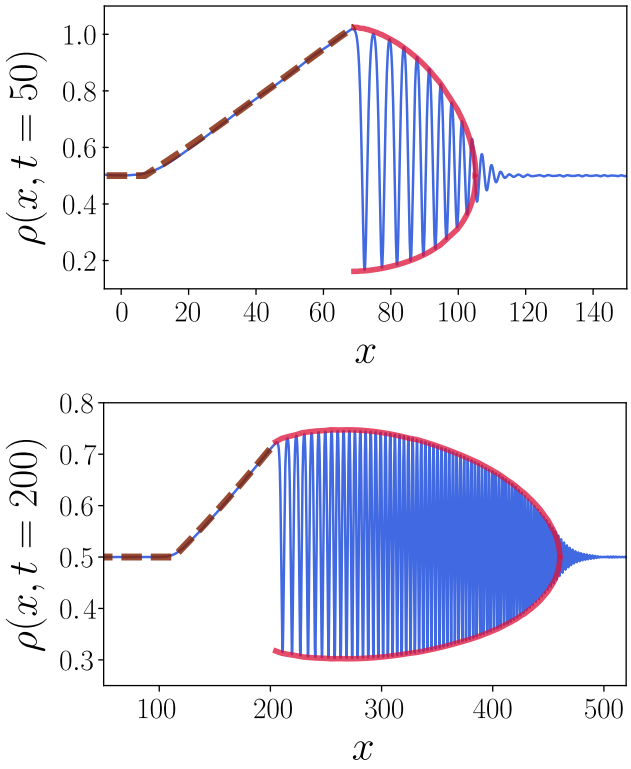

FIGURE 57: Comparison between theory and numerical simulations for the density profile $\rho(x,t)$ at $t = 50$ (upper plot) and $t = 200$ (lower plot). The initial profile is given by expression (450), with $\rho_0 = 0.5$, $\rho_1 = 1.5$ and $x_0 = 20$ [and $u(x, t = 0) = 0$]. The blue curves are the numerical results. The red solid lines are the envelopes of the density (490) where the λ_i's are calculated by the procedure described at the beginning of this section. The dashed brown lines correspond to the the dispersionless part of the profile, determined using Riemann's method exposed in Chapter 6.

The results for the density profile using Whitham modulational theory are shown in Figure 57 at different values of time for the initial distributions (450) (with $\rho_0 = 0.5$, $\rho_1 = 1.5$, $x_0 = 20$) and (451). The agreement with numerical simulations is excellent. Note that Whitham's theory leads to a correct determination of the envelopes but not of the phase along the DSW. This parameter indeed vary too fast in the shock region to be properly described by the Whitham equations[13].

In Figure 58 we also compare the wavelength of the nonlinear oscillations within the DSW as determined by Whitham approach [see equation (494)] with the results of numerical simulations, and the agreement is again very good.

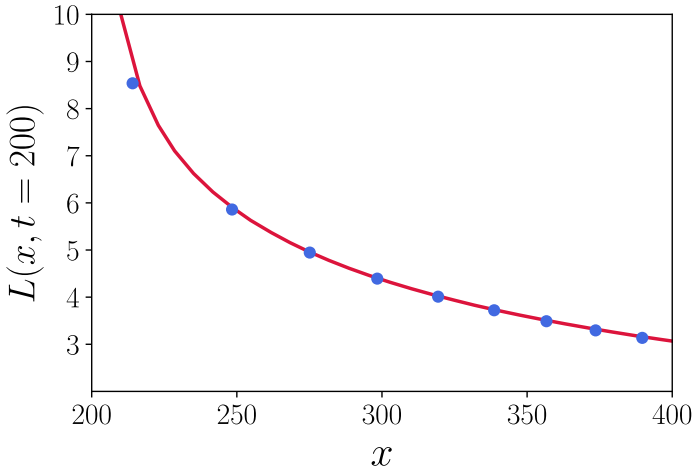

FIGURE 58: Wavelength of the nonlinear oscillations within the DSW for $t = 200$. The theoretical red curve is calculated from equation (494). The blue points are extracted from simulations.

7.3 EXPERIMENTAL CONSIDERATIONS

In Section 7.2.4, and more generally in this chapter and the previous one, we proved that Riemann's method and Whitham modulational theory are powerful tools to describe the propagation of nonlinear pulses governed by the nonlinear Schrödinger equation. However, the results derived above require a good grasp of these methods.

This is the reason why we would like to show in this section that some parameters can be extracted from our theoretical results, and, in particular, from the weak shock theory described in Section 7.2.3. This will give accurate, albeit approximate, analytic expressions.

The contrast of the fringes in the DSW is an example of an experimentally relevant parameter. Indeed, if one wish to observe experimentally the formation of a dispersive shock wave, it might be interesting to tune carefully the initial parameters of the pulse to maximize the visibility

13 Some studies have been conducted by T. Grava to describe the phase along the DSW in the case of the Korteweg-de Vries equation, see, e.g., [136].

of the oscillations in the shock region. This question has been actually studied in Ref. [200] by Xu *et al.* in a nonlinear optical fiber, by varying the intensity of the background. In this case, the dynamics in the optical fiber is governed by the following equation [7]:

$$-i\partial_z A = -\frac{\beta_2}{2}\partial_t^2 A + \gamma|A|^2 A + i\frac{\alpha}{2}A, \tag{549}$$

where A is the envelope amplitude [as in equation (358)], β_2 encompasses dispersive effects, γ the nonlinear coefficient and α accounts for the linear loss. Therefore, one sees immediately that equation (549) is a one-dimensional nonlinear Schrödinger equation, where time is played by the variable x in equation (489).

In Ref. [200], the fiber has a fixed length $L = 3$ km and the initial profile is a Gaussian bump — i.e., different from (450) — on top of a background:[14]

$$|A(t, z = 0)|^2 = P_0 + P_1\, e^{-2\,t^2/t_0^2}, \tag{550}$$

with $t_0 = 18.3$ ps, $P_1 = 5.9$ W and P_0 is the background power, which varies in the experiment. In addition, in this experiment [200], $\gamma = 3\,(\mathrm{W.km})^{-1} > 0$ and $\beta_2 = 2.5\,10^{-26}\,\mathrm{s}^2/\mathrm{m} > 0$, leading to a self-defocusing behavior of equation (549).

As we proceeded in Section 5.1, we can work with dimensionless quantities. We choose a reference power $P_{\mathrm{ref}} = 1$ W and define an effective time $\tau = \gamma\, P_{\mathrm{ref}} z$, an effective transverse length $x = t\sqrt{\frac{\gamma P_{\mathrm{ref}}}{\beta_2}}$ and the quantity $\psi = A/\sqrt{P_{\mathrm{ref}}}$, solution of the one-dimensional nonlinear Schrödinger equation

$$-i\,\partial_\tau \psi = -\frac{1}{2}\partial_x^2\psi + |\psi|^2\psi + i\,\alpha_{\mathrm{eff}}\psi, \tag{551}$$

where $\alpha_{\mathrm{eff}} = \frac{\alpha}{2\gamma P_{\mathrm{eff}}}$ is the dimensionless absorption coefficient.

The initial 'density' profile then reads

$$\rho(x, \tau = 0) = |\psi(x, 0)|^2 = \rho_0 + \rho_1\, e^{-2\,x^2/x_0^2}, \tag{552}$$

with $\rho_0 = P_0/P_{\mathrm{ref}}$, $\rho_1 = P_1/P_{\mathrm{ref}} = 5.9$ and $x_0 = t_0\sqrt{\frac{\gamma P_{\mathrm{ref}}}{\beta_2}} = 6.3$.

The final 'density' profile is imaged at the output of the fiber of length $L = 3$ km; this corresponds to an effective time $\tau^{\mathrm{out}} = \gamma P_{\mathrm{ref}} L = 9$.

A quantitative evaluation of the visibility of the oscillations near the solitonic edge of the DSW has been obtained in Ref. [200] by measuring the contrast defined as follows

$$C_{\mathrm{ont}} = \frac{\rho_{\max} - \rho_{\min}}{\rho_{\max} + \rho_{\min}}\,, \tag{553}$$

14 We recall that t plays the role of the transverse length x and z corresponds to an effective time.

where $\rho_{\max}$ and $\rho_{\min}$ are defined in graph (b) of Figure 59 (this figure has been extracted from Ref. [200]). The contrast was measured experimentally for different initial configurations (552) by keeping ρ_1 and x_0 fixed and varying ρ_0. The experimental result agreed very well with numerical simulations taking into account absorption in the fiber, as illustrated in Figure 59.

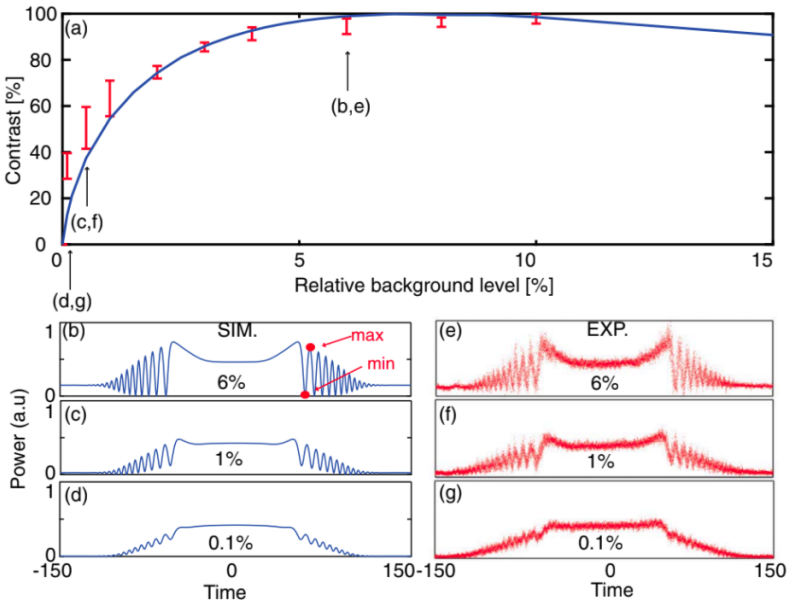

FIGURE 59: (a) Contrast of the fringes of a dispersive shock wave formed by a nonlinear pulse propagating in an optical fiber. The contrast is defined by expression (553), where $\rho_{\max}$ and $\rho_{\min}$ are shown in graph (b). The blue curve corresponds to the numerical results, while the red bars (with error bars) are obtained experimentally. Different experimental profiles are shown in figures (e), (f) and (g) for different relative background level P_0/P_1; these quantities correspond to the initial powers of the background and the bump, see equation (550). Graphs (b), (c) and (d) are the corresponding profiles obtained from simulations for the same set of initial parameters. Note that here, P_1 is left fixed, while P_0 varies.

In our case, we do not consider exactly the same initial profile and do not take damping into account, but we show that our approach gives a very reasonable analytic account of the behavior of C_{ont} considered as a function of ρ_0/ρ_1.

In addition, we do not choose exactly the same definition of $\rho_{\max}$ [appearing in equation (553)] as in Ref. [200]: we decided to take $\rho_{\max}$ as being located at the solitonic edge (see the inset of Figure 62) because it has a simple analytic expression there. Indeed, from equation (498) (i.e., when $m \to 1$, which is the relevant regime near the solitonic edge of the DSW), we obtain

$$\rho_{\max} = \tfrac{1}{4}(\lambda_{\text{S}} + c_0)^2 \ , \quad \text{and} \quad \rho_{\min} = \tfrac{1}{4}(\lambda_{\text{S}} - 3c_0)^2 \ , \tag{554}$$

yielding

$$C_{\rm ont} = \frac{4c_0(\lambda_{\rm S}-c_0)}{(\lambda_{\rm S}-c_0)^2+4c_0^2}\,. \tag{555}$$

At this stage, an exact computation of the previous expression can be performed by inverting equation (533a) to find $\lambda_{\rm S}$. As expected, the exact result, corresponding to the blue curve in Figure 62, agrees very well with the contrast determined by numerical simulations (green dots in the same figure).

However, let us now make some approximations to obtain a simple analytic expression.

First, we use the large-time expression of $\lambda_{\rm S}$ corresponding to the first equation of (542). This asymptotic expression is valid when $t \gg t_{\rm WB}$, $t = \tau^{\rm out} = 9$ being fixed here. The experimental ratio ρ_0/ρ_1 ranges from 0.1 to 10 % (see Figure 59). As we can see from Figure 60, where we have computed[15] $\tau^{\rm out}/t_{\rm WB}$ as a function of ρ_0/ρ_1, the effective time at the output of the optical fiber is at least ten times larger than the wave breaking time in the range of experimental values. This justifies the use of the asymptotic expression of $\lambda_{\rm S}$ for computing the contrast (555) and we introduce the quantity ξ defined as follows:

$$\xi = \left(\frac{\lambda_{\rm S}}{c_0}-1\right)^{3/2} \simeq \frac{\mathcal{A}}{c_0^{3/2}\,\tau^{\rm out}}, \tag{556}$$

where $\mathcal{A}$ is given by expression (541).

Second, we also use the approximation[16]

$$\begin{aligned}\mathcal{A} &\simeq -\left(\int_{c_m}^{c_0}\sqrt{r-c_0}\,\frac{{\rm d}\bar{x}^{(1)}(r)}{{\rm d}r}{\rm d}r + \int_{c_0}^{c_m}\sqrt{r-c_0}\,\frac{{\rm d}\bar{x}^{(3)}(r)}{{\rm d}r}{\rm d}r\right)\\ &= 2\int_0^{x_0}\sqrt{\lambda^+(x,0)-c_0}\;dx,\end{aligned} \tag{557}$$

where we have replaced $w_+^{(2)}(r,-c_0)$ and $w_+^{(3)}(r,-c_0)$ by $\bar{x}^{(1)}(r)$ and $\bar{x}^{(3)}(r)$, defined by expressions (453). A new change of variable yields

$$\mathcal{A} \simeq 2x_0\sqrt{c_0}\,F(\rho_0/\rho_1)\;, \tag{558}$$

where

$$F(\alpha) = \int_0^{\pi/2}\cos\theta\left(\sqrt{1+\frac{\cos^2\theta}{\alpha}}-1\right)^{1/2}d\theta. \tag{559}$$

15 Note the factor 2 of difference in the exponential between the initial density profile (552) and the one defined in equation (432) of Chapter 6. This amounts to take $t_{\rm WB}/\sqrt{2}$, with $t_{\rm WB}$ given by expression (441).

16 One can prove this result by using the symmetry property of the system $\bar{x}^{(1)}(r) = -\bar{x}^{(3)}(r)$ and making the change of variable $x = \bar{x}^{(3)}(r) \Leftrightarrow r = \lambda^+(x>0,0)$, in which $\lambda^+(x,0) = \sqrt{\rho}(x>0,0)$ where $\rho(x>0,0)$ is half of the initial density profile — whose explicit expression is given in (450).

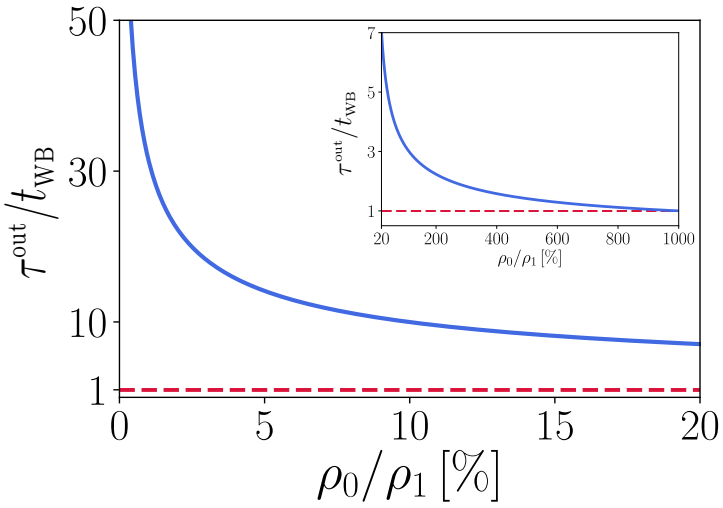

FIGURE 60: (Left) Blue curve : ratio of the effective time at the output of the fiber $\tau^{\rm out} = 9$ by the wave breaking time $t_{\rm WB}$, computed from expression (441) and for an initial Gaussian beam (552), as a function of the initial ratio ρ_0/ρ_1. The red dashed curve corresponds to $t_{\rm WB} = \tau^{\rm out}$, i.e., in the considered case, $t_{\rm WB} = 9$. The inset shows the same curves for higher density background (we recall that in the experiment $\rho_1 = 5.9$ is fixed and only ρ_0 varies).

A simple analytic expression of $F(\alpha)$ cannot be obtained, but we checked that one can devise an accurate approximation by expanding the term in the above integrand around $\theta = 0$ up to second order in θ. This yields

$$F(\alpha) \simeq \frac{(\sqrt{\alpha+1}-\sqrt{\alpha})^{1/2}}{\alpha^{1/4}} - \frac{\frac{1}{4}(\pi^2/4-2)}{\alpha^{1/4}\sqrt{1+\alpha}(\sqrt{\alpha+1}-\sqrt{\alpha})^{1/2}}\,. \tag{560}$$

A comparison between the exact result (559) and the approximate expression (560) is shown in Figure 61. The maximal relative error in the range of experimental values $\alpha \in [0, 0.1]$, i.e., ρ_0/ρ_1 between 0 and 10 %, is less than 2 %. Thus, we can safely use the approximate result (560), which is also valid for much larger values of α, see the inset of Figure 61.

Therefore, we arrive to a simple analytic equation for the contrast (555) in terms of the parameter ξ defined in (556):

$$C_{\rm ont} = \frac{4\,\xi^{2/3}}{4+\xi^{4/3}}, \quad \text{with} \quad \xi \simeq \frac{2\,x_0}{\sqrt{\rho_1}\,\tau^{\rm out}}\sqrt{\frac{\rho_1}{\rho_0}}\,F\left(\frac{\rho_0}{\rho_1}\right), \tag{561}$$

where we used the approximate expression (558) to evaluate ξ. The result is represented as a red curve in Figure 62. As one can see, it compares quite well with the value of $C_{\rm ont}$ extracted from the numerical simulations. The better agreement with the numerical result is reached for small ρ_0/ρ_1; this was expected: in this regime the wave breaking occurs rapidly ($\tau^{\rm out}/t_{\rm WB} \to \infty$, see Figure 60), and one easily fulfills the

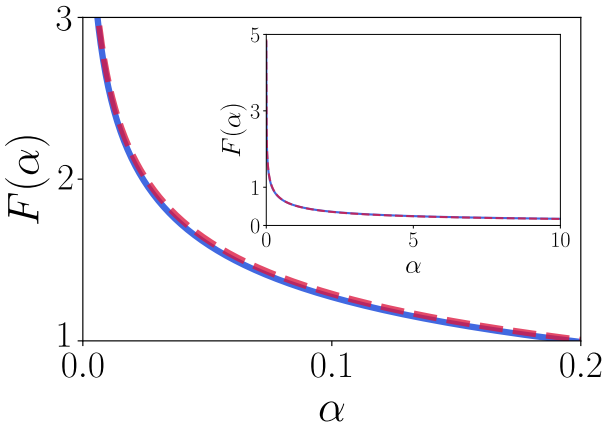

FIGURE 61: Blue curve: $F(\alpha)$ computed from the exact result (559). Dashed red curve: approximate result evaluated from expression (560). The inset shows $F(\alpha)$ for a wider range of possible values α.

condition $\tau^{\text{out}} \gg t_{\text{WB}}$ where the approximation (542) holds. Moreover, one sees that experimental data extracted from Ref. [200] and represented as brown bars in Figure 62 match well with the analytic result given by (561), despite the approximations we made and the fact that the form of the initial profile considered in this reference is not exactly the same as ours.

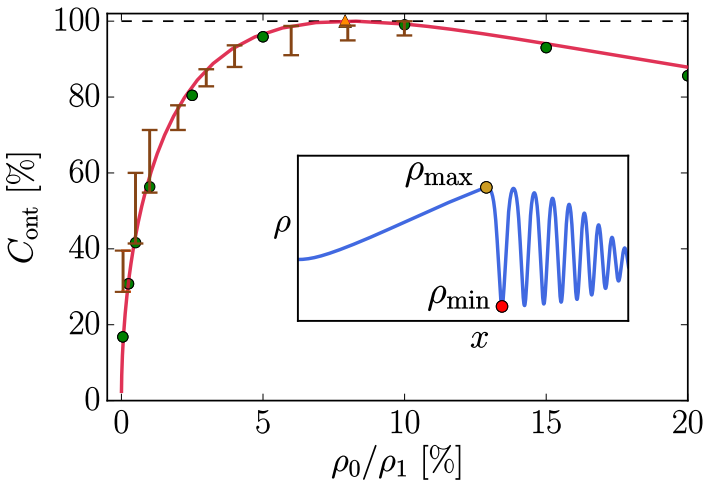

FIGURE 62: Contrast C_{ont} represented as a function of ρ_0/ρ_1. In order to follow the procedure used in Ref. [200], we fixed here the values of ρ_1, x_0 and τ^{out} [$\rho_1 = 2$, $x_0 = 20$ and $\tau^{\text{out}} = 49$ – which give the same contrast as $\rho_1 = 5.9$, $x_0 = 6.3$ and $\tau^{\text{out}} = 9$, see the text below equation (562)] and varied the value of ρ_0. The green dots correspond to the numerically determined value of the contrast, obtained from equation (553) where ρ_{min} and ρ_{max} are defined as illustrated in the inset. The yellow triangle pinpoints the density ratio ρ_0/ρ_1 for which the contrast is unity, see in particular equation (562). The red curve corresponds to the contrast computed from the approximate expression (561). The brown bars are experimental data extracted from Ref. [200].

In addition, there is a special value of ρ_0/ρ_1 for which the contrast is unity, meaning that the quantity $\rho_{\min}$ cancels. One sees from (554) that this is obtained for $\xi = 3$, i.e., $2c_0 \simeq (\mathcal{A}/\tau^{\text{out}})^{2/3}$. Using expression (558), the contrast is thus unity when

$$\frac{c_0\,\tau^{\text{out}}}{x_0} = \frac{1}{\sqrt{2}}\,F(\rho_0/\rho_1)\,. \tag{562}$$

A numerical solution of this equation gives, for the parameters of Figure 62, a contrast unity when $\rho_0/\rho_1 = 7.7\%$, while the exact equation (555) predicts a maximum contrast when $\rho_0/\rho_1 = 8.3\%$ instead (indicated by a yellow triangle in Figure 62).

Besides, one sees from equation (561) that different sets of parameters x_0, ρ_1 and τ^{out} (the effective time being fixed by the length of the fiber in this specific case) such that

$$\frac{\sqrt{\rho_1}\,\tau^{\text{out}}}{x_0} = \text{ Constant} \tag{563}$$

all lead to the same contrast C_{ont}. For instance, taking $\rho_1 = 5.9$, $x_0 = 6.3$ and $\tau^{\text{out}} = 9$ ($\sqrt{\rho_1}\,\tau^{\text{out}}/x_0 = 3.47$) yields the same result for the contrast as taking $\rho_1 = 2$, $x_0 = 20$ and $\tau^{\text{out}} = 49$ (which corresponds to the red dashed curve in Figure 62). We did not plot both curves for these two different configurations for legibility of the figure.

To conclude, we have demonstrated that our approach successfully describes the propagation of a dispersive shock wave in a system whose dynamics is governed by the nonlinear Schrödinger equation. Similar results have been also obtained for the Korteweg-de Vries equation [93], but are not reproduced in this thesis. In both cases, we were able to find the evolution of the Riemann invariants in the shock region, when two of them were varying.

However, the solutions of the problem are often implicit and require the use of numerical computations to extract, for instance, the envelopes of the DSW at a certain time t.

Nevertheless, we also proved that it was possible to extract from our approach a weak shock theory for these dispersive systems, exactly as it was done for viscous shocks [197]. This asymptotic description of the DSW can be used in some physical systems as soon as $t \gg t_{\text{WB}}$; when this condition is fulfilled, one can compute certain experimental quantities, such as the contrast of the fringes in the DSW, from simple analytic expressions derived from the weak shock theory. Therefore, beyond the mathematical description and the richness of Whitham modulational theory to describe nonlinear systems, one can also predict the behavior of parameters of experimental relevance: determining for instance the best configuration for visualizing the fringes of the DSW should be useful for future studies.

7.4 ARTICLE: LONG-TIME EVOLUTION OF PULSES IN THE KORTEWEG–DE VRIES EQUATION IN THE ABSENCE OF SOLITONS REEXAMINED: WHITHAM METHOD

This work, albeit not discussed in this thesis, was an important step in our understanding of the problem, before considering the more complicated case of the nonlinear Schrödinger equation.

↪ Long-time evolution of pulses in the Korteweg–de Vries equation in the absence of solitons reexamined: Whitham method

M. Isoard, A.M. Kamchatnov, N. Pavloff, Physical Review E **99**, 012210 (2019)

doi: https://doi.org/10.1103/PhysRevE.99.012210

We consider the long-time evolution of pulses in the Korteweg–de Vries equation theory for initial distributions which produce no soliton but instead lead to the formation of a dispersive shock wave and of a rarefaction wave. An approach based on Whitham modulation theory makes it possible to obtain an analytic description of the structure and to describe its self-similar behavior near the soliton edge of the shock. The results are compared with numerical simulations.

Long-time evolution of pulses in the Korteweg–de Vries equation in the absence of solitons reexamined: Whitham method

M. Isoard,[1] A. M. Kamchatnov,[2,3] and N. Pavloff[1]
[1]*LPTMS, CNRS, Univ. Paris-Sud, Université Paris-Saclay, 91405 Orsay, France*
[2]*Institute of Spectroscopy, Russian Academy of Sciences, Troitsk, Moscow, 108840, Russia*
[3]*Moscow Institute of Physics and Technology, Institutsky lane 9, Dolgoprudny, Moscow region, 141701, Russia*

(Received 12 October 2018; published 16 January 2019)

We consider the long-time evolution of pulses in the Korteweg–de Vries equation theory for initial distributions which produce no soliton but instead lead to the formation of a dispersive shock wave and of a rarefaction wave. An approach based on Whitham modulation theory makes it possible to obtain an analytic description of the structure and to describe its self-similar behavior near the soliton edge of the shock. The results are compared with numerical simulations.

DOI: 10.1103/PhysRevE.99.012210

I. INTRODUCTION

It is well known that pulses propagating through a nonlinear medium typically experience wave breaking. Their long-time evolution depends on which effect—in addition to the nonlinearity—dominates after the wave breaking moment: viscosity or dispersion. If viscosity dominates, then the shock corresponds to a region of localized extend in which the slow variables display a sharp transition. A typical small-amplitude viscous shock can be modeled by the Burgers' equation

$$u_t + uu_x = \nu u_{xx}, \tag{1}$$

for which a full analytic theory has been developed (see, e.g., Ref. [1]). For a positive initial profile $u(x, t = 0) \equiv u_0(x) > 0$ which is well-enough localized [i.e., $u_0(x) \to 0$ fast enough for $|x| \to \infty$] the time-evolved pulse acquires a triangle-like shape at its front edge [or at its rear edge if $u_0(x) < 0$[1]], gradually spreading out with decreasing amplitude.

The situation changes drastically if dispersive effects dominate rather than viscosity. In this case the typical evolution can be described by the celebrated Korteweg–de Vries (KdV) equation

$$u_t + 6uu_x + u_{xxx} = 0, \tag{2}$$

which admits oscillating solutions ranging from linear waves to bright solitons. A positive localized initial pulse $u_0(x) > 0$, after an intermediate stage of wave breaking and complicated deformation, eventually evolves into a sequence of solitons with some amount of linear dispersive waves. The characteristics of the solitons are determined by the initial distribution $u_0(x)$. If this initial pulse is intense enough—so that the number of solitons is large—one may determine the parameters of these solitons by means of the asymptotic formula of Karpman [2] which is obtained in the framework of the inverse scattering transform method discovered by Gardner, Green, Kruskal, and Miura [3]. However, if $u_0(x) < 0$, since Eq. (2) does not admit dark (i.e., "negative") solitons, then wave breaking does not result in the production of solitons, but it rather leads to the formation of a dispersive shock wave (DSW) connected to a triangle-like rarefaction wave which is the remnant of the initial trough. The shape and the time evolution of this oscillatory structure are highly nontrivial and considerable efforts have been invested in their study.

In an early investigation of Berezin and Karpman [4] it was shown that the KdV equation admits solutions of the form

$$u(x, t) = \frac{1}{t^{2/3}} f\left(\frac{x}{t^{1/3}}\right), \tag{3}$$

and numerical simulations of these authors demonstrated that some region of the evolving wave structure is indeed described by solutions of type (3). The existence of such a region was confirmed by the inverse scattering transform method in Refs. [5,6] and its "quasi-linear" part was studied in Ref. [7]. An extensive study of the asymptotic evolution of the pulse in the absence of solitons was performed in Ref. [8] where different characteristic parts of the wave structure were distinguished and their main parameters were calculated. However, in this reference, Ablowitz and Segur—who first explicitly point to the formation of a dispersive shock wave—confined themselves to the analytic study of typical limiting cases and explicit formulas for the whole dispersive shock wave region were found much later [9] with the use of a quite involved analysis of the associated Riemann-Hilbert problem. This approach was developed further in Refs. [10–12] and other papers.

Although the above-mentioned approaches are mathematically strict, the methods used are difficult and the theory developed has not found applications to concrete problems related with other integrable evolution equations. Since the question of evolution of pulses in the absence of solitons is related with experiments in physics of water waves [13,14], Bose-Einstein condensates [15,16], and nonlinear optics [17,18], the development of a simpler and more transparent physically approach is desirable. Such an approach, based on the Whitham theory

[1]A so-called N-wave appears if $u_0(x)$ has both polarities; see, e.g., Ref. [1].

of modulations of nonlinear waves [19], was suggested long ago by Gurevich and Pitaevskii [20] and since that time it has developed into a powerful method with numerous applications (see, e.g., the review article [21]). Despite the facts that some elements of the Whitham theory were used in Refs. [6,8] and that the general solution of the solitonless initial value problem has been obtained in Ref. [22], no asymptotic analysis has been performed within Whitham's formalism, so that its relationship with the previous results remained unclear.

The main goal of the present paper is to fill this gap and to apply the Whitham theory to the description of the asymptotic evolution of initial pulses in the small dispersion limit (or for wide pulses) under the condition of absence of solitons. We show that the combination of two ideas—self-similarity of the solution and quasisimple character [23] of the dispersive shock wave—permits an asymptotic analysis of the solution. The relatively simple theory developed in the present work should be useful in the analysis of experiments devoted to the evolution of pulses of this type.

The paper is organized as follows. In Sec. II we present the main aspects of Whitham theory and of the generalized hodograph method applying to quasisimple waves (following Refs. [22–28]). In Sec. III, the application of the ideas of Ref. [23] to the soliton edge of the DSW makes it possible to find the law of motion of this edge and suggests a self-similar asymptotic behavior consistent with Eq. (3). In Sec. IV we perform the large-time asymptotic analysis of the rear (soliton) part of the dispersive shock wave by the Whitham method within this self-similarity assumption. This yields a surprisingly simple derivation of the solution first explicitly obtained in Ref. [9]. The description of the DSW in its full range by the method of El and Khodorovskii [22] is presented in a self-contained manner in Sec. V. In this section we consider the time evolution of several initial profiles illustrating the possible different behaviors in the shock region and compare the theoretical results with numerical simulations. We present our conclusions in Sec. VI.

II. WHITHAM THEORY AND THE GENERALIZED HODOGRAPH METHOD

A. The smooth part of the profile

We consider an initial pulse with nonpositive profile $u(x, t = 0) = u_0(x)$ defined on finite interval of x and having a single minimum $\min_{x\in\mathbb{R}}\{u_0(x)\} = -1$ (this value can be changed by an appropriate rescaling on u, x, and t). We consider a initial profile of finite extend x_0, and assume that $x_0 \gg 1$, so that in a first stage of evolution one can neglect dispersive effects. This amounts to replace the KdV dynamics by the Hopf equation,

$$r_t + 6\,r\,r_x = 0. \tag{4}$$

We changed notation here to mark the difference between $r(x, t)$, solution of the approximate equation (4), and $u(x, t)$, which is the exact solution of the KdV equation (2). The solution of the Hopf equation is well known (see, e.g., Ref. [29]) and it is given in implicit form in terms of functions inverse to $u_0(x)$, as explained now.

In the case we consider, $u_0(x)$ has a single minimum and its inverse function is two valued. We denote its two branches

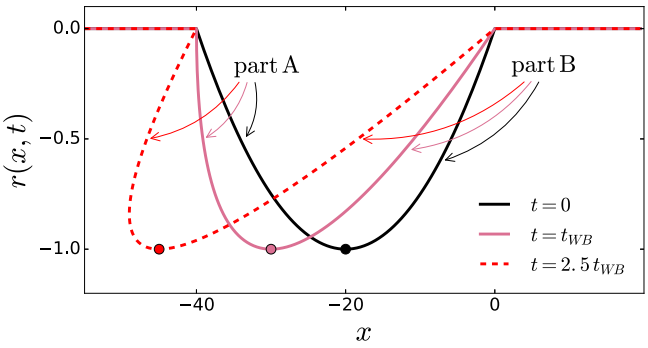

FIG. 1. The solid black, solid pink, and dashed red lines represent $r(x, t)$ solution of (4) for times $t = 0$, $t = t_{\rm WB}$, and $t = 2.5\,t_{\rm WB}$ for an initial condition $r(x, 0)$ given by the parabolic profile $u_0(x)$ defined in Eq. (6) with $x_0 = 40$. The dots represent the position of the minimum $\min_{x\in\mathbb{R}}\{r(x, t)\}$ which separates parts A (at the left) and B (at the right) of the profile.

as $w^{\rm A}(r)$ and $w^{\rm B}(r)$, where the first function refers to the part of the pulse to the left of its minimum and the second one to its right. Then the solution of the Hopf equation is given by the formulas

$$x - 6\,r\,t = w^{\rm A}(r), \tag{5a}$$

$$x - 6\,r\,t = w^{\rm B}(r). \tag{5b}$$

For example, in case of a parabolic initial pulse

$$u_0(x) = \begin{cases} 4\,x(x + x_0)/x_0^2 & \text{for } -x_0 \leqslant x \leqslant 0, \\ 0 & \text{elsewhere,} \end{cases} \tag{6}$$

the inverse functions are equal to

$$\begin{aligned} w^{\rm A}(r) &= \tfrac{x_0}{2}(-1 - \sqrt{1 + r}\,), \\ w^{\rm B}(r) &= \tfrac{x_0}{2}(-1 + \sqrt{1 + r}\,), \end{aligned} \quad \text{where } r \in [-1, 0]. \tag{7}$$

Figure 1 represents the initial profile (6) and its time evolution as computed from Eqs. (5), i.e., without taking dispersive effects into account. Figure 2 represents the corresponding functions $w^{\rm A}(r)$ and $w^{\rm B}(r)$. In the following we shall perform the explicit computations using this initial profile. Other types

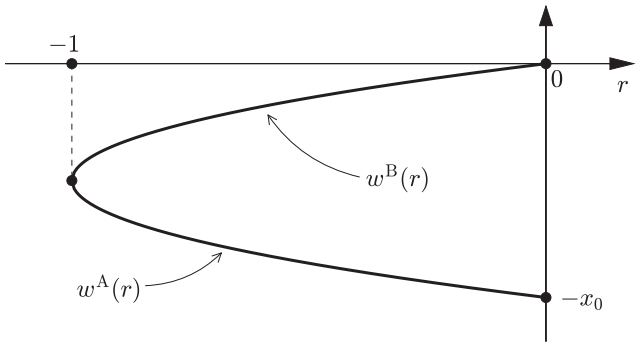

FIG. 2. The two branches $w^{\rm A}(r)$ and $w^{\rm B}(r)$ of the reciprocal function of $u_0(x)$. The figure is drawn for the initial parabolic profile (6) [the corresponding expressions of $w^{\rm A}(r)$ and $w^{\rm B}(r)$ are given in Eq. (7)] but the behavior is the generic one.

of profiles, with less generic behaviors, will be presented and discussed in Sec. V.

The wave-breaking time is the time $t_{\rm WB} = 1/\max(-6\,du_0/dx)$ at which the solution of (4) becomes infinitely steep (see, e.g., Ref. [1]). In the present work we consider initial profiles for which the largest slope $\max(-du_0/dx)$ is reached at $x = -x_0$ for $r = 0$ and thus

$$t_{\rm WB} = -\frac{1}{6}\left(\frac{dw^{\rm A}}{dr}\right)_{r=0}. \tag{8}$$

For the initial profile (6) we get $t_{\rm WB} = x_0/24$. For $t \geqslant t_{\rm WB}$ the dispersionless approximation fails (the corresponding formal solution of the Hopf equation is multivalued), and a DSW is formed, initially around $x = -x_0$, which then expands toward the negative x direction. We now explain how it can be described within Whitham modulational theory.

B. Periodic solutions and their modulations

The KdV equation (2) admits nonlinear periodic solutions which can be written in terms of three parameters $r_1 \leqslant r_2 \leqslant r_3$ as (see, e.g., Ref. [29])

$$u(x,t) = r_3 + r_2 - r_1 - 2(r_2 - r_1) \times \mathrm{sn}^2(\sqrt{r_3 - r_1}(x - Vt), m), \tag{9}$$

where

$$V = 2(r_1 + r_2 + r_3) \tag{10}$$

and

$$m = \frac{r_2 - r_1}{r_3 - r_1}. \tag{11}$$

The notation "sn" in formula (9) refers to the Jacobi sine function (see, e.g., Ref. [30]). For constant parameters r_i expression (9) is an exact (single phase) solution of the KdV equation, periodic in time and space with wavelength

$$L = \frac{2K(m)}{\sqrt{r_3 - r_1}}, \tag{12}$$

where $K(m)$ is the complete elliptic integral of the first kind.

According to the Gurevich-Pitaevskii scheme, a DSW may be described as a modulated nonlinear periodic wave of type (9) for which the r_i's slowly depend on time and position and evolve according to the Whitham equations (see, e.g, Refs. [21,29])

$$\partial_t r_i + v_i(r_1, r_2, r_3)\partial_x r_i = 0, \quad i = 1, 2, 3. \tag{13}$$

The quantities v_i in these equations are the Whitham velocities. Their explicit expressions have first been derived by Whitham [19] and can also be obtained from the relation

$$v_i = \left(1 - \frac{L}{\partial_i L}\,\partial_i\right)V = V - 2\,\frac{L}{\partial_i L}, \tag{14}$$

where L is the wavelength (12), V the phase velocity (10) of the nonlinear periodic solution (9), and ∂_i stands for ∂_{r_i}. One gets

$$\begin{aligned} v_1 &= 2(r_1 + r_2 + r_3) + \frac{4(r_2 - r_1)K(m)}{E(m) - K(m)}, \\ v_2 &= 2(r_1 + r_2 + r_3) - \frac{4(r_2 - r_1)(1 - m)K(m)}{E(m) - (1 - m)K(m)}, \\ v_3 &= 2(r_1 + r_2 + r_3) + \frac{4(r_3 - r_1)(1 - m)K(m)}{E(m)}, \end{aligned} \tag{15}$$

where $E(m)$ is the complete elliptic integral of the second kind.

Since Eqs. (13) have a diagonal form (that is, they include derivatives of a single parameter r_i in each equation), the variables r_i are called Riemann invariants of the Whitham equations—Riemann was the first who introduced such variables in the theory of nonlinear waves.

The two edges of the DSW are denoted as $x_{\rm L}(t)$ and $x_{\rm R}(t)$. The first one is the small-amplitude edge; it is at the left of the DSW in the case we consider. Within the Whitham approximation, it makes contact between the DSW and the undisturbed profile: $u(x,t) = 0$ for $x \leqslant x_{\rm L}(t)$. The small-amplitude version of (9) corresponds to the limit $m \ll 1$ and takes the form

$$u(x,t) = r_3 + (r_2 - r_1)\cos[2\sqrt{r_3 - r_1}(x - Vt)]. \tag{16}$$

In this harmonic linear limit, $r_2 \to r_1$ $(m \to 0)$ and the Whitham velocities (15) reduce to

$$\begin{aligned} v_1|_{r_2=r_1} &= v_2|_{r_2=r_1} = 12\,r_1 - 6\,r_3, \\ v_3|_{r_2=r_1} &= 6\,r_3. \end{aligned} \tag{17}$$

Around the left boundary of the DSW, the amplitude $2(r_2 - r_1)$ of the oscillations is small and since this edge propagates along a zero background, we arrive at the conclusion that $r_3 = 0$ and $r_1 = r_2$ for $x = x_{\rm L}(t)$.

The other edge, at the right side of the DSW, is the large-amplitude soliton edge, with $m = 1$. Therefore we must have here $r_2 = r_3$ and in this limit the nonlinear pattern (9) degenerates into a soliton solution of the form

$$u(x,t) = r_1 + \frac{2(r_2 - r_1)}{\cosh^2[\sqrt{r_2 - r_1}(x - Vt)]}. \tag{18}$$

This implies that the right of the DSW is bounded by a soliton for which the Whitham velocities are given by

$$\begin{aligned} v_1|_{r_2=r_3} &= 6\,r_1, \\ v_2|_{r_2=r_3} &= v_3|_{r_2=r_3} = 2\,r_1 + 4\,r_3. \end{aligned} \tag{19}$$

C. Generalized hodograph method

The dispersionless approach of Sec. II A leads, after the wave-breaking time, to an nonphysical, multivalued solution. The form, displayed in Fig. 1, of $r(x, t \geqslant t_{\rm WB})$ in the region of multivaluedness suggests that the DSW accounting for the post wave-breaking dynamics should be described by Whitham-Riemann invariants arranged in a configuration such that $r_3 = 0$ (thus ensuring matching with the unperturbed profile at the left), whereas r_2 and r_1 both depend on x and t, with always $r_3 \geqslant r_2 \geqslant r_1$.

The contact of the DSW with the smooth profile which prevails for $x \geqslant x_{\rm R}(t)$ imposes the condition

$r_1(x_R(t), t) = r(x_R(t), t)$, where $r(x, t)$ is a solution of the Hopf equation (4) with initially $r(x, 0) = u_0(x)$. Therefore the description of the DSW for $x \in [x_L(t), x_R(t)]$ imposes the boundary conditions

$$r_1(x_R(t), t) = r(x_R(t), t) \equiv r_R(t), \quad r_2(x_R(t), t) = 0, \tag{20a}$$

$$r_1(x_L(t), t) = r_2(x_L(t), t) \equiv r_L(t). \tag{20b}$$

Note that all the above functions are only defined after the wave breaking time, i.e., for $t \geqslant t_{WB}$.

This type of structure, in which two Riemann invariants (r_1 and r_2) change along the DSW, is not a simple wave solution; it belongs to the class of "quasisimple waves" introduced in Ref. [23]. In this case, Eq. (13) with $i = 3$ is trivially satisfied and for solving the remaining two Whitham equations we use the so-called generalized hodograph method of Tsarev [31]. To this end, one introduces two functions $W_i(r_1, r_2)$ ($i = 1$ or 2), making it possible to write a vector generalization of Eq. (5) for the Whitham system:

$$x - v_i(r_1, r_2)t = W_i(r_1, r_2), \quad i = 1, 2. \tag{21}$$

For the sake of brevity we have noted in the above equation $v_i(r_1, r_2) = v_i(r_1, r_2, r_3 = 0)$ for $i \in \{1, 2\}$; we will keep this notation henceforth. The W_i's must satisfy the compatibility equation found by substituting (21) into (13). This leads to the Tsarev equations:

$$\frac{\partial_j W_i}{W_i - W_j} = \frac{\partial_j v_i}{v_i - v_j}, \text{ for } i \neq j. \tag{22}$$

One can show (see, e.g., Refs. [25,27,28]) that (22) is solved for W_i's of the form

$$W_i = \left(1 - \frac{L}{\partial_i L}\partial_i\right)\mathscr{W} = \mathscr{W} + \left(\frac{1}{2}v_i - r_1 - r_2\right)\partial_i \mathscr{W}, \tag{23}$$

where $\mathscr{W}(r_1, r_2)$ is solution of the Euler-Poisson equation

$$\partial_{12}\mathscr{W} = \frac{\partial_1 \mathscr{W} - \partial_2 \mathscr{W}}{2(r_1 - r_2)}. \tag{24}$$

There is, however, a subtle point here, which was first understood in Ref. [23] (see also Ref. [22]). After the wave breaking time, the development of the dispersive shock wave occurs in *two* steps:

(A) Initially (when t is close to t_{WB}), the DSW is connected at its right edge to the smooth profile coming from the time evolution of part A of the initial profile. In this case, for a given time t, the lower value of $u(x, t)$ is reached within the smooth part of the profile and keeps its initial values (-1).

(B) Then, after a while, the left part of the initial profile (part A) has been "swallowed" by the DSW which is then connected at its right to the smooth profile coming from the time evolution of part B of $u_0(x)$. In this case, the minimum $\min_{x\in\mathbb{R}}\{u(x, t)\}$ is reached inside the DSW (or at its boundary), is negative and larger than -1 (i.e., less pronounced than in the previous case A), and asymptotically tends to 0 for large time.

We denote the region of the DSW [and of the (x, t) plane] in which r_1 is a decreasing function of x as region A, the part where it increases as region B. In region A of the (x, t) plane, we denote by $\mathscr{W}^A(r_1, r_2)$ the solution of the Euler-Poisson equation; in region B we denote it instead as $\mathscr{W}^B(r_1, r_2)$. These two forms are joined by the line $r_1 = -1$ (cf. the upper plots of Fig. 5) along which

$$\mathscr{W}^A(-1, r_2) = \mathscr{W}^B(-1, r_2). \tag{25}$$

Since the general solution of the Euler-Poisson equation with the appropriate boundary conditions, and the construction of the resulting nonlinear pattern are quite involved, we shall first consider some particular—but useful—results which follow from general principles of the Whitham theory.

III. MOTION OF THE SOLITON EDGE OF THE SHOCK

During the first stage of evolution of the DSW, its right (solitonic) edge is connected to the smooth dispersionless solution described by formula (5a), that is we have here

$$x_R - 6r_R t = w^A(r_R). \tag{26}$$

On the side of the DSW, in vicinity of this boundary, the Whitham equations (13) with the limiting expressions (19) (where $r_3 = 0$) for the velocities v_i are given by

$$\partial_t r_1 + 6r_1\partial_x r_1 = 0, \qquad \partial_t r_2 + 2r_1\partial_x r_2 = 0. \tag{27}$$

For solving these equations one can perform a classical hodograph transformation (see, e.g., Ref. [29]), that is, one assume that x and t are functions of the independent variables r_1 and r_2: $t = t(r_1, r_2)$, $x = x(r_1, r_2)$. We find from Eqs. (27) that these functions must satisfy the linear system

$$\frac{\partial x}{\partial r_1} - 2r_1\frac{\partial t}{\partial r_1} = 0, \qquad \frac{\partial x}{\partial r_2} - 6r_1\frac{\partial t}{\partial r_2} = 0.$$

At the boundary with the dispersionless solution [where $r_1 = r_R$, see (20a)] the first equation reads

$$\frac{\partial x_R}{\partial r_R} - 2\,r_R\frac{\partial t}{\partial r_R} = 0, \tag{28}$$

and this must be compatible with Eq. (26). Differentiation of Eq. (26) with respect to r_R and elimination of $\partial x_R/\partial r_R$ with the use of Eq. (28) yield the differential equation for the function $t(r_R) \equiv t(r_R, 0)$:

$$4\,r_R\frac{dt}{dr_R} + 6\,t = -\frac{dw^A(r_R)}{dr_R}. \tag{29}$$

At the wave-breaking time, $r_R = 0$, and (29) gives the correct definition (8) of the wave-breaking time: $t_{WB} = t(0)$. Elementary integration then yields

$$\begin{aligned} t(r_R) &= \frac{1}{4(-r_R)^{3/2}}\int_0^{r_R}\sqrt{-r}\,\frac{dw^A(r)}{dr}\,dr \\ &= \frac{1}{8(-r_R)^{3/2}}\int_0^{r_R}\frac{w^A(r)}{\sqrt{-r}}dr - \frac{w^A(r_R)}{4\,r_R}. \end{aligned} \tag{30}$$

Substituting this into (26) we get the following expression for the function $x_R(r_R) \equiv x(r_R, 0)$:

$$\begin{aligned} x_R(r_R) &= -\frac{3}{2\sqrt{-r_R}}\int_0^{r_R}\sqrt{-r}\,\frac{dw^A(r)}{dr}dr + w^A(r_R) \\ &= -\frac{3}{4\sqrt{-r_R}}\int_0^{r_R}\frac{w^A(r)}{\sqrt{-r}}dr - \frac{1}{2}w^A(r_R). \end{aligned} \tag{31}$$

The two formulas (30) and (31) define in an implicit way the law of motion $x = x_{\rm R}(t)$ of the soliton edge of the DSW.

The above expressions are correct as long as the soliton edge is located inside region A, that is up to the moment

$$t_{\rm A/B} = t(-1) = \frac{1}{4}\int_0^{-1} \sqrt{-r}\,\frac{dw^{\rm A}(r)}{dr}dr, \tag{32}$$

after which the soliton edge connects with part B of the smooth profile. Concretely, for a time $t > t_{\rm A/B}$, we have to solve the differential equation

$$4\,r_{\rm R}\frac{dt}{dr_{\rm R}} + 6\,t = -\frac{dw^{\rm B}(r_{\rm R})}{dr_{\rm R}}$$

with the initial condition $t(-1) = t_{\rm A/B}$. This yields

$$t(r_{\rm R}) = \frac{1}{4(-r_{\rm R})^{3/2}}\left[\int_0^{-1}\sqrt{-r}\,\frac{dw^{\rm A}(r)}{dr}dr + \int_{-1}^{r_{\rm R}}\sqrt{-r}\,\frac{dw^{\rm B}(r)}{dr}dr\right] \tag{33}$$

and

$$x_{\rm R}(r_{\rm R}) = -\frac{3}{2(-r_{\rm R})^{1/2}}\left[\int_0^{-1}\sqrt{-r}\,\frac{dw^{\rm A}(r)}{dr}dr + \int_{-1}^{r_{\rm R}}\sqrt{-r}\,\frac{dw^{\rm B}(r)}{dr}dr\right] + w^{\rm B}(r_{\rm R}). \tag{34}$$

At asymptotically large time $t \to \infty$ one is at stage B of evolution, with furthermore $r_{\rm R} \to 0$. Hence the upper limit of integration in the second integrals of formulas (33) and (34) can be put equal to zero. Integration over r in the resulting expressions can be replaced by integration over x with account of the fact that $w^{\rm A,B}(r)$ represent two branches of the inverse function of $r = u_0(x)$, so we get

$$t(r_{\rm R}) \simeq \frac{\mathcal{A}}{4(-r_{\rm R})^{3/2}}, \quad \text{where} \quad \mathcal{A} = \int_{\mathbb{R}}\sqrt{-u_0(x)}\,dx$$

is a measure of the amplitude of the initial trough. Consequently, we obtain

$$r_{\rm R}(t) = -\left(\frac{\mathcal{A}}{4t}\right)^{2/3}, \quad x_{\rm R}(t) = -\frac{3\mathcal{A}^{2/3}}{2^{1/3}}t^{1/3}, \tag{35}$$

where we have neglected a term of order x_0 which is small compared to the infinitely increasing time-dependent ones.

At large time, the dispersionless part of the profile between $x = 0$ and $x_{\rm R}(t)$ is stretched to a quasilinear behavior $u(x,t) = x\,r_{\rm R}(t)/x_{\rm R}(t)$, and one thus has

$$\int_{x_{\rm R}(t)}^{0} dx\sqrt{-u(x,t)} = -\frac{2}{3}x_{\rm R}(t)\sqrt{-r_{\rm R}(t)} = \mathcal{A}, \tag{36}$$

which means that the quantity $\mathcal{A}$ is conserved, at least at the level of the present asymptotic analysis. This situation is reminiscent of—but different from—the dissipative case where nonlinear patterns of triangular shape may also appear at the rear edge of a (viscous) shock. In the dissipative case there also exists a conserved quantity. For Burgers' equation, for instance, with an initial condition of type (6), a single viscous shock appears which is followed by an asymptotically triangular wave. This means that the details of the initial distribution are lost (as in the present case), but for Burgers' equation the conserved quantity is not the quantity $\mathcal{A}$ defined in Eq. (36), but the integral $\int_{I(t)} dx\,u(x,t)$, where $I(t)$ is the support of the triangular wave (equivalent to our segment $[x_{\rm R}(t), 0]$).

Formulas (35) suggest that in the vicinity of the soliton edge, the behavior of the DSW must be self-similar, and we now turn to the investigation of this possibility in the framework of Whitham theory.

IV. SIMILARITY SOLUTION AT THE SOLITON EDGE OF THE SHOCK

In this section we use the Whitham approach to obtain the long-time asymptotic behavior of the shock close to $x_{\rm R}(t)$, valid up to $x \sim -t^{1/3}(\ln t)^{3/2}$ (see Refs. [8,9]).

Equations (35) suggest that, close to the soliton edge of the DSW, the Riemann invariants r_1 and r_2 have the following scaling form:

$$r_i = \frac{1}{t^{2/3}}R_i\left(\frac{x}{t^{1/3}}\right). \tag{37}$$

Here $x < 0$ and since $r_1 < r_2 < 0$, we have $R_1 < R_2 < 0$. The scaling (37) agrees with the scaling (3) of the full KdV equation first noticed in Refs. [4–6]. Written in terms of the rescaled Riemann parameters R_1 and R_2 and of the self-similar variable $z = x/t^{1/3}$, the Whitham equations (13) read

$$\frac{dR_i}{dz} = -\frac{2R_i}{z - 3R_1V_i(m)}, \qquad i = 1, 2, \tag{38}$$

where

$$m = 1 - R_2/R_1, \tag{39}$$

and the velocities $V_1(m)$ and $V_2(m)$ are given by

$$\begin{aligned} V_1(m) &= 2(2-m) - \frac{4mK(m)}{E(m)-K(m)}, \\ V_2(m) &= 2(2-m) + \frac{4m(1-m)K(m)}{E(m)-(1-m)K(m)}. \end{aligned} \tag{40}$$

The two equations (38) can be reduced to a single one if we introduce the variable

$$\zeta = z/R_1 \tag{41}$$

and look for the dependence of ζ on m. A simple calculation yields the differential equation

$$\frac{d\zeta}{dm} = \frac{[\zeta - V_1(m)][\zeta - 3V_2(m)]}{2(1-m)[V_2(m) - V_1(m)]}, \tag{42}$$

whose basic properties can be studied in the phase plane (m, ζ). The phase portrait in this plane is displayed in Fig. 3. It admits the singular points

$$\begin{array}{llll} (0,12), & (0,36) & \text{for} & m = 0; \\ (1,6), & (1,6) & \text{for} & m = 1. \end{array} \tag{43}$$

As is clear from Fig. 3, the point (0,12) is a node and the point (0,36) is a saddle. At $m = 1$ the two singular points merge into one (1,6) of a mixed saddle-node type. Numerical solution of

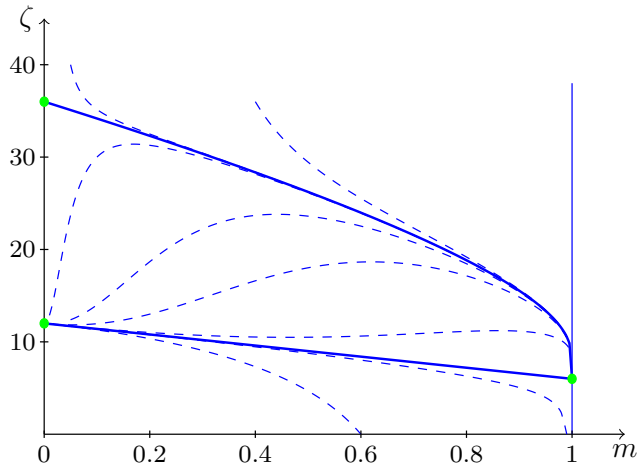

FIG. 3. Integral curves of Eq. (42). The separatices are depicted as solid thick lines. The dots are the singular points (43).

Eq. (42) suggests that the separatrix joining the singular points (0,12) and (1,6) is a straight line

$$\zeta = 6(2-m), \tag{44}$$

which, after returning to the variables R_1, R_2, and z, leads to the assumption that the system (38) admits the following integral:

$$R_1 + R_2 = \tfrac{1}{6}z. \tag{45}$$

A direct check shows that indeed $d(R_1+R_2)/dz = 1/6$ under the condition (45), so that this assumption is proved. The integral curves beginning in vicinity of this separatrix are attracted to it when m decreases, so one can expect that just this separatrix realizes the self-similar regime of the DSW near its soliton edge.

To determine the dependence of m on z, we find, with the use of Eqs. (38),

$$\frac{dm}{dz} = \frac{6\zeta(m)(1-m)(V_2(m)-V_1(m))}{z[\zeta(m)-3V_1(m)][\zeta(m)-3V_2(m)]}. \tag{46}$$

Substituting Eq. (44) and the expressions (40) in the above, we get the following equation:

$$\frac{dm}{dz} = -\frac{2-m}{zmK(m)}F(m), \tag{47}$$

where

$$F(m) = (2-m)E(m) - 2(1-m)K(m). \tag{48}$$

The solution of this equation determines $m = m(z)$ along the separatrix.

The form of expression (48) suggests that it can be obtained as a result of the calculation of some elliptic integral in which the integration limits may play the role of more convenient variables. Inspection of tables of such integrals shows that the formula 3.155.9 in Ref. [30] (which we write down here with notations slightly different from the original reference),

$$\begin{aligned} I &= 3\int_{q_2}^{q_1}\sqrt{(q_1^2-y^2)(y^2-q_2^2)}\,dy \\ &= q_1\big[(q_1^2+q_2^2)E(m) - 2q_2^2K(m)\big], \end{aligned} \tag{49}$$

has the necessary structure. In Eq. (49) one has $q_1 > q_2 > 0$ and $m = 1-(q_2/q_1)^2$.

To establish the link between the two expressions (48) and (49), it is enough to take

$$q_1^2 + q_2^2 = 1, \tag{50}$$

so that $1-m = q_2^2/q_1^2$, $2-m = 1/q_1^2$. Assuming that the variables q_1, q_2 satisfy (50), we obtain

$$q_1^2 = \frac{1}{2-m}, \qquad q_2^2 = \frac{1-m}{2-m}, \tag{51}$$

and then, imposing $m = m$, we get $F(m) = (2-m)^{3/2}I$.

Since $dq_1/dm = q_1^3/2$, Eq. (47) can be cast under the form

$$\frac{dq_1}{d\ln(-z)} = -\frac{q_1}{2mK(m)}F(m), \tag{52}$$

which is more convenient for further calculations. On the other hand, the integral (49) with account of Eqs. (51) simplifies to

$$I = q_1\big[E(m) - 2\big(1-q_1^2\big)K(m)\big],$$

and its differentiation with respect to q_1 gives

$$\frac{dI}{dq_1} = 3q_1^2mK(m). \tag{53}$$

With the help of the formulas obtained we transform Eq. (52) to

$$\frac{dI}{I} = -\frac{3}{2}d\ln(-z).$$

Then, integration of this equation with the boundary condition $z = z_1$ at $m = 1$ yields z as a function of m:

$$z = z_1\,I^{-2/3}(m) = z_1\,\frac{2-m}{F^{2/3}(m)}, \tag{54}$$

where

$$z_1 = \frac{x_R(t)}{t^{1/3}} = -6(\mathcal{A}/4)^{2/3} \tag{55}$$

is the value of z for $m = 1$ (at the soliton edge of the DSW, see Sec. III).

From the formulas (39) and (51) we find the relationship between the R_i's and the q_i's:

$$R_1 = \frac{q_1^2}{6}z, \quad R_2 = \frac{q_2^2}{6}z, \tag{56}$$

so that for the dependence of the Riemann invariants on m we obtain:

$$\begin{aligned} R_1(m) &= \frac{z_1}{6(2-m)I^{3/2}}, \\ R_2(m) &= \frac{(1-m)z_1}{6(2-m)I^{3/2}}. \end{aligned} \tag{57}$$

Formulas (54), (55), and (57), together with Eq. (37), completely determine the self-similar solution of the Whitham equations: For fixed t we have $x(m) = t^{1/3}z(m)$, so that all functions are defined parametrically, with m playing the role of the parameter. Up to notations, this solution coincides with the one obtained in Ref. [9] by means of an asymptotic study of a Riemann-Hilbert problem in the framework of the inverse scattering transform method.

In the harmonic limit $m \ll 1$, the relation (54) reads

$$m = m_1 z^{-3/4}, \quad \text{where} \quad m_1 = \frac{2^{11/4}}{\sqrt{3\pi}}(-z_1)^{3/4}, \tag{58}$$

which leads to the expressions

$$r_1 = \frac{x}{12t} - \frac{m_1}{24}\frac{(-x)^{1/4}}{t^{3/4}}, \quad r_2 = \frac{x}{12t} + \frac{m_1}{24}\frac{(-x)^{1/4}}{t^{3/4}}. \tag{59}$$

It is important to notice that the difference $r_2 - r_1$, that is, the amplitude of the oscillations in the "quasilinear" region of Zakharov and Manakov [7], increases with growing distance from the soliton edge [as $(-x)^{1/4}$] but $r_2/r_1 \to 1$ and $m \to 0$ here. Hence, this limit is not a small-amplitude one and therefore the self-similar regime cannot be realized along the whole DSW; it takes place close enough to the soliton edge only; see Figs. 6(e), 6(f), and 8. Consequently, we have to turn to the general solution of the Whitham equations to obtain a full description of the DSW.

V. GENERAL SOLUTION

In this section, following Ref. [22], we turn to the general solution of the Whitham equations given by the formulas of Sec. II C. Our task now is to express the functions $W_i(r_1, r_2)$, $i = 1, 2$, in terms of the initial form $u_0(x)$ of the pulse. As was indicated above, at the first stage of evolution the DSW is located inside the region A and after the moment $t_{A/B}$ [see Eq. (32)] a second stage begins where it also reaches region B. Correspondingly, the expressions for W_i and $\mathscr{W}$ are given by different formulas and should be considered separately.

A. Solution in region A

In region A one can follow the procedure explained in Ref. [25]. One imposes the matching of the right edge of the DSW with the dispersionless solution (5): Just at $x = x_R(t)$, we have $r_1 = r(x, t)$, where $r(x, t)$ is the solution of (4), and $v_1(r_1, 0) = 6r_1$ [this follows from Eq. (19)]. Comparing in this case Eqs. (5) and (21) one obtains

$$W_1^{A}(r_1, 0) = w^{A}(r_1), \tag{60}$$

which embodies the same information as Eq. (20a). In terms of $\mathscr{W}$ this corresponds to the equation

$$\mathscr{W}^{A}(r_1, 0) + 2r_1\,\partial_1\mathscr{W}^{A}(r_1, 0) = w^{A}(r_1), \tag{61}$$

whose solution is

$$\mathscr{W}^{A}(r_1, 0) = \frac{1}{2\sqrt{-r_1}}\int_{r_1}^{0}\frac{w^{A}(\rho)\,d\rho}{\sqrt{-\rho}}. \tag{62}$$

This will serve as a boundary condition for the Euler-Poisson equation (24) whose general solution has been given by Eisenhart [32] in the form

$$\mathscr{W}^{A}(r_1, r_2) = \int_{r_1}^{0}\frac{\varphi^{A}(\mu)\,d\mu}{\sqrt{(\mu - r_1)|r_2 - \mu|}} + \int_{r_2}^{0}\frac{\psi^{A}(\mu)\,d\mu}{\sqrt{(\mu - r_1)(\mu - r_2)}}, \tag{63}$$

where the functions φ^{A} and ψ^{A} are arbitrary functions to be determined from the appropriate boundary conditions. By taking $r_2 = 0$ in this expression one sees that $\varphi^{A}(\mu)/\sqrt{-\mu}$ is the Abel transform of $\mathscr{W}^{A}(r_1, 0)$. The inverse transform reads [33]

$$\frac{\varphi^{A}(\mu)}{\sqrt{-\mu}} = -\frac{1}{\pi}\frac{d}{d\mu}\int_{\mu}^{0}\frac{\mathscr{W}^{A}(r, 0)\,dr}{\sqrt{r - \mu}}. \tag{64}$$

Plugging expression (62) for $\mathscr{W}^{A}(r, 0)$ in this formula and changing the order of integration, one obtains

$$\varphi^{A}(\mu) = \frac{1}{2\pi\sqrt{-\mu}}\int_{\mu}^{0}\frac{w^{A}(\rho)\,d\rho}{\sqrt{\rho - \mu}}. \tag{65}$$

For the initial profile (6), w^{A} is given in Eq. (7) and one gets explicitly

$$\varphi^{A}(\mu) = -\frac{x_0}{4\pi}\left(3 + \frac{1+\mu}{\sqrt{-\mu}}\tanh^{-1}\sqrt{-\mu}\right).$$

In order to determine the function ψ^{A}, one considers the left boundary of the DSW where, according to (20b), r_1 and r_2 are asymptotically close to each other. Let us write $r_1 = r$ and $r_2 = r + \epsilon$ with $r \in [-1, 0]$ and ϵ small and positive. One gets from (63)

$$\mathscr{W}^{A}(r, r+\epsilon) = \int_{r+\epsilon}^{0} d\mu\,\frac{\varphi^{A}(\mu) + \psi^{A}(\mu)}{\sqrt{(\mu - r)(\mu - r - \epsilon)}} + \int_{r}^{r+\epsilon}\frac{\varphi^{A}(\mu)\,d\mu}{\sqrt{(\mu - r)(r + \epsilon - \mu)}}. \tag{66}$$

In the right-hand side of the above equality, the second term converges when ϵ tends to 0 [toward $\pi\varphi^{A}(r)$], whereas the first one diverges unless $\varphi^{A}(r) + \psi^{A}(r) = 0$, this being true for all $r \in [-1, 0]$. This imposes that the functions φ^{A} and ψ^{A} should be opposite one the other and the final form of the Eisenhart solution in case A thus reads

$$\mathscr{W}^{A}(r_1, r_2) = \int_{r_1}^{r_2}\frac{\varphi^{A}(\mu)\,d\mu}{\sqrt{(\mu - r_1)(r_2 - \mu)}}, \tag{67}$$

where φ^{A} is given by formula (65).

B. Solution in region B

One looks for a solution of the Euler-Poisson equation in region B of the form

$$\mathscr{W}^{B}(r_1, r_2) = \mathscr{W}^{A}(r_1, r_2) + \int_{-1}^{r_1}\frac{\varphi^{B}(\mu)\,d\mu}{\sqrt{(r_1 - \mu)(r_2 - \mu)}}. \tag{68}$$

Indeed, this ensures that $\mathscr{W}^{B}$, (i) being the sum of two solutions of the Euler-Poisson equation is also a solution of this equation and (ii) verifies the boundary condition (25) since the second term of the right-hand side of (68) vanishes when $r_1 = -1$.

At the right boundary of the DSW, $\mathscr{W}^{B}(r_1, 0)$ verifies the same equation (61) as $\mathscr{W}^{A}(r_1, 0)$ does, where all the superscripts A should be replaced by B. The solution with the appropriate integration constant reads

$$\mathscr{W}^{B}(r_1, 0) = \frac{1}{2\sqrt{-r_1}}\int_{r_1}^{-1}\frac{w^{B}(\rho)\,d\rho}{\sqrt{-\rho}} + \frac{1}{2\sqrt{-r_1}}\int_{-1}^{0}\frac{w^{A}(\rho)\,d\rho}{\sqrt{-\rho}}. \tag{69}$$

The same procedure than the one previously used in part A of the DSW leads here to

$$\varphi^{\mathrm{B}}(\mu) = \frac{1}{2\pi\sqrt{-\mu}} \int_{-1}^{\mu} d\rho \, \frac{w^{\mathrm{A}}(\rho) - w^{\mathrm{B}}(\rho)}{\sqrt{\mu - \rho}}. \tag{70}$$

For the initial profile (6) one gets explicitly

$$\varphi^{\mathrm{B}}(\mu) = -\frac{x_0}{4} \frac{1+\mu}{\sqrt{-\mu}}.$$

In the generic case, Eqs. (68) and (70) give the solution of the Euler-Poisson equation in region B.

C. Characteristics of the DSW at its edges

It is important to determine the boundaries $x_{\mathrm{R}}(t)$ and $x_{\mathrm{L}}(t)$ of the DSW, as well as the values of the Riemann invariants r_1 and r_2 at these points. The law of motion of the soliton edge was already found in Sec. III and it is instructive to show how this result can be obtained from the general solution.

At the soliton edge we have $r_2 = r_3 = 0$ and $r_1 = r_{\mathrm{R}}(t)$. The corresponding Whitham velocities are $v_1 = 6\,r_{\mathrm{R}}$ and $v_2 = 2\,r_{\mathrm{R}}$ [see Eqs. (19)], and the two equations (21) read

$$\begin{aligned} x_{\mathrm{R}} - 6 r_{\mathrm{R}} t &= W_1(r_{\mathrm{R}}, 0) = w(r_{\mathrm{R}}), \\ x_{\mathrm{R}} - 2 r_{\mathrm{R}} t &= W_2(r_{\mathrm{R}}, 0) = \mathscr{W}(r_{\mathrm{R}}, 0). \end{aligned} \tag{71}$$

These formulas apply to both stages of evolution and therefore the superscripts A and B are dropped out. They give at once

$$\begin{aligned} t(r_{\mathrm{R}}) &= \frac{1}{4 r_{\mathrm{R}}} [\mathscr{W}(r_{\mathrm{R}}, 0) - w(r_{\mathrm{R}})], \\ x_{\mathrm{R}}(r_{\mathrm{R}}) &= \frac{1}{2} [3\mathscr{W}(r_{\mathrm{R}}, 0) - w(r_{\mathrm{R}})]. \end{aligned} \tag{72}$$

Let us consider the stage A, for instance. Equation (62) yields

$$\mathscr{W}^{\mathrm{A}}(r_{\mathrm{R}}, 0) = -\frac{1}{2\sqrt{r_{\mathrm{R}}}} \int_0^{r_{\mathrm{R}}} \frac{w^{\mathrm{A}}(\rho) d\rho}{\sqrt{-\rho}},$$

which, inserted into Eqs. (72), gives immediately the results (30) and (31). For instance, for the initial profile (6), when the right boundary is still in region A, one obtains explicitly

$$t(r_{\mathrm{R}}) = \frac{x_0}{16\, r_{\mathrm{R}}} \left(\sqrt{1 + r_{\mathrm{R}}} - \frac{\arcsin \sqrt{-r_{\mathrm{R}}}}{\sqrt{-r_{\mathrm{R}}}} \right). \tag{73}$$

At the wave-breaking time, $r_{\mathrm{R}} = 0$ and this yields $t_{\mathrm{WB}} = t(r_{\mathrm{R}} = 0) = x_0/24$ as already obtained [cf. Eq. (8)]. Stage A ends at time $t_{\mathrm{A/B}}$ at which the minimum (-1) of the smooth part of the profile enters the DSW. This corresponds to $t_{\mathrm{A/B}} = t(r_{\mathrm{R}} = -1)$ and yields, for the initial parabolic profile (6), $t_{\mathrm{A/B}} = \pi\, x_0/32$.

Let us now turn to the determination of the location $x_{\mathrm{L}}(t)$ of the left boundary of the DSW and of the common value $r_{\mathrm{L}}(t)$ of r_1 and r_2 at this point. In the typical situation the left boundary is located in region A. In this case the equations (21) for $i = 1$ and 2 are equivalent and read

$$x_{\mathrm{L}} - 12\, r_{\mathrm{L}} t = W_1^{\mathrm{A}}(r_{\mathrm{L}}, r_{\mathrm{L}}). \tag{74}$$

An equation for r_{L} alone is obtained by demanding that the velocity dx_{L}/dt of the left boundary is equal to the common value $12\, r_{\mathrm{L}}$ of v_1 and v_2 at this point [cf. Eqs. (17)]. The time derivative of Eq. (74) then yields

$$t = -\frac{1}{12} \frac{dW_1^{\mathrm{A}}(r_{\mathrm{L}}, r_{\mathrm{L}})}{dr_{\mathrm{L}}}. \tag{75}$$

Once $r_{\mathrm{L}}(t)$ has been determined by solving this equation, $x_{\mathrm{L}}(t)$ is given by Eq. (74).

Note that the relation $dx_{\mathrm{L}}/dt = 12\, r_{\mathrm{L}}$ is a consequence of the general statement that the small-amplitude edge of the DSW propagates with the group velocity corresponding to the wave number determined by the solution of the Whitham equations. Indeed, the KdV group velocity of a linear wave with wave-vector k moving over a zero background is $v_g = -3k^2$, and here $k = 2\pi/L = 2\sqrt{-r_{\mathrm{L}}}$ [cf. Eq. (12)], hence $v_g = 12\, r_{\mathrm{L}} = dx_{\mathrm{L}}/dt$, as it should. This property of the small-amplitude edge is especially important in the theory of DSWs for nonintegrable equations (see Refs. [34,35]).

We also study below a case different from (6) for which the left boundary of the DSW belongs to region B and corresponds to $r_1 = r_2 = -1$ [in the so-called triangular case corresponding to $u_0(x)$ given by Eq. (77)]. Then, at the small-amplitude edge $v_1 = v_2 = -12$ and Eqs. (21) yield $x_{\mathrm{L}} + 12 \cdot t = C^{\mathrm{st}}$, the constant being the common value of $W_1^{\mathrm{B}}(-1, -1)$ and $W_2^{\mathrm{B}}(-1, -1)$. It can be determined at $t = t_{\mathrm{WB}}$, leading in this case to

$$x_{\mathrm{L}} = -x_0 - 12(t - t_{\mathrm{WB}}). \tag{76}$$

It is worth noticing that the velocity $dx_{\mathrm{L}}/dt = -12$ agrees with the leading term in Eq. (59) for $r_1 = -1$ in spite of a nonvanishing amplitude of the self-similar solution in this limit. For a more detailed study of the small-amplitude region beyond the Whitham approximation, see, e.g., Ref. [12].

D. The global picture

We now compare the results of the Whitham approach with the numerical solution of the KdV equation for the initial profile (6) and also for a profile

$$u_0(x) = \begin{cases} -1 + \left| \frac{2x}{x_0} + 1 \right| & \text{for} \quad -x_0 \leqslant x \leqslant 0, \\ 0 & \text{elsewhere.} \end{cases} \tag{77}$$

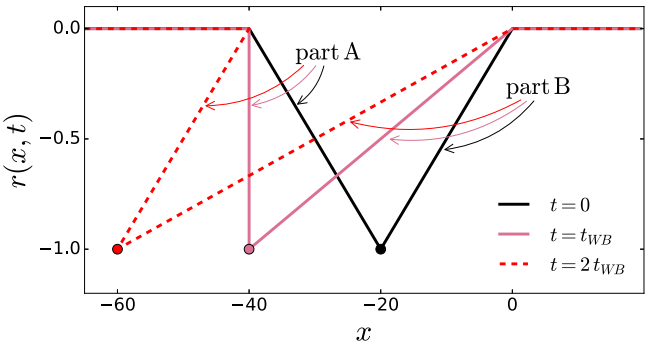

FIG. 4. Dispersionless evolution of the initial triangular profile (77) with $x_0 = 40$. The solid black, solid pink, and dashed red lines represent $r(x, t)$ solution of (4) for times $t = 0$, $t = t_{\mathrm{WB}}$ and $t = 2\,t_{\mathrm{WB}}$.

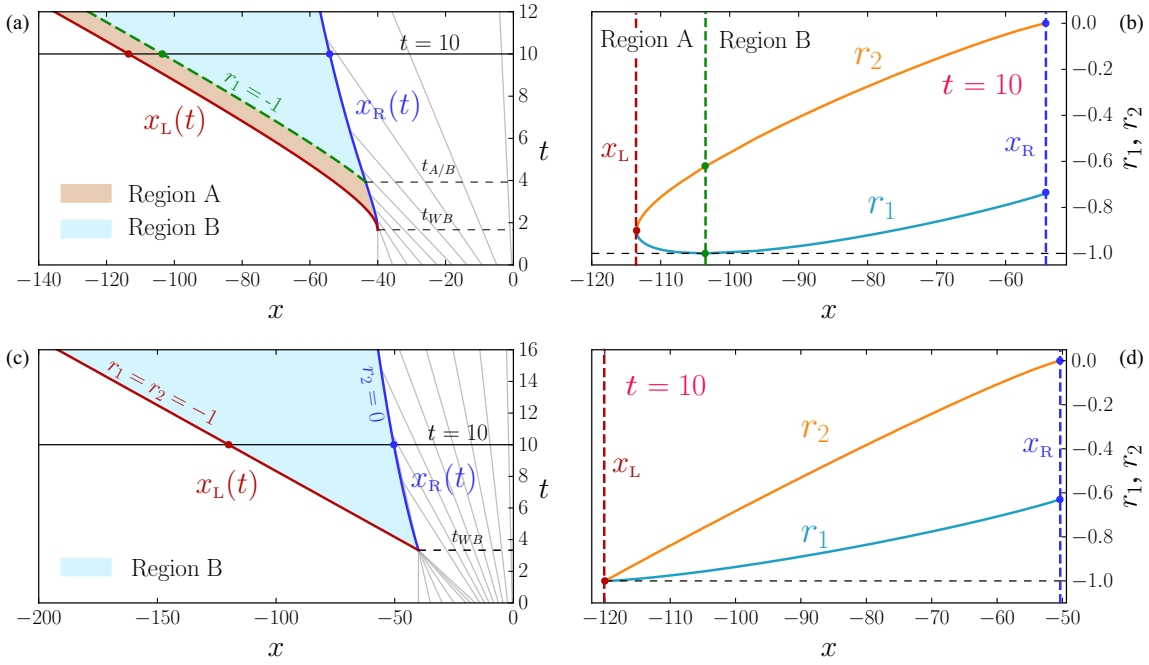

FIG. 5. The upper plots (a) and (b) refer to the parabolic initial profile, and the lower ones (c) and (d) to the triangular initial profile. Left column: Different regions in the (x, t) plane. The DSW occurs in the colored regions. The characteristics of the dispersionless evolution are represented as gray lines. In plot (a) the time $t_{A/B}$ is the time where part A of the initial profile has been completely absorbed by the DSW. For the triangular profile in plot (c) one has $t_{A/B} = t_{WB}$. Right column: Plot of the two varying Riemann invariants $r_1(x, t)$ and $r_2(x, t)$ at fixed $t = 10$ for $x_L(t) \leqslant x \leqslant x_R(t)$. In plots (a) and (b) the green dashed line marks the separation between regions A and B.

This profile is represented in Fig. 4 at $t = 0$, at wave-breaking time, which in the present case is equal to $t_{WB} = x_0/12$ and also at $t = 2\,t_{WB}$ (using the dispersionless approximation presented in Sec. II A).

We henceforth denote the initial profile (6) as "parabolic" and the initial profile (77) as "triangular." As was indicated above, the triangular profile has the particularity of having a DSW within the region B only. This is clear from Fig. 4: Part A of the initial profile does not penetrate into the DSW region before part B does. Or, phrasing this differently, according to the dispersionless evolution, at $t = t_{WB}$ both parts A and B penetrate into the region of multivaluedness at $x \leqslant -x_0$.

The DSW is described by Whitham method as explained in Secs. II B and II C. For this purpose one needs to determine r_1 and r_2 as functions of x and t ($r_3 \equiv 0$). This is performed as follows:

(i) First, we pick up a given $r_1 \in [-1,\ r_R]$, where r_R is the value of r_1 at the soliton edge, the point where the DSW is connected to the rarefaction wave (how to compute it has been explained in Sec. V C).

(ii) Second, at fixed t and r_1, we find the corresponding value r_2 as a solution of the difference equation obtained from Eqs. (21),

$$(v_1 - v_2) \cdot t = W_2(r_1, r_2) - W_1(r_1, r_2)\,, \tag{78}$$

where W_1 and W_2 are computed from Eq. (23).

(iii) Last, the corresponding value of x is determined by $x = W_1 + v_1 t$ (or, equivalently, $x = W_2 + v_2 t$).

This procedure gives, for each $r_1 \in [-1,\ r_R]$ and t, the value of r_2 and x. In practice, it makes it possible to associate to each (x, t) a couple (r_1, r_2). The result is shown in Figs. 5 for the two initial profiles (6) and (77).

Note that the characteristics of the DSW are different for the initial profiles (6) and (77): For the parabolic profile, in Fig. 5(a), the edge point of the DSW—at (x_0, t_{WB})—pertains to region A and corresponds to $r_1 = 0$, while for the triangular profile, in Fig. 5(b), the edge point of the DSW belongs to region B, with $r_1 = -1$. For the parabolic profile, the value $r_1 = -1$ defines a line which separates the regions A and B of the plane (x, t), see Fig. 5(a). This line reaches a boundary of the DSW only at $x_R(t_{A/B})$, where $t_{A/B}$ is the time where part A of the initial profile has just been completely absorbed within the DSW. On the other hand, for the triangular profile, the whole left boundary of the DSW corresponds to the line $r_1 = -1$, see Fig. 5(c).

The knowledge of $r_1(x, t)$ and $r_2(x, t)$ makes it possible to determine, for each time $t > t_{WB}$, $u(x, t)$ as given by the Whitham approach, for all $x \in \mathbb{R}$:

(i) In the regions $x \geqslant 0$ and $x \leqslant x_L(t)$, we have $u(x, t) = 0$.

(ii) In the region $[x_R(t), 0]$, one has $u(x, t) = r(x, t)$ which is solution of the Hopf equation (obtained by the method of characteristics, as explained in Sec. II A).

(iii) Inside the DSW, for $x \in [x_L(t), x_R(t)]$, the function $u(x, t)$ is given by expression (9), with $r_3 = 0$ and r_1 and r_2 determined as functions of x and t by the procedure just explained.

The corresponding profiles are shown in Fig. 6 for the parabolic and triangular initial distributions. The agreement with the numerical solution of Eq. (2) is excellent in both cases. The numerical simulations are performed using a

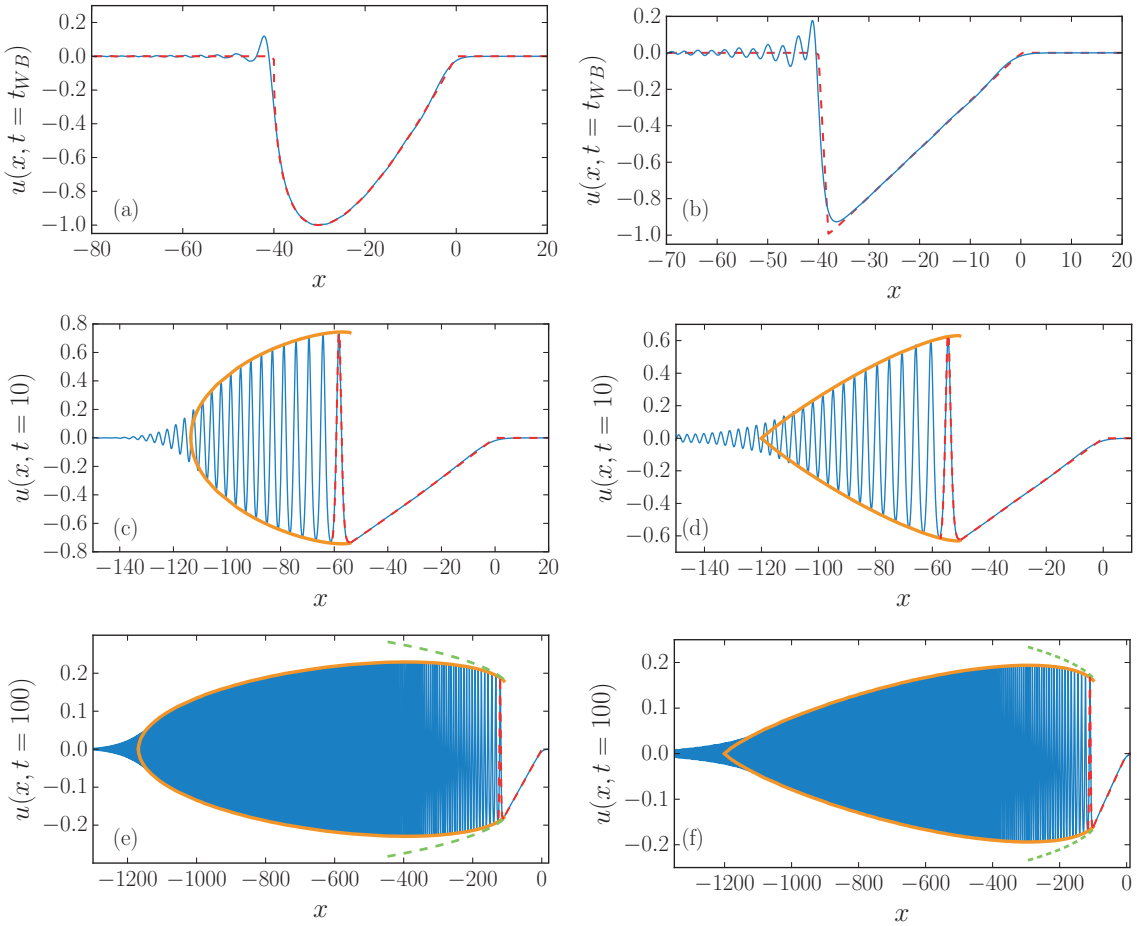

FIG. 6. $u(x,t)$ as a function of x for fixed t. The left column refers to the parabolic initial profile and the right one to the triangular initial profile. The upper row [(a) and (b)] corresponds to the wave-breaking time t_{WB}, the central row [(c) and (d)] to $t = 10$, and the lower one [(e) and (f)] to $t = 100$. The blue solid line corresponds to the numerical solution of Eq. (2). The thick envelopes correspond to the results of Whitham modulation theory. The dashed red lines represent the dispersionless profile $r(x,t)$ and also, in (c)–(f), the Whitham result for the soliton at the large-amplitude boundary of the DSW. The green dashed envelopes in (e) and (f) are the asymptotic self-similar results obtained in Sec. IV.

spatial mesh $h = 0.1$, evaluating the spatial derivatives u_x and u_{xxx} by means of, respectively, two- and four-point formulas (i.e., with an accuracy h^2), and time propagated using a fourth-order Runge-Kutta method with a time step $\Delta t = 10^{-3}$.

In Fig. 7 we also compare the wavelength of the nonlinear oscillations within the DSW as determined by Whitham approach [Eq. (12)] with the results of numerical simulations, and the agreement is again very good.

E. The initial square profile

In this section we discuss another type of initial condition, which we denote as a "square profile":

$$u_0(x) = \begin{cases} -1 & \text{for} \quad -x_0 \leqslant x \leqslant 0, \\ 0 & \text{elsewhere.} \end{cases} \tag{79}$$

El and Grimshaw already theoretically studied the same initial condition by using the method just explained [36]. We will here compare the theory with numerical simulations to indicate some limitations of the one-phase Whitham method which we use in the present work.

For this initial profile, wave breaking occurs instantaneously (i.e., $t_{\mathrm{WB}} = 0$), and until $t = x_0/4$ a plateau (i.e., a segment with constant $u(x,t) = -1$) separates the DSW (at the right) from a rarefaction wave (at the left). In this configuration, the DSW corresponds to the standard Gurevich-Pitaevskii scheme for a steplike initial profile with a single varying Riemann invariant (r_2 in this case). This DSW can be described using the self-similar variable $\zeta = (x + x_0)/t$; in this case Eq. (13) for $i = 2$ reads $\zeta = v_2(-1, r_2)$. One also obtains $x_{\mathrm{L}}(t) = -x_0 - 2t$, $x_{\mathrm{R}}(t) = -6t$ and the rarefaction wave corresponds to $r(x,t) = x/6t$ for $x \in [x_{\mathrm{R}}(t), 0]$.

It is interesting to remark that the Gurevich-Pitaevskii DSW can also be described within the approach exposed in Secs. II C and V D by solving Eq. (21) for $i = 2$. Here W_2^{A} should be computed from

$$\mathscr{W}^{\mathrm{A}}(r_1, r_2) = -x_0 \tag{80}$$

by means of Eq. (23). The form (80) of $\mathscr{W}^{\mathrm{A}}$ comes from (67) with $w^{\mathrm{A}}(r) = -x_0$.

At $t = x_0/4$ the plateau disappears, and one enters into region B with now, as usual, two varying Riemann invariants.

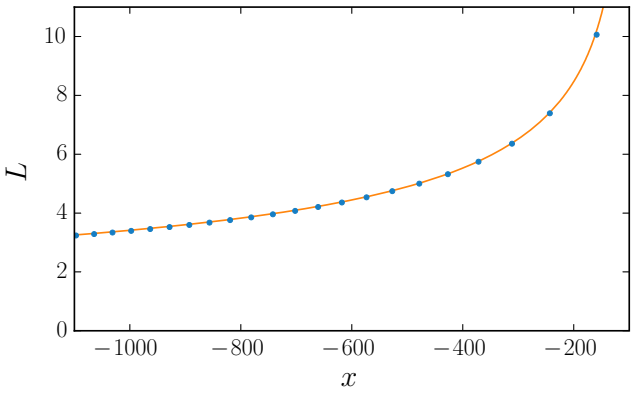

FIG. 7. Evolution of the wavelength of the nonlinear oscillations within the DSW as a function of position x. The figure corresponds to the time evolution of the parabolic initial profile represented in the lower left plot of Fig. 6 ($t = 100$). The continuous line represents the results of Whitham theory and the points are the value of the wavelength extracted from the numerical simulations.

Formulas (68) and (70) lead here to

$$\mathscr{W}^{\mathrm{B}}(r_1, r_2) = -x_0 - \frac{x_0}{\pi}\int_{-1}^{r_1} \frac{\sqrt{\mu+1}\, d\mu}{\sqrt{-\mu(r_1-\mu)(r_2-\mu)}},$$
$$= -x_0 + \frac{2\,x_0/\pi}{\sqrt{-r_1(1+r_2)}} \times\left\{\Pi\left(\frac{1+r_1}{r_1}, m\right) - K(m)\right\}, \quad (81)$$

where $m = (1 + 1/r_1)/(1 + 1/r_2)$ and Π is the complete elliptic integral of the third kind.

The predictions of Whitham theory are compared in Fig. 8 with numerical simulations. Surprisingly enough, the agreement between simulation and theory decreases at large time: At $t = 100$ one can notice oscillations in the envelope of the front part of the DSW (Gurevich-Pitaevskii part). Inspection of the dynamics of formation of the nonlinear structure reveals that, during the formation of the rear rarefaction wave, oscillations appear due to dispersive effects associated with the discontinuity of the initial condition (79): Their interference with the oscillations of the DSW leads to the modulated structure which can be observed in the lower plot of Fig. 8. Such a behavior requires a two-phase approach for a correct description. Note also that for numerical purposes the initial condition is smoothed[2] and that the beating phenomenon increases for sharper initial condition (or for lower values of x_0).

The predictions of the self-similar solution of Sec. IV are also displayed in Fig. 8. In this figure, the envelopes of the DSW expected from Eqs. (37) and (57) are represented by red dashed lines. In the vicinity of its soliton edge, the DSW is accurately described by the similarity solution. However this approach is not able to tackle the other, small-amplitude,

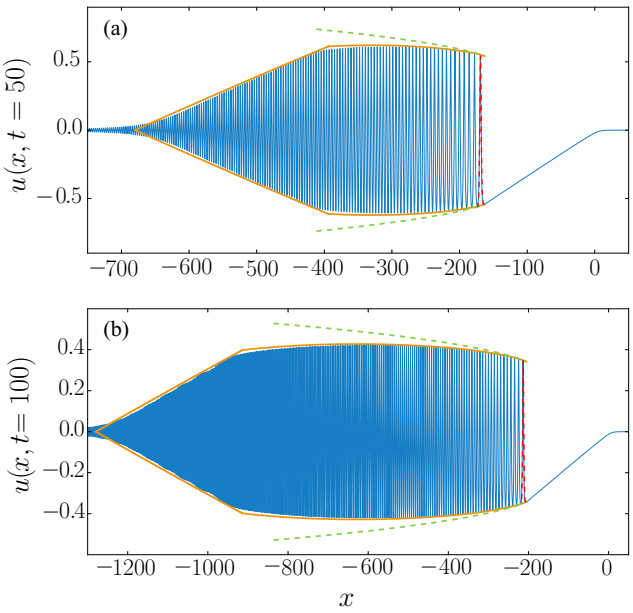

FIG. 8. Evolution of an initial square profile of type (79) with $x_0 = 80$ after a time $t = 50$ (a) and $t = 100$ (b). The blue solid lines are the results of numerical simulations. The orange envelopes are determined by Whitham method. The green dashed envelopes are the asymptotic self-similar results obtained in Sec. IV. The dashed red lines represent the Whitham result for the soliton at the large-amplitude boundary of the DSW. Note the change of scale in the axis of the two plots.

boundary of the shock. This is expected since—as discussed above—in the small-amplitude region a scaling different from the one of Eq. (3) holds, with the relevant self-similar parameter $\zeta = (x + x_0)/t$; see Refs. [9,37] for a general discussion.

VI. CONCLUSION

In the present work we have studied asymptotic solutions of the KdV equation for which no soliton is formed. We used the Whitham modulation theory combined with the generalized hodograph method for describing the DSW which is formed after wave breaking. The results typically compare very well with numerical simulations (see Sec. V D), except in the case of a initial square distribution (Sec. V E) where we argue that a two-phase approach would be needed for a correct description of the shock region.

A simple similarity description has been also obtained near the large-amplitude region of the shock, still within the framework of Whitham's approach. Our results confirm, simplify, and extend in some respects the previous works on this subject (see Sec. IV). We also showed in Sec. III that this theory provides a practical tool for the description of the nonlinear evolution of pulses and can be used for comparison with experimental data, since it yields simple analytic formulas for some characteristic features of DSWs. In particular our work reveals the existence of a conserved quantity which has remained unnoticed until now, see Eq. (36).

Extensions of the present approach to noncompletely integrable equations [35] and to other systems of physical interest are under study.

[2]In the numerical simulations presented in Fig. 8 we take $u_0(x) = \frac{1}{4}[\tanh(x/\Delta) - 1] \times \{1 + \tanh[(x + x_0)/\Delta]\}$ with $\Delta = 2$. This profile tends to (79) when $\Delta \to 0$.

ACKNOWLEDGMENTS

A.M.K. thanks Laboratoire de Physique Théorique et Modèles Statistiques (Université Paris-Saclay), where this work was started, for kind hospitality. This work was supported by the French ANR under Grant No. ANR-15-CE30-0017 (Haralab project).

[1] G. B. Whitham, *Linear and Nonlinear Waves* (Wiley Interscience, New York, 1974).
[2] V. I. Karpman, Phys. Lett. A **25**, 708 (1967).
[3] C. S. Gardner, J. M. Green, M. D. Kruskal, and R. M. Miura, Phys. Rev. Lett. **19**, 1095 (1967).
[4] I. A. Berezin and V. I. Karpman, Zh. Eksp. Teor. Fiz. **46**, 1880 (1964) [Sov. Phys. JETP **19**, 1265 (1964)].
[5] A. B. Shabat, Doklady AN SSSR **211**, 1310 (1973) [Sov. Mathem. Dokl. **14**, 1266 (1973)].
[6] M. J. Ablowitz and A. C. Newell, J. Math. Phys. **14**, 1277 (1973).
[7] V. E. Zakharov and S. V. Manakov, Zh. Eksp. Teor. Fiz. **71**, 203 (1976) [Sov. Phys. JETP **44**, 106 (1976)].
[8] M. J. Ablowitz and H. Segur, Stud. Appl. Math. **57**, 13 (1977).
[9] P. Deift, S. Venakides, and Z. Zhou, Commun. Pure Appl. Math. **47**, 199 (1994).
[10] G. A. El, A. L. Krylov, and S. Venakides, Commun. Pure Appl. Math. **54**, 1243 (2001).
[11] T. Claeys and T. Grava, Commun. Math. Phys. **286**, 979 (2009).
[12] T. Claeys and T. Grava, Commun. Pure Appl. Math. **63**, 203 (2010).
[13] J. L. Hammack and H. Segur, J. Fluid Mech. **65**, 289 (1974); **84**, 337 (1978).
[14] S. Trillo, M. Klein, G. F. Clauss, and M. Onorato, Physica D **333**, 276 (2016).
[15] A. M. Kamchatnov, A. Gammal, and R. A. Kraenkel, Phys. Rev. A **69**, 063605 (2004).
[16] M. A. Hoefer, M. J. Ablowitz, I. Coddington, E. A. Cornell, P. Engels, and V. Schweikhard, Phys. Rev. A **74**, 023623 (2006).
[17] W. Wan, S. Jia, and J. W. Fleischer, Nat. Phys. **3**, 46 (2007).
[18] G. Xu, M. Conforti, A. Kudlinski, A. Mussot, and S. Trillo, Phys. Rev. Lett. **118**, 254101 (2017).
[19] G. B. Whitham, Proc. R. Soc. A **283**, 238 (1965).
[20] A. V. Gurevich and L. P. Pitaevskii, Zh. Eksp. Teor. Fiz. **65**, 590 (1973) [Sov. Phys. JETP **38**, 291 (1974)].
[21] G. A. El and M. A. Hoefer, Physica D **333**, 11 (2016).
[22] G. A. El and V. V. Khodorovsky, Phys. Lett. A **182**, 49 (1993).
[23] A. V. Gurevich, A. L. Krylov, and N. G. Mazur, Zh. Eksp. Teor. Fiz. **95**, 1674 (1989) [Sov. Phys. JETP **68**, 966 (1989)].
[24] A. V. Gurevich, A. L. Krylov, and G. A. El, Pis'ma Zh. Eksp. Teor. Fiz. **54**, 104 (1991) [JETP Lett. **54**, 102 (1991)].
[25] A. V. Gurevich, A. L. Krylov, and G. A. El, Zh. Eksp. Teor. Fiz. **101**, 1797 (1992) [Sov. Phys. JETP **74**, 957 (1992)].
[26] A. L. Krylov, V. V. Khodorovskii, and G. A. El, Pis'ma Zh. Eksp. Teor. Fiz. **56**, 325 (1992) [JETP Lett. **56**, 323 (1992)].
[27] O. C. Wright, Commun. Pure Appl. Math. **46**, 423 (1993).
[28] F. R. Tian, Commun. Pure Appl. Math. **46**, 1093 (1993).
[29] A. M. Kamchatnov, *Nonlinear Periodic Waves and Their Modulations—An Introductory Course* (World Scientific, Singapore, 2000).
[30] I. S. Gradshteyn and I. M. Ryzhik, *Table of Integrals, Series, and Products* (Academic Press, New York, 1966).
[31] S. P. Tsarev, Math. USSR Izv. **37**, 397 (1991).
[32] L. P. Eisenhart, Ann. Math. **120**, 262 (1918).
[33] G. Arfken and H. J. Weber, *Mathematical Methods for Physicists* (Academic Press, Orlando, FL, 2005).
[34] G. A. El, Chaos **15**, 037103 (2005); **16**, 029901 (2006).
[35] A. M. Kamchatnov, Phys. Rev. E **99**, 012203 (2019).
[36] G. A. El and R. H. J. Grimshaw, Chaos **12**, 1015 (2002).
[37] H. Segur and M. J. Ablowitz, Physica D **3**, 165 (1981).

7.5 ARTICLE: WAVE BREAKING AND FORMATION OF DISPERSIVE SHOCK WAVES IN A DEFOCUSING NONLINEAR OPTICAL MATERIAL

↪ Wave breaking and formation of dispersive shock waves in a defocusing nonlinear optical material

M. Isoard, A.M. Kamchatnov, N. Pavloff, Physical Review A **99**, 053819 (2019)

doi: https://doi.org/10.1103/PhysRevA.99.053819

We describe theoretically the quasi-one-dimensional transverse spreading of a light beam propagating in a nonlinear optical material in the presence of a uniform background light intensity. For short propagation distances the pulse can be described within a nondispersive (geometric optics) approximation by means of Riemann's approach. For larger distances, wave breaking occurs, leading to the formation of dispersive shocks at both edges of the beam. We describe this phenomenon within Whitham modulation theory, which yields excellent agreement with numerical simulations. Our analytic approach makes it possible to extract the leading asymptotic behavior of the parameters of the shock, setting up the basis for a theory of nondissipative weak shocks.

Wave breaking and formation of dispersive shock waves in a defocusing nonlinear optical material

M. Isoard,[1] A. M. Kamchatnov,[2,3] and N. Pavloff[1]

[1]*LPTMS, UMR 8626, CNRS, Univ. Paris–Sud, Université Paris–Saclay, 91405 Orsay, France*

[2]*Institute of Spectroscopy, Russian Academy of Sciences, Troitsk, Moscow 108840, Russia*

[3]*Moscow Institute of Physics and Technology, Institutsky Lane 9, Dolgoprudny, Moscow Region 141701, Russia*

(Received 19 February 2019; published 14 May 2019)

We describe theoretically the quasi-one-dimensional transverse spreading of a light beam propagating in a nonlinear optical material in the presence of a uniform background light intensity. For short propagation distances the pulse can be described within a nondispersive (geometric optics) approximation by means of Riemann's approach. For larger distances, wave breaking occurs, leading to the formation of dispersive shocks at both edges of the beam. We describe this phenomenon within Whitham modulation theory, which yields excellent agreement with numerical simulations. Our analytic approach makes it possible to extract the leading asymptotic behavior of the parameters of the shock, setting up the basis for a theory of nondissipative weak shocks.

DOI: 10.1103/PhysRevA.99.053819

I. INTRODUCTION

It has long been known that light propagating in a nonlinear medium is amenable to a hydrodynamic treatment (see, e.g., Refs. [1–3]). In the case of a defocusing nonlinearity, this rich analogy has not only triggered experimental research, but also made it possible to get an intuitive understanding of observations of, e.g., the formation of rings in the far field beyond a nonlinear slab [4,5], dark solitons [6–8], vortices [9–11], wave breaking [12,13], dispersive shock waves [14–19], spontaneously self-accelerated Airy beams [20], an optical event horizon [21], ergo regions [22], stimulated Hawking radiation [23], soniclike dispersion relations [24,25], and superfluid motion [26]. Very similar phenomena have also been observed in the neighboring fields of cavity polaritons and Bose-Einstein condensation of atomic vapors. They all result from the interplay between nonlinearity and dispersion, whose effects become prominent near a gradient catastrophe region.

In this work we present a theoretical treatment of a model configuration which has been realized experimentally in a one-dimensional situation in Refs. [15,18]: the nonlinear spreading of a region of increased light intensity in the presence of a uniform constant background. In the absence of background and for a smooth initial intensity pattern, the spreading is mainly driven by the nonlinear defocusing and can be treated analytically in some simple cases [1]. The situation is more interesting in the presence of a constant background: The pulse splits in two parts, each eventually experiencing nonlinear wave breaking, leading to the formation of a dispersive shock wave (DSW) which cannot be described within the framework of perturbation theory, even if the region of increased intensity corresponds to a weak perturbation of the flat pedestal. This scenario indeed fits with the hydrodynamic approach of nonlinear light propagation and is nicely confirmed by the experimental observations of Refs. [15,18]. Although the numerical treatment of the problem is relatively simple [27–29], a theoretical approach to both the initial splitting of the pulse and the subsequent shock formation requires a careful analysis. The goal of this article is to present such an analysis. A most significant outcome of our detailed treatment is a simple asymptotic description of some important shock parameters. This provides a nondissipative counterpart of the usual weak viscous shock theory (see, e.g., Ref. [30]) and paves the way for a quantitative experimental test of our predictions.

The paper is organized as follows. In Sec. II we present the model and the setup we study. After a brief discussion of the shortcomings of the linearized approach, the spreading and splitting stage of evolution is accounted for in Sec. III within a dispersionless approximation which holds when the pulse region initially presents no large intensity gradient. It is well known that in such a situation the light flow can be described by hydrodynamiclike equations which can be cast into a diagonal form for two new position and time-dependent variables: the so-called Riemann invariants. The difficulty here lies in the fact that the splitting involves simultaneous variations of both of them: One does not have an initial simple wave within which one of the Riemann invariants remains constant, as occurs, for instance, in a similar unidirectional propagation case modeled by the Korteweg–de Vries equation (see, e.g., Ref. [31]). We treat the problem in Secs. III A and III B using an extension of the Riemann method due to Ludford [32] (also used in Ref. [33]) and compare the results with numerical simulations in Sec. III C. During the spreading of the pulse, nonlinear effects induce wave steepening, which results in a gradient catastrophe and wave breaking. After the wave breaking time, dispersive effects can no longer be omitted and a shock is formed; in this case we resort to Whitham modulation theory [30] to describe the time evolution of the pulse. Such a treatment was initiated long ago by Gurevich and Pitaevskii [34], and since that time it has developed into a powerful method with numerous applications (see, e.g., the review article in [35]). Here there is an additional complexity which lies, as for the initial nondispersive stage of evolution, in the fact that two of the (now four) Riemann invariants which describe the modulated nonlinear oscillations vary in

the shock region. Such a wave has been termed quasisimple in Ref. [36], and a thorough treatment within Whitham theory has been achieved in the Korteweg–de Vries case in Refs. [37–40]. In Sec. IV we generalize this approach to the nonlinear Schrödinger equation (NLS), which describes light propagation in the nonlinear Kerr medium (see also Ref. [41]). An interesting outcome of our theoretical treatment is the asymptotic determination of experimentally relevant parameters of the dispersive shock (Sec. V). In Sec. VI we present the full Whitham treatment of the after-shock evolution and compare the theoretical results with numerical simulations. We present in Sec. VII a panorama of the different regimes we have identified and discuss how our approach can be used to get a simple estimate of the contrast of the fringes of the DSW. This should be helpful in determining the best experimental configuration for studying the wave breaking phenomenon and the subsequent dispersive shock. Our conclusions and a summary of our results are presented in Sec. VIII.

II. MODEL AND LINEAR APPROXIMATION

In the paraxial approximation, the stationary propagation of the complex amplitude $A(\vec{r})$ of the electric field of a monochromatic beam is described by the equation (see, e.g., Ref. [42])

$$i\partial_z A = -\frac{1}{2n_0k_0}\nabla_\perp^2 A - k_0\delta n A. \tag{1}$$

In this equation, n_0 is the linear refractive index, $k_0 = 2\pi/\lambda_0$ is the carrier wave vector, z is the coordinate along the beam, $\nabla_\perp^2$ is the transverse Laplacian, and δn is a nonlinear contribution to the index. In a nonabsorbing defocusing Kerr nonlinear medium we can write $\delta n = -n_2|A|^2$, with $n_2 > 0$.

We define dimensionless units by choosing a reference intensity $I_{\rm ref}$ and introducing the nonlinear length $z_{\rm NL} = (k_0 n_2 I_{\rm ref})^{-1}$ and the transverse healing length $\xi_\perp = (z_{\rm NL}/n_0k_0)^{1/2}$. We consider a geometry where the transverse profile is translationally invariant and depends on a single Cartesian coordinate. We thus write $\nabla_\perp^2 = \xi_\perp^{-2}\partial_x^2$, where x is the dimensionless transverse coordinate and we define an effective time $t = z/z_{\rm NL}$. The quantity $\psi(x,t) = A/\sqrt{I_{\rm ref}}$ is then a solution of the dimensionless NLS equation

$$i\psi_t = -\tfrac{1}{2}\psi_{xx} + |\psi|^2\psi. \tag{2}$$

In the following we consider a system with a uniform background light intensity, on top of which an initial pulse is added at the entrance of the nonlinear cell. The initial $\psi(x, t = 0)$ is real (i.e., no transverse velocity or, in an optical context, no focusing of the light beam at the input plane), with a dimensionless intensity $\rho(x,t) = |\psi|^2$ which departs from the constant background value (which we denote by ρ_0) only in the region near the origin where it forms a bump. To be specific, we consider the typical case where

$$\rho(x,0) = \begin{cases} \rho_0 + \rho_1\left(1 - x^2/x_0^2\right) & \text{if } |x| < x_0 \\ \rho_0 & \text{if } |x| \geqslant x_0. \end{cases} \tag{3}$$

The maximal density of the initial profile is defined as $\rho_m = \rho_0 + \rho_1$. It would be natural to choose the reference light intensity $I_{\rm ref}$ to be equal to the background one; in this case we would have $\rho_0 = 1$. However, we prefer to be more general and to allow for values of ρ_0 different from unity.

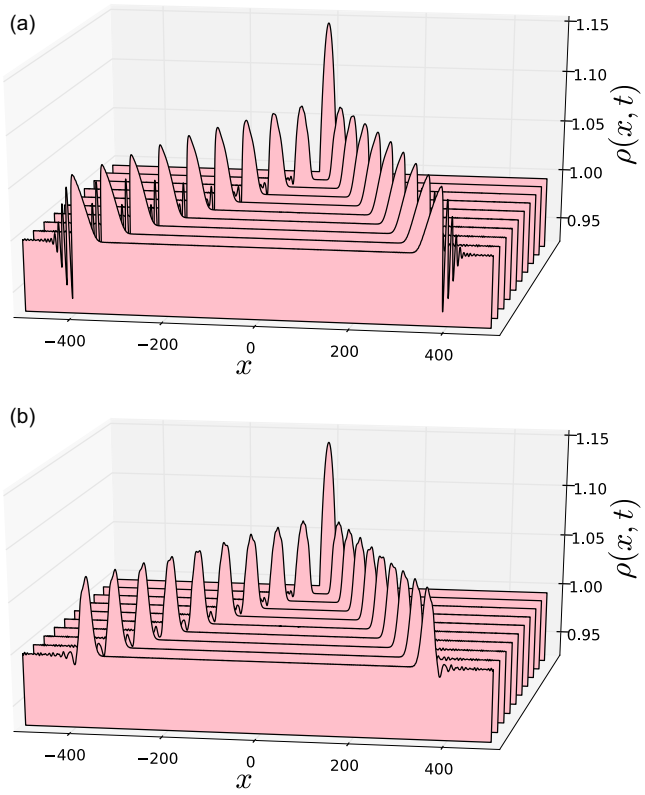

FIG. 1. Density profiles $\rho(x,t)$ for an initial condition $u(x,0) = 0$ and $\rho(x,0)$ given by (3) with $\rho_0 = 1$, $\rho_1 = 0.15$, and $x_0 = 20$. Results are shown for (a) the numerical solution of Eq. (2) and (b) the linearized version (4). The profiles are plotted from time $t = 0$ to $t = 360$ with a time step equal to 40.

We stress here the paramount importance of nonlinear effects for large time, i.e., for large propagation distance in the nonlinear medium. Even for a bump which weakly departs from the background density, a perturbative approach fails after the wave breaking time. This is illustrated in Fig. 1, which compares numerical simulations of the full Eq. (2) with its linearized version. The linearized treatment is obtained by writing $\psi(x,t) = \exp(-i\rho_0 t)[\sqrt{\rho_0} + \delta\psi(x,t)]$ and assuming that $|\delta\psi|^2 \ll \rho_0$, which yields the evolution equation

$$i\partial_t\delta\psi = -\tfrac{1}{2}\partial_x^2\delta\psi + \rho_0(\delta\psi + \delta\psi^*) \tag{4}$$

and then $\rho(x,t) \simeq \rho_0 + \sqrt{\rho_0}(\delta\psi + \delta\psi^*)$. In the case illustrated in Fig. 1, the initial profile has, at its maximum, a weak 15% density increase with respect to the background. The initial splitting of the bump is correctly described by the linearized approach, but after the wave breaking time the linearized evolution goes on predicting a roughly global displacement of the two humps at constant velocity (with additional small dispersive corrections) and clearly fails to reproduce both the formation of DSWs and the stretching of the dispersionless part of the profile (which reaches a quasitriangular shape).

III. DISPERSIONLESS STAGE OF EVOLUTION

In view of the shortcomings of the linearized approximation illustrated in Fig. 1, we include nonlinear effects at all stages of the dynamical study of the model. By means of the Madelung substitution

$$\psi(x,t)=\sqrt{\rho(x,t)}\exp\left(i\int^{x}u(x',t)dx'\right), \tag{5}$$

the NLS equation (2) can be cast into a hydrodynamiclike form for the density $\rho(x,t)$ and the flow velocity $u(x,t)$:

$$\begin{aligned}\rho_t+(\rho u)_x&=0,\\ u_t+uu_x+\rho_x+\left(\frac{\rho_x^2}{8\rho^2}-\frac{\rho_{xx}}{4\rho}\right)_x&=0.\end{aligned} \tag{6}$$

These equations are to be solved with the initial conditions (3) and $u(x,0)=0$.

The last term on the left-hand side of the second of Eqs. (6) accounts for the dispersive character of the fluid of light. In the first stage of spreading of the bump, if the density gradients of the initial density are weak, i.e., if $x_0\gg\max\{\rho_0^{-1/2},\rho_1^{-1/2}\}$, the effects of dispersion can be neglected and the system (6) then simplifies to

$$\rho_t+(\rho u)_x=0,\quad u_t+uu_x+\rho_x=0. \tag{7}$$

These equations can be written in a more symmetric form by introducing the Riemann invariants

$$\lambda^{\pm}(x,t)=\frac{u(x,t)}{2}\pm\sqrt{\rho(x,t)}, \tag{8}$$

which evolve according to the system [equivalent to (7)]

$$\partial_t\lambda^{\pm}+v_{\pm}(\lambda^{-},\lambda^{+})\partial_x\lambda^{\pm}=0, \tag{9}$$

with

$$v_{\pm}(\lambda^{-},\lambda^{+})=\tfrac{1}{2}(3\lambda^{\pm}+\lambda^{\mp})=u\pm\sqrt{\rho}. \tag{10}$$

The Riemann velocities (10) have a simple physical interpretation for a smooth velocity and density distribution: v_+ (v_-) corresponds to a signal which propagates downstream (upstream) at the local velocity of sound $c=\sqrt{\rho}$ and which is dragged by the background flow u.

The system (9) can be linearized by means of the hodograph transform (see, e.g., Ref. [43]), which consists in considering x and t as functions of λ^+ and λ^-. We readily obtain

$$\partial_{\pm}x-v_{\mp}\partial_{\pm}t=0, \tag{11}$$

where $\partial_{\pm}\equiv\partial/\partial\lambda^{\pm}$. We introduce two auxiliary (yet unknown) functions $W_{\pm}(\lambda^{+},\lambda^{-})$ such that

$$x-v_{\pm}(\lambda^{-},\lambda^{+})t=W_{\pm}(\lambda^{-},\lambda^{+}). \tag{12}$$

Inserting the above expressions in (11) shows that the $W^{\pm}$ are solutions of Tsarev equations [44]

$$\frac{\partial_-W_+}{W_+-W_-}=\frac{\partial_-v_+}{v_+-v_-},\quad \frac{\partial_+W_-}{W_+-W_-}=\frac{\partial_+v_-}{v_+-v_-}. \tag{13}$$

From Eqs. (10) and (13) we can verify that $\partial_-W_+=\partial_+W_-$, which shows that W_+ and W_- can be sought in the form

$$W_{\pm}=\partial_{\pm}\chi, \tag{14}$$

where $\chi(\lambda^{-},\lambda^{+})$ plays the role of a potential. Substituting expressions (14) in one of the Tsarev equations shows that χ is a solution of the Euler-Poisson equation

$$\frac{\partial^2\chi}{\partial\lambda^{+}\partial\lambda^{-}}-\frac{1}{2(\lambda^{+}-\lambda^{-})}\left(\frac{\partial\chi}{\partial\lambda^{+}}-\frac{\partial\chi}{\partial\lambda^{-}}\right)=0, \tag{15}$$

which can be written under the standard form

$$\frac{\partial^2\chi}{\partial\lambda^{+}\partial\lambda^{-}}+a(\lambda^{-},\lambda^{+})\frac{\partial\chi}{\partial\lambda^{+}}+b(\lambda^{-},\lambda^{+})\frac{\partial\chi}{\partial\lambda^{-}}=0, \tag{16}$$

with

$$a(\lambda^{-},\lambda^{+})=-b(\lambda^{-},\lambda^{+})=-\frac{1}{2(\lambda^{+}-\lambda^{-})}. \tag{17}$$

A. Solution of the Euler-Poisson equation

We can use Riemann's method to solve Eq. (16) in the $(\lambda^{+},\lambda^{-})$ plane, which we refer to below as the characteristic plane. We follow here the procedure given in Refs. [32,33], which applies to nonmonotonic initial distributions, such as the one corresponding to Eq. (3).

We first schematically depict in Fig. 2 the initial spatial distributions $\lambda^{\pm}(x,0)$ of the Riemann invariants [Fig. 2(a)] and their later typical time evolution [Figs. 2(b) and 2(c)]. We introduce notation for several special initial values of the Riemann invariants: $\lambda^{\pm}(-x_0,0)=\lambda^{\pm}(x_0,0)=\pm\sqrt{\rho_0}=\pm c_0$ and $\lambda^{\pm}(0,0)=\pm\sqrt{\rho_m}=\pm c_m$. We also define as part A (B) the branch of the distribution of the $\lambda^{\pm}$ which is at the right (left) of the extremum. All the notation is summarized in Fig. 2(a).

At a given time, the x axis can be considered as divided into five domains, each requiring a specific treatment. Each region is characterized by the behavior of the Riemann invariant and is identified in Figs. 2(b) and 2(c). The domains in which both Riemann invariants depend on position are labeled by arabic numbers and the ones in which only one Riemann invariant depends on x are labeled by roman numbers. For instance, in region III, λ^+ is a decreasing function of x while $\lambda^-=-c_0$ is a constant; in region 3, λ^+ is decreasing while λ^- is increasing; in region 2 both are increasing; etc.

The values of the Riemann invariants at time corresponding to Fig. 2(b) are represented in the characteristic plane in Fig. 3(a). In this plot the straight solid lines correspond to the simple-wave regions (I and III) while the curvy lines corresponds to regions where both Riemann invariants depend on position: domains 1, 2, and 3. In each of these three domains the solution χ of the Euler-Poisson equation has a different expression. In order to describe these three branches, following Ludford [32], we introduce several sheets in the characteristic plane by unfolding the domain $[c_0,c_m]\times[-c_m,-c_0]$ into a four times larger region as illustrated in Fig. 3(b). The potential $\chi(\lambda^{-},\lambda^{+})$ can now take a different form in each of the regions labeled 1, 2, and 3 in Fig. 3(b) and still be considered as single valued.

We consider a flow where initially $u(x,0)=0$, which implies that $\lambda^{+}(x,0)=-\lambda^{-}(x,0)$. This condition defines the

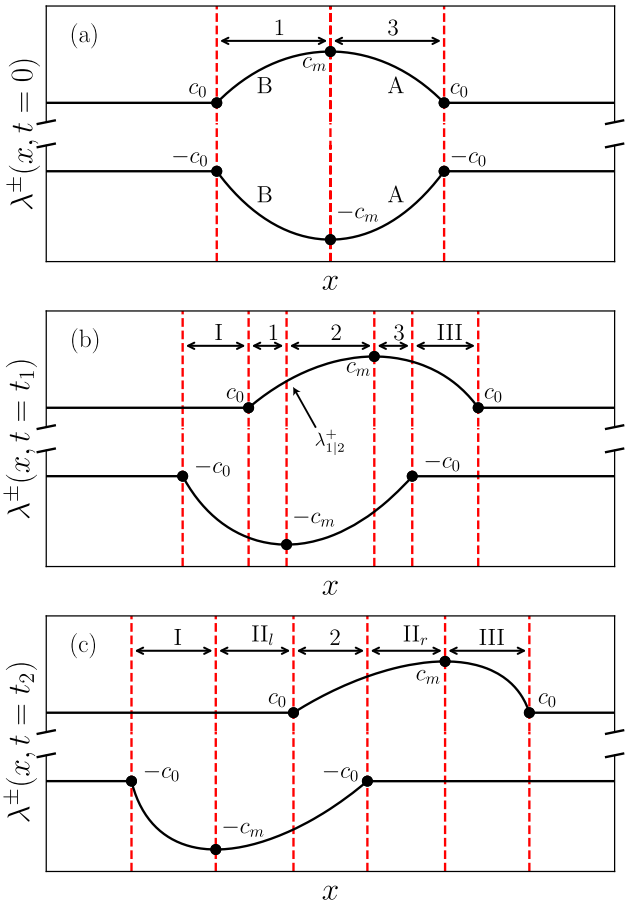

FIG. 2. Sketch of the distributions $\lambda^{\pm}(x, t)$ at several times. In each panel the top solid curve represent λ^+ (always larger than c_0) and the bottom one λ^- (always lower than $-c_0$), both plotted as functions of x. (a) Initial distribution, in which part B corresponds to region 1 and part A to region 3 (see the text). Two subsequent relevant stages of evolution are represented in (b) and (c). They correspond to times $t_1 < t_{\mathrm{SW}}(c_m) < t_2$, where $t_{\mathrm{SW}}(c_m)$ is defined in Sec. III B (see also Fig. 4). For $t > 0$, λ^+ (λ^-) moves to the right (to the left) and part B of λ^+ starts to overlap with part A of λ^-. This behavior initially leads to the configuration represented in (b), where a new region (labeled region 2) has appeared. For later convenience, we spot in this panel the value $\lambda^+_{1|2}(t_1)$ of the Riemann invariant λ^+ at the boundary between regions 1 and 2 (see the discussion in Sec. III C). For longer time [in (c)], region 2 remains while regions 1 and 3 vanish and new simple-wave regions II_l and II_r appear. At even larger times (not represented), region 2 also vanishes and only simple-wave regions remain: The initial pulse has split into two simple-wave pulses propagating in opposite directions.

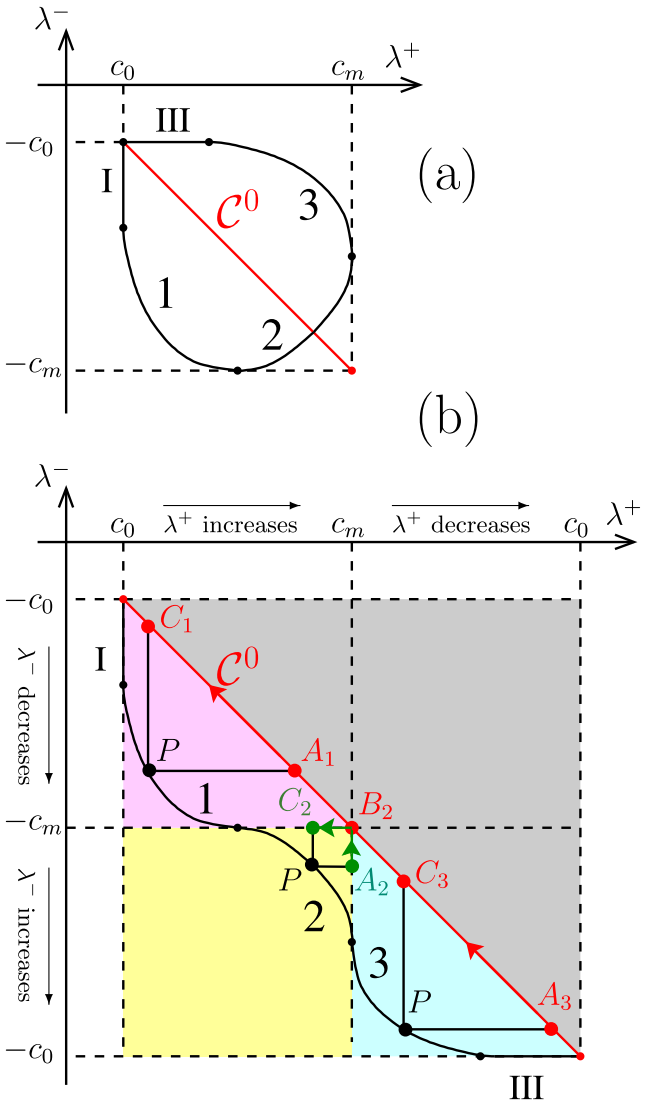

FIG. 3. (a) Behavior of the Riemann invariants in the characteristic plane at a given time t. (b) Same curve on the four-sheeted unfolded surface. The red curve $\mathcal{C}^0$ corresponds to the initial condition $[\lambda^-(x, 0) = -\lambda^+(x, 0)]$. At later time, the relation between $\lambda^+(x, t)$ and $\lambda^-(x, t)$ is given by the black solid curve, which is denoted by $\mathcal{C}^t$ in the text. A generic point P of $\mathcal{C}^t$ has coordinates (λ^+, λ^-) and points C_1, A_1, B_2, C_3, and A_3 lie on the initial curve $\mathcal{C}^0$. Points A_2 and C_2 lie on a boundary between two regions. The arrows indicate the direction of integration in Eqs. (21) and (28). In our problem, the whole gray shaded domain above $\mathcal{C}^0$ is unreachable.

curve of initial conditions of our problem in the characteristic plane. It is represented by a red solid curve labeled $\mathcal{C}^0$ in Fig. 3. We remark here that the whole region above $\mathcal{C}^0$ [shaded in Fig. 3(b)] is unreachable for the initial distribution we consider: For instance, the upper shaded triangle in region 1 would correspond to a configuration in which $\lambda^+_{\mathrm{region1}}(x, t) > |\lambda^-_{\mathrm{region1}}(x, t)|$, which does not occur in our case [see Fig. 2(b)].

Before establishing that the expression for χ is the three relevant regions of Fig. 3, it is convenient to define the inverse functions of the initial λ profiles in both parts A and B of Fig. 2(a). The symmetry of the initial conditions makes it possible to use the same functions for $\lambda^+ \in [c_0, c_m]$ and $\lambda^- \in [-c_m, -c_0]$:

$$x = \begin{cases} w^{\mathrm{A}}(\lambda^{\pm}) = x_0\sqrt{1 - \frac{(\lambda^{\pm})^2 - \rho_0}{\rho_m - \rho_0}} & \text{if } x > 0 \\ w^{\mathrm{B}}(\lambda^{\pm}) = -x_0\sqrt{1 - \frac{(\lambda^{\pm})^2 - \rho_0}{\rho_m - \rho_0}} & \text{if } x < 0. \end{cases} \tag{18}$$

For $t = 0$, using Eqs. (12) and (14), the boundary conditions read

$$\left.\frac{\partial\chi}{\partial\lambda^{\pm}}\right|_{\lambda^{\pm}(x,t=0)} = x = w^{\mathrm{A(B)}}(\lambda^{\pm}), \tag{19}$$

where the superscript B holds in region 1 (when $x < 0$) and A holds in region 3 ($x > 0$). Formula (19) requires some explanation: Its left-hand side is a function of two variables λ^+ and λ^- which is evaluated for $\lambda^- = -\lambda^+$; its right-hand side is expressed by the same function in terms of λ^+ or λ^- since the functions w^{A} and w^{B} depend only on the square of their argument. The boundary conditions (19) correspond to a potential χ which takes the form along $\mathcal{C}^0$,

$$\chi^{(n)}(\lambda^- = -\lambda^+, \lambda^+) = \int_{c_0}^{\lambda^+} w^{\mathrm{A(B)}}(r)dr + \int_{-c_0}^{\lambda^-} w^{\mathrm{A(B)}}(r)dr, \tag{20}$$

where $n = 1$ or 3 and, on the right-hand side, the superscript A (B) holds when $n = 3$ ($n = 1$). For the specific initial condition we consider [$u(x, 0) \equiv 0$ and $\rho(x, 0)$ an even function of x], w^{A} and w^{B} are even functions and thus our choice of integration constants yields $\chi = 0$ along $\mathcal{C}^0$.

Let us now consider a point P, lying in either region 1 or 3 (the case of region 2 is considered later), with coordinates (λ^+, λ^-) in the characteristic plane. We introduce points A_1, A_3, C_1, and C_3 which are located on the curve $\mathcal{C}^0$, with geometrical definitions obvious from Fig. 3(b). Note the different subscripts for C and A: Subscript 1 (3) is to be used if P is in region 1 (3). We can obtain the value of χ at the point P from Riemann's method (see, e.g., Ref. [45]); the general solution reads

$$\chi^{(n)}(P) = \frac{1}{2}\chi(C_n)R(C_n) + \frac{1}{2}\chi(A_n)R(A_n) - \int_{A_n}^{C_n} V\,dr + U\,ds, \tag{21}$$

with

$$U(s,r) = \frac{1}{2}\left(R\frac{\partial\chi}{\partial s} - \chi\frac{\partial R}{\partial s}\right) + aR\chi,$$
$$V(s,r) = \frac{1}{2}\left(\chi\frac{\partial R}{\partial r} - R\frac{\partial\chi}{\partial r}\right) - bR\chi, \tag{22}$$

where

$$R(s,r) = \frac{2}{\pi}\sqrt{\frac{r-s}{\lambda^+ - \lambda^-}}\mathsf{K}[m(s,r)], \tag{23}$$

with K the complete elliptic integral of the first kind and

$$m(s,r) = \frac{(\lambda^+ - r)(\lambda^- - s)}{(r-s)(\lambda^+ - \lambda^-)} \tag{24}$$

the associated parameter (we follow here the convention of Ref. [46]). In our case, the symmetries of the initial profile lead to many simplifications in formulas (21) and (22). Along the curve $\mathcal{C}^0$ we have $\chi = 0$. This implies that $\chi^{(n)}(A_n) = \chi^{(n)}(C_n) = 0$, and along the integration path going from A_n to C_n we have

$$U = \tfrac{1}{2}w^{\mathrm{A(B)}}(r)R(s = -r, r) = -V, \tag{25}$$

where the superscript A (B) holds when P is in region 3 (region 1). Explicit evaluation of expression (21) then yields

$$\chi^{(n)}(P) = \frac{2\sqrt{2}}{\pi\sqrt{\lambda^+ - \lambda^-}}\int_{-\lambda^-}^{\lambda^+}\sqrt{r}\mathsf{K}[m(r)]w^{\mathrm{A(B)}}(r)dr, \tag{26}$$

where

$$m(r) \equiv m(-r, r) = \frac{(\lambda^+ - r)(\lambda^- + r)}{2r(\lambda^+ - \lambda^-)}. \tag{27}$$

To calculate $\chi(P)$ in region 2 we define three points: A_2, B_2, and C_2 [see Fig. 3(b)]. Point B_2 is on the curve $\mathcal{C}^0$, at the junction between regions 1, 2, and 3. Point A_2 lies on the characteristic curve $\lambda^+ = c_m$, on the boundary between regions 2 and 3, whereas point C_2 lies on the characteristic $\lambda^- = -c_m$, on the boundary between regions 1 and 2. Then, from Eqs. (21)–(24), we can easily find that in region 2,

$$\chi^{(2)}(P) = \chi(B_2)R(B_2) + \int_{B_2}^{C_2}\left(\frac{\partial\chi}{\partial r} + b\chi\right)R_1(r)dr - \int_{A_2}^{B_2}\left(\frac{\partial\chi}{\partial s} + a\chi\right)R_2(s)ds, \tag{28}$$

where

$$R_1(r) \equiv \frac{2}{\pi}\sqrt{\frac{r + c_m}{\lambda^+ - \lambda^-}}\mathsf{K}[m_1(r)],$$
$$m_1(r) = \frac{(r - \lambda^+)(c_m + \lambda^-)}{(r - \lambda^-)(\lambda^+ + c_m)} \tag{29}$$

and

$$R_2(s) = \frac{2}{\pi}\sqrt{\frac{c_m - s}{\lambda^+ - \lambda^-}}\mathsf{K}[m_2(s)],$$
$$m_2(s) = \frac{(c_m - \lambda^+)(\lambda^- - s)}{(c_m - \lambda^-)(\lambda^+ - s)}. \tag{30}$$

Note that in formula (28) we have $\chi(B_2) = 0$ and the value of χ along the integration lines B_2C_2 and A_2B_2 is known from the previous result (26). After some computation we eventually get the expression for $\chi(P)$ in region 2,

$$\chi^{(2)}(P) = \frac{2\sqrt{2}}{\pi\sqrt{\lambda^+ - \lambda^-}}\left[\int_{c_m}^{\lambda^+}\sqrt{r}\mathsf{K}[m_0(r;\lambda^+)]w^{\mathrm{B}}(r)dr + \int_{-\lambda^-}^{c_m}\sqrt{r}\mathsf{K}[m_0(r;-\lambda^-)]w^{\mathrm{A}}(r)dr\right] + \frac{4\sqrt{2}}{\pi^2\sqrt{\lambda^+ - \lambda^-}}\left[\int_{c_m}^{\lambda^+}\sqrt{r}w^{\mathrm{B}}(r)f_1(r)dr + \int_{-\lambda^-}^{c_m}\sqrt{r}w^{\mathrm{A}}(r)f_2(r)dr\right], \tag{31}$$

where we have introduced the notation

$$f_1(r) = \int_{\lambda^+}^{r}\mathsf{K}[m_0(r;u)]\frac{\partial\mathsf{K}[m_1(u)]}{\partial u}du,$$
$$f_2(r) = \int_{-\lambda^-}^{r}\mathsf{K}[m_0(r;u)]\frac{\partial\mathsf{K}[m_2(-u)]}{\partial u}du, \tag{32}$$

with

$$m_0(r;u) = \frac{(r-u)(c_m - r)}{2r(u + c_m)}. \tag{33}$$

In many instances we can actually simplify the expressions (26) and (31): for reasonable values of c_m (chosen to be of same order as c_0 in our simulations) the elliptic integral $\mathsf{K}(m)$ turns out to be approximately equal to $\pi/2$ for all points P in the three regions. In this case, the exact expressions (26) and (31) can be replaced by a simple approximation $\chi(P) \simeq \chi_{\rm app}(P)$ which reads, when P is in region $n = 1$ or 3,

$$\chi^{(n)}_{\rm app}(\lambda_-, \lambda_+) = \frac{\sqrt{2}}{\sqrt{\lambda^+ - \lambda^-}} \int_{-\lambda^-}^{\lambda^+} \sqrt{r} w^{\rm A(B)}(r) dr, \qquad (34)$$

where the superscript A (B) holds when $n = 3$ ($n = 1$). When P is in region 2 we get

$$\chi^{(2)}_{\rm app}(\lambda_-, \lambda_+) = \frac{\sqrt{2}}{\sqrt{\lambda^+ - \lambda^-}} \int_{c_m}^{\lambda^+} \sqrt{r} w^{\rm B}(r) dr + \frac{\sqrt{2}}{\sqrt{\lambda^+ - \lambda^-}} \int_{-\lambda^-}^{c_m} \sqrt{r} w^{\rm A}(r) dr. \qquad (35)$$

This approximation greatly simplifies the numerical determination of the integrals involved in the solution of the problem. We have checked that it is very accurate in all the configurations we study in the present work. The reason for its validity is easy to understand in regions 1 and 3: The argument of the elliptic integral K in Eq. (26) is zero at the two boundaries of the integration domain ($r = -\lambda^-$ and $r = \lambda^+$) and reaches a maximum when $r = \sqrt{-\lambda^-\lambda^+}$, taking the value

$$0 \leqslant m_{\rm max} = \frac{1}{2}\left(1 - \frac{2\sqrt{-\lambda^-\lambda^+}}{\lambda^+ - \lambda^-}\right) \leqslant \frac{1}{2}. \qquad (36)$$

As time varies, the largest value of $m_{\rm max}$ is reached at the point where region 3 disappears, when $\lambda^+ = c_m$ and $\lambda^- = -c_0$. For $c_m/c_0 \sim 1$ this value is typically much lower than the upper bound $\frac{1}{2}$ of Eq. (36). For instance, in the numerical simulations below, we take $\rho_0 = 0.5$ and $\rho_m = 2$ and we get accordingly $c_0 = \sqrt{0.5}$ and $c_m = \sqrt{2}$ and the corresponding largest value of $m_{\rm max}$ is $\simeq 2.9 \times 10^{-2}$.

B. Simple-wave regions

Once χ has been computed in the domains 1, 2, and 3 where two Riemann invariants depend on position, it remains to determine the values of λ^+ and λ^- in the simple-wave regions. Let us focus on, for instance, region III, in which $\lambda^- = -c_0$ and λ^+ depends on x and t. The behavior of the characteristics in the (x, t) plane is sketched in Fig. 4. We see in this figure that the characteristic of a given value of λ^+ enters the simple-wave region III at a given time, which we denote by $t_{\rm SW}(\lambda^+)$, and a given position $x_{\rm SW}(\lambda^+)$. Beyond this point the characteristic becomes a straight line and the general solution of Eq. (9) for λ^+ is known to be of the form

$$x - v_+(-c_0, \lambda^+)t = h(\lambda^+), \qquad (37)$$

where the unknown function h is determined by boundary conditions. From Eq. (12) we see that just at the boundary between regions 3 and III we have

$$x_{\rm SW}(\lambda^+) - v_+(-c_0, \lambda^+)t_{\rm SW}(\lambda^+) = W_+^{(3)}(-c_0, \lambda^+), \qquad (38)$$

where $W_+^{(3)} = \partial_+\chi^{(3)}$. This shows that in Eq. (37) the unknown function $h(\lambda^+)$ is equal to $W_+^{(3)}(-c_0, \lambda^+)$. The

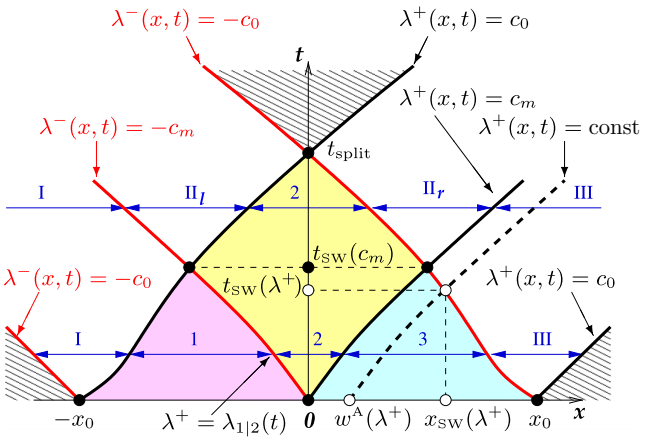

FIG. 4. Sketch of the characteristics in the (x, t) plane. The black (red) solid lines are specific characteristics for λ^+ (λ^-) stemming from the edges of the hump and from its maximum. The thick dashed line is a generic characteristic of λ^+. In the hatched regions both Riemann invariants are constant [$\lambda^\pm(x, t) = \pm c_0$] and the profile is flat. In the colored regions both Riemann invariants depend on position (the color code is the same as in Fig. 3: region 1 is pink, region 2 is yellow, and region 3 is cyan). In the white regions only one Riemann invariant depends on position: We have a simple wave. The notation is explained in the text.

equation of the characteristic in region III thus reads

$$x - v_+(-c_0, \lambda^+)t = W_+^{(3)}(-c_0, \lambda^+). \qquad (39)$$

Similar reasoning shows that in region I we have

$$x - v_-(\lambda^-, c_0)t = W_-^{(1)}(\lambda^-, c_0). \qquad (40)$$

For time larger than $t_{\rm SW}(c_m)$, regions 1 and 3 disappear and two new simple-wave regions appear, which we denote by II_l and II_r [see Fig. 4 and also Fig. 2(c)]. The same reasoning as above shows that in these regions the characteristics are determined by

$$x - v_+(-c_0, \lambda^+)t = W_+^{(2)}(-c_0, \lambda^+) \quad \text{in } \text{II}_r \qquad (41)$$

and

$$x - v_-(\lambda^-, c_0)t = W_-^{(2)}(\lambda^-, c_0) \quad \text{in } \text{II}_l. \qquad (42)$$

C. Solution of the dispersionless problem and comparison with numerical simulations

The problem is now solved: Having determined χ in regions 1, 2, and 3 (see Sec. III A), we obtain $W_\pm$ in these regions from Eqs. (14).

(i) It is then particularly easy to find the values of λ^+ and λ^- in the simple-wave regions. For instance, in region III, we have $\lambda_- = -c_0$, and for given x and t, λ^+ is obtained from Eq. (39). The same procedure is to be employed in the simple-wave regions I, II_r, and II_l, where the relevant equations are then Eqs. (40), (41), and (42), respectively.

(ii) To determine the values of λ^+ and λ^- as functions of x and t in regions 1, 2, and 3 we follow a different procedure which is detailed below, but which essentially consists in the following: For a given time t and a given region n ($n = 1$, 2,

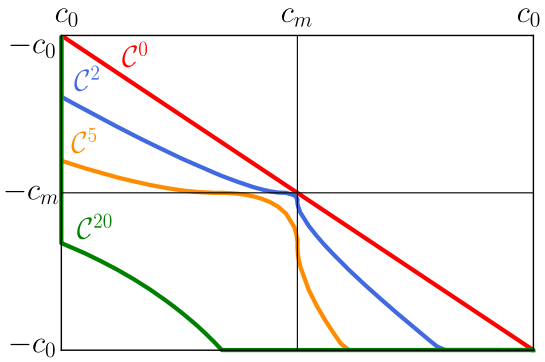

FIG. 5. Theoretical curves $\mathcal{C}^t$ representing λ^- as a function of λ^+ at a given time in the characteristic plane. The curves are plotted for $t = 0$ ($\mathcal{C}^0$, in red), $t = 2$ (blue), $t = 5$ (orange), and $t = 20 > t_{\rm SW}(c_m)$ (green). The corresponding initial distribution $\lambda^{\pm}(x, 0)$ is schematically represented in Fig. 2(a). We take here $c_0 = 1/\sqrt{2}$ and $c_m = \sqrt{2}$.

or 3) we pick one of the possible values of λ^+. From Eqs. (12) λ^- is then solution of

$$\frac{W_+^{(n)}(\lambda^-, \lambda^+) - W_-^{(n)}(\lambda^-, \lambda^+)}{v_+(\lambda^-, \lambda^+) - v_-(\lambda^-, \lambda^+)} + t = 0 \qquad (43)$$

and x is determined by either one of Eqs. (12). So, for given t and λ^+ in region n, we have determined the values of λ^- and x. In practice, this makes it possible to associate a couple (λ^-, λ^+) in region n to each (x, t).

The procedure for determining the profile in regions 1, 2, and 3 which has just been explained has to be implemented with care, because the relevant regions to be considered and their boundaries change with time; for instance, regions 1 and 3 disappear when $t > t_{\rm SW}(c_m)$. It would be tedious to list here all the possible cases so instead we explain the specifics of the procedure by means of an example: the determination of λ^+ and λ^- in region 1 when $t < t_{\rm SW}(c_m)$.

We start by determining the value of λ^+ along the characteristic $\lambda^- = -c_m$ at time t (see Fig. 4). This value of λ^+ defines the boundary between regions 1 and 2 and we accordingly denote it by $\lambda^+_{1|2}(t)$; it is represented in Fig. 2(b). From Eqs. (12) it is a solution of

$$\frac{W_+^{(1)}(-c_m, \lambda^+_{1|2}) - W_-^{(1)}(-c_m, \lambda^+_{1|2})}{v_+(-c_m, \lambda^+_{1|2}) - v_-(-c_m, \lambda^+_{1|2})} + t = 0. \qquad (44)$$

We then know that, in region 1, at time t, λ^+ takes all possible values between c_0 and $\lambda^+_{1|2}(t)$. Having determined the precise range of variation of λ^+ we can now, for each possible λ^+, determine λ^- from Eq. (43) (with $n = 1$) and follow the above-explained procedure.

(iii) The approach described in the present section makes it possible to determine the curve $\mathcal{C}^t$ representing, at time t, the profile in the unfolded characteristic plane. A sketch of $\mathcal{C}^t$ was given in Fig. 3(b); it is now precisely represented in Fig. 5 for several values of t, along with the initial curve $\mathcal{C}^0$.

Once λ^+ and λ^- have been determined as functions of x and t, the density and velocity profiles are obtained through Eqs. (8). We obtain an excellent description of the initial dispersionless stage of evolution of the pulse, as demonstrated

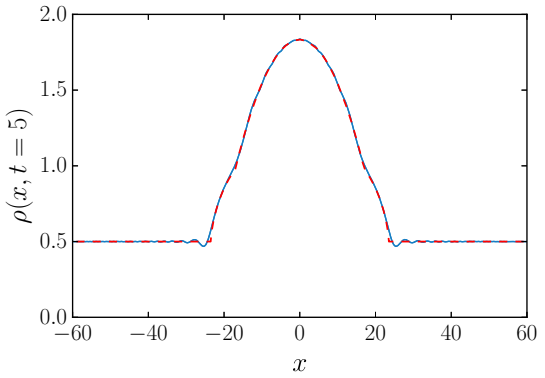

FIG. 6. Comparison between theory and simulations for $t = 5$. The red dashed curve is extracted from the exact solution of the dispersionless system (9) (see the text), while the blue curve displays the numerical solution of Eq. (2) with the initial conditions $u(x, 0) = 0$ and $\rho(x, 0)$ given by Eq. (3) taking $\rho_0 = 0.5$, $\rho_1 = 1.5$ (i.e., $\rho_m = 2$), and $x_0 = 20$. The corresponding initial distributions $\lambda^{\pm}(x, 0)$ are drawn schematically in Fig. 2(a), here with $c_0 = \sqrt{\rho_0} = \sqrt{0.5}$ and $c_m = \sqrt{\rho_m} = \sqrt{2}$.

by the very good agreement between theory and numerical simulations illustrated in Figs. 6 and 7. These figures, together with Fig. 8, compare at different times the theoretical density profile $\rho(x, t)$ with the one obtained by numerical integration of Eq. (2), taking the initial condition $u(x, 0) = 0$ and $\rho(x, 0)$ given by (3) with $\rho_0 = 0.5$, $\rho_m = 2$, and $x_0 = 20$. Similar agreement is obtained for the velocity profile $u(x, t)$. Note that for time $t = 5$, some small diffractive contributions at the left and right boundaries of the pulse are not accounted for by our dispersionless treatment (see Fig. 6). At larger time, the density profile at both ends of the pulse steepens and the amplitude of these oscillations accordingly increases. There exists a certain time, the wave breaking time $t_{\rm WB}$, at which nonlinear spreading leads to a gradient catastrophe; the dispersionless approximation subsequently predicts a nonphysical multivalued profile, as can be seen in Fig. 7 and more clearly in Fig. 8. The time $t_{\rm WB}$ can be easily computed if the wave breaking occurs at the simple-wave edges of the pulse (see, e.g., [47]) as it happens in our case, when the simple

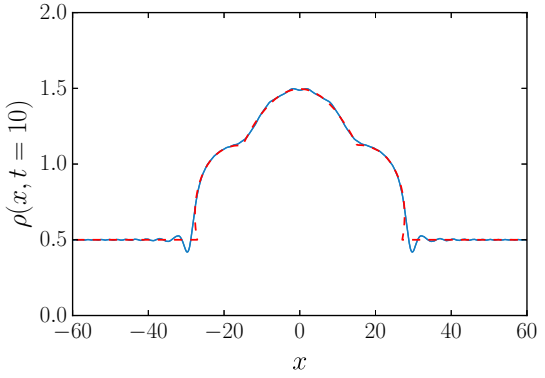

FIG. 7. Same as Fig. 6 but with $t = 10$. Notice that the dispersionless treatment leads to small regions of multivalued profile at both edges of the pulse.

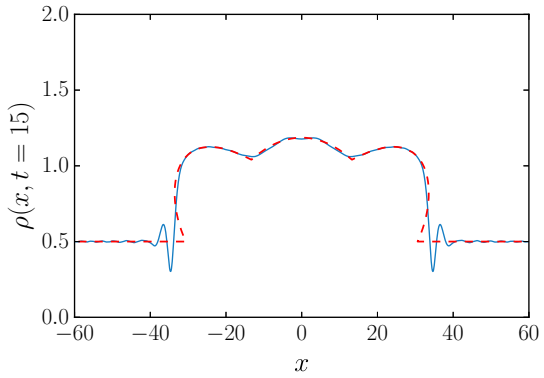

FIG. 8. Same as Figs. 6 and 7 but with $t = 15$. The multivaluedness of the theoretical profile is obvious here. It is associated with the formation of dispersive shocks at both edges of the pulse.

waves I and III break. These edges propagate with the sound velocity c_0 over a flat background and, at the wave breaking moment, the profile of λ^+ in region III (or λ^- in region I) has a vertical tangent line in the limit $\lambda^+ \to c_0$ ($\lambda^- \to -c_0$), that is, $\partial x/\partial\lambda^\pm \to 0$ as $\lambda^\pm \to \pm c_0$. Then differentiation of the simple-wave solution (39) or (40) gives at once

$$t_{\rm WB} = \frac{2}{3}\left|\frac{dW_+^{(3)}(-c_0, \lambda^+)}{d\lambda^+}\right|_{\lambda^+=c_0} \tag{45}$$

(for definiteness we consider the simple wave in the region III). Substitution of the expression for $W_+^{(3)}(-c_0, \lambda^+)$ in the relation (45) yields, after simple calculations [48],

$$t_{\rm WB} = \frac{2}{3}\left|\frac{dw^{\rm A}}{d\lambda^+}\right|_{\lambda^+=c_0}. \tag{46}$$

The numerical value of $t_{\rm WB}$ is $\simeq$6.3 for our choice of initial condition, in excellent agreement with the onset of double valuedness of the solution of the Euler-Poisson equation. In dispersive nonlinear systems the wave breaking is regularized by formation of regions with large oscillations of density and flow velocity, whose extent increases with time. This situation is typical for the formation of dispersive shock waves and requires a nonlinear treatment able to account for dispersive effects. Such an approach is introduced in the next section, but before turning to this aspect, we now compute an important characteristics time: the time $t_{\rm split}$ at which the initial bump has exactly split into two separated parts. For $t > t_{\rm split}$ a plateau of constant density ρ_0 develops between the two separated humps, as illustrated, for instance, in Fig. 1. We can see from Fig. 4 that $t_{\rm split} = t_{\rm SW}(c_0)$ and can thus be computed from Eqs. (12) as

$$t_{\rm split} = \frac{W_-^{(2)}(-c_0, c_0) - W_+^{(2)}(-c_0, c_0)}{v_+(-c_0, c_0) - v_-(-c_0, c_0)}. \tag{47}$$

On the right-hand side of this equation we have $W_\pm^{(2)} = \partial_\pm \chi^{(2)}$, where it is legitimate to use the expression (35) since we are in the limiting case where $\lambda^+ = -\lambda^-$. This yields at once

$$t_{\rm split} = \frac{x_0}{c_0} + \frac{1}{4c_0^{5/2}}\int_{c_0}^{c_m} \sqrt{r}[w^{\rm A}(r) - w^{\rm B}(r)]dr. \tag{48}$$

In the limit of a very small initial bump, c_m is very close to c_0 and the second term on the right-hand side of Eq. (48) is negligible. In this case a linear approach is valid: The two subparts of the bump move, one to the right, the other to the left, at velocities $\pm c_0$ and a time $t_{\rm split} \simeq x_0/c_0$ is needed for their complete separation. The second term on the right-hand side of Eq. (48) describes the nonlinear correction to this result. For the initial profile (3) the expressions of $w^{\rm A}$ and $w^{\rm B}$ are given in Eq. (18) and we directly obtain, from Eq. (48),

$$t_{\rm split} = \frac{x_0}{c_0}[1 + G(\rho_1/\rho_0)], \tag{49}$$

where

$$G(X) = \frac{X}{4}\int_0^1 \frac{\sqrt{1-u}}{(1+Xu)^{1/4}}du. \tag{50}$$

In the simulations, we took $x_0 = 20$, $c_0 = \sqrt{0.5}$, and $\rho_1/\rho_0 = 3$ and formula (49) then yields $t_{\rm split} \simeq 40.1$. Note that in this case the simple linear estimate would be $x_0/c_0 \simeq 28.3$. The accuracy of the result (49) can be checked against numerical simulations by plotting the numerically determined central density of the hump $\rho(x = 0, t)$ as a function of time and checking that it just reaches the background value at $t = t_{\rm split}$. This is indeed the case: For the case we consider here $\rho(x = 0, t = 40.1)$ departs from ρ_0 by only 3%.

For a small bump with $\rho_1 \ll \rho_0$, the weak nonlinear correction to the linear result is obtained by evaluating the small-X behavior of the function G in (50). This yields

$$t_{\rm split} \simeq \frac{x_0}{c_0}\left[1 + \frac{1}{6}\frac{\rho_1}{\rho_0} - \frac{1}{60}\left(\frac{\rho_1}{\rho_0}\right)^2 + \cdots\right]. \tag{51}$$

For the numerical values for which we performed the simulations, stopping expansion (51) at first order in ρ_1/ρ_0 yields $t_{\rm split} \simeq 42.4$. At the next order we get $t_{\rm split} \simeq 38.2$. These values are reasonable upper and lower bounds for the exact result. Of course, the expansion is more efficient for lower values of ρ_1/ρ_0: Even for the relatively large value $\rho_1/\rho_0 = 1$, expansion (51) gives an estimate which is off the exact result (49) by only 0.3%.

IV. WHITHAM THEORY AND GENERALIZED HODOGRAPH METHOD

In this section we first give a general presentation of Whitham modulational theory (Sec. IV A) and then discuss specific features of its implementation for the case in which we are interested (Sec. IV B).

A. Periodic solutions and their modulations

The NLS equation (2) is equivalent to the system (6) which admits nonlinear periodic solutions that can be written in terms of four parameters $\lambda_1 \leqslant \lambda_2 \leqslant \lambda_3 \leqslant \lambda_4$ in the form (see, e.g., Ref. [43])

$$\rho(x, t) = \frac{1}{4}(\lambda_4 - \lambda_3 - \lambda_2 + \lambda_1)^2 + (\lambda_4 - \lambda_3)(\lambda_2 - \lambda_1) \times {\rm sn}^2(\sqrt{(\lambda_4 - \lambda_2)(\lambda_3 - \lambda_1)}(x - Vt), m),$$
$$u(x, t) = V - \frac{C}{\rho(x, t)}, \tag{52}$$

where sn is the Jacobi elliptic sine function (see, e.g., Ref. [46]),

$$V = \frac{1}{2}\sum_{i=1}^{4}\lambda_i, \quad m = \frac{(\lambda_2-\lambda_1)(\lambda_4-\lambda_3)}{(\lambda_4-\lambda_2)(\lambda_3-\lambda_1)}, \tag{53}$$

and

$$C = \tfrac{1}{8}(-\lambda_1-\lambda_2+\lambda_3+\lambda_4)(-\lambda_1+\lambda_2-\lambda_3+\lambda_4) \times (\lambda_1-\lambda_2-\lambda_3+\lambda_4). \tag{54}$$

For constant λ_i, expressions (52)–(54) correspond to an exact (single-phase) solution of the NLS equation, periodic in time and space, where oscillations have the amplitude

$$a = (\lambda_2-\lambda_1)(\lambda_4-\lambda_3) \tag{55}$$

and the spatial wavelength

$$L = \frac{2\mathsf{K}(m)}{\sqrt{(\lambda_4-\lambda_2)(\lambda_3-\lambda_1)}}. \tag{56}$$

In the limit $m \to 0$ ($\lambda_1 = \lambda_2$ or $\lambda_3 = \lambda_4$), $\mathrm{sn}(x, m) \to \sin(x)$ and Eq. (52) describes a small-amplitude sinusoidal wave oscillating around a constant background. In the other limiting case $m \to 1$ ($\lambda_2 = \lambda_3$), $\mathrm{sn}(x, m) \to \tanh(x)$ and Eq. (52) describes a dark soliton (for which $L \to \infty$).

The great insight of Gurevich and Pitaevskii [34] was to describe a dispersive shock wave as a slowly modulated nonlinear wave, of type (52), for which the λ_i are functions of x and t which vary weakly over one wavelength and one period. Their slow evolution is governed by the Whitham equations [30,43]

$$\partial_t\lambda_i + v_i(\lambda_1,\lambda_2,\lambda_3,\lambda_4)\partial_x\lambda_i = 0, \quad i = 1,2,3,4. \tag{57}$$

Comparing with Eqs. (9), we see that the λ_i are the Riemann invariants of the Whitham equations first found in Refs. [49,50]. The v_i are the associated characteristic velocities; their explicit expressions can be obtained from the relation [38,43]

$$v_i = V - \frac{1}{2}\frac{L}{\partial_i L}, \quad i = 1,2,3,4, \tag{58}$$

where $\partial_i = \partial/\partial\lambda_i$. This yields

$$\begin{aligned} v_1 &= V - \frac{(\lambda_4-\lambda_1)(\lambda_2-\lambda_1)\mathsf{K}(m)}{(\lambda_4-\lambda_1)\mathsf{K}(m)-(\lambda_4-\lambda_2)\mathsf{E}(m)},\\ v_2 &= V + \frac{(\lambda_3-\lambda_2)(\lambda_2-\lambda_1)\mathsf{K}(m)}{(\lambda_3-\lambda_2)\mathsf{K}(m)-(\lambda_3-\lambda_1)\mathsf{E}(m)},\\ v_3 &= V - \frac{(\lambda_4-\lambda_3)(\lambda_3-\lambda_2)\mathsf{K}(m)}{(\lambda_3-\lambda_2)\mathsf{K}(m)-(\lambda_4-\lambda_2)\mathsf{E}(m)},\\ v_4 &= V + \frac{(\lambda_4-\lambda_3)(\lambda_4-\lambda_1)\mathsf{K}(m)}{(\lambda_4-\lambda_1)\mathsf{K}(m)-(\lambda_3-\lambda_1)\mathsf{E}(m)}, \end{aligned} \tag{59}$$

where m is given by Eq. (53) and $\mathsf{E}(m)$ is the complete elliptic integrals of the second kind.

In the soliton limit $m \to 1$, i.e., $\lambda_3 \to \lambda_2$, the Whitham velocities reduce to

$$\begin{aligned} &v_1 = \tfrac{1}{2}(3\lambda_1+\lambda_4), \quad v_2 = v_3 = \tfrac{1}{2}(\lambda_1+2\lambda_2+\lambda_4),\\ &v_4 = \tfrac{1}{2}(\lambda_1+3\lambda_4). \end{aligned} \tag{60}$$

In a similar way, in the small-amplitude limit $m \to 0$, i.e., $\lambda_2 \to \lambda_1$, we obtain

$$\begin{aligned} v_1 = v_2 &= 2\lambda_1 + \frac{(\lambda_4-\lambda_3)^2}{2(\lambda_3+\lambda_4-2\lambda_1)},\\ v_3 &= \frac{1}{2}(3\lambda_3+\lambda_4), \quad v_4 = \frac{1}{2}(\lambda_3+3\lambda_4), \end{aligned} \tag{61}$$

and in another small-amplitude limit ($m \to 0$ when $\lambda_3 \to \lambda_4$), we have

$$\begin{aligned} &v_1 = \frac{1}{2}(3\lambda_1+\lambda_2), \quad v_2 = \frac{1}{2}(\lambda_1+3\lambda_2),\\ &v_3 = v_4 = 2\lambda_4 + \frac{(\lambda_2-\lambda_1)^2}{2(\lambda_1+\lambda_2-2\lambda_4)}. \end{aligned} \tag{62}$$

B. Generalized hodograph method

In Sec. III we have provided a nondispersive description of the spreading and splitting of the initial pulse in two parts (one propagating to the left and the other to the right). During this nonlinear process the leading wavefront steepens and leads to wave breaking. This occurs at a certain time t_{WB} after which the approach of Sec. III predicts a nonphysical multivalued profile (see, e.g., Fig. 8), since it does not take into account dispersive effects. The process of dispersive regularization of the gradient catastrophe leads to the formation of a dispersive shock wave, as first predicted by Sagdeev in the context of collisionless plasma physics (see, e.g., Ref. [51]).

For the specific case we are interested in, the Gurevich-Pitaevskii approach, which consists in using Whitham theory for describing the DSW as a slowly modulated nonlinear wave, holds, but it is complicated by the fact that two of the four Riemann invariants vary in the shock region. As already explained in the Introduction, we adapt here the method developed in Refs. [37–40] for treating a similar situation for the Korteweg–de Vries equation. The general case of NLS dispersive shock with all four Riemann invariants varying was considered in Ref. [52].

In all the following we concentrate our attention on the shock formed at the right edge of the pulse propagating to the right. Due to the symmetry of the problem, the same treatment can be employed for the left pulse. The prediction of multivalued λ^+ resulting from the dispersionless approach of Sec. III suggests that after wave breaking of the simple-wave solution, the correct Whitham-Riemann invariant should be sought in a configuration such that $\lambda_1 = \lambda^- = -c_0$, $\lambda_2 = \lambda^+(x \to \infty) = c_0$, and λ_3 and λ_4 both depend on x and t. In this case the Whitham equations (57) with $i = 1, 2$ are trivially satisfied, and to solve them for $i = 3$ and 4, we introduce two functions $W_i(\lambda_3, \lambda_4)$ ($i = 3$ or 4), exactly as we did in Sec. III with $W_\pm(\lambda^-, \lambda^+)$:

$$x - v_i(\lambda_3,\lambda_4)t = W_i(\lambda_3,\lambda_4), \quad i = 3,4. \tag{63}$$

For the sake of brevity we have defined in this equation $v_i(\lambda_3, \lambda_4) = v_i(\lambda_1 = -c_0, \lambda_2 = c_0, \lambda_3, \lambda_4)$ for $i \in \{3, 4\}$; we will keep this notation henceforth.

Then we can derive Tsarev equations for $W_i(\lambda_3, \lambda_4)$ [replacing the subscripts + and − by 4 and 3 in (13)] and we can show (see, e.g., Refs. [38,52–54]) that these are solved for W_i

of the form

$$W_i = \left(1 - \frac{L}{\partial_i L}\partial_i\right)\mathscr{W} = \mathscr{W} + 2(v_i - V)\partial_i \mathscr{W}, \tag{64}$$

where $\mathscr{W}(\lambda_3, \lambda_4)$ is solution of the Euler-Poisson equation

$$\partial_{34}\mathscr{W} = \frac{\partial_3 \mathscr{W} - \partial_4 \mathscr{W}}{2(\lambda_3 - \lambda_4)}. \tag{65}$$

As was first understood in Ref. [36], after the wave breaking time, the development of the dispersive shock wave occurs in *two* steps. Initially (when t is close to t_{WB}), the DSW is connected at its left edge to the smooth profile coming from the time evolution of the right part of the initial profile of λ^+ (part A), which is gradually absorbed in the DSW. This process of absorption is complete at a time we denote by $t_{\mathrm{A|B}}$. Then, for $t > t_{\mathrm{A|B}}$, the DSW is connected to the smooth profile coming from the time evolution of part B of λ^+ [this is case B, region B of the (x, t) plane]. During the initial step (for $t < t_{\mathrm{A|B}}$), for a given time t, the highest value of the largest Riemann invariant is reached within the smooth part of the profile and keeps the constant value c_m. Then, in the subsequent time evolution, this highest value is reached within the DSW (or at its right boundary) where there exists a point where λ_4 takes its maximal value (c_m). We illustrate these two steps of development of the DSW in Fig. 9. We refer to the region of the DSW where λ_4 is a decreasing function of x as region A and the part where it increases as region B.

In region A of the (x, t) plane, we denote by $\mathscr{W}^{\mathrm{A}}(\lambda_3, \lambda_4)$ the solution of the Euler-Poisson equation and in region B we denote it instead by $\mathscr{W}^{\mathrm{B}}(\lambda_3, \lambda_4)$. These two forms are joined by the line $\lambda_4 = c_m$, where

$$\mathscr{W}^{\mathrm{A}}(\lambda_3, c_m) = \mathscr{W}^{\mathrm{B}}(\lambda_3, c_m). \tag{66}$$

We denote the position where this matching condition is realized by $x_m(t)$ [see Fig. 9(b)]. The corresponding boundary in the (x, t) plane is represented as a green solid curve in Fig. 10.

Since the general solution of the Euler-Poisson equation with the appropriate boundary conditions and the construction of the resulting nonlinear pattern are quite involved, we will first consider some particular but useful results which follow from general principles of the Whitham theory.

V. MOTION OF THE SOLITON EDGE OF THE SHOCK

During the first stage of evolution of the DSW, its left (solitonic) edge is connected to the smooth dispersionless solution whose dynamics is described by formula (39), that is, we have here

$$x_{\mathrm{S}} - v_+(-c_0, \lambda_{\mathrm{S}})t = W_+^{(3)}(-c_0, \lambda_{\mathrm{S}}), \tag{67}$$

where $x_{\mathrm{S}}(t)$ is the position of the left edge of the DSW and $\lambda_{\mathrm{S}}(t) \equiv \lambda^+(x_{\mathrm{S}}(t), t)$. We recall that in all the following we focus on the DSW formed in the right part of the pulse. Hence Eq. (67) concerns the right part of the nondispersive part of the profile. According to the terminology of Sec. III, this corresponds to region III.

On the other hand, in vicinity of this boundary, the Whitham equations (57) with the limiting expressions (60)

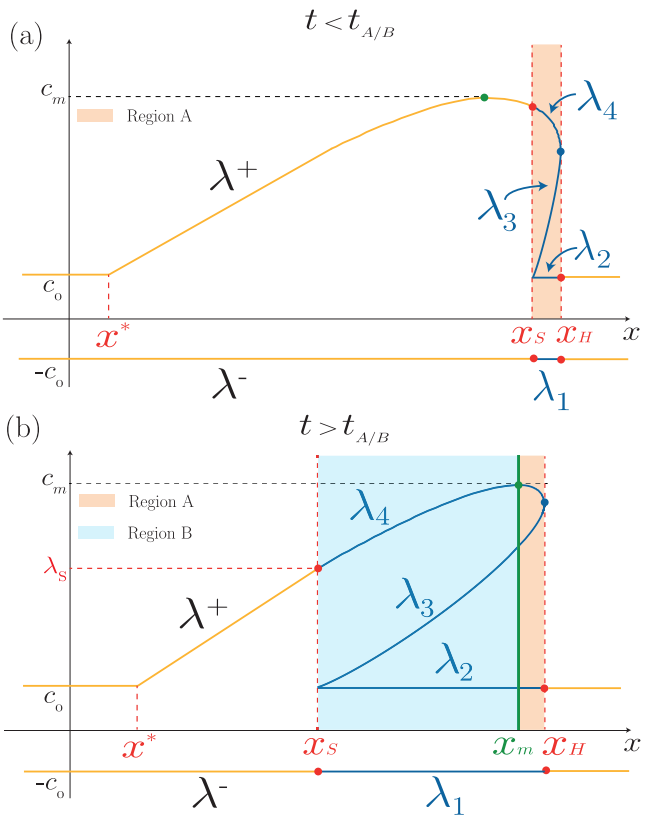

FIG. 9. Schematic plots of the position dependence of the Riemann invariants inside (blue solid curves) and outside (yellow solid curves) the DSW (colored region). (a) For $t < t_{\mathrm{A|B}}$, the DSW is connected to the smooth profile coming from the time evolution of part A of the initial pulse. At $t = t_{\mathrm{A|B}}$, part A is completely absorbed by the DSW. Thus, for this time, the shock wave connects to the smooth profile exactly at $\lambda_+(x_{\mathrm{S}}(t), t) = c_m$. (b) For $t > t_{\mathrm{A|B}}$, the DSW is connected at its left edge at a point belonging to part B of the dispersionless profile. In this case the shock wave is divided into two regions A and B, separated by the green vertical line in the plot. The continuity along the separation line between the two regions, i.e., at $x = x_m(t)$, is ensured by Eq. (66).

(where $\lambda_2 = \lambda_3 = c_0$) for the velocities v_i are given by

$$\partial_t \lambda_3 + \tfrac{1}{2}(\lambda_4 + c_0)\partial_x \lambda_3 = 0,$$
$$\partial_t \lambda_4 + \tfrac{1}{2}(3\lambda_4 - c_0)\partial_x \lambda_4 = 0. \tag{68}$$

To solve these equations we can perform a classical hodograph transform, that is, we assume that x and t are functions of the independent variables λ_3 and λ_4: $t = t(\lambda_3, \lambda_4)$ and $x = x(\lambda_3, \lambda_4)$. We find from Eqs. (68) that these functions must satisfy the linear system

$$\frac{\partial x}{\partial \lambda_3} - \frac{1}{2}(3\lambda_4 - c_0)\frac{\partial t}{\partial \lambda_3} = 0,$$
$$\frac{\partial x}{\partial \lambda_4} - \frac{1}{2}(\lambda_4 + c_0)\frac{\partial t}{\partial \lambda_4} = 0.$$

At the left edge of the DSW, the second equation reads

$$\frac{\partial x_{\mathrm{S}}}{\partial \lambda_{\mathrm{S}}} - \frac{1}{2}(\lambda_{\mathrm{S}} + c_0)\frac{\partial t}{\partial \lambda_{\mathrm{S}}} = 0, \tag{69}$$

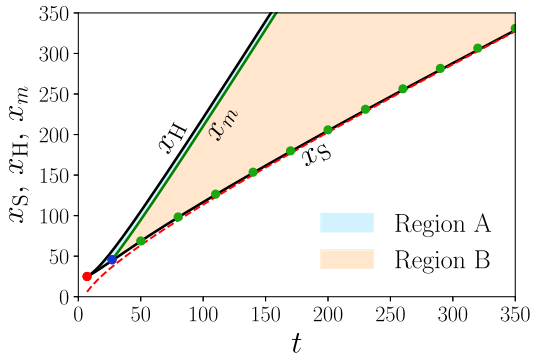

FIG. 10. Black solid curves show the time evolution of $x_S(t)$ and $x_H(t)$ calculated from Eqs. (96) and (99), respectively. The green solid curve shows the time evolution of $x_m(t)$, for which $\lambda_4(x_m(t), t) = c_m$, which marks the separation between regions A and B. The red dashed curve shows the asymptotic behavior of $x_S(t)$, from Eq. (81). The green points indicate the positions $x_S(t)$ extracted from simulations, for an initial condition (3) with $\rho_0 = 0.5$, $\rho_m = 2$, and $x_0 = 20$. The red point marks the birth of the DSW (at time $t_{WB} \simeq 6.3$), while the blue one initiates region B (at time $t_{A|B} \simeq 25.9$).

which must be compatible with Eq. (67). Differentiation of Eq. (67) with respect to λ_S and elimination of $\partial x_S/\partial\lambda_S$ with the use of Eq. (69) yields a differential equation for the function $t(\lambda_S) \equiv t(c_0, \lambda_S)$:

$$(\lambda_S - c_0)\frac{dt}{d\lambda_S} + \frac{3}{2}t = -\frac{dW_+^{(3)}(-c_0, \lambda_S)}{d\lambda_S}. \tag{70}$$

At the wave breaking time, $\lambda_S = c_0$, which corresponds to the definition $t_{WB} = t(c_0)$, and Eq. (70) then yields

$$t_{WB} = -\frac{2}{3}\left.\frac{dW_+^{(3)}(-c_0, \lambda_S)}{d\lambda_S}\right|_{\lambda_S = c_0}, \tag{71}$$

in agreement with Eq. (46), which should be expected since at the wave breaking moment the DSW reduces to a point in the Whitham approximation. For the concrete case of our initial distribution we can get a simple explicit expression for t_{WB} which reads [see Eq. (46) and note [48]]

$$t_{WB} = -\frac{2}{3}\left.\frac{dw^A(\lambda_S)}{d\lambda_S}\right|_{\lambda_S = c_0} = \frac{2c_0x_0}{3\rho_1}, \tag{72}$$

where the right-hand side is the form of the central formula corresponding to the initial profile (3). Taking $\rho_0 = 0.5$, $\rho_m = 2$, and $x_0 = 20$, we find $t_{WB} \simeq 6.3$, in excellent agreement with the numerical simulations.

The solution of Eq. (70) reads

$$\begin{aligned} t(\lambda_S) &= \frac{-1}{(\lambda_S - c_0)^{3/2}}\int_{c_0}^{\lambda_S}\sqrt{r - c_0}\frac{dW_+^{(3)}(-c_0, r)}{dr}dr \\ &= \frac{1}{2(\lambda_S - c_0)^{3/2}}\int_{c_0}^{\lambda_S}\frac{W_+^{(3)}(-c_0, r)}{\sqrt{r - c_0}}dr \\ &\quad - \frac{W_+^{(3)}(-c_0, \lambda_S)}{\lambda_S - c_0}. \end{aligned} \tag{73}$$

Substituting this expression into (67), we obtain the function $x_S(\lambda_S) \equiv x(c_0, \lambda_S)$:

$$x_S(\lambda_S) = \tfrac{1}{2}(3\lambda_S - c_0)t(\lambda_S) + W_+^{(3)}(-c_0, \lambda_S). \tag{74}$$

The two formulas (73) and (74) define, in an implicit way, the law of motion $x = x_S(t)$ of the soliton edge of the DSW.

The above expressions are correct as long as the soliton edge is located inside region A of the DSW, that is, up to the moment $t_{A|B} = t(c_m)$. From (73) we obtain the explicit expression

$$t_{A|B} = \frac{-1}{(c_m - c_0)^{3/2}}\int_{c_0}^{c_m}\sqrt{r - c_0}\frac{dW_+^{(3)}(-c_0, r)}{dr}dr. \tag{75}$$

In the case we consider, this yields $t_{A|B} = 25.9$. For time larger than $t_{A|B}$ the soliton edge connects with region B of the dispersionless profile, which corresponds to region II_r (see Fig. 4). Concretely, for a time $t > t_{A|B}$, instead of Eq. (70) we have to solve the differential equation

$$(\lambda_S - c_0)\frac{dt}{d\lambda_S} + \frac{3}{2}t = -\frac{dW_+^{(2)}(-c_0, \lambda_S)}{d\lambda_S}, \tag{76}$$

with the initial condition $t(c_m) = t_{A|B}$. The solution of Eq. (76) reads

$$\begin{aligned} t(\lambda_S) = \frac{-1}{(\lambda_S - c_0)^{3/2}}\Bigg(&\int_{c_m}^{\lambda_S}\sqrt{r - c_0}\frac{dW_+^{(2)}(-c_0, r)}{dr}dr \\ &+ \int_{c_0}^{c_m}\sqrt{r - c_0}\frac{dW_+^{(3)}(-c_0, r)}{dr}dr\Bigg) \end{aligned} \tag{77}$$

and $x_S(\lambda_S)$ is determined by Eq. (41):

$$x_S(\lambda_S) = \tfrac{1}{2}(3\lambda_S - c_0)t(\lambda_S) + W_+^{(2)}(-c_0, \lambda_S). \tag{78}$$

At asymptotically large time $t \to \infty$ we are in stage B of evolution of the DSW with furthermore $\lambda_S \to c_0$. In this case the upper limit of integration in the first integral of formula (77) can be set equal to c_0. Thus, we get in this limit

$$t(\lambda_S) \simeq \frac{\mathcal{A}}{(\lambda_S - c_0)^{3/2}}, \tag{79}$$

where the expression for the constant $\mathcal{A}$ is

$$\begin{aligned} \mathcal{A} = -\Bigg(&\int_{c_m}^{c_0}\sqrt{r - c_0}\frac{dW_+^{(2)}(-c_0, r)}{dr}dr \\ &+ \int_{c_0}^{c_m}\sqrt{r - c_0}\frac{dW_+^{(3)}(-c_0, r)}{dr}dr\Bigg). \end{aligned} \tag{80}$$

Consequently, we obtain the asymptotic expressions

$$\lambda_S(t) = c_0 + \left(\frac{\mathcal{A}}{t}\right)^{2/3}, \quad x_S(t) = c_0t + \frac{3\mathcal{A}^{2/3}}{2}t^{1/3}. \tag{81}$$

We denote the position of the rear point of the simple wave by $x^*(t)$ (see Fig. 9). It is clear from Fig. 4 that $x^* = 0$ at time $t = t_{SW}(c_0)$, i.e., just when region 2 disappears, whereafter the dispersionless approach of Sec. III predicts a profile with only simple waves and plateau regions. The rear edge of the simple wave then propagates over a flat background at constant velocity c_0; we thus have

$$x^*(t) = c_0[t - t_{SW}(c_0)]. \tag{82}$$

Asymptotically, i.e., at time much larger than $t_{SW}(c_0)$, we have $x^*(t) \simeq c_0 t$ and, in the simple-wave profile between $x^*(t)$ and $x_S(t)$, λ^+ depends on the self-similar variable $[x - x^*(t)]/t$ while λ^- is constant. Then Eqs. (9) readily yield

$$\lambda^+ = c_0 + \frac{2}{3}\frac{x - x^*(t)}{t}, \quad \lambda^- = -c_0 \quad \text{for } x \in [x^*(t), x_S(t)]. \tag{83}$$

Equation (8) then yields the explicit expression of ρ in this region (which was roughly described at the end of Sec. II as having a quasitriangular shape), and using (81) we obtain

$$\int_{x^*(t)}^{x_S(t)} [\sqrt{\rho(x,t)} - c_0]^{1/2} dx = \frac{1}{\sqrt{2}}\mathcal{A}. \tag{84}$$

The asymptotic situation at the rear of the DSW is reminiscent of what occurs in the theory of weak dissipative shocks where (i) a nonlinear pattern of triangular shape may also appear at the rear edge of a (viscous) shock, (ii) the details of the initial distribution are lost at large time (as in the present case), and (iii) a conserved quantity of the type (84) also exists. Hence the above results provide, for a conservative system, the counterpart of the weak viscous shock theory (presented, for instance, in Ref. [30]). Note, however, that the boundary conditions at the large-amplitude edge of the shock are different depending on whether we consider a dissipative or a conservative system and that the corresponding velocity and conserved quantity are accordingly also different. Note also that equivalent relations for the behavior of a rarefaction wave in the rear of a dispersive shock in the similar situation for the Korteweg–de Vries equation have been obtained in Ref. [31].

Formulas (81) and (84) are important because they provide indirect evidence making it possible to assert if a given experiment has indeed reached the point where a bona fide dispersive shock wave should be expected.

In the next section we give an explicit theoretical description of the whole region of the dispersive shock.

VI. SOLUTION IN THE SHOCK REGION

In this section we turn to the general solution of the Whitham equations given by the formulas of Sec. IV B. Our task is to express the functions W_3 and W_4 in terms of the initial distribution of the light pulse. As was indicated above, we need to distinguish two regions, A and B, in which $\mathscr{W}$ takes different values.

A. Solution in region A

In region A we can straightforwardly adapt the procedure explained in Ref. [38]. We impose the matching of the left edge of the DSW with the dispersionless solution (see Sec. III B): Just at $x = x_S(t)$, we have $\lambda_4 = \lambda^+$, $\lambda_3 = \lambda_2 = c_0$, and $\lambda_1 = -c_0$ (see Fig. 9) and Eq. (60) yields $v_4(\lambda_3, \lambda_4) = (3\lambda_4 - c_0)/2 = v_+(-c_0, \lambda^+)$. Then, at this point, the conditions (39) and (63) with $i = 4$ are simultaneously satisfied, which implies

$$W_4^{\mathrm{A}}(\lambda_3 = c_0, \lambda_4 = \lambda^+) = W_+^{(3)}(-c_0, \lambda^+), \tag{85}$$

where $W_+^{(3)}$ is the form of W_+ corresponding to region 3. Note that here the first argument of the function $W_+^{(3)}$ is $\lambda^- = -c_0$ for all times. Indeed, the boundary condition (85) corresponds to the matching in physical space at $x_S(t)$. When the DSW starts to form at time t_{WB}, the edge $x_S(t_{WB})$ lies on the characteristic issued from x_0 [x_0 defines the initial extent of the pulse; see Eq. (3)]. The Riemann invariant λ^- is constant and equal to $-c_0$ along this characteristic (cf. Fig. 4). Then, because the characteristics of λ^- in the dispersionless region close to x_S are oriented to the left whereas x_S moves to the right, it is clear that $\lambda^-(x_S(t), t) = -c_0$ for $t \geqslant t_{WB}$.

In terms of $\mathscr{W}$ the relation (85) corresponds to the equation

$$\mathscr{W}^{\mathrm{A}}(c_0, \lambda_4) + 2(\lambda_4 - c_0)\partial_4 \mathscr{W}^{\mathrm{A}}(c_0, \lambda_4) = W_+^{(3)}(-c_0, \lambda_4), \tag{86}$$

whose solution is

$$\mathscr{W}^{\mathrm{A}}(c_0, \lambda_4) = \frac{1}{2\sqrt{\lambda_4 - c_0}} \int_{c_0}^{\lambda_4} \frac{W_+^{(3)}(-c_0, r)dr}{\sqrt{r - c_0}}. \tag{87}$$

This will serve as a boundary condition for the Euler-Poisson equation (65) whose general solution has been given by Eisenhart [55] in the form

$$\mathscr{W}^{\mathrm{A}}(\lambda_3, \lambda_4) = \int_{c_0}^{\lambda_3} \frac{\psi^{\mathrm{A}}(\mu)d\mu}{\sqrt{\lambda_3 - \mu}\sqrt{\lambda_4 - \mu}} + \int_{c_0}^{\lambda_4} \frac{\varphi^{\mathrm{A}}(\mu)d\mu}{\sqrt{|\lambda_3 - \mu|}\sqrt{\lambda_4 - \mu}}, \tag{88}$$

where $\varphi^{\mathrm{A}}(\mu)$ and $\psi^{\mathrm{A}}(\mu)$ are arbitrary functions to be determined from the appropriate boundary conditions. By taking $\lambda_3 = c_0$ in this expression we see that $\varphi^{\mathrm{A}}(\mu)/\sqrt{\mu - c_0}$ is the Abel transform of $\mathscr{W}^{\mathrm{A}}(c_0, \lambda_4)$. Using the inverse transformation [56] and expression (87) we can show that

$$\varphi^{\mathrm{A}}(\mu) = \frac{1}{2\pi\sqrt{\mu - c_0}} \int_{c_0}^{\mu} \frac{W_+^{(3)}(-c_0, r)dr}{\sqrt{\mu - r}}, \tag{89}$$

where we recall that $W_+^{(3)} = \partial_+ \chi^{(3)}$. In order to determine the other unknown function ψ^{A}, we consider the right boundary of the DSW where λ_3 and λ_4 are asymptotically close to each other. We can show (see, e.g., equivalent reasoning in Ref. [31]) that in order to avoid divergence of $\mathscr{W}^{\mathrm{A}}(\lambda_3, \lambda_4 = \lambda_3)$, we need to impose $\psi^{\mathrm{A}}(\lambda) = -\varphi^{\mathrm{A}}(\lambda)$. The final form of the Eisenhart solution in region A thus reads

$$\mathscr{W}^{\mathrm{A}}(\lambda_3, \lambda_4) = \int_{\lambda_3}^{\lambda_4} \frac{\varphi^{\mathrm{A}}(\mu)d\mu}{\sqrt{\mu - \lambda_3}\sqrt{\lambda_4 - \mu}}, \tag{90}$$

where φ^{A} is given by formula (89).

B. Solution in region B

We look for a solution of the Euler-Poisson equation in region B in the form

$$\mathscr{W}^{\mathrm{B}}(\lambda_3, \lambda_4) = \mathscr{W}^{\mathrm{A}}(\lambda_3, \lambda_4) + \int_{\lambda_4}^{c_m} \frac{\varphi^{\mathrm{B}}(\mu)d\mu}{\sqrt{\mu - \lambda_3}\sqrt{\mu - \lambda_4}}, \tag{91}$$

where c_m is the maximum value for λ_4. This expression ensures that $\mathscr{W}^{\mathrm{B}}$, (i) being the sum of two solutions of the

Euler-Poisson equation, is also a solution of this equation and (ii) verifies the boundary condition (66) since the second term on the right-hand side of (91) vanishes when $\lambda_4 = c_m$.

At the left boundary of the DSW, $\mathscr{W}^{\mathrm{B}}(c_0, \lambda_4)$ verifies an equation similar to (86):

$$\mathscr{W}^{\mathrm{B}}(c_0, \lambda_4) + 2(\lambda_4 - c_0)\partial_4 \mathscr{W}^{\mathrm{B}}(c_0, \lambda_4) = W_+^{(2)}(-c_0, \lambda_4). \tag{92}$$

The solution with the appropriate integration constant reads

$$\mathscr{W}^{\mathrm{B}}(r_1, 0) = \frac{1}{2\sqrt{\lambda_4 - c_0}} \int_{\lambda_4}^{c_m} \frac{W_+^{(2)}(-c_0, r)}{\sqrt{r - c_0}} dr + \frac{1}{2\sqrt{\lambda_4 - c_0}} \int_{c_0}^{c_m} \frac{W_+^{(3)}(-c_0, r)}{\sqrt{r - c_0}} dr, \tag{93}$$

where $W_+^{(2)}$ is the form of W_+ corresponding to region 2. The same procedure as the one previously used for region A of the DSW leads here to

$$\varphi^{\mathrm{B}}(\mu) = \frac{1}{2\pi\sqrt{\mu - c_0}} \int_{\mu}^{c_m} \frac{W_+^{(3)}(-c_0, r) - W_+^{(2)}(-c_0, r)}{\sqrt{\mu - r}} dr. \tag{94}$$

Equations (91) and (94) give the solution of the Euler-Poisson equation in region B.

C. Characteristics of the DSW at its edges

It is important to determine the boundaries $x_{\mathrm{S}}(t)$ and $x_{\mathrm{H}}(t)$ of the DSW, as well as the values of the Riemann invariants λ_3 and λ_4 at these points. The law of motion of the soliton edge was already found in Sec. V and it is instructive to show how this result can be obtained from the general solution.

At the soliton edge we have $\lambda_2 = \lambda_3 = c_0$ and $\lambda_4 = \lambda_{\mathrm{S}}(t)$. The corresponding Whitham velocities are $v_3 = (\lambda_{\mathrm{S}} + c_0)/2$ and $v_4 = (3\lambda_{\mathrm{S}} - c_0)/2$ [see Eqs. (60)], and Eqs. (63) read

$$\begin{aligned} x_{\mathrm{S}} - \tfrac{1}{2}(3\lambda_{\mathrm{S}} - c_0)t &= W_4^{\alpha}(c_0, \lambda_{\mathrm{S}}) = W_+^{(n)}(-c_0, \lambda_{\mathrm{S}}), \\ x_{\mathrm{S}} - \tfrac{1}{2}(\lambda_{\mathrm{S}} + c_0)t &= W_3^{\alpha}(c_0, \lambda_{\mathrm{S}}) = \mathscr{W}^{\alpha}(c_0, \lambda_{\mathrm{S}}), \end{aligned} \tag{95}$$

where, in order to have formulas applying to both stages of evolution of the DSW, we have introduced dummy indices α and n with $\alpha = \mathrm{A}$ or B and $n = 3$ or 2, respectively. This gives at once

$$\begin{aligned} t(\lambda_{\mathrm{S}}) &= \frac{1}{\lambda_{\mathrm{S}} - c_0}[\mathscr{W}^{\alpha}(c_0, \lambda_{\mathrm{S}}) - W_+^{(n)}(-c_0, \lambda_{\mathrm{S}})], \\ x_{\mathrm{S}}(\lambda_{\mathrm{S}}) &= c_0 t + \frac{1}{2}[3\mathscr{W}^{\alpha}(c_0, \lambda_{\mathrm{S}}) - W_+^{(n)}(-c_0, \lambda_{\mathrm{S}})]. \end{aligned} \tag{96}$$

Let us consider stage A, for instance. Equation (87) yields

$$\mathscr{W}^{A}(c_0, \lambda_{\mathrm{S}}) = \frac{1}{2\sqrt{\lambda_{\mathrm{S}} - c_0}} \int_{c_0}^{\lambda_{\mathrm{S}}} \frac{W_+^{(3)}(-c_0, r) dr}{\sqrt{r - c_0}},$$

which inserted into Eqs. (96) gives immediately the results (73) and (74).

Figure 10 shows the time evolution of $x_{\mathrm{S}}(t)$. The black curve is calculated from Eqs. (96), while the red dashed curve corresponds to the asymptotic behavior of x_{S}, given by Eq. (81). The green points are extracted from simulations and exhibit very good agreement with the theory. The same excellent agreement is obtained for the time evolution of λ_{S}, as shown in Fig. 11.

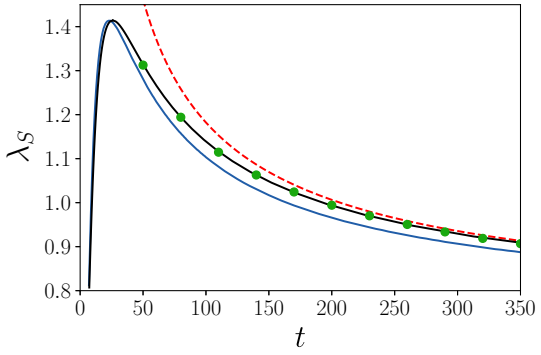

FIG. 11. The black solid curve shows the time evolution of $\lambda_{\mathrm{S}}(t)$ from Eq. (96), or equivalently from Eq. (73) and then (77). The red dashed curve shows the asymptotic behavior from Eq. (81). The green points are extracted from simulations for different times, for the initial profile (3) with $\rho_0 = 0.5$, $\rho_m = 2$, and $x_0 = 20$. The blue solid curve is an approximation obtained by schematically describing the initial splitting by assuming $\lambda^- \simeq$ const for all t during the evolution of the right pulse (see the text).

We demonstrated in Sec. III the accuracy of the Riemann method for describing the spreading and splitting of the initial pulse into two parts. The matching between the left edge of the DSW and the dispersionless profile at the point of coordinates $(x_{\mathrm{S}}, \lambda_{\mathrm{S}})$ is given in Eq. (67). Since the splitting occurs rapidly, a simpler approach would be to make the approximation $\lambda^-(x, t) = -c_0 =$ const for the dispersionless right part of the profile. In this case, the Riemann equation (9) for λ^+ reduces to

$$\frac{\partial \lambda^+}{\partial t} + \left(\frac{3}{2}\lambda^+ - \frac{1}{2}c_0\right)\frac{\partial \lambda^+}{\partial x} = 0. \tag{97}$$

This equation can be solved by the method of characteristics, which yields the implicit solution for $\lambda^+(x, t)$,

$$x - \left(\tfrac{3}{2}\lambda^+ - \tfrac{1}{2}c_0\right)t = w^{\mathrm{A(B)}}(\lambda^+), \tag{98}$$

where $w^{\mathrm{A(B)}}$ is the inverse function of the initial $\lambda^+(x)$ profile in part A (B) [in our case the explicit expressions are given in Eqs. (18)].

Within this approximation the DSW is described through $\mathscr{W}$ by the same equations (89)–(91) and (94) as before, replacing $W_+^{(3/2)}(-c_0, r)$ by $w^{\mathrm{A(B)}}(r)$ everywhere. Further, λ_{S} computed using this approximation is represented in Fig. 11 as a function of t (blue solid curve), where it is also compared with the results obtained using the full Riemann method (black solid curve) and the results extracted from numerical simulations (green points). As we can see, an accurate description of the spreading and splitting stage is important since the blue curve does not precisely agree with the results of the simulations, mainly at large times. However, this approximation gives a correct description of the initial formation of the DSW: This is discussed in Ref. [48], where it is argued that, close to the wave breaking time, the approximation $W_+^{(3)}(-c_0, r) \simeq w^{\mathrm{A}}(r)$ is very accurate.

Let us now turn to the determination of the location $x_{\mathrm{H}}(t)$ of the small-amplitude harmonic boundary of the DSW and of

the common value $\lambda_H(t)$ of λ_3 and λ_4 at this point (see Fig. 9). In the typical situation the left boundary is located in region A. In this case the equations (63) for $i = 3$ and 4 are equivalent and read

$$x_H - v_H t = W_i^A(\lambda_H, \lambda_H), \quad i = 3 \text{ or } 4, \tag{99}$$

where $v_H = v_i(\lambda_H, \lambda_H) = 2\lambda_H - c_0^2/\lambda_H$ [cf. Eqs. (62)]. An equation for λ_H alone is obtained by demanding that the velocity dx_H/dt of the left boundary is equal to the common value v_H of v_3 and v_4. The differentiation of Eq. (99) with respect to time then yields

$$t = -\frac{1}{dv_H/d\lambda_H}\frac{dW_4^A(\lambda_H, \lambda_H)}{d\lambda_H}. \tag{100}$$

Note that the relation $dx_H/dt = v_H$ is a consequence of the general statement that the small-amplitude edge of the DSW propagates with the group velocity corresponding to the wave number determined by the solution of the Whitham equations. Indeed, the NLS group velocity of a linear wave with wave vector k moving over a background $\rho_0 = c_0^2$ is the group velocity of the so-called Bogoliubov waves

$$v_g(k) = \frac{k^2/2 + c_0^2}{\sqrt{k^2/4 + c_0^2}}, \tag{101}$$

where $k = 2\pi/L = 2\sqrt{\lambda_H^2 - c_0^2}$ [L is computed from Eq. (56)]. This yields $v_g = 2\lambda_H - c_0^2/\lambda_H = v_H$, as it should. This property of the small-amplitude edge is especially important in the theory of DSWs for nonintegrable equations (see, e.g., Refs. [57,58]).

The value of $W_4^A(\lambda_H, \lambda_H)$ in Eq. (99) is computed through (63) and (90). We get

$$W_4^A(\lambda_H, \lambda_H) = \pi\varphi^A(\lambda_H) + \pi\left(\lambda_H - \frac{c_0^2}{\lambda_H}\right)\frac{d\varphi^A}{d\mu}(\lambda_H) \tag{102}$$

and

$$\frac{dW_4^A(\lambda_H, \lambda_H)}{d\lambda_H} = \pi\left(2 + \frac{c_0^2}{\lambda_H^2}\right)\frac{d\varphi^A}{d\mu}(\lambda_H) + \pi\left(\lambda_H - \frac{c_0^2}{\lambda_H}\right)\frac{d^2\varphi^A}{d\mu^2}(\lambda_H), \tag{103}$$

where φ^A is given by Eq. (89). Once expression (103) has been used to obtain $\lambda_H(t)$ by solving Eq. (100), the position $x_H(t)$ of the harmonic edge of the DSW is determined by (99). The time evolution of $x_H(t)$ is displayed in Fig. 10.

The position of the point $x_m(t)$ where $\lambda_4 = c_m$ (cf. Fig. 9) can be obtained from Eqs. (63). First, for a given time t, we need to find the corresponding value λ_3, the solution of the equation

$$t = \frac{W_3(\lambda_3, c_m) - W_4(\lambda_3, c_m)}{v_4(\lambda_3, c_m) - v_3(\lambda_3, c_m)}. \tag{104}$$

Note that in this equation we did not write the superscript A or B, because this formula equally holds in both cases since it is to be determined at the boundary between the two regions A and B of the DSW [cf. Eq. (66) and Fig. 9]. Then $x_m(t)$ is determined using either of Eqs. (63). The result is shown in Fig. 10, where the curve $x_m(t)$ represents the position of the boundary between the two regions A and B at time t.

D. Global picture

We now compare the results of the Whitham approach with the numerical solution of the NLS equation (2) for the initial profile (3). The DSW is described by Whitham method as explained in Secs. IV A and IV B. For this purpose we need to determine λ_3 and λ_4 as functions of x and t (whereas $\lambda_1 = -c_0$ and $\lambda_2 = c_0$). This is performed as follows. First, we pick up a given $\lambda_4 \in [c_0, \lambda_S]$, where λ_S is the value of λ_4 at the soliton edge, the point where the DSW is connected to the rarefaction wave (it has been explained in Secs. V and VI C how to compute it). Second, at fixed t and λ_4, we find the corresponding value λ_3 as a solution of the difference of Eqs. (63),

$$(v_4 - v_3)t = W_3(\lambda_3, \lambda_4) - W_4(\lambda_3, \lambda_4), \tag{105}$$

where W_3 and W_4 are computed from Eq. (64), with a superscript A or B, as appropriate. Finally, the corresponding value of x is determined by $x = W_3 + v_3 t$ (or equivalently $x = W_4 + v_4 t$). This procedure gives, for each $\lambda_4 \in [c_0, \lambda_S]$ and t, the values of λ_3 and x. In practice, it makes it possible to associate with each (x, t) a couple (λ_3, λ_4). The results confirm the schematic behavior depicted in Fig. 9.

The knowledge of $\lambda_3(x, t)$ and $\lambda_4(x, t)$ completes our study and enable us to determine, for each time $t > t_{WB}$, $\rho(x, t)$ and $u(x, t)$ as given by the Whitham approach, for all $x \in \mathbb{R}^+$. Denoting by $x^*(t)$ the left boundary of the hump [recall that we concentrate on the right part of the light intensity profile (see Fig. 9)], we have the following.

(i) In the two regions $x \geqslant x_H(t)$ and $0 \leqslant x \leqslant x^*(t)$, we have $u(x, t) = 0$ and $\rho(x, t) = \rho_0$.

(ii) In the dispersionless region $[x^*(t), x_S(t)]$, $u(x, t)$ and $\rho(x, t)$ are computed from (7) in terms of λ^+ and λ^-, which are computed as explained in Sec. III. The profile in this region rapidly evolves to a rarefaction wave [with $\lambda^- = -c_0$ (see Fig. 9)] of triangular shape.

(iii) Inside the DSW, for $x \in [x_S(t), x_H(t)]$, the functions $\rho(x, t)$ and $u(x, t)$ are given by the expression (52), with $\lambda_1 = -c_0 = -\lambda_2$ and λ_3 and λ_4 determined as functions of x and t by the procedure just explained.

The corresponding density profiles are shown in Fig. 12 at different values of time for the initial distribution (3) (with $\rho_0 = 0.5$, $\rho_1 = 1.5$, and $x_0 = 20$). The agreement with the numerical simulation is excellent. The same level of accuracy is reached for the velocity profile $u(x, t)$.

In Fig. 13 we also compare the wavelength of the nonlinear oscillations within the DSW as determined by Whitham approach [Eq. (56)] with the results of numerical simulations. The agreement is again very good.

VII. DISCUSSION AND EXPERIMENTAL CONSIDERATIONS

The different situations we have identified are summarized in Fig. 14, which displays several typical density profiles in a phase space with coordinates ρ_1/ρ_0 and t. The curves $t_{split}(\rho_1/\rho_0)$ [as given by Eq. (49)] and $t_{WB}(\rho_1/\rho_0)$ [Eq. (72)]

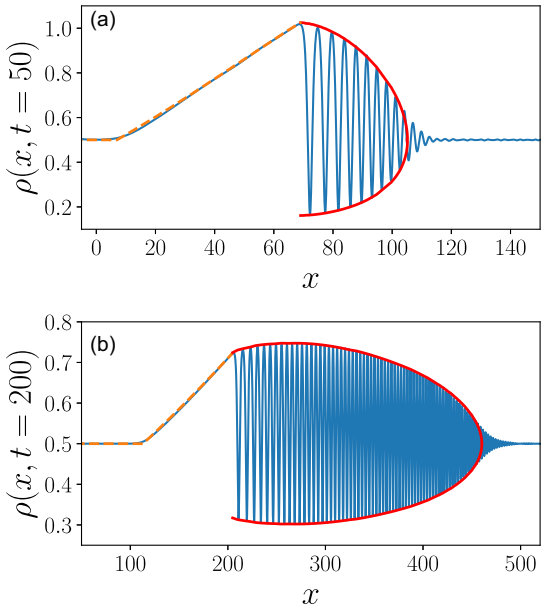

FIG. 12. Comparison between theory and numerical simulations for the density profile $\rho(x,t)$ at (a) $t = 50$ and (b) $t = 200$. The initial profile is the same as that used in all the previous figures. The blue curves are the numerical results. The red solid curves are the envelopes of the density (52) where the λ_i are calculated by the procedure described in Sec. VI D. The dashed orange curves correspond to the dispersionless part of the profile, determined using the method given in Sec. III.

separate this plane into four regions, labeled as (a), (b), (c), and (d) in the figure. These two curves cross at a point represented by an open circle whose coordinates we determined numerically as being $\rho_1/\rho_0 = 0.608\,14$ and $c_0 t/x_0 = 1.096\,23$. These coordinates are universal in the sense that they have the same value for any initial profile of inverted parabola type, such as given by Eq. (3), with $u(x,0) = 0$. Other types of initial profile would yield different precise arrangements of these curves in phase space, but we expect the qualitative behavior illustrated by Fig. 14 to be generic, because the different regimes depicted in this figure correspond to physical intuition: A larger initial hump (larger ρ_1/ρ_0) experiences

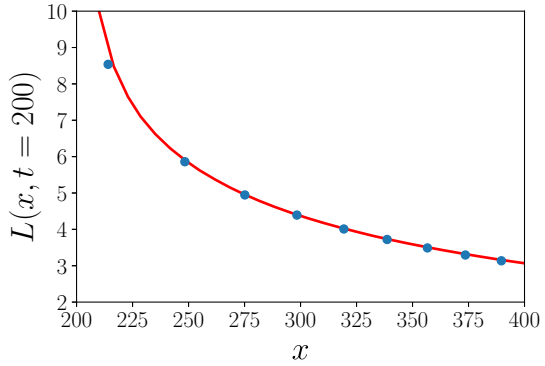

FIG. 13. Wavelength of the nonlinear oscillations within the DSW for $t = 200$. The theoretical red curve is calculated from Eq. (56). The blue points are extracted from simulations.

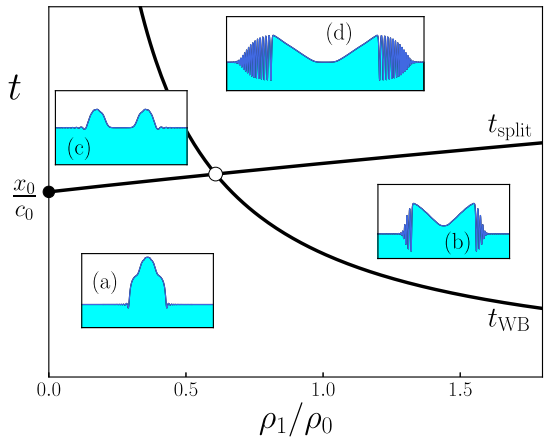

FIG. 14. Behavior of the light intensity profile in the plane $(\rho_1/\rho_0, t)$. The plane is separated into four regions by the curves $t = t_{\rm WB}$ and $t = t_{\rm split}$. These curves cross at the point represented by an open circle (of coordinates $\rho_1/\rho_0 = 0.608\,14$ and $c_0 t/x_0 = 1.096\,23$). Typical profiles are displayed in the insets (a)–(d), which represent $\rho(x,t)$ plotted as a function of x for fixed t.

earlier wave breaking and needs a longer time to be separated into two counterpropagating pulses. Also, the evolution of a small initial pulse can initially be described by perturbation theory and first splits into two humps which experience wave breaking in a later stage (as illustrated in Fig. 1): This is the reason why $t_{\rm split} < t_{\rm WB}$ for small ρ_1/ρ_0. In the opposite situation where $t_{\rm WB} < t < t_{\rm split}$, the wave breaking has already occurred while the profile has not yet split into two separate humps. This is the situation represented by inset (b) and which has been considered in Refs. [15,18].

In Ref. [18], Xu *et al.* studied the formation of a DSW in a nonlinear optic fiber[1] varying the intensity of the background. In particular, they quantitatively evaluated the visibility of the oscillations near the solitonic edge of the DSW by measuring the contrast

$$C_{\rm ont} = \frac{\rho_{\rm max} - \rho_{\rm min}}{\rho_{\rm max} + \rho_{\rm min}}, \tag{106}$$

where $\rho_{\rm max}$ and $\rho_{\rm min}$ are defined in the inset of Fig. 15. In Ref. [18], the contrast was studied for a fiber of fixed length, for an initial Gaussian bump, i.e., different from (3), keeping the quantities analogous to ρ_1 and x_0 fixed and varying ρ_0. The experimental results agreed very well with numerical simulations taking into account absorption in the fiber. Here we do not consider exactly the same initial profile and do not take damping into account, but we show that our approach gives a very reasonable analytic account of the behavior of $C_{\rm ont}$ considered as a function of ρ_0/ρ_1.

From Eq. (52) in the limit $m \to 1$ (which is the relevant regime near the solitonic edge of the DSW) we get

$$\rho_{\rm max} = \tfrac{1}{4}(\lambda_S + c_0)^2, \quad \rho_{\rm min} = \tfrac{1}{4}(\lambda_S - 3c_0)^2, \tag{107}$$

[1]In this case the role of variable x in Eq. (2) is played by time, but the phenomenology is very similar to the one we describe in the present work (see, e.g., [59]).

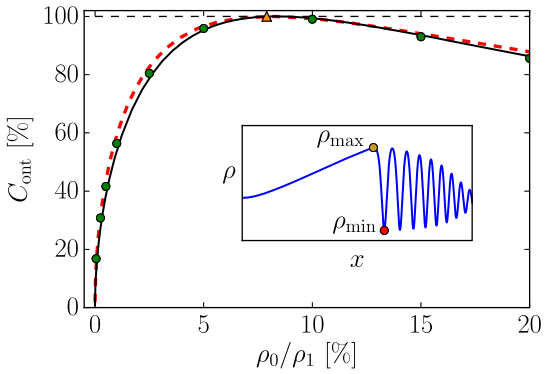

FIG. 15. Contrast $C_{\rm cont}$ represented as a function of ρ_0/ρ_1. We follow here the procedure of Ref. [18] and use the same dimensionless parameters: The value of ρ_0 varies while $\rho_1 = 5.9$, $x_0 = 6.3$, and $t = 9$ are fixed. The green circles correspond to the numerically determined value of the contrast, obtained from Eq. (106), where $\rho_{\rm min}$ and $\rho_{\rm max}$ are defined as illustrated in the inset. The black solid curve corresponds to expression (108), where $\lambda_{\rm S}$ is obtained from (77). The red dashed curve is the approximate result obtained from the same align (108), but evaluating $\lambda_{\rm S}$ from Eqs. (81), (110), and (112). The triangle marks the point of contrast unity.

yielding

$$C_{\rm cont} = \frac{4c_0(\lambda_{\rm S} - c_0)}{(\lambda_{\rm S} - c_0)^2 + 4c_0^2}. \tag{108}$$

The results presented in Fig. 15 demonstrate that, as expected, this expression (black solid curve in the figure) agrees very well with the contrast determined from the numerical solution of Eq. (2) (green points).

At this point, the computation of $C_{\rm cont}$ through (108) relies on the determination of $\lambda_{\rm S}$ by means of (77), a task which requires a good grasp of the Riemann approach. However, we can get an accurate, though approximate, analytic determination of $C_{\rm cont}$ in a simpler way: by using the large-time expression (81) for $\lambda_{\rm S}$, together with the approximation

$$\mathcal{A} \simeq -\left(\int_{c_m}^{c_0} \sqrt{r - c_0}\frac{dw^{\rm B}(r)}{dr}dr + \int_{c_0}^{c_m} \sqrt{r - c_0}\frac{dw^{\rm A}(r)}{dr}dr\right)$$
$$= 2\int_0^{x_0} \sqrt{\lambda^+(x,0) - c_0}dx. \tag{109}$$

In the above, we approximated in expression (80) $W_+^{(3/2)}(-c_0, r)$ by $w^{\rm A(B)}(r)$, used the symmetry of these functions, and made the change of variable $x = w^{\rm A}(r) \Leftrightarrow r = \lambda^+(x,0)$, in which $\lambda^+(x,0) = \sqrt{\rho}(x,0)$, where $\rho(x,0)$ is the initial density profile (3). A new change of variable yields

$$\mathcal{A} \simeq 2x_0\sqrt{c_0}F(\rho_0/\rho_1), \tag{110}$$

where

$$F(\alpha) = \int_0^{\pi/2} \cos\theta\left(\sqrt{1 + \frac{\cos^2\theta}{\alpha}} - 1\right)^{1/2} d\theta. \tag{111}$$

A simple analytic expression of $F(\alpha)$ cannot be obtained, but we checked that one can devise an accurate approximation by expanding the term in parentheses in the above integrand around $\theta = 0$ up to second order in θ. This yields

$$F(\alpha) \simeq \frac{(\sqrt{\alpha+1} - \sqrt{\alpha})^{1/2}}{\alpha^{1/4}}$$
$$- \frac{\frac{1}{4}(\pi^2/4 - 2)}{\alpha^{1/4}\sqrt{1+\alpha}(\sqrt{\alpha+1} - \sqrt{\alpha})^{1/2}}. \tag{112}$$

In the domain $10^{-3} \leqslant \alpha \leqslant 50$, $F(\alpha)$ varies over two orders of magnitude (from 4.8 to 7.8×10^{-2}) and the approximation (112) gives an absolute error ranging from 5.8×10^{-2} to 1.8×10^{-3} and a relative one ranging from 1.1% to 2.4%.

Combining Eqs. (108), (81), (110), and (112) yields an analytic expression for the contrast $C_{\rm cont}$. This expression is represented as a dashed red curve in Fig. 15. As we can see, it compares quite well with the value of $C_{\rm cont}$ extracted from the numerical simulations.[2] The better agreement with the numerical result is reached for small ρ_0/ρ_1; this was expected: In this regime the wave breaking occurs rapidly and we easily fulfill the condition $t \gg t_{\rm WB}$ where the approximation (81) holds. We note here that the behavior of the contrast illustrated in Fig. 15 is very similar to the one obtained in Ref. [18]. In both cases there is a special value of ρ_0/ρ_1 for which the contrast is unity, meaning that the quantity $\rho_{\rm min}$ cancels. From (107) and (81) this is obtained for $2c_0 \simeq (\mathcal{A}/t)^{2/3}$, i.e., using (110), for

$$\frac{c_0 t}{x_0} = \frac{1}{\sqrt{2}}F(\rho_0/\rho_1). \tag{113}$$

A numerical solution of this equation gives, for the parameters of Fig. 15, a contrast unity when $\rho_0/\rho_1 = 7.9\%$, while the exact Eq. (108) predicts a maximum contrast when $\rho_0/\rho_1 = 8.3\%$ instead (the exact result at $\rho_0/\rho_1 = 7.9\%$ is $C_{\rm cont} = 0.999$). These two values are marked with a single triangle in Fig. 15 because they cannot be distinguished on the scale of the figure. This shows that the solution of Eq. (113) gives a simple way to determine the best configuration for visualizing the fringes of the DSW; this should be useful for future experimental studies.

Note that formula (108) demonstrates that the contrast depends only on $\lambda_{\rm S}/c_0$ and using the approximate relations (81) and (113) leads to the conclusion that $C_{\rm cont}$ can be considered as a function of the single variable

$$X = \frac{x_0}{t\sqrt{\rho_1}}\sqrt{\frac{\rho_1}{\rho_0}}F(\rho_0/\rho_1). \tag{114}$$

Hence, for a configuration different from the one considered in Fig. 15 but for which the combination of parameters $t\sqrt{\rho_1}/x_0$ takes the same value (namely, 3.47), the curve $C_{\rm cont}(\rho_0/\rho_1)$ should superimpose on the one displayed in Fig. 15. We checked that this is indeed the case by taking $\rho_1 = 2$, $x_0 = 20$, and $t = 49$, but did not plot the corresponding contrast in Fig. 15 for legibility.

Figure 15 and the discussion of this section illustrate the versatility of our approach which not only gives an excellent

[2]Computing the contrast using expression (111) instead of the approximation (112) yields a result which is barely distinguishable from the dashed curve in Fig. 15.

account of the numerical simulations at the prize of an elaborate mathematical treatment, but also provides simple limiting expressions, such as Eq. (81), which make it possible to obtain an analytic and quantitative description of experimentally relevant parameters such as the contrast of the fringes of the DSW.

VIII. CONCLUSION

In this work we presented a detailed theoretical treatment of the spreading of a light pulse propagating in a nonlinear medium. A hydrodynamic approach to both the initial nondispersive spreading and the subsequent formation of an optical dispersive shock compares extremely well with the results of numerical simulations. Although in reality the transition between these two regimes is gradual, it is sharp within the Whitham approximation. An exact expression has been obtained for the theoretical wave breaking time which separates these two regimes [Eq. (72)], which may be used to evaluate the experimental parameters necessary to observe a DSW in a realistic setting (see Fig. 14). In addition, our theoretical treatment provides valuable insight into simple features of the shocks which are relevant to future experimental studies, such as the coordinates of its trailing edge x_S, the large-time nondispersive intensity profile which follows it (Sec. V), and the best regime for visualizing the fringes of the DSW (Sec. VII). We note also that our treatment reveals the existence of an asymptotically conserved quantity, see Eq. (84).

A possible extension of the present work would be to consider an initial configuration for which, at variance with the situation we study here, the largest intensity gradient is not reached exactly at the extremity of the initial hump. In this case, wave breaking occurs within a simple wave (not at its boundary) and the DSW has to be described by four position- and time-dependent Riemann invariants [52]. In the vicinity of the wave breaking moment, one of the Riemann invariants can be considered as constant and a generic dispersionless solution can be represented by a cubic parabola; a detailed theory was developed in Ref. [60] for this simpler case. In Refs. [61,62] the general situation was considered for the Korteweg–de Vries equation.

We conclude by stressing that the present treatment focused on quasi-one-dimensional spreading; future developments should consider non-exactly-integrable systems, for instance, light propagation in a photorefractive medium, in a bidimensional situation with cylindrical symmetry.

ACKNOWLEDGMENTS

We thank T. Bienaimé, Q. Fontaine, and Q. Glorieux for fruitful discussions. We also thank an anonymous referee for suggestions that improved the manuscript. A.M.K. thanks Laboratoire de Physique Théorique et Modèles Statistiques (Université Paris–Saclay), where this work started, for kind hospitality. This work was supported by the French ANR under Grant No. ANR-15-CE30-0017 (Haralab project).

[1] V. I. Talanov, Radiophys. **9**, 138 (1965).
[2] S. A. Akhmanov, A. P. Sukhorukov, and R. V. Khokhlov, Zh. Eksp. Teor. Fiz. **50**, 1537 (1966) [Sov. Phys. JETP **23**, 1025 (1966)].
[3] S. A. Akhmanov, A. P. Sukhorukov, and R. V. Khokhlov, Usp. Fiz. Nauk **93**, 19 (1967) [Sov. Phys. Usp. **10**, 609 (1968)].
[4] S. A. Akhmanov, D. P. Krindach, A. P. Sukhorukov, and R. V. Khokhlov, Pis'ma Zh. Eksp. Teor. Fiz. **6**, 509 (1967) [JETP Lett. **6**, 38 (1967)].
[5] R. G. Harrison, L. Dambly, D. Yu, and W. Lu, Opt. Commun. **139**, 69 (1997).
[6] P. Emplit, J. P. Hamaide, F. Reynaud, C. Froehly, and A. Barthelemy, Opt. Commun. **62**, 374 (1987).
[7] D. Krökel, N. J. Halas, G. Giuliani, and D. Grischkowsky, Phys. Rev. Lett. **60**, 29 (1988).
[8] A. M. Weiner, J. P. Heritage, R. J. Hawkins, R. N. Thurston, E. M. Kirschner, D. E. Leaird, and W. J. Tomlinson, Phys. Rev. Lett. **61**, 2445 (1988).
[9] F. T. Arecchi, G. Giacomelli, P. L. Ramazza, and S. Residori, Phys. Rev. Lett. **67**, 3749 (1991).
[10] M. Vaupel, K. Staliunas, and C. O. Weiss, Phys. Rev. A **54**, 880 (1996).
[11] D. Vocke, K. Wilson, F. Marino, I. Carusotto, E. M. Wright, T. Roger, B. P. Anderson, P. Öhberg, and D. Faccio, Phys. Rev. A **94**, 013849 (2016).
[12] J. E. Rothenberg and D. Grischkowsky, Phys. Rev. Lett. **62**, 531 (1989).
[13] N. Ghofraniha, C. Conti, G. Ruocco, and S. Trillo, Phys. Rev. Lett. **99**, 043903 (2007).
[14] G. Couton, H. Maillotte, and M. Chauvet, J. Opt. B **6**, S223 (2004).
[15] W. Wan, S. Jia, and J. W. Fleischer, Nat. Phys. **3**, 46 (2007).
[16] C. Barsi, W. Wan, C. Sun, and J. W. Fleischer, Opt. Lett. **32**, 2930 (2007).
[17] J. Fatome, C. Finot, G. Millot, A. Armaroli, and S. Trillo, Phys. Rev. X **4**, 021022 (2014).
[18] G. Xu, A. Mussot, A. Kudlinski, S. Trillo, F. Copie, and M. Conforti, Opt. Lett. **41**, 2656 (2016).
[19] G. Xu, M. Conforti, A. Kudlinski, A. Mussot, and S. Trillo, Phys. Rev. Lett. **118**, 254101 (2017).
[20] M. Karpov, T. Congy, Y. Sivan, V. Fleurov, N. Pavloff, and S. Bar-Ad, Optica **2**, 1053 (2015).
[21] M. Elazar, V. Fleurov, and S. Bar-Ad, Phys. Rev. A **86**, 063821 (2012).
[22] D. Vocke, C. Maitland, A. Prain, F. Biancalana, F. Marino, E. M. Wright, and D. Faccio, Optica **5**, 1099 (2018).
[23] J. Drori, Y. Rosenberg, D. Bermudez, Y. Silberberg, and U. Leonhardt, Phys. Rev. Lett. **122**, 010404 (2019).
[24] D. Vocke, T. Roger, F. Marino, E. M. Wright, I. Carusotto, M. Clerici, and D. Faccio, Optica **2**, 484 (2015).
[25] Q. Fontaine, T. Bienaimé, S. Pigeon, E. Giacobino, A. Bramati, and Q. Glorieux, Phys. Rev. Lett. **121**, 183604 (2018).
[26] C. Michel, O. Boughdad, M. Albert, P.-É. Larré, and M. Bellec, Nat. Commun. **9**, 2108 (2018).
[27] A. M. Kamchatnov, A. Gammal, and R. A. Kraenkel, Phys. Rev. A **69**, 063605 (2004).
[28] G. A. El, A. Gammal, E. G. Khamis, R. A. Kraenkel, and A. M. Kamchatnov, Phys. Rev. A **76**, 053813 (2007).

[29] M. Conforti and S. Trillo, in *Rogue and Shock Waves in Nonlinear Dispersive Media*, edited by M. Onorato, S. Residori, and F. Baronio, Lecture Notes in Physics Vol. 926 (Springer International, Cham, 2016).

[30] G. B. Whitham, *Linear and Nonlinear Waves* (Wiley Interscience, New York, 1974).

[31] M. Isoard, A. M. Kamchatnov, and N. Pavloff, Phys. Rev. E **99**, 012210 (2019).

[32] G. S. S. Ludford, Proc. Cambridge Philos. Soc. **48**, 499 (1952).

[33] M. G. Forest, C.-J. Rosenberg, and O. C. Wright III, Nonlinearity **22**, 2287 (2009).

[34] A. V. Gurevich and L. P. Pitaevskii, Zh. Eksp. Teor. Fiz. **65**, 590 (1973) [Sov. Phys. JETP **38**, 291 (1974)].

[35] G. A. El and M. A. Hoefer, Physica D **333**, 11 (2016).

[36] A. V. Gurevich, A. L. Krylov, and N. G. Mazur, Zh. Eksp. Teor. Fiz. **95**, 1674 (1989) [Sov. Phys. JETP **68**, 966 (1989)].

[37] A. V. Gurevich, A. L. Krylov, and G. A. El, Pis'ma Zh. Eksp. Teor. Fiz. **54**, 104 (1991) [JETP Lett. **54**, 102 (1991)].

[38] A. V. Gurevich, A. L. Krylov, and G. A. El, Zh. Eksp. Teor. Fiz. **101**, 1797 (1992) [Sov. Phys. JETP **74**, 957 (1992)].

[39] A. L. Krylov, V. V. Khodorovskii, and G. A. El, Pis'ma Zh. Eksp. Teor. Fiz. **56**, 325 (1992) [JETP Lett. **56**, 323 (1992)].

[40] G. A. El and V. V. Khodorovsky, Phys. Lett. A **182**, 49 (1993).

[41] G. A. El, A. M. Kamchatnov, V. V. Khodorovskii, E. S. Annibale, and A. Gammal, Phys. Rev. E **80**, 046317 (2009).

[42] L. D. Landau, E. M. Lifshitz, and L. P. Pitaevskii, *Electrodynamics of Continuous Media*, Landau and Lifshitz Course of Theoretical Physics Vol. 8 (Elsevier Butterworth-Heinemann, Oxford, 2006).

[43] A. M. Kamchatnov, *Nonlinear Periodic Waves and Their Modulations: An Introductory Course* (World Scientific, Singapore, 2000).

[44] S. P. Tsarev, Math. USSR Izv. **37**, 397 (1991).

[45] A. Sommerfeld, *Partial Differential Equations in Physics*, Lectures on Theoretical Physics Vol. VI (Academic, New York, 1964).

[46] *Handbook of Mathematical Functions: With Formulas, Graphs, and Mathematical Tables*, edited by M. Abramowitz and I. A. Stegun (Dover, New York, 1970).

[47] L. D. Landau and E. M. Lifshitz, *Fluid Mechanics* (Pergamon, Oxford, 1987).

[48] It should not be a surprise that, to determine the wave breaking time, it is legitimate to replace $W_+^{(3)}(-c_0, \lambda^+)$ by $w^{\mathrm{A}}(\lambda^+)$ in Eq. (45). Indeed, the wave breaking phenomenon occurs when several characteristics issued from the right region of the edge of the bump cross (in region III for the case considered). For all these characteristics, we intuitively expect that we can neglect the weak dependence of λ^- on x. This is indeed the case: We can rigorously show that $W_+^{(3)}(-c_0, \lambda^+)$ and $w^{\mathrm{A}}(\lambda^+)$ coincide in the limit $\lambda^+ = c_0$, which is the relevant one for evaluating (45).

[49] M. G. Forest and J. E. Lee, in *Oscillation Theory, Computation, and Methods of Compensated Compactness*, edited by C. Dafermos, J. L. Ericksen, D. Kinderlehrer, and M. Slemrod, IMA Volumes on Mathematics and its Applications Vol. 2 (Springer, New York, 1986), p. 35.

[50] M. V. Pavlov, Teor. Mat. Fiz. **71**, 351 (1987) [Theor. Math. Phys. **71**, 584 (1987)].

[51] R. Z. Sagdeev, in *Reviews of Plasma Physics*, edited by M. A. Leontovich (Consultants Bureau, New York, 1966), Vol. 4, p. 23.

[52] G. A. El and A. L. Krylov, Phys. Lett. **203**, 77 (1995).

[53] O. C. Wright, Commun. Pure Appl. Math. **46**, 423 (1993).

[54] F. R. Tian, Commun. Pure Appl. Math. **46**, 1093 (1993).

[55] L. P. Eisenhart, Ann. Math. **120**, 262 (1918).

[56] G. Arfken and H. J. Weber, *Mathematical Methods for Physicists* (Academic, Orlando, 2005).

[57] G. A. El, Chaos **15**, 037103 (2005); **16**, 029901 (2006).

[58] A. M. Kamchatnov, Phys. Rev. E **99**, 012203 (2019).

[59] Y. S. Kivshar and G. P. Agrawal, *Optical Solitons* (Academic, San Diego, 2003).

[60] A. M. Kamchatnov, R. A. Kraenkel, and B. A. Umarov, Phys. Rev. E **66**, 036609 (2002).

[61] G. A. El, A. L. Krylov, and S. Venakides, Commun. Pure Appl. Math. **54**, 1243 (2001).

[62] T. Grava and C. Klein, Commun. Pure Appl. Math. **60**, 1623 (2007).

8 CONCLUSION

Analogue gravity has been initially proposed by Unruh as a tool making it possible to observe "experimental black hole evaporation" [182]. Today, analogue gravity has become an active field of research that represents a new source of inspiration to deepen our understanding of fundamental processes at the interface of general relativity, condensed matter, hydrodynamics and optics.

In this thesis, we have shown that analogue systems in Bose-Einstein condensates were excellent candidates to explore the analogous Hawking radiation. By taking into account zero modes whose contribution had been overlooked in previous studies, we have obtained a self-grounded theory and we have been able to compare successfully our theoretical results with experimental data obtained by J. Steinhauer's group in 2019 [131]. The observation of such a signal in an analogue quantum system is undoubtedly the result of strong experimental improvements and theoretical developments in the last years.

We have also revealed that the expected Hawking signal in Bose-Einstein condensates was not thermal due to dispersive effects. In particular, we have questioned the data analysis performed by J. Steinhauer's group [131] and we have conjectured that a self-consistent procedure might have led them to the erroneous conclusion that the analogue Hawking radiation is fully thermal. This departure from the predicted thermal radiation emitted by black holes [87] shows the significant role played by dispersion in analogue systems. Interestingly, this important effect does not kill the spontaneous emission from the sonic horizon, but, instead, enhances it, see e.g., the right graph of Figure 31. We think that the role of dispersion that leads to a departure from thermality should be explored in more detail in the future; in addition, the fact that complete dispersive systems in optics, i.e., without sonic branches in the dispersion relation, also reveal the existence of an analogue Hawking radiation is an intriguing path to scrutinize [97, 98].

The correct theoretical description of density correlations at the vicinity of the acoustic black hole is also an important step towards the exploration of backreaction: the objective in the future will be to understand what is the effect of the analogous Hawking radiation on the density background[1]. Our recent results should make it possible to quantify this backreaction effect and this is one of the directions we would like to follow in the near future.

In Chapter 4, we have proved that sonic black holes in Bose-Einstein condensates reveal tripartite entanglement shared among quanta emitted from the sonic horizon. We showed in particular that the process

1 Backreaction in general relativity is the effect of Hawking radiation to the spacetime geometry near the event horizon; this is one possible path to delve into the information loss paradox.

behind these entanglement properties was a Bogoliubov transformation, i.e., a mixing of positive and negative energy modes, leading to the existence of two different vacua. This has confirmed the fundamental role played by Bogoliubov transformations in effective curved spacetimes generated by analogue systems, in close connection with the results discussed in Chapter 2.

The existence of tripartite entanglement is a novel aspect, not yet explored, in the context of Bose-Einstein analogue systems. A lot of work remains to be done: we would like to analyze the effect of temperature on the entanglement and propose a measurement procedure able to experimentally reveal tripartite entanglement in these systems.

In the second part of this thesis, we have been interested in nonlinear effects leading to a gradient catastrophe and to the formation of dispersive shock waves. We stressed in particular the universality of hydrodynamics equations to describe many physical models in various physics fields; for instance, the non-dispersive approximation of the nonlinear Schrödinger equation, which describes the dynamics of Bose-Einstein condensates or optical beams in nonlinear media, is a particular case of the equations governing the dynamics of polytropic gases, themselves being a particular case of inviscid nonlinear hydrodynamics equations. Therefore, a better grasp of this type of equations will be certainly a further step in the theoretical description and comprehension of numerous physical phenomena.

In Chapter 6, we considered the general case of inviscid nonlinear pulses. We described the first stage of spreading of a bump on top of a uniform background by means of Riemann's method. Then, we applied our results in the case of the nonlinear Schrödinger equation. Furthermore, we showed that approximate solutions of Riemann's method were accurate to describe correctly the dynamics of nonlinear pulses. Likewise, this approach was also effective in the case of non-integrable equations; we took the specific example of a Bose-Einstein condensate transversely confined in an atomic wave guide.

In Chapter 7, we studied in more detail the propagation of dispersive shock waves in the case of the nonlinear Schrödinger equation. Our theoretical approach, based on a hodograph transform and the resolution of an Euler-Poisson equation with the use of the method proposed in Refs. [56, 82], compared very well with numerical simulations. We have been able in particular to extract a weak shock theory and have obtained simple analytic expressions to describe some experimental parameters, such as the contrast of the fringes of a dispersive shock wave.

In the near future, we hope to compare the theoretical results obtained during this PhD with experimental data. Indeed, dispersive shock waves have been recently observed experimentally by a group at LKB. They sent an optical pulse in the presence of a background light intensity through a vapour of rubidium atoms and noticed the formation of oscillations at both edges of the bump, see Figure 63. The dynamics of such a fluid of light is governed by a non-integrable equation, which

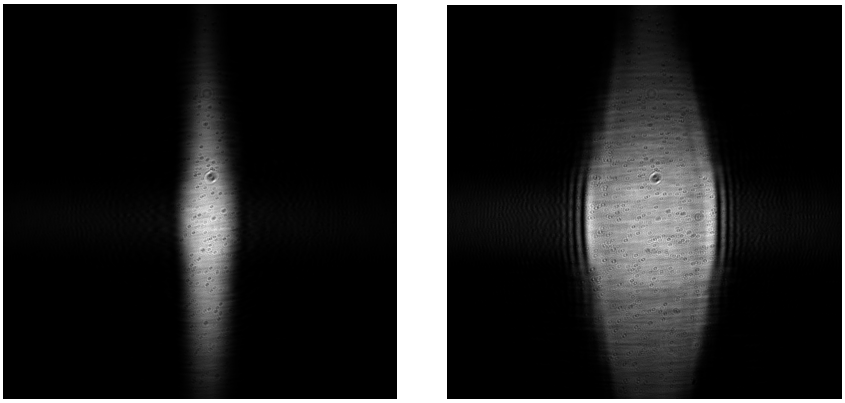

FIGURE 63: (Left) Initial optical beam. (Right) After propagation through the vapour of Rubidium atoms. The franges at both edges of the pulse correspond to the formation of dispersive shock waves, courtesy of Tom Bienaimé, LKB, for providing these experimental images.

reduces to the nonlinear Schrödinger equation when there is no saturation of the nonlinearity nor absorption [162]. However, it seems that the effects of saturation and absorption might play an important role in these systems. In this case, it would be very interesting to extend the theoretical description of dispersive shock waves to non-integrable equations in order to take into account these effects and to consider 2D dynamics.

The work presented in this manuscript illustrates how the fields of quantum and nonlinear fluctuations in quantum fluids can dialog one with the other. This corresponds to a vivid domain of research in which the fields of nonlinear optics and of quantum matter waves benefit from the cross fertilization of many body physics and quantum optics [51] to explore emerging areas, such as quantum information science [17, 46, 68, 121, 138, 147, 150, 198], and even probe the foundations of quantum physics [151].

Part III

APPENDIX

A

COMPARISON BETWEEN DIFFERENT THEORETICAL PARAMETERS FOR A WATERFALL CONFIGURATION

Theoretically, we need to impose the following conditions:

$$\frac{V_d}{V_u} = \frac{n_u}{n_d} = \frac{1}{m_u^2} = m_d = \left(\frac{\xi_d}{\xi_u}\right)^2 = \left(\frac{c_u}{c_d}\right)^2 , \tag{564}$$

see (116), Section 3.1.3.

The experiment performed by J. Steinhauer's group is not in a true waterfall configuration. We should fix the right parameter(s) to obtain the best configuration with respect to the experimental setup [131]. Table 1 shows the different experimental and theoretical parameters; we compare different configurations, whose parameters are fixed by one of the equalities of (564). For instance, the experimental downstream Mach number is $m_d^{\text{exp}} = 2.9$ [131]. If we choose the same value for the theoretical downstream Mach number (column 5 of Table 1), then, all the other theoretical parameters can be calculated with conditions (564). Actually, this choice (fixing $m_d = 2.9$) leads to the best agreement between experimental and theoretical parameters, see Table 1.

Parameters	Exp. val.	$(c_u/c_d)^2$	$(\xi_d/\xi_u)^2$	m_d	$1/m_u^2$	V_d/V_u
c_u	0.52	**0.52**	**0.52**	0.52	**0.52**	**0.52**
c_d	0.31	0.31	0.31	**0.31**	0.23	0.26
ξ_u	1.4	**1.4**	**1.4**	1.39	**1.4**	**1.4**
ξ_d	2.36	2.34	2.36	**2.36**	3.16	2.77
$\xi = \sqrt{\xi_u \xi_d}$	1.82	1.81	1.82	1.81	2.1	1.97
m_d	2.9	2.81	2.84	2.9	5.11	3.91
m_u	0.44	0.6	0.59	0.59	0.44	0.51
V_u	0.23	**0.23**	**0.23**	0.31	**0.23**	**0.23**
V_d	0.9	0.65	0.65	**0.9**	1.18	0.9

Table 1: The experimental values are extracted from Ref. [131] and written in the second column. Then, the theoretical parameters in each column (from column 3 to column 7) are obtained by fixing one of conditions (564). The condition that we decide to fix is indicated on top of each column and the corresponding parameter(s) is(are) colored in red. The bold numbers can be chosen freely (indeed, in most cases, only the ratio is fixed – for example, conditions (564) only fixes the ratio c_u/c_d; thus, one can choose either c_u or c_d equal to the experimental value, and then fix the other parameter by means of c_u/c_d).

B

ZERO MODES IN BOSE-EINSTEIN CONDENSATES

In this appendix, we detail the determination of the zero modes introduced in Section 3.2.2.

The zero modes are given by

$$P = \begin{pmatrix} \psi(x) \\ -\psi^\star(x) \end{pmatrix}, \quad \text{and} \quad Q = \begin{pmatrix} q(x) \\ -q^\star(x) \end{pmatrix}, \tag{565}$$

and satisfy

$$\mathcal{L}_{\text{BG}}\, P = 0, \quad \mathcal{L}_{\text{BG}}\, Q = 0, \tag{566}$$

where $\psi(x)$ is the condensate wave function and $\mathcal{L}_{\text{BG}}$ is the Bogoliubov-De Gennes Hamiltonian defined in equation (135). The fact that Q is also an eigenvector of $\mathcal{L}_{\text{BG}}$, with eigenvalue zero, comes from the absence of phase diffusion in our system, i.e., M_{eff} in equation (147), see the discussion in Section 3.2.3 for more details.

B.1 FLAT PROFILE

For the flat profile configuration

$$\psi(x) = \sqrt{n_0}\exp(\mathrm{i}k_0 x), \tag{567}$$

see Section 3.1.3. We look for the most general solutions of equations (566):

$$P_\alpha = A^P_\alpha \begin{pmatrix} e^{\mathrm{i}k_0 x} \\ -e^{-\mathrm{i}k_0 x} \end{pmatrix}, \tag{568}$$

and

$$\begin{aligned} Q_d = {} & A \begin{pmatrix} e^{\mathrm{i}k_0 x} \\ -e^{-\mathrm{i}k_0 x} \end{pmatrix} + B\, e^{i\,K_0\,X_d} \begin{pmatrix} \left(\frac{K_0}{2} - m_d\right) e^{\mathrm{i}k_0 x} \\ \left(\frac{K_0}{2} + m_d\right) e^{-\mathrm{i}k_0 x} \end{pmatrix} \\ & + B\, e^{i\,\alpha} e^{-i\,K_0\,X_d} \begin{pmatrix} \left(-\frac{K_0}{2} - m_d\right) e^{\mathrm{i}k_0 x} \\ \left(-\frac{K_0}{2} + m_d\right) e^{-\mathrm{i}k_0 x} \end{pmatrix} \end{aligned} \tag{569a}$$

$$Q_u = C \begin{pmatrix} e^{\mathrm{i}k_0 x} \\ -e^{-\mathrm{i}k_0 x} \end{pmatrix} + D\, e^{\Lambda_u\, X_u} \begin{pmatrix} \left(-i\,\frac{\Lambda_u}{2} - m_u\right) e^{\mathrm{i}k_0 x} \\ \left(-i\,\frac{\Lambda_u}{2} + m_u\right) e^{-\mathrm{i}k_0 x} \end{pmatrix}, \tag{569b}$$

with $K_0 = 2\sqrt{m_d^2 - 1}$ and $\Lambda_u = 2\sqrt{1 - m_u^2}$, and where the subscripts hold for the upstream (u) or the downstream (d) region.

The matching conditions at the horizon read

$$\begin{aligned} P_u(x=0) &= P_d(x=0), \\ \partial_x P_u(x=0) &= \partial_x P_d(x=0), \end{aligned} \tag{570}$$

and

$$\begin{aligned} Q_u(x=0) &= Q_d(x=0,) \\ \partial_x Q_u(x=0) &= \partial_x Q_d(x=0). \end{aligned} \tag{571}$$

We see immediately that $A_u^P = A_d^P$ and can be fixed arbitrarily to 1.

For Q_α the conditions are

$$\begin{cases} A + B\left(\frac{K_0}{2} - m_d\right) + B\,e^{i\,\alpha}\left(-\frac{K_0}{2} - m_d\right) = C + D\left(-i\,\frac{\Lambda_u}{2} - m_u\right) \\ -A + B\left(\frac{K_0}{2} + m_d\right) + B\,e^{i\,\alpha}\left(-\frac{K_0}{2} + m_d\right) = -C + D\left(-i\,\frac{\Lambda_u}{2} + m_u\right) \\ iBK_0\,\xi_d^{-1}\left[\left(\frac{K_0}{2} - m_d\right) - e^{i\,\alpha}\left(-\frac{K_0}{2} - m_d\right)\right] = D\,\Lambda_u\,\xi_u^{-1}\left(-i\,\frac{\Lambda_u}{2} - m_u\right) \\ iBK_0\,\xi_d^{-1}\left[\left(\frac{K_0}{2} + m_d\right) - e^{i\,\alpha}\left(-\frac{K_0}{2} + m_d\right)\right] = D\,\Lambda_u\,\xi_u^{-1}\left(-i\,\frac{\Lambda_u}{2} + m_u\right) \end{cases} \tag{572}$$

After solving this system of equations we find that

$$\begin{aligned} &B = D\,E \quad \text{and} \quad B\,e^{i\,\alpha} = D\,E^*, \\ &A = C + D\,[m_d\,(E + E^*) - m_u] \\ &\text{with} \quad E = -\frac{\Lambda_u}{2\,m_d\,K_0^2}\,\frac{\xi_d}{\xi_u}\,(\Lambda_u\,m_d + i\,m_u\,K_0) \end{aligned} \tag{573}$$

Then, the zero modes have zero norm, that is to say

$$Q_\alpha^\dagger\,\sigma_z\,Q_\alpha = 0 \quad \text{and} \quad P_\alpha^\dagger\,\sigma_z\,P_\alpha = 0, \tag{574}$$

where σ_z is the Pauli matrix. The norm of P_α is immediately zero from expression (568). For Q_u, equation (574) leads to

$$i\,\Lambda_u\,C^*\,D\,e^{\Lambda_u\,X_u} + c.c = 0. \tag{575}$$

We can take $C = 0$ without loss of generality.

Then, the value of D is determined numerically. The procedure is the following: we know that the field operator $\delta\hat{\psi}$ should be correctly normalized, see equation (159):

$$\left[\delta\hat{\psi}(x,t), \delta\hat{\psi}^\dagger(x',t)\right] = \delta(x - x')\ . \tag{576}$$

Then, we can extract the zero modes contribution to the expansion of the quantum field operator (155), denoted as

$$\hat{\psi}_{ZM} = i\,Q\hat{P} - i\,P\,\hat{Q}. \tag{577}$$

If $\delta\hat{\psi}$ is correctly normalized, one should have

$$[\hat{\psi}_1(x,t),\hat{\psi}_1^\dagger(x',t)] - \delta(x-x') = -[\hat{\psi}_{ZM}(x,t),\hat{\psi}_{ZM}^\dagger(x',t)], \quad (578)$$

where we have introduced $\hat{\psi}_1 = \delta\hat{\psi} - \hat{\psi}_{ZM}$, i.e., the operator $\delta\hat{\psi}$ without taking into account the zero modes contribution. The solid blue and green curves (real and imaginary parts, respectively) in the left graph of Figure 64 show the numerical computation of $[\hat{\psi}_1(x,t),\hat{\psi}_1^\dagger(x',t)] - \delta(x-x')$ in the downstream region for a specific configuration ($m_u = 0.5$, $m_d = 4$, with $x = 75\,\xi_u$ and x' ranging from $x' = 60\,\xi_u$ to $x' = 90\,\xi_u$). One sees that, indeed, the absence of zero modes in expansion (155) leads to an incorrect normalization; one observes spurious oscillations. The dashed red and pink curves (real and imaginary parts, respectively) are obtained from the calculation of $-[\hat{\psi}_{ZM}(x,t),\hat{\psi}_{ZM}^\dagger(x',t)]$ with the use of expressions (568) and (569a) and by fixing D such that both curves agree. Therefore, by choosing a correct value of D (here $D = 0.079$), one can remove the spurious oscillations and obtain a correct normalization of the total field operator $\delta\psi$, see, e.g., Figure 22. In fact, these oscillations are nothing but the contribution of the zero modes in expression (155).

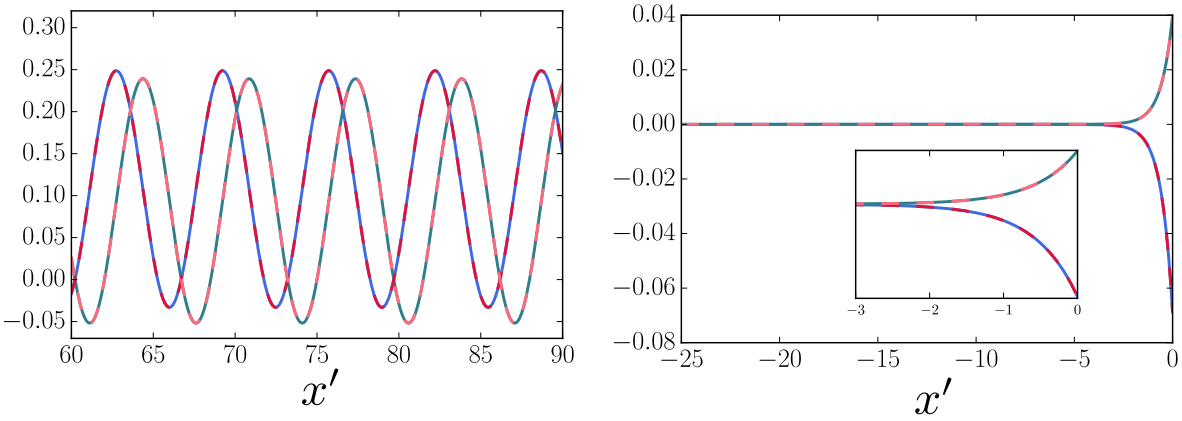

FIGURE 64: Numerical determination of D for the flat profile configuration. (Left) Downstream region: $x > 0$, $x' > 0$, with $x = 75\,\xi_u$. Solid blue and green curve: real and imaginary parts of $[\hat{\psi}_1(x,t),\hat{\psi}_1^\dagger(x',t)] - \delta(x-x')$, respectively; dashed red and pink curve: real part and imaginary parts of $-[\hat{\psi}_{ZM}(x_a,t),\hat{\psi}_{ZM}^\dagger(x_b,t)]$. (Right) Upstream region: $x < 0$, $x' < 0$, with $x = -20$. Same color code as the left plot.

A final check consists of performing the same calculation in the upstream region. The value of D found in the downstream region should be the same as the one in the upstream region. The solid blue and green curves (real and imaginary parts, respectively) in the right graph of Figure 64 show the numerical computation of $[\hat{\psi}_1(x,t),\hat{\psi}_1^\dagger(x',t)] - \delta(x-x')$ in the upstream region for the same configuration ($m_u = 0.5$, $m_d = 4$, with $x = -20\,\xi_u$ and x' ranging from $x' = -25\,\xi_u$ to $x' = 0$). The dashed red and pink curves (real and imaginary parts, respectively) are

obtained from the calculation of $-[\hat{\psi}_{ZM}(x,t), \hat{\psi}^{\dagger}_{ZM}(x',t)]$ with the use of expressions (568) and (569b), and with D determined from the above procedure in the downstream region. Both curves nicely agree.

One can then repeat this procedure for different flat profile configurations, i.e., varying the upstream and downstream Mach number m_u and m_d. This is how we found the approximate expressions given by (150).

In conclusion, once D is determined, one obtains the expressions given in Chapter 3, see equations (148) and (149).

B.2 WATERFALL CONFIGURATION

For the waterfall configurations, the determination of the zero modes is similar to the previous section; the main difference here lies in the fact that the condensate wave function is now given by

$$\psi(x) = \begin{cases} \sqrt{n_u}\exp(\mathrm{i}k_u x)\phi_u(x) & \text{for} \quad x<0\,, \\ \sqrt{n_d}\exp(\mathrm{i}k_d x)\phi_d(x) & \text{for} \quad x>0\,, \end{cases} \tag{579}$$

with ϕ_u and ϕ_d given by expressions (115).

One finds the general solutions of equations (566) given by[1]

$$Q_\alpha = \begin{pmatrix} e^{i\,k_\alpha\,x} & 0 \\ 0 & e^{-i\,k_\alpha\,x} \end{pmatrix} \bar{Q}_\alpha, \tag{580}$$

with

$$\begin{aligned} \bar{Q}_u &= D\left[\chi(X_u) - \frac{\Lambda}{2}\right]^2 e^{\Lambda_u\,X_u}\begin{pmatrix}1\\1\end{pmatrix}\,, \\ \bar{Q}_d &= A\begin{pmatrix}\phi_d\\-\phi_d^\star\end{pmatrix} \\ &\quad + E\,e^{i\,K_0\,X_d}\begin{pmatrix}[\frac{K_0}{2}-m_d]\,\phi_d\\[\frac{K_0}{2}+m_d]\,\phi_d^\star\end{pmatrix} + E\,e^{-i\,K_0\,X_d}\begin{pmatrix}[-\frac{K_0}{2}-m_d]\,\phi_d\\[-\frac{K_0}{2}+m_d]\,\phi_d^\star\end{pmatrix}\,. \end{aligned} \tag{581}$$

Then, one uses the continuity equations (570) and (571) to determine the relations between A, D and E. We find in particular a system very similar to (572) leading to expressions (152) of Chapter 3. We use exactly the same procedure as the one detailed in the previous section to determine the value of D for different waterfall configurations; we obtain expression (153).

1 We only detail the expressions for Q_α, since P_α is given in (565), with ψ made explicit in expression (579).

C

FOURIER TRANSFORM OF THE DENSITY CORRELATION FUNCTION

In this appendix we detail the calculation leading to expression (178) of Chapter 3.

Let us introduce

$$\begin{aligned} I(\omega) &= \frac{1}{\sqrt{n_u n_d L_u L_d}} \int_{-L_u}^{0} dx \int_{0}^{L_d} dx'\, e^{-i(k_{\rm H} x + k_{\rm P} x')}\, g^{(2)}(x,x') \\ &= \frac{1}{\sqrt{n_u\, n_d\, L_u\, L_d}} \int_{-\infty}^{+\infty} dx \int_{-\infty}^{+\infty} dx' e^{-i(k_{\rm H} x + k_{\rm P} x')}\, g^{(2)}(x,x')\, \Pi_u(x)\, \Pi_d(x), \end{aligned} \tag{582}$$

where $k_{\rm H}(\omega)$ and $k_{\rm P}(\omega)$ are the momenta relative to the condensate of the Hawking quantum and of its partner at a frequency ω, and where

$$\Pi_u(x) = \Theta(x+L_u) - \Theta(x), \quad \text{and} \quad \Pi_d(x) = \Theta(x) - \Theta(x-L_d). \tag{583}$$

In the previous expression Θ is the Heaviside function. By expanding the $g^{(2)}$ function with the use of expressions (170), (163), (164) and (166), it is not difficult to show that

$$I(k_{\rm H}, k_{\rm P}) = \int \frac{d\omega'}{2\,\pi} A(\omega') \Pi_u[k_{\rm H}(\omega) - q_{u|\rm out}(\omega')]\, \Pi_d[k_{\rm P}(\omega) + q_{d2|\rm out}(\omega')], \tag{584}$$

with

$$A(\omega) = \frac{1}{\sqrt{L_u\, L_d}}\, (\mathcal{U}_{k_{\rm H}} + \mathcal{V}_{k_{\rm H}})\, (\mathcal{U}_{k_{\rm P}} + \mathcal{V}_{k_{\rm P}})\, S_{ud2}(\omega)\, S^*_{d2d2}(\omega). \tag{585}$$

In expression (584), $q_{\alpha|\rm out}(\omega')$, $\alpha \in \{u, d\}$, are the wave vectors associated to the $u|$out and $d2|$out modes, calculated from the dispersion relation, see in particular Figure 20. Note that, with this notation, $k_{\rm H} = q_{u|\rm out}(\omega) < 0$ and $k_{\rm P} = -q_{d2|\rm out}(\omega) < 0$.

In equation (585), $\mathcal{U}_{k_{\rm H}} \equiv \mathcal{U}_{u|\rm out}$ ($\mathcal{V}_{k_{\rm H}} \equiv \mathcal{V}_{u|\rm out}$) and $\mathcal{U}_{k_{\rm P}} \equiv \mathcal{U}_{d2|\rm out}$ ($\mathcal{V}_{k_{\rm P}} \equiv \mathcal{V}_{d2|\rm out}$), where $\mathcal{U}_{\alpha|\rm out}$ and $\mathcal{V}_{\alpha|\rm out}$ are defined in equation (138).

The Fourier transforms of Π_α are

$$\Pi_\alpha(q) = L_\alpha\, e^{i\, q\, L_\alpha/2}\, \mathrm{sinc}(q\, L_\alpha/2). \tag{586}$$

In the following, we consider the case where L_u, $L_d \to +\infty$; in this limit the windows Π_α are well peaked around zero. This means that the only significant contribution in the integral arises when $\omega' \simeq \omega$. In this case, one has

$$\begin{cases} q_{u|\rm out}(\omega') \simeq q_{u|\rm out}(\omega) + q'_{u|\rm out}(\omega)\, (\omega' - \omega), \\ q_{d2|\rm out}(\omega') = q_{d2|\rm out}(\omega) + q'_{d2|\rm out}(\omega)\, (\omega' - \omega), \end{cases} \tag{587}$$

where $q'_{\alpha|\mathrm{out}} = \frac{\mathrm{d}q_{\alpha|\mathrm{out}}}{\mathrm{d}\omega}$. Expressions (587) can be rewritten in the form

$$\begin{cases} q_{u|\mathrm{out}}(\omega') - q_{u|\mathrm{out}}(\omega) \simeq \dfrac{\omega' - \omega}{V_g(k_{\mathrm{H}})}, \\ q_{d2|\mathrm{out}}(\omega') - q_{d2|\mathrm{out}}(\omega) \simeq \dfrac{\omega' - \omega}{V_g(k_{\mathrm{P}})}, \end{cases} \tag{588}$$

where we noticed that $q'_{u|\mathrm{out}}(\omega) = 1/V_g(k_{\mathrm{H}})$ and $q'_{d2|\mathrm{out}}(\omega) = 1/V_g(k_{\mathrm{P}})$. Then, we make the following change of variable in (584):

$$s = |V_g(k_{\mathrm{H}})|\,[k_{\mathrm{H}} - q_{u|\mathrm{out}}(\omega')]. \tag{589}$$

Using relations (588), we see immediately that

$$s = V_g(k_{\mathrm{P}})[k_{\mathrm{P}} + q_{d2|\mathrm{out}}(\omega')]. \tag{590}$$

Integral (584) becomes

$$I(\omega) = A(\omega) \int \frac{ds}{2\,\pi}\, \Pi_u \left(\frac{s}{|V_g(k_{\mathrm{H}})|} \right) \Pi_d \left(\frac{s}{V_g(k_{\mathrm{P}})} \right). \tag{591}$$

With a new change of variable

$$I(\omega) = A(\omega) \frac{|V_g(k_{\mathrm{H}})|\, L_d}{\pi} \int dt\, \mathrm{sinc}(t)\, \mathrm{sinc}\left(t\, \frac{L_d\, |V_g(k_{\mathrm{H}})|}{L_u\, V_g(k_{\mathrm{P}})} \right) \times \exp\left[i \left(\frac{L_d\, |V_g(k_{\mathrm{H}})|}{L_u\, V_g(k_{\mathrm{P}})} - 1 \right) t \right]. \tag{592}$$

The previous integral can be rewritten

$$I(\omega) = A(\omega) \sqrt{L_u\, L_d} \sqrt{|V_g(k_{\mathrm{H}})|\, V_g(k_{\mathrm{P}})}\, d(\omega), \tag{593}$$

with

$$d(\omega) = \frac{\sqrt{a(\omega)}}{\pi} \int dt\, \mathrm{sinc}(t)\, \mathrm{sinc}\,[a(\omega)\, t]\; e^{i\,[a(\omega)-1]\,t}, \tag{594}$$

and

$$a(\omega) = \frac{L_d\, |V_g(k_{\mathrm{H}})|}{L_u\, V_g(k_{\mathrm{P}})}. \tag{595}$$

The explicit computation of integral (594) gives

$$d(\omega) = \begin{cases} \sqrt{a(\omega)}, & \text{if } a(\omega) \leq 1 \\ \dfrac{1}{\sqrt{a(\omega)}}, & \text{if } a(\omega) \geq 1. \end{cases} \tag{596}$$

One can recast expression (593) in the form

$$I(\omega) = \mathcal{S}_0\, d(\omega)\, S_{ud2}(\omega)\, S^*_{d2d2}(\omega) = \mathcal{S}_0\, d(\omega)\, \langle \hat{c}_U(\omega)\, \hat{c}_{D2}(\omega) \rangle, \tag{597}$$

where $\mathcal{S}_0 = \sqrt{|V_{u|\mathrm{out}}|\; V_{d2|\mathrm{out}}}\, (\mathcal{U}_{k_{\mathrm{H}}} + \mathcal{V}_{k_{\mathrm{H}}})\, (\mathcal{U}_{k_{\mathrm{P}}} + \mathcal{V}_{k_{\mathrm{P}}})$.

Note that $u_{k_{\mathrm{H}},k_{\mathrm{P}}} = \sqrt{|V_{\alpha|\mathrm{out}}|}\, \mathcal{U}_{k_{\mathrm{H}},k_{\mathrm{P}}}$ and $v_{k_{\mathrm{H}},k_{\mathrm{P}}} = \sqrt{|V_{\alpha|\mathrm{out}}|}\, \mathcal{V}_{k_{\mathrm{H}},k_{\mathrm{P}}}$ ($\alpha = u$ if $k = k_{\mathrm{H}}$, $\alpha = d2$ if $k = k_{\mathrm{P}}$), where the u_k's and the v_k's are the standard Bogoliubov amplitudes of excitations of momentum k (see, e.g., Refs. [148, 153]).

The final expression (597) is exactly the same as equation (178) of Chapter 3.

D

HODOGRAPH TRANSFORM

The goal of this appendix is to prove expressions (397) of Chapter 6. We start from the partial differential equations

$$\partial_t \lambda^{\pm} + v_{\pm}(\lambda^+, \lambda^-)\, \partial_x \lambda^{\pm} = 0, \tag{598}$$

and we consider x and t as functions of the Riemann invariants λ^+ and λ^-:

$$x = x(\lambda^+, \lambda^-), \quad t = t(\lambda^+, \lambda^-). \tag{599}$$

Let us now introduce an unknown function $\Phi(x,t) = \Phi[x(\lambda^+, \lambda^-), t(\lambda^+, \lambda^-)]$. By differentiating with respect to λ^+ and λ^-, we obtain the system:

$$\begin{cases} \Phi_x\, x_{\lambda^+} + \Phi_t\, t_{\lambda^+} = \Phi_{\lambda^+}, \\ \Phi_x\, x_{\lambda^-} + \Phi_t\, t_{\lambda^-} = \Phi_{\lambda^-}, \end{cases} \tag{600}$$

where we used the shortcut notations $\Phi_x = \partial\Phi/\partial x$, $x_{\lambda^+} = \partial x/\partial\lambda^+$, ...

The solutions of the set of equations (600) are given by

$$\begin{cases} \Phi_x = D^{-1}\,(\Phi_{\lambda^+}\, t_{\lambda^-} - \Phi_{\lambda^-}\, t_{\lambda^+}), \\ \Phi_t = D^{-1}\,(\Phi_{\lambda^-}\, x_{\lambda^+} - \Phi_{\lambda^+}\, x_{\lambda^-}), \end{cases} \tag{601}$$

with $D = x_{\lambda^+}\, t_{\lambda^-} - x_{\lambda^-}\, t_{\lambda^+}$. Then, taking $\Phi = \lambda^+$ or $\Phi = \lambda^-$ leads to

$$\begin{aligned} \lambda^+_x &= D^{-1}\, t_{\lambda^-}, \quad \lambda^+_t = -D^{-1}\, x_{\lambda^-}, \\ \lambda^-_x &= -D^{-1}\, t_{\lambda^+}, \quad \lambda^-_t = D^{-1}\, x_{\lambda^+}, \end{aligned} \tag{602}$$

Inserting the previous expressions in equations (598) yields immediately the set of linear equations (397).

E

SOLUTIONS OF THE EULER-POISSON EQUATION

We consider the Euler-Poisson equation

$$\frac{\partial^2 W}{\partial\lambda_3\partial\lambda_4} - \frac{1}{2(\lambda_3-\lambda_4)}\left(\frac{\partial W}{\partial\lambda_3} - \frac{\partial W}{\partial\lambda_4}\right) = 0. \tag{603}$$

A general solution of equation (603) has been found by Eisenhart in 1918 [53] in the form

$$W(\lambda_3,\lambda_4) = \int_{c_0}^{\lambda_3} \frac{\psi(\mu)\,d\mu}{\sqrt{\lambda_3-\mu}\sqrt{\lambda_4-\mu}} + \int_{c_0}^{\lambda_4} \frac{\varphi(\mu)\,d\mu}{\sqrt{|\lambda_3-\mu|}\sqrt{\lambda_4-\mu}}, \tag{604}$$

where c_0 is a constant and plays the role of the sound velocity in our case.

In this appendix, we detail the calculations to obtain the explicit expressions of ψ and φ in both regions A and B [see Section 7.2.2, from equation (526) to equation (530)].

REGION A We seek for a solution of (603) in the form

$$W^{\mathrm{A}}(\lambda_3,\lambda_4) = \int_{c_0}^{\lambda_3} \frac{\psi^{\mathrm{A}}(\mu)\,\mathrm{d}\mu}{\sqrt{\lambda_3-\mu}\sqrt{\lambda_4-\mu}} + \int_{c_0}^{\lambda_4} \frac{\varphi^{\mathrm{A}}(\mu)\,\mathrm{d}\mu}{\sqrt{|\lambda_3-\mu|}\sqrt{\lambda_4-\mu}}. \tag{605}$$

we know two boundary conditions for W^{A}, given by (524a) and (525):

$$W^{\mathrm{A}}(c_0,\lambda_{\mathrm{S}}) = \frac{1}{2\sqrt{\lambda_{\mathrm{S}}-c_0}} \int_{c_0}^{\lambda_{\mathrm{S}}} \frac{w_+^{(3)}(r,-c_0)}{\sqrt{r-c_0}}\,\mathrm{d}r, \tag{606a}$$

$$W^{\mathrm{A}}(\lambda_3=\lambda_{\mathrm{H}},\lambda_4=\lambda_{\mathrm{H}}) \text{ does not diverge.} \tag{606b}$$

Taking the limit $\lambda_3 \to c_0$ in equation (605) and using expression (606a), yields

$$\int_{c_0}^{\lambda_4} \frac{\varphi^{\mathrm{A}}(\mu)\,\mathrm{d}\mu}{\sqrt{\mu-c_0}\sqrt{\lambda_4-\mu}} = \frac{1}{2\sqrt{\lambda_{\mathrm{S}}-c_0}} \int_{c_0}^{\lambda_{\mathrm{S}}} \frac{w_+^{(3)}(r,-c_0)}{\sqrt{r-c_0}}\,\mathrm{d}r. \tag{607}$$

The inverse Abel transformation amounts to perform the following transformation: given two functions ϕ and w such that

$$\int^{\lambda} \frac{\phi(\mu)}{\sqrt{\lambda-\mu}}\,\mathrm{d}\mu = w(r), \tag{608}$$

one obtains after transformation [1, 14]

$$\phi(\mu) = \frac{1}{\pi}\frac{\mathrm{d}}{\mathrm{d}\mu}\int^{\mu} \frac{w(r)}{\sqrt{\mu-r}}\,\mathrm{d}r. \tag{609}$$

Therefore, using this transformation in the case of expression (607) leads to

$$\frac{\varphi^{\mathrm{A}}(\mu)}{\sqrt{\mu-c_0}}=\frac{1}{2\pi}\frac{\mathrm{d}}{\mathrm{d}\mu}\int_{c_0}^{\mu}\frac{\mathrm{d}r}{\sqrt{\mu-r}\sqrt{r-c_0}}\int_{c_0}^{r}\frac{w_+^{(3)}(x,-c_0)}{\sqrt{x-c_0}}\,\mathrm{d}x. \tag{610}$$

Inverting both integrals gives

$$\frac{\varphi^{\mathrm{A}}(\mu)}{\sqrt{\mu-c_0}}=\frac{1}{2\pi}\frac{\mathrm{d}}{\mathrm{d}\mu}\int_{c_0}^{\mu}\mathrm{d}x\,\frac{w_+^{(3)}(x,-c_0)}{\sqrt{x-c_0}}\int_{x}^{\mu}\frac{\mathrm{d}r}{\sqrt{\mu-r}\sqrt{r-c_0}}. \tag{611}$$

Then, we compute the second integral over r:

$$\int_{x}^{\mu}\frac{\mathrm{d}r}{\sqrt{\mu-r}\sqrt{r-c_0}}=2\arctan\left(\sqrt{\frac{x-\mu}{c_0-x}}\right), \tag{612}$$

and thus,

$$\frac{\varphi^{\mathrm{A}}(\mu)\,d\mu}{\sqrt{\mu-c_0}}=\frac{1}{\pi}\frac{\mathrm{d}}{\mathrm{d}\mu}\int_{c_0}^{\mu}\mathrm{d}x\,\frac{w_+^{(3)}(x,-c_0)}{\sqrt{x-c_0}}\arctan\left(\sqrt{\frac{\mu-x}{x-c_0}}\right). \tag{613}$$

The last step consists of taking the derivative with respect to μ to obtain exactly equation (526):

$$\varphi^{\mathrm{A}}(\mu)=\frac{1}{2\pi\sqrt{\mu-c_0}}\int_{c_0}^{\mu}\frac{w_+^{(3)}(r,-c_0)\,dr}{\sqrt{\mu-r}}\,. \tag{614}$$

Then, we use the second boundary condition (606b) when $\lambda_3\to\lambda_4\equiv\lambda_{\mathrm{H}}$. We introduce a small parameter ε such that

$$\lambda_3=\lambda_{\mathrm{H}}-\varepsilon,\quad \lambda_4=\lambda_{\mathrm{H}}. \tag{615}$$

In this case, equation (605) can be written as

$$\begin{aligned}W^{\mathrm{A}}(\lambda_{\mathrm{H}}-\varepsilon,\lambda_{\mathrm{H}})=\int_{c_0}^{\lambda_{\mathrm{H}}-\varepsilon}\mathrm{d}\mu\frac{\psi^{\mathrm{A}}(\mu)+\varphi^{\mathrm{A}}(\mu)}{\sqrt{\lambda_{\mathrm{H}}-\varepsilon-\mu}\sqrt{\lambda_{\mathrm{H}}-\mu}}\\ +\int_0^{\varepsilon}\frac{\varphi^{\mathrm{A}}(\lambda_{\mathrm{H}}+\mu-\varepsilon)\,\mathrm{d}\mu}{\sqrt{\mu(\varepsilon-\mu)}}.\end{aligned} \tag{616}$$

When $\varepsilon\to 0$, the second integral of equation (616) converges to $\pi\varphi^{\mathrm{A}}(\lambda_{\mathrm{H}})$. However, if $\psi^{\mathrm{A}}+\varphi^{\mathrm{A}}\neq 0$, the first integral clearly diverges. Consequently, W^{A} converges when $\lambda_3\to\lambda_4=\lambda_{\mathrm{H}}$ if and only if

$$\psi^{\mathrm{A}}(\mu)=-\varphi^{\mathrm{A}}(\mu), \tag{617}$$

and, in this case,

$$W^{\mathrm{A}}(\lambda_{\mathrm{H}},\lambda_{\mathrm{H}})=\pi\varphi^{\mathrm{A}}(\lambda_{\mathrm{H}}). \tag{618}$$

This value exactly coincides with the first term of expression (537). The explicit expression of φ^{A} given by (614), as well as condition (617), lead to the solution of the Euler-Poisson equation (603) in region A [see equation (528)]

REGION B In this region, we seek for a solution of (603) in the form

$$W^{\mathrm{B}}(\lambda_3,\lambda_4) = W^{\mathrm{A}}(\lambda_3,\lambda_4) + \int_{\lambda_4}^{c_m} \frac{\varphi^{\mathrm{B}}(\mu)\,d\mu}{\sqrt{\mu-\lambda_3}\sqrt{\mu-\lambda_4}}. \tag{619}$$

This expression ensures the continuity between W^{A} and W^{B}, when $\lambda_4 \to c_m$ [see condition (519)]. The boundary condition in region B reads

$$\begin{aligned} W^{\mathrm{B}}(c_0,\lambda_{\mathrm{S}}) = &-\frac{1}{2\sqrt{\lambda_{\mathrm{S}}-c_0}}\int_{\lambda_{\mathrm{S}}}^{c_m}\frac{w_+^{(2)}(r,-c_0)}{\sqrt{r-c_0}}dr \\ &+\frac{1}{2\sqrt{\lambda_{\mathrm{S}}-c_0}}\int_{c_0}^{c_m}\frac{w_+^{(3)}(r,-c_0)}{\sqrt{r-c_0}}dr\,. \end{aligned} \tag{620}$$

Inserting expressions (606a) and (620) in equation (627) yields

$$\int_{\lambda_{\mathrm{S}}}^{c_m}\frac{\varphi^{\mathrm{B}}(\mu)\,\mathrm{d}\mu}{\sqrt{\mu-c_0}\sqrt{\mu-\lambda_{\mathrm{S}}}} = \int_{\lambda_{\mathrm{S}}}^{c_m}\frac{w_+^{\mathrm{diff}}(r)\,\mathrm{d}r}{\sqrt{r-c_0}}, \tag{621}$$

with $w_+^{\mathrm{diff}}(r) = w_+^{(3)}(r,-c_0) - w_+^{(2)}(r,-c_0)$. Similarly to region A, we can perform an inverse Abel transform to obtain in this case

$$\frac{\varphi^{\mathrm{B}}(\mu)}{\sqrt{\mu-c_0}} = -\frac{1}{\pi}\frac{\mathrm{d}}{\mathrm{d}\mu}\int_{\mu}^{c_m}\mathrm{d}x\,\frac{w_+^{\mathrm{diff}}(x)}{\sqrt{x-c_0}}\operatorname{arcsinh}\left(\sqrt{\frac{x-\mu}{\mu-c_0}}\right). \tag{622}$$

Taking the derivative with respect to μ leads immediately to the result (530):

$$\varphi^{\mathrm{B}}(\mu) = \frac{1}{2\pi\sqrt{\mu-c_0}}\int_{\mu}^{c_m}\frac{w_+^{(3)}(r,-c_0)-w_+^{(2)}(r,-c_0)}{\sqrt{r-\mu}}dr\,. \tag{623}$$

COMPLETE ELLIPTIC INTEGRALS The solutions of the Euler-Poisson equation W^{A} and W^{B} can be expressed in terms of a single integral by means of the complete elliptic integrals of the first kind[1]. Indeed,

$$\begin{aligned} W^{\mathrm{A}}(\lambda_3,\lambda_4) &= \frac{1}{2\pi}\int_{\lambda_3}^{\lambda_4}\mathrm{d}\mu\int_{c_0}^{\mu}\frac{w_+^{(3)}(r,-c_0)\,\mathrm{d}r}{\sqrt{\mu-\lambda_3}\sqrt{\lambda_4-\mu}\sqrt{\mu-c_0}\sqrt{\mu-r}} \\ &= \frac{1}{2\pi}\int_{c_0}^{\lambda_3}\mathrm{d}r\int_{\lambda_3}^{\lambda_4}\frac{w_+^{(3)}(r,-c_0)\,\mathrm{d}\mu}{\sqrt{\mu-\lambda_3}\sqrt{\lambda_4-\mu}\sqrt{\mu-c_0}\sqrt{\mu-r}} \\ &+ \frac{1}{2\pi}\int_{\lambda_3}^{\lambda_4}\mathrm{d}r\int_{r}^{\lambda_4}\frac{w_+^{(3)}(r,-c_0)\,\mathrm{d}\mu}{\sqrt{\mu-\lambda_3}\sqrt{\lambda_4-\mu}\sqrt{\mu-c_0}\sqrt{\mu-r}}, \end{aligned} \tag{624}$$

where we have inserted expression (614) in equation (528) and have inverted both integrals. Both integrals over μ on the right-hand side of equation (624) are complete elliptic integrals of the first kind [77]. Therefore,

$$\begin{aligned} W^{\mathrm{A}}(\lambda_3,\lambda_4) = &\frac{1}{\pi}\int_{c_0}^{\lambda_3} w_+^{(3)}(r,-c_0)\,f_{\mathrm{A}}(\lambda_3,r)\,\mathrm{d}r \\ &+\frac{1}{\pi}\int_{\lambda_3}^{\lambda_4} w_+^{(3)}(r,-c_0)\,f_{\mathrm{A}}(r,\lambda_3)\,\mathrm{d}r, \end{aligned} \tag{625}$$

1 The formulae below are easier to compute numerically.

with

$$\begin{cases} f_{\mathrm{A}}(x_1, x_2) = \dfrac{\mathrm{K}\left[m_{\mathrm{A}}(x_1, x_2)\right]}{\sqrt{x_1 - c_0}\sqrt{\lambda_4 - x_2}}, \\ m_{\mathrm{A}}(x_1, x_2) = \dfrac{(\lambda_4 - x_1)\,(x_2 - c_0)}{(\lambda_4 - x_2)\,(x_1 - c_0)}, \end{cases} \tag{626}$$

$\mathrm{K}(m_{\mathrm{A}})$ being a complete elliptic integral of the first kind. The same procedure gives in region B:

$$W^{\mathrm{B}}(\lambda_3, \lambda_4) = W^{\mathrm{A}}(\lambda_3, \lambda_4) + \frac{1}{\pi}\int_{\lambda_4}^{c_m} w_{+}^{\mathrm{diff}}(r)\, f_{\mathrm{B}}(r)\, \mathrm{d}r, \tag{627}$$

with

$$f_{\mathrm{B}}(r) = \frac{1}{\sqrt{r - \lambda_3}\sqrt{\lambda_4 - c_0}}\, \mathrm{K}\left[\frac{(\lambda_3 - c_0)\,(r - \lambda_4)}{(\lambda_4 - c_0)\,(r - \lambda_3)}\right]. \tag{628}$$

BIBLIOGRAPHY

[1] N.H. Abel. "Auflösung Einer Mechanischen Aufgabe." In: *Journal für die reine und angewandte Mathematik (Crelles Journal)* 1826 (1826), pp. 153–157. DOI: 10.1515/crll.1826.1.153.

[2] M. Abramowitz and I. A. Stegun. *Handbook of Methematical Functions*. New-York: Dover Publications, 1970.

[3] Gerardo Adesso and Fabrizio Illuminati. "Gaussian Measures of Entanglement versus Negativities: Ordering of Two-Mode Gaussian States." In: *Physical Review A* 72 (2005), p. 032334. DOI: 10.1103/PhysRevA.72.032334.

[4] Gerardo Adesso and Fabrizio Illuminati. "Continuous Variable Tangle, Monogamy Inequality, and Entanglement Sharing in Gaussian States of Continuous Variable Systems." In: *New Journal of Physics* 8 (2006), pp. 15–15. DOI: 10.1088/1367-2630/8/1/015.

[5] Gerardo Adesso, Alessio Serafini, and Fabrizio Illuminati. "Extremal Entanglement and Mixedness in Continuous Variable Systems." In: *Physical Review A* 70 (2004), p. 022318. DOI: 10.1103/PhysRevA.70.022318.

[6] Gerardo Adesso, Alessio Serafini, and Fabrizio Illuminati. "Quantification and Scaling of Multipartite Entanglement in Continuous Variable Systems." In: *Physical Review Letters* 93 (2004), p. 220504. DOI: 10.1103/PhysRevLett.93.220504.

[7] G. Agrawal. *Nonlinear Fiber Optics*. Elsevier, 2013. DOI: 10.1016/C2011-0-00045-5.

[8] S. A. Akhmanov, A. P. Sukhorukov, and R. V. Khokhlov. "Self-Focusing and Self-Trapping of Intense Light Beams in a Nonlinear Medium." In: *Sov. Phys. JETP* 23 (1966), p. 1025.

[9] S. A. Akhmanov, A. P. Sukhorukov, and R. V. Khokhlov. "Self-Focusing and Self-Trapping of Intense Light Beams in a Nonlinear Medium." In: *Zh. Eksp. Teor. Fiz* 50 (1966), p. 1537.

[10] S. A. Akhmanov, A. P. Sukhorukov, and R. V. Khokhlov. "Self-Focusing and Diffraction of Light in a Nonlinear Medium." In: *Usp. Fiz. Nauk* 93 (1967), p. 19.

[11] S. A. Akhmanov, A. P. Sukhorukov, and R. V. Khokhlov. "Self-Focusing and Diffraction of Light in a Nonlinear Medium." In: *Sov. Phys. Usp.* 10 (1968), p. 609.

[12] Ahmed Almheiri, Donald Marolf, Joseph Polchinski, and James Sully. "Black Holes: Complementarity or Firewalls?" In: *Journal of High Energy Physics* 2013 (2013), p. 62. DOI: 10.1007/JHEP02(2013)062.

[13] M. R. Andrews, D. M. Kurn, H.-J. Miesner, D. S. Durfee, C. G. Townsend, S. Inouye, and W. Ketterle. "Propagation of Sound in a Bose-Einstein Condensate." In: *Physical Review Letters* 79 (1997), pp. 553–556. DOI: 10.1103/PhysRevLett.79.553.

[14] G. Arfken and H. J. Weber. *Mathematical Methods for Physicists*. Orlando: Academic Press, 2005.

[15] Roberto Balbinot, Alessandro Fabbri, Serena Fagnocchi, Alessio Recati, and Iacopo Carusotto. "Nonlocal Density Correlations as a Signature of Hawking Radiation from Acoustic Black Holes." In: *Physical Review A* 78 (2008), p. 021603. DOI: 10.1103/PhysRevA.78.021603.

[16] R. Balian and E. Brezin. "Nonunitary Bogoliubov Transformations and Extension of Wick's Theorem." In: *Il Nuovo Cimento B Series 10* 64 (1969), pp. 37–55. DOI: 10.1007/BF02710281.

[17] Luca Barbiero, Christian Schweizer, Monika Aidelsburger, Eugene Demler, Nathan Goldman, and Fabian Grusdt. "Coupling Ultracold Matter to Dynamical Gauge Fields in Optical Lattices: From Flux Attachment to $\mathbb{Z}_2$ Lattice Gauge Theories." In: *Science Advances* 5 (2019). DOI: 10.1126/sciadv.aav7444.

[18] Carlos Barceló, S. Liberati, and Matt Visser. "Probing Semiclassical Analog Gravity in Bose-Einstein Condensates with Widely Tunable Interactions." In: *Physical Review A* 68 (2003), p. 053613. DOI: 10.1103/PhysRevA.68.053613.

[19] Carlos Barceló, Stefano Liberati, and Matt Visser. "Towards the Observation of Hawking Radiation in Bose–Einstein Condensates." In: *International Journal of Modern Physics A* 18 (2003), pp. 3735–3745. DOI: 10.1142/S0217751X0301615X.

[20] Carlos Barceló, Stefano Liberati, and Matt Visser. "Analogue Gravity." In: *Living Reviews in Relativity* 8 (2005), p. 12. DOI: 10.12942/lrr-2005-12.

[21] Carlos Barceló, Stefano Liberati, and Matt Visser. "Analogue Gravity." In: *Living Reviews in Relativity* 14 (2011), p. 3. DOI: 10.12942/lrr-2011-3.

[22] Christopher Barsi, Wenjie Wan, Can Sun, and Jason W. Fleischer. "Dispersive Shock Waves with Nonlocal Nonlinearity." In: *Optics Letters* 32 (2007), p. 2930. DOI: 10.1364/OL.32.002930.

[23] F. Belgiorno, S. L. Cacciatori, M. Clerici, V. Gorini, G. Ortenzi, L. Rizzi, E. Rubino, V. G. Sala, and D. Faccio. "Hawking Radiation from Ultrashort Laser Pulse Filaments." In: *Physical Review Letters* 105 (2010), p. 203901. DOI: 10.1103/PhysRevLett.105.203901.

[24] Nicolas Bilas and Nicolas Pavloff. "Dark Soliton Past a Finite-Size Obstacle." In: *Physical Review A* 72 (2005), p. 033618. DOI: 10.1103/PhysRevA.72.033618.

[25] N. D. Birrell and P. C. W. Davies. *Quantum Fields in Curved Space*. Cambridge University Press, 1982. DOI: 10.1017/CBO9780511622632.

[26] Jean-Paul Blaizot and Georges Ripka. *Quantum Theory of Finite Systems*. Cambridge, Mass: MIT Press, 1986.

[27] H. M. J. M. Boesten, C. C. Tsai, J. R. Gardner, D. J. Heinzen, and B. J. Verhaar. "Observation of a Shape Resonance in the Collision of Two Cold Rb 87 Atoms." In: *Physical Review A* 55 (1997), pp. 636–640. DOI: 10.1103/PhysRevA.55.636.

[28] N.N. Bogoliubov. "On the Theory of Superfluidity." In: *Journal of Physics (Union of Soviet Socialist Republics)* 11 (1947), pp. 23–32.

[29] T. Bonnemain. "Quadratic Mean Field Games with Negative Coordination." PhD thesis. Université Cergy-Pointoise, 2020.

[30] T. Bonnemain, T. Gobron, and D. Ullmo. "Universal Behavior in Non Stationary Mean Field Games." In: *arXiv:1907.05374 [cond-mat, physics:physics]* (2019). arXiv: 1907.05374 [cond-mat, physics:physics].

[31] R. Boyd. *Nonlinear Optics*. Academic Press, 2008.

[32] Xavier Busch and Renaud Parentani. "Dynamical Casimir Effect in Dissipative Media: When Is the Final State Nonseparable?" In: *Physical Review D* 88 (2013), p. 045023. DOI: 10.1103/PhysRevD.88.045023.

[33] Xavier Busch, Renaud Parentani, and Scott Robertson. "Quantum Entanglement Due to a Modulated Dynamical Casimir Effect." In: *Physical Review A* 89 (2014), p. 063606. DOI: 10.1103/PhysRevA.89.063606.

[34] Iacopo Carusotto. "Superfluid Light in Bulk Nonlinear Media." In: *Proceedings of the Royal Society A: Mathematical, Physical and Engineering Sciences* 470 (2014), p. 20140320. DOI: 10.1098/rspa.2014.0320.

[35] Iacopo Carusotto and Cristiano Ciuti. "Quantum Fluids of Light." In: *Reviews of Modern Physics* 85 (2013), pp. 299–366. DOI: 10.1103/RevModPhys.85.299.

[36] Iacopo Carusotto, Serena Fagnocchi, Alessio Recati, Roberto Balbinot, and Alessandro Fabbri. "Numerical Observation of Hawking Radiation from Acoustic Black Holes in Atomic Bose–Einstein Condensates." In: *New Journal of Physics* 10 (2008), p. 103001. DOI: 10.1088/1367-2630/10/10/103001.

[37] Yvan Castin. *Mécanique Quantique : Seconde Quantification et Résolvante; Master 2ème Année : Concepts Fondamentaux de La Physique*. 2011.

[38] Pisin Chen and Gerard Mourou. "Accelerating Plasma Mirrors to Investigate the Black Hole Information Loss Paradox." In: *Physical Review Letters* 118 (2017), p. 045001. DOI: 10.1103/PhysRevLett.118.045001.

[39] R. Y. Chiao. "Bogoliubov Dispersion Relation for a Photon Fluid: Is This a Superfluid?" In: *Optics Communications* 179 (2000), p. 157.

[40] Valerie Coffman, Joydip Kundu, and William K. Wootters. "Distributed Entanglement." In: *Physical Review A* 61 (2000), p. 052306. DOI: 10.1103/PhysRevA.61.052306.

[41] Steven Corley. "Particle Creation via High Frequency Dispersion." In: *Physical Review D* 55 (1997), pp. 6155–6161. DOI: 10.1103/PhysRevD.55.6155.

[42] Steven Corley and Ted Jacobson. "Hawking Spectrum and High Frequency Dispersion." In: *Physical Review D* 54 (1996), pp. 1568–1586. DOI: 10.1103/PhysRevD.54.1568.

[43] Gilles Couton, Hervé Maillotte, and Mathieu Chauvet. "Self-Formation of Multiple Spatial Photovoltaic Solitons." In: *Journal of Optics B: Quantum and Semiclassical Optics* 6 (2004), S223–S230. DOI: 10.1088/1464-4266/6/5/009.

[44] D. Daems, F. Bernard, N. J. Cerf, and M. I. Kolobov. "Tripartite Entanglement in Parametric Down-Conversion with Spatially Structured Pump." In: *Journal of the Optical Society of America B* 27 (2010), p. 447. DOI: 10.1364/JOSAB.27.000447.

[45] Franco Dalfovo, Stefano Giorgini, Lev P. Pitaevskii, and Sandro Stringari. "Theory of Bose-Einstein Condensation in Trapped Gases." In: *Reviews of Modern Physics* 71 (1999), pp. 463–512. DOI: 10.1103/RevModPhys.71.463.

[46] Jean Dalibard, Fabrice Gerbier, Gediminas Juzeliūnas, and Patrik Öhberg. "*Colloquium* : Artificial Gauge Potentials for Neutral Atoms." In: *Reviews of Modern Physics* 83 (2011), pp. 1523–1543. DOI: 10.1103/RevModPhys.83.1523.

[47] P C W Davies. "Scalar Production in Schwarzschild and Rindler Metrics." In: *Journal of Physics A: Mathematical and General* 8 (1975), pp. 609–616. DOI: 10.1088/0305-4470/8/4/022.

[48] P. C. W. Davies and S. A. Fulling. "Radiation from Moving Mirrors and from Black Holes." In: *Proceedings of the Royal Society of London. A. Mathematical and Physical Sciences* 356 (1977), pp. 237–257. DOI: 10.1098/rspa.1977.0130.

[49] Bryce S. DeWitt. "Quantum Field Theory in Curved Spacetime." In: *Physics Reports* 19 (1975), pp. 295–357. DOI: 10.1016/0370-1573(75)90051-4.

[50] Jonathan Drori, Yuval Rosenberg, David Bermudez, Yaron Silberberg, and Ulf Leonhardt. "Observation of Stimulated Hawking Radiation in an Optical Analogue." In: *Physical Review Letters* 122 (2019), p. 010404. DOI: 10.1103/PhysRevLett.122.010404.

[51] Peter D. Drummond and Mark Hillery. *The Quantum Theory of Nonlinear Optics*. Cambridge: Cambridge University Press, 2014. DOI: 10.1017/CBO9780511783616.

[52] Lu-Ming Duan, G. Giedke, J. I. Cirac, and P. Zoller. "Inseparability Criterion for Continuous Variable Systems." In: *Physical Review Letters* 84 (2000), pp. 2722–2725. DOI: 10.1103/PhysRevLett.84.2722.

[53] Luther Pfahler Eisenhart. "Triply Conjugate Systems with Equal Point Invariants." In: *The Annals of Mathematics* 20 (1919), p. 262. DOI: 10.2307/1967119.

[54] G. A. El. "Resolution of a Shock in Hyperbolic Systems Modified by Weak Dispersion." In: *Chaos: An Interdisciplinary Journal of Nonlinear Science* 15 (2005), p. 037103. DOI: 10.1063/1.1947120.

[55] G. A. El. "Erratum: "Resolution of a Shock in Hyperbolic Systems Modified by Weak Dispersion" [Chaos 15, 037103 (2005)]." In: *Chaos: An Interdisciplinary Journal of Nonlinear Science* 16 (2006), p. 029901. DOI: 10.1063/1.2186766.

[56] G.A. El' and V.V. Khodorovsky. "Evolution of a Solitonless Large-Scale Perturbation in Korteweg-de Vries Hydrodynamics." In: *Physics Letters A* 182 (1993), pp. 49–52. DOI: 10.1016/0375-9601(93)90051-Z.

[57] M. Elazar, V. Fleurov, and S. Bar-Ad. "All-Optical Event Horizon in an Optical Analog of a Laval Nozzle." In: *Physical Review A* 86 (2012), p. 063821. DOI: 10.1103/PhysRevA.86.063821.

[58] Christopher Eltschka and Jens Siewert. "Monogamy Equalities for Qubit Entanglement from Lorentz Invariance." In: *Physical Review Letters* 114 (2015), p. 140402. DOI: 10.1103/PhysRevLett.114.140402.

[59] L.-P. Euvé, F. Michel, R. Parentani, T. G. Philbin, and G. Rousseaux. "Observation of Noise Correlated by the Hawking Effect in a Water Tank." In: *Physical Review Letters* 117 (2016), p. 121301. DOI: 10.1103/PhysRevLett.117.121301.

[60] Léo-Paul Euvé, Scott Robertson, Nicolas James, Alessandro Fabbri, and Germain Rousseaux. "Scattering of Co-Current Surface Waves on an Analogue Black Hole." In: *arXiv:1806.05539 [gr-qc, physics:physics]* (2018). arXiv: 1806.05539 [gr-qc, physics:physics].

[61] Léo-Paul Euvé, Scott Robertson, Nicolas James, Alessandro Fabbri, and Germain Rousseaux. "Scattering of Co-Current Surface Waves on an Analogue Black Hole." In: *Physical Review Letters* 124 (2020), p. 141101. DOI: 10.1103/PhysRevLett.124.141101.

[62] Alessandro Fabbri and Nicolas Pavloff. "Momentum Correlations as Signature of Sonic Hawking Radiation in Bose-Einstein Condensates." In: *SciPost Physics* 4 (2018), p. 019. DOI: 10.21468/SciPostPhys.4.4.019.

[63] Daniele Faccio, Francesco Belgiorno, Sergio Cacciatori, Vittorio Gorini, Stefano Liberati, and Ugo Moschella, eds. *Analogue Gravity Phenomenology*. Vol. 870. Lecture Notes in Physics. Cham: Springer International Publishing, 2013. DOI: 10.1007/978-3-319-00266-8.

[64] J. Fatome, C. Finot, G. Millot, A. Armaroli, and S. Trillo. "Observation of Optical Undular Bores in Multiple Four-Wave Mixing." In: *Physical Review X* 4 (2014), p. 021022. DOI: 10.1103/PhysRevX.4.021022.

[65] Alexander L Fetter. "Nonuniform States of an Imperfect Bose Gas." In: *Annals of Physics* 70 (1972), pp. 67–101. DOI: 10.1016/0003-4916(72)90330-2.

[66] Q. Fontaine, T. Bienaimé, S. Pigeon, E. Giacobino, A. Bramati, and Q. Glorieux. "Observation of the Bogoliubov Dispersion in a Fluid of Light." In: *Physical Review Letters* 121 (2018), p. 183604. DOI: 10.1103/PhysRevLett.121.183604.

[67] M. Gregory Forest and Jong-Eao Lee. "Geometry and Modulation Theory for the Periodic Nonlinear Schrodinger Equation." In: *Oscillation Theory, Computation, and Methods of Compensated Compactness*. Ed. by George R. Sell, Hans Weinberger, Constantine Dafermos, J. L. Ericksen, David Kinderlehrer, and Marshall Slemrod. Vol. 2. New York, NY: Springer New York, 1986, pp. 35–69. DOI: 10.1007/978-1-4613-8689-6_3.

[68] Kieran A. Fraser and Francesco Piazza. "Topological Soliton-Polaritons in 1D Systems of Light and Fermionic Matter." In: *Communications Physics* 2 (2019), p. 48. DOI: 10.1038/s42005-019-0149-1.

[69] S. A. Fulling and P. C. W. Davies. "Radiation from a Moving Mirror in Two Dimensional Space-Time: Conformal Anomaly." In: *Proceedings of the Royal Society of London. A. Mathematical and Physical Sciences* 348 (1976), pp. 393–414. DOI: 10.1098/rspa.1976.0045.

[70] Stephen A. Fulling. "Nonuniqueness of Canonical Field Quantization in Riemannian Space-Time." In: *Physical Review D* 7 (1973), pp. 2850–2862. DOI: 10.1103/PhysRevD.7.2850.

[71] L. J. Garay, J. R. Anglin, J. I. Cirac, and P. Zoller. "Sonic Analog of Gravitational Black Holes in Bose-Einstein Condensates." In: *Physical Review Letters* 85 (2000), pp. 4643–4647. DOI: 10.1103/PhysRevLett.85.4643.

[72] C. Gardiner and P. Zoller. *Quantun Noise*. Berlin: Springer-Verlag, 1999.

[73] F Gerbier. "Quasi-1D Bose-Einstein Condensates in the Dimensional Crossover Regime." In: *Europhysics Letters (EPL)* 66 (2004), pp. 771–777. DOI: 10.1209/epl/i2004-10035-7.

[74] Christopher Gerry and Peter Knight. *Introductory Quantum Optics*. Cambridge University Press, 2004. DOI: 10.1017/CBO9780511791239.

[75] S. Gilbert. *Linear Algebra and Its Applications*. Stamford, CT: Cengage Learning, 2005.

[76] S. Giovanazzi, C. Farrell, T. Kiss, and U. Leonhardt. "Conditions for One-Dimensional Supersonic Flow of Quantum Gases." In: *Physical Review A* 70 (2004), p. 063602. DOI: 10.1103/PhysRevA.70.063602.

[77] I.S. Gradshteyn and I.M. Ryzhik. *Table of Integrals, Series, and Products*. Elsevier, 1980. DOI: 10.1016/C2013-0-10754-4.

[78] E. P. Gross. "Structure of a Quantized Vortex in Boson Systems." In: *Il Nuovo Cimento* 20 (1961), pp. 454–477. DOI: 10.1007/BF02731494.

[79] W. Guerin. "Source Atomique Cohérente Dans Des Pièges Optique et Magnétique: Réalisation d'un Laser à Atomes Guidé." PhD thesis. Université Paris-Sud - Paris XI, 2007.

[80] A. Gullstrand. *Allgemeine Lösung Des Statischen Einkörperproblems in Der Einsteinschen Gravitationstheorie*. Vol. 16. Arkiv För Matematik, Astronomi Och Fysik. Stockholm: Almqvist & Wiksell, 1922.

[81] A.V. Gurevich, A.L. Krylov, and G.A. El. "Breaking of a Riemann Wave in Dispersive Hydrodynamics." In: *Pis'ma Zh. Exp. Teor. Fiz.* 54 (1991), p. 104.

[82] A.V. Gurevich, A.L. Krylov, and G.A. El. "Evolution of a Riemann Wave in Dispersive Hydrodynamics." In: *Zh. Eksp. Teor. Fiz* 101 (1992), p. 1797.

[83] A.V. Gurevich, A.L. Krylov, and N.G. Mazur. "Quasi-Simple Waves in Korteweg-De Vries Hydrdynamics." In: *Zh. Eksp. Teor. Fiz* 95 (1989), p. 1674.

[84] A.V. Gurevich and L. Pitaevskii. "Nonstationary Structure of a Collisionless Shock Wave." In: *Zh. Eksp. Teor. Fiz* 65 (1973), p. 590.

[85] Sasha Haco, Stephen W. Hawking, Malcolm J. Perry, and Andrew Strominger. "Black Hole Entropy and Soft Hair." In: *Journal of High Energy Physics* 2018 (2018), p. 98. DOI: 10.1007/JHEP12(2018)098.

[86] D. S. Hall, M. R. Matthews, J. R. Ensher, C. E. Wieman, and E. A. Cornell. "Dynamics of Component Separation in a Binary Mixture of Bose-Einstein Condensates." In: *Physical Review Letters* 81 (1998), pp. 1539–1542. DOI: 10.1103/PhysRevLett.81.1539.

[87] S. W. Hawking. "Black Hole Explosions?" In: *Nature* 248 (1974), p. 30. DOI: 10.1038/248030a0.

[88] S. W. Hawking. "Particle Creation by Black Holes." In: *Communications In Mathematical Physics* 43 (1975), p. 199. DOI: 10.1007/BF02345020.

[89] S. W. Hawking. "Loss of Information in Black Holes." In: *The Geometric Universe*. Oxford University Press, 1998, p. 125.

[90] S. W. Hawking and G. F. R. Ellis. *The Large Scale Structure of Space-Time*. Cambridge University Press, 1973. DOI: 10.1017/CBO9780511524646.

[91] M. A. Hoefer, M. J. Ablowitz, I. Coddington, E. A. Cornell, P. Engels, and V. Schweikhard. "Dispersive and Classical Shock Waves in Bose-Einstein Condensates and Gas Dynamics." In: *Physical Review A* 74 (2006), p. 023623. DOI: 10.1103/PhysRevA.74.023623.

[92] P. C. Hohenberg. "Existence of Long-Range Order in One and Two Dimensions." In: *Physical Review* 158 (1967), pp. 383–386. DOI: 10.1103/PhysRev.158.383.

[93] M. Isoard, A. M. Kamchatnov, and N. Pavloff. "Long-Time Evolution of Pulses in the Korteweg–de Vries Equation in the Absence of Solitons Reexamined: Whitham Method." In: *Physical Review E* 99 (2019), p. 012210. DOI: 10.1103/PhysRevE.99.012210.

[94] S. K. Ivanov and A. M. Kamchatnov. "Collision of Rarefaction Waves in Bose-Einstein Condensates." In: *Physical Review A* 99 (2019), p. 013609. DOI: 10.1103/PhysRevA.99.013609.

[95] A. D. Jackson, G. M. Kavoulakis, and C. J. Pethick. "Solitary Waves in Clouds of Bose-Einstein Condensed Atoms." In: *Physical Review A* 58 (1998), pp. 2417–2422. DOI: 10.1103/PhysRevA.58.2417.

[96] Ted Jacobson. *Introductory Lectures on Black Hole Thermodynamics*. 1996.

[97] Maxime J. Jacquet. *Negative Frequency at the Horizon*. Springer Theses. Cham: Springer International Publishing, 2018. DOI: 10.1007/978-3-319-91071-0.

[98] Maxime J. Jacquet and Friedrich Koenig. "The Influence of Spacetime Curvature on Quantum Emission in Optical Analogues to Gravity." In: *arXiv:2001.05807 [cond-mat, physics:gr-qc, physics:quant-ph]* (2020). arXiv: 2001.05807 [cond-mat, physics:gr-qc, physics:quant-ph].

[99] A. M. Kamchatnov. "Propagation of Ultrashort Periodic Pulses in Nonlinear Fiber Light Guides." In: *Zh. Eksp. Teor. Fiz* 97 (1990), p. 144.

[100] A. M. Kamchatnov. *Nonlinear Periodic Waves and Their Modulations: An Introductory Course*. World Scientific, 2000.

[101] A. Kamchatnov and V. Shchesnovich. "Dynamics of Bose-Einstein Condensates in Cigar-Shaped Traps." In: *Physical Review A* 70 (2004), p. 023604. DOI: 10.1103/PhysRevA.70.023604.

[102] Victor I. Kolobov, Katrine Golubkov, Juan Ramón Muñoz de Nova, and Jeff Steinhauer. "Spontaneous Hawking Radiation and beyond: Observing the Time Evolution of an Analogue Black Hole." In: *arXiv:1910.09363 [gr-qc]* (2019). arXiv: 1910.09363 [gr-qc].

[103] V.R. Kudashev. "Conservation of Number of Waves and Inheritance of Simmetries under Whitham Averaging." In: *Pis'ma Zh. Exp. Teor. Fiz.* 54 (1991), p. 179.

[104] Yasunari Kurita and Takao Morinari. "Formation of a Sonic Horizon in Isotropically Expanding Bose-Einstein Condensates." In: *Physical Review A* 76 (2007), p. 053603. DOI: 10.1103/PhysRevA.76.053603.

[105] Oren Lahav, Amir Itah, Alex Blumkin, Carmit Gordon, Shahar Rinott, Alona Zayats, and Jeff Steinhauer. "Realization of a Sonic Black Hole Analog in a Bose-Einstein Condensate." In: *Physical Review Letters* 105 (2010), p. 240401. DOI: 10.1103/PhysRevLett.105.240401.

[106] L. D. Landau and E. M. Lifshitz. *Mécanique Quantique — Théorie Non-Relativiste*. Vol. 3. Union soviétique, 1967.

[107] L. D. Landau and E. M. Lifshitz. *Fluids Mechanics*. Oxford: Pergamon, 1987.

[108] L. D. Landau, E. M. Lifshitz, and L. P. Pitaevskii. *Electrodynamics of Continuous Media*. Vol. 8. Landau and Lifshitz Course of Theoretical Physics. Elsevier Butterworth-Heinemann, Oxford, 2006.

[109] P.-É. Larré. "Fluctuations Quantiques et Effets Non-Linéaires Dans Les Condensats de Bose-Einstein. Des Ondes de Choc Dispersives Au Rayonnement de Hawking Acoustique." PhD thesis. Université Paris-Sud, 2013.

[110] P.-É. Larré, A. Recati, I. Carusotto, and N. Pavloff. "Quantum Fluctuations around Black Hole Horizons in Bose-Einstein Condensates." In: *Physical Review A* 85 (2012), p. 013621. DOI: 10.1103/PhysRevA.85.013621.

[111] Pierre-Élie Larré and Iacopo Carusotto. "Optomechanical Signature of a Frictionless Flow of Superfluid Light." In: *Physical Review A* 91 (2015), p. 053809. DOI: 10.1103/PhysRevA.91.053809.

[112] P.D. Lax. "Development of Singularities of Solutions of Nonlinear Hyperbolic Partial Differential Equations." In: *J. Math. Phys.* 5 (1964), pp. 611–613.

[113] P. Leboeuf and N. Pavloff. "Bose-Einstein Beams: Coherent Propagation through a Guide." In: *Physical Review A* 64 (2001), p. 033602. DOI: 10.1103/PhysRevA.64.033602.

[114] P. Leboeuf, N. Pavloff, and S. Sinha. "Solitonic Transmission of Bose-Einstein Matter Waves." In: *Physical Review A* 68 (2003), p. 063608. DOI: 10.1103/PhysRevA.68.063608.

[115] U. Leonhardt, T. Kiss, and P. Öhberg. "Theory of Elementary Excitations in Unstable Bose-Einstein Condensates and the Instability of Sonic Horizons." In: *Physical Review A* 67 (2003), p. 033602. DOI: 10.1103/PhysRevA.67.033602.

[116] U Leonhardt, T Kiss, and P hberg. "Bogoliubov Theory of the Hawking Effect in Bose Einstein Condensates." In: *Journal of Optics B: Quantum and Semiclassical Optics* 5 (2003), S42–S49. DOI: 10.1088/1464-4266/5/2/357.

[117] U. Leonhardt and T. G. Philbin. *Geometry and Light: The Science of Invisibility*. New-York: Dover Publications, 2010.

[118] M. Lewenstein and L. You. "Quantum Phase Diffusion of a Bose-Einstein Condensate." In: *Physical Review Letters* 77 (1996), pp. 3489–3493. DOI: 10.1103/PhysRevLett.77.3489.

[119] Stefano Liberati, Giovanni Tricella, and Andrea Trombettoni. "The Information Loss Problem: An Analogue Gravity Perspective." In: *Entropy* 21 (2019), p. 940. DOI: 10.3390/e21100940.

[120] Geoffrey S. S. Ludford. "On an Extension of Riemann's Method of Integration, with Applications to One-Dimensional Gas Dynamics." In: *Mathematical Proceedings of the Cambridge Philosophical Society* 48 (1952), pp. 499–510. DOI: 10.1017/S0305004100027900.

[121] M. D. Lukin. "*Colloquium* : Trapping and Manipulating Photon States in Atomic Ensembles." In: *Reviews of Modern Physics* 75 (2003), pp. 457–472. DOI: 10.1103/RevModPhys.75.457.

[122] Dieter Lüst and Ward Vleeshouwers. *Black Hole Information and Thermodynamics*. SpringerBriefs in Physics. Cham: Springer International Publishing, 2019. DOI: 10.1007/978-3-030-10919-6.

[123] Xin Ma and William Rhodes. "Multimode Squeeze Operators and Squeezed States." In: *Physical Review A* 41 (1990), pp. 4625–4631. DOI: 10.1103/PhysRevA.41.4625.

[124] Jean Macher and Renaud Parentani. "Black-Hole Radiation in Bose-Einstein Condensates." In: *Physical Review A* 80 (2009), p. 043601. DOI: 10.1103/PhysRevA.80.043601.

[125] Juan Maldacena. "The Large-N Limit of Superconformal Field Theories and Supergravity." In: *International Journal of Theoretical Physics* 38 (1999), pp. 1113–1133. DOI: 10.1023/A:1026654312961.

[126] Samir D Mathur. "The Information Paradox: A Pedagogical Introduction." In: *Classical and Quantum Gravity* 26 (2009), p. 224001. DOI: 10.1088/0264-9381/26/22/224001.

[127] N. D. Mermin and H. Wagner. "Absence of Ferromagnetism or Antiferromagnetism in One- or Two-Dimensional Isotropic Heisenberg Models." In: *Physical Review Letters* 17 (1966), pp. 1133–1136. DOI: 10.1103/PhysRevLett.17.1133.

[128] Claire Michel, Omar Boughdad, Mathias Albert, Pierre-Élie Larré, and Matthieu Bellec. "Superfluid Motion and Drag-Force Cancellation in a Fluid of Light." In: *Nature Communications* 9 (2018), p. 2108. DOI: 10.1038/s41467-018-04534-9.

[129] C. W. Misner, K. S. Thorne, and J. A. Wheeler. *Gravitation*. W. H. Freeman, Princeton University Press, 1973.

[130] Christophe Mora and Yvan Castin. "Extension of Bogoliubov Theory to Quasicondensates." In: *Physical Review A* 67 (2003), p. 053615. DOI: 10.1103/PhysRevA.67.053615.

[131] Juan Ramón Muñoz de Nova, Katrine Golubkov, Victor I. Kolobov, and Jeff Steinhauer. "Observation of Thermal Hawking Radiation and Its Temperature in an Analogue Black Hole." In: *Nature* 569 (2019), pp. 688–691. DOI: 10.1038/s41586-019-1241-0.

[132] H. S. Nguyen, D. Gerace, I. Carusotto, D. Sanvitto, E. Galopin, A. Lemaître, I. Sagnes, J. Bloch, and A. Amo. "Acoustic Black Hole in a Stationary Hydrodynamic Flow of Microcavity Polaritons." In: *Physical Review Letters* 114 (2015), p. 036402. DOI: 10.1103/PhysRevLett.114.036402.

[133] E. Noether. "Invariante Variationsprobleme." In: *Nachr. König. Gesellsch. Wiss. Göttingen, Math.-Phys. Klasse* (1918), pp. 235–237.

[134] J R M de Nova, F Sols, and I Zapata. "Entanglement and Violation of Classical Inequalities in the Hawking Radiation of Flowing Atom Condensates." In: *New Journal of Physics* 17 (2015), p. 105003. DOI: 10.1088/1367-2630/17/10/105003.

[135] M. Olshanii. "Atomic Scattering in the Presence of an External Confinement and a Gas of Impenetrable Bosons." In: *Physical Review Letters* 81 (1998), pp. 938–941. DOI: 10.1103/PhysRevLett.81.938.

[136] Miguel Onorato, Stefania Resitori, and Fabio Baronio, eds. *Rogue and Shock Waves in Nonlinear Dispersive Media*. Vol. 926. Lecture Notes in Physics. Cham: Springer International Publishing, 2016. DOI: 10.1007/978-3-319-39214-1.

[137] J. R. Oppenheimer and G. M. Volkoff. "On Massive Neutron Cores." In: *Physical Review* 55 (1939), pp. 374–381. DOI: 10.1103/PhysRev.55.374.

[138] Tomoki Ozawa et al. "Topological Photonics." In: *Reviews of Modern Physics* 91 (2019), p. 015006. DOI: 10.1103/RevModPhys.91.015006.

[139] Don N. Page. "Particle Emission Rates from a Black Hole: Massless Particles from an Uncharged, Nonrotating Hole." In: *Physical Review D* 13 (1976), pp. 198–206. DOI: 10.1103/PhysRevD.13.198.

[140] P. Painlevé. "La Mécanique Classique et La Théorie de La Relativité." In: *Les Comptes Rendus de l'Académie des Sciences de Paris* 173 (1921), p. 677.

[141] Leonard Parker. "Probability Distribution of Particles Created by a Black Hole." In: *Physical Review D* 12 (1975), pp. 1519–1525. DOI: 10.1103/PhysRevD.12.1519.

[142] Leonard Parker. "The Production of Elementary Particles by Strong Gravitational Fields." In: *Asymptotic Structure of Space-Time*. Ed. by F. Paul Esposito and Louis Witten. Boston, MA: Springer US, 1977, pp. 107–226. DOI: 10.1007/978-1-4684-2343-3_2.

[143] M. V. Pavlov. "Nonlinear Schrodinger Equation and the Bogolyubov-Whitham Method of Averaging." In: *Theoretical and Mathematical Physics* 71 (1987), pp. 584–588. DOI: 10.1007/BF01017090.

[144] O. Penrose. "CXXXVI. On the Quantum Mechanics of Helium II." In: *The London, Edinburgh, and Dublin Philosophical Magazine and Journal of Science* 42 (1951), pp. 1373–1377. DOI: 10.1080/14786445108560954.

[145] Oliver Penrose and Lars Onsager. "Bose-Einstein Condensation and Liquid Helium." In: *Physical Review* 104 (1956), pp. 576–584. DOI: 10.1103/PhysRev.104.576.

[146] R. Penrose. "Gravitational Collapse: The Role of General Relativity." In: *Rivista del Nuovo Cimento, Numero Speziale* 1 (1969), p. 252.

[147] J. Perczel, J. Borregaard, D. E. Chang, S. F. Yelin, and M. D. Lukin. "Topological Quantum Optics Using Atomlike Emitter Arrays Coupled to Photonic Crystals." In: *Physical Review Letters* 124 (2020), p. 083603. DOI: 10.1103/PhysRevLett.124.083603.

[148] Christopher Pethick and Henrik Smith. *Bose-Einstein Condensation in Dilute Gases*. Cambridge ; New York: Cambridge University Press, 2008.

[149] T. G. Philbin, C. Kuklewicz, S. Robertson, S. Hill, F. Konig, and U. Leonhardt. "Fiber-Optical Analog of the Event Horizon." In: *Science* 319 (2008), p. 1367. DOI: 10.1126/science.1153625.

[150] Francesco Piazza and Philipp Strack. "Umklapp Superradiance with a Collisionless Quantum Degenerate Fermi Gas." In: *Physical Review Letters* 112 (2014), p. 143003. DOI: 10.1103/PhysRevLett.112.143003.

[151] Igor Pikovski, Michael R. Vanner, Markus Aspelmeyer, M. S. Kim, and Časlav Brukner. "Probing Planck-Scale Physics with Quantum Optics." In: *Nature Physics* 8 (2012), pp. 393–397. DOI: 10.1038/nphys2262.

[152] L. P. Pitaevskiĭ. "Vortex Lines in an Imperfect Bose Gas." In: *Soviet Physics — Journal of Experimental and Theoretical Physics* 13 (1961), p. 451.

[153] L. P. Pitaevskiĭ and S. Stringari. *Bose-Einstein Condensation and Superfluidity*. International Series of Monographs on Physics. Oxford, United Kingdom: Oxford University Press, 2016.

[154] V. N. Popov. "Functional Integrals in Quantum Field Theory and Statistical Physics." In: *D. Reidel Pub., Dordrecht* (1983).

[155] John Preskill. "Do Black Holes Destroy Information?" In: *arXiv:hep-th/9209058* (1992). arXiv: hep-th/9209058.

[156] A. Recati, N. Pavloff, and I. Carusotto. "Bogoliubov Theory of Acoustic Hawking Radiation in Bose-Einstein Condensates." In: *Physical Review A* 80 (2009), p. 043603. DOI: 10.1103/PhysRevA.80.043603.

[157] Peter Ring and Peter Schuck. *The Nuclear Many Body Problem.* Texts and Monographs in Physics. Berlin: Springer, 2004.

[158] Scott J Robertson. "The Theory of Hawking Radiation in Laboratory Analogues." In: *Journal of Physics B: Atomic, Molecular and Optical Physics* 45 (2012), p. 163001. DOI: 10.1088/0953-4075/45/16/163001.

[159] Germain Rousseaux, Christian Mathis, Philippe Maïssa, Thomas G Philbin, and Ulf Leonhardt. "Observation of Negative-Frequency Waves in a Water Tank: A Classical Analogue to the Hawking Effect?" In: *New Journal of Physics* 10 (2008), p. 053015. DOI: 10.1088/1367-2630/10/5/053015.

[160] Germain Rousseaux, Philippe Maïssa, Christian Mathis, Pierre Coullet, Thomas G Philbin, and Ulf Leonhardt. "Horizon Effects with Surface Waves on Moving Water." In: *New Journal of Physics* 12 (2010), p. 095018. DOI: 10.1088/1367-2630/12/9/095018.

[161] L. Salasnich, A. Parola, and L. Reatto. "Effective Wave Equations for the Dynamics of Cigar-Shaped and Disk-Shaped Bose Condensates." In: *Physical Review A* 65 (2002), p. 043614. DOI: 10.1103/PhysRevA.65.043614.

[162] Neven Šantić, Adrien Fusaro, Sabeur Salem, Josselin Garnier, Antonio Picozzi, and Robin Kaiser. "Nonequilibrium Precondensation of Classical Waves in Two Dimensions Propagating through Atomic Vapors." In: *Physical Review Letters* 120 (2018), p. 055301. DOI: 10.1103/PhysRevLett.120.055301.

[163] R. Schley, A. Berkovitz, S. Rinott, I. Shammass, A. Blumkin, and J. Steinhauer. "Planck Distribution of Phonons in a Bose-Einstein Condensate." In: *Physical Review Letters* 111 (2013), p. 055301. DOI: 10.1103/PhysRevLett.111.055301.

[164] Ralf Schützhold. "Detection Scheme for Acoustic Quantum Radiation in Bose-Einstein Condensates." In: *Physical Review Letters* 97 (2006), p. 190405. DOI: 10.1103/PhysRevLett.97.190405.

[165] K. Schwarzschild. "Uber Das Gravitationsfeld Eines Massenpunktes Nach Der Einsteinschen Theorie." In: *Sitz. der K. Preuss. Akad. der Wiss.* 7 (1916), pp. 189–196.

[166] Alessio Serafini. "Multimode Uncertainty Relations and Separability of Continuous Variable States." In: *Physical Review Letters* 96 (2006), p. 110402. DOI: 10.1103/PhysRevLett.96.110402.

[167] Alessio Serafini. "Detecting Entanglement by Symplectic Uncertainty Relations." In: *Journal of the Optical Society of America B* 24 (2007), p. 347. DOI: 10.1364/JOSAB.24.000347.

[168] Alessio Serafini, Gerardo Adesso, and Fabrizio Illuminati. "Unitarily Localizable Entanglement of Gaussian States." In: *Physical Review A* 71 (2005), p. 032349. DOI: 10.1103/PhysRevA.71.032349.

[169] Alessio Serafini, Fabrizio Illuminati, and Silvio De Siena. "Symplectic Invariants, Entropic Measures and Correlations of Gaussian States." In: *Journal of Physics B: Atomic, Molecular and Optical Physics* 37 (2004), pp. L21–L28. DOI: 10.1088/0953-4075/37/2/L02.

[170] I. Shammass, S. Rinott, A. Berkovitz, R. Schley, and J. Steinhauer. "Phonon Dispersion Relation of an Atomic Bose-Einstein Condensate." In: *Physical Review Letters* 109 (2012), p. 195301. DOI: 10.1103/PhysRevLett.109.195301.

[171] R. Simon. "Peres-Horodecki Separability Criterion for Continuous Variable Systems." In: *Physical Review Letters* 84 (2000), pp. 2726–2729. DOI: 10.1103/PhysRevLett.84.2726.

[172] R. Simon, N. Mukunda, and Biswadeb Dutta. "Quantum-Noise Matrix for Multimode Systems: U(n) Invariance, Squeezing, and Normal Forms." In: *Physical Review A* 49 (1994), pp. 1567–1583. DOI: 10.1103/PhysRevA.49.1567.

[173] A. Sommerfeld. *Partial Differential Equations in Physics*. New-York: Academic Press, 1964.

[174] J. Michael Steele. *The Cauchy-Schwarz Master Class: An Introduction to the Art of Mathematical Inequalities*. Cambridge University Press, 2004. DOI: 10.1017/CBO9780511817106.

[175] Jeff Steinhauer. "Observation of Self-Amplifying Hawking Radiation in an Analogue Black-Hole Laser." In: *Nature Physics* 10 (2014), pp. 864–869. DOI: 10.1038/nphys3104.

[176] Jeff Steinhauer. "Measuring the Entanglement of Analogue Hawking Radiation by the Density-Density Correlation Function." In: *Physical Review D* 92 (2015), p. 024043. DOI: 10.1103/PhysRevD.92.024043.

[177] Jeff Steinhauer. "Observation of Quantum Hawking Radiation and Its Entanglement in an Analogue Black Hole." In: *Nature Physics* 12 (2016), pp. 959–965. DOI: 10.1038/nphys3863.

[178] L. Susskind. *The Black Hole War: My Battle with Stephen Hawking to Make the World Safe for Quantum Mechanics*. United States: Little, Brown and Company, 2008.

[179] V. I. Talanov. "Self Focusing of Wave Beams in Nonlinear Media." In: *ZhETF Pisma Redaktsiiu 2* 9 (1965), p. 218.

[180] S P Tsarëv. "The Geometry of Hamiltonian Systems and Hydrodynamic Type. The Generalized Hodograph Method." In: *Mathematics of the USSR-Izvestiya* 37 (1991), pp. 397–419. DOI: 10.1070/IM1991v037n02ABEH002069.

[181] W. G. Unruh. "Notes on Black-Hole Evaporation." In: *Physical Review D* 14 (1976), pp. 870–892. DOI: 10.1103/PhysRevD.14.870.

[182] W. G. Unruh. "Experimental Black-Hole Evaporation?" In: *Physical Review Letters* 46 (1981), p. 1351. DOI: 10.1103/PhysRevLett.46.1351.

[183] W. G. Unruh. "Sonic Analogue of Black Holes and the Effects of High Frequencies on Black Hole Evaporation." In: *Physical Review D* 51 (1995), pp. 2827–2838. DOI: 10.1103/PhysRevD.51.2827.

[184] W. G. Unruh and R. Schützhold. "Hawking Radiation from "Phase Horizons" in Laser Filaments?" In: *Physical Review D* 86 (2012), p. 064006. DOI: 10.1103/PhysRevD.86.064006.

[185] William G Unruh and Robert M Wald. "Information Loss." In: *Reports on Progress in Physics* 80 (2017), p. 092002. DOI: 10.1088/1361-6633/aa778e.

[186] G. Vidal and R. F. Werner. "Computable Measure of Entanglement." In: *Physical Review A* 65 (2002), p. 032314. DOI: 10.1103/PhysRevA.65.032314.

[187] David Vocke, Thomas Roger, Francesco Marino, Ewan M. Wright, Iacopo Carusotto, Matteo Clerici, and Daniele Faccio. "Experimental Characterization of Nonlocal Photon Fluids." In: *Optica* 2 (2015), p. 484. DOI: 10.1364/OPTICA.2.000484.

[188] David Vocke, Kali Wilson, Francesco Marino, Iacopo Carusotto, Ewan M. Wright, Thomas Roger, Brian P. Anderson, Patrik Öhberg, and Daniele Faccio. "Role of Geometry in the Superfluid Flow of Nonlocal Photon Fluids." In: *Physical Review A* 94 (2016), p. 013849. DOI: 10.1103/PhysRevA.94.013849.

[189] David Vocke, Calum Maitland, Angus Prain, Kali E. Wilson, Fabio Biancalana, Ewan M. Wright, Francesco Marino, and Daniele Faccio. "Rotating Black Hole Geometries in a Two-Dimensional Photon Superfluid." In: *Optica* 5 (2018), p. 1099. DOI: 10.1364/OPTICA.5.001099.

[190] Robert M. Wald. "On Particle Creation by Black Holes." In: *Communications in Mathematical Physics* 45 (1975), pp. 9–34. DOI: 10.1007/BF01609863.

[191] Wenjie Wan, Shu Jia, and Jason W. Fleischer. "Dispersive Superfluid-like Shock Waves in Nonlinear Optics." In: *Nature Physics* 3 (2007), pp. 46–51. DOI: 10.1038/nphys486.

[192] Silke Weinfurtner, Edmund W. Tedford, Matthew C. J. Penrice, and William G. Unruh. "Measurement of Stimulated Hawking Emission in an Analogue System." In: *Physical Review Letters* 106 (2011), p. 021302. DOI: 10.1103/PhysRevLett.106.021302.

[193] R. F. Werner and M. M. Wolf. "Bound Entangled Gaussian States." In: *Physical Review Letters* 86 (2001), pp. 3658–3661. DOI: 10.1103/PhysRevLett.86.3658.

[194] G. B. Whitham. "A General Approach to Linear and Non-Linear Dispersive Waves Using a Lagrangian." In: *Journal of Fluid Mechanics* 22 (1965), pp. 273–283. DOI: 10.1017/S0022112065000745.

[195] G. B. Whitham. "Non-Linear Dispersive Waves." In: *Proceedings of the Royal Society of London. Series A. Mathematical and Physical Sciences* 283 (1965), pp. 238–261. DOI: 10.1098/rspa.1965.0019.

[196] G. B. Whitham. "Two-Timing, Variational Principles and Waves." In: *Journal of Fluid Mechanics* 44 (1970), p. 373. DOI: 10.1017/S002211207000188X.

[197] G. B. Whitham. *Linear and Nonlinear Waves*. New-York: Wiley-Interscience, 1974.

[198] K. Wintersperger, M. Bukov, J. Näger, S. Lellouch, E. Demler, U. Schneider, I. Bloch, N. Goldman, and M. Aidelsburger. "Parametric Instabilities of Interacting Bosons in Periodically Driven 1D Optical Lattices." In: *Physical Review X* 10 (2020), p. 011030. DOI: 10.1103/PhysRevX.10.011030.

[199] S. Wüster and C. M. Savage. "Limits to the Analog Hawking Temperature in a Bose-Einstein Condensate." In: *Physical Review A* 76 (2007), p. 013608. DOI: 10.1103/PhysRevA.76.013608.

[200] G. Xu, A. Mussot, A. Kudlinski, S. Trillo, F. Copie, and M. Conforti. "Shock Wave Generation Triggered by a Weak Background in Optical Fibers." In: *Optics Letters* 41 (2016), p. 2656. DOI: 10.1364/OL.41.002656.

[201] Gang Xu, Matteo Conforti, Alexandre Kudlinski, Arnaud Mussot, and Stefano Trillo. "Dispersive Dam-Break Flow of a Photon Fluid." In: *Physical Review Letters* 118 (2017), p. 254101. DOI: 10.1103/PhysRevLett.118.254101.

[202] I Zapata, M Albert, R Parentani, and F Sols. "Resonant Hawking Radiation in Bose–Einstein Condensates." In: *New Journal of Physics* 13 (2011), p. 063048. DOI: 10.1088/1367-2630/13/6/063048.

[203] B. Zwiebach. *A First Course in String Theory*. New-York: Cambridge University Press, 2004.

[204] Karol Życzkowski, Paweł Horodecki, Anna Sanpera, and Maciej Lewenstein. "Volume of the Set of Separable States." In: *Physical Review A* 58 (1998), pp. 883–892. DOI: 10.1103/PhysRevA.58.883.

COLOPHON

This document was typeset using the typographical look-and-feel `classicthesis` developed by André Miede. The style was inspired by Robert Bringhurst's seminal book on typography "*The Elements of Typographic Style*". `classicthesis` is available for both LaTeX and LyX:

https://bitbucket.org/amiede/classicthesis/

Happy users of `classicthesis` usually send a real postcard to the author, a collection of postcards received so far is featured here:

http://postcards.miede.de/

université PARIS-SACLAY | ÉCOLE DOCTORALE Physique en l'Île-de-France (PIF)

Titre: Étude Théorique des Corrélations Quantiques et des Fluctuations Non-linéaires dans les Gaz Quantiques

Mots clés: Gravité analogue, Rayonnement de Hawking, Condensats de Bose-Einstein, Fluides non-linéaires, Ondes de chocs dispersives

Résumé: Cette thèse est dédiée à l'étude des phénomènes nonlinéaires dans deux fluides quantiques qui partagent de nombreuses similitudes : les condensats de Bose-Einstein et les "fluides de lumière".

Dans une première partie, nous étudions les analogues soniques des trous noirs. Il est possible de créer une configuration stationnaire d'un condensat de Bose-Einstein en écoulement d'une région subsonique vers une région supersonique. Ce fluide transsonique joue alors le rôle d'un trou noir puisque les ondes sonores ne peuvent s'échapper de la région supersonique. En outre, en quantifiant le champ sonore, il est possible de montrer qu'un rayonnement de Hawking analogue émerge des fluctuations quantiques du vide. Dans cette thèse, nous montrons que la prise en compte des "modes zéros" – omis jusqu'alors dans le contexte de la gravité analogue – est essentielle pour obtenir une description précise du processus de Hawking, menant alors à un excellent accord avec les résultats expérimentaux. Enfin, nous étudions l'intrication entre les différentes excitations quantiques et montrons que notre système crée de l'intrication tripartite.

Dans une second temps, nous étudions la propagation des fluides nonlinéaires grâce à une approche hydrodynamique et à des méthodes mathématiques développées par Riemann et Whitham. Nous étudions la structure oscillante et la dynamique des ondes de chocs dispersives qui se forment à la suite d'un déferlement. Notre approche permet de trouver des expressions analytiques simples qui décrivent les propriétés asymptotiques du choc. Cela donne accès à des paramètres d'intérêt expérimental, comme le temps de déferlement, la vitesse de l'onde de choc ou encore le contraste de ses franges.

Title: Theoretical Study of Quantum Correlations and Nonlinear Fluctuations in Quantum Gases

Keywords: Analogue Gravity, Hawking radiation, Bose-Einstein condensates, Nonlinear fluids ,Dispersive shock waves

Abstract: This thesis is dedicated to the study of nonlinear-driven phenomena in two quantum gases which bear important similarities: Bose-Einstein condensates of ultracold atomic vapors and "fluids of light".

In a first part, we study sonic analogues of black holes. In a Bose-Einstein condensate, it is possible to implement a stationary configuration with a current flowing from a subsonic region to a supersonic one. This mimics a black hole, since sonic excitations cannot escape the supersonic region. Besides, quantizing the phonon field leads to a sonic analogue of Hawking radiation. In this thesis, we show that a correct account of "zero modes" – overlooked so far in the context of analogue gravity – is essential for an accurate description of the Hawking process, and results in a excellent comparison with recent experimental data. In addition, we characterize the entanglement shared among quantum excitations and show that they exhibit tripartite entanglement.

In a second part, we investigate the short and long time propagation of nonlinear fluids within a hydrodynamic framework and by means of mathematical methods developed by Riemann and Whitham. In particular, we study the oscillating structure and the dynamics of dispersive shock waves which arise after a wave breaking event. We obtain a weak shock theory, from which we can extract a quantitative description of experimentally relevant parameters, such as the wave breaking time, the velocity of the solitonic edge of the shock or the contrast of its fringes.

Université Paris-Saclay
Espace Technologique / Immeuble Discovery
Route de l'Orme aux Merisiers RD 128 / 91190 Saint-Aubin, France